

REPORT DOCUMENTATION PAGE			2	Form Approved OMB NO. 0704-0188	
<p>The public reporting burden for this collection of information is estimated to average 1 hour per response, including the time for reviewing instructions, searching existing data sources, gathering and maintaining the data needed, and completing and reviewing the collection of information. Send comments regarding this burden estimate or any other aspect of this collection of information, including suggestions for reducing this burden, to Washington Headquarters Services, Directorate for Information Operations and Reports, 1215 Jefferson Davis Highway, Suite 1204, Arlington VA, 22202-4302. Respondents should be aware that notwithstanding any other provision of law, no person shall be subject to any penalty for failing to comply with a collection of information if it does not display a currently valid OMB control number.</p> <p>PLEASE DO NOT RETURN YOUR FORM TO THE ABOVE ADDRESS.</p>					
1. REPORT DATE (DD-MM-YYYY) 13-08-2014		2. REPORT TYPE Final Report		3. DATES COVERED (From - To) 1-May-2008 - 30-Apr-2014	
4. TITLE AND SUBTITLE Final Report: Spray and Combustion of Gelled Hypergolic Propellants for Future Rocket and Missile Engines			5a. CONTRACT NUMBER W911NF-08-1-0124		
			5b. GRANT NUMBER		
			5c. PROGRAM ELEMENT NUMBER 611103		
6. AUTHORS S. T. Thynell, J. H. Adair, W. A. Goddard, III, R. K. Hanson, C.K. Law, J. Lee, H. A. Rabitz, G. A. Risha, F. A. Williams, V. Yang, R. A. Yetter			5d. PROJECT NUMBER		
			5e. TASK NUMBER		
			5f. WORK UNIT NUMBER		
7. PERFORMING ORGANIZATION NAMES AND ADDRESSES Pennsylvania State University 110 Technology Center  University Park, PA 16802 -7000			8. PERFORMING ORGANIZATION REPORT NUMBER		
9. SPONSORING/MONITORING AGENCY NAME(S) AND ADDRESS (ES) U.S. Army Research Office P.O. Box 12211 Research Triangle Park, NC 27709-2211			10. SPONSOR/MONITOR'S ACRONYM(S) ARO		
			11. SPONSOR/MONITOR'S REPORT NUMBER(S) 54232-EG-MUR.76		
12. DISTRIBUTION AVAILABILITY STATEMENT Approved for Public Release; Distribution Unlimited					
13. SUPPLEMENTARY NOTES The views, opinions and/or findings contained in this report are those of the author(s) and should not be construed as an official Department of the Army position, policy or decision, unless so designated by other documentation.					
14. ABSTRACT This final report contains a summary of findings associated with research related to the development of gelled and nongelled hypergolic propellant spray and combustion technologies for future rocket and missile propulsion systems. The research has utilized recent breakthroughs in modeling and diagnostic techniques to substantially improve the state of knowledge. New diagnostic and numerical techniques were developed to resolve the entire range of length and time scales (from atomistic to device levels). Emphasis was placed on both microscale and mesoscale processes that dictate the propellant interfacial dynamics and chemical initiation mechanisms, as well as					
15. SUBJECT TERMS Hypergolic propellants, ignition, combustion, droplet dynamics, impinging jets, jet atomization, chemical kinetics, condensed-phase reactions, gas-phase reactions, gelling agents, property measurements, monomethyl hydrazine, red fuming nitric acid					
16. SECURITY CLASSIFICATION OF:			17. LIMITATION OF ABSTRACT UU	15. NUMBER OF PAGES	19a. NAME OF RESPONSIBLE PERSON Stefan Thynell
a. REPORT UU	b. ABSTRACT UU	c. THIS PAGE UU			19b. TELEPHONE NUMBER 814-863-0977

## **Report Title**

### **Final Report: Spray and Combustion of Gelled Hypergolic Propellants for Future Rocket and Missile Engines**

#### **ABSTRACT**

This final report contains a summary of findings associated with research related to the development of gelled and nongelled hypergolic propellant spray and combustion technologies for future rocket and missile propulsion systems. The research has utilized recent breakthroughs in modeling and diagnostic techniques to substantially improve the state of knowledge. New diagnostic and numerical techniques were developed to resolve the entire range of length and time scales (from atomistic to device levels). Emphasis was placed on both microscale and macroscale processes that dictate the propellant interfacial dynamics and chemical initiation mechanisms, as well as the propellant atomization, mixing, and flame development. In this research program, the team of researchers made significant progress in several areas, including, a) property measurements of gelled and nongelled fuels, b) examination of dynamics of droplet collisions, c) jet atomization, spray formation, and mixing of nonreacting gelled and nongelled liquid streams, d) simulation of interfacial reactions at atomistic & molecular scales, e) laser spectroscopy of reactions at interfaces, f) confined interaction and droplet studies of various gelled and nongelled hydrazine fuels and nitric acid, g) flow visualization studies of impinging liquid streams in a microreactor, h) modeling and experiments of MMH/NO<sub>2</sub> reaction mechanism and reduction, i) modeling and simulation of nonreacting liquid stream impingement and spray formation, and j) design of subscale combustor testing and diagnostics.



**Enter List of papers submitted or published that acknowledge ARO support from the start of the project to the date of this printing. List the papers, including journal references, in the following categories:**

**(a) Papers published in peer-reviewed journals (N/A for none)**

<u>Received</u>	<u>Paper</u>
03/30/2011 17.00	J. Roslund, M. Roth, L. Guyon, V. Boutou, F. Courvoisier, J. Wolf, H. Rabitz. Resolution of strongly competitive product channels with optimal dynamic discrimination: Application to flavins, Journal of Chemical Physics, (01 2011): . doi:
04/12/2011 19.00	C. Tang, P. Zhang, C. Law. Bouncing, Coalescence and Separation in Head-on Collision of Unequal-size Droplets, , (03 2011): . doi:
04/12/2011 22.00	S. Wang, S. Thynell. EXPERIMENTAL STUDY ON HYPERGOLIC INTERACTION BETWEEN MONOMETHYLHYDRAZINE AND NITRIC ACID, , (04 2011): . doi:
04/12/2011 21.00	P. Zhang, H. Sun, C. Law. Secondary Channels in the Thermal Decomposition of Monomethylhydrazine (CH <sub>3</sub> NHNH <sub>2</sub> ), , (03 2011): . doi:
04/12/2011 20.00	H. Sun, P. Zhang, C. Law. Thermal Decomposition of Monomethylhydrazine: Reaction Mechanism and Kinetic Modeling, , (03 2011): . doi:
04/12/2011 18.00	W. Liu, J. Kock, D. Zhu, C. Law. Nonpremixed ignition of C7-C16 normal alkanes in stagnating liquid pool, , (03 2011): . doi:
06/22/2011 24.00	R. Cook, S. Pyun, D. Davidson, R. Hanson. MMH Pyrolysis and Oxidation: Species Time-History Measurements behind Reflected Shock Waves, , (07 2011): . doi:
06/22/2011 26.00	S. Fakhri, J. Lee, R. Yetter. EFFECT OF NOZZLE GEOMETRY ON THE ATOMIZATION AND SPRAY CHARACTERISTICS OF GELLED-PROPELLANT SIMULANTS FORMED BY TWO IMPINGING JETS, Atomization and Sprays, (01 2011): . doi:
06/22/2011 25.00	W. Liu, S. Dasgupta, S. Zybin, W. Goddard III. First Principles Study of the Ignition Mechanism for Hypergolic Bipropellants: N,N,N',N'-Tetramethylethylenediamine (TMEDA) and N,N,N',N'-Tetramethylmethylenediamine (TMMDA) with Nitric Acid, Journal of Physical Chemistry A, (01 2011): . doi:
07/23/2014 70.00	N. Kumbhakarna, S.T. Thynell. Development of a reaction mechanism for liquid-phase decomposition of guanidinium 5-amino tetrazolate, Thermochemica Acta, (04 2014): 25. doi: 10.1016/j.tca.2014.02.014
07/23/2014 72.00	David F. Davidson, Ronald K. Hanson, Sijie Li. Shock tube study of ethylamine pyrolysis and oxidation, Combustion and Flame, (04 2014): 0. doi: 10.1016/j.combustflame.2014.04.002

- 07/23/2014 71.00 Xiaodong Chen, Vigor Yang. Thickness-based adaptive mesh refinement methods for multi-phase flow simulations with thin regions,  
Journal of Computational Physics, (07 2014): 22. doi: 10.1016/j.jcp.2014.02.035
- 08/13/2014 77.00 Sijie Li, David F. Davidson, Ronald K. Hanson. Shock tube study of the pressure dependence of monomethylhydrazine pyrolysis,  
Combustion and Flame, (08 2014): 16. doi:
- 08/13/2014 78.00 Sijie Li, Enoch Dames, David F. Davidson, Ronald K. Hanson. High-Temperature Measurements of the Reactions of OH with Ethylamine and Dimethylamine,  
The Journal of Physical Chemistry A, (01 2014): 0. doi: 10.1021/jp411141w
- 09/09/2013 63.00 Roberto Rey-de-Castro, Zaki Leghtas, Herschel Rabitz. Manipulating Quantum Pathways on the Fly,  
Physical Review Letters, (05 2013): 0. doi: 10.1103/PhysRevLett.110.223601
- 09/09/2013 55.00 Wei-Guang Liu, Shiqing Wang, Siddharth Dasgupta, Stefan T. Thynell, William A. Goddard, Sergey Zybin, Richard A. Yetter. Experimental and quantum mechanics investigations of early reactions of monomethylhydrazine with mixtures of NO<sub>2</sub> and N<sub>2</sub>O<sub>4</sub>,  
Combustion and Flame, (05 2013): 970. doi: 10.1016/j.combustflame.2013.01.012
- 09/09/2013 66.00 Ulrich Niemann, Kalyanasundaram Seshadri, Forman A. Williams. Effect of addition of a non-equidiffusional reactant to an equidiffusional diffusion flame,  
Combustion Theory and Modelling, (06 2013): 0. doi: 10.1080/13647830.2013.791724
- 09/09/2013 67.00 Sijie Li, David F. Davidson, Ronald K. Hanson, Nicole J. Labbe, Phillip R. Westmoreland, Patrick Oßwald, Katharina Kohse-Höinghaus. Shock tube measurements and model development for morpholine pyrolysis and oxidation at high pressures,  
Combustion and Flame, (09 2013): 0. doi: 10.1016/j.combustflame.2013.03.027
- 09/10/2012 34.00 Wei-Guang Liu, William A. Goddard. First-Principles Study of the Role of Interconversion Between NO<sub>2</sub>, N<sub>2</sub>O<sub>4</sub>, cis-ONONO<sub>2</sub> and trans-ONONO<sub>2</sub> in Chemical Processes,  
Journal of the American Chemical Society, (08 2012): 12970. doi: 10.1021/ja300545e
- 09/10/2012 39.00 Hongyan Sun, Peng Zhang, Chung K. Law. Ab Initio Kinetics for Thermal Decomposition of CH<sub>3</sub>N•NH<sub>2</sub>, cis-CH<sub>3</sub>NHN•H, Trans-CH<sub>3</sub>NHN•H, and C•H<sub>2</sub>NNH<sub>2</sub> Radicals,  
The Journal of Physical Chemistry A, (07 2012): 8419. doi: 10.1021/jp3045675
- 09/10/2012 37.00 Chenglong Tang, Peng Zhang, Chung K. Law. Bouncing, coalescence, and separation in head-on collision of unequal-size droplets,  
Physics of Fluids, (02 2012): 0. doi: 10.1063/1.3679165
- 09/10/2012 38.00 Hongyan Sun, Peng Zhang, Chung K. Law. Gas-Phase Kinetics Study of Reaction of OH Radical with CH,  
The Journal of Physical Chemistry A, (05 2012): 5045. doi: 10.1021/jp3021529
- 09/10/2012 36.00 Chung K. Law. Fuel Options for Next-Generation Chemical Propulsion,  
AIAA Journal, (01 2012): 19. doi: 10.2514/1.J051328
- 09/10/2012 35.00 Robert D. Cook, Sung Hyun Pyun, Jungwan Cho, David F. Davidson, Ronald K. Hanson. Shock tube measurements of species time-histories in monomethyl hydrazine pyrolysis,  
Combustion and Flame, (04 2011): 790. doi: 10.1016/j.combustflame.2011.01.001
- 09/19/2011 27.00 S.T. Thynell, S.Q. Wang. An experimental study on the hypergolic interaction between monomethylhydrazine and nitric acid,  
Combustion and Flame, (9 2011): 0. doi: 10.1016/j.combustflame.2011.07.009
- 09/19/2011 28.00 Sung Hyun Pyun, Jungwan Cho, David F Davidson, Ronald K Hanson. Interference-free mid-IR laser absorption detection of methane,  
measurement science and technology, (02 2011): 0. doi: 10.1088/0957-0233/22/2/025303

- 10/01/2010 10.00 L. Zhang, A. van Duin, S. Zybin, W. Goddard III. Thermal Decomposition of Hydrazines from Reactive Dynamics Using the ReaxFF Reactive Force Field  
, Journal of Physical Chemistry B, (01 2009): . doi:
- 10/01/2010 11.00 A. Chowdhury, C. Bapat, S. Thynell. Apparatus for probing preignition behavior of hypergolic materials, Review of Scientific Instruments, (04 2009): . doi:
- 10/01/2010 12.00 F. Williams. Simplified Theory for Ignition Times of Hypergolic Gelled Propellants, Journal of Propulsion and Power, (12 2009): . doi:
- 10/01/2010 7.00 H. Sun, L. Catoire, C. Law. Thermal Decomposition of Monomethylhydrazine: Shock Tube Experiments and Kinetic Modeling, International Journal of Chemical Kinetics, (05 2008): . doi:
- 10/01/2010 8.00 W. Liu, S. Zybin, S. Dasgupta, T. Klapotke, W. Goddard III. Explanation of the Colossal Detonation Sensitivity of Silicon Pentaerythritol Tetranitrate (Si-PETN) Explosive, Journal American Chemical Society, (05 2009): . doi:
- 10/01/2010 9.00 K. Chenoweth, A. van Duin, W. Goddard III. The ReaxFF Monte Carlo Reactive Dynamics Method for Predicting Atomistic Structures of Disordered Ceramics: Application to the Mo3VOx Catalyst, Angew Chem Int Ed Engl, (01 2009): . doi:
- 10/01/2010 3.00 V. Beltrani, P. Ghosh, H. Rabitz. Exploring the capabilities of quantum optimal dynamic discrimination, Journal of Chemical Physics, (04 2009): . doi:
- 10/01/2010 4.00 M. Roth, L. Guyon, J. Roslund, V. Boutou, F. Courvoisier, J. Wolf, H. Rabitz. Quantum Control of Tightly Competitive Product Channels, Physical Review Letters, (06 2009): . doi:
- 10/01/2010 5.00 L. Zhang, S. Zybin, A. van Duin, S. Dasgupta, W. Goddard III, E. Kober. Carbon Cluster Formation during Thermal Decomposition of Octahydro-1,3,5,7-tetranitro-1,3,5,7-tetrazocine and 1,3,5-Triamino-2,4,6-trinitrobenzene High Explosives from ReaxFF Reactive Molecular Dynamics Simulations, Journal of Physical Chemistry A, (10 2009): . doi:
- 10/01/2010 6.00 S. Zybin, W. Goddard III, P. Xu, A. van Duin, A. Thompson. Physical mechanism of anisotropic sensitivity in pentaerythritol tetranitrate from compressive-shear reaction dynamics simulations, Applied Physics Letters, (02 2010): . doi:
- 11/18/2010 14.00 P. Zhang, S. Klippenstein, H. Sun, C. Law. Ab initio kinetics for the decomposition of monomethylhydrazine (CH<sub>3</sub>NHNH<sub>2</sub>), The Combustion Institute, (01 2010): . doi:
- 11/29/2010 16.00 H. Sun, C. Law. Kinetics of Hydrogen Abstraction Reactions of Butene Isomers by OH Radical, Journal of Physical Chemistry A, (10 2010): . doi:

**TOTAL: 38**

---

**(b) Papers published in non-peer-reviewed journals (N/A for none)**

<u>Received</u>	<u>Paper</u>
02/27/2012 29.00	C. Tang, P. Zhang, C. Law. Bouncing, coalescence, and separation in head-on collision of unequal size droplets, Physics of Fluids, (2 2012): . doi:
02/27/2012 30.00	P. Zhang, C. Law. An analysis of head-on droplet collision with large deformation in gaseous medium, Physics of Fluids, (04 2011): . doi:
02/27/2012 31.00	X. Hong, H. Sun, C. Law. Rate coefficients of the reactions of isopentane with H and CH3 radicals: Quantum mechanical approach, Computational and Theoretical Chemistry, (10 2010): . doi:
02/27/2012 32.00	P. Zhang, S. Klippenstein, H. Sun, C. Law. Ab initio kinetics for the decomposition of monomethylhydrazine (CH <sub>3</sub> NHNH <sub>2</sub> ), Proceedings of the Combustion Institute, (08 2010): . doi:
02/27/2012 33.00	S. Wang, S. Thynell. An experimental study on the hypergolic interaction between monomethylhydrazine and nitric acid, Combustion and Flame, (07 2011): . doi:
<b>TOTAL:</b>	<b>5</b>

---

Number of Papers published in non peer-reviewed journals:

---

**(c) Presentations**

---

**Non Peer-Reviewed Conference Proceeding publications (other than abstracts):**

<u>Received</u>	<u>Paper</u>
09/09/2013 59.00	D. E. Bittner, J. L. Sell, G. A. Risha. Effect of Jet Momentum Ratio and Equivalence Ratio on the Ignition Process of TMEDA and White Fuming Nitric Acid (WFNA), 49th AIAA/ASME/SAE/ASEE Joint Propulsion Conference. 14-JUL-13, . : ,
09/09/2013 65.00	R. K. Gehmlich, K. Seshadri. THE INFLUENCE OF NITROUS OXIDE ADDITION ON THE AUTOIGNITION OF ETHANE/AIR FLAMES, JANNAF, 45th Combustion Joint Subcommittee Meeting, Monterey, California. 03-DEC-12, . : ,
09/13/2012 50.00	Hongyan Sun, Peng Zhang, Chung K. Law. A DETAILED CHEMICAL KINETIC MECHANISM FOR THE OXIDATION OF MONOMETHYLHYDRAZINE, The 7th International Conference on Chemical Kinetics. 10-JUL-11, . : ,
<b>TOTAL:</b>	<b>3</b>

**Peer-Reviewed Conference Proceeding publications (other than abstracts):**

Received

Paper

- 09/09/2013 62.00 X. Chen, V. Yang. Numerical Simulation of Primary Atomization of Non-Newtonian Impinging Jets, ILASS Americas, 25th Annual Conference on Liquid Atomization and Spray Systems. 01-MAY-13, . : ,
- 09/09/2013 61.00 P. Khare, V. Yang. Drag Coefficients of Deforming and Fragmenting Liquid Droplets, ILASS Americas, 25th Annual Conference on Liquid Atomization and Spray Systems. 01-MAY-13, . : ,
- 09/09/2013 60.00 D. Ma, X. Chen, V. Yang, P. Khare. Breakup of Liquid Droplets, ICLASS 2012, 12th Triennial International Conference on Liquid Atomization and Spray Systems. 02-SEP-12, . : ,
- 09/09/2013 58.00 S. Wang, S. T. Thynell. Decomposition and Combustion of Monomethylhydrazinium Nitrates, 8th U. S. National Combustion Meeting, Salt Lake City, Utah. 21-MAY-13, . : ,
- 09/09/2013 57.00 S. Q. Wang, S. T. Thynell. Experimental Investigation of Pressure Effect on Ignition Delay of Monomethylhydrazine, 1,1-Dimethylhydrazine, Tetramethylethylenediamine and 2-Dimethylaminoethylazide with Nitric Acid, 8th U. S. National Combustion Meeting Organized by the Western States Section of the Combustion Institute and hosted by the University of Utah. 23-MAY-13, . : ,
- 09/09/2013 64.00 K. Seshadri, X.-S. Bai, F. A. Williams. Rate-Ratio Asymptotic Analysis of the Influence of Addition of Hydrogen on the Structure and Mechanisms of Extinction of Nonpremixed Methane Flame, 8th US National Combustion Meeting, Salt Lake City, Utah. 19-MAY-13, . : ,
- 09/13/2012 44.00 P. Khare, D. Ma, X. Chen and V. Yang. Breakup and Dynamics of Liquid Droplets, ILASS Americas, 24th Annual Conference on Liquid Atomization and Spray Systems. 01-MAY-12, . : ,
- 09/13/2012 53.00 Peng Zhang, Chung K. Law. Density Functional Theory Study of the Ignition Mechanism of 2-Azido-N, N-Dimethylethanamine (DMAZ), Fall Technical Meeting of the Eastern States Section of the Combustion Institute, Hosted by the University of Connecticut, Storrs, CT. 09-OCT-11, . : ,
- 09/13/2012 52.00 Hongyan Sun, Chung K. Law. Ab initio Multireference Study of the Reactions of  $\text{CH}_3\text{N} \cdot \text{NH}_2 + \text{OH}$ , Fall Technical Meeting of the Eastern States Section of the Combustion Institute, Hosted by the University of Connecticut, Storrs, CT. 09-OCT-11, . : ,
- 09/13/2012 51.00 Hongyan Sun, Peng Zhang, Chung K. Law. A Theoretical Study of H-Abstraction Reactions of Monomethylhydrazine by OH Radical, Fall Technical Meeting of the Eastern States Section of the Combustion Institute Hosted by the University of Connecticut, Storrs, CT. 09-OCT-11, . : ,
- 09/13/2012 43.00 Xiaodong Chen and Vigor Yang. A Multi-Scale Study of Droplet Collision Dynamics: From Gas Film Lubrication to Liquid Phase Mixing, ILASS Americas, 24th Annual Conference on Liquid Atomization and Spray Systems. 01-MAY-12, . : ,
- 09/13/2012 49.00 Prashant Khare, Dongjun Ma, Xiaodong Chen, Vigor Yang. Phenomenology of Secondary Breakup of Newtonian Liquid Droplets, 50th AIAA Aerospace Sciences Meeting including the New Horizons Forum and Aerospace Exposition. 09-JAN-12, . : ,

09/13/2012 48.00 Xiaodong Chen, Dongjun Ma, Vigor Yang. Mechanism Study of Impact Wave in Impinging JetsAtomization, 50th AIAA Aerospace Sciences Meeting including the New Horizons Forum and Aerospace Exposition. 09-JAN-12, . : ,

09/13/2012 47.00 Xiaodong Chen, Dongjun Ma, Vigor Yang. High-Fidelity Numerical Simulations of Impinging Jet Atomization, 48th AIAA/ASME/SAE/ASEE Joint Propulsion Conference & Exhibit. 30-JUL-12, . : ,

09/13/2012 46.00 Xiaodong Chen, Dongjun Ma and Vigor Yang. Dynamics and Stability of Impinging Jets, ILASS Americas, 24th Annual Conference on Liquid Atomization and Spray Systems. 01-MAY-12, . : ,

09/13/2012 45.00 Xiaodong Chen, Dongjun Ma, and Vigor Yang. Collision Outcome and Mass Transfer of Unequal-sized Droplet Collision, 50th AIAA Aerospace Sciences Meeting including the New Horizons Forum and Aerospace Exposition. 09-JAN-12, . : ,

09/14/2013 69.00 Hongyan Sun, Chung K. Law, Karol Kowalski, Kiran Bhaskaran-Nair. Kinetics Study of Reaction  $\text{CH}_3\text{N}^\bullet + \text{NH}_2 + \text{OH}$  by Multireference Second-Order Perturbation Theory and Multireference Coupled-Cluster Theory, 8th U. S. National Combustion Meeting, Salt Lake City, Utah. . : ,

**TOTAL: 17**

**(d) Manuscripts**

<u>Received</u>	<u>Paper</u>
07/23/2014 74.00	Sijie Li, David F. Davidson, Ronald K. Hanson. Shock tube study of dimethylamine oxidation, International Symposium on Combustion (11 2013)
07/23/2014 75.00	Peng Zhang, Lidong Zhang, Chung K. Law. Density Functional Theory Study of the Reactions of 2-Azido-N, N-Dimethylethanamine with Nitric Acid and Nitrogen Dioxide, Combustion and Flame (07 2014)
07/23/2014 73.00	David F. Davidson, Ronald K. Hanson, Sijie Li, Enoch Dames. High-Temperature Measurements of the Reactions of OH with Ethylamine and Dimethylamine, Journal of Physical Chemistry A (Submitted) (11 2013)
09/09/2013 68.00	Sijie Li, David F. Davidson, Ronald K. Hanson. Shock tube study of the pressure dependence of monomethylhydrazine pyrolysis, Combustion and Flame (06 2013)
09/12/2012 41.00	Robert D. Cook, David F. Davidson, and Ronald K. Hanson. Shock Tube Measurements of Species Time-Histories in Monomethyl Hydrazine Oxidation, Combustion and Flame (07 2012)
09/12/2012 42.00	Roberto Rey-de-Castro, Zaki Leghtas, and Herschel Rabitz. Measuring and Manipulating Quantum Control Pathway Amplitudes on the Fly, New Journal of Physics (07 2012)
09/14/2012 54.00	Tei Newman-Lehman, Roberto Grana, Kalyanasundaram Seshadri, Forman Williams. The structure and extinction of nonpremixed methane/nitrous oxide and ethane/nitrous oxide flames, Proceedings of the Combustion Institute (01 2012)
11/29/2010 15.00	H. Sun, C. Law. Rate coefficients of the reactions of isopentane with H and CH <sub>3</sub> radicals: Quantum mechanical TST and VTST approaches, (11 2010)
12/04/2009 1.00	C. Norscia, K. Seshadri, F. Williams. The Structure and Extinction of Methane/Nitrogen Dioxide Flames, (12 2009)
<b>TOTAL:</b>	<b>9</b>



Books

Received

Book

09/12/2012

40.00

S. Wang and S.T. Thynell. Book Chapter: Decomposition and Combustion of Ionic Liquid Compound Synthesized from N,N,N',N'-Tetramethylethylenediamine and Nitric Acid, Washington, D.C.: American Chemical Society, (07 2012)

TOTAL:

1

Received

Book Chapter

09/09/2013

56.00

S. Wang, S. T. Thynell. Decomposition and Combustion of Ionic Liquid Compound Synthesized from N,N,N?,N?-Tetramethylethylenediamine and Nitric Acid, ACS Symposium Series, Ionic Liquids: Science and Applications: American Chemical Society, (12 2012)

TOTAL:

1

Patents Submitted

None

---

Patents Awarded

None

---

## Awards

Professor V. Yang received the AIAA Propellants and Combustion Award 2009

---

Professor R. K. Hanson presented the H. Hottel Memorial Lecture at the 33rd International Symposium on Combustion, Tsinghua University, Beijing China, August 2, 2010.

Prof. R. K. Hanson received Humboldt Senior Research Award from the Alexander von Humboldt Foundation in 2010.

Prof. R. K. Hanson received the R. I. Soloukhin Award, 2011

Professor R.A. Yetter received PSEAS Outstanding Research Award 2010

Professor R.A. Yetter received the AIAA Propellants and Combustion Award 2011

Professor R.A. Yetter received the PSEAS Premier Research Award 2014

Professor F. A. Williams, elected Fellow of the American Academy of Arts and Sciences, 2010.

Professor R. K. Hanson received the 2013 SAE Arch T. Colwell Merit Award, co-winner

Professor W. A. Goddard received the 7th World Congress on Oxidation Catalysis award for outstanding achievement in oxidation catalysis (June 2013)

Professor V. Yang received Lifetime Achievement Award from JANNAF 2014

Professor V. Yang received ASME's Worcester Reed Warner Medal 2014

---

## Graduate Students

<u>NAME</u>	<u>PERCENT SUPPORTED</u>	<u>Discipline</u>
T. Morgan	0.05	
A. Tabakovic	0.05	
G. Hayes	0.05	
Olisa Pinto	0.05	
M. Li	0.05	
D. Liu	0.05	
C. Tang	0.05	
P. Zhang	0.05	
S. A. K. Fakhri	0.05	
S. Etheridge	0.05	
C. Ramasubramanian	0.05	
N. Notaro	0.05	
P. Saksena	0.50	
W.G. Liu	0.40	
M.J. Cheng	0.20	
S. Wang	0.50	
R.D. Cook	0.30	
S. Li	0.20	
S.H. Pyun	0.20	
X. Hong	0.10	
V. Amin	0.10	
R. Gehmlich	0.20	
U. Niemann	0.20	
P. Khare	0.50	
<b>FTE Equivalent:</b>	<b>4.00</b>	
<b>Total Number:</b>	<b>24</b>	

### Names of Post<sup>14</sup> Doctorates

<u>NAME</u>	<u>PERCENT SUPPORTED</u>
D. Ma	0.15
X.Chen	0.15
Y. Wang	0.15
A. Saha	0.10
P. Zhang	0.10
H. Sun	0.40
J. Song	0.20
A. Goun	0.50
Y. Liu	0.06
S. Zybin	0.06
A. Jaramillo-Botero	0.04
S. Dasgupta	0.01
<b>FTE Equivalent:</b>	<b>1.92</b>
<b>Total Number:</b>	<b>12</b>

### Names of Faculty Supported

<u>NAME</u>	<u>PERCENT SUPPORTED</u>	National Academy Member
J. Adair	0.05	
C.K. Law	0.01	Yes
J.G. Lee	0.08	
H. Rabitz	0.01	
R. Yetter	0.08	
W.A. Goddard	0.01	Yes
S.T. Thynell	0.08	
R.K. Hanson	0.01	Yes
F.A. Williams	0.01	Yes
V. Yang	0.01	
G. Risha	0.08	
<b>FTE Equivalent:</b>	<b>0.43</b>	
<b>Total Number:</b>	<b>11</b>	

### Names of Under Graduate students supported

<u>NAME</u>	<u>PERCENT SUPPORTED</u>	Discipline
C. Cain	0.05	Aerospace Engineering
A. Stubblebine	0.05	Aerospace Engineering
Y. Zhou	0.05	Mechanical Engineering
J. Harmon	0.05	Mechanical Engineering
R. Glass	0.05	Mechanical Engineering
V. Yeager	0.05	Mechanical Engineering
N. Becker	0.05	Mechanical Engineering
D. Bittner	0.15	Mechanical Engineering
J. Sell	0.15	Mechanical Engineering
J. Pratt	0.05	Mechanical Engineering
<b>FTE Equivalent:</b>	<b>0.70</b>	
<b>Total Number:</b>	<b>10</b>	

15  
**Student Metrics**

This section only applies to graduating undergraduates supported by this agreement in this reporting period

The number of undergraduates funded by this agreement who graduated during this period: ..... 3.00

The number of undergraduates funded by this agreement who graduated during this period with a degree in science, mathematics, engineering, or technology fields:..... 3.00

The number of undergraduates funded by your agreement who graduated during this period and will continue to pursue a graduate or Ph.D. degree in science, mathematics, engineering, or technology fields:..... 2.00

Number of graduating undergraduates who achieved a 3.5 GPA to 4.0 (4.0 max scale):..... 0.00

Number of graduating undergraduates funded by a DoD funded Center of Excellence grant for Education, Research and Engineering:..... 0.00

The number of undergraduates funded by your agreement who graduated during this period and intend to work for the Department of Defense ..... 0.00

The number of undergraduates funded by your agreement who graduated during this period and will receive scholarships or fellowships for further studies in science, mathematics, engineering or technology fields: ..... 0.00

**Names of Personnel receiving masters degrees**

NAME

S. A. K. Fakhri

**Total Number:** 1

**Names of personnel receiving PHDs**

NAME

S. Wang

Pulkit Saxena

S. Li

P. Khare

**Total Number:** 4

**Names of other research staff**

NAME

PERCENT SUPPORTED

C. Di Norscia 0.05

T. Newman-Lehman 0.10

D. F. Davidson 0.09

J. B. Jeffries 0.05

**FTE Equivalent:** 0.29

**Total Number:** 4

**Sub Contractors (DD882)**

**Inventions (DD882)**

**Scientific Progress**

**Technology Transfer**

N/A



## TABLE OF CONTENTS

	Page Number
Table of Contents.....	ii
List of Figures and Tables.....	ix
<b>INTRODUCTION.....</b>	<b>1</b>
<b>I. GELLED MATERIALS FORMULATION, PROCESSING, AND CHARACTERIZATION (Adair, Penn State).....</b>	<b>3</b>
1. Abstract.....	3
2. Background.....	3
3. Experimental Facilities and Algorithms .....	4
4 Major Findings.....	5
4.1 Preparation of model hypergolic fluids .....	5
4.2 Preparation of hypergolic fluids with a variety of material systems.....	8
5. References.....	16
<b>II. JET ATOMIZATION, SPRAY FORMATION AND DROPLET DYNAMICS.....</b>	<b>17</b>
<b>II.1 Studies on Droplet Collision Dynamics (Law, Princeton University) .....</b>	<b>17</b>
1. Objectives.....	17
2. Background.....	17
3. Experimental Facilities and Algorithms Developed or Used .....	18
3.1 Experimental Facilities .....	18
3.2 Algorithms Developed or Used .....	19
4. Major Findings.....	20
4.1 Experimental Observations of Droplet Collision .....	20
4.2 Experimental Observations of Jet Collision .....	25
4.3 Numerical Simulations in Front Tracking Method .....	26
4.3.1 Stationary Coalescence of Unequal-size Droplets.....	26
4.3.2 Head-on Collision of Unequal-size Droplets .....	27
4.4 Theoretical Analysis .....	32
5. References .....	33
<b>II.2 Jet Atomization and Spray Formation in Impinging Jets (Lee, U. Cincinnati).....</b>	<b>35</b>
1. Abstract .....	35
2. Nomenclature.....	35
3. Introduction.....	36
4. Experimental Details.....	38
4.1 Nozzle configurations.....	38
4.2 Experimental setup .....	38
4.3 Rheological characterization of gelled simulants.....	39
4.4 Diagnostics .....	40
5. Results and Discussion .....	41
5.1 Effect of nozzle geometry on the atomization at an atmospheric chamber pressure .....	41
5.1.1 Nozzle & near-field jet stream characterization.....	41

5.1.2 Sheet formation and break-up .....	44
5.1.3 Droplet size variation and distribution .....	47
5.2 Effect of Chamber Pressure on the Atomization .....	49
5.2.1 Breakup regimes .....	49
5.2.1.1 Breakup regimes for water .....	49
5.2.1.2 Breakup regimes for ethanol/water mixture .....	51
5.2.1.3 Breakup regimes for particle-based gel .....	52
5.2.1.4 Regime map .....	52
5.2.2 Breakup length .....	54
5.2.3 Characterization of pre-impingement jet and post-impingement sheet .....	55
5.2.3.1 Disturbances on the surface of the jet before impingement .....	56
5.2.3.2 Surface wavelength after impingement .....	58
5.2.3.3 Ligament wavelength .....	58
6. References .....	59
<b>III. INTERFACANTERFACIAL REACTIONS AND TRANSPORT AT ATOMISTIC, MOLECULAR, MICRO, AND MESO SCALES .....</b>	<b>62</b>
<b>III.1 Enhanced Spectroscopic Analysis of Interfacial Reactions and Transport (Rabitz, Princeton University) .....</b>	<b>62</b>
1. Abstract .....	62
2. Background and Scientific Objectives .....	62
3. Enhanced Spectroscopy through Optimal Dynamic Discrimination .....	62
4. Optimized CARS .....	64
5. Interrogating Mixing Systems With Chemically Sensitive Imaging .....	67
6. Impulsive CARS for Interrogation of Mixing Systems .....	70
6.1 White Light Supercontinuum Driven CARS .....	70
6.2 TOPAS-White Commercial NOPA Driven CARS .....	74
7. Conclusions .....	75
8. References .....	76
<b>III.2 Study of Condensed-phase Reactions in Hypergolic Propellants using Microreactors (Yetter, Penn State) .....</b>	<b>77</b>
1. Abstract .....	77
2. Introduction .....	77
3. Drop Tests .....	80
4. Reactor Fabrication .....	80
5. Experiment .....	82
6. Cold Flow Characterization in Microreactor .....	84
7. Drop Test Results .....	90
8. Micro-reactor Test Results .....	90
8.1 TMEDA with Nitric Acid Micro-Reactor Experiment .....	91
8.2 DMAZ with Nitric Acid Micro-Reactor Experiment .....	93
8.3 Triethylamine with White Fuming Nitric Acid Micro-Reactor Experiment .....	94
8.4 Dicyclopentadiene with White Fuming Nitric Acid Micro-Reactor Experiment .....	94
8.5 Indene with White Fuming Nitric Acid Micro-Reactor Experiment .....	95
8.6 TMEDA-DMAZ mixtures with Nitric Acid Micro-Reactor Experiment .....	96
9. Numerical Simulations .....	98
10. Discussion .....	105

11. Conclusions .....	108
12. References .....	109
<b>III.3 Reaction Mechanisms for Hypergolic Propellants (Goddard, California Institute of Technology)</b> .....	112
1. Abstract of Objectives .....	112
2. Background and Scientific Objectives .....	112
3. Methods .....	113
4. Results and Discussions .....	114
4.1 DFT study of ignition mechanism of hypergolic bipropellant: TMEDA, TMMDA and nitric acid .....	114
4.1.1 Exothermicity of the formation of dinitrate salt of TMEDA and TMMDA .....	114
4.1.2 Bond energies in TMEDA, TMMDA and their alkane analogues .....	115
4.1.3 Reaction mechanism of TMEDA+NO <sub>2</sub> .....	116
4.1.3.1 Initiating stage .....	117
4.1.3.2 Reactions after INT1. ....	118
4.1.3.3 Reactions after INT2 .....	118
4.1.4 Reaction mechanism of TMMDA+NO <sub>2</sub> .....	119
4.1.4.1. Initiating stage: H-abstraction .....	120
4.1.4.2. Reactions after INT20 .....	120
4.1.5 Comparison between reaction mechanisms of TMEDA/NTO and TMMDA/NTO .....	121
4.1.6 Conclusion .....	121
4.2 DFT Investigations of Early Reactions of Monomethylhydrazine with Mixtures of NO <sub>2</sub> and N <sub>2</sub> O <sub>4</sub> .....	122
4.2.1 H-atom abstraction from MMH .....	122
4.2.2 H-atom abstraction from CH <sub>3</sub> NNH <sub>2</sub> or CH <sub>3</sub> NHNH .....	123
4.2.3 H-atom abstraction from CH <sub>3</sub> N=NH .....	124
4.2.4 Formation of MMH·HONO aerosol and its lower reactivity .....	124
4.2.5 Reactions of asymmetric dimer of NO <sub>2</sub> , ONONO <sub>2</sub> in gas phase .....	125
4.2.6 Reactions facilitated by aerosol to form CH <sub>3</sub> ONO <sub>2</sub> .....	126
4.2.7 Conclusions .....	129
4.3. DFT Investigations of Early Reactions of Unsymmetric Dimethylhydrazine (UDMH) with Mixtures of NO <sub>2</sub> and N <sub>2</sub> O <sub>4</sub> .....	130
4.3.1 H-atom abstraction from UDMH .....	131
4.3.2 Formation of UDMH·HONO aerosol .....	131
4.3.3 Reactions facilitated by aerosol to form CH <sub>3</sub> N <sub>3</sub> and then CH <sub>3</sub> ONO <sub>2</sub> .....	131
4.3.4 Conclusions .....	132
5. References .....	132
<b>III.4 Experimental Studies of Condensed-phase Interactions of Hypergolic Propellants (Thynell, Penn State)</b> .....	135
1. Abstract .....	135
2. Introduction .....	135
2.1 Background .....	135
2.2 Objectives .....	136
3. Experimental Setups .....	137
3.1 Drop-test Setup .....	137



3.2 Confined-interaction Setup .....	138
3.3 Strand Burner .....	138
3.4 Confined rapid Thermolysis (CRT)/FTIR Setup .....	139
4. Results and Discussion .....	139
4.1 Drop-on-pool Impingement Tests .....	140
4.1.1 MMH/90% $\text{HNO}_3$ .....	140
4.1.2 MMH/WFNA .....	141
4.1.3 MMH/RFNA .....	143
4.1.4 TMEDA/90% $\text{HNO}_3$ .....	143
4.2 Results from confined-interaction/FTIR studies .....	144
4.2.1 IR analysis of MMH/ $\text{HNO}_3$ interaction .....	144
4.2.2 Early reactions between MMH and $\text{HNO}_3$ .....	147
4.2.3 IR analysis of TMEDA/ $\text{HNO}_3$ interaction .....	150
4.2.4 Early reactions between TMEDA and $\text{HNO}_3$ .....	152
4.3 Study on nitrates MMH·2 $\text{HNO}_3$ and TMEDA·8 $\text{HNO}_3$ .....	153
4.3.1 Preparation .....	153
4.3.2 Combustion of TMEDA·8 $\text{HNO}_3$ .....	154
4.3.3 Combustion of MMH·2 $\text{HNO}_3$ .....	156
4.3.4 Decomposition of TMEDA·8 $\text{HNO}_3$ .....	157
4.3.5 Decomposition of MMH·2 $\text{HNO}_3$ .....	160
4.4 Pressure effect on ignition delay .....	163
5. References .....	164
<b>IV. IGNITION AND REACTION MECHANISMS IN GAS PHASE .....</b>	<b>170</b>
<b>IV.1 Aerosol Shock Tube Experiments (Hanson, Stanford University) .....</b>	<b>170</b>
1. Abstract .....	170
2. Experimental Facilities and Methods .....	170
2.1 Shock Tube Facility .....	170
2.2 Stanford High Pressure Shock Tube (HPST) .....	170
2.3 Stanford Kinetic Shock Tube (KST) .....	171
2.4 Stanford NASA Shock Tube (NASA) .....	171
2.5 Laser Absorption Strategy .....	171
2.6 Ring Dye Laser Diagnostics .....	172
3. Summary of Results .....	172
3.1 MMH Pyrolysis and Oxidation .....	172
3.1.1 Experimental Setup .....	174
3.2 MMH Pyrolysis .....	176
3.2.1 Kinetic and Gasdynamic Modeling .....	176
3.2.2 Results and Discussion .....	177
3.3 MMH Oxidation .....	181
3.3.1 Kinetics and Gasdynamics Modeling .....	181
3.3.2 Results and Discussion .....	183
3.4 Conclusions .....	187
3.5 Morpholine and Related Chemistry .....	188
3.5.1 Morpholine .....	190
3.5.2 OH + DMA, OH + EA .....	191
3.5.3 Dimethylamine Oxidation .....	192

3.5.4 Ethylamine Pyrolysis and Oxidation .....	193
3.5.5 MMH Pyrolysis .....	195
3.5.6 Conclusions .....	197
3.5.6.1 Morpholine Oxidation .....	197
3.5.6.2 Dimethylamine and Ethylamine Combustion .....	197
3.5.6.3 MMH Pyrolysis .....	198
4. References .....	199
<b>IV.2 Studies on MMH Reaction Mechanism (Law, Princeton University) .....</b>	<b>200</b>
1. Objective .....	200
2. Background .....	200
3. Theoretical Approach .....	200
3.1 Multireference second-order perturbation theory (CASPT2) .....	200
3.2 High-accuracy Multireference coupled-cluster theory with Brillouin-Wigner (BW-MRCCSD(T)) and Mukherjee (Mk-MRCCSD(T)) approaches .....	201
3.3 Variable reaction coordinate transition state (VRC-TST) theory .....	201
3.4. Rice–Ramsperger–Kassel–Marcus (RRKM) theory .....	201
4. Major Findings .....	201
4.1 <i>Ab Initio</i> Kinetics for the Primary Decomposition of Monomethylhydrazine .....	201
4.2 <i>Ab Initio</i> Kinetics for the Secondary Decomposition of Monomethylhydrazine .....	203
4.3 Gas-phase Kinetics Study of Reaction of OH Radical with CH <sub>3</sub> NHNH <sub>2</sub> by Second-Order Multireference Perturbation Theory and Two-Transition State Theory .....	204
4.4 <i>Ab Initio</i> Kinetics for Thermal Decomposition of CH <sub>3</sub> N•NH <sub>2</sub> , cis-CH <sub>3</sub> NHN•H, trans-CH <sub>3</sub> NHN•H, and C•H <sub>2</sub> NNH <sub>2</sub> Radicals .....	207
4.5 Kinetics of CH <sub>3</sub> N•NH <sub>2</sub> + OH by Multireference Second-Order Perturbation Theory and Multireference Coupled-Cluster Theory .....	211
4.6 Kinetic Modeling of Monomethylhydrazine Decomposition and Product Formation .....	213
5. References .....	215
<b>IV.3 Theoretical and Experimental Counterflow Ignition and Combustion Studies (Williams, University of California at San Diego) .....</b>	<b>216</b>
1. Abstract .....	216
2. Background and Scientific Objectives .....	216
3. Facilities .....	217
4. Major Findings .....	217
4.1 A Generic Model for Hypergolic Ignition of Gelled Propellants .....	217
4.2 The Structure and Extinction of Methane/Nitrogen Dioxide Flames .....	217
4.3 The Structure and Extinction of Nonpremixed Methane/Nitrous Oxide and Ethane/Nitrous Oxide Flames .....	218
4.4 Experimental and Computational Studies of Ignition of Nonpremixed C <sub>2</sub> H <sub>6</sub> /N <sub>2</sub> with oxidizer mixtures of N <sub>2</sub> O/O <sub>2</sub> /N <sub>2</sub> .....	224
4.5 Rate-Ratio Asymptotic Analysis of the Structure and Mechanisms of Extinction of Nonpremixed CH <sub>4</sub> /N <sub>2</sub> -O <sub>2</sub> /N <sub>2</sub> O/N <sub>2</sub> Flames .....	226
4.6 Experimental and Computational Studies of the Influence of Hydrogen and Carbon Monoxide on the Structure and Extinction of Methane Flames .....	229

<b>V. MODELING, SIMULATION, AND DIAGNOSTICS OF OVERALL PROCESSES</b>	234
<b>V.1 High-Fidelity Modeling and Simulation of Spray and Combustion of Gelled Hypergolic Propellants (Yang, Georgia Institute of Technology)</b>	234
1. Abstract	234
2. Research objectives	234
3. Theoretical formulation	235
3.1 Governing equations	236
3.2 Numerical model and spatial discretization	238
4. Impinging jet atomization	239
4.1 Flow patterns of impinging jets	240
4.2 Impact wave dynamics and atomization	240
4.3 Non-Newtonian impinging jets	242
4.3.1 Rim instability	244
4.3.2 Impact wave	244
4.3.3 Shear thinning effect	246
5. Deforming and fragmenting Newtonian liquid droplets	247
5.1 Bag breakup	249
5.2 Multimode breakup	252
5.3 Shear breakup	254
5.4 Time averaged drag coefficient of deforming and fragmenting droplets	254
5.5 Generalized regime diagram and child droplet size distributions	257
6. Dynamics and mass transfer of unequal-sized droplet collision	261
7. Equal-sized droplet collision and mixing	264
8. Non-Newtonian droplet breakup and dynamics	266
9. References	268
<b>V.2 Impinging Jet Experimentation (Risha, Penn State – Altoona)</b>	271
1. Summary	271
2. Nomenclature	271
3. Introduction	271
4. Background	272
5. Experimental Method of Approach	275
5.1 Injector Configuration	275
5.1.1 Inert Impingement Results	277
5.1.2 Single Element Characterization with Liquid Water	277
5.1.3 Gel Preparation for Inert Materials	278
5.1.4 Gel Preparation for Reactive Materials	283
5.2 Reactant Delivery System	285
5.3 Curved Surface Impingement	286
5.4 Propellant Formulation and Reservoir Filling Process	287
6. Results and Discussion	289
6.1 Effect of Volumetric Flow Rate and Oxidizer Type	290
6.2 Effect of Momentum Ratio and Equivalence Ratio	291
6.3 Effect of Gellant of Ignition Delay	293
6.4 Effect of Fuel and Oxidizer Leads	294
6.5 Effect of Length-to-Diameter Ratio of Injector	295

6.6 Effect of DMAZ Fuel Additive .....	296
6.7 Effect of Curved Wall Impingement .....	298
7. Conclusions.....	299
8. References.....	299
<b>ARCHIVAL PUBLICATIONS AND PRESENTATIONS IN CHRONOLOGICAL ORDER .....</b>	<b>301</b>
Archival Publications.....	301
Papers Presented at Conferences .....	304
<b>LIST OF TEAM MEMBERS IN ALPHABETICAL ORDER .....</b>	<b>309</b>

## LIST OF FIGURES AND TABLES

<b>INTRODUCTION</b> .....	1
<b>Figure 1.</b> Summary of the defined task areas and associated investigators. ....	2
<b>Figure 2.</b> Summary of some of the fuels, oxidizers, and gelling agents considered in the research effort. ....	2
<b>I. GELLED MATERIALS FORMULATION, PROCESSING, AND CHARACTERIZATION (Adair, Penn State)</b> .....	3
<b>Figure 1.</b> Top: Summary of gelation ranges for each of the fuels with weight percent of commercial silica added to each fuel also shown in detail in Table 1. Bottom: representative samples for silica in DMAZ; the 2 and 4 weight percent silica samples were Newtonian while the right hand sample was a gel. ....	6
<b>Figure 2.</b> Top: Shear stress and viscosity as a function of shear rate for 3 weight percent silica in TMEDA. Middle: Viscosity as a function of shear rate for 6 weight percent silica in MMH, and; Bottom: Shear stress for 6 weight percent silica in MMH. ....	6
<b>Figure 3.</b> Summary of evaluation for nanoscale magnesium synthesized using a modified process originally developed by Rieke (Rieke 1981). (A) Basic synthetic steps and (B,C) Thermophysical characterization in our prior studies (Eklund 2007) revealed that the nanoscale Mg was stable in air for long times (up to at least three months). Moreover, the material when suspended in water slowly converted to magnesium hydroxide without a robust reaction (Eklund 2007). As shown in (B), X-ray diffraction analysis indicated magnesium metal was the predominant phase even after three months in ambient conditions of temperature and relative humidity. As shown in (C), Raman spectroscopy revealed that aromatic carbon rings, likely from the naphthalene present during the synthetic procedures, provide a passivation surface barrier to metal oxidation. However the larger batch scales used in the current project lead to agglomeration that several dispersion strategies could not prevent or eliminate. The dense agglomerates shown in (D) prevented the nanoscale Mg from forming a gel in the TMEDA. Efforts are continuing to provide better dispersion for this interesting material. ....	8
<b>Figure 4.</b> (Top) Basic design and basis for timed flow using pressure changes, and; (Bottom) Gen 1 capillary rheometer based on a modified Parr Instruments Teflon-lined hydrothermal reactor. ....	11
<b>Figure 5.</b> (A) Gen 3 capillary rheometer; (B), Argon dry box in which the capillary rheometer can be placed to provide a carefully controlled environment; (C) Gen 4 design for capillary rheometer, and; (D) Gen 4 capillary rheometer showing valving and digital pressure meters. ....	11
<b>Figure 6.</b> (Top) Viscosity measured for water with and without calibration. While the general trend toward decreasing viscosity with temperature is shown, the deviation becomes more profound as temperature increases. (Bottom) measured viscosity for TMEDA as a function of temperature with 3 <sup>rd</sup> order non-linear regression for the corrected value based on the calibration with was in the top figure. The range of temperatures was from 20 to 40°C at a pressure of 10psi Ar. ....	12
<b>Figure 7.</b> (Left) High pressure-high temperature vessel for surface tension determinations, and; (Right) overhead view of apparatus built for high pressure – high temperature determinations of surface tension. ....	13
<b>Figure 8.</b> Schematic of the 316L stainless steel apparatus for high pressure – high temperature determination of surface tension for fuels and other potentially reactive liquids.	

(Top) 3D schematic drawing of vessel with ports and gas ports highlighted. (Bottom, Left) Overhead view of the arrangement of ports for gas and tensiometer probes. (Bottom, Right) Dimensions of the pressure vessel. ....	14
<b>Figure 9.</b> Detailed schematic of the high pressure – high temperature surface tension measurement head with ports and other apparatus indicated in the schematic. One of the intrinsic limitations of the dynamic tensiometer is the maximum pressure for the transducers used to determine surface tension is 200 psi. ....	15
<b>Figure 10.</b> Surface tension values determined for TMEDA in an argon atmosphere at 10 psi applied pressure from 20 to 117.2°C. The virial equation was linear over this temperature and pressure range. The virial coefficients are summarized in Table 1. ....	15
<b>Table 1.</b> Provisional virial coefficients for viscosity and surface tension as a function of temperature in the relationship, $\eta$ or $\gamma_{lv} = ax^3+bx^2+cx+d$ , where $x$ is temperature in °C. ....	5
<b>Table 2.</b> Range of gelation and solidification for the weight percent of as-received Cab-O-Sil nanoscale silica in MMH, TMEDA, DMAZ, and hydrazine. Figure summarizes gelation ranges for each of the fuel. ....	7
<b>II. JET ATOMIZATION, SPRAY FORMATION AND DROPLET DYNAMICS</b> .....	17
<b>II.1 Studies on Droplet Collision Dynamics (Law, Princeton University)</b> .....	17
<b>Figure 1.</b> Photographic images showing representative bouncing collision sequences for tetradecane droplet collisions. (a) $(We_s, \Delta) = (8.5, 1.0)$ ; (b) $(7.3, 1.46)$ ; (c) $(7.3, 1.87)$ ; (d) $(7.0, 2.33)$ . ....	22
<b>Figure 2.</b> Photographic images showing representative coalescence collision sequences for tetradecane droplet collisions. (a) $(We_s, \Delta) = (16.1, 1.0)$ ; (b) $(13.8, 1.46)$ ; (c) $(17.6, 1.87)$ ; (d) $(16.5, 2.33)$ . ....	23
<b>Figure 3.</b> Photographic images showing representative separation collision sequences for tetradecane droplet collisions. (a) $(We_s, \Delta) = (39.1, 1.0)$ ; (b) $(52.8, 1.50)$ ; (c) $(58.8, 1.78)$ ; (d) $(68.0, 2.50)$ . Separation at $\Delta = 2.5$ was not observed up to $We_s = 68$ . ....	24
<b>Figure 4.</b> Comparison between experimentally measured and model predicted transition Weber numbers as a function of the size ratio for Tetradecane, Decane, and Water droplet collision. ....	25
<b>Figure 5.</b> Time sequence for the initially stationary coalescence of unequal-size droplets for $\lambda = 0.5$ , $\xi = 1.0$ , (a) $\zeta = 1.0$ , $Oh = 0.025$ and (b) $\zeta = 0.01$ , $Oh = 0.0025$ . ....	27
<b>Figure 6.</b> Time sequence for the collision of unequal-size tetradecane droplets at 1atm air for (a) Scheme 1 and (b) Scheme 2. $d = 200\mu m$ , $D = 200\mu m$ , $U = 0.7m/s$ , $\tau = 1.13 ms$ $\eta = 0.5$ , $Oh = 0.025$ , $We = 6.0$ . ....	29
<b>Figure 7.</b> Comparison of Schemes 1 and 2 for the droplet contour after coalescence. ....	29
<b>Figure 8.</b> Energy budget of the colliding droplets for (a) Scheme 1 and (b) Scheme 2. KE denotes the total kinetic energy, DE the total dissipation energy, SE the surface energy, TE the total energy, and VDR the viscous dissipation rate multiplied by unit time, each normalized by the initial energy of a single droplet. ....	30
<b>Figure 9.</b> Time sequence for the collision of unequal-size tetradecane droplets at 1atm air for (a) Scheme 1 and (b) Scheme 2. $\eta = 0.3$ , $Oh = 0.025$ , $We = 6.0$ . ....	31
<b>Figure 10.</b> Viscosity dissipation rate for different size ratios. ....	31
<b>Figure 11.</b> Internal flow structure at $\bar{t} = 2.0$ for $\lambda = 0.5$ . ....	32
<b>Figure 12.</b> Internal flow structure at $\bar{t} = 2.0$ for $\lambda = 0.3$ . ....	32
<b>Table I.</b> Comparison of the predicted and experimental transition $We$ for the collision of tetradecane and water droplets in air. ....	33

<b>II.2 Jet Atomization and Spray Formation in Impinging Jets (Lee, U. Cincinnati)</b> .....	35
<b>Figure 1.</b> Schematic drawings of angled inlet (left) and straight inlet (right) .....	38
<b>Figure 2.</b> Schematic drawing of a gelled water simulant feed system into a high pressure chamber.....	38
<b>Figure 3.</b> Rheology of simulant gel: (a)Viscosity vs. Shear rate for gels (b) Storage and Loss moduli plotted versus time for particle-based gel .....	40
<b>Figure 4.</b> Flow rate vs. the root of pressure drop across nozzle for non-gelled water (a) straight-edge inlet nozzle and (b) angled-edge inlet nozzle.....	41
<b>Figure 5.</b> Images of near-field jet streams exiting orifice for non-gelled water with straight edge inlet: images on the top row for short nozzles ( $L/D=5$ ) and the bottom row for long nozzles ( $L/D=20$ ). .....	42
<b>Figure 6.</b> Flow rate vs. the root of pressure drop across nozzle for gelled water (a) straight-edge inlet nozzle and (b) angled-edge inlet nozzle.....	43
<b>Figure 7.</b> Images of near-field jet streams exiting orifice for gelled water with straight edge inlet: images on the top row for short nozzles ( $L/D=5$ ) and the bottom row for long nozzles ( $L/D=20$ ) .....	44
<b>Figure 8.</b> Typical instantaneous images of impinging doublets for (a) non-gelled and (b) gelled water cases for different orifice configurations .....	45
<b>Figure 9.</b> Break-up length vs. Reynolds number for (a) non-gelled and (b) gelled water and for nozzles with various orifice configurations.....	46
<b>Figure 10.</b> Comparison of breakup length .....	46
<b>Figure 11.</b> For non-gelled water (a) spatial distribution of drop size across spray for various flow rates and (b) mean drop size at the center of spray vs. Reynolds number for various orifice inlet configurations .....	47
<b>Figure 12.</b> Comparison of atomization characteristics of impinging doublets using non-gelled and gelled water: (a) Spatial distribution of mean drop size ( $D_{32}$ ) across spray for similar Reynolds number ( $\sim 2200$ ), (b) Mean drop size vs. Reynolds number and (c) drop size distribution at the center of spray for similar Reynolds number ( $\sim 2200$ ). .....	48
<b>Figure 13.</b> A typical instantaneous image of a liquid sheet formed by two impinging jets issuing water jet (Flow direction is from left to right).....	49
<b>Figure 14.</b> Shadowgraph of impinging jet spray taken for various pressures and flow rates (Non-gelled water) .....	50
<b>Figure 15.</b> Shadowgraph of impinging jet spray taken for various pressures and flow rates (Non-gelled Ethanol-Water mixture).....	52
<b>Figure 16.</b> Common regime diagram presenting the location of breakup regimes for various gelled and non-gelled fluids over a range of pressures and flow rates. (Data for other fluids are plotted from DLR Group [21,22] and Fakhri [23]). .....	53
<b>Figure 17.</b> The normalized sheet breakup length plotted as function of ambient pressure for all working fluids: (a) Distilled water, (b) Ethanol-water, and (c) Gelled Ethanol-water. (Solid lines represent the empirical correlation obtained from Jung et al. [7]). .....	55
<b>Figure 18.</b> The normalized breakup length plotted as a function of Reynolds number of gas (The legend should be interpreted for three major fluids $\circ$ for water $\diamond$ for non-gelled ethanol/water and $\square$ for the gelled ethanol/water. Also, in these fluids, different symbols or colors signify various ambient pressures. For an example, * enclosed in $\circ$ signifies breakup length for water at 3.45 MPa).. .....	56

<b>Figure 19.</b> Shadowgraphs of single jet stream of water for various pressures and flow rates. ....	57
<b>Figure 20.</b> Typical shadowgraph of a single jet illustrating the method of measurement for □ Disturbance which is subsequently plotted as a function of $Re_g$ in Wave-Breakup regimes for water. ....	57
<b>Figure 21.</b> The surface wavelength between adjacent waves plotted: (a) as a function of pressure in wave breakup regime for non-gelled water and (b) as a function of $Re_{gas}$ in the wave breakup regime for non-gelled water. ....	58
<b>Figure 22.</b> The ligament wavelength vs. ambient pressure for (a) Distilled water, (b) Non-gelled ethanol-water, and (c) Gelled Ethanol-water at operating conditions corresponding to the wave-breakup regimes. ....	59
<b>Figure 23.</b> Ligament wavelength measured as a function of $Re_g$ for non-gelled water. ....	59
<b>Table 1.</b> Properties of working fluids at STP. ....	39
<b>III. INTERFACANTERFACIAL REACTIONS AND TRANSPORT AT</b>	
<b>ATOMISTIC, MOLECULAR, MICRO, AND MESO SCALES</b> .....	62
<b>III.1 Enhanced Spectroscopic Analysis of Interfacial Reactions and Transport (Rabitz, Princeton University)</b> .....	62
<b>Figure 1.</b> (a) schematic representation of the closed-loop optimization algorithm (b) schematic of laser pulse shaper: the broadband ultra-short laser pulse is dispersed into its component frequencies, which are individually addressed by computer controlled light modulator before being recombined into a tailored pulse and sent to the experiment. ....	63
<b>Figure 2.</b> Optimal Dynamic Discrimination of Rhodamin 101 and Sulfo-Rhodamin 101. A portion of the fluorescence spectrum of each dye is manipulated by optimized stimulated emission depletion. ....	64
<b>Figure 3.</b> Diagram of 3-Beam, OPA-Driven CARS.....	66
<b>Figure 4.</b> Raman line of spectroscopic standard Acetonitrile ( $2954\text{ cm}^{-1}$ $\text{CH}_3$ sym-stretch) measured with 3-beam OPA-Driven CARS. Optimization (black trace) produces slight improvement of CARS signal but marked reduction of Non-Resonant Background. ....	67
<b>Figure 5.</b> Shift of florescence maximum of HPTS dye caused by chemical environment.....	68
<b>Figure 6.</b> Laser Induced Fluorescent imaging of colliding droplets to observe and evaluate configuration of microdroplet generators. ....	69
<b>Figure 7.</b> Analysis of droplet mixing post coalescence. Flourescence ratios have been converted to Volume Fraction of Methanol v. Water. The averaged volume fraction of each species through a strip in the center of the droplets (outlined by red lines) is plotted against the image backdrop. ....	69
<b>Figure 8.</b> Fluorescent imaging of cross-flow micro-channel reactor (edges of microchannels outlined in red). Methanol carrying a chemically sensitive dye flows into the chamber from the bottom and collides in the center with pure water flowing from the top. As the two species mix the dye in the methanol is transferred to the water causing a shift in the fluorescence to longer wavelength. ....	70
<b>Figure 9.</b> Schematic of White Light CARS system.....	71
<b>Figure 10.</b> Representative spectra of Raman spectrographic standards measured with single laser shot of White Light CARS system. ....	73
<b>Figure 11.</b> Measuring Impulsive CARS of mixing dyes in microchannel cross-flow reactor. At right integrated peak heights for peaks associated with each dye are plotted versus position in the reactor. ....	74



<b>Figure 12.</b> Spectrum of TOPAS-White commercial NOPA in Ultra-broadband configuration (orange), compared to spectra of TOPAS in Standard configuration (blue) and the House-Built NOPA (red).	74
<b>Figure 13.</b> Optimized NOPA-Driven Impulsive-CARS of Raman spectroscopic standard Acetonitrile. Before shaping, the natural phase of the NOPA creates strong Non-resonant 4WM. The Optimization not only brings the CARS signal out of the noise but nearly eliminates the Non-resonant background.	75
<b>III.2 Study of Condensed-phase Reactions in Hypergolic Propellants using Microreactors (Yetter, Penn State)</b>	77
<b>Figure 1.</b> Schematic of fabrication process for the microreactors. Steps (a), (b) and (c) illustrate the photolithography process for one side of the double side polished silicon wafer. Step (d) shows the deep reactive ion etching (DRIE) of the silicon wafer to create the reactor channels. Steps (e), (f) and (g) illustrate the photolithography process for the back side of the etched silicon wafer. Step (h) shows the DRIE process for the back side of the wafer to create the inlet and outlet ports. Step (i) illustrates the anodic bonding of the etched silicon wafer to a borosilicate glass wafer.	81
<b>Figure 2.</b> (a) Fabricated microreactors using etched silicon bonded to borosilicate glass. (b) Microreactor with stainless steel manifold setup.	82
<b>Figure 3.</b> Schematic of the experimental setup showing the microreactor assembly under an upright microscope.	82
<b>Figure 4.</b> Schematic of Micro-PIV setup.	83
<b>Figure 5.</b> (a) Cold flow testing of microreactor using micro-spheres to visualize flow at stagnation zone. (b) Cold flow visualization downstream of the stagnation zone showing very little broadening of diffusion interface.	84
<b>Figure 6.</b> Typical average velocity flow-field calculated from PIV measurements. Magnitude of velocity is shown by using colored vectors in the image with blue vectors indicating a low velocity magnitude while red indicates a high velocity magnitude.	85
<b>Figure 7.</b> Fluid velocity from opposite inlets of the stagnation flow reactor as the flow decelerates towards the stagnation point. Solid line indicates FLUENT simulation results while the points indicate experimental PIV measurements.	85
<b>Figure 8.</b> Fluid velocity as the flow decelerates towards the stagnation point. Lines indicate FLUENT simulation results while the points indicate experimental PIV measurements.	86
<b>Figure 9.</b> Velocity profiles at (a) inlet to stagnation zone and (b) outlet to stagnation zone.	87
<b>Figure 10.</b> Shifting of the stagnation plane from the centre of the microreactor towards one inlet or the other.	87
<b>Figure 11.</b> Position of stagnation plane at various heights in the deep-etched microreactor.	88
<b>Figure 12.</b> Schematic of the cross-sectional view of the stagnation zone of the microreactor showing the stagnation plane (red line) between the two fluid flows. (a) shows a stable stagnation plane between the two fluids at low flow rates and (b) shows the unstable stagnation plane at high flow rates in which the plane shifts towards one inlet or the other.	89

<b>Figure 13.</b> Still frames from reactive flow in micro-reactor using the various fuels with 30% WFNA. All flow rates for the reactants are at 500 uL/min and the images were captured at 1000 fps. ....	91
<b>Figure 14.</b> Change in exit temperatures for TMEDA and Nitric Acid in the micro-reactors with increasing flow rates of reactants. ....	92
<b>Figure 15.</b> Change in exit temperatures for DMAZ and Nitric Acid in the micro-reactors with increasing flow rates of reactants. ....	93
<b>Figure 16.</b> Change in exit temperatures for Triethylamine and White Fuming Nitric Acid in the micro-reactors with increasing flow rates of reactants. ....	94
<b>Figure 17.</b> Change in exit temperatures for Dicyclopentadiene and White Fuming Nitric Acid in the micro-reactors with increasing flow rates of reactants. ....	95
<b>Figure 18.</b> Change in exit temperatures for Indene and White Fuming Nitric Acid in the micro-reactors with increasing flow rates of reactants. ....	96
<b>Figure 19.</b> Ignition delay results from drop-tests carried out by Stevenson using mixtures of TMEDA and DMAZ as the fuel and Nitric Acid as the oxidizer [18]. ....	97
<b>Figure 20.</b> Change in exit temperatures for TMEDA-DMAZ mixtures and 30% Nitric Acid in the micro-reactors with increasing flow rates of reactants. ....	98
<b>Figure 21.</b> Heating rate along the stagnation centerline. Inlet velocity for both fuel and oxidizer is 0.1 cm/s while the reaction rate constant = $2 \times 10^7 \text{ L}^2 \cdot \text{mol}^{-2} \cdot \text{s}^{-1}$ . ....	101
<b>Figure 22.</b> Heating rate and temperature profile along the stagnation centerline. Inlet velocity for both fuel and oxidizer is 0.1 cm/s while the reaction rate constant = $2 \times 10^7 \text{ L}^2 \cdot \text{mol}^{-2} \cdot \text{s}^{-1}$ . $\dot{q}_l = 1 \text{ KW/cm}^3 \cdot \text{K}$ . ....	102
<b>Figure 23.</b> Heating rate and temperature profile along the stagnation centerline. Inlet velocity for both fuel and oxidizer is 50 cm/s while the reaction rate constant = $2 \times 10^7 \text{ L}^2 \cdot \text{mol}^{-2} \cdot \text{s}^{-1}$ . $\dot{q}_l = 1 \text{ KW/cm}^3 \cdot \text{K}$ . ....	103
<b>Figure 24.</b> Maximum temperature profile at the stagnation zone from numerical simulations of flow in the microreactor with reaction rate constant $K = 2 \times 10^7 \text{ L}^2 \cdot \text{mol}^{-2} \cdot \text{s}^{-1}$ . In addition to the temperature trends from the original simulation, temperature trends with the added heat loss term in the energy equation are also shown. ....	104
<b>Figure 25.</b> Maximum temperature profile at the stagnation zone from numerical simulations of flow in the microreactor with reaction rate constant $K = 2 \times 10^9 \text{ L}^2 \cdot \text{mol}^{-2} \cdot \text{s}^{-1}$ . In addition to the temperature trends from the original simulation, temperature trends with the added heat loss term in the energy equation are also shown. ....	105
<b>Table 1.</b> Summary of Ignition Delay times for various fuels with WFNA as well as flow rates at which peak temperatures occur in the micro-reactor. ....	106
<b>III.3 Reaction Mechanisms for Hypergolic Propellants (Goddard, California Institute of Technology) ....</b>	
<b>Figure 1.</b> Structures of several fuel molecules (a) MMH (b) UDMH (c) TMEDA (d) TMMDA (e) DMPipZ (f) TMTZ. ....	113
<b>Table 1.</b> Bond energies in TMEDA, TMMDA, and their corresponding alkane analogues. ....	116
<b>Scheme 1.</b> Reactions between TMEDA and $\text{NO}_2$ . Enthalpy and Gibbs free energy (in parentheses) of each species are provided. Unit in kcal/mol. ....	117
<b>Scheme 2.</b> Reactions between TMMDA and $\text{NO}_2$ . Enthalpy and Gibbs free energy (in parentheses) of each species are provided. Unit in kcal/mol. ....	120

<b>Scheme 3.</b> Reactions between MMH and NO <sub>2</sub> in gas phase. Barriers of all H-abstractions from N of MMH to form HONO are about 10 kcal/mol, and the same H-abstraction from methyl group is 16.1 kcal/mol endothermic and has ~10 kcal/mol higher barrier, rendering the oxidation of carbon slower at low temperature. Enthalpies and Gibbs free energies (in the parentheses) are calculated at 298.15K and 1 atm. <i>cis</i> -HONO at standard state is used as reference product.....	123
<b>Scheme 4.</b> The formation of aerosol MMH•HONO and MMH•2HONO followed by H-abstraction and HONO formation. The barriers of H-abstraction from MMH•2HONO aerosol are 7~9 kcal/mol higher than the ones from MMH. Enthalpies and Gibbs free energies (in the parentheses) are calculated at 298.15K and 1 atm.....	125
<b>Scheme 5.</b> The reactions between ONONO <sub>2</sub> , MMH, GInt5 and GInt6 in gas phase. These reactions have low barriers and produce HNO <sub>3</sub> as the source of nitrate anion observed experimentally. Enthalpies and Gibbs free energies (in the parentheses) are calculated at 298.15K and 1 atm. ....	126
<b>Scheme 6.</b> The reactions between ONONO <sub>2</sub> and MMH in water to simulate potential energy surface in the aerosol. Enthalpies is calculated at 298.15K and 1 atm. Several gas products, such as CH <sub>3</sub> ONO <sub>2</sub> and N <sub>2</sub> O, can desorb from the aerosol and be observed via IR spectra.....	127
<b>Scheme 7.</b> The reactions between CH <sub>3</sub> N <sub>3</sub> and ONONO <sub>2</sub> in water to simulate potential energy surface in the aerosol. The reaction path via SInt14, SInt15, SInt16 and STS12 has low barriers to form CH <sub>3</sub> ONO <sub>2</sub> . Enthalpies are calculated at 298.15K and 1 atm. ....	128
<b>Scheme 8.</b> The reactions between CH <sub>3</sub> N <sub>3</sub> and ONONO <sub>2</sub> in gas phase. All barriers are significant higher than the corresponding reactions in water, indicating the importance of solvation effect. Enthalpies and Gibbs free energies (in the parentheses) are calculated at 298.15K and 1 atm. ....	129
<b>Scheme 9.</b> Reactions between UDMH and NO <sub>2</sub> in gas phase. Barriers of all H-abstractions from N of UDMH to form HONO ranges 10~15 kcal/mol, and the same H-abstraction from methyl group is ~18 kcal/mol endothermic and has ~10 kcal/mol higher barrier, rendering the oxidation of carbon slower at low temperature. Enthalpies and Gibbs free energies (in the parentheses) are calculated at 298.15K and 1 atm. <i>cis</i> -HONO at standard state is used as reference product.....	130
<b>Scheme 10.</b> Formation of UDMH•HONO aerosol. Enthalpies and Gibbs free energies (in the parentheses) are calculated at 298.15K and 1 atm. ....	131
<b>Scheme 11.</b> Reactions between UDMH and <i>trans</i> -ONONO <sub>2</sub> in or on the surface of aerosol. Enthalpies with solvation energy are reported. STS2 is the rate-determining-step to form the final product, CH <sub>3</sub> N <sub>3</sub> . The enthalpic barrier height is 26.8 kcal/mol. ....	132
<b>III.4 Experimental Studies of Condensed-phase Interactions of Hypergolic Propellants (Thynell, Penn State).....</b>	135
<b>Figure 3.1.</b> Drop-test setup. ....	137
<b>Figure 3.2.</b> a) Overall view of the confined interaction setup, and b) top view and dimensions in inches of the interaction zone machined in block I.....	138
<b>Figure 3.3.</b> Strand burner.....	138
<b>Figure 4.1.</b> a) Selected images from a drop test of MMH (drop) / 90%HNO <sub>3</sub> (pool); and b) signals acquired by photodiode (PD) and microphone (MIC). ....	140
<b>Figure 4.2.</b> Liquid-phase temperature trace (a) and gas-phase temperature traces (b) in a drop test of MMH (drop) / 90%HNO <sub>3</sub> (pool). ....	141

<b>Figure 4.3.</b> a) Selected images from a drop test of MMH (drop) / WFNA (Case I); and b) signals acquired by photodiode (PD) and microphone (MIC). .....	142
<b>Figure 4.4.</b> a) Selected images from a drop test of MMH (drop) / WFNA (Case II); and b) signals acquired by photodiode (PD) and microphone (MIC). .....	142
<b>Figure 4.5.</b> Selected images from a drop test of MMH (drop) / RFNA (80 $\mu$ L) .....	143
<b>Figure 4.6.</b> Selected frames from a high-speed video for TMEDA (drop) and 90% HNO <sub>3</sub> (pool), $t = -5, 0, 10, 30, 45, 60, 75, 90, 110, 130$ ms, respectively.....	143
<b>Figure 4.7.</b> Temperature traces of the liquid pool (a) and the gases above the pool (b) in a drop test involving 80 $\mu$ L of 90% HNO <sub>3</sub> and a 7 $\mu$ L drop of TMEDA. ....	144
<b>Figure 4.8.</b> a) Average IR spectrum of the first 30 spectra obtained from confined interaction between MMH and HNO <sub>3</sub> at 20°C and 1 atm N <sub>2</sub> ; b) average IR spectrum of the last 30 spectra obtained from the same test; and c) Time-resolved IR absorption of species evolved from the same test (maximum absorption of all species were normalized to 1). .....	145
<b>Figure 4.9.</b> IR spectrum from a confined interaction of MMH/HNO <sub>3</sub> at 200°C. ....	146
<b>Figure 4.10.</b> a) Average IR spectra from confined interaction between MMH and WFNA at 250°C and 1 atm N <sub>2</sub> ; b) IR spectrum obtained by subtracting H <sub>2</sub> O from (a); and c) IR spectrum obtained by subtracting HONO, CH <sub>3</sub> ONO <sub>3</sub> , N <sub>2</sub> O, CO <sub>2</sub> , and CH <sub>4</sub> from b).....	146
<b>Figure 4.11.</b> Liquid-phase reactions of MMH/HNO <sub>3</sub> .....	148
<b>Figure 4.12.</b> Gas-phase pre-ignition reactions of MMH/HNO <sub>3</sub> . ....	150
<b>Figure 4.13.</b> Selected IR spectrum of species evolved from confined interaction between TMEDA and HNO <sub>3</sub> at 20°C and 1 atm N <sub>2</sub> . ....	151
<b>Figure 4.14.</b> Selected IR spectrum of species evolved from confined interaction between TMEDA and HNO <sub>3</sub> at 100 and 200°C, 1 atm N <sub>2</sub> . ....	151
<b>Figure 4.15.</b> IR spectrum of species evolved from confined interaction between TMEDA and HNO <sub>3</sub> at 250°C and 1 atm N <sub>2</sub> ; (A – original spectrum; B – spectrum after subtraction of H <sub>2</sub> O, NO <sub>2</sub> and CO <sub>2</sub> from the original spectrum; C – spectrum after subtraction of H <sub>2</sub> O, NO <sub>2</sub> , CO <sub>2</sub> , N <sub>2</sub> O, NO, CH <sub>2</sub> O and (CH <sub>3</sub> ) <sub>2</sub> NNO from the original spectrum.).....	152
<b>Figure 4.16.</b> Pre-ignition reactions of TMEDA/HNO <sub>3</sub> . ....	153
<b>Figure 4.17.</b> a) MMH·2HNO <sub>3</sub> ; b) TMEDA·2HNO <sub>3</sub> ; and c) TMEDA·8HNO <sub>3</sub> .....	154
<b>Figure 4.18.</b> Combustion of TMEDA·8HNO <sub>3</sub> at various gauge pressures (unit: psig) ..	155
<b>Figure 4.19.</b> Burn rate of TMEDA·8HNO <sub>3</sub> .....	156
<b>Figure 4.20.</b> Combustion of MMH·2HNO <sub>3</sub> at gauge pressure 400 (a) and 1000 psig (b).....	157
<b>Figure 4.21.</b> Burn Rates of MMH·2HNO <sub>3</sub> .....	157
<b>Figure 4.22.</b> IR spectra of gaseous species evolved from rapid thermolysis of TMEDA·8HNO <sub>3</sub> at various temperatures: a) 40°C; b) 80°C; ad c) 120°C. ....	158
<b>Figure 4.23.</b> Temporal evolution of species from rapid thermolysis of TMEDA·8HNO <sub>3</sub> at 80°C and 1 atm N <sub>2</sub> . ....	159
<b>Figure 4.24.</b> Oxidation of TMEDA cation by HNO <sub>3</sub> .....	160
<b>Figure 4.25.</b> a) Average IR spectrum of a total 150 spectra obtained from MMH·2HNO <sub>3</sub> decomposition at 160°C and 1 atm N <sub>2</sub> ; b) IR spectrum obtained by subtracting H <sub>2</sub> O and HNO <sub>3</sub> bands from (a). ....	161
<b>Figure 4.26.</b> Proposed MMH·2HNO <sub>3</sub> decomposition reactions. ....	162
<b>Figure 4.27.</b> Drop tests: a) MMH/WFNA at -20 kPa; b) MMH/WFNA at 50 kPa.....	163
<b>Figure 4.28.</b> Ignition delay of MMH/WFNA and UDMH/WFNA .....	163
<b>Figure 4.29.</b> Ignition delay of TMEDA, DMAZ and their mixture with WFNA.....	164

<b>Table 4.1.</b> IR frequencies of species in Fig. 4.10 (vs=very strong, s=strong, m=medium) .....	147
<b>IV. IGNITION AND REACTION MECHANISMS IN GAS PHASE</b> .....	170
<b>IV.1 Aerosol Shock Tube Experiments (Hanson, Stanford University)</b> .....	170
<b>Figure 1.</b> Schematic of shock tube operation.....	171
<b>Figure 2.</b> Ring dye laser diagnostic of $\text{NH}_2$ , using the fundamental output of a Spectra Physics 380 ring dye laser.....	172
<b>Figure 3.</b> Comparison of measured absorbance in the pyrolysis of 1% MMH/Ar mixtures at 244 nm, 306 nm and 10.22 $\mu\text{m}$ . .....	176
<b>Figure 4.</b> Room temperature FTIR spectra of $\text{NH}_3$ (dotted line) and MMH (solid line), and $\text{CO}_2$ laser line chosen for the MMH diagnostic. ( $\text{NH}_3$ absorption extends beyond the scale of the plot near 10.35 $\mu\text{m}$ ) .....	176
<b>Figure 5.</b> Comparison of measured pressure to constant volume and constant pressure models. Initial conditions are $T_5 = 1188 \text{ K}$ and $P_5 = 2.62 \text{ atm}$ . .....	177
<b>Figure 6.</b> Comparison of modeled temperature using constant volume and constant pressure models. Initial conditions are $T_5 = 1188 \text{ K}$ and $P_5 = 2.62 \text{ atm}$ . .....	177
<b>Figure 7(a).</b> Comparison of measured $\text{NH}_3$ (solid line) with the original Princeton mechanism (dashed line).....	178
<b>Figure 7(b).</b> $\text{NH}_3$ sensitivity at 991 K and 1.837 atm. ....	178
<b>Figure 8(a).</b> Comparison of measured $\text{NH}_2$ (solid line) with the original Princeton mechanism (dashed line).....	178
<b>Figure 8(b).</b> $\text{NH}_2$ sensitivity at 1111 K and 2.64 atm. ....	178
<b>Figure 9(a).</b> Comparison of measured $\text{NH}_2$ (solid line) with the Princeton mechanism (dashed line), the Princeton mechanism with modified $k_1$ and $k_2$ (dotted line), and the Princeton mechanism with modified $k_1$ , $k_2$ , and $k_4$ (dashed-dotted line) at 1111 K.....	179
<b>Figure 9(b).</b> Comparison of measured $\text{NH}_2$ (solid line) with the Princeton mechanism (dashed line), the Princeton mechanism with modified $k_1$ and $k_2$ (dotted line), and the Princeton mechanism with modified $k_1$ , $k_2$ , and $k_4$ (dashed-dotted line) at 1252 K.....	179
<b>Figure 10(a).</b> Comparison of measured $\text{NH}_3$ (solid line) with the Princeton mechanism (dashed line) and the Princeton mechanism with modified $k_1$ and $k_2$ (gray line) at 991 K.....	179
<b>Figure 10(b).</b> Comparison of measured $\text{NH}_3$ (solid line) with the Princeton mechanism (dashed line) and the Princeton mechanism with modified $k_1$ and $k_2$ (gray line) at 1207 K.....	179
<b>Figure 11(a).</b> Comparison of measured MMH with the Princeton mechanism (dashed line) and the Princeton mechanism with modified $k_1$ and $k_2$ (gray line) at 1111 K.....	180
<b>Figure 11(b).</b> Comparison of measured MMH with the Princeton mechanism (dashed line) and the Princeton mechanism with modified $k_1$ and $k_2$ (gray line) at 1252 K.....	180
<b>Figure 12(a)</b> Comparison of measured pressure to constant volume model. Initial conditions are $T_5 = 1279 \text{ K}$ and $P_5 = 1.48 \text{ atm}$ . ....	183
<b>Figure 12(b)</b> Comparison of measured pressure to 1-D model. Initial conditions are $T_5 = 1279 \text{ K}$ and $P_5 = 1.48 \text{ atm}$ . ....	183
<b>Figure 13.</b> Comparison of measured OH to Catoire (black, dash), Anderson (black, dash-dot), Modified Catoire (gray, dash), and Modified Anderson (gray, dash-dot) mechanisms using measured pressure (a) over the entire test time and (b) at early times. Initial conditions are $T_5 = 1180 \text{ K}$ and $P_5 = 1.59 \text{ atm}$ . ....	183

<b>Figure 14.</b> Comparison of measured $\text{NH}_2$ to Catoire (black, dash), Anderson (black, dash-dot), Modified Catoire (gray, dash), and Modified Anderson (gray, dash-dot) mechanisms using measured pressure. Initial conditions are $T_5 = 1200 \text{ K}$ and $P_5 = 1.59 \text{ atm}$ .....	184
<b>Figure 15.</b> Comparison of measured $\text{NH}_2$ to Modified Anderson mechanism using measured P (dashed) and 1-D model (dotted). Initial conditions are $T_5 = 1136 \text{ K}$ and $P_5 = 1.63 \text{ atm}$ .....	185
<b>Figure 16.</b> Comparison of measured $\text{NH}_2$ to Modified Anderson mechanism using measured P (dashed), 1-D model (dotted), and constant U,V model (gray). Initial conditions are $T_5 = 1200 \text{ K}$ and $P_5 = 1.59 \text{ atm}$ . ....	185
<b>Figure 17.</b> Comparison of measured $\text{NH}_2$ to Modified Anderson mechanism using measured P (dashed) and 1-D model (dotted). Initial conditions are $T_5 = 1287 \text{ K}$ and $P_5 = 1.51 \text{ atm}$ .....	185
<b>Figure 18.</b> Comparison of measured OH to Modified Anderson mechanism using measured P (dashed) and 1-D model (dotted) (a) over the entire test time and (b) at early times. Initial conditions are $T_5 = 1156 \text{ K}$ and $P_5 = 1.66 \text{ atm}$ . ....	186
<b>Figure 19.</b> Comparison of measured OH to Modified Anderson mechanism using measured P (dashed), 1-D model (dotted), and constant U,V model (gray) (a) over the entire test time and (b) at early times. Initial conditions are $T_5 = 1180 \text{ K}$ and $P_5 = 1.59 \text{ atm}$ .....	186
<b>Figure 20.</b> Comparison of measured OH to Modified Anderson mechanism using measured P (dashed) and 1-D model (dotted) (a) over the entire test time and (b) at early times. Initial conditions are $T_5 = 1279 \text{ K}$ and $P_5 = 1.48 \text{ atm}$ . ....	187
<b>Figure 21.</b> Comparison of model predictions to morpholine/air ignition delay time measurements for stoichiometric mixtures around 15 and 25 atm respectively. Dashed lines: Simulation results using the previous mechanism [19]. Solid lines: Simulation results using the current mechanism. ....	191
<b>Figure 22.</b> Comparison of the measured reaction rates and theoretical study results for DMA + OH and EA + OH. ....	192
<b>Figure 23.</b> Measured dimethylamine ignition delay times in 4% $\text{O}_2$ /argon, scaled to $\Phi = 1$ and $P = 1.5 \text{ atm}$ , in comparison with the simulations with and without the changes recommended in Table 1.....	193
<b>Figure 24.</b> Comparison of the simulated OH time-histories, using the morpholine mechanism with and without the modifications in Table 2, to the experiment in stoichiometric mixture of 500 ppm DMA/ $\text{O}_2$ /argon at 1417 K and 2.2 atm.....	193
<b>Figure 25.</b> Measurements of ethylamine ignition delay times near 0.85, 1.35 and 2 atm in stoichiometric mixture of ethylamine/4% $\text{O}_2$ /Ar; simulation results utilize the Modified morpholine mechanism. ....	194
<b>Figure 26.</b> Measured $\text{NH}_2$ time-histories in 2000 ppm ethylamine/Ar mixtures; simulation results are based on the Modified morpholine mechanism.....	195
<b>Figure 27.</b> OH time-histories in 500 ppm ethylamine/0.2% $\text{O}_2$ /Ar mixtures: measurements (solid lines) and simulation results using the Modified morpholine mechanism (dash-dotted lines).....	195
<b>Figure 28.</b> Representative MMH N-N bond scission reaction rate constants in comparison with the previous studies.....	196
<b>Figure 29.</b> Pressure dependence of the measured $k$ at representative temperatures, in comparison with the theoretical study by Zhang et al. [9].....	197

<b>Table 1.</b> Summary of rate recommendations based on new $\text{NH}_2$ , $\text{NH}_3$ , and MMH measurements in MMH pyrolysis.....	181
<b>Table 2.</b> Summary of MMH mechanisms used in this work.....	181
<b>IV.2 Studies on MMH Reaction Mechanism (Law, Princeton University)</b> .....	200
<b>Figure 1.</b> Potential curves for $\text{NH}_2 + \text{CH}_3\text{NH}$ (solid line), and the front (dotted line) and back (dashed line) sides of $\text{CH}_3 + \text{NHNH}_2$ .....	202
<b>Figure 2.</b> Total potential correction curves for $\text{NH}_2 + \text{CH}_3\text{NH}$ (solid line), and the front (dotted line) and back (dashed line) sides of $\text{CH}_3 + \text{NHNH}_2$ .....	202
<b>Figure 3.</b> Comparison of the predicted total decomposition rate constant through $\text{MMH} \rightarrow \text{NH}_2 + \text{CH}_3\text{NH}$ and $\text{MMH} \rightarrow \text{CH}_3 + \text{NHNH}_2$ with previous experimental and simulation data for the overall thermal decomposition of MMH.....	204
<b>Figure 4.</b> Transition state geometry of abstracting central amine H of MMH optimized at the CASPT2(3e,3o)/aug-cc-pVTZ level, with mesh contour showing the active space (3e,3o) of the $\sigma$ , $\sigma^*$ orbital pair of the central amine hydrogen being abstracted and the OH radical orbital. (a) $\sigma$ orbital of central amine H, (b) $\sigma^*$ orbital of central amine H, and (c) $p$ orbital of the OH.....	205
<b>Figure 5.</b> Potential energy surface of the reactions of $\text{MMH} + \text{OH}$ calculated at the QCISD(T)/CBS//CASPT2/aug-cc-pVTZ level, except the geometry of OH radical was optimized at the UCCSD(T)/cc-pVTZ level and the geometries of radical products were optimized at the B3LYP/6-311++G(d,p) level.....	206
<b>Figure 6.</b> Theoretical rate coefficients for the abstraction of different H atoms in MMH by OH radical, with a total rate compared with the experimental data.....	207
<b>Figure 7.</b> Potential energy surface of decomposition of the $\text{CH}_3\text{N}\bullet\text{NH}_2$ , $\text{cis-CH}_3\text{NHN}\bullet\text{H}$ , $\text{trans-CH}_3\text{NHN}\bullet\text{H}$ , and $\text{C}\bullet\text{H}_2\text{NHNH}_2$ radicals calculated at the QCISD(T)/cc-pV $\infty$ Z//CASPT2/aug-cc-pVTZ level (data marked by blue) and at the QCISD(T)/cc-pV $\infty$ Z//B3LYP/6-311++G(d,p) level (data marked by black).....	208
<b>Figure 8.</b> The temperature dependence of rate coefficients in the dissociation channel of $\text{C}\bullet\text{H}_2\text{NHNH}_2 \rightarrow \text{CH}_2=\text{NH} + \text{NH}_2$ at pressures of $p = 0.01, 0.1, 1, 5, 10, 50, 100$ atm, and high pressure limit.....	209
<b>Figure 9.</b> A plot of $k/k_\infty$ as a function of pressure at $T = 300, 400, 500, 800, 1000, 1200, 1500, 1800$ , and $2500$ K, for the dissociation channel of $\text{C}\bullet\text{H}_2\text{NHNH}_2 \rightarrow \text{CH}_2=\text{NN} + \text{NH}_2$ .....	209
<b>Figure 10.</b> Theoretical rate coefficients of the dissociation channels of $\text{C}\bullet\text{H}_2\text{NHNH}_2 \rightarrow \text{CH}_2=\text{NH} + \text{NH}_2$ and $\text{C}\bullet\text{H}_2\text{NHNH}_2 \rightarrow \text{CH}_2=\text{NNH}_2 + \text{H}$ as functions of temperature and pressure.....	210
<b>Figure 11.</b> Theoretical rate coefficients for the dissociation of $\text{CH}_3\text{N}\bullet\text{NH}_2$ radical to three product channels of $\text{CH}_2=\text{NNH}_2 + \text{H}$ , $\text{transCH}_3\text{N}=\text{NH} + \text{H}$ , and $\text{cisCH}_3\text{N}=\text{NH} + \text{H}$ as functions of temperature and pressure.....	210
<b>Figure 12.</b> Potential energy surface of $\text{CH}_3\text{N}\bullet\text{NH}_2 + \text{OH}$ calculated by several <i>ab initio</i> methods.....	212
<b>Figure 13.</b> Modeling of experimental data of $\text{NH}_3$ product formation. Experimental condition: $991\text{K}, 1.84\text{atm}, 1\%\text{MMH}$ in Ar.....	214
<b>Figure 14.</b> Modeling of experimental data of MMH decomposition. Experimental condition: $1112\text{K}, 1.89\text{atm}, 1\%\text{MMH}$ in Ar.....	214

**Figure 15.** Modeling of experimental data of  $\text{NH}_3$  product formation. Experimental condition: 1207K, 1.73atm, 1%MMH in Ar.....215

### IV.3 Theoretical and Experimental Counterflow Ignition and Combustion Studies

(Williams, University of California at San Diego) .....216

**Figure 1.** Schematic illustration of the counterflow configuration. ....219

**Figure 2.** Photograph of a nonpremixed  $\text{CH}_4/\text{N}_2\text{--N}_2\text{O}/\text{O}_2/\text{N}_2$  flame. Strain rate,  $a_2 = 175 \text{ s}^{-1}$ . ....220

**Figure 3.** The mass fraction of nitrous oxide,  $Y_{\text{N}_2\text{O},2}$ , as a function of the strain rate at extinction,  $a_{2,e}$  at fixed values of  $Z_{\text{st}}$  and  $T_{\text{st}}$ . The fuel is methane. The symbols represent experimental data and the lines are predictions of the San Diego Mechanism. ....220

**Figure 4.** The mass fraction of nitrous oxide,  $Y_{\text{N}_2\text{O},2}$ , as a function of the strain rate at extinction,  $a_{2,e}$  at fixed values of  $Z_{\text{st}}$  and  $T_{\text{st}}$ . The fuel is ethane. The symbols represent experimental data and the lines are predictions of the San Diego Mechanism. ....221

**Figure 5.** Computed structure of  $\text{CH}_4/\text{N}_2\text{--N}_2\text{O}/\text{O}_2/\text{N}_2$  flames at fixed values of  $T_{\text{st}} = 2200\text{K}$ ,  $Z_{\text{st}} = 0.054$ , and  $Y_{\text{N}_2\text{O},2} = 0.102$ . The left side shows flame structure at strain rate of  $100 \text{ s}^{-1}$ , and the right side the flame structure at strain rate of  $180 \text{ s}^{-1}$ . The computations were done using the San Diego Mechanism.....221

**Figure 6.** Contribution of elementary reactions to rates of production of  $\text{CH}_4$ ,  $\text{N}_2\text{O}$ ,  $\text{O}_2$ , and  $\text{H}$ . Positive values indicate production and negative values consumption. The computations were done using the San Diego Mechanism at  $T_{\text{st}} = 2200$ ,  $Z_{\text{st}} = 0.054$ ,  $Y_{\text{N}_2\text{O},2} = 0.102$ , and  $a_2 = 100 \text{ s}^{-1}$ . ....223

**Figure 7.** Net rates of production of  $\text{CH}_4$ ,  $\text{N}_2\text{O}$ ,  $\text{O}_2$ , and  $\text{H}$ . The computations were done using the San Diego Mechanism at  $T_{\text{st}} = 2200$ ,  $Z_{\text{st}} = 0.054$ ,  $Y_{\text{N}_2\text{O},2} = 0.102$ , and  $a_2 = 100 \text{ s}^{-1}$ . ....223

**Figure 8.** Photograph of an Ignition Event of  $\text{C}_2\text{H}_6/\text{N}_2\text{--N}_2\text{O}/\text{O}_2/\text{N}_2$ ,  $Y_{\text{F},1} = 0.15$ ,  $T_1 = 298 \text{ K}$ ;  $Y_{\text{N}_2\text{O},2} = 0.4$ ,  $Y_{\text{O}_2,2} = 0.088$ ,  $T_2 = 1189\text{K}$ ; Strain rate  $a_2 = 350 \text{ s}^{-1}$ . ....225

**Figure 9.** Critical conditions of ignition  $\text{C}_2\text{H}_6/\text{N}_2\text{--Air}$ . Symbols represent experimental data and the line is the prediction obtained using the San Diego Mechanism. ....226

**Figure 10.** Critical conditions of ignition  $\text{C}_2\text{H}_6/\text{N}_2\text{--N}_2\text{O}/\text{O}_2/\text{N}_2$ . Symbols represent experimental data and the line is the prediction obtained using the San Diego Mechanism. ....226

**Figure 11.** Schematic illustration of the outer structure of the flame. ....227

**Figure 12.** The flame temperature  $T_p$  as a function of  $\chi_p^{-1}$  for various values of  $Y_{\text{N}_2\text{O}}$  .....228

**Figure 13.** The ratio  $a_q/a_{q,0}$  at extinction for various values of  $Y_{\text{N}_2\text{O}}$ . The symbols represent experimental data and the lines are predictions of the asymptotic analysis. ....228

**Figure 14.** The strain rate at extinction, as a function of mass fraction of hydrogen in the oxidizer stream,  $Y_{\text{H}_2,2}$ , at fixed  $Z_{\text{st}} = 0.055$ , and  $T_{\text{st}} = 2000 \text{ K}$ . The symbols represent experimental data and the curve represents predictions obtained using the San Diego Mechanism. ....230

**Figure 15.** The strain rate at extinction, as a function of mass fraction of hydrogen in the fuel stream,  $Y_{\text{H}_2,1}$ , at fixed  $Z_{\text{st}}$  and  $T_{\text{st}}$ . The symbols represent experimental data and the curve represents predictions obtained using the San Diego Mechanism. ....230



<b>Figure 16.</b> The normalized strain rate at extinction, as a function of $r$ at fixed $Z_{st} = 0.055$ , and $T_{st} = 2000$ K. The symbols represent experimental data and the curves represent predictions obtained using the San Diego Mechanism. ....	231
<b>Figure 17.</b> The strain rate at extinction, as a function of mass fraction of CO in the oxidizer stream, $Y_{CO,2}$ , and mass fraction of CO in the fuel stream, $Y_{CO,1}$ at fixed $Z_{st} = 0.055$ , and $T_{st} = 2000$ K. The symbols represent experimental data and the solid line and broken line are predictions obtained using the San Diego Mechanism. ....	232
<b>Figure 18.</b> The strain rate at extinction, as a function of mass fraction of CO in the oxidizer stream, $Y_{CO,2}$ , and mass fraction of CO in the fuel stream, $Y_{CO,1}$ at fixed $Z_{st} = 0.055$ , and $T_{st} = 2100$ K. The symbols represent experimental data and the solid line and broken line are predictions obtained using the San Diego Mechanism. ....	232
<b>Figure 19.</b> The predicted normalized strain rate at extinction, as a function of $r$ at fixed $Z_{st} = 0.3$ , and $T_{st} = 2000$ K, for CO addition to the fuel side and to the oxidizer side. Predictions were made using the San Diego Mechanism. ....	233
<b>V. MODELING, SIMULATION, AND DIAGNOSTICS OF OVERALL PROCESSES</b> ..	234
<b>V.1 High-Fidelity Modeling and Simulation of Spray and Combustion of Gelled Hypergolic Propellants (Yang, Georgia Institute of Technology)</b> .....	234
<b>Figure 1.</b> Combustion of impinging jets of gelled hypergolic propellants. ....	235
<b>Figure 2.</b> Schematic of doublet impinging liquid jets and resultant sheet. ....	239
<b>Figure 3.</b> Impinging-jet flow patterns of glycerin-water solution obtained from simulations. $D = 400 \mu\text{m}$ , $2\alpha = 60^\circ$ , (a) liquid chain ( $u_j = 2.2$ m/s, $We=27.5$ , $Re=1000$ ); (b) closed rim ( $u_j = 3.3$ m/s, $We=58.8$ , $Re=40.4$ ); (c) open rim ( $u_j = 5.3$ m/s, $We=152$ , $Re=294$ ); (d) unstable rim ( $u_j = 7.9$ m/s, $We=343.5$ , $Re=3536$ ); (e) impact wave ( $u_j = 11.2$ m/s, $We=687$ , $Re=5000$ ). ....	240
<b>Figure 4.</b> Spatial distribution of flow-field predicted by level-9 simulation: (a) front view; (b) side view. Various regions in impinging-jet atomization dominated by impact wave. A: jet impingement region; B: flapping sheet region; C: ligaments region; D: droplet region. (water jets, $D = 635 \mu\text{m}$ , $u_j = 18.5$ m/s, $2\alpha = 60^\circ$ , $We = 2987$ , $Re = 11724$ ). ....	241
<b>Figure 5.</b> Detailed image showing the process of ligament formation with interface colored by $z$ coordinate. (a) oblique view; (b) side view. (glycerine-water jets, $D = 400 \mu\text{m}$ , $u_j = 11.2$ m/s, $2\alpha = 60^\circ$ , $We = 687$ , $Re = 5000$ ). ....	242
<b>Figure 6.</b> Variation of average drag coefficient with Weber number. ....	243
<b>Figure 7.</b> Comparison of flow patterns under different Weber numbers. (Images in left column obtained from experiments by Fakhri (2009), right column depicts present simulation results. The Weber numbers for the three cases from top to bottom are 1549, 6195 and 12390, respectively). ....	243
<b>Figure 8.</b> Development of flow pattern under $We = 1549$ (interface colored by $y$ coordinate). ....	244
<b>Figure 9.</b> Development of flow pattern under $We = 6195$ (interface colored by $y$ coordinate). ....	245
<b>Figure 10.</b> Development of flow pattern under $We = 12390$ (interface colored by $y$ coordinate). ....	246
<b>Figure 11.</b> Locking-on of Strouhal number. ....	246
<b>Figure 12.</b> Distribution of shear rate on the interface under different Weber numbers. (a) $We=1549$ ; (b) $We=6195$ ; (c) $We=12390$ . ....	247

<b>Figure 13.</b> Computational Setup. ....	248
<b>Figure 14.</b> Comparison of present results for $We = 24$ , $\rho_l / \rho_g = 8.29$ with results for $We = 18.7$ , $\rho_l / \rho_g = 10$ . ....	249
<b>Figure 15.</b> Perspective view of the temporal evolution of droplet structure for bag breakup mechanism. $We = 80$ , $Re = 13951$ , $\rho_l / \rho_g = 8.29$ , $t = T^*U/D$ . ....	250
<b>Figure 16.</b> Bottom view of the temporal evolution of droplet structure for bag breakup mechanism. $We = 80$ , $Re = 13951$ , $\rho_l / \rho_g = 8.29$ , $t = T^*U/D$ . ....	250
<b>Figure 17.</b> Time evolution of momentum and surface energy for $We = 80$ . ....	251
<b>Figure 18.</b> Time history of drag coefficient for bag breakup. ....	251
<b>Figure 19.</b> Multimode breakup mechanism. $We = 365$ , $Re = 29805$ , $\rho_l / \rho_g = 8.29$ , $t = T^*U/D$ . ....	252
<b>Figure 20.</b> Time evolution of momentum and surface energy for $We = 365$ . ....	253
<b>Figure 21.</b> Time history of drag coefficient for multimode breakup. ....	253
<b>Figure 22.</b> Multimode breakup mechanism (bottom view). $We = 365$ , $Re = 29805$ , $\rho_l / \rho_g = 8.29$ , $t = T^*U/D$ . ....	254
<b>Figure 23.</b> Shear breakup mechanism. $We = 1112$ , $Re = 52000$ , $\rho_l / \rho_g = 8.29$ , $t = T^*U/D$ . ....	255
<b>Figure 24.</b> Bottom view of the shear breakup mechanism. $We = 1112$ , $Re = 52000$ , $\rho_l / \rho_g = 8.29$ , $t = T^*U/D$ . ....	255
<b>Figure 25.</b> Time evolution of momentum and surface energy for $We = 1112$ . ....	256
<b>Figure 26.</b> Evolution of coefficient of drag with time for $We = 1112$ . ....	256
<b>Figure 27.</b> Variation of average drag coefficient with Weber number. ....	257
<b>Figure 28.</b> Generalized regime diagram. ....	258
<b>Figure 29.</b> PDF of child droplet diameter for Weber numbers of 365, 537, 636, 742, 858 and 981. ....	259
<b>Figure 30.</b> Sauter mean diameter, $d_{32}$ , correlated using an analytical model. ....	260
<b>Figure 31.</b> Rendered results of collision of unequal-sized droplets. ....	261
<b>Figure 32.</b> Evolution of shape parameters during bouncing process. Water droplets in air at 1 atm: (a) $We=1$ , $Re=85.2$ , $B=0$ , $D_s=100 \mu\text{m}$ , $U=0.85 \text{ m/s}$ ; (b) $We=10$ , $Re=269.4$ , $B=0$ , $D_s=100 \mu\text{m}$ , $U=2.69 \text{ m/s}$ . ....	262
<b>Figure 33.</b> Liquid phase mixing during head-on collision for $We = 50$ and $100$ with diameter ratio of (a) $0.5$ and (b) $0.25$ . ....	263
<b>Figure 34.</b> Rendered results for simulation of head-on and off-center bouncing outcome. Conditions: (a) Tetradecane droplets in 1 atm. Nitrogen, $We=8.6$ , $Re=105.9$ , $B=0$ , $D=306 \mu\text{m}$ , $U_{\text{relative}}=0.97 \text{ m/s}$ ; (b) Tetradecane droplets in 1 atm. Nitrogen, $We=48.8$ , $Re=260.3$ , $B=0.9$ , $D=306 \mu\text{m}$ , $U_{\text{relative}}=2.31 \text{ m/s}$ . ....	264
<b>Figure 35.</b> Comparison of unequal reflexive separation with experimental images. Conditions: water droplets with diameter ratio of $0.50$ in 1 atm. air, $We_{\text{small}} = 102$ , $B=0$ , $D_{\text{larger}}=400 \mu\text{m}$ , $U_{\text{relative}}=6.10 \text{ m/s}$ (Ashgriz & Poo 1990). ....	265
<b>Figure 36.</b> Results and modeling of mass transfer ratio under different diameter ratios: (a) results under diameter ratio of $0.5$ ; (b) results under diameter ratio of $0.25$ ; (c) modeling under diameter ratio of $0.5$ ; (d) modeling under diameter ratio of $0.25$ . ....	266

<b>Figure 37.</b> Non-Newtonian droplet breakup - $We = 2411$ . Perspective view of temporal evolutions of 3D droplet structure in non-dimensional time. Non-dimensional time, $t = T*U/D$ .	267
<b>Figure 38.</b> Beads-on-a-string structure during the breakup of non-Newtonian liquid drops.	267
<b>Figure 39.</b> Helical instability, liquid drop ejection sites and formation of primary and satellite droplets during the breakup of non-Newtonian liquid drops.	268
<b>Table 1.</b> Maximum value of drag coefficient as a function of Weber number.	257
<b>Table 2.</b> Correlation coefficients $\mu$ and $\sigma$ for a range of Weber numbers.	259
<b>V.2 Impinging Jet Experimentation (Risha, Penn State – Altoona)</b>	271
<b>Figure 1.</b> Ignition delays from drop tests and rocket engine firings of TMEDA/DMAZ blends. <sup>14</sup>	273
<b>Figure 2.</b> Schematic diagram of the injector configuration	274
<b>Figure 3.</b> Effect of oxidizer jet diameter on momentum ratio and equivalence ratio	275
<b>Figure 4.</b> Schematic and photographs of the injector assembly	276
<b>Figure 5.</b> Schematic of the injector assembly purge passage	276
<b>Figure 6.</b> Impinging water jets: (a) impingement angle of $60^\circ$ , (b) fan created by jet impingement.	277
<b>Figure 7.</b> Captured images of single and impinging injectors using water as the liquid.	278
<b>Figure 8.</b> Images of the effect of water type of fan characteristics using Carbopol gels.	279
<b>Figure 9.</b> High-speed images of the fan and impingement gel streams at 100 cc/min for each stream.	280
<b>Figure 10.</b> High-speed images of the fan and impingement gel streams at 300 cc/min for each stream.	280
<b>Figure 11.</b> High-speed images of the fan and impingement gel streams at 500 cc/min for each stream.	281
<b>Figure 12.</b> Sequence of images of the gel stream evolution at a flow rate of 100 cc/min.	281
<b>Figure 13.</b> Sequence of images of the gel stream evolution at a flow rate of 300 cc/min.	282
<b>Figure 14.</b> Sequence of images of the gel stream evolution at a flow rate of 500 cc/min.	282
<b>Figure 15.</b> Series of images of jet atomization for flow rates ranging from 100 to 500 cc/min.	283
<b>Figure 16.</b> Photograph of the volumetric proportions of the gelling agent (Cab-O-sil) and the liquid.	284
<b>Figure 17.</b> Drop test results of gelled TMEDA with WFNA and RFNA	284
<b>Figure 18.</b> Images of various gelled reactants including TMEDA (at two different Cab-O-sil wt%) and WFNA.	285
<b>Figure 19.</b> Schematic diagram of hypergolic experiment.	286
<b>Figure 20.</b> Diagram of the curved impingement wall configuration.	287
<b>Figure 21.</b> Photographs of the filling/evacuation station configuration during reactant filling and air evacuating processes.	288
<b>Figure 22.</b> Series of captured images of the impingement and ignition processes of TMEDA and WFNA.	289
<b>Figure 23.</b> Ignition delay as a function of total flow rate.	290
<b>Figure 24.</b> Influence of oxidizer type on ignition delay for various flow conditions	291
<b>Figure 25.</b> Effect of equivalence ratio and momentum ratio on ignition delay.	292
<b>Figure 26.</b> Momentum Ratio versus ignition delay for TMEDA/WFNA reactants.	292

<b>Figure 27.</b> Influence of momentum and equivalence ratios on ignition delay.....	293
<b>Figure 28.</b> Ignition delay for both non-gelled and gelled reactants as a function of reactant flow rate. ....	293
<b>Figure 29.</b> Ignition delay for both non-gelled and gelled reactants as a function of reactant flow lead time. ....	294
<b>Figure 30.</b> Effect of oxidizer and fuel lead time on ignition delay .....	294
<b>Figure 31.</b> Effect of oxidizer and fuel lead time on ignition delay. ....	295
<b>Figure 32.</b> Ignition delay as a function of L/D ratio for one flow rate.....	295
<b>Figure 33.</b> Ignition delays for TMEDA and DMAZ as a function of fuel flow rate.....	296
<b>Figure 34.</b> Effect of DMAZ additive in the TMEDA fuel on ignition delay.....	297
<b>Figure 35.</b> Ignition delay of DMAZ additive superimposed on the data for engine tests by Stevenson. <sup>14</sup> .....	297
<b>Figure 36.</b> Effect of curved surface on ignition delay.....	298
<b>Figure 37.</b> Captured high speed images of a typical TMEDA and WFNA ignition event: (a) without curved quartz wall; (b) with curved quartz wall tangent to the nozzle exit.....	298
<b>Table 1.</b> Properties of selected fuels and oxidizers. ....	287

## INTRODUCTION

Gelled hypergolic propellants (GHPs) provide many unique advantages that no other systems can deliver, and they represent a technology critical to DoD's Future Combat Systems for compact munitions. These benefits include improved safety in storage and handling; better compliance with insensitive munitions (IM) requirements; lower toxicity and fire hazards; reduced leakage, spillage, and slosh problems; and higher energy density (with reactive gellants loaded). In addition, the inherent thrust modulation capability provides excellent application flexibility for smart tactical missiles, divert and attitude-control systems, launch-vehicle boost and upper-stage engines, and even air breathing propulsion systems. Extensive worldwide efforts have been made in the past 35 years to formulate and process GHPs; identify potential applications; characterize the rheological, flow, injection, and combustion properties; and develop engines for laboratory and flight tests. Much of the existing knowledge, however, is empirically based and established through time-consuming and costly processes of trial and error. The major obstacles arose from the difficulties in conducting experiments and theoretical studies at scales required to resolve local chemical and transport processes that dictate the global behavior of ignition and combustion in an engine. The extreme working conditions of severe toxicity and high pressure and temperature, along with complications associated with gelled materials, pose other serious challenges. In addition, the effects of intrinsic and constitutive properties of GHPs on the thermophysical, ignition, and combustion characteristics are not well understood.

The overall objective of the research program was to understand the flow, ignition and combustion behavior of two impinging streams of hypergolic liquids. The specific objectives include:

- examine liquid stream break-up, droplet formation, and atomization,
- study interfacial processes leading to ignition and complete combustion,
- determine the role of gellants, and
- enhance knowledge base on GHP spray and combustion technologies.

As a result, the following five task areas were defined:

1. thermophysical, constitutive, and chemical properties of GHPs, and effects of gelling,
2. injection, atomization, spray formation, droplet interaction, and mixing of GHPs,
3. hypergolic-propellant interfacial fluid transport and chemical reactions,
4. detailed and reduced reaction mechanisms for ignition and combustion of GHPs, and
5. modeling and simulation of multiphase, chemically reacting flows for GHPs, and injector and subscale engine testing, diagnostics, and evaluation.

These five task areas and the associated investigators are shown in Fig. 1. Collaboration between the investigators occurred within each task area as well as across the task areas.

The baseline liquid propellants were neat and gelled monomethylhydrazine (MMH) and inhibited red fuming nitric acid (IRFNA). In the gas-phase, reactions between MMH and nitrogen dioxide and its dimers were also examined experimentally and computationally. The chemical kinetics of many other relevant product molecules was also examined in the gas phase. As the program evolved, new gellant materials and fuels were also considered as shown in Fig. 2, in order to maximize the benefits of the research to the Army.

In this report, a summary of major findings by each investigator are presented. These summaries are grouped according to the task areas, in order to give the reader a focus of his or her

examination of this report. At the end of the report, a list of publications is included and these publications contains additional details of the research findings, as well as contact information of the various investigators..

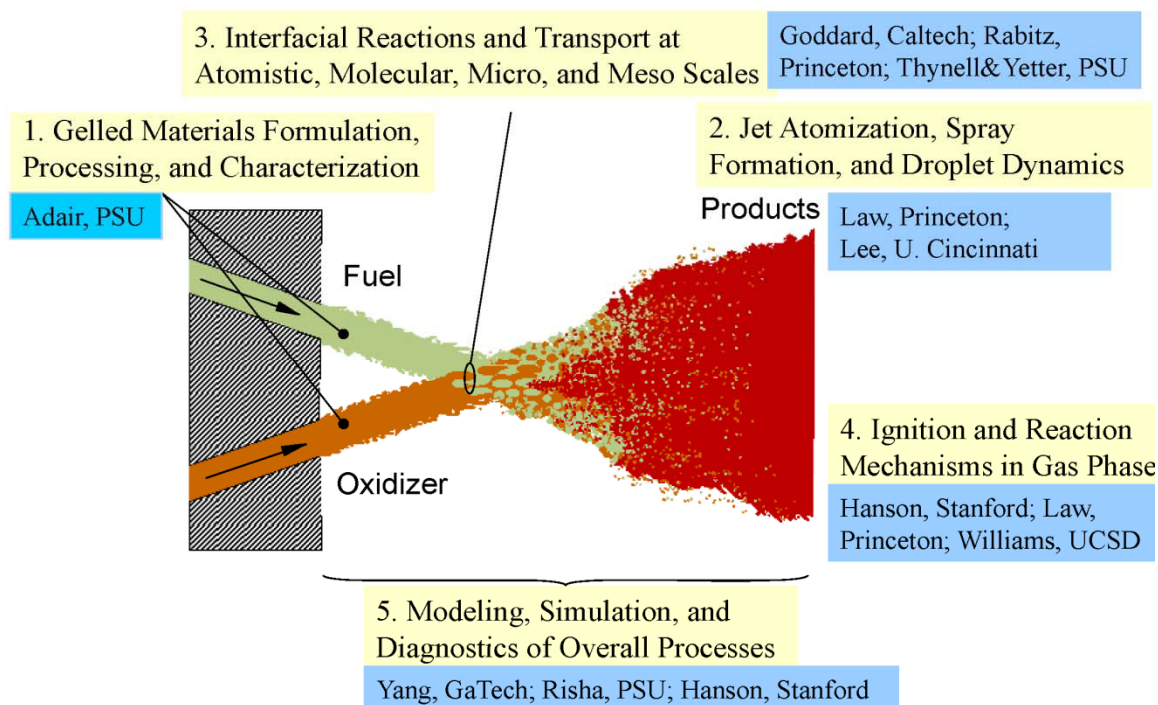


Figure 1. Summary of the defined task areas and associated investigators.

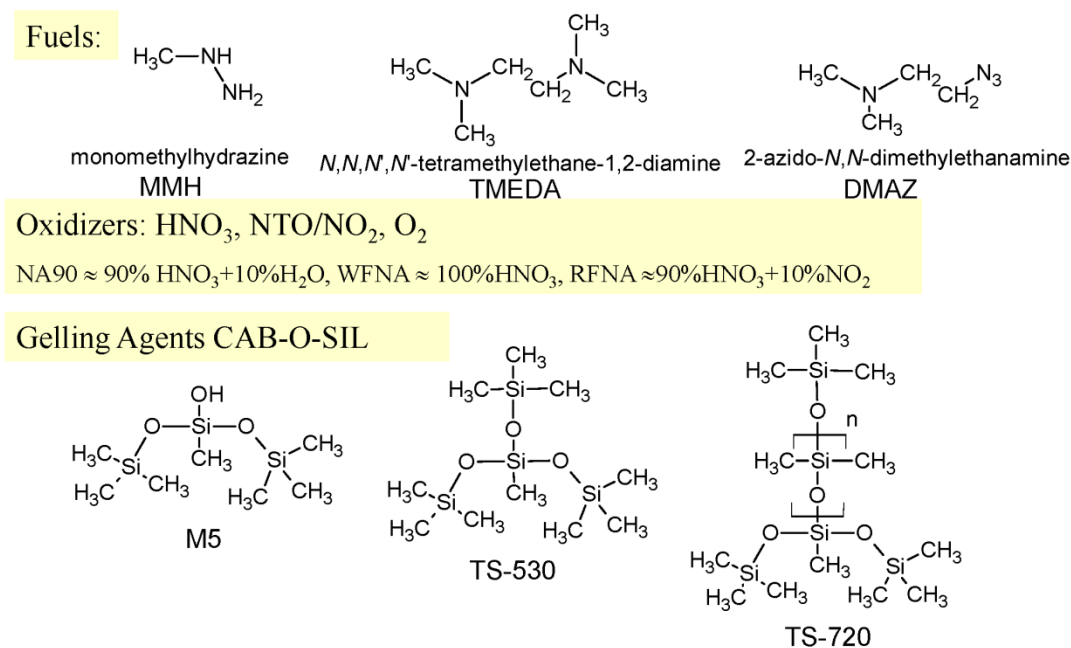


Figure 2. Summary of some of the fuels, oxidizers, and gelling agents considered in the research effort.

## **I. Gelled Materials Formulation, Processing, and Characterization (Adair, Penn State)**

### **1. Abstract**

The objective of this task is to provide characterization support and develop methodologies to measure the intrinsic and constitutive properties of gelled propellants. A secondary goal was to provide a hierarchy of particulates based on our prior work in developing particulate synthetic schemes for ceramic and metal colloids from the nanoscale to submicron scale. This activity is thus central to the overarching goal of the MURI project to develop a fundamental understanding of the processes and mechanisms that control droplet formation, droplet collision and mixing, ignition, and energy release in gelled hypergolic propellants. Another aspect of the project was to develop cost-effective viscosity and surface tension determinations as a function of temperature up to 500 K. In this latter objective, partial success was achieved. The low cost viscometers designed from a generation 1 system through a gen 4 system improved but significant experimental error was present even in the gen 4 system. In contrast, the development of a high temperature method to determine surface tension was more successful.

### **2. Background**

The approaches used in this subtask included the following:

- Preparation of model hypergolic fluids
- Preparation of hypergolic fluids with a variety of material systems
- Gelled propellants properties to be determined for intrinsic and constitutive characteristics
- Achieve property measurements under the high pressure (6-8MPa, 1ksi, modified to less than 200 psi) and temperature (up to 500°K)

A commercially available colloidal silica (Cab-O-Sil, Grade EH-5, Cabot Corp.) was used to prepare model gelled fuels, mostly in tetraethylene diamine (TMEDA), but in preliminary development, also in hydrazine, monomethyl hydrazine (MMH), 2-diethylaminoethylazide (DMAZ). Both the MMH and DMAZ were difficult to process and efforts associated with these fuels were abandoned in early stages of the project. It was anticipated that silane coupling agents would be necessary to wet the colloidal silica, but this was not required for any of the fuels. Several gel formulations were prepared for each fuel and flow behavior was determined as a function of solid content by qualitative observation. The rheological behavior for the silica in the fuels was Newtonian at low solid content but became shearing within the regime where gelation took place. Therefore, a cup and cone viscometer was used to determine shear stress-shear rate behavior and viscosity as a function of shear rate. Several silica-TMEDA gels were also provided to other members of the Penn State MURI team for analyses in high shear rate systems.

Several other commercial systems were also evaluated including an aluminum particulate material by Yetter at Penn State. In prior research, we developed a nanoscale magnesium () that was further investigated in the current project. The synthetic scheme was originally reported by Rieke (Rieke 1981). All syntheses were performed in our Argon dry box with control over both humidity and oxygen. The Rieke synthesis uses magnesium chloride, dissolved in tetrahydrofuran (THF) with naphthalene present and lithium metal added as flakes to reduce the magnesium to metallic Mg nanoparticles. The Mg nanoparticles were evaluated for properties to use as an aid in fuels. Unfortunately, the as-synthesized nanoparticles were highly agglomerated and could not be used to create gelled fuels.

The major objectives of the project were to develop measurement systems to determine constitutive properties of hypergolic fluids originally at high pressures (6-8MPa, 1ksi) and temperature (up to 1,273 K) in the original goals. More pragmatic goals became 0.2ksi (1 to 2MPa) and 500 K early in the program. Another goal was to develop measurement devices that were relatively inexpensive and transportable. The two major properties to be determined were high shear rate (greater than 500 s<sup>-1</sup>) viscosity and surface tension for the hypergolic fluids. For viscosity determinations, a capillary viscometer design was developed through 4 generations, but using water as a model material, there are a consistently larger values (20 to 80 percent greater than those reported in the literature. One of the problems with the small diameter high performance liquid chromatography tubing utilized to keep cost low is the flexibility in the tubing even at relatively modest driving pressures of less than 25 psi. This is a fatal flaw in the basic design.

In contrast, the development of a high temperature dynamic tensiometer using a commercial instrument tensiometer acquired in the 1990s (M&H Technologies, Inc. SensaDyne Instrument Division, <http://www.sensadyne.com/tensiometer-accuracy-1>, Flagstaff, AZ) proceeded with fewer complications. The dynamic tensiometer method uses a two capillary droppers, originally designed with glass, but modified to use 316 L stainless steel in the present project, combined with piezoelectric transducers that measure the pressure required for a test gas (Argon was used during this project) to generate a bubble of a prescribed diameter (Christian 1995). Thus, dynamic tensiometry measures the pressure per unit area directly related to the surface tension for the liquid-vapor interface,  $\gamma_{lv}$ . We adapted the pressure vessel systems described earlier for a system suitable for the fuel (Christian 1995).

### 3. Experimental Facilities and Algorithms

Most of the research took place in the Adair labs at Penn State housed in about 1,300 sq. ft. in the Steidle Building on the Penn State campus. The Adair Lab has an argon dry box with a high purity argon with both humidity and oxygen levels monitored.

The rheological properties were determined using a capillary viscometer described by Adamson (Adamson, 1990). Inert gas (argon) was used to drive the fuels at high shear rates through the capillary rheometer. The flow rate as a function of pressure drop was used to determine the viscosity as a function of shear rate. The relationship for flow rate as a function of pressure drop is given by the Hagen-Poiseuille relationship (Adamson 1990):

$$\eta = \left( \frac{\Delta P}{l} \right) \left( \frac{\pi r^4}{8Q} \right) \quad \text{Eq. 1}$$

where  $\Delta P$  is the measured pressure drop,  $l$  is the tubing length,  $r$  is the inner radius of the capillary, and  $Q$  is the volumetric flow rate. The shear rate is given by:

$$\dot{\gamma} = \frac{du}{dr} = \frac{\Delta P}{2\mu L} r = \frac{4Q}{\pi r^3} \quad \text{Eq. 2}$$

where  $\mu$  is dynamic viscosity  $\eta/\rho$  where  $\rho$  is density. Finally, the Reynolds Number is given by,

$$\text{Re} = \left( \frac{\rho v D}{\eta} \right) \quad \text{Eq. 3}$$



where  $u$  is the linear fluid flow rate and  $D$  is capillary diameter. All units for Eqs. 1 through 3 are in mks. Data were recorded, analyzed and plotted using MS Excel software.

The SensaDyne dynamic tensiometer interfaced with a Windows computer with software was used to determine surface tension. The SensaDyne software developed for modest temperatures was adapted to determine the surface tension of the TMEDA fuel at elevated temperatures. We utilized 316L stainless steel tubing with 1/8 in. ID and 3/16 in. ID rather than  $\text{Si}_3\text{N}_4$  as originally proposed. Stainless steel was both less expensive and more durable than the ceramic material.

Other facilities that were used for nanoparticle characterization were located in the Materials Characterization Lab housed in the Millennium Science Complex on the Penn State campus. Particle size distribution in the surrogate systems was determined via light scattering using a Malvern Zetasizer S system which can perform either static light scattering or dynamic light scattering. Particle size and morphology were also determined using a field emission scanning electron microscopy (FEI). In addition, the user-facility Particulate Characterization Laboratory has an array of additional characterization capabilities including specific surface area, density, and surface potential analyses that were used in some of the analyses.

#### 4. Major Findings

The major findings include verification to prepare surrogate gel systems with colloidal silica, the preparation of air stable nano-Mg, development of a capillary rheometer, and measurement of surface tension for TMEDA fuel to almost 120°C (390K). Limitations include agglomerates in the as-synthesized nanoscale magnesium that prevented gel formation, errors in the capillary viscometer viscosity determinations particularly at low (20°C) temperatures, and determination of surface tension to the target temperature at 230°C (500K). We have preliminary constitutive equations for calibrated viscosity and surface tension over these limited ranges. Both the capillary viscometer and the dynamic tensiometer have been moved to the High Pressure Combustion Lab that permits a better controlled environment for the higher pressure and temperature measurements. We intend to continue efforts with our collaborators to expand the range of the current measurements for TMEDA and other fuels. The provisional constitutive equations are summarized in Table 1 with the specifics associated the determinations provided in subsequent sections.

Table 1. Provisional virial coefficients for viscosity and surface tension as a function of temperature in the relationship,  $\eta$  or  $\gamma_{lv} = ax^3 + bx^2 + cx + d$ , where  $x$  is temperature in °C.

Liquid	High Shear Viscosity (cP)				Surface Tension (mN/m)			
	a	b	c	d	a	b	c	d
Water (20 to 80°C)	9.0E-07	6.0E-05	7.0E-03	0.0326	Not measured			
TMEDA (20 to 40°C)	0	8.0E-04	7.02E-02	2.352	0	0	-1.1E-01	23.85

Elaboration on both the major findings and limitations we established for our approaches follow.

##### 4.1 Preparation of model hypergolic fluids

A summary of the activities on model hypergolic fluids is given in Table 2 and Figures 1 through 2. The fuels, MMH, TMEDA, and DMAZ all displayed weight percent ranges where gelation,

defined as a shear thinning material, were present at relatively low solid weight percent,

## Qualitative Gel Evaluation

- MMH  $5% < \text{Gel} < 6\%$
- TMEDA  $6% < \text{Gel} < 7\%$
- DMAZ  $5% < \text{Gel} < 6\%$
- Hydrazine  $10% < \text{Gel}$

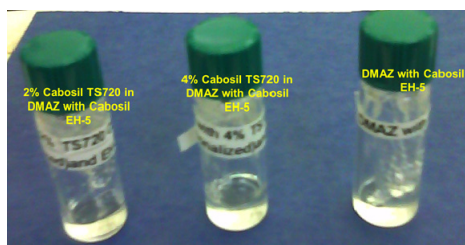


Figure 1. Top: Summary of gelation ranges for each of the fuels with weight percent of commercial silica added to each fuel also shown in detail in Table 1. Bottom: representative samples for silica in DMAZ; the 2 and 4 weight percent silica samples were Newtonian while the right hand sample was a gel.

summarized in Figure 1. In contrast, the as-received silica in hydrazine had no gelation weight percent up to 10 weight percent solid. This suggests that the acidic surface groups for silica, silanols,  $\equiv\text{SiOH}$ , can readily associate with the nitrogen associated with the amine groups in the hydrazine, but not with the sterically shielded nitrogen –containing groups associated with MMH, TMEDA, and DMAZ.

However, the weight percent required for gelation of the nanoscale silica significant Cab-O-Sil silica is composed of highly agglomerated approximately 6nm amorphous silica particles with a fractal shape, a great deal of both pearls on a string structure as well as multiple branch points. Thus, the free volume for each agglomerate in a Cab-O-Sil powder is quite large, leading to a magnifying effect for the solid loading with the highly branched, large free volume agglomerates. However, up to the ‘percolation’ weight percent where a continuous network of agglomerates are associated, the relatively low solids content gives a Newtonian flow behavior, that is, where the viscosity is independent of the shear rate of the fuel. The Newtonian behavior is presented in Figure 2 (Top) for 3 weight percent silica in TMEDA where there is modest effects at very low shear rates and virtually no hysteresis in the shear stress-shear rate behavior. In contrast, within the gelation range for the silica in DMAZ. Furthermore, specifically for a 6

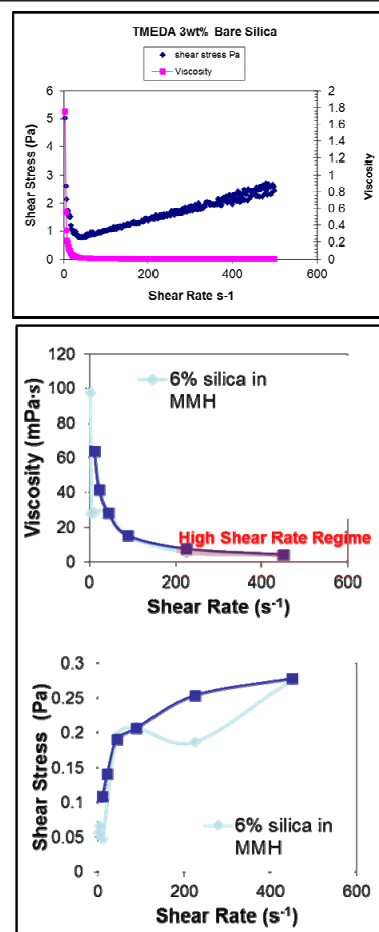


Figure 2. Top: Shear stress and viscosity as a function of shear rate for 3 weight percent silica in TMEDA. Middle: Viscosity as a function of shear rate for 6 weight percent silica in MMH, and; Bottom: Shear stress for 6 weight percent silica in MMH.

weight percent silica content in DMAZ, the rheological behavior shown in Figure 2 (Middle and Bottom) is shear thinning with viscosity decreasing as a function of shear rate and the shear stress-shear rate curve displaying hysteresis as shear rate is first decreased and increased, the shear rate values are different. The hysteresis behavior is the subject of a great deal of research, but one can conclude that the presence of hysteresis is due to adhesion among the flow units in the suspension, specifically the silica agglomerates adhering to one another leading to long range structure formation and breakdown over the course of the decreasing – and then increasing shear rate cycle during rheological determinations.

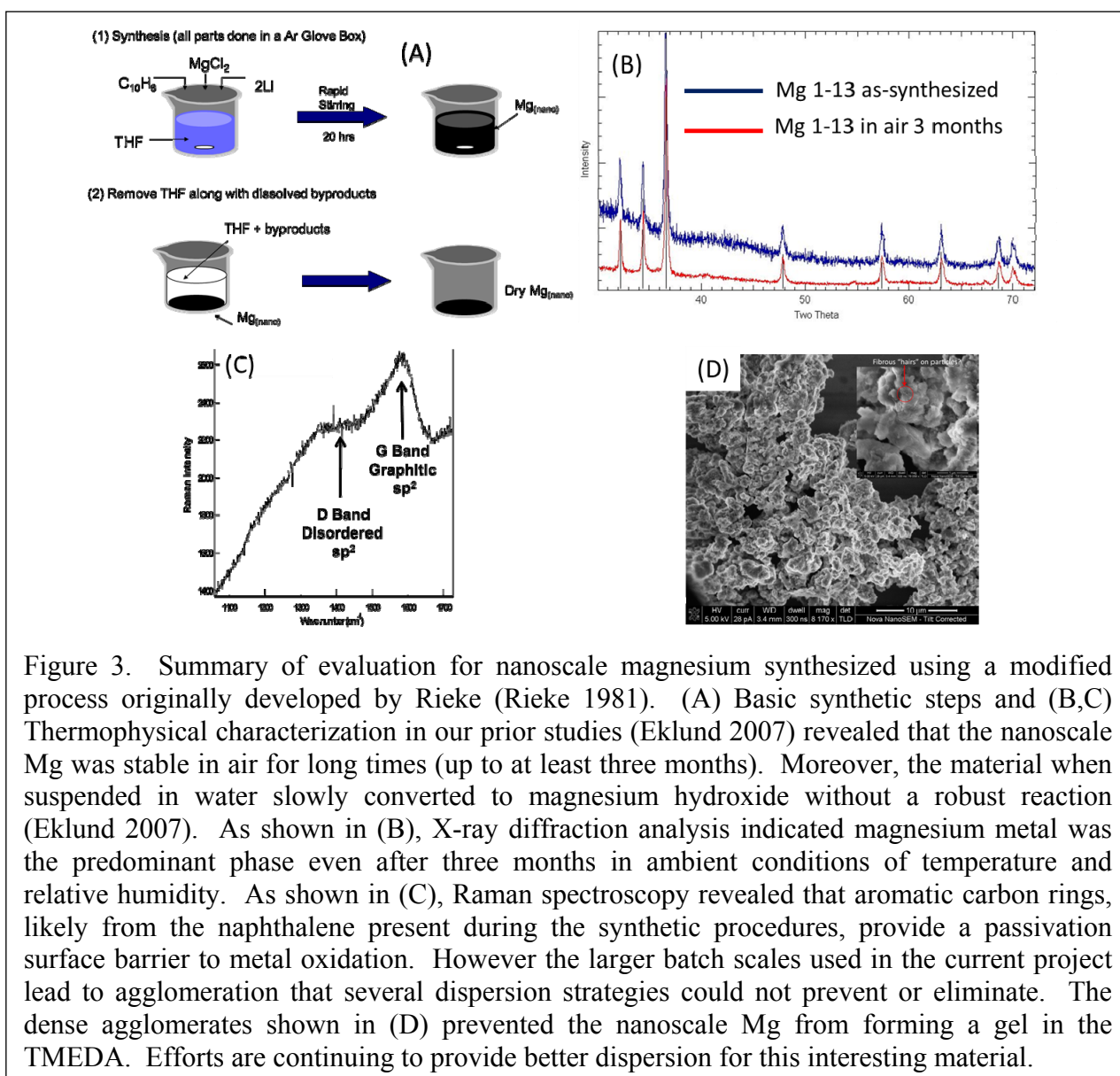
Selected silica-TMEDA gels were provided to the other Penn State team members, but proved too viscous for the flow conditions in the experiments.

Table 2. Range of gelation and solidification for the weight percent of as-received Cab-O-Sil nanoscale silica in MMH, TMEDA, DMAZ, and hydrazine. Figure summarizes gelation ranges for each of the fuel.

Solvent	Silica Content	Gel
MMH	5%	No
MMH	6%	Yes
MMH	7%	Yes
MMH	10%	Solid
TMEDA	5%	No
TMEDA	6%	No
TMEDA	7%	Yes
TMEDA	10%	Solid
DMAZ	5%	No
DMAZ	6%	Yes
DMAZ	7%	Yes
DMAZ	10%	Solid
Hydrazine	5%	No
Hydrazine	6%	No
Hydrazine	7%	No
Hydrazine	10%	No

## 4.2 Preparation of hypergolic fluids with a variety of material systems

Two materials were evaluated for effects on hypergolic fluid performance, a nanoscale magnesium prepared in our labs using a synthetic process first reported by Rieke et al. (Rieke 1981) and a commercial nanoscale aluminum obtained by Yetter as part of his research. The latter results on nanoscale Al are thus reported by Dr. Yetter. Here we will focus on the nanoscale Mg. The nanoMg powder was introduced at the end of the third year of the project. The material had been developed in association with palladium coatings in an earlier industrially supported project on hydrogen storage (Eklund 2007). Most of the effort on this material did not focus on the state of agglomeration, but on the thermophysical stability of the material as partially summarized in Figure 3. The nanoscale Mg prepared by the wet chemical method summarized in Figure 3(A) was evaluated in our prior work for thermophysical stability. For example the dry powder could be stored in an ambient environment (air and a variable relative humidity and lab temperature) for up to three months with converting to a reduced form as



shown by the X-ray diffraction patterns in Figure 3(B). Raman spectroscopy revealed, Figure 3(C), disordered, D-band, and G-band  $sp^2$  carbon, associated with graphitic carbon were present in the material. We hypothesized that the naphthalene used in the Rieke synthetic process lead to condensed graphitic coatings that passivated the nanoscale Mg particles against oxidation. Furthermore, it was observed that the nanoscale Mg introduced directly into water required 8 to 12 hours to oxidize to magnesium hydroxide and without a robust reaction.

Efforts to disperse the nanoscale Mg have not been successful to date. It is hypothesized that during the formation of the graphitic surface coatings that passivate the nanoscale Mg also are likely cross-linked leading to the persistent agglomeration. However, the primary particle size, shown in Figure 3(D), the submicron range are attractive for hypergolic fluids. Furthermore, analysis of the XRD patterns in Figure 3(B) indicates that the primary crystallite size is 20 to 30nm. Dispersion methods have been limited to what we could do in a TMEDA environment, but efforts are continuing in other liquid environments. The metallic nature of these particulates mean that our chemically aided milling approach cannot be used because of the greater ductility associated with the nanoscale Mg as well as the likelihood that milling will compromise the passivation layer also leading to a much more reactive nanoscale metal particulate to handle. Therefore, we evaluated the charge on the surface of the nanoscale Mg in TMEDA and found a highly negative surface potential (ZETAPALS, Brookhaven Instruments) at -56mV. We also measured the charge in a 70 volume percent ethanol-30 volume percent water mixture and established that  $\sim$ -30mV develops on the novel surface of the Rieke process synthesized material. These findings suggest that manipulation of the surface potential during synthesis could lead to less agglomerated material. We are pursuing this approach as well as additional funding through other venues to further develop this dispersion approach.

- Gelled propellants properties to be determined for intrinsic and constitutive characteristics
- Achieve property measurements under the high pressure (6-8MPa, 1ksi, modified to less than 200 psi) and temperature (up to 500K)

These two goals have been joined as inevitably the determination of constitutive relationships and measurements at high pressure and temperature inseparable. As noted above, efforts to determine both the viscosity and surface tension were not entirely successful, particularly the former property with the capillary rheometer designed as part of the project. However, the surface tension measurements are unique to these classes of reactive materials and efforts will continue through other funding to more fully develop this capability to both higher and lower temperatures. Also as noted above, both the capillary rheometer and the dynamic tensiometer have been moved to Penn State's High Pressure Combustion Lab under the direction of Dr. Yetter. This venue permits evaluation of the measurements at higher pressures and temperatures where an unexpected and abrupt high pressure and/or high temperature event can be much more easily contained.

Much of the effort has been directed toward developing a relatively inexpensive and readily deployable capillary rheometer for high pressure/high temperature/high shear rate experiments. The approach is summarized in Figure 4, which also includes the first generation pressure vessels used for initial viscosity determinations with test fluids including water and ethanol. The viscosity is calculated using Eq. 1. The flow rate is measured from the time required for transport of approximately 23 mL of the fluid from vessel 1 into vessel 2, determined via the

change in pressure when all 23mL have been blown out of the capillary tubing. The viscosity data has been documented in prior reports, and is not shown for the Gen 1 rheometer. The Gen 1 rheometer was a modified Parr Instruments 23mL Teflon-lined hydrothermal bomb rated to 250 °C and over 1000 psi pressures. However, the Teflon proved too soft to reliably machine fittings to permit the high pressure flow of liquid from vessel 1 to vessel 2 to measure the time flow. Therefore, subsequent designs were based on 316L steel vessels manufactured by the College of Earth and Mineral Sciences Machine Shop co-located with the Adair research labs in the Steidle Building on the Penn State campus. The 316L SS was chosen as this material is relative inexpensive, easy to machine, but both corrosion resistant and pressure fittings and tubing is commercially available. The Gen 4 vessel and set up is shown in Figure 5. The approximately 3 meters of tubing was wound on an Al cylinder designed for the large thermal mass and temperature stability provided. This length of tubing provided flow for about 180 sec with an error of less than 2 seconds. At least five measurements were taken at each temperature. The virial coefficients for the 3<sup>rd</sup> order non-linear fit to the data are summarized in Table 1. There were issues with the calibration even the Gen 4 rheometer. Therefore, the virial coefficients in Table 1 are provisional values as additional evaluation and verification are required before the data is published. Furthermore, we also need to evaluate the validity of the current approach. While the use of the pressure change to monitor fluid flow is perhaps a clever way to measure the overall fluid flow, it may lead to significant error. For example, we seek to determine viscosity of the fluid of interest, implying that only while the fluid is in transit through the capillary tubing are we obtaining a valid determination of the viscosity. At the beginning and end of the fluid flow, we are not measuring the viscosity, but instead the complicated wetting and other complicated phenomena as the fluid front is driven through the tubing and towards the end of the current determination out of the tubing. Thus, we need to modify, not necessarily the apparatus, but the fluid flow measurement boundaries. Thus, the fluid rate needs to be corrected to avoid measuring the beginning and end of the fluid flow. This correction will be made in current and future work to refine this measurement technique in future research efforts.

The development and initial surface tension determinations are shown in Figures 7 through 10. Although Christensen et al. (Christensen 1995) have previously described a higher pressure-higher temperature apparatus, sufficient detail and the design of the apparatus was limited to non-reactive liquids. Therefore, extensive detail is provided in this report regarding the design of the high pressure-high temperature surface tension measurement. The pressure vessel is composed of 316L stainless steel for the low cost, ease of machining and readily available valves, ports and other fixture in this material. In Figure 7, the transducer heads are shown in the left hand side of the figure with the stainless steel capillaries inserted into the head. The heating tape used to heat the relatively large thermal mass of the vessel is not shown. The right hand side of Figure 7 shows details for the closures and ports and argon gas through the Teflon tubing in the top of the photograph. The schematic drawings in Figure 8 show the relative positions of the ports for the gas and tensiometer probes. The side view in the bottom right of Figure 8 provides the dimensions for the vessel. Approximately 25 mL of fluid is the minimum volume that can be used to determine the surface tension of the fluid. Argon has been used to date for surface tension determinations, but virtually any gas can be used. The current system is designed to be used in either an explosion proof fume hood or within an isolated bay. The computer interface (not shown) can be remotely isolated from the apparatus through pressure relief walls.



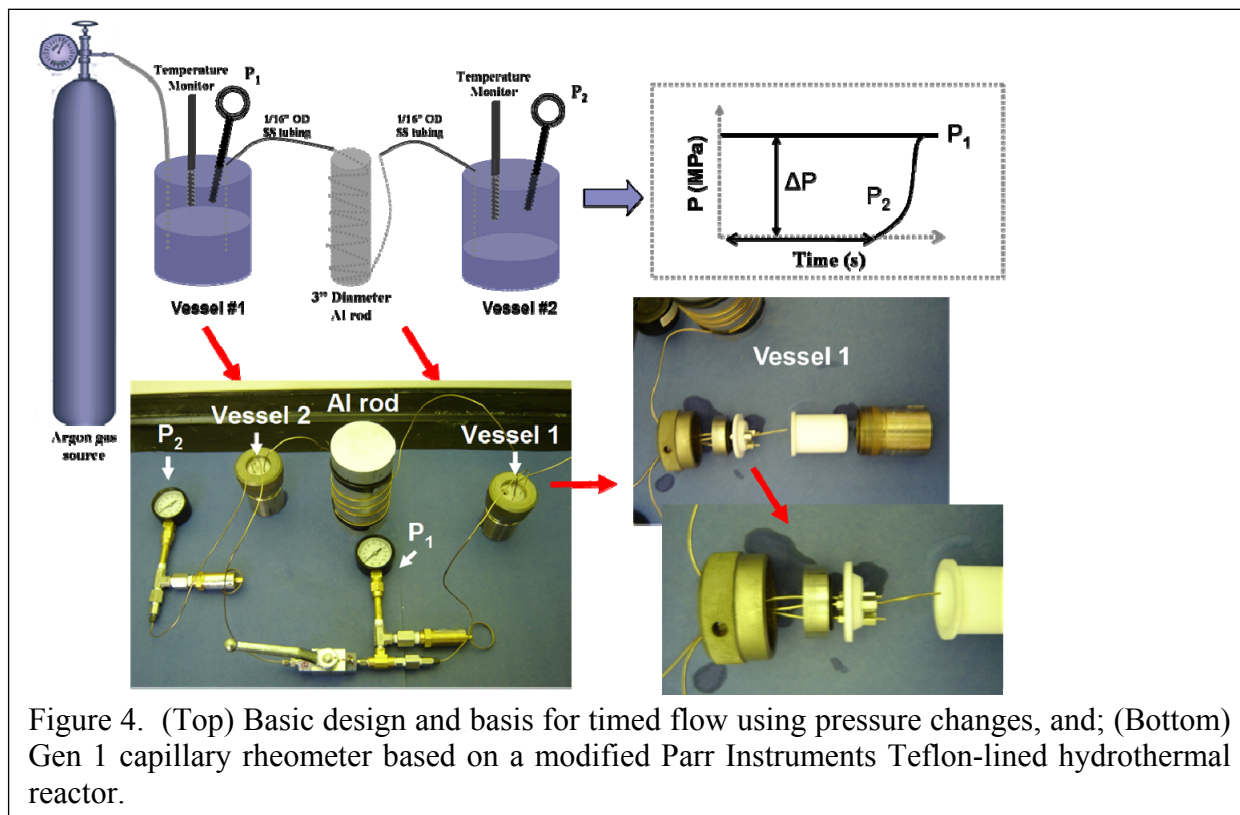


Figure 4. (Top) Basic design and basis for timed flow using pressure changes, and; (Bottom) Gen 1 capillary rheometer based on a modified Parr Instruments Teflon-lined hydrothermal reactor.

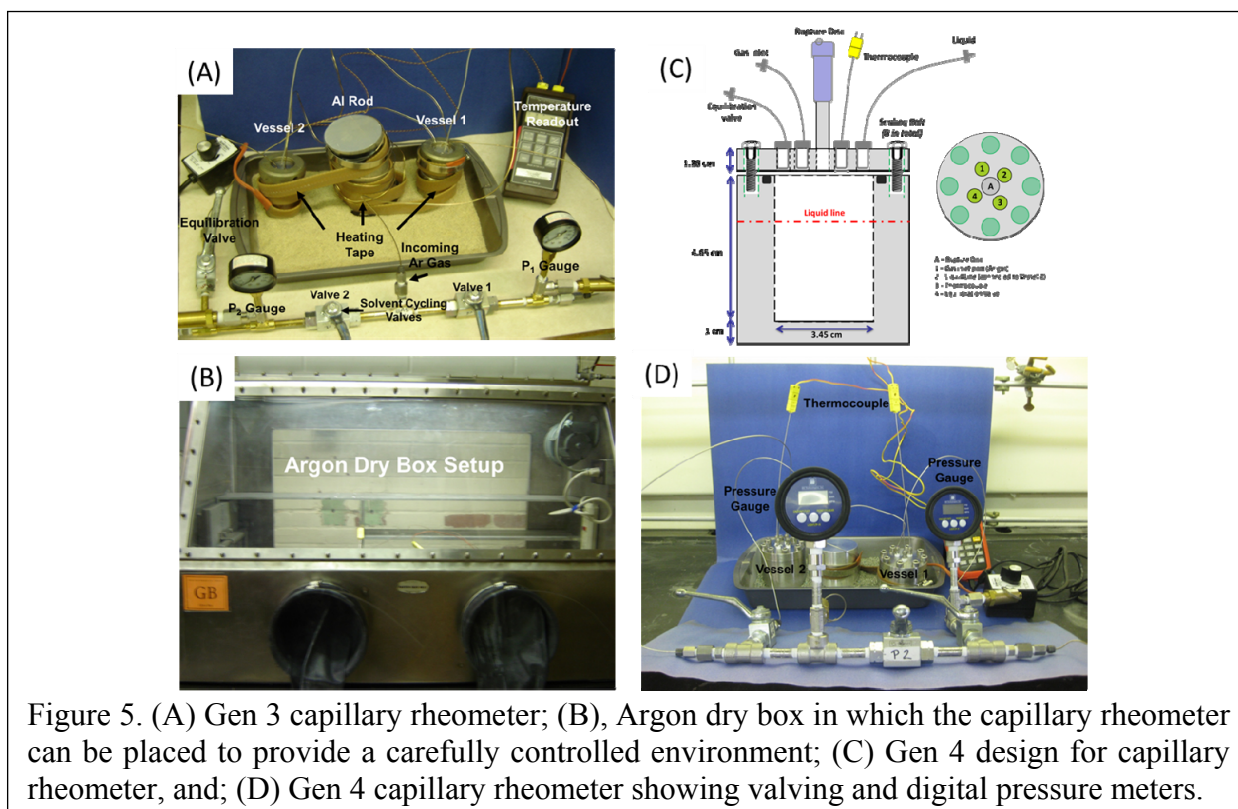


Figure 5. (A) Gen 3 capillary rheometer; (B), Argon dry box in which the capillary rheometer can be placed to provide a carefully controlled environment; (C) Gen 4 design for capillary rheometer, and; (D) Gen 4 capillary rheometer showing valving and digital pressure meters.

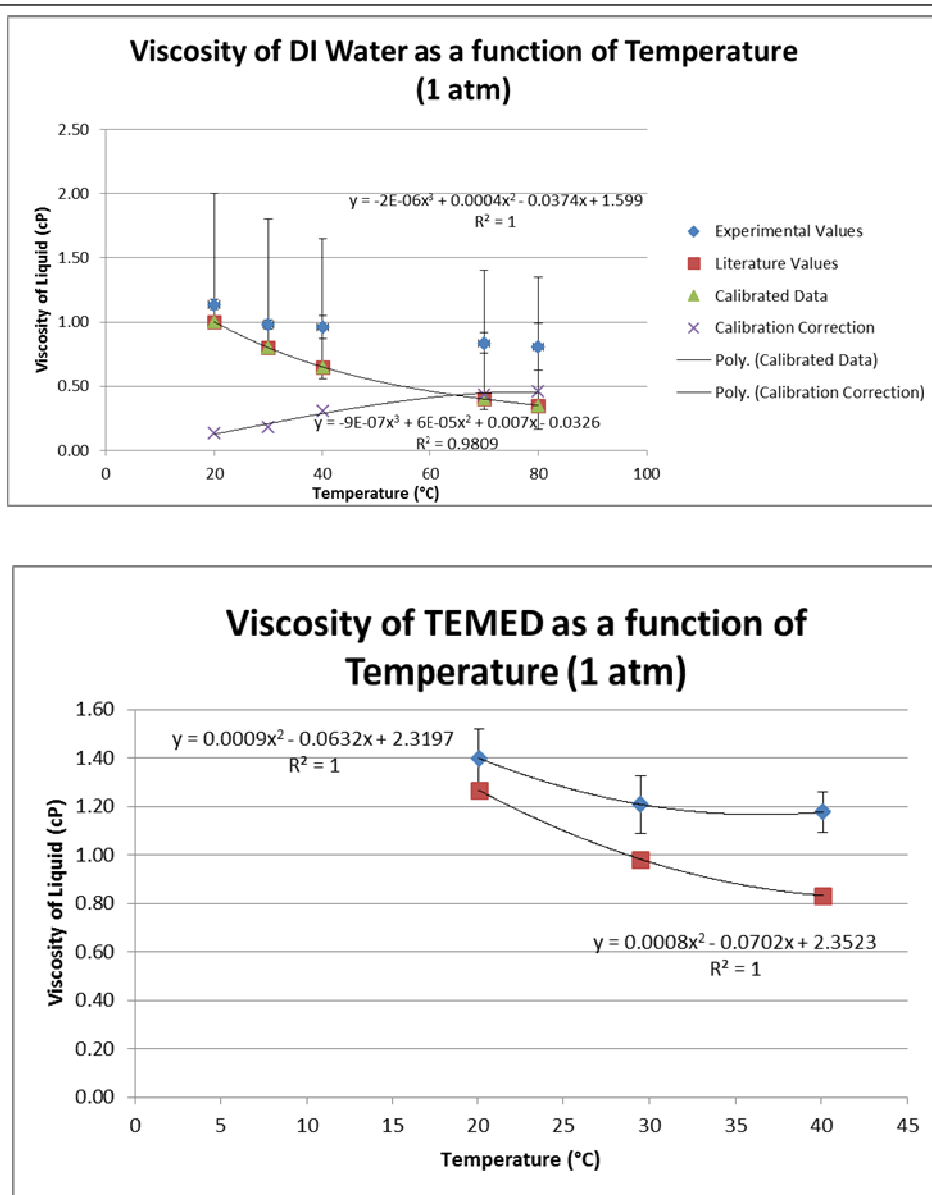
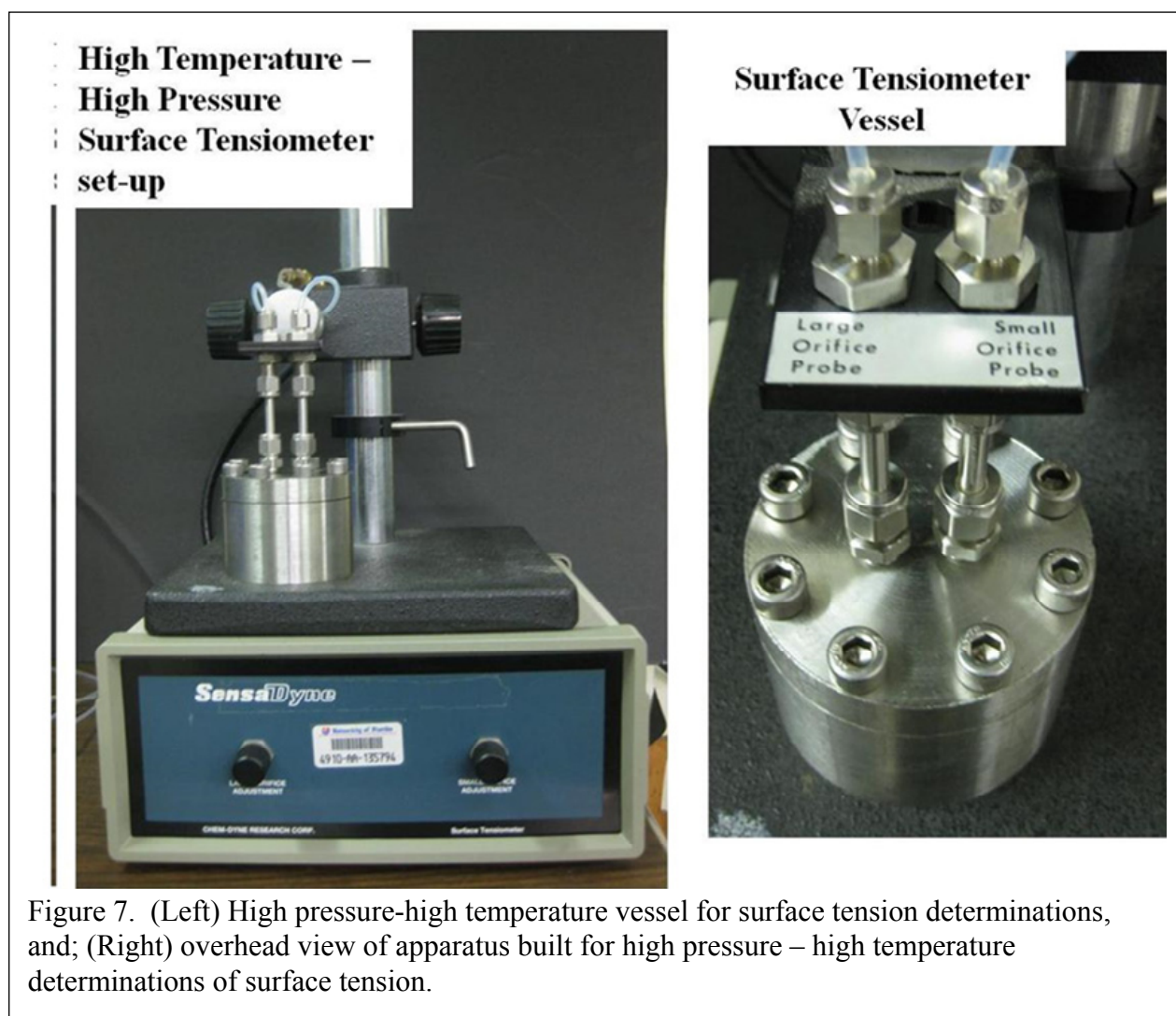


Figure 6. (Top) Viscosity measured for water with and without calibration. While the general trend toward decreasing viscosity with temperature is shown, the deviation becomes more profound as temperature increases. (Bottom) measured viscosity for TMEDA as a function of temperature with 3<sup>rd</sup> order non-linear regression for the corrected value based on the calibration with was in the top figure. The range of temperatures was from 20 to 40°C at a pressure of 10psi Ar.





The apparatus is not designed to be used in a dry box because of the close proximity required for the transducers. The schematic in Figure 9 shows a more detailed schematic of the tensiometer apparatus head assembly. The pressure gauge has now been replaced with a pressure relief valve as the maximum pressures for the pressure transducers is less than 200 psi, above which fracture occurs. The system was relatively straightforward to design, with the only serious issue being the limited head space for both the tensiometer tubes, thermal couple, and pressure monitoring/pressure relief valve. A double Viton O-ring is used to ensure a gas type or vacuum tight seal in the face of the head closure and top crown.

The surface tension for TMEDA is summarized in Figure 10. Many preliminary measurements were made with test liquids including water, ethanol, and ethanol-water mixtures that are not shown, but that validated the test procedures. The summary of the virial coefficients for TMEDA from 31.9°C (305.15K) up to 117.2°C (390.35K) are given in Table 1. The surface tension of

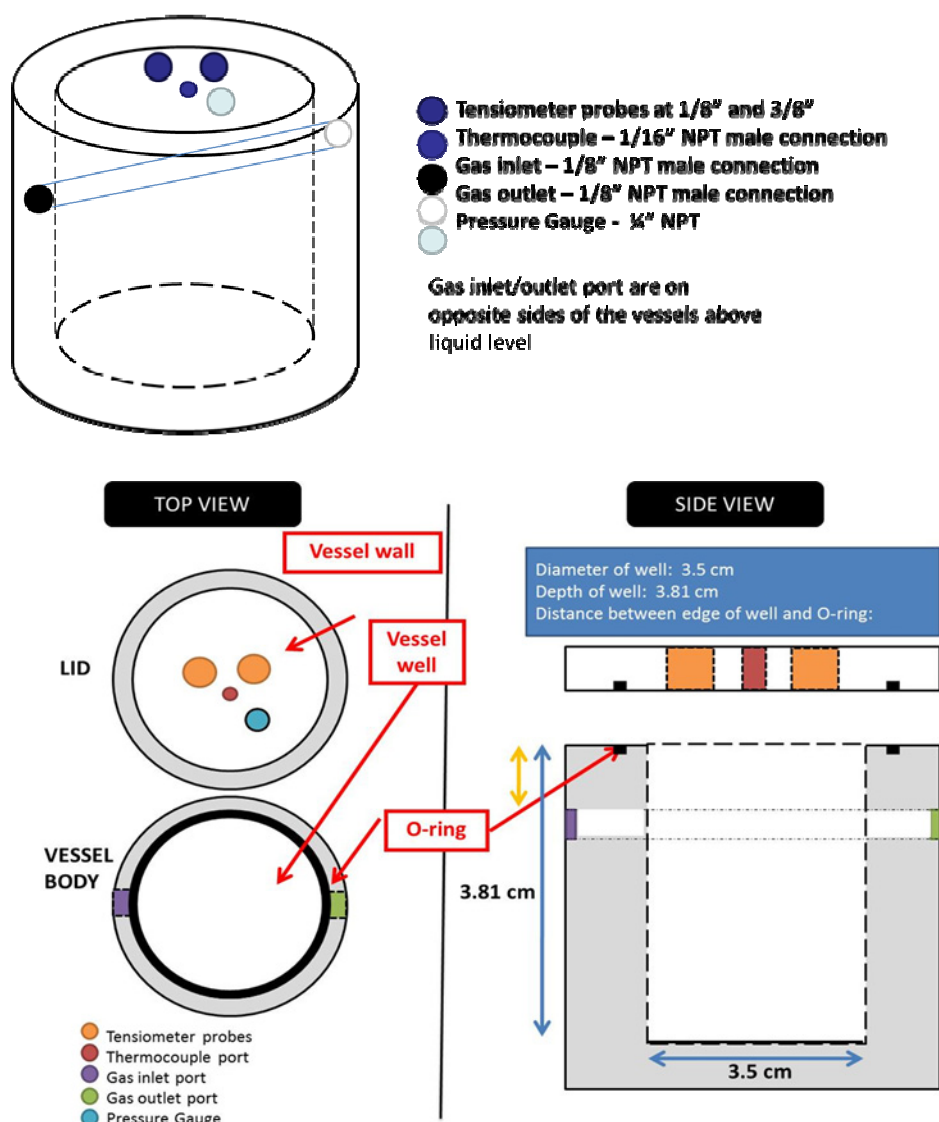


Figure 8. Schematic of the 316L stainless steel apparatus for high pressure – high temperature determination of surface tension for fuels and other potentially reactive liquids. (Top) 3D schematic drawing of vessel with ports and gas ports highlighted. (Bottom, Left) Overhead view of the arrangement of ports for gas and tensiometer probes. (Bottom, Right) Dimensions of the pressure vessel.

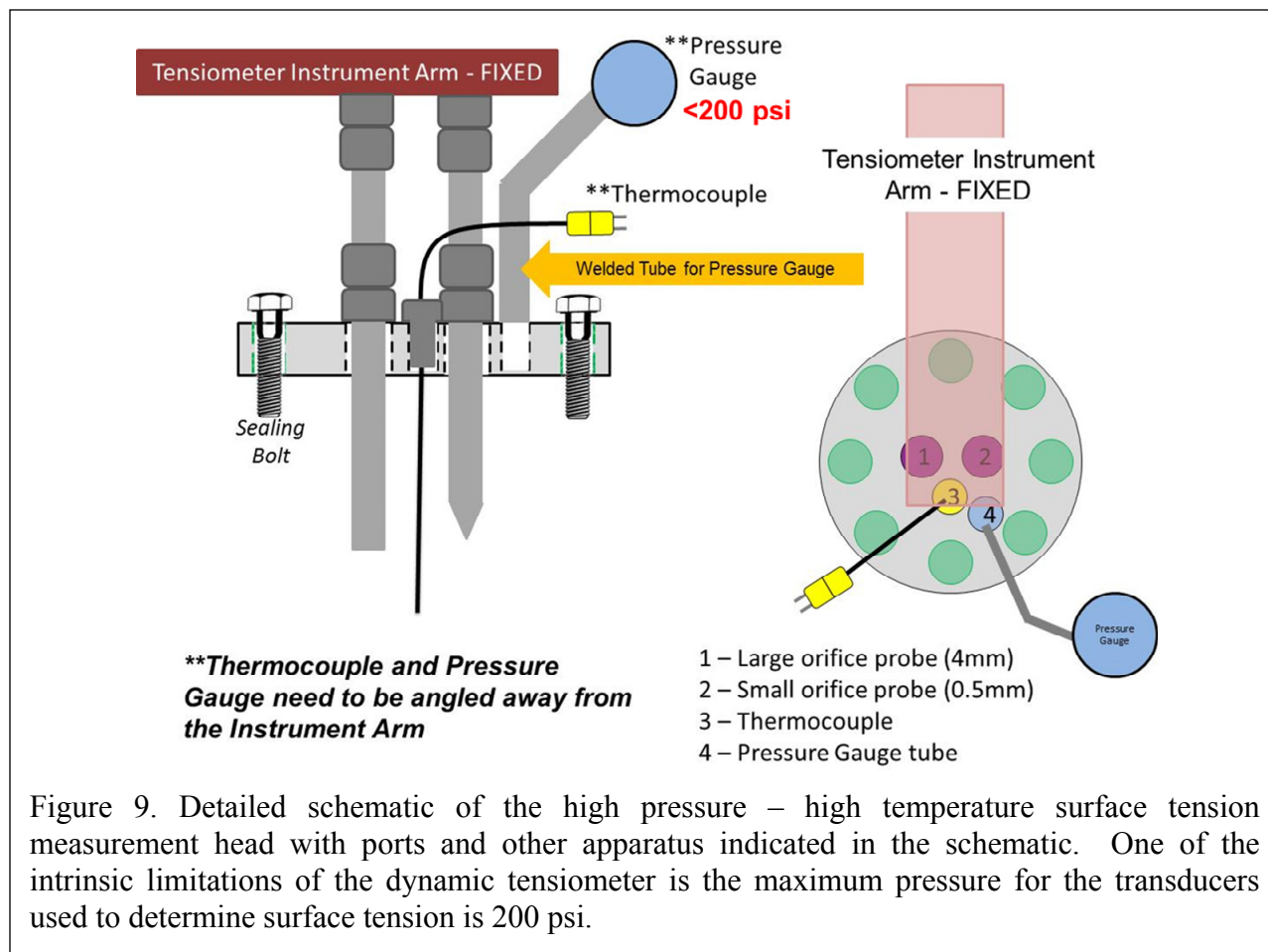


Figure 9. Detailed schematic of the high pressure – high temperature surface tension measurement head with ports and other apparatus indicated in the schematic. One of the intrinsic limitations of the dynamic tensiometer is the maximum pressure for the transducers used to determine surface tension is 200 psi.

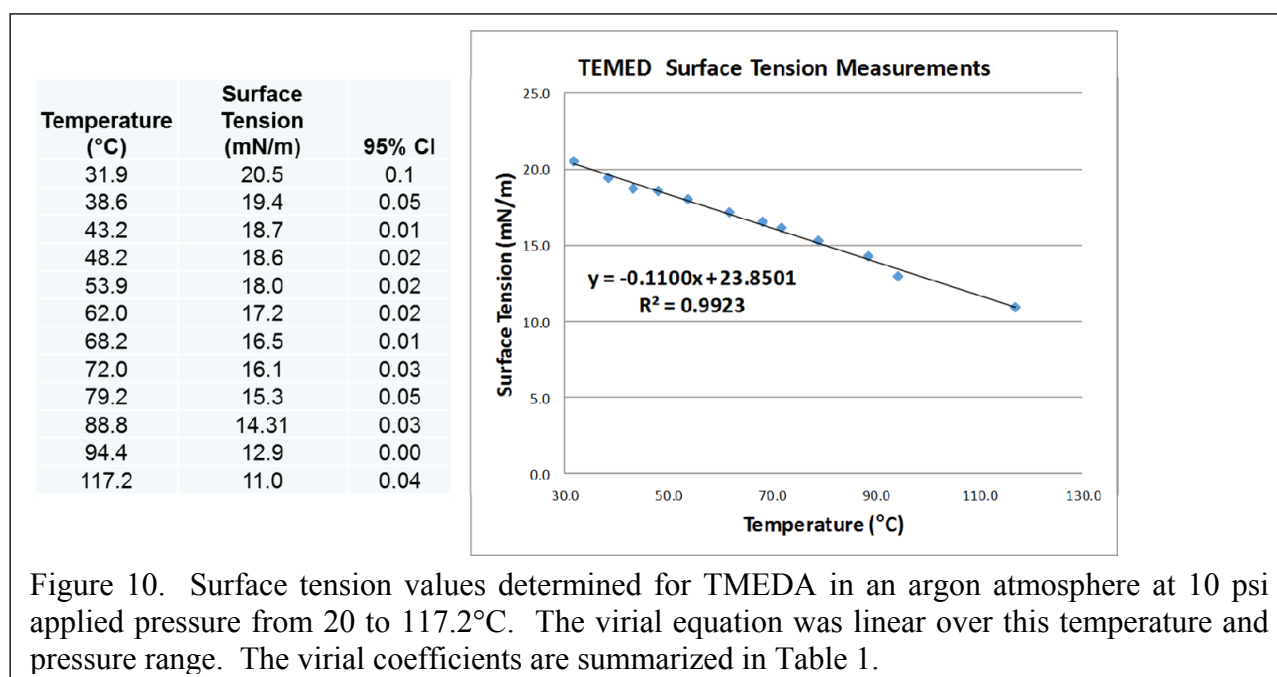


Figure 10. Surface tension values determined for TMEDA in an argon atmosphere at 10 psi applied pressure from 20 to 117.2°C. The virial equation was linear over this temperature and pressure range. The virial coefficients are summarized in Table 1.

TMEDA ranges linearly from 20.5 mN/m to 11.0 mN/m over this temperature range with an  $R^2$  value of 0.9923 for the linear regression. Once the pressure relief valve is in place, measurements to 230°C (over 500K) will be conducted. The apparatus is now in place in the High Pressure Combustion Lab under the direction of Dr. Yetter which is a much more amenable venue for the measurements that will be conducted in the future. Future development of this apparatus will include computer instrumentation to automatically collect the surface temperature as a function of time and temperature as well as pressure determinations to generate the vapor pressure as a function of both autogenous TMEDA pressure and over pressures of various gases. It is anticipated once additional measurements on TMEDA and other fuels are made that a manuscript will be developed that documents the values and utility of this variable in both models and experimental studies.

## 5. References

- Adamson, A. W. (1990) *Physical Chemistry of Surfaces*, New York, John Wiley & Sons, Inc.
- Christensen, T. C., Janule, V.P., Teichmann, A.F. (1995) Surface Tension Measurements in a Pressurized Environment. *International Symposium on Micelles, Microemulsions, and Monolayers*. Gainesville, FL, Center for Surface Science & Engineering, pp. 1-11.
- Eklund, P.C., Furuta, T., Goto, H., Fujiwara, Y., Adair, J.H., Nelson, J.A., Srinivasan, K., "Hydrogen Storage Material Based on Platelets and/or Multilayered Core/Shell Structure," U.S. Patent 7,288,325 B2, Oct 30, 2007.
- Rieke, R.D., Li, P. T.-J., Burns, T.P., Uhm, S.T. (1981), Preparation of Highly Reactive Metal Powders. A New Procedure for the Preparation of Highly Reactive Zinc and Magnesium Metal Powders, *J. Org. Chem.*, 46, 4324-4326.

## II. JET ATOMIZATION, SPRAY FORMATION AND DROPLET DYNAMICS

### II.1 Studies on Droplet Collision Dynamics (Law, Princeton University)

#### 1. Objectives

In the present study, we aim to extend the previous studies on unequal-size head-on droplet collision to liquids with a wide range of rheological properties, especially the liquid viscosity which as will be shown is an essential property governing the subject phenomena. We are particularly interested in identifying distinct collision outcomes and interpreting their size-ratio dependence on the dynamic and rheological aspects of the problem.

We implemented a front tracking method to simulate the collision of equal- and unequal-size droplets. The conversion of the surface energy of the merged interface to the kinetic energy of the neighboring fluid was taken into account in the simulations in order to keep the total energy conserved. We shall clarify in due course the different roles of the energy of merged interfaces in determining the different outcomes for the merging between equal- and unequal-size droplets;<sup>[3]</sup> In spite of the worthy advances in our understanding of droplet collision, a unified theoretical description of the transitions straddling regimes(I), (II), and(III), corresponding to  $We=O(1-10)$  which largely controls the collision dynamics, and  $Ca \ll 1$  which characterizes the early stage of droplet deformation, has, however, not been attempted. This is perhaps one of the most complex aspects of the phenomena and the primary objective of the present study is therefore to provide such a formulation. The task is a challenging one because of the nonmonotonic nature of the two transition boundaries with respect to  $We$ , of the large deformation of the droplets, of the need to describe the experimental observations of the presence/absence of regime (II) for different collision situations and materials, and of other features that will become evident as the formulation evolves.

#### 2. Background

The dynamics of droplet collision is relevant to many phenomena in nature such as the raindrop formation,<sup>1,2</sup> ocean mist production,<sup>3</sup> and atmospheric aerosols circulation.<sup>4</sup> Droplet collision is also ubiquitous in many industrial processes, especially those involving spraying.<sup>5</sup> A prominent example is the propensity of droplet collision in the dense spray region downstream of the injector in diesel and rocket engines. The frequent collisions and subsequent coalescence and separation can significantly modify the size and velocity distributions of the droplets in the spray, which in turn affect the eventual combustor performance.<sup>6</sup>

Earlier experimental studies on droplet collision were focused on the binary collision of identical water droplets in atmospheric air.<sup>7,8,9</sup> These studies showed that, depending on the collision Weber number,  $We$ , which measures the relative importance of the translational kinetic energy and the surface energy of the droplets, and the impact parameter,  $B$ , which measures the deviation of the trajectory of the droplets from that of head-on impact, collision may result in either permanent coalescence or separation after temporary coalescence. Subsequent experiments on hydrocarbons by Jiang, Umemura, and Law<sup>10</sup> identified a bouncing regime in the  $B-We$  parameter space, which divides the permanent coalescence regime into two regimes, namely, a coalescence regime after small droplet deformation, compared with the original droplet size, and a coalescence regime with large deformation. Qian and Law<sup>11</sup> extended the study to include effects of ambient pressures that are either lower or higher than atmospheric, for both water and hydrocarbon droplets, and found that the bouncing regime can be recovered for water at elevated pressures and suppressed for hydrocarbons at reduced pressures. A refined regime diagram consisting of five distinct collision regimes was consequently identified in the parameter space of

*B-We*: (I) permanent coalescence after small droplet deformation, (II) bouncing, (III) permanent coalescence after large deformation, (IV) near head-on separation after temporary coalescence, and (V) off-center separation after temporary coalescence.

Other studies on droplet collision have been mainly focused on two equal-size droplets, with emphasis on identifying and interpreting distinct collision outcomes and their dependence on the collision parameters. Pan et al.<sup>12</sup> numerically simulated Regimes (I) to (III) by using a front tracking method, in which the experimentally determined interface merging instants were used as an input parameter in the simulation. Excellent agreement was found between their simulations and experimental observations. Zhang and Law<sup>13</sup> developed a comprehensive theory to explain the nonmonotonic transitions from Regime (I) to (II) and from (II) to (III). Several important physical factors, such as the rarefied gas flow between the two colliding interfaces, the viscous dissipation of the droplet internal motion, and the van der Waals force between the droplet interfaces, were identified and incorporated into the theory. The theoretical results agree well with the reported experimental observations. Various models have also been proposed to explain the transition between Regime (III) to (IV)<sup>11,14,15,16</sup> and the formation of satellite droplets for Regime (V)<sup>17,18</sup>. In addition, Koch<sup>14,15</sup> studied extensively the response in Regime I for its practical relevance in colloidal and emulsion stability.

It is of obvious fundamental and practical interest to be able to theoretically predict the dynamics of droplet collision in different regimes, together with the transition boundaries between them. To formulate the droplet dynamics, the droplet is characterized by its density  $\rho_l$ , viscosity  $\mu_l$ , surface tension  $\sigma$ , and initial radius  $R_0$  and impact velocity  $V_0$ . The surrounding gas has density  $\rho_g$ , viscosity  $\mu_g$ , and pressure  $p_\infty$ . For situations of  $We=O(10)$  or higher, Qian and Law<sup>14</sup> analyzed the transition from regimes (III) to (IV) as the boundary across which the total energy of the merged mass cannot be contained by its surface energy at maximum deformation. For situations of  $We=O(10^2-10^3)$  (regime IV), Roisman<sup>15</sup> proposed a theoretical model that describes the droplet deformation after coalescence. A considerable number of theoretical studies have also been reported for the collision between two weakly deformed droplets with  $We \ll 1$ . For such situations, it is recognized that  $We$  may not act as the controlling similarity parameter as it does when  $We \gg 1$ . Other similarity parameters should be considered together with  $We$  for a complete description of droplet collision. An example is the prediction of strong droplet bouncing for  $We \ll 1$  together with the requirements of the capillary number  $Ca = \frac{\mu_g V_0}{\sigma} \ll 1$  and the Stokes

number  $St = 2 \frac{\rho_l V_0 R_0}{9 \mu_g} \gg 1$ .<sup>16,17</sup>

### 3. Experimental Facilities and Algorithms Developed or Used

#### 3.1 Experimental Facilities

The experimental apparatus and procedure employed in the present study are similar to those of References 10 and 11, in which two identical streams of droplets of uniform and controlled size, produced by the ink-jet printing technique, impinged on each other. Time-resolved images were obtained through stroboscopy synchronized with the droplet generation circuit. The entire apparatus was housed in a chamber whose internal pressure could be varied between  $0 \pm 1$  and 20 atm. Vibrations in the laboratory were found to have no influence on the experimentation. Pure hydrocarbons and de-ionized water were used to produce droplets with diameters ranging from

about 200 to 400  $\mu\text{m}$ . The experiments were performed at room temperature and the collision phenomena observed were repeatable from run to run.

A video image software (Mediagrab) was used to grab the collision images from the video camera and store them for subsequent analysis of the instantaneous droplet size and velocity. This image acquisition system allows the fine resolution of the collision events and consequently the transition behaviour and boundaries between different regimes. In all the experimental collision images, the stroboscope provided a uniform source of back lighting for the images. Thus areas of different shading indicate different amounts of light transmission through the colliding masses which act as optical lens in diffracting the light. This additional information may be useful in exploring the three-dimensional nature of the collision process through computational simulation.

### 3.2 Algorithms Developed or Used

The front tracking method adopted herein has been discussed in great details in<sup>12,19</sup>. In summary, the unsteady Navier–Stokes equation is solved for both gas and liquid phases in a unified computation domain:

$$\partial_t(\rho\mathbf{v}) + \nabla \cdot (\rho\mathbf{v}\mathbf{v}) = -\nabla p + \nabla \cdot \mu \left[ \nabla \mathbf{v} + (\nabla \mathbf{v})^T \right] + \mathbf{F} \quad (1)$$

where  $\mathbf{v}$ ,  $\rho$ , and  $p$  are the velocity, density and pressure, respectively. The surface tension

$$\mathbf{F} = \sigma \int k \mathbf{n} \delta(\mathbf{x} - \mathbf{x}_f) dS \quad (2)$$

is added as a delta function integrated locally over the immiscible interface in order to render a singular force exerted by the droplet to the flow field. In (2),  $k$  is twice the mean curvature,  $\mathbf{n}$  the unit normal vector outwardly directing from the droplet surface, and  $\mathbf{x}$  the space vector with the subscript  $f$  designating the interface.

For head-on droplet collision, a cylindrical coordinate can be established such that the connection of the centers of mass of the two droplets forms the axial ( $z$ -) direction and the radial ( $r$ -) direction is perpendicular to it. The entire flow field is axisymmetric in the coordinate and hence (1) can be written, in the  $r$ -direction, by

$$\begin{aligned} \partial_t(\rho v_r) + r^{-1} \partial_r(r \rho v_r^2) + \partial_z(\rho v_z v_r) = \\ \partial_r p + (2\mu \partial_r v_r) + 2\mu \partial_r(r^{-1} v_r) + \partial_z[\mu(\partial_z v_r + \partial_r v_z)] + F_r \end{aligned} \quad (3)$$

and, in the  $z$ -direction, by

$$\begin{aligned} \partial_t(\rho v_z) + r^{-1} \partial_r(r \rho v_z v_r) + \partial_z(\rho v_z^2) = \\ \partial_z p + \partial_z(2\mu \partial_z v_z) + r^{-1} \partial_z[\mu(\partial_z v_r + \partial_r v_z)] + F_z \end{aligned} \quad (4)$$

Both the gas and liquid phases are assumed as incompressible, so the continuity equation gives

$$r^{-1} \partial_r(r v_r) + \partial_z v_z = 0 \quad (5)$$

Furthermore, the density and viscosity are assumed to be constants in each phase.

The smaller and large droplet of the diameters  $d$  and  $D$ , respectively, are initially placed such that  $z = z_c$  bisects the connection line of their centers of mass. The computational domain is an axisymmetric cylinder of  $3.0D$  in length and  $1.5D$  in radius. The domain is discretized by a nonuniform, orthogonal staggered mesh with 150 and 400 grid points in the radial and axial directions, respectively. Studies of grid dependence were performed and the computational



results did not show grid dependence for  $150 \times 400$  and finer meshes. An artificial body force along the  $z$  direction.

$$f = A(\rho_g)H(z - z_c)\mathbf{z} \quad (6)$$

is used to drive the smaller droplet to move toward the larger one until the relative velocity  $U$  is obtained. In (6),  $A$  is the gravity,  $\rho_g$  is the gas density,  $H(z \geq z_c)$  is the Heaviside step function, being unity for all  $z \geq z_c$ , and  $z_c$  is chosen to be so large that the droplets will not collide before the specified relative velocity can be obtained.

Following previous studies, the governing equations are normalized by adopting the length scale  $D$ , time scale  $D/U$  and the liquid density  $\rho_l$ . The normalization results in several non-dimensional parameters: the Reynolds number defined as  $Re = \rho_l U D / \mu_l$ , where  $\mu_l$  is the liquid viscosity, the Weber number  $We = \rho_l U^2 D / \sigma$ , the size ratio  $\lambda = d/D$ , the density ratio  $\xi = \rho_l / \rho_g$  and the viscosity ratio  $\zeta = \mu_l / \mu_g$ . Since the density and viscosity ratios are two or three orders of magnitude larger than unity, their influence on the droplet dynamics will be neglected in the present simulation, as suggested in previous studies<sup>12,20</sup>. Physically, this means that the gas inertia and viscous dissipation have negligible influence on the collision dynamics compared to those of the liquid phase. The surface energy associated with the merged interfaces is not simply neglected as suggested in<sup>12</sup>, but is converted to the neighboring velocity-grids by using an immersed boundary method<sup>19,21</sup> to conserve the total energy. However, caution is needed when dealing with the energy conversion. In general, adding energy to the velocity-grids would unbalance the continuity and momentum equations (through terms involving the velocities). In order to resolve this issue, we adopted the following N-time-level split method.

## 4. Major Findings

### 4.1 Experimental Observations of Droplet Collision

As baseline for comparison, we first experimented with equal-size droplets. While we have experimented with all liquids, we shall only show the images of tetradecane droplets for illustration. Specifically, Figure 1(a) shows the bouncing case at  $We_s = 8.5$ , corresponding to Regime II. It is seen that, at  $t = 0.26$  ms, the droplets have reached their maximum deformation in the  $r$ -direction, which is much larger than their initial sizes. Since coalescence does not occur, the droplets eventually bounce away from each other. Figure 2(a) shows the coalescence case at  $We_s = 16.1$ , corresponding to Regime III. The two droplets coalesce at  $t = 0.34$  ms and the coalesced droplet reaches maximum deformation in the  $r$ -direction at  $t = 0.53$  ms. Although further deformation in the  $z$ -direction tends to stretch the droplet to separate, as seen in the image at  $t = 0.93$ , separation eventually does not occur since viscous dissipation through the internal motion of the droplet reduces the available kinetic energy to separate the merged droplet. Figure 3(a) shows the separation case at  $We_s = 39.1$ , corresponding to Regime IV. At such a large Weber number, the droplets undergo substantial deformation, as shown in the images at  $t = 0.23$  and  $0.80$ . Since the surface tension of the stretched droplet cannot hold the large amount of the kinetic energy associated with the internal motion, even with the stabilization effect of viscous dissipation, the merged droplet eventually separates and a smaller, satellite droplet is concomitantly formed. To compare with previous experiments, the transition Weber numbers from Regime II to Regime III and to Regime IV were found to be 13.7 and 34 in the present experiments, which are almost identical to those reported earlier.



Similar to the equal-size situations, bouncing, coalescence and separation were observed for unequal-size droplet collisions, as shown in Figures 1, 2 and 3, respectively. Figures 1(b), (c) and (d) show the collision images for different size ratios but similar Weber numbers ( $We_s = 7.0-8.5$ ). Under such situations, the droplets come into contact and experience moderate deformation and then bounce back. Unlike the equal-size case in which droplet deformation for each droplet is identical in space and time, the unequal-size droplets show different behaviors in response to the collision. First, the extent of deformation is different for the droplets because of their different capillary pressure  $2\sigma/R$  to resist deformation. Second, the droplets reach their respective maximum deformations at different times. As shown in Figure 1(c), the larger droplet needs a longer time ( $t = 0.67\text{ms}$ ) to reach its maximum deformation in the  $r$ -direction than the smaller droplet does ( $t = 0.4\text{ms}$ ). The underlying physics is that the droplets have different characteristic response times, which is proportional to the natural oscillation time,  $t_{osc} = (\rho R^3/\sigma)^{1/2}$ , and is longer for the larger droplet. Many experimental observations have shown that the collision process usually occurs within a few droplet oscillation times for the Weber numbers of interest in the study.

Figures 2(b), (c) and (d) show coalescence for different size ratios but similar Weber number ( $We_s = 13.8-17.6$ ). An interesting observation is that a rear-face bulge is formed on the coalesced droplet and the size of the bulge depends on the size ratio, as shown at  $t = 0.3, 0.57$  and  $0.7$  ms in Figures 2(b), 2(c), and 2(d), respectively. The formation of the bulge is caused by the transfer of the kinetic energy of the smaller droplet to the larger one upon coalescence. The excess energy provides the momentum of the liquid element to push forward to cause separation, which however is suppressed due to the stabilizing effects of surface tension and viscous dissipation. The droplet therefore remains coalesced, with a bulge.

Figures 3(b), (c) and (d) show the separation cases for different size ratios. Separation is observed for the size ratios 1.5 and 1.78 but not for 2.5 even though the Weber number is larger for the  $\Delta = 2.5$  case. This implies that increasing the size ratio suppresses droplet separation. Another interesting observation is that while a satellite droplet is formed after droplet separation for  $\Delta = 1$ , it is absent for  $\Delta = 1.5$  and 1.78. The formation of satellite droplets is attributed to the capillary instability of the liquid bridge, as shown at  $t = 0.97$  in Figure 3(a). For the unequal-size situations, because of the loss of symmetry, the liquid bridge tends to stick to the larger droplet instead of forming a satellite droplet.

In order to accurately determine the cumulative viscous dissipation in the different stages of droplet collision, the unsteady flow field of the droplet internal motion and the evolution of the surface geometry was analyzed, which can be obtained only by solving the 3D Navier-Stokes equation and using various numerical techniques for gas-liquid interface tracking. Moreover, experimental measurement of the flow field within the  $100\text{ }\mu\text{m}$ -size droplet is fundamentally challenging. We shall therefore develop an approximate evaluation of the viscous dissipation through simple scaling analysis.

Figure 4 shows the comparison between our model prediction and experimental measurements for tetradecane, decane, and water droplet collision. Qualitatively, the agreement for all the liquids is close, showing that the transition Weber number,  $We_{c-s}$ , increases with the size ratio. The solid line represents the results by using the present model and the dash line presents the results by using the present model but with a constant of 11, which was found by Qian and Law for equal-size droplet collision. Two predictions are very close, indicating that the residual surface energy term  $\gamma$  in Eq. (20) is only weakly dependent on the size ratio. Quantitatively, the

model predicts well tetradecane and decane droplet collision, while the discrepancy is larger for the water droplets.

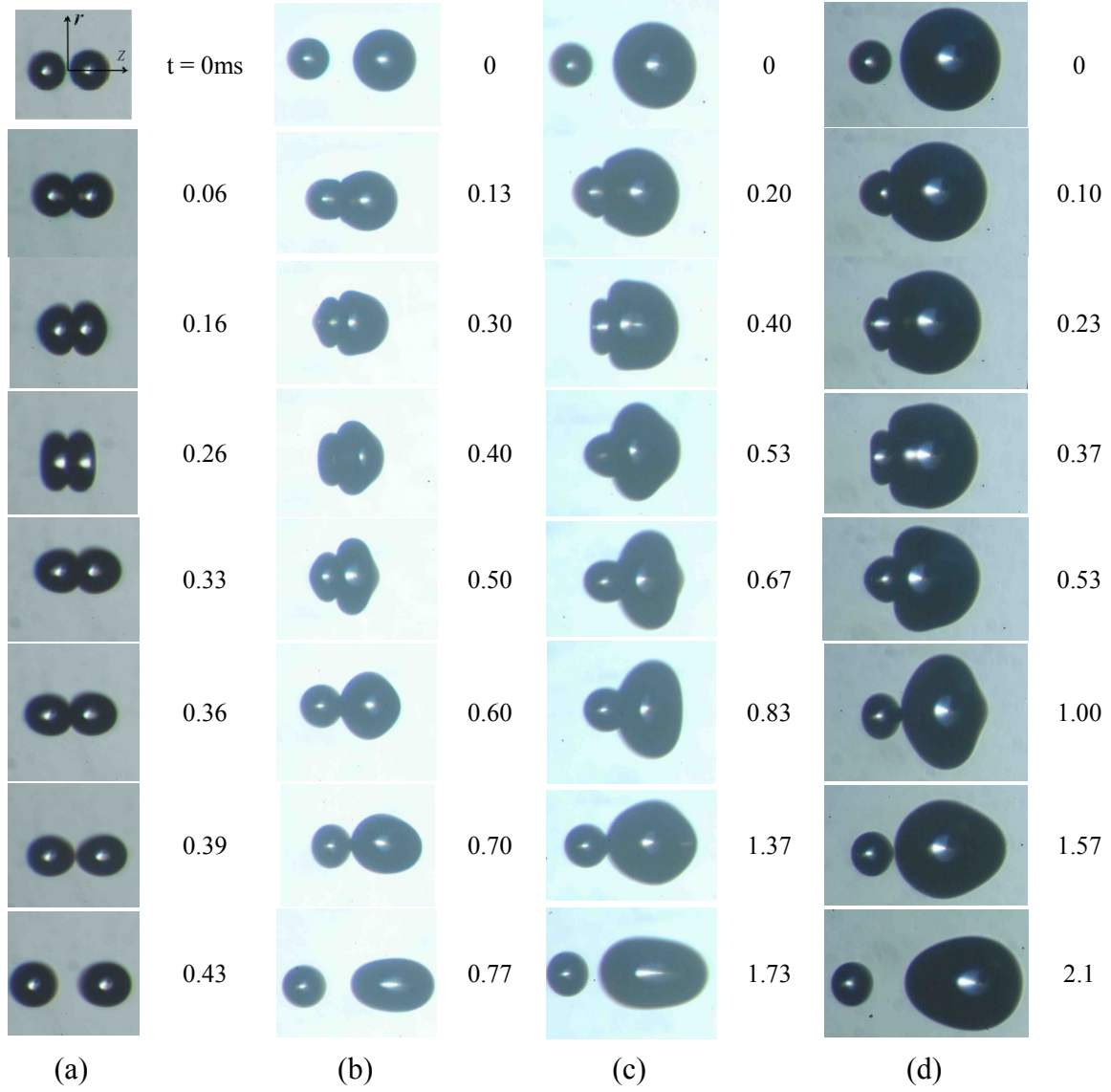


Figure 1. Photographic images showing representative bouncing collision sequences for tetradecane droplet collisions. (a)  $(We_s, \Delta) = (8.5, 1.0)$ ; (b)  $(7.3, 1.46)$ ; (c)  $(7.3, 1.87)$ ; (d)  $(7.0, 2.33)$ .

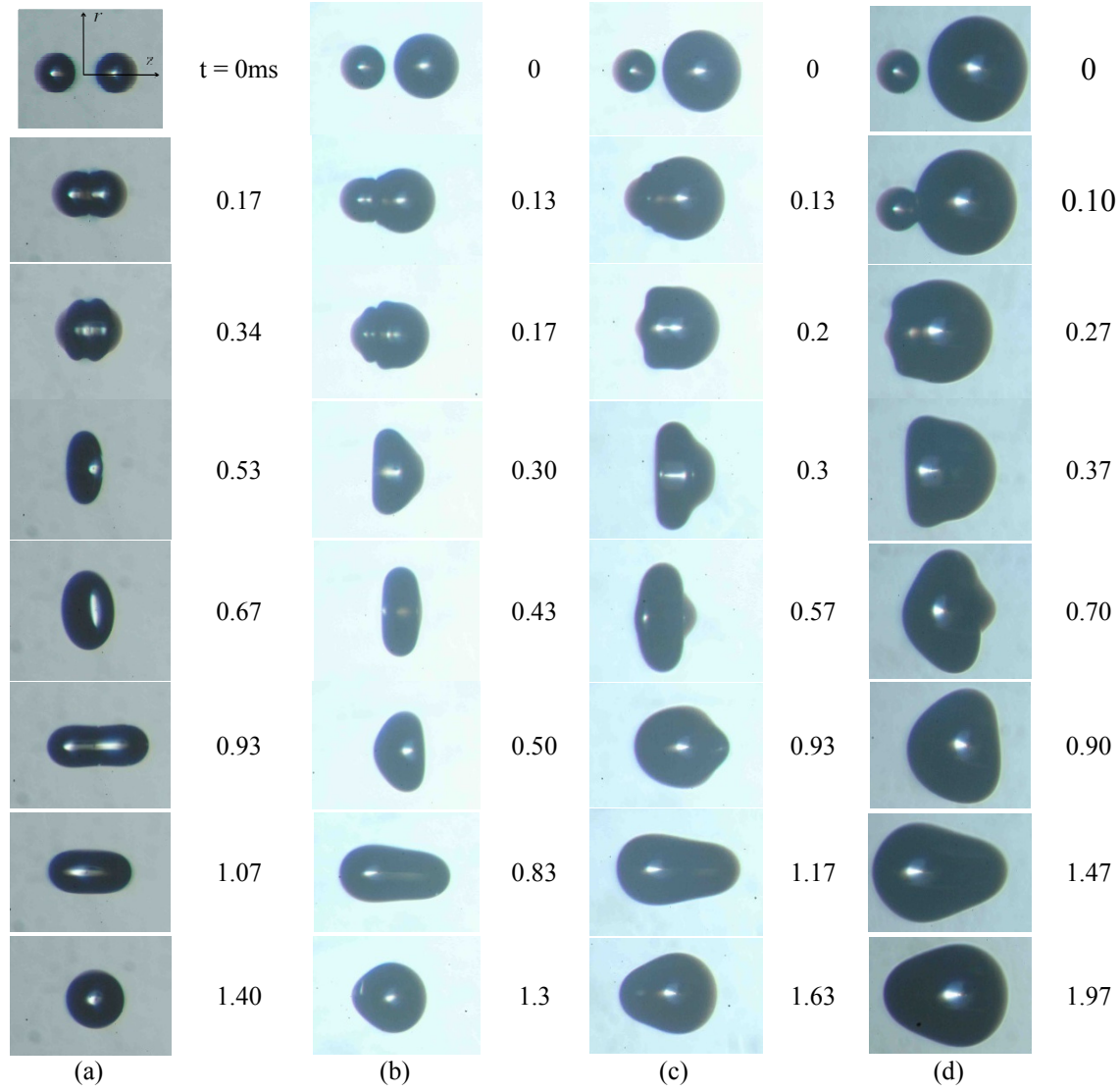


Figure 2. Photographic images showing representative coalescence collision sequences for tetradecane droplet collisions. (a)  $(We_s, \Delta) = (16.1, 1.0)$ ; (b)  $(13.8, 1.46)$ ; (c)  $(17.6, 1.87)$ ; (d)  $(16.5, 2.33)$ .

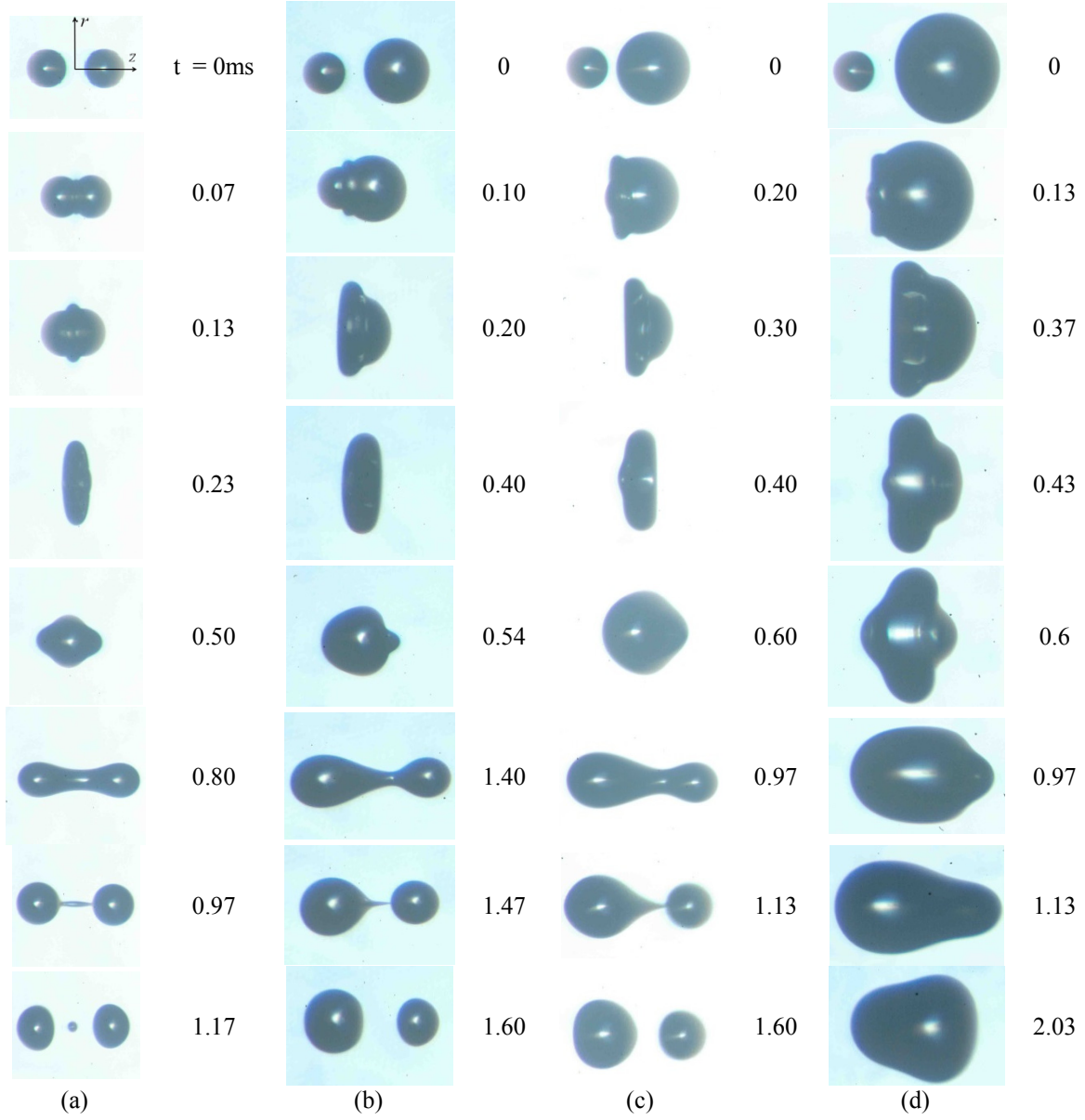


Figure 3. Photographic images showing representative separation collision sequences for tetradecane droplet collisions. (a)  $(We_s, \Delta) = (39.1, 1.0)$ ; (b)  $(52.8, 1.50)$ ; (c)  $(58.8, 1.78)$ ; (d)  $(68.0, 2.50)$ . Separation at  $\Delta = 2.5$  was not observed up to  $We_s = 68$ .

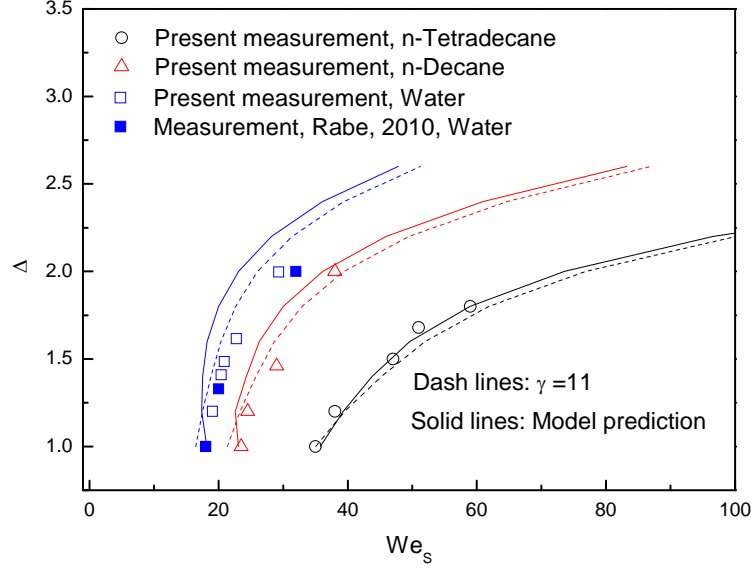


Figure 4. Comparison between experimentally measured and model predicted transition Weber numbers as a function of the size ratio for Tetradecane, Decane, and Water droplet collision.

The study was motivated by the conjecture that unequal-size droplet collision holds the potential to promote permanent coalescence and subsequently the liquid-phase ignition for gelled hypergolic propellants. Our experiment first identified a unified regime diagram in terms of bouncing, coalescence and separation for hydrocarbon and water droplets in the parameter space of the size ratio and a collision Weber number. The Experimental results support our conjecture by showing that the transition Weber number,  $We_{b-c}$ , that separates the bouncing and coalescence regimes, weakly depends on the size ratio, and that the transition Weber number,  $We_{c-s}$ , that separates the coalescence and separation regimes, significantly increases with the size ratio. A theoretical model based on energy balance and scaling analysis was developed and demonstrated to predict  $We_{c-s}$  well. Based on a sensitivity analysis, it is demonstrated that the strong influence of unequal-size droplet collision on suppressing droplet separation is mainly due to the increased viscous dissipation through the internal motion of the merged droplet before the droplet starts stretching to separation. The satisfactory agreement between the model prediction and the experimental observations for hydrocarbon droplets suggests that the model can be used for estimations of other hydrocarbon fuels.

#### 4.2 Experimental Observations of Jet Collision

It was found that jet collision exhibits a non-monotonic behavior with increasing impact inertia, which was also observed for droplet-droplet collisions. Symmetric jets of long chain hydrocarbons such as tetradecane and hexadecane were found to merge and coalesce when flow rate and impact inertia are very small. With increase in inertia through the flow rate, the jets were found to bounce away from each other from the impact point. Further increase in jet velocity, subsequently, results in merging of the jets. No more bouncing is observed with higher flow rates. However, the structure of merged jets upon collision and merging changes rapidly. It was observed that initially after merging, the jets create a chain like structure, while with increase in jet velocity transforms it into a liquid sheet, which eventually breakup to create atomized droplets.

The bouncing of the jets is facilitated by a thin air layer present between the jet surfaces. This air layer is sustained by the volume of air entrained by the moving jets before they collide. For bouncing it is imperative to maintain a steady air layer which is being squeezed out by the horizontal momentum of the jets. One can understand that the supply and sustenance of this air layer depends on its capability to withstand the compressing effect of the liquid jets. At a very small flow rate or the jet velocity, the entrainment which relates to the air boundary layer around the jets is weak to create a sustainable air layer thus the jets merge. Increase in jet velocity results in thicker boundary layer and thus strong entrainment to sustain a stable air layer. The compressing force of the jets at this stage is not strong enough to penetrate the air layer and to bring the liquid surfaces close for the Vander Waals force to promote the coalescence. However, with further increase in the jet velocity, the compression becomes stronger and eventually the jets merge.

Mechanistically, collision of two liquid jets at moderately high flow rate creates a fluid sheet in a plane perpendicular to the plane of incidence of the jets. Within the sheet, fluid is pushed out radially away from the impact point of the jets. To conserve the mass the liquid sheet thins as  $1/r$ , where  $r$  is the radial distance from the point of impact. A curvature force is generated due to surface tension acting normal to the edges of the fluid sheet and thus limits its lateral extent. Eventually, the curvature force causes the sheet to retract and ultimately close, thus forming the apex of the first link. When these rims collide at the apex of the link, it creates another thin sheet in the plane perpendicular to the first link. This process continues until the size of the link becomes too small due to viscous losses.

Increases in the flow rate of jet velocity creates larger chains until the liquid sheet becomes unstable and breaks apart before the first link retracts to form any subsequent sheets.

### 4.3 Numerical Simulations in Front Tracking Method

#### 4.3.1 Stationary Coalescence of Unequal-size Droplets

To further verify the present numerical scheme for unequal-size droplet collision, we simulated the coalescence of initially stationary unequal-size droplets, which was experimentally studied by Anilkumar et al.<sup>22</sup> and numerically studied by Nobari and Tryggvason<sup>23</sup>. Since the droplets have no initial velocity, the Weber number is not an appropriate non-dimensional parameter and can be replaced by the Ohnesorge number, defined as  $Oh = \mu_d(\rho_l D \sigma)^{-1/2}$ . Furthermore, the time scale based on the initial velocity is replaced by  $\tau = (\pi/4)[\rho_l(D^3 + d^3)/\sigma]^{1/2}$ , which corresponds to the lowest mode of natural oscillation of the merged droplet.

Following Nobari and Tryggvason, the droplets are initially placed so that they slightly overlap with each other along the symmetry axis. The overlapped surfaces are then removed to form a small opening between the droplets and as such the initial condition is completely specified. The simulations were conducted for  $Oh=0.025$  and  $0.0025$ , respectively corresponding to the large and small droplet viscosity cases studied by Anilkumar et al.<sup>22</sup> and Nobari and Tryggvason<sup>23</sup>, as shown in Figure 5. It is seen that the mushroom-like jet formation is absent for  $Oh=0.025$  while it is present for  $Oh=0.0025$ . These results agree with the previous observations<sup>22, 23, 24</sup> in that the surface energy of the merging interface plays a crucial role in the internal jet formation and that internal viscous dissipation suppresses jet formation.



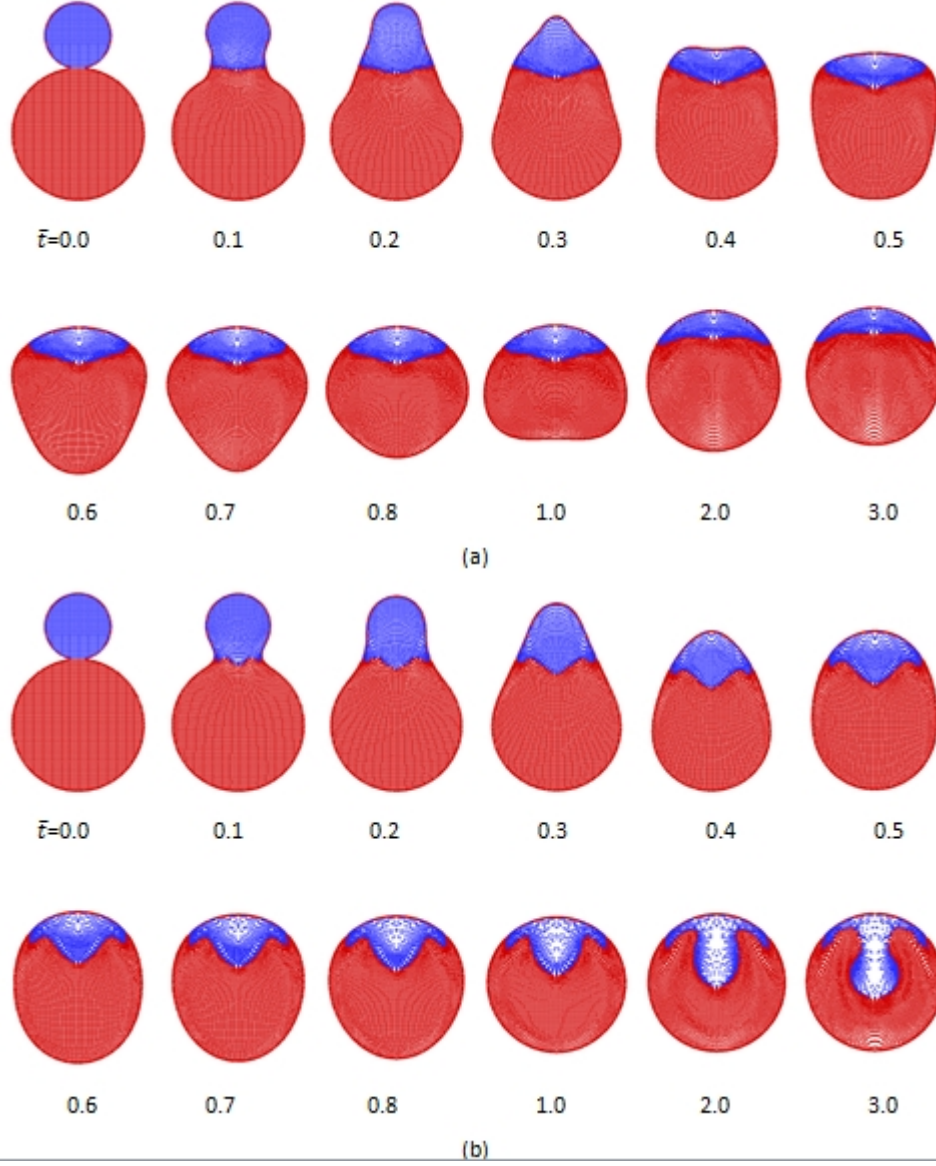


Figure 5. Time sequence for the initially stationary coalescence of unequal-size droplets for  $\lambda = 0.5$ ,  $\xi = 1.0$ , (a)  $\zeta = 1.0$ ,  $Oh = 0.025$  and (b)  $\zeta = 0.01$ ,  $Oh = 0.0025$ .

In summary, the surface energy of the merged interface appears to be unimportant in the global and internal dynamics of equal-size droplet collision while it is the driving force for jet formation in initially stationary unequal-size droplet coalescence. Furthermore, the jet formation, which indicates enhanced internal mixing after droplet coalescence, is unlikely in equal-size droplet collision due to symmetry while it can be observed for initially stationary unequal-size droplet coalescence.

#### 4.3.2 Head-on Collision of Unequal-size Droplets

Figure 6 shows the simulation results for the head-on collision of two unequal-size tetradecane droplets with  $We=6.0$ ,  $Oh=0.025$  and  $\lambda=0.5$ , with Figures 6a and 6b show the evolution of the droplet contours and mixing structure using Scheme 1 and 2, respectively. It is first noted that while one might expect a stronger inward indentation of the surface at the location of merging

when energy of the merged surface is considered, the image at  $\bar{t}=0.1$  shows the appearance of column stretching, which was also observed in experiments<sup>16,22</sup>. In Figure 6a, a mushroom-like structure, which is a salient feature of unequal-size droplet merging observed in the experiment, can be observed in simulations only by keeping the surface energy of the merged interface – this structure cannot be obtained if the surface energy is neglected, as shown in Figure 6b. The conversion of surface energy also causes a distinct difference in the droplet shape contour after coalescence, as shown in Figure 7. As such, we have conclusively demonstrated the important role of the surface energy of the merged interface in forming the jet and hence facilitating mixing upon merging. The underlying physics is demonstrated by examining the energy budget, as shown in Figure 8, in that the energy dissipation rate VDR around the merging instant is much smaller than that in the equal-size collision. Consequently the rapid viscous dissipation assumption is not valid for unequal-size collision, and the surface energy of the merged interfaces has to be kept and converted into the kinetic energy of the internal motion of droplet. This then leads to the formation of the mushroom-like mixing structure.

To study the size ratio effects on jet formation, a simulation was conducted for  $\lambda=0.3$  while keeping the other non-dimensional parameters unchanged, as shown in Figure 9. Again, a mushroom-like jet structure is formed by using Scheme 1, as shown in Figure 9a while it is absent using Scheme 2, as shown in Figure 9b. It is seen that the penetration depth of the smaller droplet into the larger one at  $\bar{t}=2.0$  for  $\lambda=0.3$  is smaller than that for  $\lambda=0.5$  at the same time. That is because, for the same Weber number, the smaller size-ratio collision results in smaller droplet deformation upon coalescence and hence a smaller surface energy to drive the jet formation. By the same token, the  $\lambda=0.3$  case is more sensitive to energy conversion than  $\lambda=0.5$ , because the viscous dissipation rate immediately after coalescence for  $\lambda=0.3$  is smaller than  $\lambda=0.5$ , as shown in Figure 10.

To study the Weber number effects on jet formation, a series of simulations were conducted with increasing Weber numbers. The internal flow structure at  $\bar{t}=2.0$ , which is sufficiently long for jet formation, is shown in Figures 11 and 12 for  $\lambda=0.5$  and  $\lambda=0.3$ , respectively. It is seen that the mushroom-like jet is absent for  $We=0.5$  for both size ratios while it is clearly developed for the higher Weber numbers. This is because, for a given size ratio and Ohnesorge number, increasing the Weber number results in increased droplet deformation upon coalescence and consequently a larger surface energy to drive the jet formation.



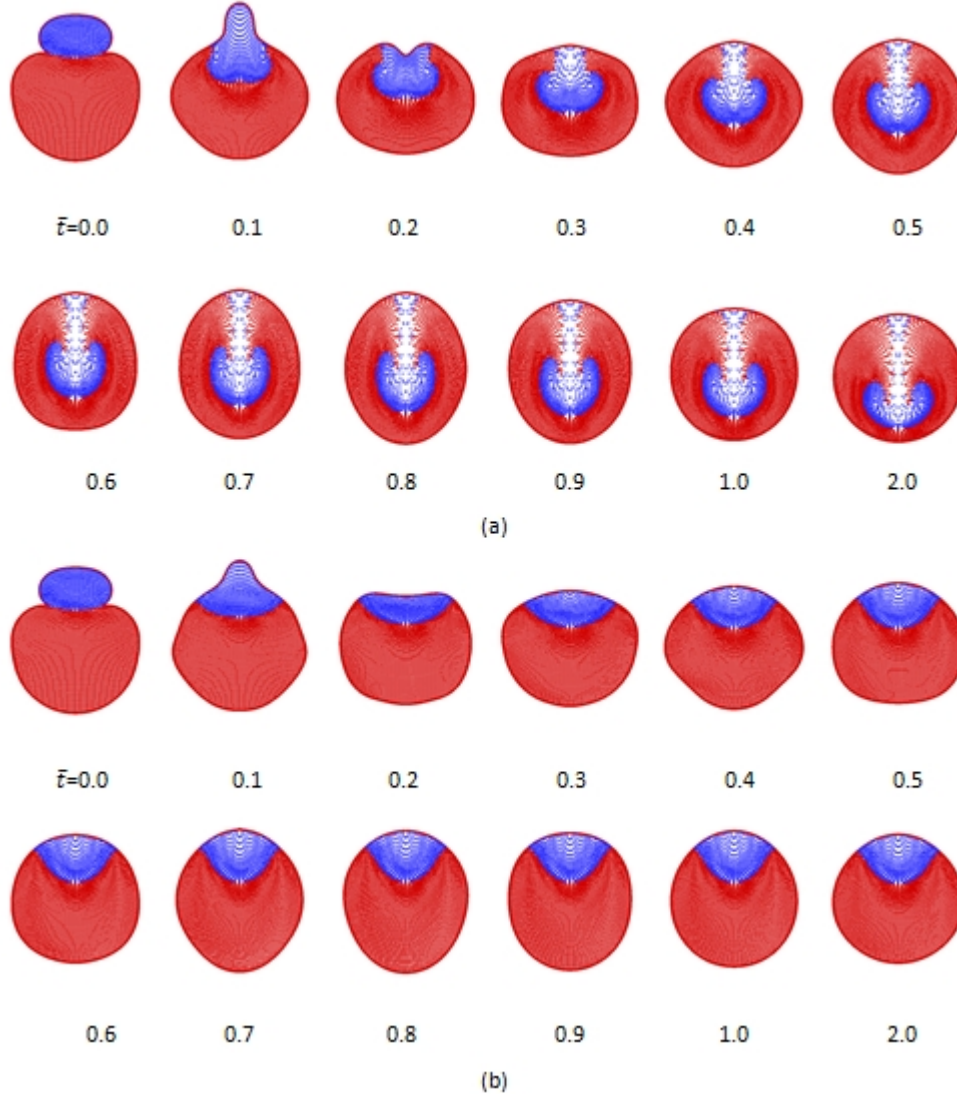


Figure 6. Time sequence for the collision of unequal-size tetradecane droplets at 1atm air for (a) Scheme 1 and (b) Scheme 2.  $d = 200\mu\text{m}$ ,  $D = 200\mu\text{m}$ ,  $U = 0.7\text{m/s}$ ,  $\tau = 1.13\text{ ms}$ ,  $\eta = 0.5$ ,  $Oh = 0.025$ ,  $We = 6.0$ .

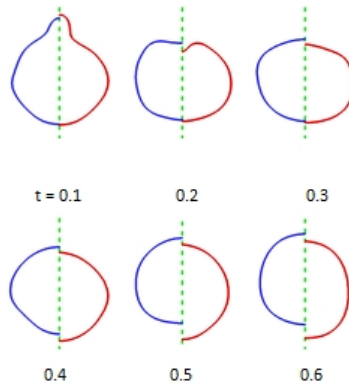


Figure 7. Comparison of Schemes 1 and 2 for the droplet contour after coalescence.

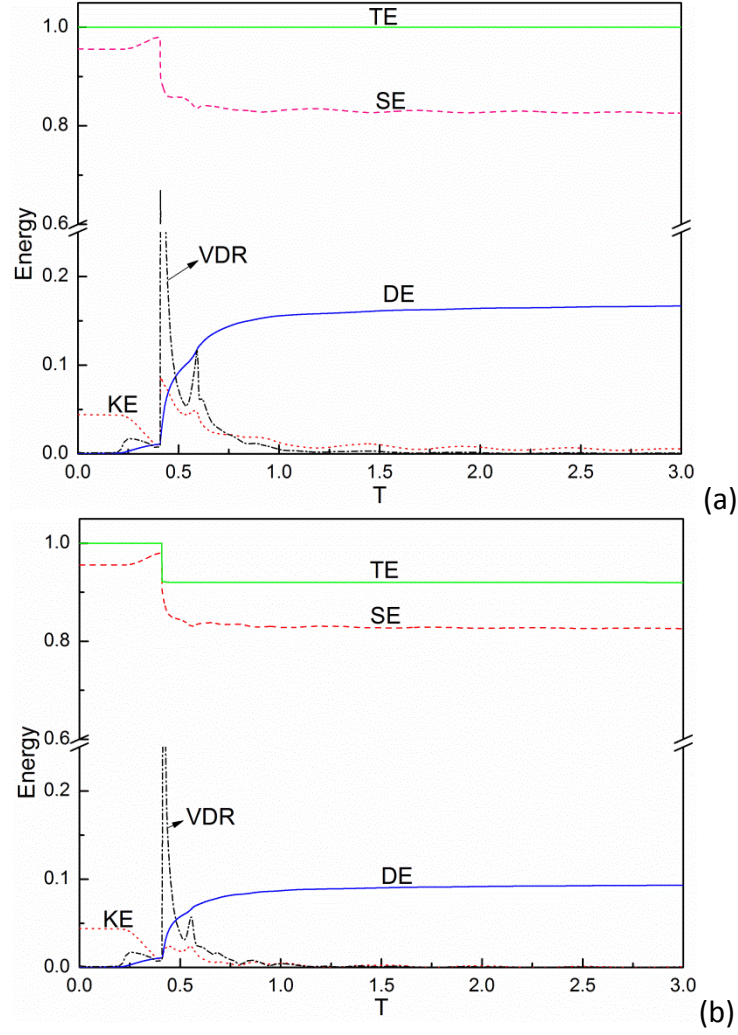


Figure 8. Energy budget of the colliding droplets for (a) Scheme 1 and (b) Scheme 2. KE denotes the total kinetic energy, DE the total dissipation energy, SE the surface energy, TE the total energy, and VDR the viscous dissipation rate multiplied by unit time, each normalized by the initial energy of a single droplet.

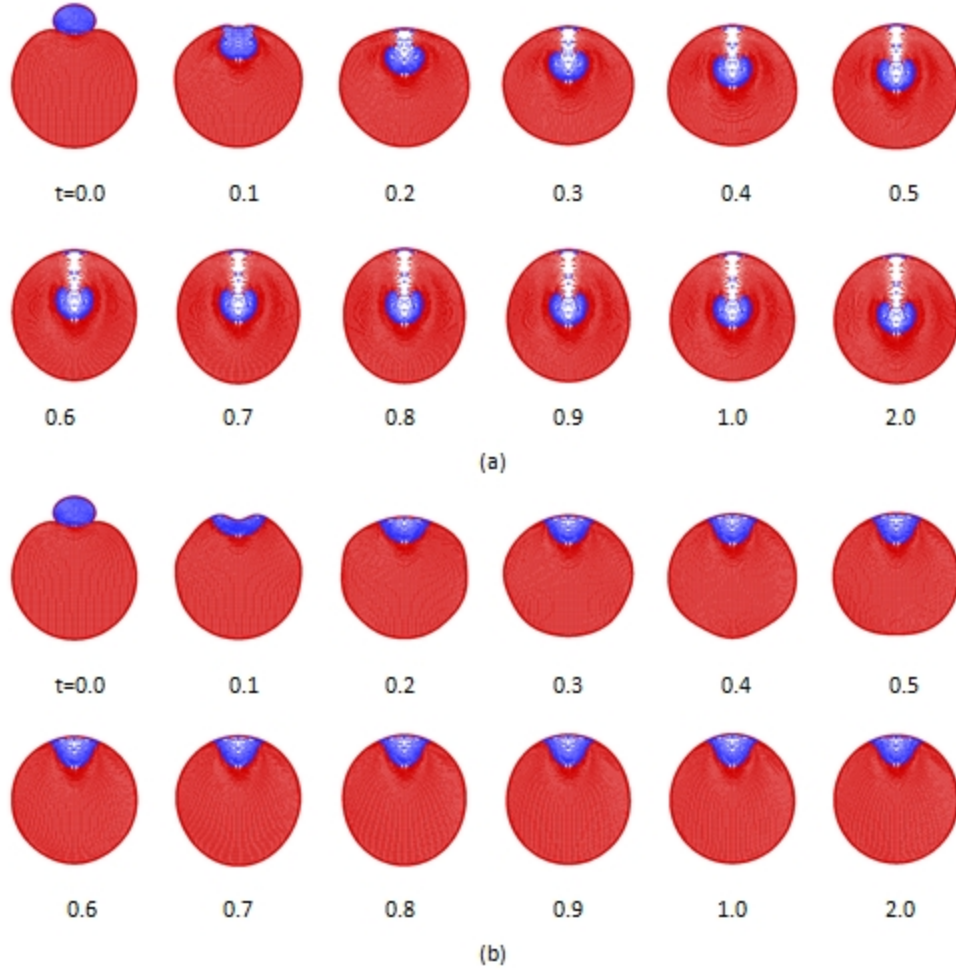


Figure 9. Time sequence for the collision of unequal-size tetradecane droplets at 1atm air for (a) Scheme 1 and (b) Scheme 2.  $\eta = 0.3$ ,  $Oh = 0.025$ ,  $We = 6.0$ .

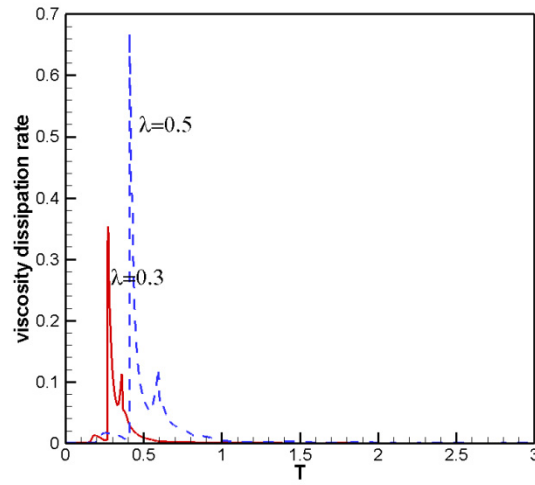


Figure 10. Viscosity dissipation rate for different size ratios.

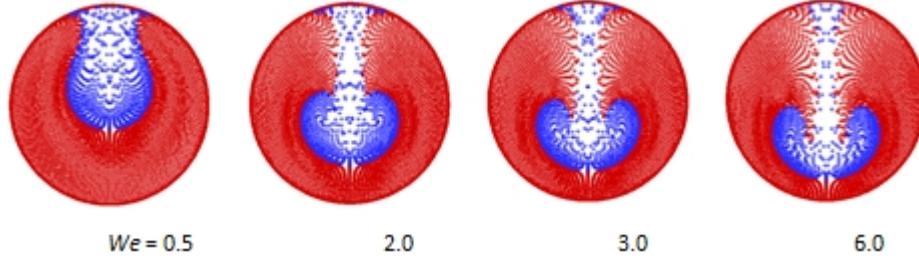


Figure 11. Internal flow structure at  $\bar{t} = 2.0$  for  $\lambda = 0.5$ .

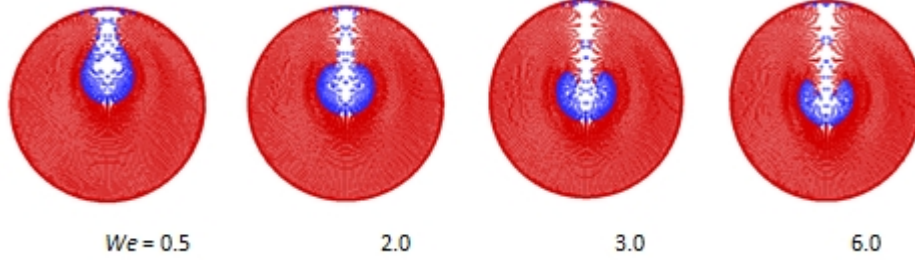


Figure 12. Internal flow structure at  $\bar{t} = 2.0$  for  $\lambda = 0.3$ .

The present study has extended the scope of droplet collision by asking what happens after merging is possible and effected. In particular we are interested to assess the extent of mixing between the two droplet masses and how it can be optimized. We have subsequently shown that an important system parameter that critically affects the efficiency of mixing is the disparity in the sizes of the colliding droplets. Thus, if the droplets are of the same or similar size, then mixing is minimized due to symmetry. On the other hand, if the droplets are of sufficiently disparate sizes, then upon merging the smaller droplet is transformed into a mushroom-like jet that penetrates into the interior of the larger droplet and consequently facilitates mixing, in accordance with previous experimental observations. Of particular significance is the demonstration that the jet acquires its energy from the surface energy of the merged interfaces. For equal-size droplets this surface energy is viscously dissipated rapidly.

#### 4.4 Theoretical Analysis

A reasonably comprehensive theoretical model of head-on droplet collision has been formulated, with  $We = O(1-10)$  and  $Ca \ll 1$ , that includes the essential physics describing the large droplet deformation, viscous loss through internal motion, rarefied flow effects of the intervening gas between the colliding interfaces, and the Van der Waals force that destroys and hence causes merging of the interfaces. Of particular interest is the verification of the experimental observation that, with increasing impact inertia, droplet collision can result in a nonmonotonic coalescence-bouncing-coalescence transition sequence. The distinctively different collision outcomes at different environment pressures and between water and hydrocarbon droplets are also theoretically confirmed. The predicted transition Weber numbers and the corresponding experimental values for tetradecane and water droplets collision at different pressures are summarized in Table I. Additional understanding gained on the characteristics of collision include the extent of viscous loss in the droplet, the motion of the interface relative to that of the

droplet mass center when coalescence is effected, the maximum deformation, and the nonmonotonic nature of the collision/coalescence time.

To simplify the fairly complex phenomena addressed in the study and facilitate the analytical effort, we made several physically reasonable approximations which are the major causes for the quantitative discrepancy between the theoretical and experimental results. First, the impacting droplet is approximated as a truncated sphere with time-dependent geometric dimensions. Although this model has succeeded in calculating the energy transfer among the different modes of energy, which is crucial for describing droplet collision with large Weber numbers, the evident difference between it and the experimentally observed droplet deformation, as well as the approximate nature of the initial conditions for it, have led to discrepancy. Second, the impacting interface is approximated as a flattened planar disk because of the large ratio of the disk radius to the gap distance. Nevertheless, the dimple formation and the gap flow instability contain additional physics such as trapping of the air bubble upon coalescence at the rim. In addition, the approximation made in studying the droplet internal motion and the neglect of the vaporized species in the intervening gas composition in the description of the van der Waals force could be other sources of the inaccuracy in the formulation. While all the above issues merit further study, the fairly comprehensive nature of the present analysis, on a complex phenomenon that involves a multitude of distinctive physical processes, is worth noting.

Table I. Comparison of the predicted and experimental transition  $We$  for the collision of tetradecane and water droplets in air.

	Tetradecane (1.0 atm)	Tetradecane (0.6 atm)	Tetradecane (2.4 atm)
$We_S$ (theory)	3.1	Coalescence only	0.4
$We_S$ (exp)	2.3	Coalescence only	Not available
$We_H$ (theory)	13.0	Coalescence only	78.5
$We_H$ (exp)	12.3	Coalescence only	30.0
	Water (1.0 atm)	Water (2.7 atm)	Water (8.0 atm)
$We_S$ (theory)	Coalescence only	0.07	0.1
$We_S$ (exp)	Coalescence only	3.0	Not available
$We_H$ (theory)	Coalescence only	9.5	28.0
$We_H$ (exp)	Coalescence only	6.0	13.0

## 5. References

1. Gunn, R., Collision Characteristics of Freely Falling Water Drops. Science 1965, 150, 695-701.
2. P. R. Brazier-Smith, S. G. J., and J. Latham,, The Interaction of Falling Water Drops: Coalescence. Proceedings of the Royal Society of London. Series A, Mathematical and Physical Sciences 1972, 326, 393-408.
3. Raes, F.; Van Dingenen, R.; Vignati, E.; Wilson, J.; Putaud, J. P.; Seinfeld, J. H.; Adams, P., Formation and cycling of aerosols in the global troposphere. Atmos Environ 2000, 34 (25), 4215-4240.
4. Raes, F., Formation and cycling of aerosols in the global troposphere. Nato Sci S Ss Iv Ear 2002, 16, 13-18.
5. Hiroyasu, H.; Kadota, T., Fuel Droplet Size Distribution in Diesel Combustion-Chamber. B Jsme 1976, 19 (135), 1064-1072.

6. Faeth, G. M., Current Status of Droplet and Liquid Combustion. *Prog Energ Combust* 1977, 3 (4), 191-224.
7. J. R. Adam, N. R. L., and Hendrick.Cd, Collision Coalescence and Disruption of Water Droplets. *Journal of Applied Physics* 1968, 39, 5173-5180.
8. Geldart, R. H. M. a. J. W., Drop Collisions under Conditions of Free Fall. *Journal of the Atmospheric Sciences* 1962, 19, 107-113.
9. Abbott, C. E., Survey of Waterdrop Interaction Experiments. *Rev Geophys* 1977, 15 (3), 363-374.
10. Jiang, Y. J.; Umemura, A.; Law, C. K., An Experimental Investigation on the Collision Behavior of Hydrocarbon Droplets. *J Fluid Mech* 1992, 234, 171-190.
11. Qian, J.; Law, C. K., Regimes of coalescence and separation in droplet collision. *J Fluid Mech* 1997, 331, 59-80.
12. Pan, K. L.; Law, C. K.; Zhou, B., Experimental and mechanistic description of merging and bouncing in head-on binary droplet collision. *Journal of Applied Physics* 2008, 103 (6).
13. Zhang, P.; Law, C. K., An analysis of head-on droplet collision with large deformation in gaseous medium. *Physics of Fluids (1994-present)* 2011, 23 (4), 042102.
14. Gopinath, A.; Koch, D. L., Collision and rebound of small droplets in an incompressible continuum gas. *J Fluid Mech* 2002, 454, 145-201.
15. Bach, G. A.; Koch, D. L.; Gopinath, A., Coalescence and bouncing of small aerosol droplets. *J Fluid Mech* 2004, 518, 157-185.
16. Ashgriz, N.; Poo, J. Y., Coalescence and Separation in Binary Collisions of Liquid-Drops. *J Fluid Mech* 1990, 221, 183-204.
17. Rabe, C.; Malet, J.; Feuillebois, F., Experimental investigation of water droplet binary collisions and description of outcomes with a symmetric Weber number. *Phys Fluids* 2010, 22 (4).
18. Tang, C.; Zhang, P.; Law, C. K., Bouncing, coalescence, and separation in head-on collision of unequal-size droplets. *Phys Fluids* 2012, 24 (2).
19. Unverdi, S. O., Numerical simulations of multi-fluid flows. PhD thesis, The University of Michigan 1990.
20. Unverdi, S. O.; Tryggvason, G., A Front-Tracking Method for Viscous, Incompressible, Multi-Fluid Flows. *J Comput Phys* 1992, 100 (1), 25-37.
21. S.O. Unverdi, G. T., Computations of multi-fluid flows. *Physica D: Nonlinear Phenomena* 1992, 60, 70-83.
22. Anilkumar, A. V.; Lee, C. P.; Wang, T. G., Surface-Tension-Induced Mixing Following Coalescence of Initially Stationary Drops. *Phys Fluids a-Fluid* 1991, 3 (11), 2587-2591.
23. M.R. Nobari, G. T., The flow induced by the coalescence of two initially stationary drops. NASA Technical Memorandum 1994.
24. Nobari, M. R., Numerical simulation of oscillation, collision, and coalescence of drops. PhD thesis, The University of Michigan 1993.



## II.2 Jet Atomization and Spray Formation in Impinging Jets (Lee, U. Cincinnati)

### 1. Abstract

Near- and far-field atomization and mixing processes of impinging doublets are experimentally characterized using non-gelled and gelled fluids as working fluids. The main emphasis of the study is on the effect of pre-impinging jet stream surface dynamics on break-up and mixing processes. Nozzle geometry - such as orifice inlet shape and aspect ratio, and spray chamber pressure affect jet stream surface dynamics before and after jet impingement and hence sheet breakup and mixing. For a given flow rate, the sheet formed by impinging jets is much more stable and the corresponding break-up length is much greater for gelled water than for non-gelled water jets. The nozzle aspect ratio has a more significant effect on the near-field jet stream characteristics for both fluids than the orifice inlet shape. Longer nozzles ( $l/d=20$ ) form more stable jet streams and delay the break-up of sheets, leading to greater break-up length than that attained with shorter nozzles ( $l/d=5$ ). The liquid breakup regimes have been quantitatively characterized for both non-gelled and gelled simulants over a range of flow conditions. For all fluids, the breakup length is found to decrease as the ambient pressure increases. Near-field imaging and its analysis show that the ambient pressure affects jet surface dynamics before impingement by increasing the jet surface disturbance length scale and sheet dynamics after impingement by shortening the surface wavelength, resulting in shorter breakup length with the increase of ambient pressure.

### 2. Nomenclature

$d_0$	= Orifice diameter (mm)	
$K$	= Pre-exponential coefficient	
$L$	= Length (mm)	
$L_b$	= Breakup length (mm)	
$n$	= Power law index	
$P$	= Pressure (MPa)	
$Re_j$	= Reynolds number of the jet	$(\rho_j U_j d_0 / \mu)$
$Re_g$	= Reynolds number of the gas	$(\rho_g U_g d_0 / \mu)$
$U$	= Velocity (m/s)	
$We_g$	= Weber number of the gas	$(\rho_g U_g^2 d_0 / \sigma)$
$We_j$	= Weber number of the jet	$(\rho_j U_j^2 d_0 / \sigma)$
Subscript		
$c$	= critical	
$g$	= gas	
$gen$	= generalized	
$GHP$	= Gelled Hypergolic Propellant	
$HBE$	= Extended Herschel Bulkley	
$j$	= jet	
Greek		
$\gamma$	= shear rate ( $s^{-1}$ )	
$\Theta$	= Half impingement angle of liquid jets ( $^\circ$ )	
$\lambda$	= wavelength (mm)	
$\mu$	= Newtonian viscosity (Pa.s)	

- $\eta$  = non-Newtonian viscosity  
 $\eta_{\infty}$  = non-Newtonian viscosity at infinite shear rate  
 $\rho$  = density ( $\text{kg/m}^3$ )  
 $\sigma$  = surface tension ( $\text{Nm}^{-1}$ )  
 $\tau$  = Yield stress (Pa)

### 3. Introduction

The flow characteristics of liquid streams before impingement have been known to have significant effects on the mixing as well as atomization processes occurring downstream. Important key parameters are the aspect ratio (length/diameter) of nozzle orifice and the orifice inlet geometry.

The effects of nozzle properties on internal flow within the nozzle have been studied by Nuric<sup>1</sup>, Jung et al.<sup>2-3</sup> and Ryan et al.<sup>4</sup>. Nurick expounds on the importance of cavitation within a nozzle which induces hydraulic flip. The onset of cavitation for a sharp-edged orifice inlet is dependent on flow conditions and nozzle aspect ratio ( $l/d$ ). As the nozzle orifice upstream pressure increases, the separation (cavitation) region at the orifice inlet increases to about four times the diameter of orifice, after which it reattaches. Rounding the nozzle orifice inlet is found to reduce the propensity of vena contracta formation. The effects of nozzle characteristics on jet streams have been reported by Jung et al.<sup>3</sup> Their study shows that turbulence strength (dependent on inlet conditions, jet velocity, and fluid properties) is an important factor affecting the breakup characteristics of liquid sheets. In their study, it is observed that the coefficient of discharge was higher for nozzles with rounded inlets than those with sharp inlets, implying better efficiency and lesser turbulence within the former. Higher cavitation is also observed for sharp inlet nozzles, which results in immediate expansion of the jet upon exit from the orifice. Although impact force decreases the break-up length, jet turbulence softens impact force effects, preventing the full development of sheet waves. The trends are observed in the results of Jung et al.<sup>2-3</sup>, where it is found that break-up of sheets formed from turbulent jets is due to the turbulence itself, whereas break-up of laminar jets is due primarily to impact force effects. Ryan et al.<sup>4</sup> report that the break-up length variation with Weber number for laminar sheets increases initially before decreasing, but in the case of turbulent sheets, break-up length is found to gradually increase with Weber number. This result contradicts the linear instability theory analysis, where a gradual decrease of break-up length with the increase of Weber number is predicted. In the study by Jung et al.<sup>2</sup>, it is reported that the break-up length gradually decreases with the increase of Weber number. Although the trend is similar, the linear instability theory consistently overestimates the break-up length. Also, straight-edge inlet nozzles are found to produce a more turbulent jet than angled-edge inlet nozzles and a change of flow rate has a less discernable effect on the break-up length for the former inlet type. The effect of impingement angle on break-up length has been studied by Ryan et al.<sup>4</sup>, where it is observed that the break-up length for laminar sheets decreases with an increase in impingement angle but the opposite trend is observed in the case of turbulent jets.

Early work<sup>5</sup> on the pressure effect on sheet formation reported no change from ambient pressure to 0.25 MPa. Dombrowski<sup>6</sup> was the first to study the effect of pressure on sheet disintegration over a wide range of pressures (vacuum to 2.1 MPa) and reported amplification of aerodynamic waves at elevated pressures. At higher pressures, the breakup length of the sheet is shortened because of impact waves generated at the impingement point<sup>7</sup> and violent ejection of droplets from the periphery of the sheet<sup>8</sup>. There has been no effort undertaken to quantify the phenomenon of impact waves and its relation to breakup length.



Despite studies<sup>6</sup> on how Reynolds number influences sheet breakup, the effects of viscosity at higher pressures has not been studied. Breakup modes, based on Reynolds number, are classified broadly under two regimes; capillary instability and Kelvin-Helmholtz instability. At higher Reynolds numbers, the closed rim sheet transitions into an open rim sheet as a result of Kelvin-Helmholtz instability. One of the major characteristics of this open rim sheet is the formation of ligament structures which eventually transitions to a turbulent regime. The breakup mode becomes more complicated in the case of gellant fuels because the addition of gellant influences the rheological properties of the fluid<sup>9</sup>. Unlike conventional fuels, Gelled Hypergolic Propellants (GHPs) are non-Newtonian shear-thinning fluids which undergo a decrease in shear viscosity with increasing shear rate. Extensive experiments<sup>10</sup> conducted on gelled propellants found the Extended Herschel Bulkley equation accurately predicts the dependency of the shear viscosity to the shear rate. Detailed investigations into the atomization behavior of GHPs in air show that regimes of particulate-based gelled propellants at low Reynolds number display pronounced ray-shaped patterns. At higher Reynolds numbers, regimes tend to overlap between non-Newtonian and Newtonian fluids<sup>11</sup>. Despite the introduction of a generalized Reynolds number for different fluids, the regime diagrams presented by Ciezki et al. are insufficient to describe breakup patterns over a wide range of flow conditions because similar regimes occur over distinct conditions. This could be attributed to the fact that the effect of pressure is not taken into account while characterizing these regimes.

The shape of the jet formed prior to impingement plays a crucial role in the structure of the sheet formed upon impact. This shape is necessary for governing combustion dynamics and for designing actual air breathing propulsion systems. One of the key phenomena occurring upstream of the impingement point is the cavitation inside the nozzle, which is found lacking at higher pressures<sup>1</sup>. This increase in pressure reduces the atomization of the jet and re-attachment of the flow takes place before the nozzle exit<sup>12</sup>. Liquid sheet dynamics are also affected by turbulence strength of the jet prior to impingement. Experimental findings<sup>3</sup> indicate that upon increasing jet turbulence, the breakup length of sheet is shortened and the wavelengths of ligaments show a marked decrease. Furthermore, there is no study conducted on ligament breakup or surface wave measurement characterization with a focus on ambient pressure.

The objective of this study is to characterize the non-reacting spray of non-gelled and gelled simulants formed by like-doublet impinging jets with respect to the change of surface tension, viscosity and pre-impingement conditions over a wide range of pressures. The jet stream dynamics before impingement are characterized for various nozzle pairs where the nozzle inlet sharpness and the aspect ratio (nozzle length/nozzle diameter) are varied. Also, in order to explain the effect of ambient pressure on the breakup length, the surface of the jet before impingement and the near field spray characteristics, such as surface wavelength, are characterized. Spray characteristics, such as ligament wavelength, are also measured in the downstream of the impingement region. Lastly, a breakup regime map is proposed to extend the understanding of breakup regimes across various fluids over a wide range of ambient pressure by introducing non-dimensionless numbers.

## 4. Experimental Details

### 4.1 Nozzle configurations

Schematic drawings of nozzles used in this study are shown in Fig. 1. The orifice diameter of the nozzles is 0.5mm and verified using a microscope to be within 2.5 % of its nominal size. The orifices were machined using EDM (Electrical Discharge Machining) in order to ensure similarly smooth internal surfaces for all nozzles. The entrance to the orifice is either straight or angled and the aspect ratios (length-to-diameter) of the nozzles are 5 and 20. For the angled-edge orifice entrance, the angle for the tapered section is 120 degrees. For all experiments, the impingement angle is set at 60 degrees and the distance from the exit of the orifice to the impingement location is fixed at 5 mm.

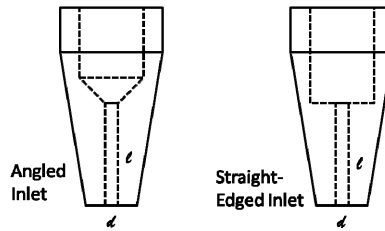


Figure 1. Schematic drawings of angled inlet (left) and straight inlet (right).

### 4.2 Experimental setup

The experimental setup is shown in Fig. 2. Also shown is the feed system of gelled simulants.

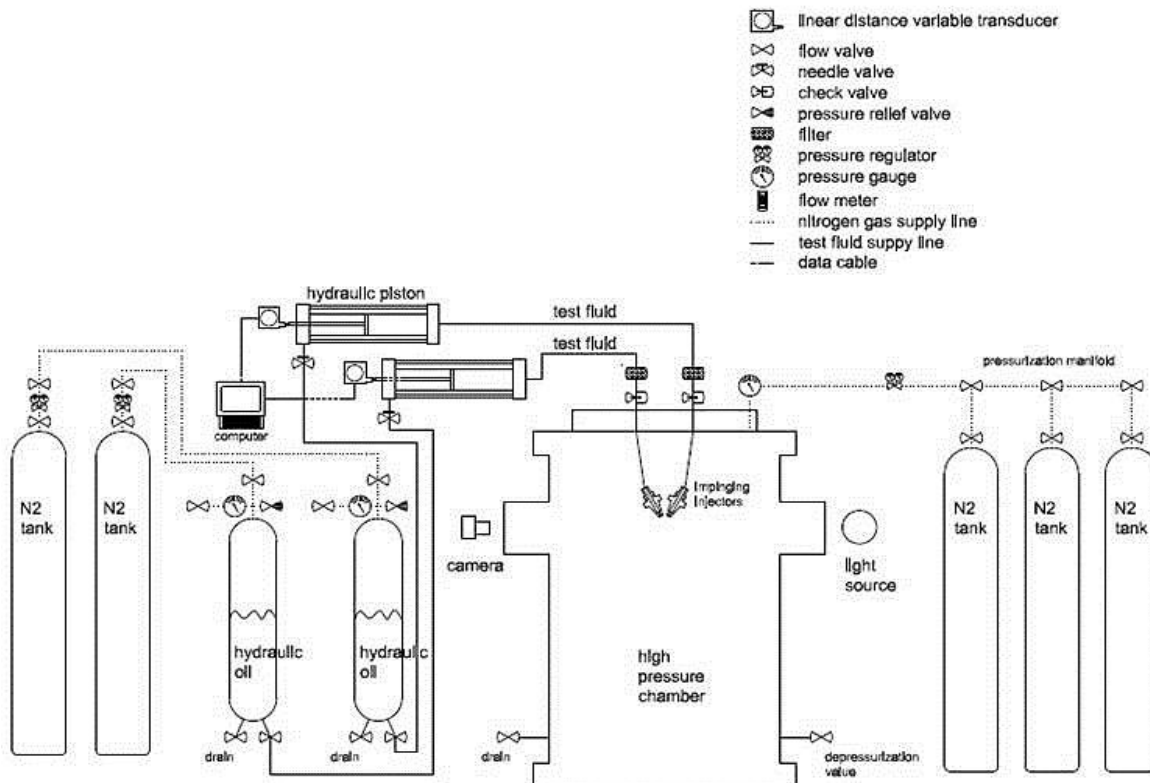


Figure 2. Schematic drawing of a gelled water simulant feed system into a high pressure chamber.

Nitrogen gas at constant pressure is used to drive hydraulic oil into a double-acting cylinder and the piston dispenses the gel into the injectors. Fresh batches of gel are used each time since some leakage across seals in the cylinder is observed when batches are kept stagnant for an extended period of time. The flow rate of gel is controlled by varying the flow rate of hydraulic oil using a needle valve and is determined by measuring the displaced volume of the cylinder using LVDTs (Linear Variable Displacement Transducer, UniMeasure LX-PA-25) attached to the piston of cylinder. The flow rates of each nozzle in the doublet are kept the same for each set of operating conditions. LabView is used to measure, display and record the flow rate. In the case of non-gelled distilled water, pressurized nitrogen is used to drive water through the nozzles directly from pressure vessels. Flow rates for the Newtonian fluids are monitored using standard high pressure flow meters with an accuracy of  $\pm 2\%$  (Brooks Flowmeters MT3809). They are then dispensed into the chamber. The pressure chamber is rated for pressures up to 6.8 MPa and allows optical access to its inside through 7.6 cm diameter quartz windows.

#### 4.3 Rheological characterization of gelled simulants

The working fluids are listed in Table 1. The two Newtonian fluids are distilled water and an ethanol-water mixture in the volumetric ratio of 3:1 to simulate the base of the gellant. Two gelled-simulants are used: one is a polymer (Carbopol 981A, Lubrizol)-based gel where 0.5% Wt. Carbopol is mixed in water and the other is a particle-based gel where a fumed silica (Cabosil TS-720-Cabot Corp) is mixed in 75 % ethanol - 25 % water mixture with 0.1% Carbopol (Carbopol 981A, Lubrizol). Various batches of the simulant gel are rheologically matched with the standard GHPs such as MMH, IRFNA and Hydrazine<sup>13</sup>. A cup and cone arrangement of the rheometer (TA Instruments AR200) is used to determine the change of viscosity with applied shear. Fresh batches of gel are prepared and rheologically tested to maintain conformity with standard GHPs in terms of the relation of viscosity to shear rate. The rheometer offers torque control (0.0003  $\mu\text{N}\cdot\text{m}$  - 200  $\text{mN}\cdot\text{m}$ ) with a resolution of 0.1  $\text{nN}\cdot\text{m}$ . The experimental values are used to curve fit the models as shown in Figure 3a. The relation of viscosity to shear rate for the gelled simulant falls into a region where those of gelled hydrazine and IRFNA cover. Also, the dynamic viscosity measurement for a fresh batch is made and a typical result for the particle-based gel is shown in Figure 3b where it shows that the storage modulus ( $G'$ ) is greater than the loss modulus ( $G''$ ), indicating that the mixture is weakly gel and elastic. Compared to similar measurements for polymeric gel, the value of  $G''/G'$  is less for the particle-based gel, indicating the latter exhibits more elastic behavior than the former.

Table 1. Properties of working fluids at STP.

Test Fluid			Surface tension ( $\text{N}\cdot\text{m}^{-1}$ )	Density ( $\text{kg}\cdot\text{m}^{-3}$ )	Newtonian Viscosity ( $\text{Pa}\cdot\text{sec}$ )	Power law index, $n$	Pre-exponential coefficient, $K$	Non-Newtonian viscosity at infinite shear rate, $\eta_\infty$
Water			0.072	1000	0.001	N/A	N/A	N/A
Ethanol/Water			0.0254	866.9	0.00195	N/A	N/A	N/A
Polymeric gel			0.072	1000	N/A	0.464	7.26	N/A
Particle-based gel	0.0254	866.9	N/A	0.5	2.5		8	

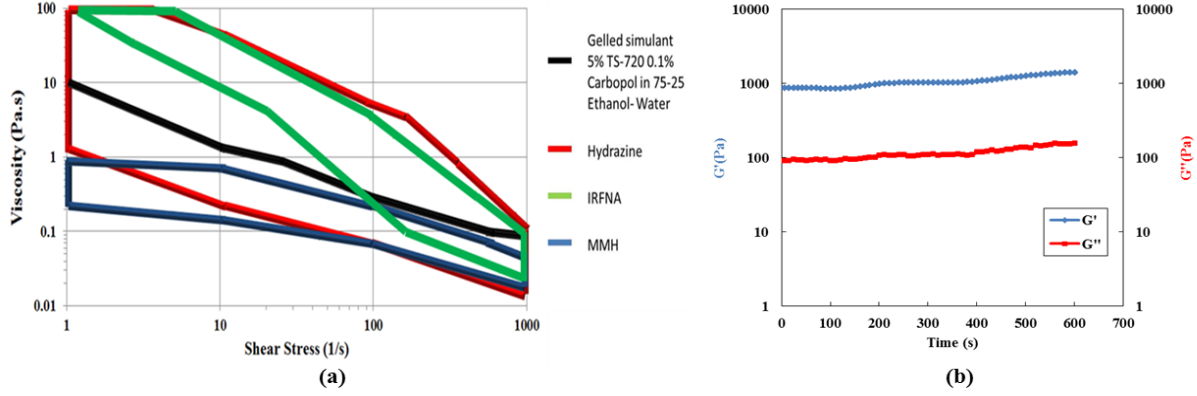


Figure 3. Rheology of simulant gel: (a) Viscosity vs. Shear rate for gels (b) Storage and Loss moduli plotted versus time for particle-based gel.

In this study, to characterize the rheological behavior, one employs the Extended Herschel-Bulkley [5] model. This model considers the constant viscosity of the gel at infinite shear and presents viscosity in the form of:

$$\eta = \frac{\tau_o}{\gamma} + K\gamma^{n-1} + \eta_\infty \quad (1)$$

This value of viscosity is then used to fit into the Extended Herschel-Bulkley based  $Re_{gen}^{11}$  which has shown good correlation when applied at lower shear rates for gels.

$$Re_{gen,HBE} = \frac{\rho u^{2-n} d_o^n}{\frac{\tau_o}{8} \frac{D}{u} + K \left( \frac{3m+1}{4m} \right)^n 8^{n-1} + \eta_\infty \left( \frac{3m+1}{4m} \right) \left( \frac{D}{u} \right)^{n-1}} \quad (2)$$

where  $m$  is written as:

$$m = \frac{nK \left( \frac{8u}{D} \right)^n + \eta_\infty \left( \frac{8u}{D} \right)}{\tau_o + K \left( \frac{8u}{D} \right)^n + \eta_\infty \left( \frac{8u}{D} \right)} \quad (3)$$

#### 4.4 Diagnostics

The shadowgraph technique is used to characterize near-field atomization processes. The light source used is a Xenon Nanopulser 737B which is capable of emitting 5 mJ with a pulse duration of 10 ns. The light is collimated using a lens (ThorLabs LA1131 N-BK7, 1" diameter and 50mm focal length). The collimated light is directed onto the optical access window of the high pressure chamber and is focused onto a digital single-lens reflex (DSLR) camera (Nikon D7000 equipped with a 180 mm macro lens). Typical settings for the camera are an exposure time of 1/6th of a second, an ISO sensitivity setting of 1600, and an f/4.5. Once the images are captured, they are processed using ImageJ software<sup>15</sup>. This procedure is used to obtain quantitative data such as breakup length, surface wavelength, and ligament wavelength. Surface disturbances are calculated by thresholding near-field jet streams. For each flow condition, 100 images are obtained.

The planar laser-induced fluorescence is used to characterize mixing. A second-harmonic of Nd:YAG laser at 532 nm is used to excite a dye (Rhodamine 610) resolved in base fluid. Typical laser energy is 20 mJ/pulse and dye concentration is kept at 3mg/liter. The laser beam is formed in a sheet (width of 2") using a train of optics. The resulting fluorescence is collected using a DSLR lens, filtered using a long wave pass filter (OG 590) and a band pass filter (610 $\pm$ 10 nm) and detected using an ICCD (Intensified CCD camera, PIMAX 3, Princeton Instruments). The imaging plane is located 2" downstream of impinging location and the imaging is made at 45° with respect to the laser sheet plane. Therefore, a correction for the perspective distortion is required for each image taken. ImageJ software is used to analyze the acquired images.

## 5. Results and Discussion

The results are presented in two subsections describing results for an atmospheric chamber pressure and high-chamber pressure. For the former, the effect of nozzle geometry on the atomization characteristics is mainly investigated and for the latter the effect of jet surface dynamics on the atomization at high chamber pressure is studied.

### 5.1 Effect of nozzle geometry on the atomization at an atmospheric chamber pressure

#### 5.1.1 Nozzle & near-field jet stream characterization

Sheet formation, break-up, and subsequent atomization are known to depend on the flow conditions of the jet prior to impact<sup>2,3</sup>. Therefore, each nozzle is characterized in terms of flow rate with respect to pressure drop across the nozzle as shown in Figure 4, where results for non-gelled water are presented. In the case of the shorter straight edge nozzles ( $l/d=5$ ), the flow rate increases linearly with the root of the pressure drop to a certain level, beyond which the flow rate begins to stop increasing, indicating the onset of cavitation within the orifice. A maximum discharge coefficient ( $C_d$ ) of 0.8 (+0.02) is reached consistently at a flow rate corresponding to 205 cc/min. For the angled edge inlet nozzles ( $l/d=5$ ), the occurrence of cavitation appears to be delayed to a higher pressure drop. The maximum discharge coefficient ( $C_d$ ) reached is 0.81 (+0.02) at a flow rate corresponding to 225 cc/min, after which the  $C_d$  was found to drop. Overall, these results lead us to conclude that angling the inlet allows slightly higher flow rate across a

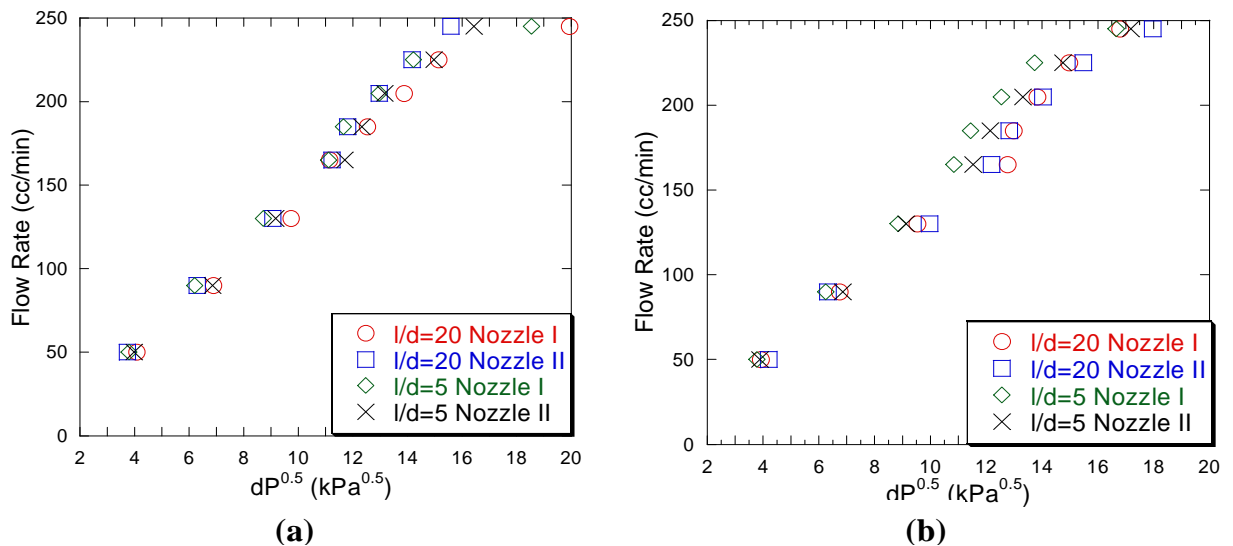


Figure 4. Flow rate vs. the root of pressure drop across nozzle for non-gelled water (a) straight-edge inlet nozzle and (b) angled-edge inlet nozzle.

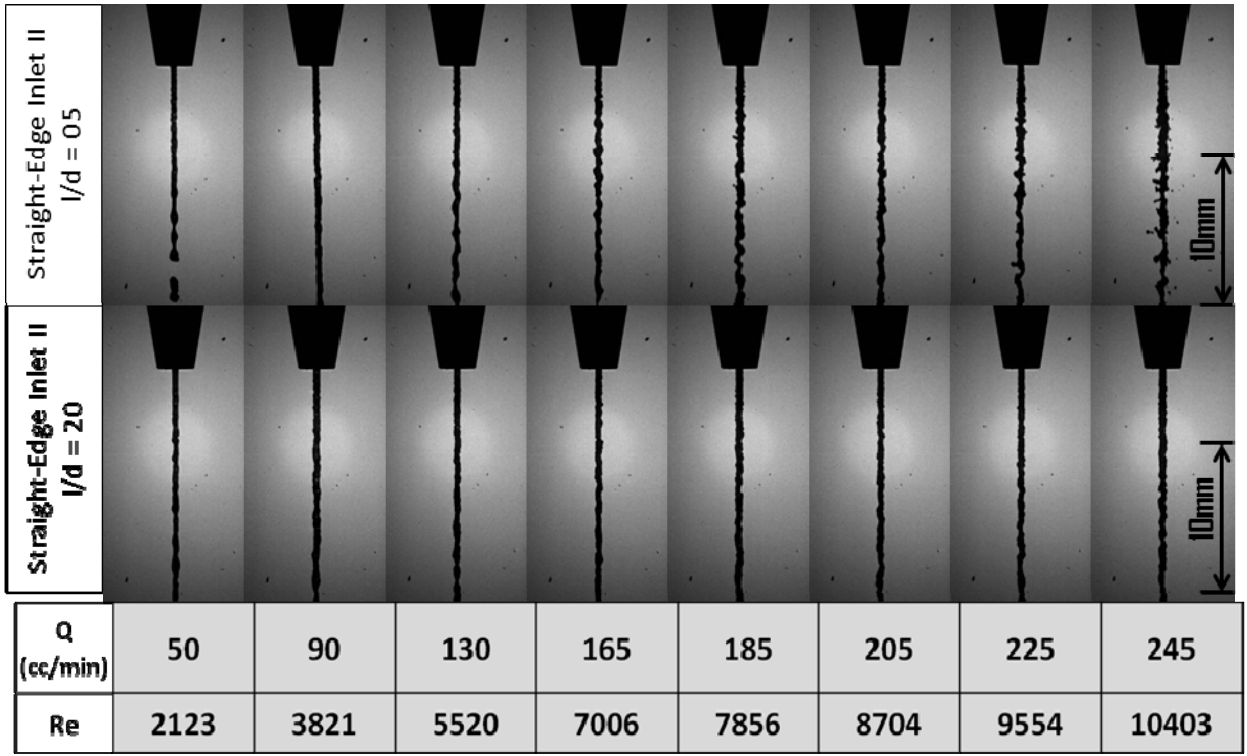


Figure 5. Images of near-field jet streams exiting orifice for non-gelled water with straight edge inlet: images on the top row for short nozzles ( $L/D=5$ ) and the bottom row for long nozzles ( $L/D=20$ ).

nozzle before the losses become significant. Although these results mirror those of Jung et. al.<sup>3</sup>, the differences in the effect of nozzle inlet are not as significant as what they have found. Also, it can be noted that any given pair of nozzles do not behave identically, as evident from the relationship between flow rate and pressure drop shown to be not being exactly the same.

Nurick<sup>1</sup> uses a cavitation model to determine a critical value at which cavitation would occur for a given model (Eq. 4). The nozzle used in his study has a critical cavitation number of 1.45 (for an aspect ratio,  $l/d = 20$ ). Using this model, the critical cavitation number for the longer nozzles ( $l/d = 20$ ) was determined to be 1.44, which corresponds well with the results of Nurick. For the shorter nozzles ( $l/d = 5$ ), the critical cavitation number was found to be 1.65.

$$\text{Cavitation No.} = \frac{P_1 - P_v}{P_1 - P_B} \quad (4)$$

Near-field images of non-gelled jet streams exiting the nozzles are shown in Figure 5. They show that disturbances on the jet surface are observed at Reynolds number greater than 2000. These disturbances increase as the flow rate increases and are more evident for shorter nozzles than for longer ones, for any given flow rate. A similar observation has been made by Asghriz et al.<sup>14</sup> who report that jet streams from shorter nozzles are subject to higher fluctuations due to turbulence and spread out on exiting due to cavitation. As shown in Figure 5a, for short nozzles ( $l/d=5$ ), the jet streams are observed to have already undergone hydraulic flip at high flow rates ( $Q > 250$  cc/min), due to stagnation of flow rate with increase in upstream pressure, indicating the presence of hydraulic flip in the orifice. However, longer nozzles ( $l/d=20$ ) do not show any evidence of hydraulic flip for flow rates of up to 250 cc/min, as the trend shows the flow rate to

increase uniformly with increase in upstream pressure. In terms of jet surface disturbance and cavitation, angled-edge inlet nozzles are observed to behave in a very similar manner as the straight-edge inlet nozzles. Quantitative characterization of disturbances on the jet streams with respect to nozzle orifice inlet type is difficult. However, the effects of nozzle aspect ratio on the jet stream's surface disturbances are very evident.

Figure 6 shows plots of flow rate with respect to pressure drop across the nozzle for gelled water cases. Contrary to non-gelled cases, the flow rate increases linearly with the root of pressure drop, without showing any evidence of cavitation, even at flow rates about twice as much as that of non-gelled cases. Further, it is observed that a higher pressure drop is required across the nozzle to deliver the same amount of flow compared to the non-gelled cases. Similar to non-gelled cases, the effect of nozzle inlet orifice geometry (straight vs. angled edge inlets) on the relationship between the flow rate and the pressure drop across the nozzle is even less evident for gelled jet streams. The  $C_d$  attained for the nozzles at a maximum flow rate of 500cc/min (experimentally limited) was 0.7 (+0.02), and still increasing. This is significantly lesser than what was observed for the non-gelled case. This  $C_d$  is consistent for the gelled case, irrespective of inlet geometry (i.e. straight or angled). At the maximum flow rate of 500cc/min, the pressure upstream of the nozzle was 240psig. Since the gellant content for the fluid is very small (0.5%), and since the magnitude of vapor pressure is much smaller relative to the upstream pressure and the atmospheric pressure, the vapor pressure of the gel was assumed to be similar to that of water.

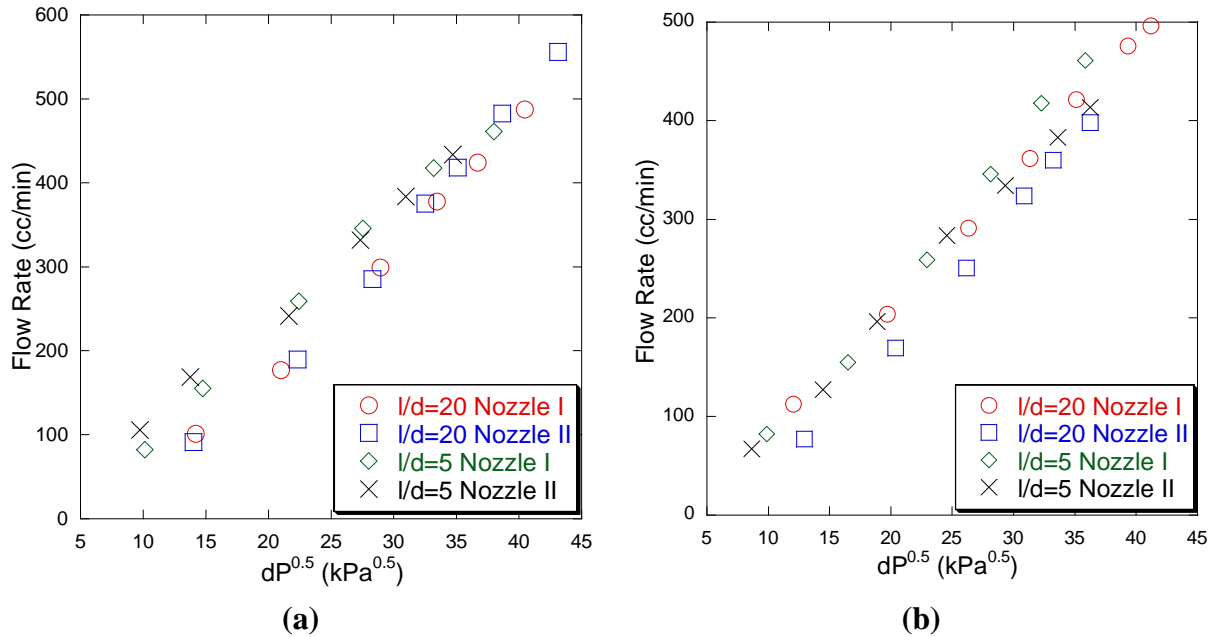


Figure 6. Flow rate vs. the root of pressure drop across nozzle for gelled water (a) straight-edge inlet nozzle and (b) angled-edge inlet nozzle.

This was used to determine the cavitation number. Under this assumption and at the maximum experimental flow rate, the cavitation number for the gel was found to be 1.06. Note that since there was no evidence of decreasing  $C_d$ , this does not reflect the critical cavitation number for the gel.

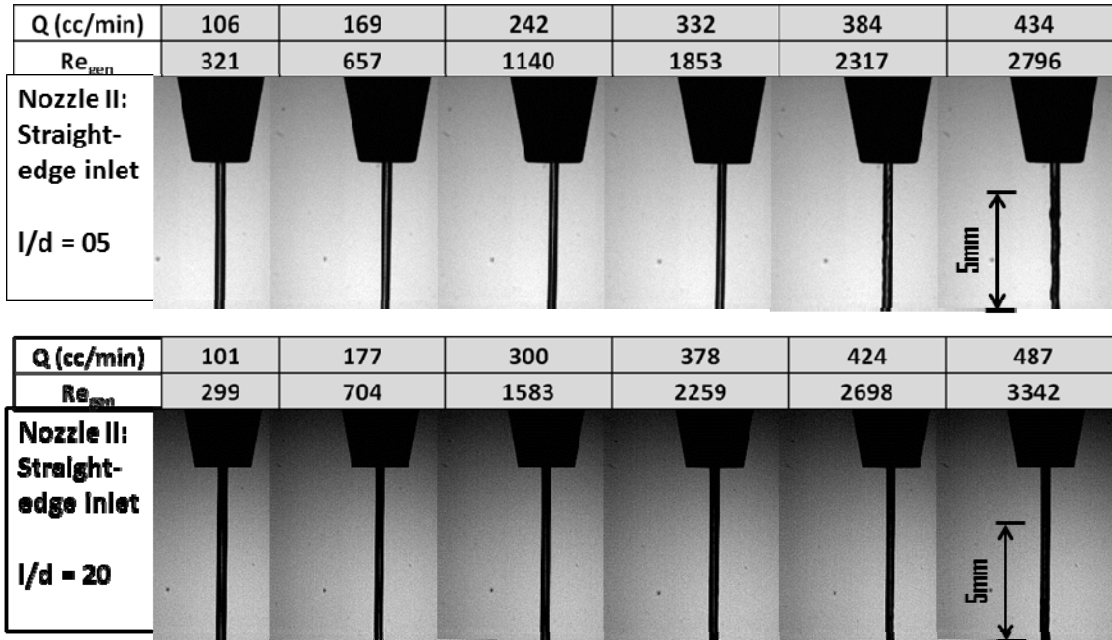


Figure 7. Images of near-field jet streams exiting orifice for gelled water with straight edge inlet: images on the top row for short nozzles ( $L/D=5$ ) and the bottom row for long nozzles ( $L/D=20$ ).

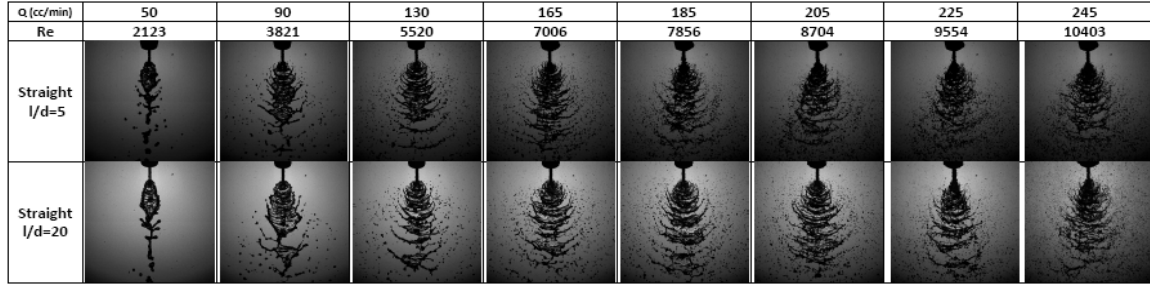
Near-field images of gelled jet streams at the exit of nozzles are shown in Figure 7. Considerably smaller disturbances exist on the jet surface as compared to the non-gelled cases. It is apparent that the flow of gelled water through the nozzle is much more laminar than that of non-gelled water, even at much higher flow rates. However, it should be noted that the corresponding Reynolds numbers at similar flow rates are lower due to the higher viscosity of the gel. As for the shorter nozzles, some evidence of surface disturbance is observed at flow rates where the generalized Reynolds numbers are around the critical value of 2620, as given by Eq. (2). However, no surface disturbance is observed for the long nozzle for the flow rates employed in this study and for generalized Reynolds numbers of up to 3300.

Findings from this section indicate that the nozzle aspect ratio has more noticeable effects on the near-field jet stream characteristics for gelled as well as non-gelled jet stream than the nozzle inlet shape. These surface disturbances will propagate downstream and affect far field spray characteristics as well as jet break up processes.

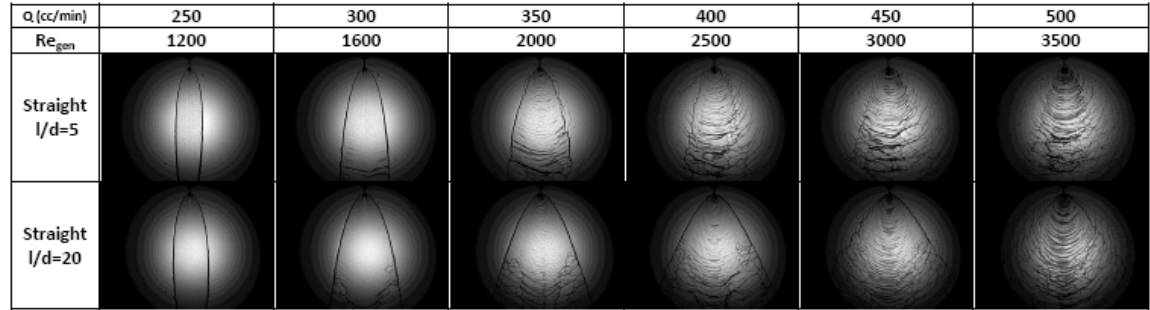
### 5.1.2 Sheet formation and break-up

The sheets formed at different flow rates using various pairs of nozzles are imaged using a high-speed camera. About 200 images are taken per operating condition and they are filtered and averaged above a threshold to determine break-up length. This is determined as the distance from impingement point of doublets to the first location where the sheet is disconnected. Figure 8 shows typical instantaneous images of impinging doublets. As the flow rate is varied, the sheet formation and controlling break-up mechanism changes. For non-gelled water cases at low flow rates, the sheet is not fully developed yet and the break-up occurs predominantly along the rim of the sheet. As the flow rate increases, instead of droplets separating from the rim, ligaments start fragmenting from the rim. The sheet surface ligaments fragment at periodic intervals from the





(a)



(b)

Figure 8. Typical instantaneous images of impinging doublets for (a) non-gelled and (b) gelled water cases for different orifice configurations.

periphery of the impingement point and a wave-like structure emanating from near the impingement point is observed. Increasing disturbance on the sheet surface eventually leads to the separation of ligaments. These ligaments then disintegrate into droplets further downstream.

Sheet formation for gelled water is quite different from that of non-gelled water. At low flow rates, the sheet is very stable, showing no evidence of disturbances on most parts of the sheet

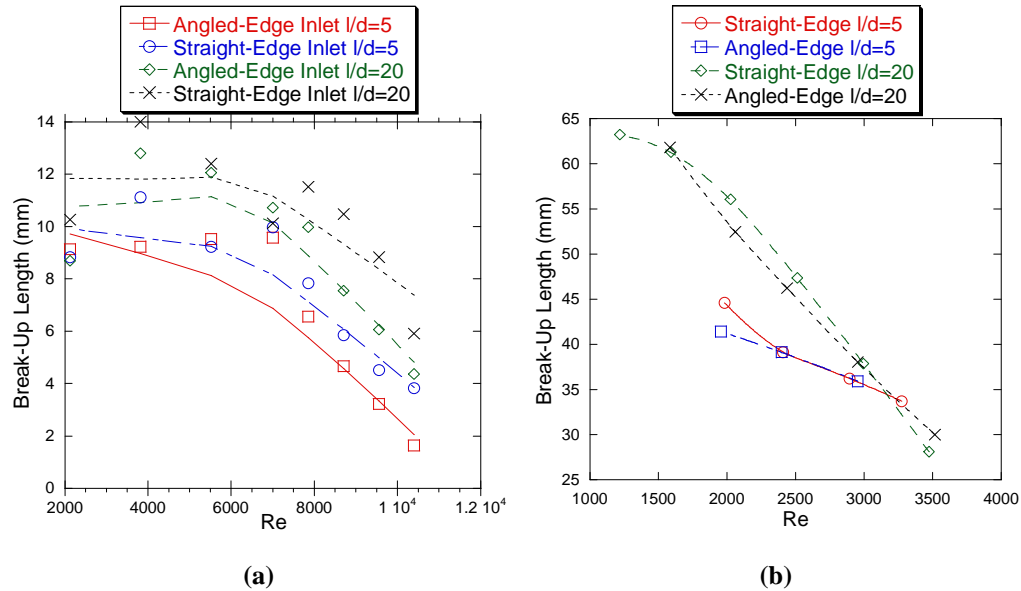


Figure 1. Break-up length vs. Reynolds number for (a) non-gelled and (b) gelled water and for nozzles with various orifice configurations.

except at the boundary. As the flow rate is increased, the propagated disturbances appear to cause break-up of the sheet starting from its periphery and a relatively smaller-scale, wave-like structure is observed near the center portion of the sheet. However, the ligament formation as observed in non-gelled cases is not observed and droplets are separated from the sheet almost immediately upon its break-up, without the formation of intermediate ligaments. As the flow rate is increased further, the break-up region of the sheet moves towards the centerline and periodic ligament formation is also observed. The formation of ligaments is initiated by the appearance of holes caused by surface waves on the sheet. At further downstream, the ligaments form a web-like structure after which they disintegrate into droplets. The pattern of sheet formation and disintegration is similar to that found by Kampen et al.<sup>16</sup> The web-like structure was also reported by Miller et al.<sup>17</sup> where the retardation of the breakup of fluid element due to the large extensional viscosities of the fluid is suggested as its formation mechanism.

Figure 9a shows plots of measured break-up length vs. Reynolds number for non-gelled water and for various orifices. As the Reynolds number increases, the break-up length initially increases slightly and then starts decreasing. This behavior is due to the fact that at lower flow rates the sheet is not fully developed yet, and the sheet break-up occurs not only in the downstream area, but also along the rim. It can be observed that pre-impingement jet stream conditions play a significant role in the break-up process: for all Reynolds numbers the break-up length for both pairs of nozzles with  $l/d=20$  is larger than that for nozzles with  $l/d=5$ . However, the effect of orifice inlet geometry on break-up length does not seem to be as significant. For the gelled water cases, due to the nature of the break-up processes described previously, two different downstream sheet break-up locations can be used to determine break-up length: edge (left and right) and center of the sheet, the latter being longer than the former. Plots of the break-up length measured using distance to break-up at the center of the sheet vs. Reynolds number for non-gelled water utilizing various orifices are shown in Figure 9b. The apparent viscosity of the gel is dependent on the level of shear rate in the orifice, which is dependent on two primary factors, nozzle characteristics and the nozzle exit jet velocity. This suggests that the higher

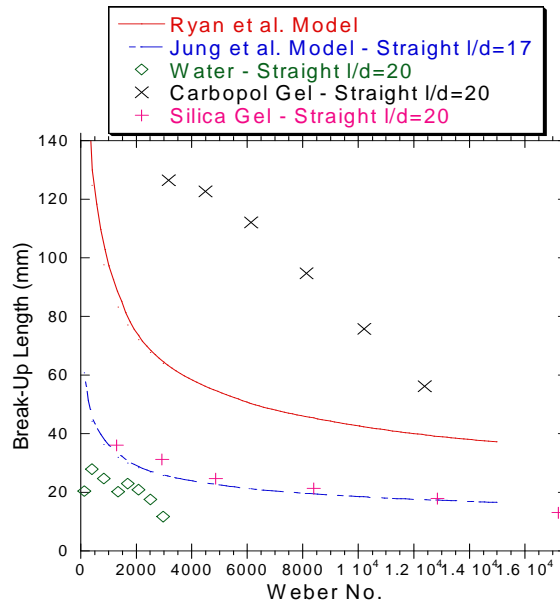


Figure 2. Comparison of breakup length.

viscosity of gelled water will require relatively more turbulent conditions for sheet break-up. Figure 9b shows that the break-up length for gelled water is indeed significantly greater than that of non-gelled water for a given Reynolds number. However, similar to non-gelled water cases, it can be observed that the pre-impingement jet stream conditions play an important role in the break-up process: break-up process is delayed significantly for the long nozzles ( $l/d=20$ ) compared to the short nozzles ( $l/d=5$ ). As the Reynolds number increases, the break-up lengths seem to converge for both nozzles. Also observed at higher flow rates is the relatively minor effect of orifice inlet geometry (aspect ratio) on the break-up length, i.e., the break-up length is more or less the same for short and long nozzle pairs.

Figure 10 shows plots of break-up length variation with Weber number including models developed by Ryan et al.<sup>11</sup> and the empirical correlation by Jung et al.<sup>9</sup> Weber number is dependent on surface tension and flow rate, and since surface tension is a constant for Newtonian and non-Newtonian fluids, flow rate is the only variable. The Weber number is defined by:

$$We = \frac{\rho u^2 d}{\sigma} \quad (4)$$

where  $\rho$  is density of fluid,  $u$  is mean flow velocity,  $d$  is orifice diameter and  $\sigma$  is surface tension of fluid. Surface tension was measured for both the gelled and non-gelled fluids and was found to be approximately the same ( $\sim 4\%$  variation of gel from the non-gelled fluid). It can be seen that for the non-gelled water case, Ryan et al.'s model<sup>4</sup>, which is based on linear stability theory, tends to overestimate the break-up length. Since the surface tension of Carbopol gel is the same as that of water, this suggests that the higher viscosity of the Carbopol gel plays a significant role in its break-up, i.e., break-up of the sheet is inhibited due to high viscosity.

### 5.1.3 Droplet size variation and distribution

Figure 11a shows the spatial distribution of mean drop size ( $D_{32}$ ) across the width (measured perpendicular to the sheet) of the spray for various nozzle flow rates and for a straight-edge nozzle pair ( $l/d=20$ ). For a given flow rate, the mean drop size becomes a maximum at the center

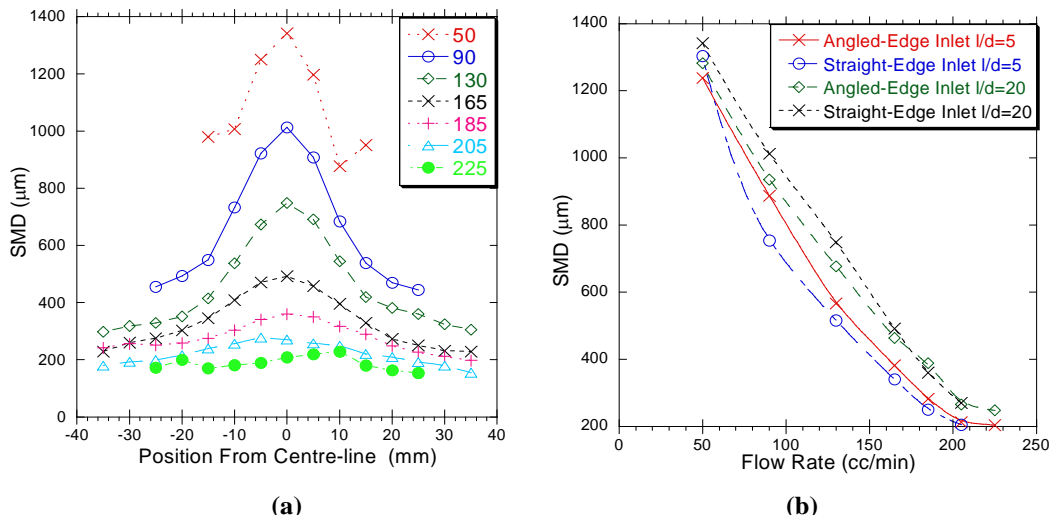


Figure 3. For non-gelled water (a) spatial distribution of drop size across spray for various flow rates and (b) mean drop size at the center of spray vs. Reynolds number for various orifice inlet configurations.

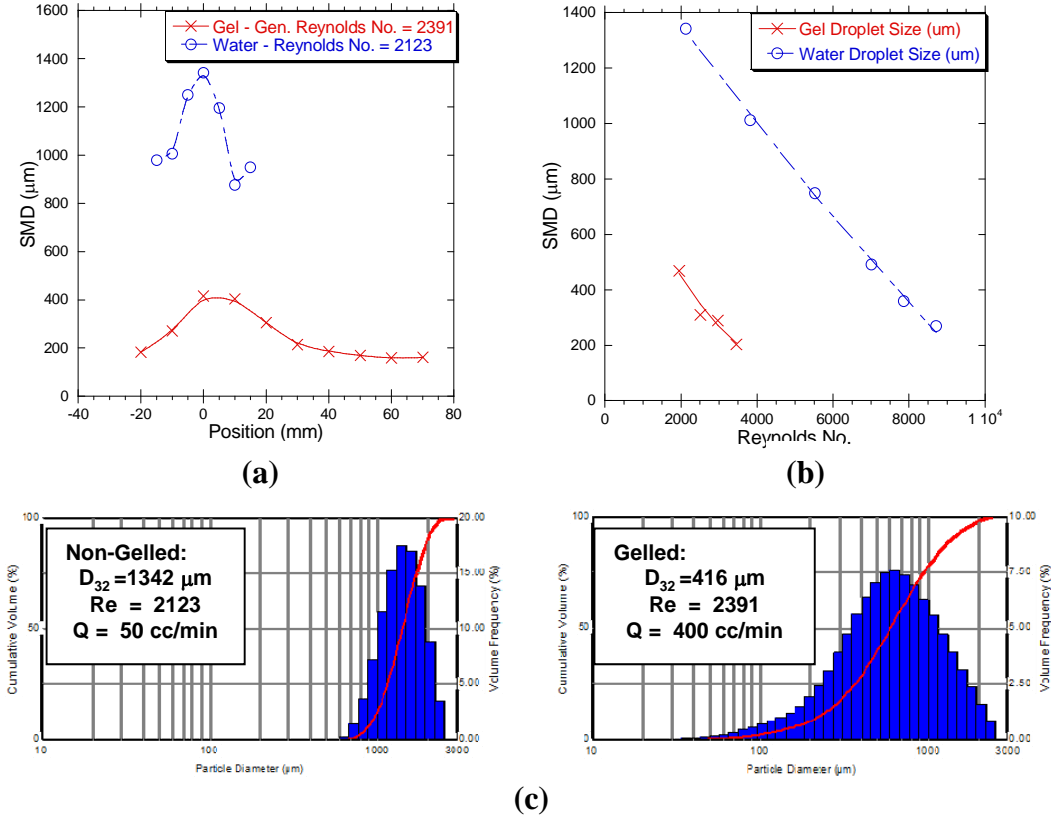


Figure 4. Comparison of atomization characteristics of impinging doublets using non-gelled and gelled water: (a) Spatial distribution of mean drop size (D<sub>32</sub>) across spray for similar Reynolds number (~2200), (b) Mean drop size vs. Reynolds number and (c) drop size distribution at the center of spray for similar Reynolds number (~2200).

of the spray and gradually decreases towards either side of the center. As the flow rate increases, the mean droplet size decreases at all locations in the spray and the spatial distribution of drop size becomes more uniform. In order to see the effect of nozzle orifice configuration on atomization, the drop size is measured at the center of the spray for various orifices. The results are shown in Fig. 11b. The mean droplet size of shorter nozzles ( $l/d=5$ ) is smaller than that of longer nozzles ( $l/d=20$ ) for both straight- and angled-edge orifice inlet nozzles. This is consistent with previous observations where the jet stream surface disturbances are more evident for shorter nozzles.

Figures 12a and 12b show that the spatial distribution of the mean drop size (D<sub>32</sub>) and centre-line droplet size distribution, respectively for gelled and non-gelled water. Figure 12a shows that the size of mean drop for the gelled water case exhibits a similar trend to a non-gelled water case at a similar Reynolds number (approximately 2200): the mean drop size becomes a maximum at the center of the spray and gradually decreases towards either side of the maximum and as the flow rate (hence Reynolds number) increases, the mean drop size gradually decreases. However, at any given location in the spray (Fig. 12b), the mean drop size is significantly smaller for the gelled water case than for the non-gelled water case, at a similar Reynolds number. Deskatyov et al.<sup>18</sup> show that droplet size for gels is larger than that for non-gelled fluids. However, their results were for similar flow rates, instead of Reynolds number. Additionally, even for high flow rates of the non-gelled water, no droplet formation was observed for the gel at similar flow rates. For

these reasons, Reynolds number was chosen as a non-dimensional independent parameter. The gel spray is distributed over a wider space (Fig. 12a) and exhibits a wider range of droplet size distribution (Fig. 12c) than the non-gelled spray. It should be noted that at similar Reynolds number, the mean jet velocity is much greater for gelled water cases than for non-gelled water cases and the break-up mechanism is quite different as previously discussed, due to the higher viscosity of the gel cases. As can be seen in the images shown in Fig. 8, ligament formation, as well as wave-like sheet structure, is observed for the non-gelled case while the sheet is not yet formed in the gelled water case at an operating condition corresponding to  $Re \sim 2200$ .

## 5.2 Effect of Chamber Pressure on the Atomization

### 5.2.1 Breakup regimes

#### 5.2.1.1 Breakup regimes for water

Shadowgraph images of the impinging jets are analyzed to gain a better understanding of breakup regimes. The breakup regimes identify a range of operating conditions where distinct mechanisms play roles in forming spray. Flow rates are varied from 50-200  $\text{cm}^3/\text{min}$  for ambient gauge pressures ranging from 0 to 4.5 MPa.

A typical spray formed by impinging jets is shown in Figure 13. After impingement of two jets, a sheet is formed. The sheet surface ligaments fragment at periodic intervals from the periphery of the impingement point and a wavelike structure emanates from near the impingement point. An increase in disturbances on the sheet surface eventually leads to the separation of ligaments.

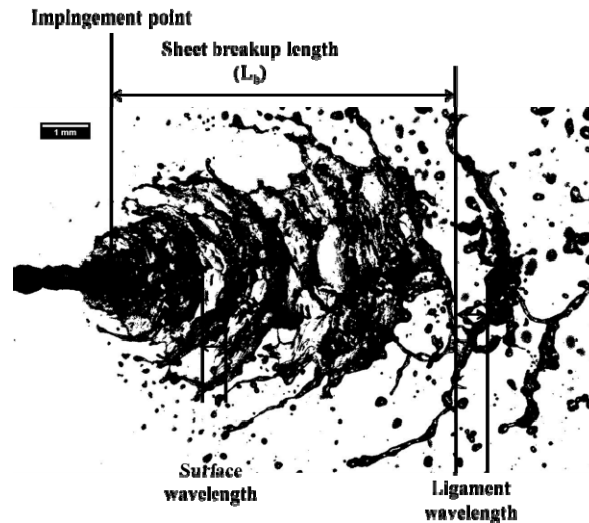


Figure 5. A typical instantaneous image of a liquid sheet formed by two impinging jets issuing water jet (Flow direction is from left to right).

These ligaments then disintegrate into droplets further downstream. Breakup length of the sheet is defined as the distance from the impingement point to the point where the sheet breaks off into ligaments. The surface wavelength is defined as the distance from the location of the first periodic wave to the very next wave as shown in Figure 13. The distance between the breakup point and the first ligaments is defined as the ligament breakup length.<sup>4</sup>

For water at atmospheric pressure, the breakup modes are divided into two primary modes. The first is closed rim sheets which are formed as a direct result of capillary instability from single jet

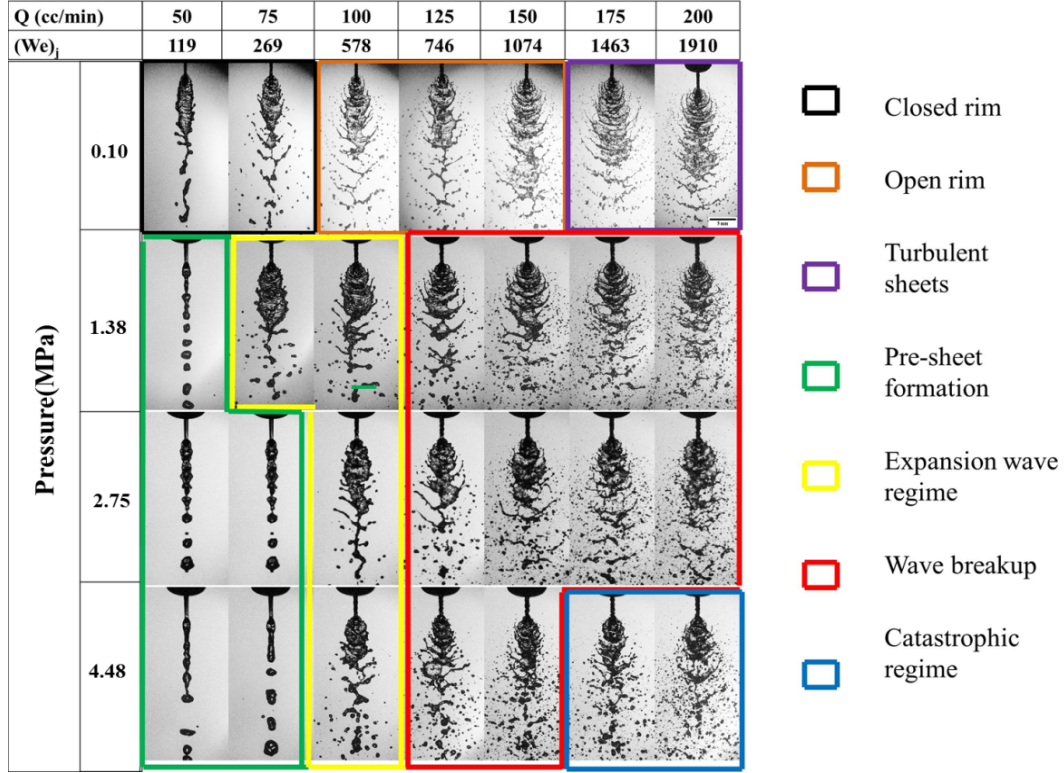


Figure 6. Shadowgraph of impinging jet spray taken for various pressures and flow rates (Non-gelled water).

instability. This is followed by open rim sheets which arise due to Kelvin-Helmholtz instability. At higher Reynolds numbers and Weber numbers greater than 2000<sup>19</sup>, closed rim sheet slowly becomes open rim sheet. This transition is clearly indicated by the amplified impact waves at impingement point and by the formation of edge ligaments. As the Reynolds number is increased further, the influence of cavitation is instrumental in forming fully developed turbulent sheets. These regimes are detailed in Figure 14.

It is clear that at elevated pressures the breakup regimes of water are distinctively different from those at atmospheric pressure as shown in Figure 14. For example, as the flow rate increases, the breakup length increases at atmospheric pressure but it decreases at pressures higher than 1.4 MPa. Also, the effect of cavitation in the nozzle on the pre-impingement jet condition and the propensity of its occurrence with respect to nozzle exit pressure affect the breakup modes. At atmospheric pressure, cavitation is observed at flow rates higher than 175cc/min. The lack of cavitation at higher pressures accounts for the difference between the regimes at these flow conditions.

A fundamental study on breakup regime for water at elevated pressures is carried out by Jung et al.<sup>7</sup> To incorporate the effect of pressure, they introduce a parameter:  $We_g$ . However, they use only one fluid (water) for their experiment and  $We_g$  only incorporates the relative effect of inertia to surface tension forces. Further investigations involving two fluids (water and kerosene) deemed Weber number alone is not sufficient to identify breakup regimes. This holds true for the test fluids employed in this study as both surface tension and viscosity vary with respect to each other. The parameters chosen to describe various breakup regimes are  $We_j$ , and  $We_g$ . The



regimes are classified by identifying visual similarities and by comparing Weber number data pertaining to flow conditions. The breakup modes observed for water at higher pressure are summarized below.

**a. Pre-sheet formation:** The breakup of the liquid sheet is delayed and no visible sheet is formed. This applies to low Weber number cases ( $We_j < 200$ ). The surface tension is unable to overcome the pressure applied on the liquid jet to cause pinch-off. In the present study, it is found that the breakup process is further delayed up to  $We_j \sim 300$  at higher pressures ranging between 2.8 MPa to 4.5 MPa.

**b. Expansion wave regime:** The common regime in all flow cases at very low Weber numbers is an expansion wave regime in which the sheet expands as jet velocity increases. Due to lack of aerodynamic waves, breakup length increases as a direct result of the increase in mass flow rate<sup>7</sup>. This regime is observed at medium Weber numbers ( $250 < We_j < 600$ ). At pressures above 1.4 MPa, this regime is delayed until  $We_j = 578$ .

**c. Wave breakup regime:** This regime refers to  $We_g > 1$ , where the presence of aerodynamic waves influences the sheet breakup and shows general agreement with the linear instability theory described in the introduction section. This phenomenon is due to the presence of waves originating at the impingement point. These waves cause the breakup by keeping the upstream portion of sheet ruffled and intact<sup>7</sup>. The breakup of the liquid sheet into ligaments is pronounced in this breakup regime. This mode of liquid sheet break up (represented by red box) dominates for many flow conditions and is shown in Figure 14.

**d. Catastrophic breakup regime:** Breakup length and breakup frequency of the sheet cannot be distinguished as the sheet is broken and is entirely atomized due to aerodynamic forces at the nozzle exit. The catastrophic regime is observed for flow conditions  $175 \text{ cm}^3/\text{min} < Q < 200 \text{ cm}^3/\text{min}$  at a pressure of 4.5 MPa.

#### 5.2.1.2 Breakup regimes for ethanol/water mixture

Apart from the breakup modes exhibited by water-water impingement, ethanol-water mixture doublets tend to display breakup modes such as periodic shedding, ligament structures, and rimless separation. The breakup of ethanol-water mixture at lower Weber numbers is termed as pre-sheet formation. This is observed at  $We_j < 300$ . This mode is followed by the periodic drop atomization at higher  $We_j$ . This is a phenomenon in which the edge of the sheet periodically sheds droplets, destabilizing the rim<sup>20</sup>. This phenomenon is observed for a range of  $We_j$  between 500 and 700. The ethanol-water mixture also exhibits a transition regime, from closed rim to open rim, which can be categorized as a rimless separation<sup>21</sup>. This transition is similar to that of sheets exhibited by n-heptane and ethylene glycol<sup>11</sup>. This breakup mode is observed in the case of 3.4 MPa for ethanol-water. Typically, at higher Weber numbers,  $We_j > 1000$ , we observe a formation of ligament structures. The characteristics of this regime are that the rim of the sheet opens out and the sheet undergoes breakup by formation of ligament shaped structures as shown in Figure 15. Subsequently, the catastrophic regime is observed for  $We_j \sim 4600$ . However, this study indicates that at elevated pressures, this breakup regime starts at  $We_j \sim 3500$ .

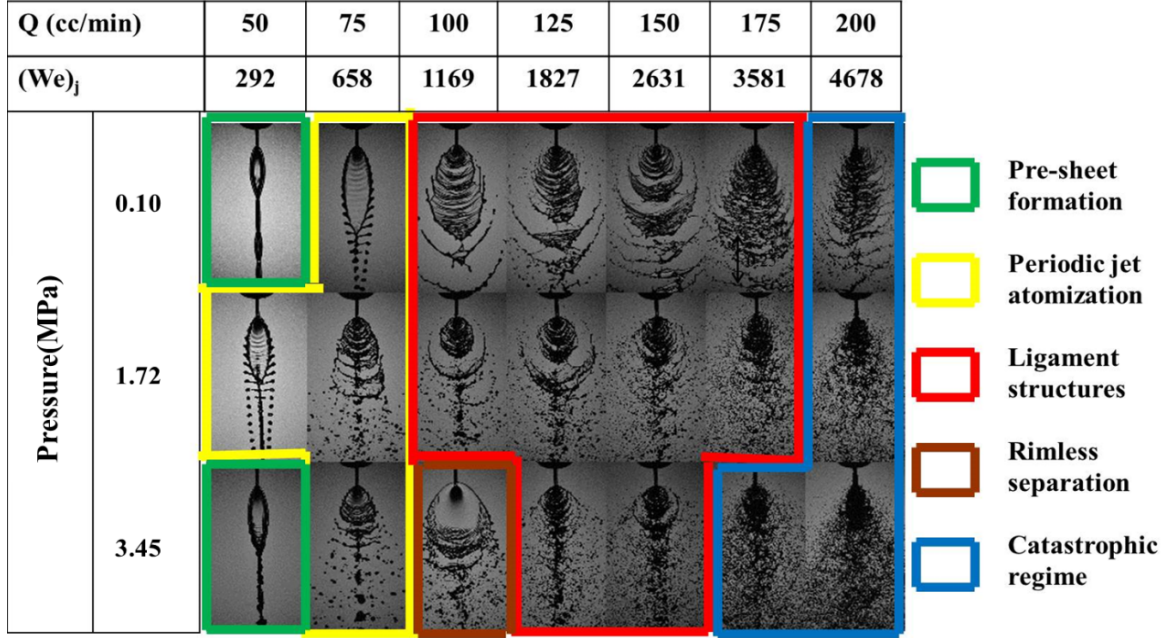


Figure 7. Shadowgraph of impinging jet spray taken for various pressures and flow rates (Non-gelled Ethanol-Water mixture).

#### 5.2.1.3 Breakup regimes for particle-based gel

Experimental results indicate that gelled fluids show four primary breakup modes such as pre-sheet formation, ray shaped pattern, ligament structures, and a fully turbulent mode.<sup>20,21</sup> At lower Reynolds numbers, a ray shaped pattern was observed. With an increase of Reynolds number, the breakup mode of gelled fluids changes from ray shaped patterns to ligament structures and catastrophic regimes similar to that of Newtonian fluids.<sup>11</sup>  $We_j$  and  $Re_{gen,HBE}$  have been used as parameters to characterize breakup regimes<sup>10,11</sup> of impinging jets for various fluids. However, it should be noted that  $Re_{gen,HBE}$  does not account for pressure effect and this fact makes it difficult to form a comparative study between the gellants at elevated pressures. The challenge lies in identifying a unique parameter encompassing all flow conditions such as pressure, flow rates, and fluid conditions in terms of surface tension and viscosity.

#### 5.2.1.4 Regime map

To identify operating conditions that result in various breakup modes for different test fluids, a regime map is constructed. Typically, common regime maps have been plotted using  $We_j$  and  $Re_j$  for Newtonian fluids<sup>22</sup> and  $We_j$  and  $Re_{gen}$  for non-Newtonian fluids<sup>11</sup>. Despite the introduction of generalized Reynolds numbers for the test fluids, the formulation does not distinguish between the regimes occurring over a range of pressures. It is observed that there are overlaps of regimes at distinct flow conditions. Therefore, a better representation of breakup regimes is required and new parameters are introduced to distinguish different modes at high pressure:  $We_g$  and  $Re_g$ , which are basically the jet Weber number and Reynolds number adjusted for ambient gas density, respectively.

$$We_g = \frac{\rho_g U_j^2 d_o}{\sigma} = \frac{\rho_j U_j^2 d_o}{\sigma} \cdot \frac{\rho_g}{\rho_j} = We_j \cdot \frac{\rho_g}{\rho_j} \quad (5)$$



$$Re_g = \frac{\rho_g U_j d_o}{\mu_j} = \frac{\rho_j U_j d_o}{\mu_j} \cdot \frac{\rho_g}{\rho_j} = Re_j \cdot \frac{\rho_g}{\rho_j} \quad (6)$$

Similarly, the generalized ambient-density-corrected  $Re_{g,gen}$  combines the effect of pressure and of viscosity for non-Newtonian fluids and is essential to derive a common basis for comparison between Newtonian and non-Newtonian fluids.

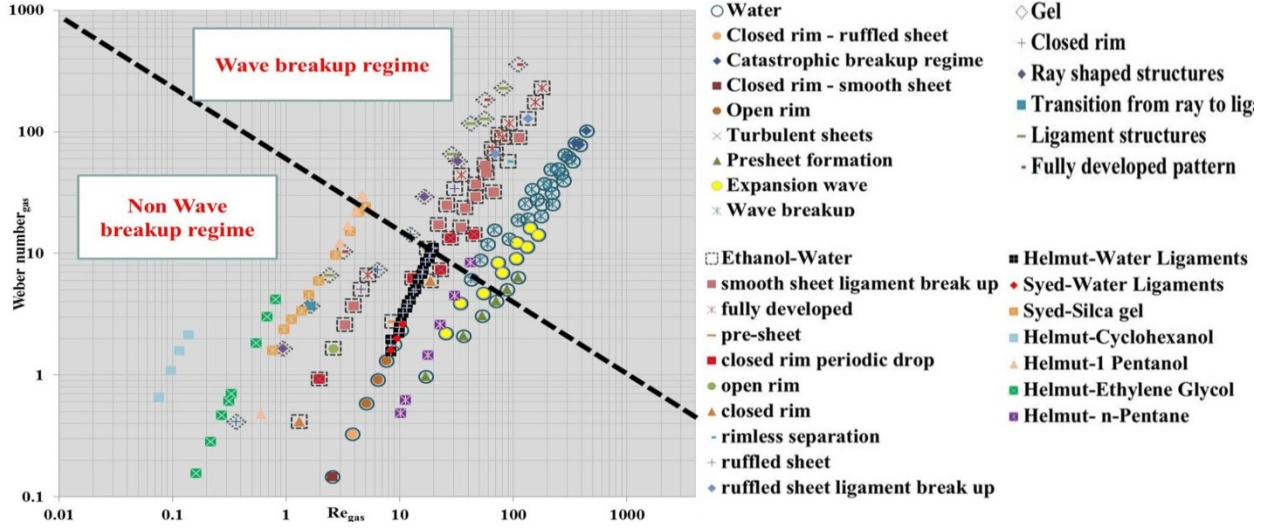


Figure 8. Common regime diagram presenting the location of breakup regimes for various gelled and non-gelled fluids over a range of pressures and flow rates. (Data for other fluids are plotted from DLR Group [21,22] and Fakhri [23]).

Using the formulation, a regime map spanning all test fluids at flow conditions mentioned in Section III.A is shown in Figure 16.<sup>21-23</sup> The legend shows three major fluids (water, non-gelled ethanol-water and ethanol-water gel) represented by different symbols ( $\circ$ ,  $\square$ , and  $\diamond$  respectively). Different characters or colors inside each symbol signify various breakup regimes. For example, \* enclosed in  $\circ$  signifies wave breakup regime for water.

The usefulness of the proposed regime diagram lies in its capability to encompass any fluid irrespective of its type and flow conditions including change of ambient pressure. A qualitative take on Figure 16 shows breakup regimes aggregating into two distinctive groups: the non-wave breakup and the wave breakup regime. The lower half of the regime map displays unique lines for each given fluid and corresponds mostly to atmospheric pressure condition. This non-wave breakup regime encompasses the regime of closed rim for water and of smooth sheet ligament breakup and ligament structures for the gelled simulant. The upper half of the regime map is the wave-breakup regime which is characterized by periodic wavy structure developed on liquid sheet followed by ligament formation. Typically, this is observed at high pressure conditions for wave-breakup mode for water, ligament shaped structures for gelled simulant, and non-gelled ethanol-water. The wave breakup modes, identified at higher pressure, tend to show no effect of cavitation<sup>24</sup>. This regime map also indicates the close link between the base of the gel used (ethanol-water) and the gel. This link highlights the role played by Weber number of the jet in determining the way liquid breakup occurs.

Also, shown in the plot are data for from others. With increasing viscosity of non-gelled fluids, the aggregated breakup modes shift towards the left top in distinct lines for all regimes. The

critical Reynolds number is defined as the Reynolds number at which the breakup mode transitions from a non-wave breakup to a wave breakup mode. We observe quantitatively that the critical Reynolds number, at least for non-gelled fluids, is found to be a function of viscosity of the fluid tested. It can be seen that upon increasing the viscosity of Newtonian fluids, its likelihood to breakup in wave breakup mode requires higher  $We_g$ . A relationship linking the critical Weber number and Reynolds number is identified and the relation governing the transition line is found out to be

$$\frac{We_c}{Re_c^{0.25}} = \text{Constant} \quad (7)$$

### 5.2.2 Breakup length

Breakup length measurements for all fluids are made from instantaneous shadowgraph images of impinging jet spray. Typically, one hundred images are taken and the standard deviation of breakup length is found to be within 10%. However, for catastrophic breakup regime, breakup lengths are difficult to measure as the sheet tends to flap continuously, blurring images. Previous studies on the effect of back pressure, with respect to impinging injectors, have reported the decrease of break up length with an increase in chamber density and injection velocity<sup>25</sup>. Figure 17 shows plots of the breakup length versus the ambient pressure for various mean flow rate for three different fluids. For all working fluids in this study, the sheet breakup lengths are inversely correlated with respect to ambient pressure and they show a close correlation with the observations of Strakey et al.<sup>25</sup> Typically, the flow rate also plays a major role in determining the breakup length. Though in the expansion wave regime (refer to Figure 15) the breakup length tends to increase as the mean flow rate increases, within the wave-breakup regime (e.g. for water at higher pressure than 0.7 MPa and flow rates higher than 75 cc/min) breakup length decreases as the flow rate of test fluid increases. Also, shown in Figure 17 (a) and (b) are lines derived from the correlation by Jung et al.<sup>7</sup> developed for turbulent sheets and  $We_g > 2$  using only water. The results with water and ethanol-water are consistent with the predicted relationship between the breakup length and pressure. However, the correlation is not highly sensitive to changes in injection velocity.

It is also evident that the breakup length clearly decreases, for fixed flow conditions of pressure and flow rate, with increasing viscosity. The addition of the gellant in ethanol-water (Figure 17c) results in the shorter breakup length than that of water (Figure 17a) and ethanol-water mixture (Figure 17b). However, decreasing the surface tension of the fluid seems to have little or no marked effect. For the same breakup regimes and flow parameters, water (Figure 17a) and ethanol-water (Figure 17b) exhibit similar breakup lengths. Building on this similarity, one can establish that, within same breakup regimes, Reynolds number ( $Re_j$ ) plays a major role in determining breakup lengths.

Figure 18 shows a plot of normalized breakup length versus  $Re_g$  for all fluids at operating conditions corresponding to the wave breakup regime. It shows that for a given fluid,  $Re_g$  is a proper parameter to characterize the breakup process over ranges of pressure and flow rate within the wave breakup regime. For non-gelled water, the normalized breakup length monotonically decreases as  $Re_g$  increases. Similar trends are shown for other fluids. However, at a given  $Re_g$ , the breakup length is much shorter for the gelled ethanol-water case and does not change as much with respect to varying ambient pressure as the water case. This clearly indicates that the viscosity of liquid plays an important role in sheet breakup by surface waves.

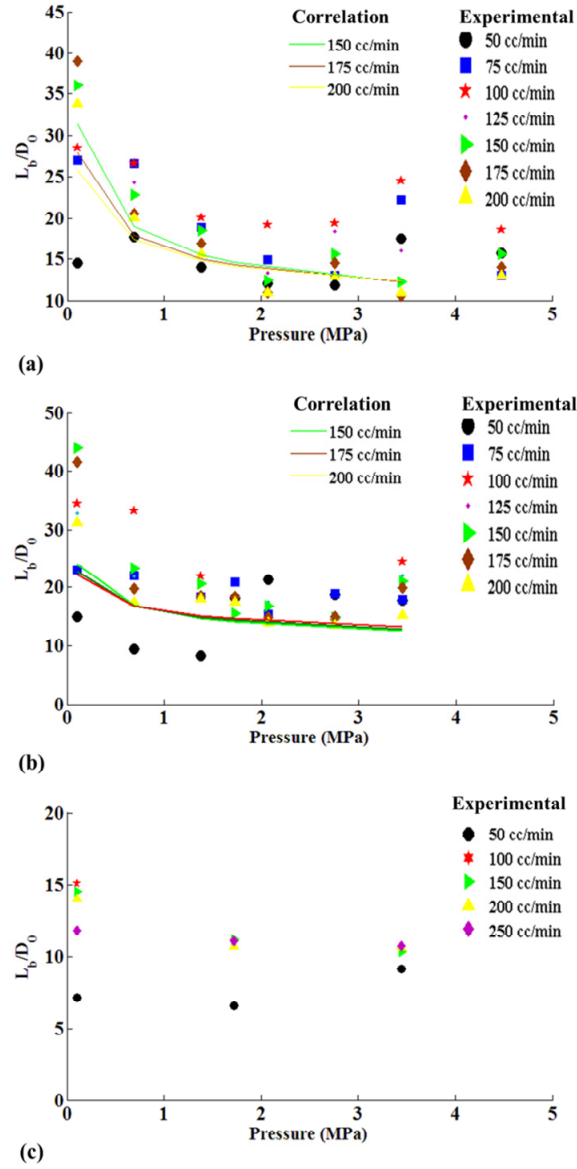


Figure 17. The normalized sheet breakup length plotted as function of ambient pressure for all working fluids: (a) Distilled water, (b) Ethanol-water, and (c) Gelled Ethanol-water. (Solid lines represent the empirical correlation obtained from Jung et al. [7]).

### 5.2.3 Characterization of pre-impingement jet and post-impingement sheet

In order to explain the effect of ambient pressure on the breakup length, the surface of jet before impingement and near field spray characteristics, such as surface wavelength and ligament wavelength in the downstream of impingement region, are quantitatively characterized.

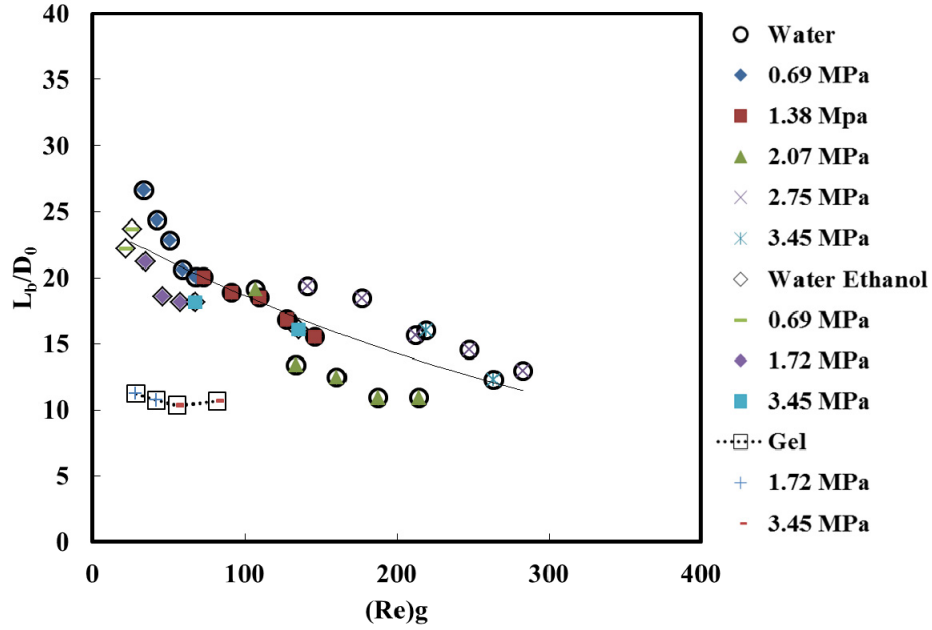


Figure 9. The normalized breakup length plotted as a function of Reynolds number of gas (The legend should be interpreted for three major fluids  $\circ$  for water  $\diamond$  for non-gelled ethanol/water and  $\square$  for the gelled ethanol/water. Also, in these fluids, different symbols or colors signify various ambient pressures. For an example, \* enclosed in  $\circ$  signifies breakup length for water at 3.45 MPa).

### 5.2.3.1 Disturbances on the surface of the jet before impingement

Figure 19 shows the typical instantaneous shadowgraph images of single jet streams of water for various pressures and flow rates. For all fluids at a given pressure and flow rate, the size of disturbance on the surface of jet tends to increase as it moves downstream from injector exit. It gets bigger at a fixed downstream distance as either the flow rate or the ambient pressure increases. Comparing non-gelled fluids at given flow rate and pressure, the ethanol-water mixture jet exhibits less perturbation than the water jet. This decrease may be due to higher viscosity of the former. Also, the former shows an evidence of cavitation in the nozzle at lower flow rates than the latter, especially at atmospheric pressure. This can be attributed to higher vapor pressure of ethanol-water mixture. Comparing gelled and non-gelled ethanol-water mixture, the disturbance on jet initiated near injector exit tends to grow at a faster rate for the gelled mixture as it moves downstream.

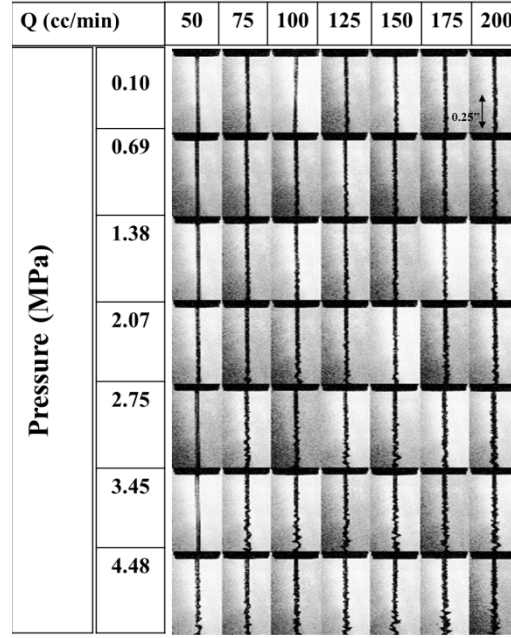


Figure 10. Shadowgraphs of single jet stream of water for various pressures and flow rates.

The shadowgraph images of pre-impinging jets for water shown in Figure 19 are analyzed to quantify the characteristic amplitude of disturbances on the pre-impingement jet ( $\lambda_{\text{Disturbance}}$ ). For other fluids (non-gelled and gelled water-ethanol mixture), the resolution of image (mm/pixel) is too big for the perturbation on the surface of jet to be accurately resolved. Figure 20 illustrates how  $\lambda_{\text{Disturbance}}$  is defined. It is defined as the maximum radial distance from the center of liquid jet to the outermost surface of the perturbed jet at the intended impingement point which is 5 mm downstream of injector exit. Each raw image is filtered and thresholded. Then  $\lambda_{\text{Disturbance}}$  is calculated from the pixel coordinates obtained from the resultant image using ImageJ. The image analysis shows that  $\lambda_{\text{Disturbance}}$  does not seem to be strongly dependent on flow rate especially at low ambient pressures. It gradually increases as the ambient pressure increases. As shown in Figure 20, the Reynolds number adjusted for ambient gas pressure,  $Re_g$ , is a proper parameter to characterize the effect of ambient pressure and flow rate on  $\lambda_{\text{Disturbance}}$ . This strongly indicates that increasing ambient pressure affects the breakup length observed in Figure 17 through the increase of  $\lambda_{\text{Disturbance}}$  in the pre-impingement state.

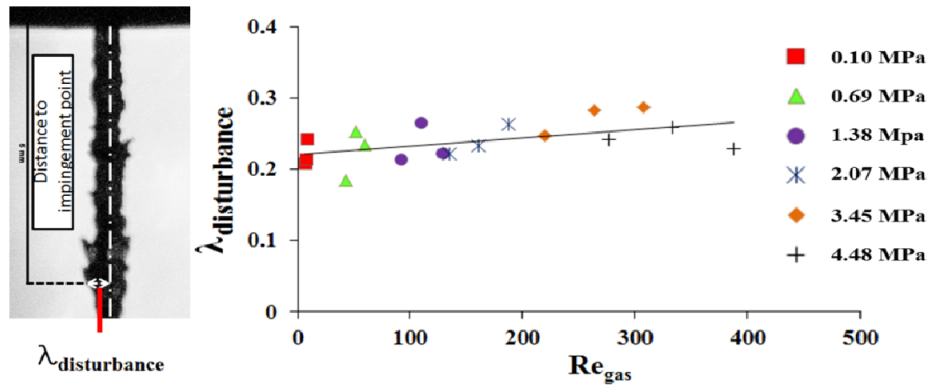


Figure 11. Typical shadowgraph of a single jet illustrating the method of measurement for  $\lambda_{\text{Disturbance}}$  which is subsequently plotted as a function of  $Re_g$  in Wave-Breakup regimes for water.

### 5.2.3.2 Surface wavelength after impingement

The second parameter chosen to characterize the effect of pressure on the liquid breakup in the near field spray is the surface wavelength ( $\lambda_{\text{Surface}}$ ). It is defined as the spacing between adjacent periodic waves formed on the liquid sheet after the impingement of two jets as shown in Figure 13. The analysis is carried out for shadowgraph images taken in operating conditions corresponding to the wave breakup regime. Other modes do not display a clear surface wave. Typically up to 100 images are analyzed and the standard deviation of analyzed result for a fixed operating condition is within 10%. Previous study<sup>4</sup> has concluded that the surface wavelength for water is independent of velocity. However, this experiment finds evidence suggesting velocity plays a key role in affecting the surface wavelength as shown in Figure 21a; the surface wavelength decreases on increasing either ambient pressure for fixed flow rate or flow rate for fixed ambient pressure. Figure 21b shows the result for water plotted in terms of  $\lambda_{\text{Surface}}$  versus the Reynolds number adjusted for ambient gas pressure,  $Re_g$ ;  $\lambda_{\text{Surface}}$  decreases as  $Re_g$  increases. It should be noted that the trend exhibited by the surface wavelength with respect to ambient pressure and flow rate is similar to that of the breakup lengths shown in Figure 10, indicating the shorter the breakup length, the shorter  $\lambda_{\text{Surface}}$ .

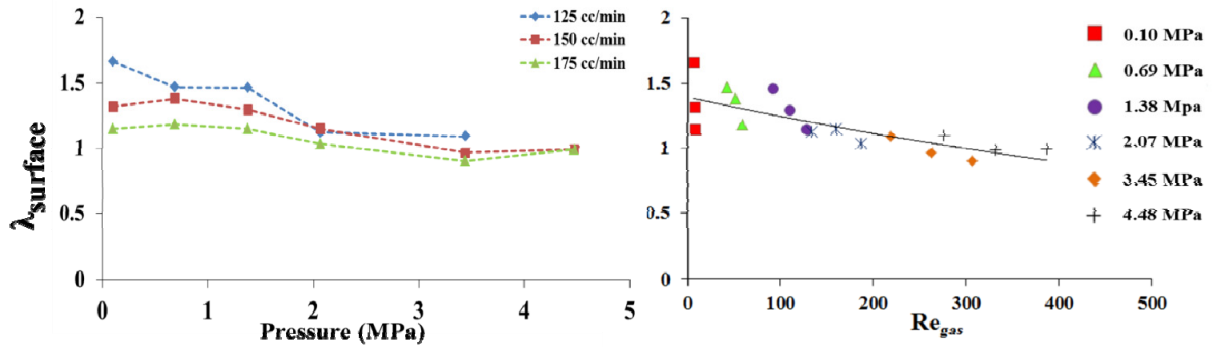


Figure 12. The surface wavelength between adjacent waves plotted: (a) as a function of pressure in wave breakup regime for non-gelled water and (b) as a function of  $Re_{\text{gas}}$  in the wave breakup regime for non-gelled water.

### 5.2.3.3 Ligament wavelength

The last parameter analyzed to characterize the effect of pressure on the liquid breakup in the near field spray is the ligament wavelength ( $\lambda_{\text{Ligament}}$ ). As shown in Figure 13, the distance between the breakup location and the first ligament is defined as the ligament breakup length. Figure 22 shows the analyzed results for water and gelled- and non-gelled water-ethanol mixture, plotted in terms of  $\lambda_{\text{Ligament}}$  versus ambient pressure. It clearly shows that for all fluids,  $\lambda_{\text{Ligament}}$  decreases on increasing either ambient pressure for fixed flow rate or flow rate for fixed ambient pressure in the same way as the surface wavelength as shown in Figure 22a. Figure 23 shows a plot of the data for water shown in Figure 22a in terms of  $\lambda_{\text{Ligament}}$  versus the Reynolds number adjusted for ambient gas pressure,  $Re_g$ . This plot indicates that  $Re_g$  is a proper parameter to characterize the effect of ambient pressure and flow rate on  $\lambda_{\text{Ligament}}$ . Also, it can be noted that the trend exhibited by  $\lambda_{\text{Ligament}}$  with respect to ambient pressure and flow rate is similar to that of breakup length as shown in Figure 18.

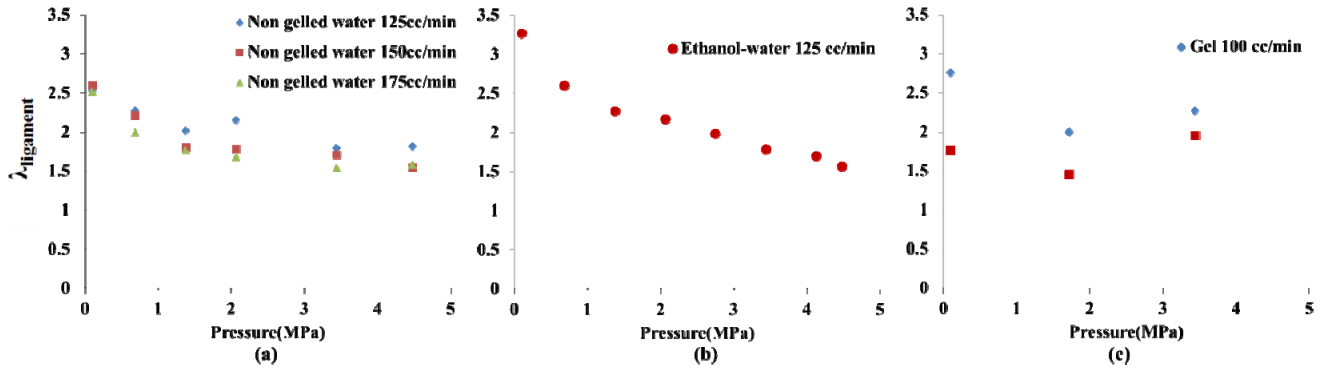


Figure 13. The ligament wavelength vs. ambient pressure for (a) Distilled water, (b) Non-gelled ethanol-water, and (c) Gelled Ethanol-water at operating conditions corresponding to the wave-breakup regimes.

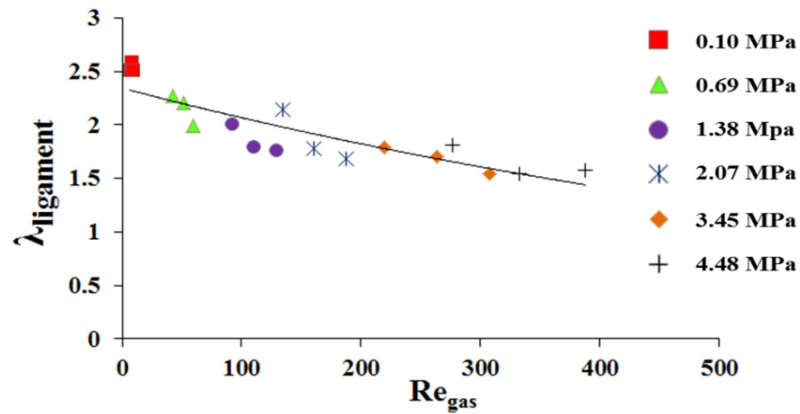


Figure 14. Ligament wavelength measured as a function of  $Re_{\text{gas}}$  for non-gelled water.

## 6. References

1. Nurick, W.H., (1976) Orifice Cavitation and its Effect on Spray Mixing, ASME Transactions Series I - Journal of Fluids Engineering, 98, pp. 681-687.
2. Jung, K., Khil, T. and Yoon, Y., (2006) Effects of Orifice Internal Flow on Breakup Characteristics of Like-Doublet Injectors, Journal of Propulsion and Power, 22(3), pp. 653-660.
3. Jung, K., Khil, T., Yoon, Y., Roh, T., (2002) The break-up Characteristics of Liquid Sheets Formed by Like-Doublet Injectors", AIAA 2002-4177, 38<sup>th</sup> Joint Propulsion Conference & Exhibit, Indianapolis, IA.
4. Ryan, H.M., Anderson, W.E., Pal, S. and Santoro, R.J., (1995) Atomization Characteristics of Impinging Liquid Jets, Journal of Propulsion and Power, 11(1), pp. 135-145.
5. Fukui, N. and Sato, T., "The Study of a Liquid Atomization by the Impingement of Two Jets," Bulletin of JSME, Vol. 15, No. 83, 1972, pp. 609-619.



6. Dombrowski, N. and Hooper, P., "A study of the sprays formed by impinging jets in laminar and turbulent flow," *Journal of Fluid Mechanics*, Vol. 18, No. 3, 1964, pp. 392–400. doi: 10.1017/S0022112064000295
7. Jung, K., Lim, B., Khil, T., and Yozon, Y., "Breakup characteristics of laminar and turbulent liquid sheets formed by impinging jets in high pressure environments," 40th AIAA Joint Propulsion Conference, Fort Lauderdale, FL, July 2004. doi: 10.2514/6.2004-3526
8. Yasuda, N., Yamamura, K., and Mori, Y. H., "Impingement of liquid jets at atmospheric and elevated pressures: an observational study using paired water jets or water and methylcyclohexane jets," *Proceedings of the Royal Society A: Mathematical, Physical and Engineering Science*, Vol. 466, No. 2124, 2010, pp. 3501–3526. doi: 10.1098/rspa.2010.0144
9. Natan, B. and Rahimi, S., "The status of gel propellants in year 2000," *International journal of energetic materials and chemical propulsion*, Vol. 5, No. 1-6, 2002. doi: 10.1615/IntJEnergeticMaterialsChemProp.v5.i1-6.200
10. Madlener, K. and Ciezki, H. K., "Estimation of Flow Properties of Gelled Fuels with Regard to Propulsion Systems," *Journal of Propulsion and Power*, Vol. 28, No. 1, 2012, pp. 113–121. doi: 10.2514/1.50422
11. von Kampen, J., Madlener, K., and Ciezki, H. K., "Characteristic flow and spray properties of gelled fuels with regard to the impinging jet injector type," 42nd AIAA Joint Propulsion Conference, Sacramento, CA, USA, 2006, pp. 9–12.
12. Tamaki, N., Shimizu, M., Nishida, K., and Hiroyasu, H., "Effects of cavitation and internal flow on atomization of a liquid jet," *Atomization and Sprays*, Vol. 8, No. 2, 1998.
13. Rahimi, S., Peretz, A., and Natan, B., "Rheological Matching of Gel Propellants," *Journal of Propulsion and Power*, Vol. 26, No. 2, 2010, pp. 376–379. doi: 10.2514/1.42904
14. Asghriz, N., Brocklehurst, W. and Talley, D., (2001) Mixing Mechanisms in a Pair of Impinging Jets, *Journal of Propulsion and Power*, 17(3), pp. 736-749.
15. Rasband, W., "WS 1997-2012. ImageJ," US National Institutes of Health, Bethesda, Maryland, USA, URL: <http://imagej.nih.gov/ij> [cited 10 November 2013].
16. Kampen, J., Ciezki, H.K., Tiedt, T. and Madlener, K., (2006) Some Aspects of the Atomization Behaviour of Newtonian and of Shear-thinning Gelled non-Newtonian Fluids with an Impinging Jet Injector, *Spray'06 Workshop*.
17. Miller, E., Gibson, B., McWilliams, E. and Rothstein J.P, (2005) Collision of Viscoelastic Jets and the Formation of Fluid Webs, *Applied Physics Letters*, 87, 014101.
18. Desyatkov, A., Adler, G., Propokov, O. and Natan, B., (2007) Atomization of Gel Fuels Using Impinging Jet Atomizers, 2<sup>nd</sup> European Conference for Aerospace Sciences, Brussels, Belgium.
19. Huang, J., "The break-up of axisymmetric liquid sheets," *Journal of Fluid Mechanics*, Vol. 43, No. 02, 1970, pp. 305–319. doi: 10.1017/S0022112070002392
20. Bremond, N., and Villermaux, E., "Atomization by jet impact," *Journal of Fluid Mechanics*, Vol. 549, No. 1, 2006, pp. 273–306. doi: 10.1017/S0022112005007962
21. Madlener, K., Ciezki, H. K., von Kampen, J., Heislbeitz, B., and Feinauer, A., "Characterization of Various Properties of Gel Fuels with Regard to Propulsion Application," 44th AIAA/ASME/SAE/ASEE Joint Propulsion Conference & Exhibit, Hartford, CT, July 2008. doi: 10.2514/6.2008-4870
22. Ciezki, H. K., Tiedt, T., Von Kampen, J., and Bartels, N., "Atomization Behavior of Newtonian Fluids with an Impinging Jet Injector in Dependence upon Reynolds and Weber



- Numbers,” 41st AIAA/ASME/SAE/ASEE Joint Propulsion Conference & Exhibit, Tucson, AZ, July 2005. doi: 10.2514/6.2005-4477
23. Fakhri, S. A. K., A Study on the Atomization and Spray Characteristics of Gelled Simulants Formed by Two Impinging Jets, M.S. Thesis, Mechanical and Nuclear Engineering Department, The Pennsylvania State University, University Park, PA, USA 2009.
  24. Ashgriz, N., Brocklehurst, W., and Talley, D., “Mixing mechanisms in a pair of impinging jets,” *Journal of Propulsion and Power*, Vol. 17, No. 3, 2001, pp. 736–749. doi: 10.2514/2.5803
  25. Strakey, P. and Talley, G., “Spray Characteristics of Impinging Jet Injectors at High Back-Pressure,” Eighth International Conference on Liquid Atomization and Spray Systems, Pasadena, CA, May 2000.

### III. INTERFACANTERFACIAL REACTIONS AND TRANSPORT AT ATOMISTIC, MOLECULAR, MICRO, AND MESO SCALES

#### III.1 Enhanced Spectroscopic Analysis of Interfacial Reactions and Transport (Rabitz, Princeton University)

##### 1. Abstract

The goal for this portion of the MURI is to develop new sensitive, selective, *in situ* optical tools for interrogation and characterization of mixing and early-stage combustion of Hypergolic propellants. We have developed a form of coherent control named Optimal Dynamic Discrimination (ODD) which exploits the unique quantum dynamics of different molecular species to yield new optical signals that are more easily measured and distinctive to the molecule of interest. We developed the theoretical framework for this method and implemented it in the laboratory. By integrating the ODD methodology with Coherent Anti-Stokes Raman Scattering (CARS) we can collect optimized vibrational spectra, yielding detailed qualitative and quantitative information about the molecular species being interrogated. We have used ODD, CARS, and Laser induced fluorescence to examine and characterize mixing in a series of experimental apparatuses developed by MURI collaborators and partnered with researchers at the Army Research Laboratory to share resources for these experiments. These experiments are ongoing, and the final state of this optical detection tool will be the ability to image the emission of these optimally excited species, producing spatially resolved chemical concentration maps for each individual species involved in a complex reaction.

##### 2. Background and Scientific Objectives

The goal of this aspect of the GHP-MURI is to improve our understanding of the complex chemical and physical processes taking place at the interface between impinging streams of gelled hypergolic fuel-oxidizer pairs. We are tasked with characterizing the interfacial reactions over a full spectrum of interaction scales - from the molecular to the macroscopic - this included analyzing the nature and role of pre-ignition mixing; observing and characterizing early condensed and mixed phase reactions between colliding streams, droplets, and vapor; and identifying early initiation reactions and products for conventional and new hypergolic fuels.

To accomplish these tasks our group developed novel optical detection capabilities for extracting chemical information from these reacting systems. The goal was to apply the tools of Optimal Coherent Control to enhance standard spectroscopic techniques (such as laser induced fluorescence, stimulated emission depletion, and coherent Raman spectroscopy and microscopy). In this fashion we can access and modify the excited state dynamics of the system to yield new optical responses that are more easily distinguishable and unique to specific molecules taking place in a reaction. This methodology is referred to as Optimal Dynamic Discrimination (ODD) and we can apply it to a number of non-linear spectroscopic techniques that interact with a molecule's dynamics to yield optical signals.

##### 3. Enhanced Spectroscopy through Optimal Dynamic Discrimination

In the first years of the program our group developed the theoretical framework for the Optimal Dynamic Discrimination method. ODD was previously demonstrated in discrimination of a pair of flavin molecules with near identical optical properties [1] and we expanded the approach to make it applicable to observation and characterization of reactive systems.

Optimal Dynamic Discrimination is based on the ability to guide the dynamics of a quantum mechanical system toward a preferred state through its interaction with the complex electric field of an ultrashort pulsed laser [2]. By manipulating the electric field of the laser through phase and amplitude pulse shaping [3] we control the response of the system. Closed-loop Optimization of this interaction allows a computer driven algorithm to discover the optimally tailored electric field patterns that drive the system to the desired objective [4]. A block diagram of the closed-loop algorithm is shown in Figure 1. The optimization algorithm used in these experiments is a modification of a “climbing” algorithm known as Covariance Matrix Adaptation (CMA) [5]. In this optimization strategy a number of shaped pulses with unique phase vectors are applied to the molecular system, and the fitness of each pulse – its success in driving the system to the desired state – is recorded by the computer. The computer then calculates the covariance matrix in the basis defined by the phase vector, a measure similar to the local ‘slope’ of the fitness measurements in the high dimensional space accessible by the phase shaper. This slope lets the computer intelligently create new phase vectors that should increase the measured fitness, driving the system toward the desired state – for the purposes of these experiments excitation of optical signaling from specified chemical species involved in a reacting mixture.

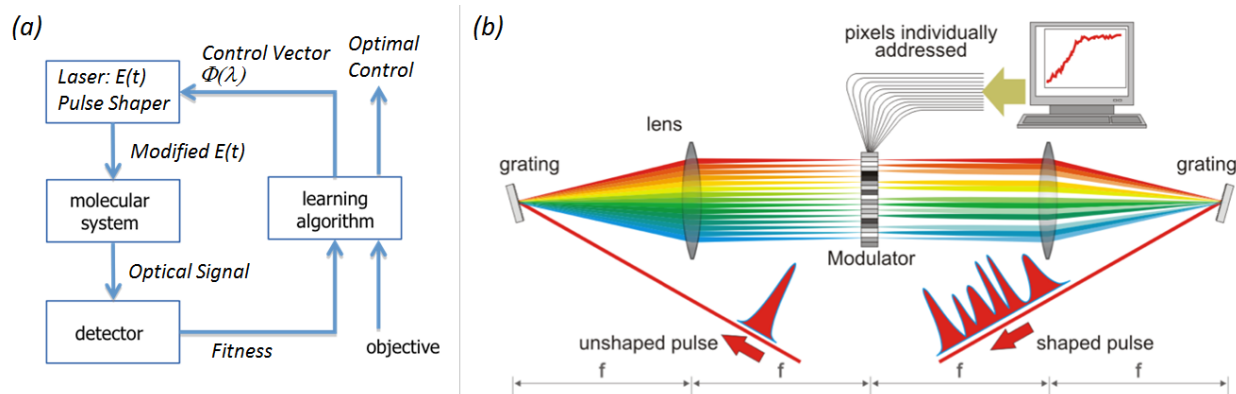


Figure 1. (a) schematic representation of the closed-loop optimization algorithm (b) schematic of laser pulse shaper: the broadband ultra-short laser pulse is dispersed into its component frequencies, which are individually addressed by computer controlled light modulator before being recombined into a tailored pulse and sent to the experiment.

To implement ODD in the laboratory we designed and constructed a broad bandwidth Non-collinear Optical Parametric Amplifier (NOPA) and matching pulse shaping system with sufficient spectral range to cover an entire electronic manifold of complex molecules. This broad bandwidth source allows us to create higher fidelity laser fields, in the same way that an instrument with more notes can play a more complex melody. The NOPA is pumped by a Spectra Physics Titanium: Sapphire amplifier with 1.0 W average power, 800 nm central wavelength, 100 fs temporal width. A small portion of the pump ( $\sim 1$  mW) is focused into a Sapphire plate to generate a weak, ultra-broadband supercontinuum seed. The remaining pump beam is frequency doubled to 400 nm and sent through delay and steering lines to be recombined with the seed in a non-linear  $\beta$ -BBO crystal. The seed and pump beams are focused into the crystal at a precise angle dictated by phase matching between the beams and the non-linear index of refraction of the crystal to create an intense broadband beam through parametric amplification. The amplified NOPA output has a spectrum 150 nm wide centered at 600 nm, and the average output power is 20 mW. This NOPA output is directed through a dual prism reflective pulse

shaper with a 128 pixel dual mask liquid crystal spatial light modulator at the focal plane to manipulate the spectral phase.

We first use this broadband system to perform proof of concept experiments discriminating two similar dye molecules by optimized excitation - stimulated emission spectroscopy. Rhodamine and Sulfo-Rhodamine dye, two common fluorescent dyes of near identical optical characteristics, have absorption bands peaking near 535 nm and emission bands peaking near 565 nm. The dyes were excited by the shaped NOPA source and their fluorescence spectrum was measured. The spectrum of the NOPA was split at 550 nm in the pulse shaper, at the equivalence point between the absorption/emission curves of the dyes. The higher energy side of the NOPA excites the dye while the lower energy side was delayed by application of a linear phase offset. This delayed sub-pulse triggers stimulated emission from the population on a particular portion of the excited state energy manifold. This technique is a single pulse version of Stimulated Emission Depletion Fluorescence spectroscopy. The optimization algorithm then shapes the NOPA's spectral phase to find 'pump/dump' pairs of sub-pulses that could access different portions of the two molecules excited state manifold. The results of the optimization are shown in Figure 2: the algorithm significantly modifies the fluorescence spectra, making the two dyes easily distinguishable.

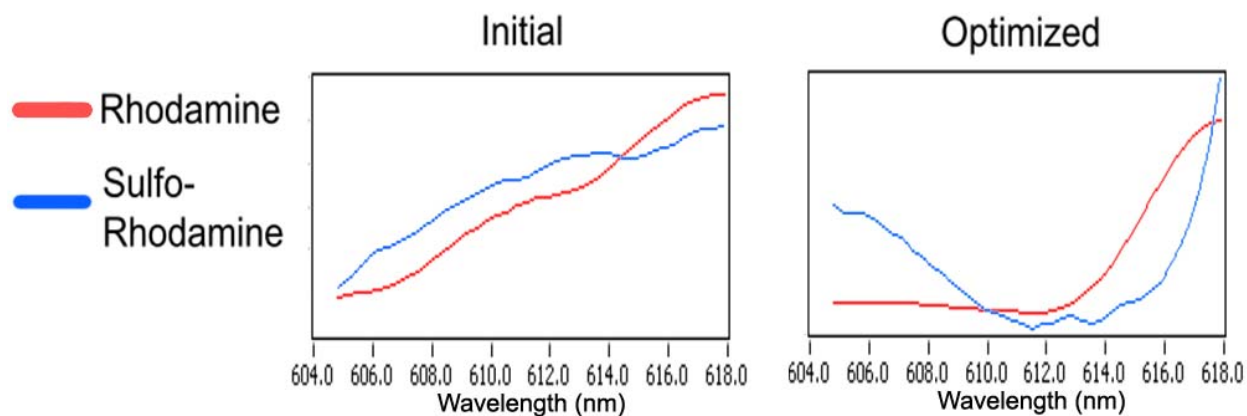


Figure 2. Optimal Dynamic Discrimination of Rhodamin 101 and Sulfo-Rhodamin 101. A portion of the fluorescence spectrum of each dye is manipulated by optimized stimulated emission depletion.

#### 4. Optimized CARS

Next we focus on applying the tools of Optimal Dynamic Discrimination to Coherent Anti-Stokes Raman Scattering (CARS) spectroscopy. CARS is a nonlinear application of Raman scattering that has already proven useful for combustion characterization [6]. CARS yields the vibrational spectrum of the sample, which is highly specific to a given molecule and so useful for identifying a large number of chemical species it is often called the molecular fingerprint. The vibrational spectrum gives us direct access to the composition of a mixture of species, and the intensity of the signal is related to the local concentration giving us quantitative characterization of the sample. In addition, coherent Raman scattering produces strong signals, several orders of magnitude larger than random Raman scattering, and the signal is coherently scattered in a beam whose direction is dictated by phase matching of the incident laser pulses, making it easy to collect and analyze the entire scattered intensity.

ODD-CARS enhances this already useful technique by manipulating the timing and coherence of the vibrational wavepacket that is produced in the excitation of CARS scattering to control the signal. By controlling the vibrational coherence produced we can selectively enhance or inhibit different peaks that would arise in the scattered signal, editing and cropping the spectra until all that remains is the signal from the molecules of interest. We are able to do this because CARS is a coherent, multiphoton process that is highly sensitive to the complex phase of the fields interacting with the molecule. We control the phase of the laser fields with ultrafast pulse shaping, which grants us control over the CARS signal.

One of the primary complications in measuring CARS spectra is the Non-Resonant Four Wave Mixing (4WM) Background signal. The source of this 4WM signal is instantaneous mixing of the 3 incoming laser fields mediated by the electronic response of the medium, and it can dwarf the scattered CARS signal if efforts are not taken to avoid it. Typically this can be achieved through tricks with the Probe pulse: rotating the polarization orthogonal to the Pump and Stokes beams to minimize mixing or delaying the Probe until the temporal overlap with the excitation pulses is small but the Vibrational resonance is still measureable. These techniques decrease the non-resonant background, but also decrease the CARS signal exponentially. Applying the tools of ODD to CARS helps to minimize the impact of this non-resonant term without sacrificing the signal of interest.

For experimental optimization of CARS by ODD we first measured coherent Raman with the home-built NOPA that was used in the Stimulated Emission Depletion experiments, acting simultaneously as the Pump and Stokes fields. After some experimental difficulties we switched to a home-built OPA to enhance the stability of the signal at the expense of spectral bandwidth. The OPA is similar in construction to the NOPA, but the seed and pump are not overlapped at a phase matching angle in the amplifier crystal. This limits the bandwidth that can be created in an OPA, but the system is typically more stable and simpler to align. The OPA is pumped by pulses from a different Ti:Sapphire amplifier (KMLabs Dragon D3). The Dragon amplifier produces high intensity ultrashort laser pulses with average power 3 W, repetition rate of 3 KHz, central wavelength 800 nm and transform-limited pulse length  $\sim 30$  fs. This primary laser source is split into the three beams of the CARS setup: 1.0 W of the primary beam pumps the OPA that acts as the Pump beam,  $\sim 200$  mW is sent into a dual-grating reflective pulse shaper yielding a 100 mW shaped Stokes beam, the remainder of the primary beam is spectrally narrowed by a bandpass filter to make the high resolution Probe beam, with a final power of  $\sim 5$  mW. The OPA output is tunable between 500 nm and 800 nm, and the bandwidth is typically  $\sim 30$  nm. For our CARS measurements the OPA was tuned to 650 nm.

With this new system we measured three-beam CARS: with the OPA beam acting as the pump laser, a shaped portion of the Ti:Sapphire amplifier beam as the Shaped Stokes laser, and a narrowband filtered portion of the 800 nm amplifier beam as the Probe laser. See Figure 3 for diagram of 3-Beam OPA-Driven CARS. Tuning the OPA to 650 nm yields a CARS spectrum  $900\text{ cm}^{-1}$  wide centered at  $3000\text{ cm}^{-1}$  allowing us to monitor the C-H stretching region of the vibrational spectrum. We monitor this region for two principle reasons: most organic molecules of interest have a strong CH stretching resonance, yielding an intense signal, and because the initial reaction steps of the Hypergolic Reactions being studied involve hydrogen abstraction from the fuel molecule and the formation of a fuel:oxidizer complex. The spectral signature of this complex is very distinctive in the  $3000\text{ cm}^{-1}$  region, transforming the singular, narrow CH stretching peak into a broad indistinct band spectrum.

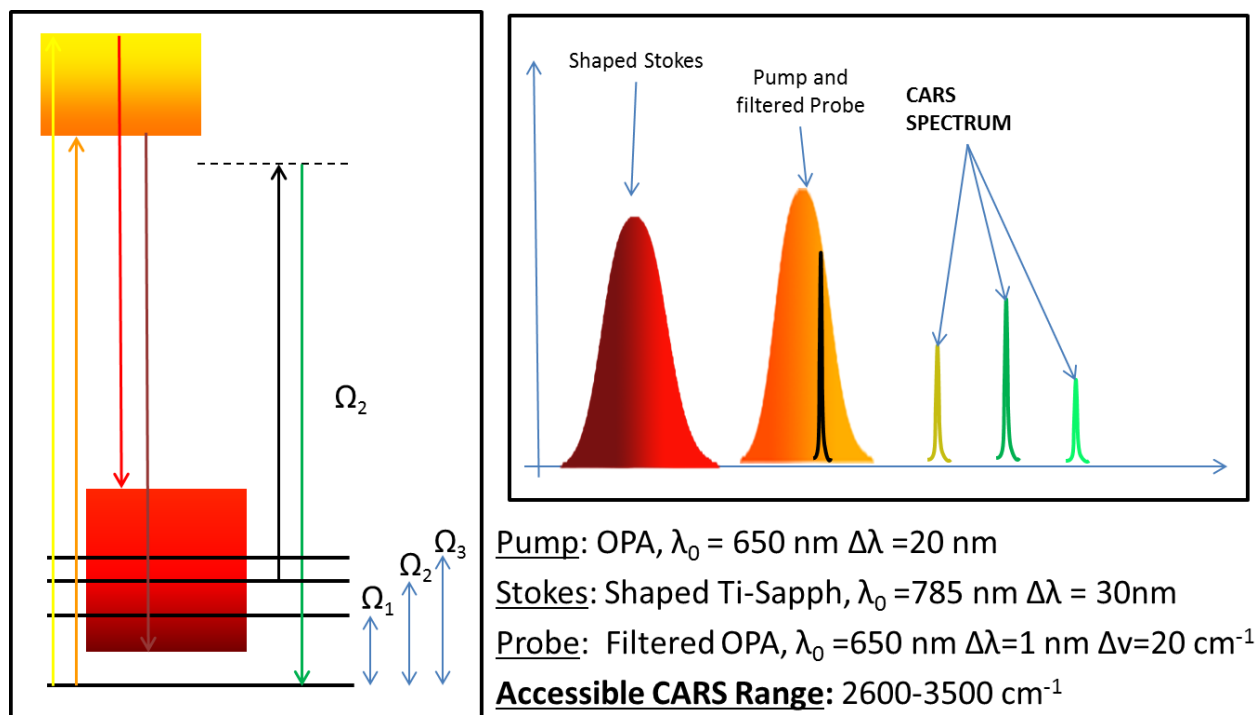


Figure 3. Diagram of 3-Beam, OPA-Driven CARS.

We measured CARS spectra from a series of bulk samples and began using the closed loop optimization to improve the signals. Figure 4 shows representative results for the optimization of the  $\text{CH}_3$  symmetric stretching vibration of acetonitrile. We were able to enhance the CARS peak only slightly, but the real strength of optimization is revealed in the reduction of the non-resonant background scattering to near zero without decreasing the resonant peak. We were also able to use the pulse shaping to manipulate the spectrum of the non-resonant background scatter through controlled coherent mixing; shaping the excitation pulses to ensure only specific portions of the pulse interacted with each other, essentially yielding a controllable bandpass filter. This result is separate from ODD, which uses the excited state dynamics of resonantly excited molecules, but can be a useful tool for selective excitation and detection.

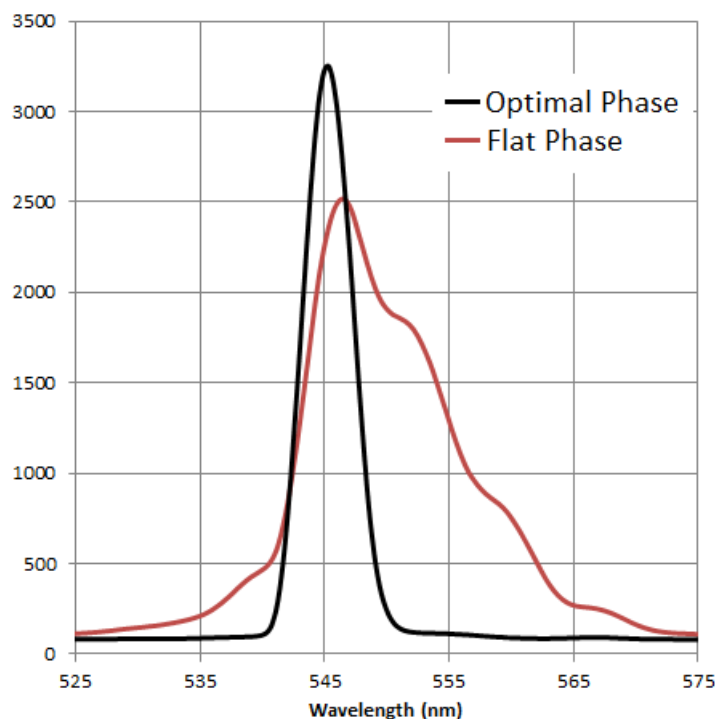


Figure 4. Raman line of spectroscopic standard Acetonitrile ( $2954\text{ cm}^{-1}$   $\text{CH}_3$  sym-stretch) measured with 3-beam OPA-Driven CARS. Optimization (black trace) produces slight improvement of CARS signal but marked reduction of Non-Resonant Background.

### 5. Interrogating Mixing Systems With Chemically Sensitive Imaging

Parallel to the development of our Optimal Dynamic Discrimination technique, our group received two experimental mixing apparatuses from our MURI collaborators which we examined and helped characterize using the optical spectroscopic tools in our lab that were unavailable to our collaborators. To observe and evaluate these apparatuses we built a Laser Induced Fluorescence (LIF) imaging system that could visualize the microscopic features of the colliding and mixing systems and yield chemical information about the system in the process. The samples were excited by 400 nm laser light from the frequency doubled Ti:Sapphire laser amplifier. For visualizing the flows and droplets, small concentrations ( $<1\mu\text{M}$ ) of a chemically sensitive dye, Hydroxypyrene Trisulfonic acid (HPTS or Pyranine), were put in either Water or Methanol solution. The different solvent environments initiated hydrogen abstraction from the HPTS molecule and shifted the fluorescence band. In Water, the hydrogen was stripped from the molecule and the band shifts to 510 nm peak emission; in Methanol HPTS retains the hydrogen and fluoresces at 440 nm peak emission, see Figure 5. Monitoring the ratio of fluorescence in the ‘green channel’ associated with water vs. the ‘blue channel’ associated with methanol gives a measure of the local concentration of each.

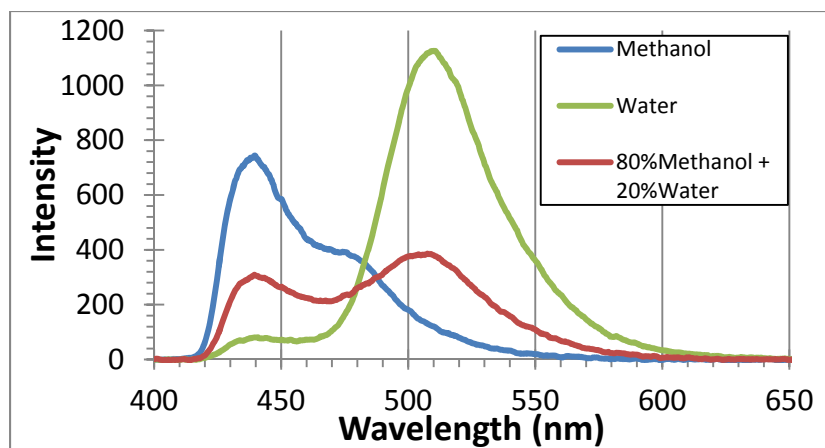


Figure 5. Shift of fluorescence maximum of HPTS dye caused by chemical environment.

We first received a pair of Piezoelectric microDroplet Generators (PDGs) designed and constructed by MURI collaborator Prof. C.K. Law of Princeton University. The PDGs produce a consistent, reproducible stream of  $\sim 100$  micron diameter spherical droplets of liquid, separated by  $\sim 30$  ms between drops. The streams from a pair of these PDGs are aligned to cross at a consistent, stable collision point and imaging the coalescence and mixing of the droplets yields insight into the nature and role of mixing in the initial reaction of these microdroplets. While installing the PDGs and setting up the crossing of the two streams we measured Laser Induced Fluorescence images of the droplet collision point and subsequent coalescence. Both streams of droplets were approximately equal in size and velocity, and collisions were in a head-on geometry. Droplets from one side were pure water, while droplets from the opposing side were methanol with a small concentration of HPTS dye. When the droplets collided and mixing occurred, the HPTS dye was carried with the methanol into the water environment and the rise of the green fluorescent signal was an indicator of degree of mixing. A schematic of the colliding droplet apparatus and representative Fluorescence Images are shown in Figure 6. Integration of the intensity at points in the image in the two fluorescent channels corresponds to a rough measure of species volume fraction of each component in the mixture. This analysis is shown in Figure 7, this image of a pair of droplets is taken after coalescence and significant mixing has occurred. The intensities of each pixel's green channel and blue channel are scaled and divided to yield a fluorescence ratio mapping that is directly related to degree of local mixing. A strip of the image through the center of the droplets is integrated to give a projected cross-section of degree of mixing.



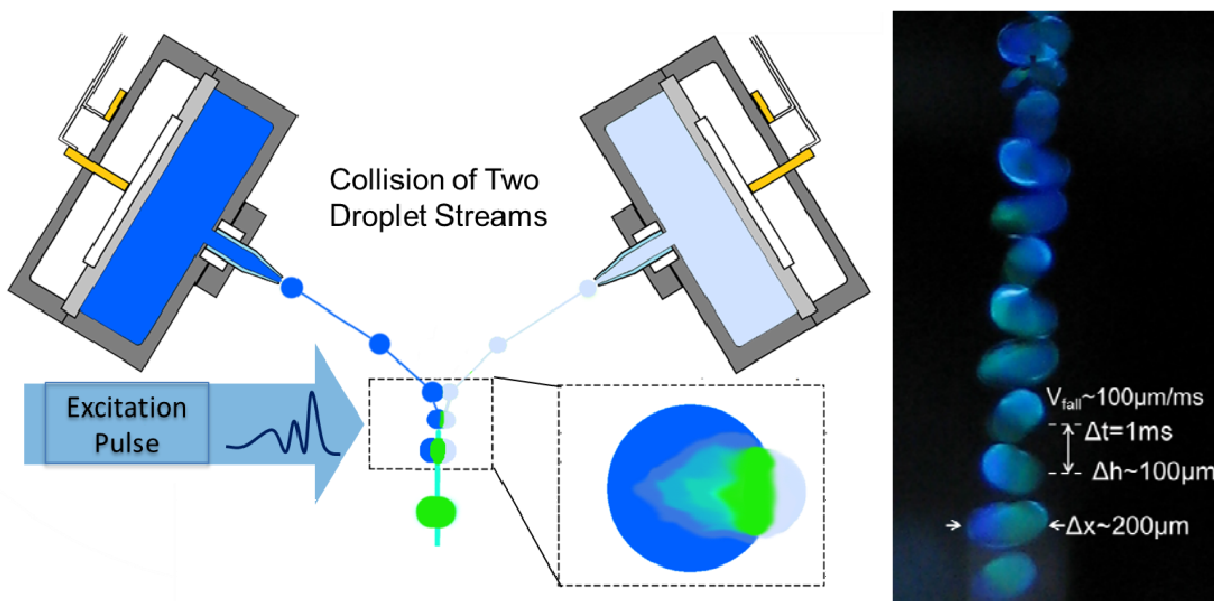


Figure 6. Laser Induced Fluorescent imaging of colliding droplets to observe and evaluate configuration of microdroplet generators.

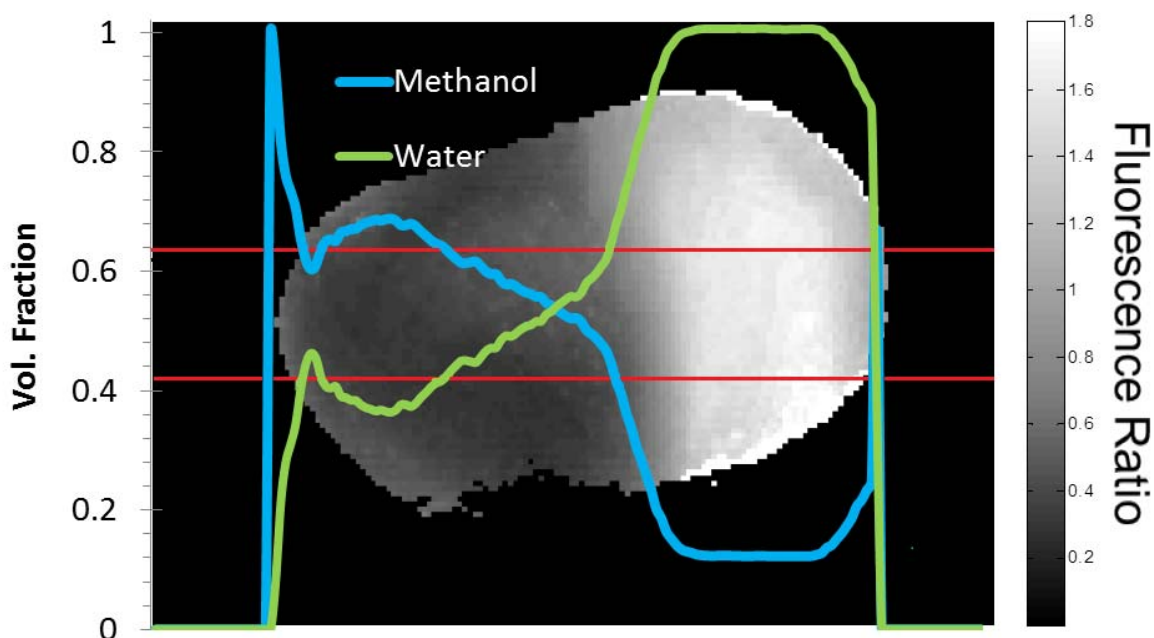


Figure 7. Analysis of droplet mixing post coalescence. Fluorescence ratios have been converted to Volume Fraction of Methanol v. Water. The averaged volume fraction of each species through a strip in the center of the droplets (outlined by red lines) is plotted against the image backdrop.

Next we received the microchannel cross-flow reactor produced by MURI collaborator Prof. R. Yetter of Penn State. In this device, narrow channels are etched into a silicon substrate bonded between thin glass windows. The channels meet at a cross junction and the streams collide and mix while traveling out of the reactor. The channels are narrow:  $200 \mu\text{m} \times 500 \mu\text{m}$  for the incoming and  $500 \mu\text{m} \times 500 \mu\text{m}$  for the outgoing channels. The flow rate and dimensions of the channel enforce laminar flow and mixing of the two streams, producing a consistent, stable

stagnation plane where the two streams collide and reproducible mixing when laminar conditions are maintained. We used the same LIF imaging technique to interrogate the microchannel reactor: a small concentration of HPTS dye in methanol was injected from the bottom of the reactor and mixed with the undyed water from the top. The flow rates of the streams were set to produce a stationary boundary and the fluorescence of the dye was excited by 400 nm pulses from the frequency-doubled Ti:Sapphire amplifier. The images shown below in Figure 8 are taken with a 10X imaging microscope and filtered by a 10 nm bandpass filter at 550 nm. The bright band in the center is the fluorescence of the dye carried by methanol into the water and deprotonated by the water, shifting the fluorescing to the longer wavelength.

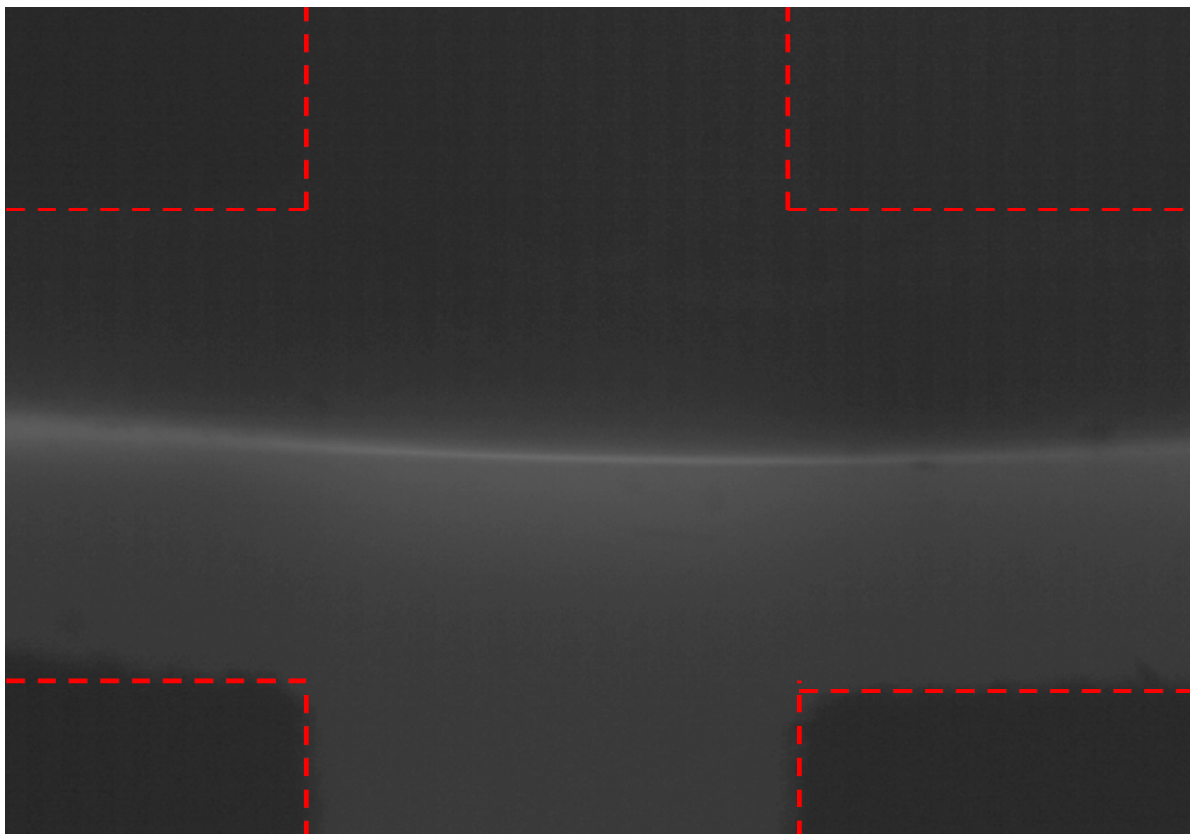


Figure 8. Fluorescent imaging of cross-flow micro-channel reactor (edges of microchannels outlined in red). Methanol carrying a chemically sensitive dye flows into the chamber from the bottom and collides in the center with pure water flowing from the top. As the two species mix the dye in the methanol is transferred to the water causing a shift in the fluorescence to longer wavelength.

## 6. Impulsive CARS for Interrogation of Mixing Systems

### 6.1 White Light Supercontinuum Driven CARS

With the laser resources of the OPA system we were unable to achieve control in the 3-beam CARS experiment. Because we were using two lasers as separate Pump and Stokes pulses and only shaping one of them our control was limited. We needed to fully control the complex phase of the excitation field, either by shaping both the pump and Stokes fields independently, or by moving to a different light source that would have sufficient broad bandwidth to contain both the Pump and Stokes spectral components within a single pulse (this is known as Impulsive excitation).

To this end we developed a collaboration with Dr. Paul Pellegrino of the Army Research Lab to attempt to measure controlled impulsively excited CARS driven by a white light supercontinuum. The broad bandwidth and stability of the supercontinuum allowed us to measure CARS from numerous bulk samples over their entire vibrational spectrum with single pulses, even in the small sample sizes and low concentrations of the Law-microdroplet and Yetter-microchannel apparatuses.

The ultra-broadband supercontinuum light source was generated by focusing approximately 1 W of power from a Ti:Sapphire amplifier (Coherent Legend Elite, 3 W average power, pulse duration 35 fs) into a 0.2 mm thick sapphire plate. The high intensity of the laser and optical nonlinearity of the sapphire generates a “white light” supercontinuum spanning from 500 nm to beyond 1200 nm in the IR. The power of the supercontinuum is fairly low, typically <5 mW. For the purposes of our CARS measurements we filter the supercontinuum to select the IR portion with wavelength longer than 800 nm. This allows us to use the remaining 2 W of power from the amplifier in the probe beam, returning moderate power even after filtering to 0.5 nm to collect higher resolution CARS spectra. This also allows us to excite CARS in a single beam, collinear geometry and use spectral filtering to separate the CARS spectra at wavelengths shorter than 800 nm from the spectrum of the driving pulse.

The white light supercontinuum is very spectrally broad, and carries sufficient power to drive nonlinear material interactions, but because its generation is a highly nonlinear, dispersion driven process the pulse comes out very temporally stretched and distorted. This lowers the instantaneous intensity of the pump pulse and also prevents temporal overlap of spectral components within the continuum, a necessary condition for achieving CARS excitation. We correct the distortions of the supercontinuum with a prism-compressor. The prism compressor directly adjusts the timing of the different spectral components in the pulse by sending them through different path lengths dictated by the dispersion of the prism glass, so that after the pulse makes a round trip through the compressor all the spectral components arrive (approximately) simultaneously. We first built a Dual Prism pulse compressor in 2012 which we upgraded to a more stable single prism pulse compressor in 2013. The prisms used in both compressors were SF10 glass. These devices compress the supercontinuum pump pulse from over 2000 femtoseconds to approximately 25 femtoseconds. A schematic of the experiment is shown in Figure 9. The compressed pulses were characterized by SHG-FROG.

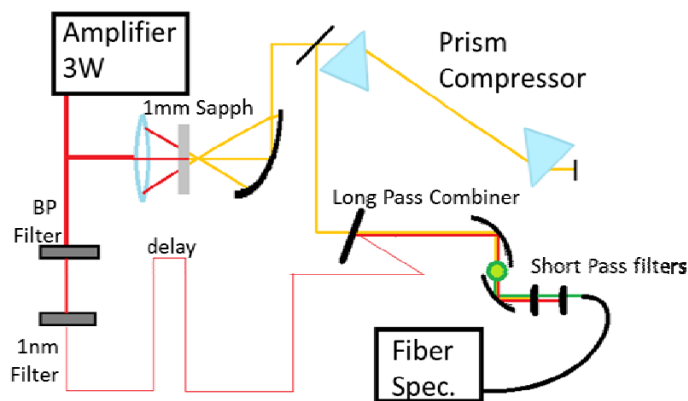


Figure 9. Schematic of White Light CARS system

After Compression the pump pulse was combined with the probe pulse on a longpass filter. The pulses were synchronized with a motorized delay stage and a probe delay of  $\sim 200$  fs added to separate the resonant CARS signal from the non-resonant Four Wave Mixing (4WM) background signal. The combined beam is focused into the sample with a 50 mm focal length gold coated off-axis parabolic reflector and the scattered CARS signal collected with a 4x Olympus microscope objective to be filtered and sent to the spectrometer. The parabolic reflector was used to avoid the optical dispersion and chromatic aberration of glass lenses; however the reflective optics made focusing to a diffraction limited spot prohibitively difficult. The measured spot size was typically 100-300 microns, making it ill-suited for point-scanning microscopy. However, even with the larger focal spot, the system was able to collect strong CARS spectra allowing for wide-angle illumination, where a large area of the sample was illuminated and the spatial information as obtained by imaging of the scatter.

After attempts to shape the supercontinuum in a dual prism, liquid crystal spatial light modulator (SLM) pulse shaper, it was learned that energy losses in the shaper were too high and the output energy of the supercontinuum was too low to drive nonlinear material interactions such as Second Harmonic Generation in BBO, Four wave mixing, or CARS excitation. Control would not be possible with this experimental system with the tools available. The principle loss of power was due to poor transmission of the low frequencies of the IR continuum through our SLM (which was purchased and designed to operate near 800 nm for shaping of Ti:Sapphire lasers). Alternate LC-SLMs with coatings for the IR or reflective SLMs are available, but we did not have access to them for this experiment, so control was not possible in this experimental system. However, the energy of the supercontinuum after correction by the prism compressor is comparable to the output power of other light sources after passing through the shaper; with this in mind the compressed, but uncontrolled, White light supercontinuum works as an effective benchmark for the intensity of signals we would expect to see from shaped driving fields from more powerful light sources.

With this setup we measured CARS from micro-droplets of Raman spectroscopic standards acetonitrile, acetone, and methanol. A single stream of droplets was generated by the Law-Group Piezoelectric microDroplet Generators described above. The stream was positioned at the focus of the CARS system, with a small distance between the PDG nozzle and the focal spot to inhibit instabilities in the stream affecting the measurements. The timing of the droplets, laser, and spectrometer were set such that spectra collected from the droplets are from a single pump-probe pair investigating a single droplet of solution. Typical spectra are presented in Figure 10; for all measured standards we observe all expected peaks to beyond  $3000\text{ cm}^{-1}$ .

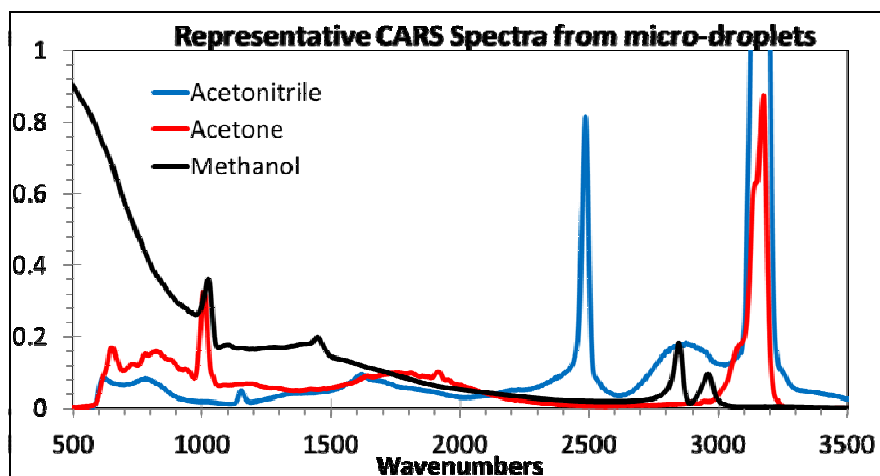


Figure 10. Representative spectra of Raman spectrographic standards measured with single laser shot of White Light CARS system.

This experiment is ongoing, with further studies being planned to investigate mixing and reaction of colliding streams of droplets as well as to apply the measurement technique for detection and characterization of smaller aerosol droplets/particles. The next stage of experimentation will be to measure CARS at the collision point of a pair of droplet streams and subsequent mixing. Once this capability is gained CARS of reactive streams will begin, starting with diffusion limited reactions such as the neutralization of organic Acid/Base pairs and moving to more complex reactions as our lab's environmental capabilities allow. The principle barriers to these continued measurements are improved synchronization, timing, and stability of the droplet streams to ensure repeatability of laser/droplet interaction; the only barriers to optical detection being improved focal optics for better spatial resolution.

With the White Light Driven CARS system we also measured CARS of mixing streams of organic dyes in the Yetter microchannel cross-flow reactor. The image of the reactor mixing region, spectra of the organic dyes, and a projection of the integrated peak intensities as a function of position in the reactor are all presented in Figure 11. With the broad accessible spectrum and high spectral resolution of the WL-driven CARS we are able to distinguish many peaks from each dye for effective identification of optical signaling. Integrating these peaks and plotting the relative intensity vs position in the reactor creates a map of the stagnation plane of the impinging flows and allows us to see a rough measure of the penetration depth and mixing at the point of stream collision. Because the low power of the supercontinuum prohibits shaping of the driving field, this is still only conventional CARS and we must raster scan the focus across the mixing region to see the change in concentration. With ODD-CARS we would be able to send optimally tailored driving pulse shapes that selectively excite only one of the two dyes and image the entire mixing region at once, similarly to LIF imaging.

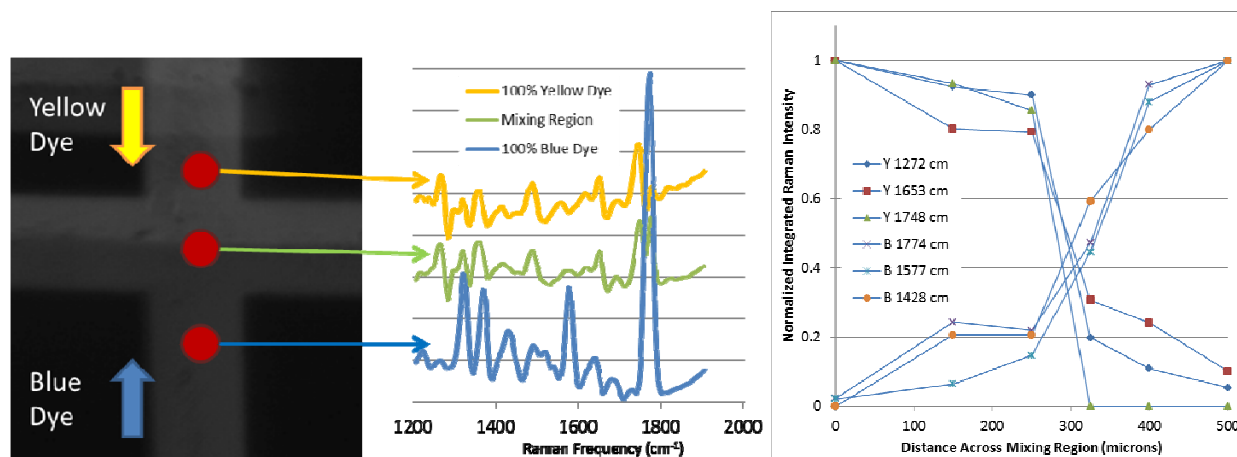


Figure 11. Measuring Impulsive CARS of mixing dyes in microchannel cross-flow reactor. At right integrated peak heights for peaks associated with each dye are plotted vs. position in the reactor.

## 6.2 TOPAS-White Commercial NOPA Driven CARS

From our experiments with the home-built NOPA, the home-built OPA, and the Sapphire Supercontinuum, we knew that we needed an ultra-broadband, stable light source that was also powerful enough to be shaped and still excite nonlinear optical interactions. To meet these requirements we purchased the TOPAS-White Non-collinear Optical Parametric Amplifier, a commercial NOPA system from Light Conversion Ltd. This light source has a broader spectral range than the home-built NOPA, but its power and field intensity are more stable than the OPA, making it the ideal source for Optimally Shaped CARS. Figure 12 charts a comparison between the original home-built NOPA, the TOPAS NOPA operating in its standard configuration, and the TOPAS NOPA running in “super broadband mode”. The NOPA spectrum is still narrower than the White Light Supercontinuum, but the pedestal width of the spectrum is  $>3000 \text{ cm}^{-1}$ , making it sufficiently broad to address the entire typical vibrational spectral range and the power is more than  $50\times$  greater.

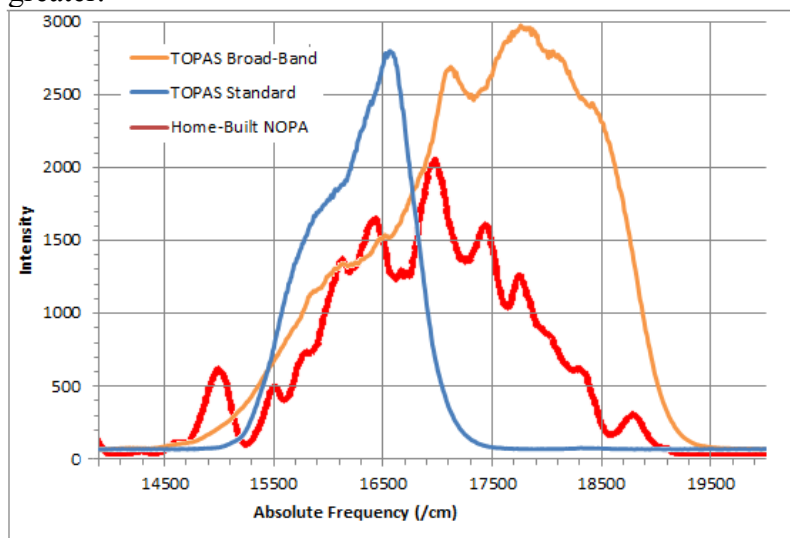


Figure 12. Spectrum of TOPAS-White commercial NOPA in ultra-broadband configuration (orange), compared to spectra of TOPAS in standard configuration (blue) and the house-built NOPA (red).



A new broad bandwidth shaping system was designed, constructed, and characterized for this NOPA, and with this system we are now able to measure impulsive excitation CARS with an optimally shaped laser pulse. We have again, begun by measuring CARS of Raman spectroscopic standards like acetonitrile, and then optimizing the collected signals to try to enhance the CARS resonant scattering or inhibit the non-resonant background. Figure 13 shows early results in the optimization of Raman scattering from acetonitrile. Here we see that the optimization has again successfully reduced the non-resonant background to essentially zero, and has also produced a large enhancement in the resonant Raman peak.

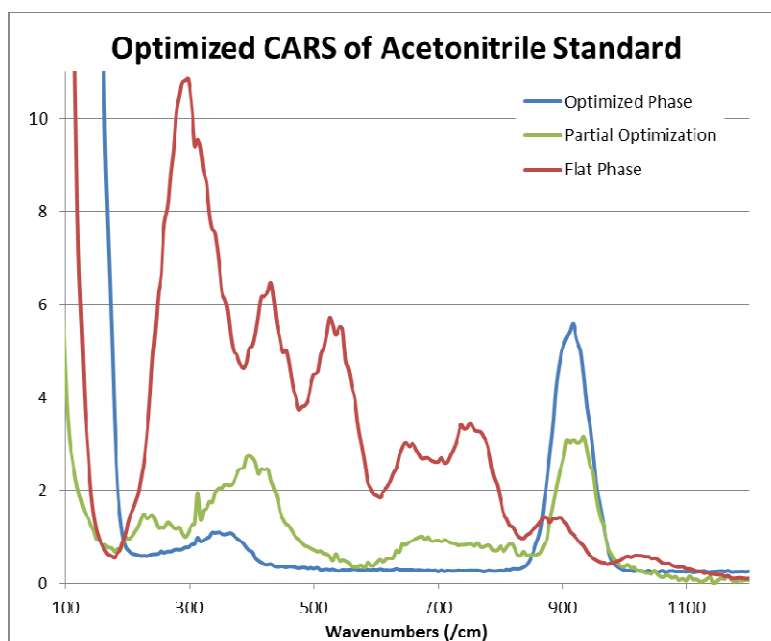


Figure 13. Optimized NOPA-Driven Impulsive-CARS of Raman spectroscopic standard Acetonitrile. Before shaping, the natural phase of the NOPA creates strong Non-resonant 4WM. The Optimization not only brings the CARS signal out of the noise but nearly eliminates the Non-resonant background.

## 7. Conclusions

Over the course of this program we have created a new detection capability in Optimal Dynamic Discrimination (ODD). Beginning by laying out the theoretical framework for the methodology, we proceeded to implement the technique through discrimination of test systems utilizing dyes with optical characteristics indistinguishable by conventional spectroscopic techniques. We then applied this methodology to Coherent Raman spectroscopy to yield chemically selective vibrational spectroscopy. This tool will yield both qualitative identification of chemicals present in a complex mixing and reacting system like hypergolic combustion as well as quantitative measure of the concentration of those species present. We collaborated with MURI partners to perform preliminary experiments in characterizing fluid mixing in microdroplet collisions and microchannel flow mixing systems. Presently we have examined nonreactive flows and mixing of water and simple solvents, and we are preparing to move on to the observation of reactive mixtures such as organic acid-base pairs in preparation to work with combustive systems. The ability to directly measure local concentrations of chemical species taking part in these combustion reactions in real time, without disturbing the reaction, will be a powerful detection

capability. These experiments are ongoing, but we are nearing the stage where we have sufficiently developed and evaluated the techniques of Optimally Enhanced CARS and other ODD techniques and can now utilize the tools to investigate and characterize complex reacting systems. This research should yield a sensitive and flexible spectroscopic toolkit for broad use in chemical analysis in many environments

## 8. References

1. M. Roth, L. Guyon, J. Roslund, V. Boutou, F. Courvoisier, J.-P. Wolf, and H. Rabitz, "Quantum Control of Tightly Competitive Product Channels", *Physical Review Letters* **102**, 253001 (2009)
2. Brif C., Chakrabarti R., Rabitz H., "Control of Quantum Phenomena: past, present, and future", *New J. Phys.* **12**, 075008 (2010)
3. Weiner, A.M., "Femtosecond pulse shaping using spatial light modulators", *Review of Scientific Instruments* **71**, 1929 (2000).
4. Judson, R.S. and H. Rabitz, Teaching Lasers to Control Molecules, *Physical Review Letters* **68**, 1500 (1992).
5. Roslund, J., Shir, O., Back, T, Rabitz, H, Accelerated optimization and automated discovery with covariance matrix adaptation for experimental quantum control, *Phys Rev A* **80**, 043415 (2009)
6. Eckbreth, A. C., *Laser Diagnostics for Combustion Temperature and Species*, CRC Press, (1996)



## **III.2 Study of Condensed-phase Reactions in Hypergolic Propellants using Microreactors (Yetter, Penn State)**

### **1. Abstract**

Unlike conventional methods of testing and studying hypergolic propellants which usually involve the use of drop tests or impinging jet tests, this work presents a newer method using micro-fabricated reactors to study the fast reactions that occur between the propellants. These reactors are able to provide us with the ability to concentrate on just the pre-ignition reactions and the interaction between the liquid propellants by isolating the liquid-phase reactions from the gas-phase reactions that actually lead up to ignition. This report provides a detailed description of the fabrication of the microreactors, the characterization of flow in the microreactors as well as description of experiments carried out in the micro-reactor using various hypergolic fuels such as tetramethylethylenediamine (TMEDA), 2-dimethylaminoethylazide (DMAZ), triethylamine, dicyclopentadiene (DCPD) and indene along with nitric acid (NA) as the oxidizer. The heat released by the reactions between the reactants was quantified using temperature measurements at the exit of the reactor. Drop tests were also conducted using the various fuel-oxidizer combinations to compare with the experimental results from the reactors. A high correlation was found to exist between the experimental drop tests and the temperature measured in the micro-reactor experiments thus proving that initial liquid-phase reactions impact the ignition process and thus the performance of the hypergols as a whole. Also discussed are numerical simulations of the reactive flow at the stagnation zone of the microreactor. A FORTRAN code meant for opposed flow diffusion flames was modified to reflect the liquid phase flow and reactions occurring in the microreactor. These simulations showed that the flow rates had an effect on the temperature observed in the stagnation zone with temperature trends from the numerical simulations being similar to those seen in the microreactor. This work thus presents the first comprehensive measurements which relate the effect of early liquid-phase reactions with the overall ignition process for various hypergols pairs.

### **2. Introduction**

Hypergolic bipropellants are a special variety of liquid propellants and are usually fuel and oxidizer combinations which chemically react on contact and produce enough heat to be able to spontaneously ignite. The spontaneous ignition process makes the use of hypergolic propellants advantageous as there is no need for complex ignition systems thus making engine design and control systems much simpler. In addition, these propellants are able to have better restart reliabilities and can be stored for long periods of time than other types of propellants and thus are ideal for space missions and spacecraft maneuvering systems and also show promise for micro-propulsion [1]. The discovery of hypergolicity occurred in Germany around 1937 and the Titan, Gemini and Apollo missions all used hypergolic bipropellants. The use of hypergolic propellants is still very popular with the Ariane, Long March, the Space Shuttle and the International Space Station programs all using hypergolic propellants [1].

Given the large area of applications for hypergolic propellants, they have been a focus of scientific research for a number of years and the use of these propellants is well understood, making the hypergolic engines, reliable and safe. But although the ignition systems may be simpler in hypergolic propellant engines, the ignition process itself is not very well understood as it is a transient phenomenon and usually involves both physical and chemical processes, the interrelation between which can be very complex. Hypergolic ignition modeling efforts [2]–[4] usually concentrate only on the gas phase reactions with all the reactants fully vaporized and

neglect the contribution of liquid phase reactions although the liquid phase reactions are highly energetic as well.

One of the most common measure to test hypergolicity as well as compare different hypergolic pairs is based on ignition delay times. Although ignition delay has been defined in various ways, the most commonly used definition was provided by Gunn [5] which states that ignition delay is the difference in time between the first contact between the two reactants and the initial change in light emission. Long ignition delay times are unfavorable as they lead to accumulation of unused propellant as well as highly explosive intermediate species inside the engine chamber. This can lead to detonation upon starting, which is referred to as a ‘hard start’ [6]. As a number of chemical and physical processes play an important role leading up to ignition, the ignition delay times are in fact a combination of the chemical delay and the physical delay times and can thus be referred to as global ignition delay times instead [6]. The chemical delay times are controlled by the reaction times between the two reactants. On the other hand, the physical delay times are a function of the time needed for atomization, heating, vaporization, diffusion and mixing of the reactants. Thus the physical delay times are highly dependent on both the physical properties of the reactants (such as viscosity, density, surface tension and miscibility) as well as the method by which the reactants are mixed together. An experimental setup which will yield better mixing between the reactants will naturally result in lower ignition delay times. In this study, ignition delay refers to the global ignition delay times for the hypergols.

The simplest way to gain an understanding into physical and chemical processes involved between the reactions of hypergols is to use a drop test. Drop tests, in their various forms, have been used for the last few decades [5]–[7] and involve release of a fuel or oxidizer droplet into a pool of the corresponding hypergolic pair. Drop tests are relatively simple to set up and use very little amounts of the propellants and are thus still used to perform initial tests on new propellants. As the ignition delay times are so dependent on mixing between the two reactants, modified versions of drop tests were also created [8], [9] which forcefully mixed the fuel and oxidizer pairs together and thus provided for a larger reaction between the two propellants. To simulate the conditions found in an actual rocket engine, impinging jet tests have also used [10], [11] in which the mixing and thus the reaction between the fuel and oxidizer took place at the intersection of two or more jets. The impinging jet tests provide a more realistic method to study hypergols than the conventional drop tests as the mixing, vaporization, chemical reactions and the ambient conditions are more comparable to actual engine conditions.

Even though the drop tests are relatively easy to setup and the impinging jets give us empirical information on what the performance of these hypergols would be like in actual rocket engine conditions, these tests suffer from a large amount of variabilities. These variabilities arise due to the fact that it is very hard to control and quantify parameters such as droplet size, impact strength, and mixing. These differences lead to large discrepancies between results from different kinds of setups as well as making it tough to separate the initial condensed-phase reaction reactions that lead to ignition from the later occurring gas-phase reactions. This study uses the advantages of fluid flow at the micron-scale to concentrate on the initial contact between the two hypergols as well as the condensed-phase reactions.

One of the advantages of using micro-reactors for testing hypergols is the fact that very low quantities of the reagents are needed for tests when compared to macro-scale experiments. Given that the reagents can be hazardous as well as corrosive, this helps in making the tests much safer. Given the low Reynolds numbers in fluid flow at the micron-scale, the fluid flow is dominated

by viscous effects and thus is laminar in nature. [12]. This laminar flow helps in ensuring that the mixing between the two fluids at the interface in the micro-reactor is due to diffusional mixing only. If now, the Péclet number is tailored (either by flow conditions or the reactor dimensions and design) to be high then the diffusional mixing can also be limited and thus it is possible to have minimal mixing between the two reactants [13]. Thus using micro-fluidics seems to be perfect for analyzing fast liquid-liquid reactions especially between hazardous reagents like hypergols.

There are a large number of hypergolic propellants with the oxidizers usually being hydrogen peroxide, fluorine, pure nitric acid (NA), white fuming nitric acid (WFNA), red fuming nitric acid (RFNA), inhibited red fuming nitric acid (IRFNA) and nitrogen tetroxide (NTO). The fuels on the other hand are usually amines, phenols or heterocyclic compounds such as hydrazine, monomethylhydrazine (MMH), unsymmetrical dimethylhydrazine (UDMH), aerazine (50% hydrazine and 50% UDMH). The most popular combination of hypergolic fuel and oxidizer is MMH with NTO. This combination provides low ignition times as well as high specific impulse [14]. Although these fuels and oxidizers provide for excellent rocket engine characteristics, they are in most cases very corrosive, toxic and in some cases even carcinogenic (as in the case of hydrazine based fuels) [15]. Thus there is a large interest in finding alternative fuels which while providing similar rocket engine characteristics, will also be safer to use [16]. To develop these fuels, we need a better understanding of the processes (both chemical and physical) leading to ignition during hypergolic combustion.

Alkyl Multiamines have been suggested as possible candidates to replace the toxic hydrazine based fuels and a series of tertiary amines have been recently developed and tested as well [17]–[19]. Among the various alkylamines, TMEDA is considered the most promising candidate because of its short ignition delay times with WFNA. And although the ignition delay times of TMEDA reacting with RFNA are larger than the corresponding times for the reaction between MMH and RFNA, TMEDA is still an attractive alternative as it is believed to be far less toxic [20]. After discovery of TMEDA as a fuel, multiple studies have been carried out using drop tests [18], [19] to evaluate its performance. And a much more detailed study has been carried out by Wang et. al. [21] which analyzed gaseous species produced by condensed and gas-phase reactions between TMEDA and 90% nitric acid.

Various 2-azidoethanamines have also been recently developed and tested by the US army as possible alternatives to the carcinogenic hydrazine fuels [22]. It was found that DMAZ was the best candidate amongst these as it had physical properties comparable to MMH and was also able to support hypergolic ignition with NTO based oxidizers. Also, much like TMEDA, DMAZ has been found to be much less toxic than MMH [20]. DMAZ when used with IRFNA has shown to have ignition characteristics similar to aerazine-IRFNA systems but is shown to be clearly less when compared to the MMH-IRFNA systems, with the main hurdle being the large ignition delays with DMAZ which lead to hard starts in rocket engines. Stevenson [18] has recently claimed that the addition of TMEDA to DMAZ helps in reducing ignition delays and it was suggested that a mixture of 66.7% TMEDA and 33.3% DMAZ was capable of producing minimum ignition delay times in both drop and engine tests. Moreover this mixture of TMEDA and DMAZ provided a higher specific impulse as well as cleaner burning by not producing as much salt precipitate as was formed by just reacting TMEDA with the oxidizer.

Numerical models for both TMEDA and DMAZ have been created [23] following in the footsteps of the much used and thus better understood MMH-RFNA mechanism. These

mechanisms, like the original MMH-RFNA mechanism [24], ignore the condensed-phase chemistry and only concentrate on the gas-phase reactions.

Given the fuels under consideration as alternatives to hydrazine based fuels, this study concentrates on comparing the performance of TMEDA and DMAZ in the micro-reactor (limited to only condensed-phase reactions) with the drop test experiments and relating how early condensed phase reactions do in fact affect the entire ignition event. Also under consideration in this study are fuels such as triethylamine, dicyclopentadiene and indene. Triethylamine has been shown to display hypergolic behavior with WFNA [25], while interaction of dicyclopentadiene and indene with WFNA have also been previously studied [26]. These additional fuels were tested in both the micro-reactor as well as the drop test setup and the results were compared to provide a baseline for the results provided by the interaction TMEDA and DMAZ with NA. It is hoped that a better understanding of the importance of condensed-phase chemistry, which has been ignored by previous studies, in the ignition process will lead to better numerical models and in turn development of safer fuels to replace MMH.

### 3. Drop Tests

Initial tests for all the fuels interacting with the WFNA were conducted using a simple drop test setup. This setup was identical to the one used by Wang et. al. [21] for their studies regarding the interaction between TMEDA and nitric acid and a schematic along with a detailed description is provided in that study. For the drop test, an excess amount of WFNA (approximately 80  $\mu\text{L}$ ) was placed at the bottom of a square glass cuvette. The cross section of the cuvette was 10 mm on each side of the square and it was about 45mm tall. The drop of fuel was produced using a plunger attached to a glass syringe which slowly produces a droplet of fuel. This fuel droplet was approximately 7~10  $\mu\text{L}$  in volume and traveled towards the centre of the oxidizer pool in the cuvette. Care was taken that no additional momentum was supplied to the droplet of fuel. A Phantom high speed camera was used to record the process from the actual release of the fuel droplet to the end of the ignition event.

### 4. Reactor Fabrication

Application of highly oxidizing fluids such as nitric acid warranted fabrication of the microreactors from silicon and glass instead of polymers such as PDMS. The microreactors were designed to be mounted on a manifold where they were held in place with a compression seal with the inlet and exhaust ports etched into the silicon from underneath. These manifolds provided a suitable method to pump reactants into the reactors while minimizing pressure drops and providing a safe and secure approach for collecting exhaust fumes and residual condensed phase products. Thus, flow channels were etched from one side of the silicon wafer while the inlet and outlet ports were etched from the back side. To etch both sides, a double side polished wafer was used. Since no electrical devices were fabricated onto the silicon reactor, the resistivity of the wafers was not an important parameter. But for the sake of uniformity, all reactors were created using 4" wide *n*-type silicon wafers with a resistivity between 2 and 5  $\Omega\text{-cm}$ .

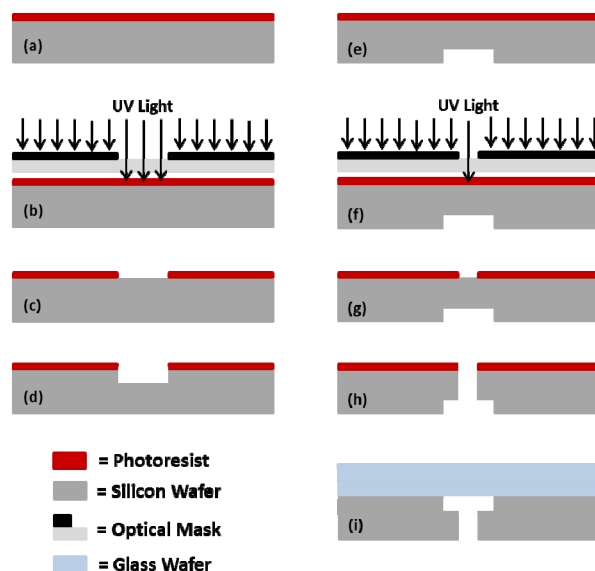


Figure 1. Schematic of fabrication process for the microreactors. Steps (a), (b) and (c) illustrate the photolithography process for one side of the double side polished silicon wafer. Step (d) shows the deep reactive ion etching (DRIE) of the silicon wafer to create the reactor channels. Steps (e), (f) and (g) illustrate the photolithography process for the back side of the etched silicon wafer. Step (h) shows the DRIE process for the back side of the wafer to create the inlet and outlet ports. Step (i) illustrates the anodic bonding of the etched silicon wafer to a borosilicate glass wafer.

A schematic of the fabrication process is shown in Figure 1. The photolithography for the pattern transfer on to the silicon substrate was carried out using the MicroChem<sup>®</sup> KMPR photoresist. KMPR is a chemically-enhanced high contrast epoxy based i-line (365 nm wavelength) photoresist and was chosen over the more traditionally used photoresists because it has superior adhesion to silicon and resistance to chemical and plasma etchants. The flow channel pattern on the silicon wafer was etched using a deep reactive ion etching (DRIE) process where the silicon was etched anisotropically using the Bosch process [27]. The same process was repeated for etching the inlet and exhaust through-holes on the back-side of the silicon wafer. Once the etching of the wafer was complete, the silicon wafer was thoroughly cleaned using a piranha clean solution (50% concentrated sulphuric acid and 50% hydrogen peroxide) and then bonded to a borosilicate glass wafer using anodic bonding. The last step of the fabrication was dicing of the bonded wafer to obtain individual reactors which was accomplished using a conventional dicing saw.

Microreactors were batch processed and designed to provide a stagnation point flow between the two counter-flowing reactants entering the microreactor (Figure 2a). The stagnation flow design was chosen such that the reaction would be positioned at the interface between the two flows preventing side-wall contact of the reaction. Each reactor had inlet and exit channel widths and depths of 240  $\mu\text{m}$  and 60  $\mu\text{m}$ , respectively. The inlet channel lengths were 0.375 cm each and the overall exit channel length were 1.5 cm.

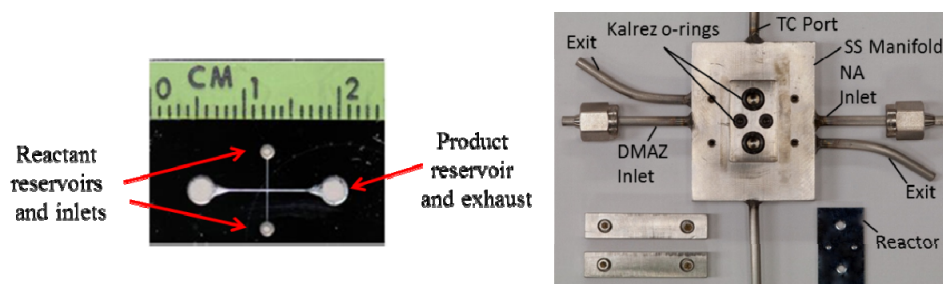


Figure 2. (a) Fabricated microreactors using etched silicon bonded to borosilicate glass. (b) Microreactor with stainless steel manifold setup.

The manifolds (Figure 2b) were fabricated from SS316 and made use of Swagelok<sup>®</sup> fittings for external connections. The inlets and outlets of the manifold were connected to the inlets and outlets of the microreactors using corrosion resistant Kalrez<sup>®</sup> O-rings with a compression seal to prevent any leakage of chemicals.

## 5. Experiment

Two experimental configurations were used to analyze the reaction between hypergols and the flow field in the microreactors. The experimental setup for hypergol analysis, which is schematically shown in Figure 3, consisted of the reactor mounted manifold placed under an upright microscope (Nikon Eclipse LV100). A high speed camera (Phantom V7.3) was mounted onto the upright microscope to optically study the reacting flow in the microreactors. A pressure driven flow was established in the microreactors with a positive pressure applied at the inlets and the exhaust open to atmospheric pressure. The fuel and oxidizer were introduced into the manifold using Teflon<sup>®</sup> tubing connected to high pressure stainless steel syringes. The syringes were controlled by two independent high pressure syringe pumps (Harvard Apparatus PHD4400). Fine-wire shielded K-type thermocouples were introduced into the exhaust reservoir of the main channels and were carefully positioned at the center of the exit of the microreactor to record the temperature of the exhaust fluids while simultaneously studying the reaction zone optically. A rise in temperature at the exit was an indication that an exothermic reaction had occurred inside the main channel of the reactor. Temperature measurements, reported elsewhere [28], have shown that the channel exit measurements follow similar trends to temperature measurements at the stagnation point. A water trap connected to a high velocity exhaust fan was attached further downstream of the exhaust to facilitate the safe disposal of the products of the reaction.

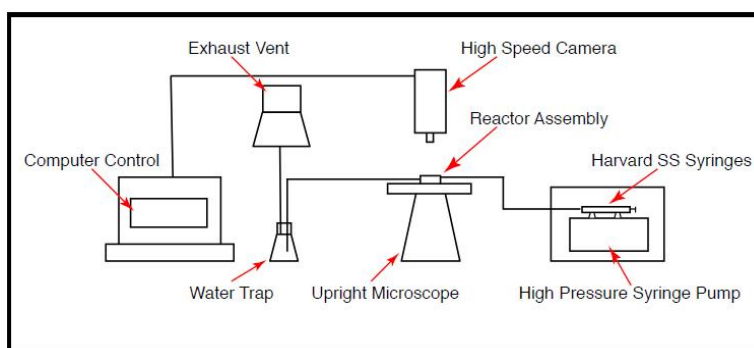


Figure 3. Schematic of the experimental setup showing the microreactor assembly under an upright microscope.

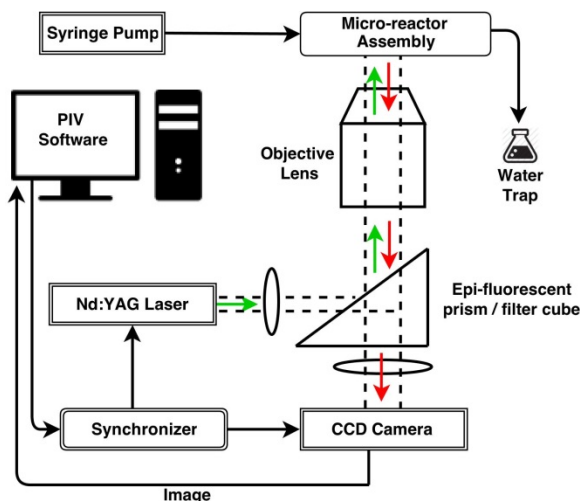


Figure 4. Schematic of Micro-PIV setup.

To quantitatively determine the velocity flow-field in the microreactor, velocity measurements were made using a micro-PIV system which is schematically shown in Figure 4. The reactor and manifold assembly were placed on an inverted microscope (Nikon Eclipse TE2000-U) and a 10x objective (Nikon Plan Fluor NA = 0.3) was used to magnify the image. The illumination for the PIV was provided by a double pulsed Nd:YAG laser ( $\lambda = 532$  nm, New Wave Research – Solo III) which provided the two pulses of 50 mJ at a repetition rate of 15 Hz. The flow in the microreactor was seeded by 2  $\mu\text{m}$  diameter fluorescent particles (Thermo Scientific Fluoro-Max Red Aqueous Fluorescent Particles) which when excited by the laser have emission peaks of 542/612 nm. The fluorescent emission from the particles passes through the high-pass filter cube in the microscope and is recorded by a 12-bit high resolution ( $1360 \times 1024$  pixel) CCD camera (TSI PIVCAM-14-10) which provides the images to the PIV software. The double pulsed laser and the CCD camera are connected to a workstation via a laser pulse synchronizer (TSI 610034) which controlled the timing of the volumetric illumination from the laser as well as the image acquisition.

A scaling factor of 0.35  $\mu\text{m}/\text{pixel}$  was used for the present study and thus the observation area was  $476 \times 360 \mu\text{m}$ . Each pulse from the double pulsed laser was recorded as a separate image (forming an image-pair) and was processed using a PIV software (TSI Insight 6.0) which managed both data acquisition as well as the analysis. The laser pulse delay, which is controlled by the synchronizer, varied depending on the flow-rate of the fluid inside the microreactor. It was calculated such that the particles moved at an average of 8 pixels from one frame of the image-pair to the other. These calculations were done using the average flow velocity in the channels of the microreactor. A total of 120 image-pairs were acquired for each experimental run so as to provide a sufficient amount of data for the averaged correlations to be accurate. The images obtained by the PIV software were processed using a Nyquist Grid. The Nyquist Grid sets vectors with the x spacing equal to half of the interrogation spot width and the y spacing equal to half of the interrogation spot height. No spot offsets are used (which provides an effective overlap of 50% between each image-pair) and the processing only uses a single pass. The correlations were computed with a FFT correlation engine and a Gaussian peak algorithm. An ensemble method of correlation was used which helps in improving signal to noise ratios when there are steady flows under observation [29]. The interrogation window was kept at 48 x



48 pixels to have multiple particles in each window and thus to form better cross-correlations while calculating the displacement of the particles as well as the velocity flow-field.

The velocity profile measurements were compared with a steady-state 3-dimensional simulation that was created using FLUENT [30]. The dimensions of the cross-section of the reactor used in the model were exactly the same as the actual fabricated microreactor and water was used as the fluid entering the microreactor from both the inlets. Owing to the small length scales and even smaller diffusion scales involved in the simulation, a large number of grid points, especially near the interface of the two liquids, had to be used to closely simulate the interface region. The fluid flow domain was created in GAMBIT and to ensure more accurate solutions, quadrilateral elements were chosen while meshing the domain. A total of 500,000 grid points were used for the simulation and to save on computational time, the overall length of the main-channel in the simulation was reduced while taking care for the flow to still develop. A uniform velocity profile was specified at the reactor inlets that corresponded to the average experimental velocities obtained from the syringe pump flow rates and microreactor inlet channel cross-sectional areas. The no-slip condition was specified as the boundary condition for the walls while the outlet had a gauge pressure of zero.

## 6. Cold Flow Characterization in Microreactor

Cold-flow studies were performed to characterize the flow field along the stagnation streamline and to determine strain rates at the stagnation point. A variety of non-reactive fluids including water, acetone, and glycerol were used to simulate the hypergol reactants. The flow in the reactor was visualized using the red fluorescent polymeric micro-spheres also used for the PIV measurements. The micro-spheres were added to one inlet of the reactor while keeping the other inlet particle free. The flow rates were varied over a Reynolds number range from 15 to 120. As expected from behavior generally observed in microchannels at low Reynolds numbers, laminar flow was achieved with a quasi-steady interface between the flows in which the particles remained only on one side of the channel, even far downstream of the stagnation zone (Figure 5a and Figure 5b).

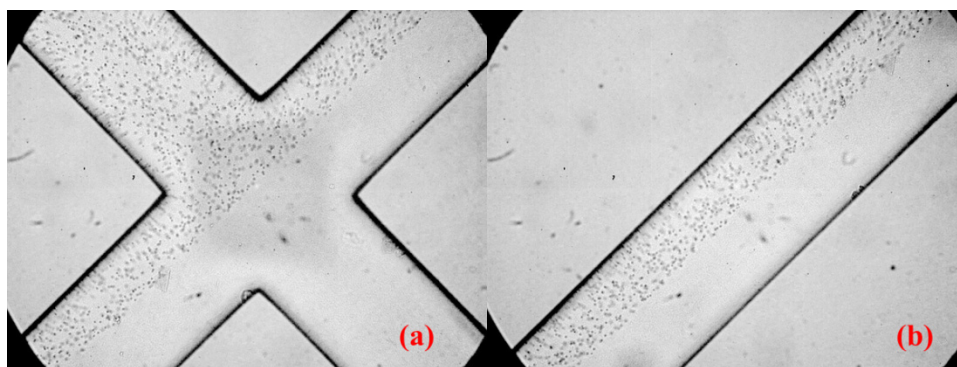


Figure 5. (a) Cold flow testing of microreactor using micro-spheres to visualize flow at stagnation zone. (b) Cold flow visualization downstream of the stagnation zone showing very little broadening of diffusion interface.

A common method for normalizing the velocities in a counter-flow configuration is usually by using the strain-rate instead of flow rates of the reactants. The strain rates at the interface for the counter-flow setup were approximated as  $(U_1 + U_2)/L$ , where  $U_1$  and  $U_2$  are the velocities of the



fluid from the two inlets respectively, and  $L$  is the separation distance between the two inlets. Figure 6 shows a typical averaged velocity profile from the PIV measurements. The velocity profile was calculated by using correlations between 120 image pairs. The flow field can be seen to be symmetrical about the stagnation point in the microreactor. Figure 7 shows the deceleration of the fluid velocities from the opposing inlets to the stagnation zone of the microreactor for one of the strain rates studied in the microreactor. The fluid velocities from both the experimental PIV measurements as well as the FLUENT simulation are plotted with the solid line showing the numerical result while the individual points showing the experimental data.

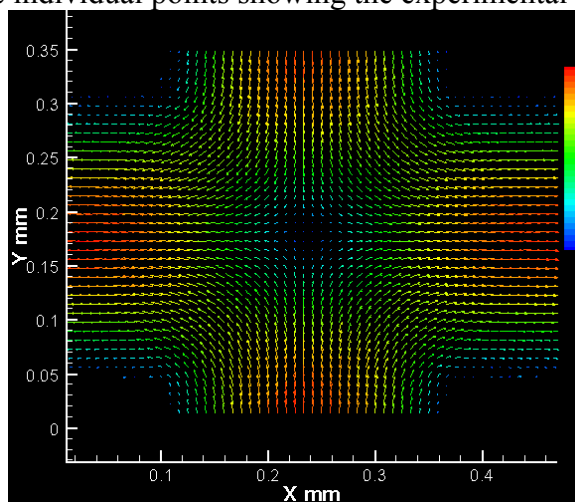


Figure 6. Typical average velocity flow-field calculated from PIV measurements. Magnitude of velocity is shown by using colored vectors in the image with blue vectors indicating a low velocity magnitude while red indicates a high velocity magnitude.

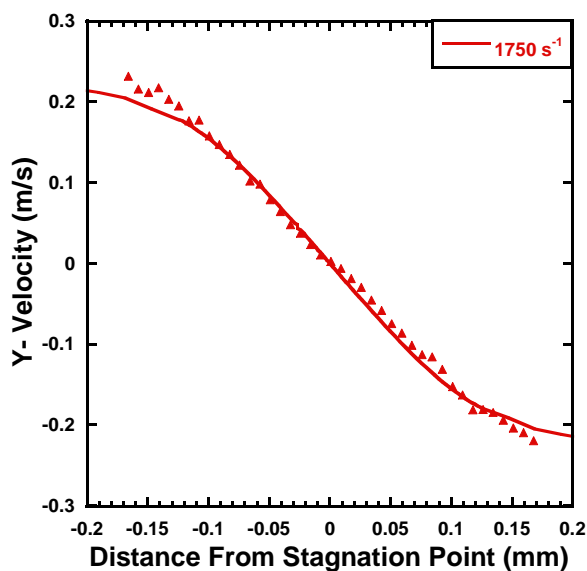


Figure 7. Fluid velocity from opposite inlets of the stagnation flow reactor as the flow decelerates towards the stagnation point. Solid line indicates FLUENT simulation results while the points indicate experimental PIV measurements

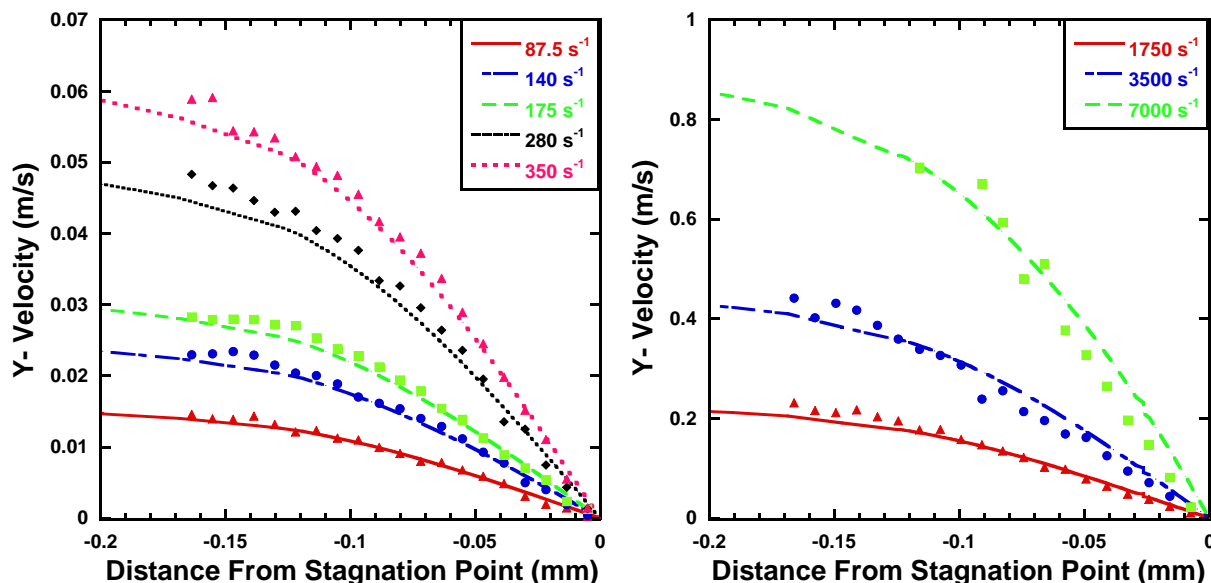


Figure 8. Fluid velocity as the flow decelerates towards the stagnation point. Lines indicate FLUENT simulation results while the points indicate experimental PIV measurements.

Both experimental data from the PIV measurements and the corresponding results from the FLUENT simulations for the various strain rates under study are shown in Figure 8. The results shown concentrate on the stagnation zone of the reactor as this is the location where the flow-field changes the most and show the decelerating velocities only from one inlet of the stagnation flow microreactor owing to the inherent symmetrical nature of the flow. The lines in the plots are the FLUENT simulation results while the points are the experimental PIV results for corresponding strain rates. The measurements from the PIV system were limited to a strain-rate of 7000 s<sup>-1</sup> since the PIV camera was not able to collect two full frames of data any faster. The maximum Reynolds number for the flows studied using the PIV was 60. Figure 9 shows the comparison of the FLUENT simulation results to the PIV experimental data by plotting the velocity profiles at the entrance and outlet to the main stagnation zone for different flow rates. As can be seen from the plots, the numerical simulations agree very well with the experimental PIV results apart from very close to the wall. The reason for this discrepancy could be due to the relatively large sized (2  $\mu\text{m}$ ) microparticles that have been used to track the flow are therefore unable to resolve the details in the flow field close to the walls.

Although very good agreements between the PIV measurements and the FLUENT simulations were observed over a range of low to moderate flow rates of the reagents into the microreactor, instabilities were seen to occur when the flow rates were raised to a critical high value. At low flow rates the flow-field is seen to be symmetric about the centre of the microreactor stagnation zone as shown in Figure 6 but when the flow rate is raised above a critical value the flow-field is no longer symmetric but instead the stagnation plane shifts towards one inlet or the other which varies with depth. The flow-field when this shift in the stagnation plane occurs is visualized in Figure 10. The direction in which the stagnation plane shifts is purely stochastic in nature and cannot be predicted. A number of experiments were conducted and it was found that there was equal probability of the stagnation plane to move towards one inlet or the other.

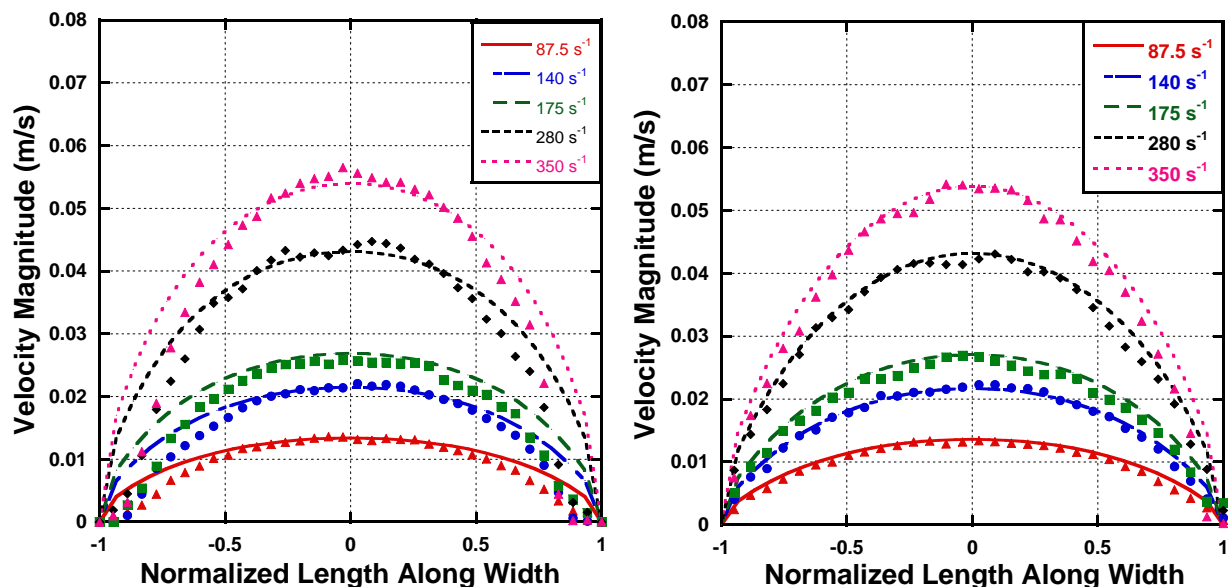


Figure 9. Velocity profiles at (a) inlet to stagnation zone and (b) outlet to stagnation zone.

Measurements were made at various heights along the width of the reactor to find the position of the stagnation plane at these various heights. Figure 11 shows the relative position of the stagnation plane at various heights for a number of experimental runs. As can be seen from the graph, the position of the stagnation plane is no longer vertical along the height of the microreactor (as would be expected in stagnation flow reactor) but instead shifts rapidly from one side of the microreactor to the other with very little change in the vertical direction.

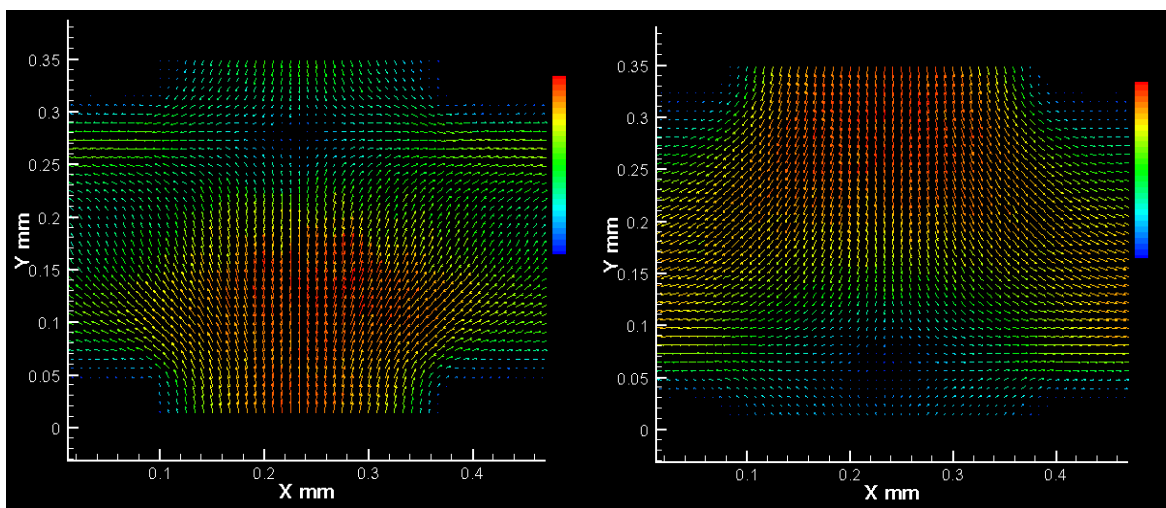


Figure 10. Shifting of the stagnation plane from the centre of the microreactor towards one inlet or the other.

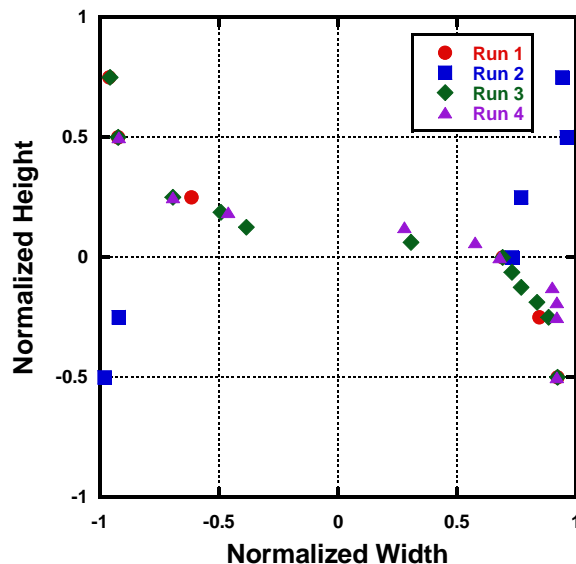


Figure 11. Position of stagnation plane at various heights in the deep-etched microreactor.

This shift in the stagnation plane is caused by the fact that the two fluids ‘slip’ over one another instead of coming to rest at the stagnation plane. Figure 12(a) shows a schematic of the cross-sectional view of the stagnation zone of the microreactor in the case of low flow rates of the fluids into the microreactor. The stagnation plane between the fluids entering the reactor is shown by the red line and is seen to be stable and vertical. When the flow rates are increased over a critical value the stagnation plane is seen to shift and can be represented by the schematic in Figure 12(b). It should be noted that multiple runs made with the same flow conditions in the microreactor resulted in the stagnation plane that would shift towards either one inlet to the other, with the direction of the shift not being predictable.

Similar bifurcation instability has also been seen in macroscopic experiments involving stagnation flows formed between opposing jets of gases [31]. The experiments from the study show that at low Reynolds number and with equal jet velocities, the flow remains symmetric about a plane between the two nozzle exits and the stagnation plane is located midway between the nozzles. When the flows from the jets were increased past a critical Reynolds number then the flow remained symmetrical no longer and stagnation plane was observed to shift away from the midway plane. Instabilities have also been noticed at higher Reynolds number flows in microfluidic devices. A number of studies [32]–[38] in the past have shown that when the fluid velocities are increased, the flow in microfluidic devices do not remain laminar in nature. Most of these studies have concentrated on the mixing efficiency in *t*-type micromixers. As the mixing in the microreactors is based on diffusional mixing alone, thus one method of increasing the mixing efficiency is by changing the flow regime from a simple laminar one to a more chaotic one.

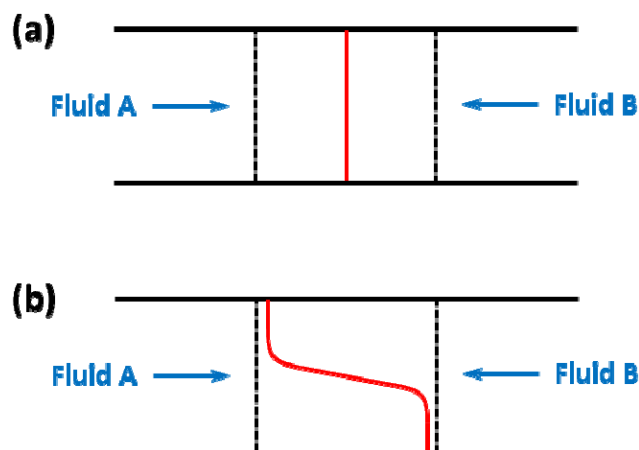


Figure 12. Schematic of the cross-sectional view of the stagnation zone of the microreactor showing the stagnation plane (red line) between the two fluid flows. (a) shows a stable stagnation plane between the two fluids at low flow rates and (b) shows the unstable stagnation plane at high flow rates in which the plane shifts towards one inlet or the other.

Studies [32], [33] have found that three kinds of laminar regimes exist in the mixing channel. At very low Reynolds numbers, the flow between two fluids is stratified in nature and the mixing occurs only due to molecular diffusion. When the Reynolds numbers are increased then the flow regimes change slightly to a more chaotic regime resulting in more mixing between the fluids. This regime is referred to as the vortex flow regime. When the Reynolds numbers are increased even further then the flow shifts to a regime called the engulfment flow regime. Engulfment flow is characterized by the creation of secondary flows and the separation of the boundary layers due to the sharp edges of the corners at the junction of the micromixer. It is believed that the instabilities seen in the present study at high Reynolds number flows are similar in nature to the engulfment flow regime. The shifting of the stagnation plane can now be explained by the creation of secondary flows in the stagnation zone.

The study of the stagnation flow between two opposed jets by Ciani et al. [31] demonstrated that the Reynolds number alone could be used to characterize the flow between two opposing jets. But in the present microreactor, these instabilities set in at different flow rates in the deep etched reactors (500  $\mu\text{m}$  deep) and the shallow etched reactors (60  $\mu\text{m}$  deep). The instabilities occurred when the flow rate of the fluids was increased over 750  $\mu\text{L}/\text{min}$  for the deep etched reactors (i.e. a Reynolds number of 24) while they occurred above a flow rate of 2000  $\mu\text{L}/\text{min}$  for the shallow etched reactors (i.e. a Reynolds number of 240). As the critical flow rate at which this bifurcation instability occurs is different when the aspect ratio of the reactor is changed, thus it can be stated that the instability depends on both the volume flow rate as well as geometrical parameters of the microreactor. Thus, Reynolds number alone cannot be used to characterize the flow and another dimensionless number is needed.

Such a dimensionless number was suggested by Soleymani et al. [39] and has been used by other studies as well to predict when the engulfment in the flow-field will set in. These studies showed that the transition to the engulfment flow regime is not governed by Reynolds number of the flow alone but is also affected by parameters such as aspect ratio, the width of the inlets and width of the mixing channel. This dimensionless number is referred to as the identification number ( $K$ ) and can be defined as:

$$K = Re^{0.82} \left(\frac{W}{h}\right)^{-0.79} \left(\frac{D_{h,in}}{D_h}\right)^{-1.5} \left(\frac{w}{h}\right)^{0.15}$$

where,  $Re$  is the Reynolds number of the flow at which transition to the engulfment regime occurs,  $W$  is the width of the inlet channels,  $h$  is the depth of the reactor channels,  $D_{h,in}$  is the hydraulic diameter of the inlet channels,  $D_h$  is the hydraulic diameter of the mixing channel and  $w$  is the width of the mixing channel. It was found by a variety of studies [32], [34]–[36], that the transition to the engulfment flow regime occurs at an identification number close to 100. But a study by Sultan et al. [37], which studied t-type micromixers with headspace, found there to be no correlation between the transition to a chaotic flow regime and the identification number. For the present study, the identification number (as defined by Soleymani et al.) for the shallow-etched reactor was found to be 27 while that for the through-etched reactor was 29. The difference between the present study and the ones before (where transition to the engulfment flow regime was related to the identification number of 100) could be attributed to the fact that the present study does not use t-type micromixers but is instead a study of a planar stagnation flow microreactor.

Considering that instabilities were only found to exist at high Reynolds number flows in the shallow-etched reactor which was to be used for the reactive hypersonic studies, care was taken to conduct the experiments in the regime where the transition to the chaotic regime did not take place.

## 7. Drop Test Results

All drop tests were conducted with the Phantom camera set at 2000 fps and with 80  $\mu$ L of the oxidizer placed at the bottom of the cuvette. Given that the inner dimensions of the cuvette were 9mm x 9mm, this provided for a depth of about 1mm of the oxidizer in the cuvette. Owing to surface tension of the oxidizer, the depth of the oxidizer pool in the cuvette varied across the width of the cuvette. The meniscus of the pool was noticed to be higher at the walls of the glass cuvette than at the centre of the cuvette. The time notation used for all the tests is such that  $t = 0$ s indicates the time at which the fuel droplet just makes contact with the oxidizer pool in the cuvette. Five tests were conducted for each fuel and oxidizer combination and the results presented below are the typical results from any one test. TMEDA was found to be the most reactive of the fuels when WFNA was the oxidizer. The interaction of TMEDA with WFNA was violent and ignition occurred within 14 ms. The second most reactive fuel was triethylamine with ignition occurring with a delay 45ms from first contact. This was followed with DMAZ where the ignition delay was 99ms. The two hydrocarbons, dicyclopentadiene and indene, failed to ignite during the drop test but a vigorous reaction was noticed for both when the fuel droplet interacted with the oxidizer pool. For dicyclopentadiene this occurred within 65 ms of contact while for indene it occurred much later at 300ms from the time of first contact.

## 8. Micro-reactor Test Results

Studies with the stagnation flow microreactor have proven that the flow in the reactor is laminar and thus well-defined when there are non-reactive fluids flowing in the reactor and even with reactive fluids forming an interface in the main channel. The interface between the reacting was found to be stable and thus the micro-reactors have been shown to be feasible for use to study these fast liquid-liquid reactions [40]. All experimental runs in the micro-reactor were made with the oxidizer being diluted with distilled water. The diluting of the oxidizer helped in reducing the

available nitric acid in the system and thus made sure that the exothermic reactions inside the micro-reactor could be properly controlled. This is of particular importance as the reaction between most hypergols is extremely exothermic and almost instantaneous with the production of large amount of gases and salts. The dilution of the oxidizer thus helped in isolation of the early condensed phase reactions in the system. Moreover the dilution helped in studying a range of conditions within the reactor. Most of the micro-reactors were tested using flow rates such that the Reynolds number of the flow in the channels ranged between 7 and 196. These flow rates yielded a residence time ranging between 0.76ms and 27us per channel width.

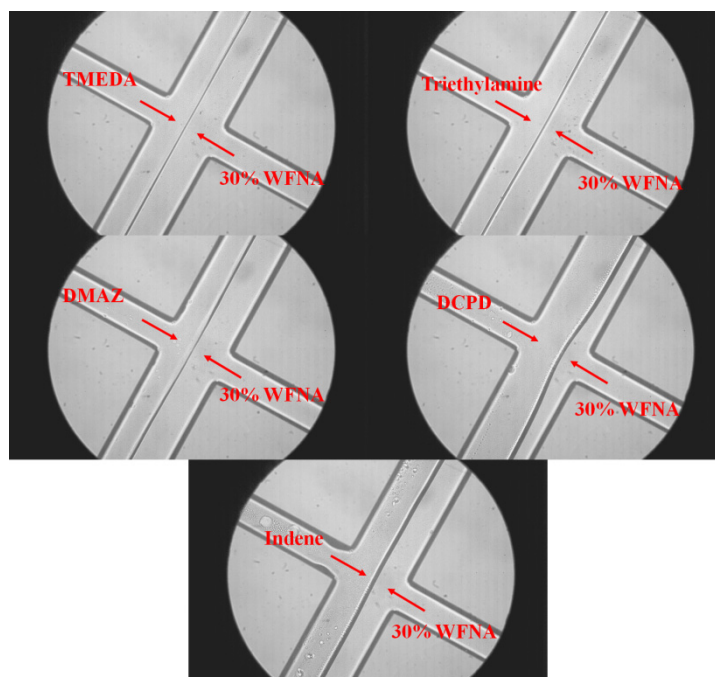


Figure 13. Still frames from reactive flow in micro-reactor using the various fuels with 30% WFNA. All flow rates for the reactants are at 500 uL/min and the images were captured at 1000 fps.

Figure 13 shows still images from high-speed videos of reacting flows between the various fuels and 30% WFNA. All images were taken at 1000 fps with the flow rate of all reactants being 500  $\mu\text{L}/\text{min}$ . As can be seen from the images the reaction fronts are very stable with very few perturbations even with a reaction occurring at the interfaces and a laminar flow was achieved using all the fuel and oxidizer combinations. It can be theorized that due to the reaction being diffusion controlled and very little mixing taking place in the reactor, the system will always remain a liquid-liquid interaction and the reaction zone can be properly controlled to study the interactions in the condensed phase as well as the impact of diffusion on the reactions. It should be noted from the high speed images of the reaction front that the reaction diffusion zone is extremely thin for the TMEDA – nitric acid case but grows to become thicker when indene and WFNA were used in the micro-reactor.

### 8.1 TMEDA with Nitric Acid Micro-Reactor Experiment

Care was taken while running TMEDA along with nitric acid in the micro-reactors as the reaction between the two is extremely exothermic and also instantaneous. As one of the first heat



releasing reactions between the two is a salt formation reaction [21], to isolate the early condensed phase reactions, the micro-reactors were run at very low concentrations of the oxidizer. Exit temperatures were measured using the fine wire thermocouples attached to the stainless steel manifold for a variety of flow rates and oxidizer concentrations. Figure 14 shows the change in exit temperatures with changing flow rates of the reactants as well as changes in oxidizer concentration.

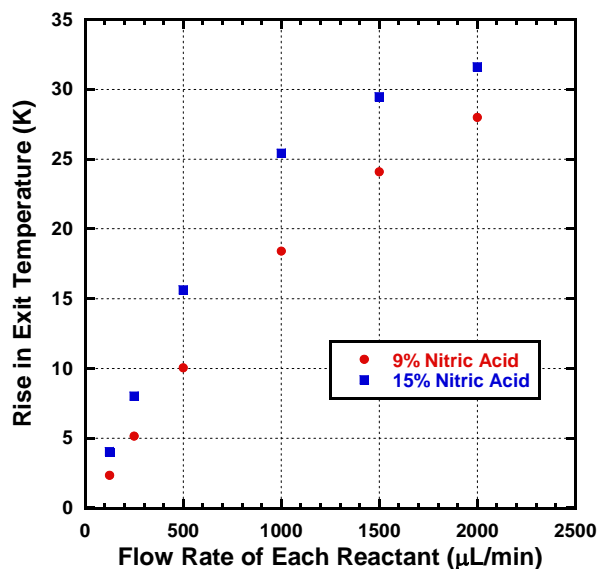


Figure 14. Change in exit temperatures for TMEDA and Nitric Acid in the micro-reactors with increasing flow rates of reactants.

As can be seen from the plotted graph, a rise in exit temperature is observed even at very low concentrations of the oxidizer. This can be expected due to the highly exothermic nature of the TMEDA – nitric acid reaction. This rise in exit temperature of the fluids was noticed to increase with an increase in concentration of the oxidizer. The diluting of the oxidizer concentration, which resulted in a drop in the temperature of the products at the exit is because of the lowering in the reaction rates between the reactants that are able to diffuse across the interface and thus cause a reaction to occur. With the dilution of nitric acid, there are lesser reaction-causing nitric acid molecules that are available to diffuse across the interface to interact with the TMEDA molecules. Thus it is natural that the amount of reaction occurring between diluted nitric acid mixtures and TMEDA is far lesser than the reaction that occurs with undiluted nitric acid and TMEDA. When more reactants are available to diffuse across the interface, the reactions that occur see an increase and the temperature of the products at the exit rises accordingly. Also seen in the temperature plot (Figure 14), is that rise in exit temperatures is also seen to increase with an increase in flow rates of the reactants into the microreactor. Care was taken to limit the flow rate of each of the reagents into the microreactor to 2000  $\mu\text{L}/\text{min}$  so as to ensure that the flow-field in the reactor did not transition into an unstable regime.

It should also be noted that the experimental runs for TMEDA and nitric acid using the micro-reactor were only possible at very low concentrations of the oxidizer. At lower concentrations the salt produced by the reaction between TMEDA and nitric acid was low and stayed in solution without precipitating out. At higher concentrations of the oxidizer, there was a large amount of salt precipitation that occurred in the main channel of the reactor and the system no longer remained a simple condensed phase laminar flow one and gave way to a transient multi-phase



system. Given that the early condensed phase chemistry could no longer be isolated in the micro-reactors with high concentrations of the oxidizer, care was taken to always maintain a low concentration of nitric acid while running it along with TMEDA in the micro-reactor.

## 8.2 DMAZ with Nitric Acid Micro-Reactor Experiment

With the setup and the environmental conditions being the same as that used for the TMEDA-NA experiments, the experiments for DMAZ with nitric acid were started with a similar concentration of nitric acid. In this case as well it was noticed that the rise temperature observed at the exits increased with an increase in flow rates of the reactants (Figure 15). An interesting point to note when comparing to the TMEDA – nitric acid system is that the rise in exit temperatures for similar concentrations of the oxidizer and the flow rates are much higher for TMEDA than they are for DMAZ. Also when the flow rates were continued to increase the rise in exit temperatures eventually reached a peak value and any further increase in the flow rates of the reactants caused a drop in the exit temperatures. This peak was usually around 750  $\mu\text{L}/\text{min}$  for the DMAZ – nitric acid system and was consistent across multiple runs as well as when the concentration of the nitric acid was changed.

Also as in the case of the TMEDA – nitric acid system, the rise in temperature increased when the concentration of the oxidizer was increased. As there was no problem with salt formation when DMAZ was flowed in the micro-reactor with the nitric acid, thus higher concentrations of the oxidizer could be tested with DMAZ. An interesting point to note when comparing to the TMEDA – nitric acid system is that the rise in exit temperatures for similar concentrations of the oxidizer and the flow rates are much higher for TMEDA than they are for DMAZ. Also, the peak temperatures for the TMEDA – nitric acid system occur at a much higher flow rate ( $\sim 2500$   $\mu\text{L}/\text{min}$ ) than they do in the case of when DMAZ and nitric acid are used in the system ( $\sim 750$   $\mu\text{L}/\text{min}$ ).

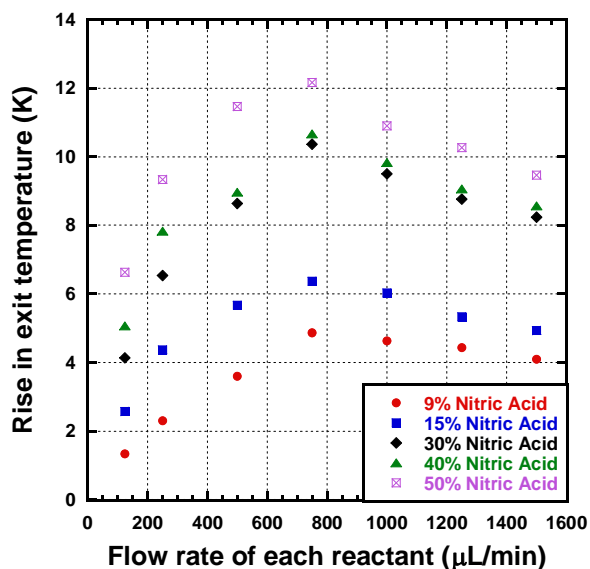


Figure 15. Change in exit temperatures for DMAZ and Nitric Acid in the micro-reactors with increasing flow rates of reactants.

### 8.3 Triethylamine with White Fuming Nitric Acid Micro-Reactor Experiment

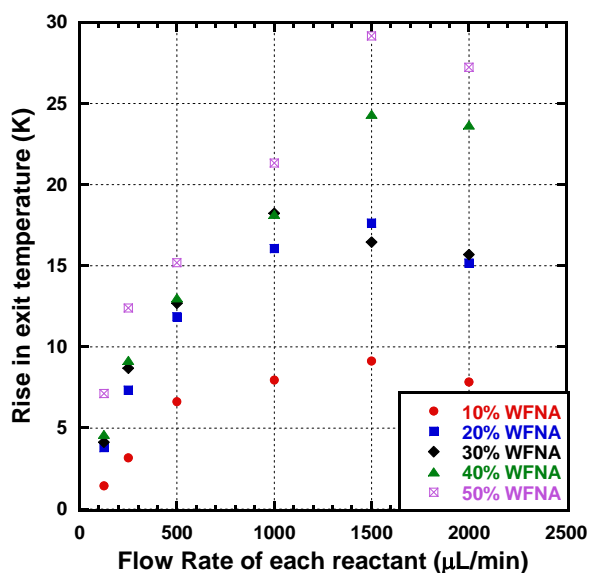


Figure 16. Change in exit temperatures for Triethylamine and White Fuming Nitric Acid in the micro-reactors with increasing flow rates of reactants.

As shown in the fuel drop-tests, triethylamine was able to undergo vigorous reaction with the WFNA and actually was able to achieve ignition. This ignition delay, though longer than the TMEDA – WFNA combination, was shorter than the ignition delay of the DMAZ – WFNA combination. To test the triethylamine in the microreactor it was reacted with WFNA to create an system of hypergols similar to the one studied by Schala et al. [25]. Similar to the runs made with TMEDA and DMAZ, with triethylamine too, an exothermic reaction was observed with a very low concentration of the oxidizer (10%). Much like earlier, the rise in exit temperatures rose with an increase in flow rates as well as oxidizer concentrations (Figure 16). Interestingly, the amount of heat release observed via the measurement of the exit temperatures showed that the reaction between triethylamine and WFNA was less exothermic than the liquid-liquid reaction between TMEDA and nitric acid but was more than the one observed between DMAZ and nitric acid.

In the case of the triethylamine – WFNA system a peak in exit temperature similar to the one observed in the DMAZ – nitric acid system was observed when the flow rates of the reactants were increases. The flow rate at which this peak in rise of exit temperatures was observed (1500 μL/min) was higher than the flow rate at which the peak was observed in the DMAZ – nitric acid system (750 μL/min). Once again, the flow rates of the reactants into the microreactor were limited to a value of 2000 μL/min to ensure stable laminar flow in the microreactor with no transition to a chaotic flow regime.

### 8.4 Dicyclopentadiene with White Fuming Nitric Acid Micro-Reactor Experiment

Drop tests earlier in this study showed that the reaction between dicyclopentaidene with WFNA was quite slow when compared to fuels like TMEDA and triethylamine and ignition was achieved in only one of the drop tests. When the fuel was ran through the micro-reactor with WFNA the heat release measured using the thermocouples at the exit of the micro-reactor showed very low temperature rise when compared to the other fuels, with almost no noticeable rise in temperature at low concentrations of the oxidizer. Even when the flow rates of the

reactants into the micro-reactor were increased, the rise in temperatures at the exit remained small. Though the rise in exit temperatures was very low when compared to the earlier fuels, the trends in temperature with a change in flow rate were very similar. Also the peak value in the temperature vs. flow rate plot (Figure 17) was noticed to be at a much lower value even when compared to the DMAZ – nitric acid combination. In this case the peak was consistently noticed to be at a flow rate of around 500  $\mu\text{L}/\text{min}$ .

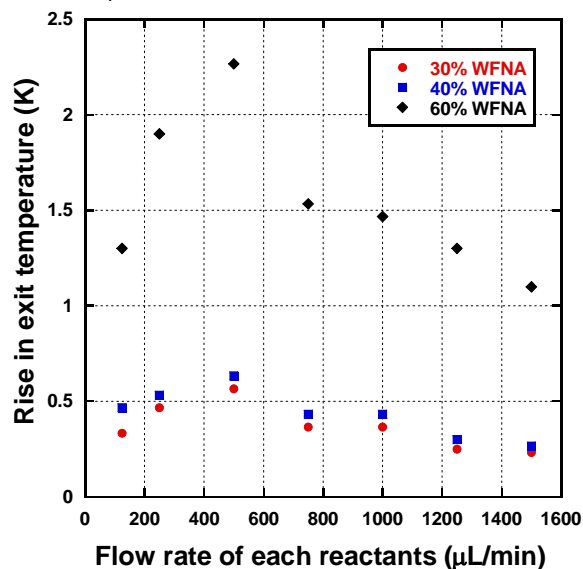


Figure 17. Change in exit temperatures for Dicyclopentadiene and White Fuming Nitric Acid in the micro-reactors with increasing flow rates of reactants.

### 8.5 Indene with White Fuming Nitric Acid Micro-Reactor Experiment

Indene was the final fuel used along with WFNA as the oxidizer in the micro-reactor. Although the temperature trends were similar as to that seen for the other fuels, the rise in exit temperatures were very low with the rise being almost negligible for an oxidizer concentration less than 40% WFNA (Figure 18). The peak temperatures as well as the flow rates at which these peaks occurred were lesser than even those observed for the dicyclopentadiene – WFNA combination and occurred at a flow rate of around 400  $\mu\text{L}/\text{min}$ . The reaction between indene and WFNA produces a viscous, sticky black substance as can be seen from the drop tests, thus it was not possible to run the micro-reactor with very high concentrations of WFNA as it was noticed that the sticky substance ended up clogging either the ports in the manifold or the main channel of the micro-reactor itself. This residue, much like the salt produced by the TMEDA – nitric acid reaction, was tough to remove from the reactor and made it impossible to maintain a purely laminar flow in the reactor. Thus the tests for indene were run at a maximum oxidizer concentration of 60% WFNA to avoid issues of clogging the micro-reactor.

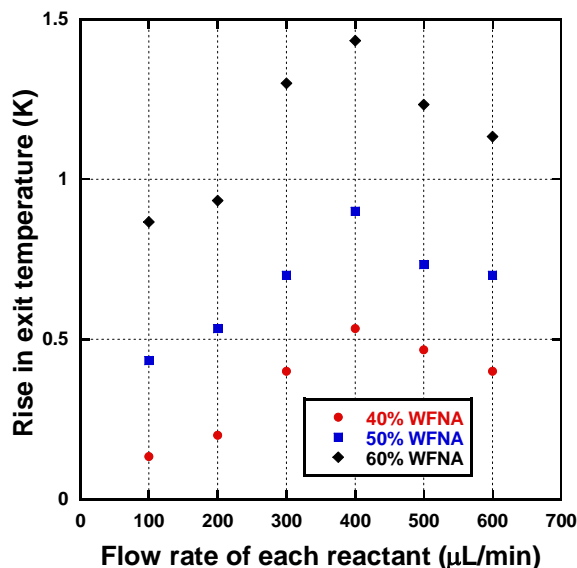


Figure 18. Change in exit temperatures for Indene and White Fuming Nitric Acid in the micro-reactors with increasing flow rates of reactants.

### 8.6 TMEDA-DMAZ mixtures with Nitric Acid Micro-Reactor Experiment

In a recent study, Stevenson [18] found that mixtures of hypergolic fuels sometimes perform better than the individual fuels themselves in drop and rocket tests. In particular the study concentrated on mixing hypergolic tertiary diamines (like TMEDA) with hypergolic amine azides (like DMAZ). In drop tests with inhibited red fuming nitric acid (IRFNA) TMEDA had an ignition delay of 14ms while DMAZ on itself had an ignition delay of over 26 ms. But when the two fuels were mixed in various proportions the ignition delay seemed to change and in certain cases the ignition delay was found to be lesser than even the ignition delay for pure TMEDA with IRFNA. The results from the study have been re-plotted in Figure 19. As can be seen from the plot the minimum ignition delay (9ms) was noticed for a mixture in which there was 66.6% TMEDA and 33.3% DMAZ.

A hypothesis proposed by the study was that the ignition delay times were dependent both on the heat released by the hypergolic reaction as well as the ignition temperature of the reactants. The reaction between the tertiary diamine and nitric acid provided a larger heat release than the reaction between the amine azide and nitric acid owing to the higher amine content in the diamine (and thus higher basicity). But the ignition temperature of the amine azide was noticed to be much lower than that of the much heavier tertiary diamine. A combination of the two fuels thus provided for a mixture which provided for a large heat release as well as for a lower ignition temperature thus making the ignition delays much shorter in the case of mixtures. It was also noticed that the mixtures of TMEDA and DMAZ burned in a much cleaner manner, leaving lesser residues behind, with IRFNA than when pure TMEDA was used. An improvement in ignition delay times as well as having lower residues while burning makes the mixtures of TMEDA and DMAZ an attractive replacement for the more toxic MMH.

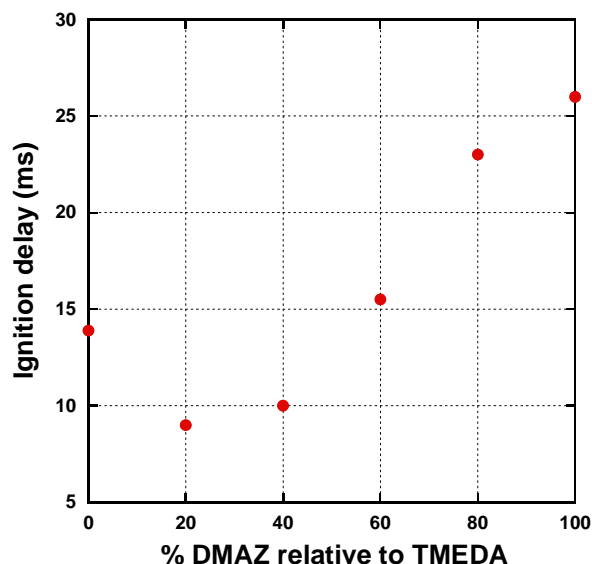


Figure 19. Ignition delay results from drop-tests carried out by Stevenson using mixtures of TMEDA and DMAZ as the fuel and Nitric Acid as the oxidizer [18].

Mixtures of TMEDA and DMAZ were then created to be tested in the micro-reactor along with diluted nitric acid. For the tests using these fuel mixtures the concentration of nitric acid was kept at 30% and the tests were run at two flow rates of 250  $\mu\text{L}/\text{min}$  and 500  $\mu\text{L}/\text{min}$ . The heat released from the reaction between these fuel mixtures and the nitric acid was again related to the rise in temperature at the exit of the micro-reactor. Temperature trends from these tests (Figure 14) seemed to be similar to the trends noticed in the drop tests by Stevenson and were consistent even with a change in flow rate. In that, a maximum heat release was actually seen for a mixture of TMEDA and DMAZ rather than for pure TMEDA. Moreover the maximum heat release was noticed for a mixture of 60% TMEDA and 40% DMAZ mirroring very closely the drop tests results in the study by Stevenson. The significance of having a higher heat release in the case of mixtures of TMEDA and DMAZ rather than for one of the fuels separately is that rather than just having TMEDA-NA provide the high heat release and DMAZ provide for the lowering of the ignition temperature, as suggested by Stevenson in his study, the current results indicate that there is a new mechanism present wherein all three reactants, namely TMEDA, DMAZ and nitric acid, react together via new pathways which provide for a higher heat release and thus a shorter ignition delay time. Another reason for the similar trends found between the drop test and the micro-reactor experiments for the TMEDA-DMAZ blends could be that the reactions that occur in the liquid phase between the hypergols are very similar to the reactions that occur later on in the gas phase. Thus, the liquid phase reaction will affect the later occurring reactions and will have a large role to play in the ignition of the hypergols. The relative importance of the liquid phase reactions in the reaction between blends of TMEDA and DMAZ with nitric acid has also been shown in a recent study [41] which conducted ignition drop tests at elevated pressures. The study found very little variation in ignition delay times of the TMEDA-DMAZ blend when reacted with nitric acid, leading to the conclusion that the ignition was controlled by the early liquid phase reactions whose rates do not depend on the applied pressure.

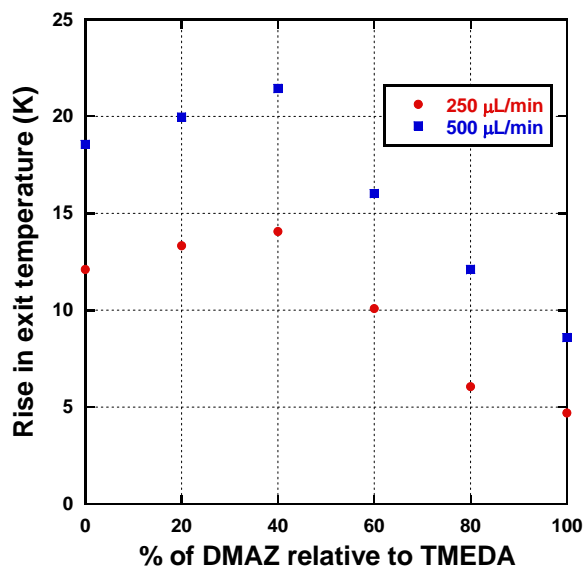


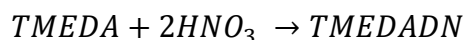
Figure 14. Change in exit temperatures for TMEDA-DMAZ mixtures and 30% Nitric Acid in the micro-reactors with increasing flow rates of reactants.

## 9. Numerical Simulations

The stagnation flow microreactors used to study the fast condensed phase reactions occurring between hypergols can be compared to an opposed-flow or counter-flow diffusion flame system. Like in the counter-flow diffusion flame the reactions at the interface of the liquids in the microreactor are dependent both on the diffusion of the reagents across the interface as well as the reaction rate of the reactions in the chemical mechanism.

The reactive flow in the stagnation-flow microreactor was analyzed with liquid flows using the same set of governing equations as described in the previous section. The governing equations for the counter-flow diffusion flame were solved using a FORTRAN code developed by the Sandia National Laboratories – Oppdif [42]. The original code for the numerical simulations of a counter-flow diffusion flame was written for gas-phase chemistry and thus uses the ideal gas law to calculate mass density values. As the flow in the microreactor is in the liquid phase, the fluids are incompressible in nature and all the mass density values were set to be constant in the governing equations.

The numerical simulations were performed for a variety of inlet flow rates for the TMEDA – nitric acid system. The concentration of the nitric acid was kept at 20% by diluting the oxidizer inlet with liquid water (similar to the experiments carried out with the microreactor). The inlet temperature for both the fuel and oxidizer was kept at 300 K. A single step reaction suggested by Wang et al. [21] was used as the reaction mechanism for the system with the heat of the reaction being - 45 Kcal/mol as suggested by Liu et al. [43]. This mechanism involves the reaction of one molecule of TMEDA with two molecules of nitric acid to form a di-nitrate salt (TMEDADN) along with the evolution of heat:



No activation energy was used for the one-step reaction and thus the reaction was assumed to be temperature independent. The rate of the reaction for the single step in the reaction mechanism was varied so as to provide information on the effect of reaction rates on the temperature

profiles. Viscosity, thermal conductivity and mass diffusivity values for each of the fluids are required for the numerical simulation of the reactive flow. As the binary molecular diffusion coefficients (mass diffusivities) for the various chemical species were not known, the values for the numerical simulations were estimated using the Wilke-Chang estimation [44]. The estimation can be expressed as:

$$D = 7.4 \times 10^{-8} \frac{(xM)^{1/2} \cdot T}{\eta V^{0.6}}$$

where,  $D$  is the binary molecular diffusion coefficient,  $x$  is the association parameter which is 2.6 for water and 1 for non-associated solvents,  $M$  is the molecular weight of the solvent,  $T$  is the temperature,  $\eta$  is the viscosity of the solvent and  $V$  is the molal volume of the solute at the boiling point.

Heat transfer plays a critical role in microfluidic devices. As heat transfer coefficients are inversely proportional to the hydraulic diameter of a channel, thus the small dimensions of a microfluidic device will imply a large increase in heat transfer coefficients. Heat transfer on the micron-scale has been extensively studied over the past two decades and behavior of heat and mass transfer in the fluid on the micron-scale has been compared to the behavior observed on the macro-scale. Different experimental studies have shown widely disparate results, with some studies showing heat transfer coefficients that have been far lower [45], [46] or far greater [47] than those observed for macro-scale flow. More recent studies [48], [49], on the other hand, have suggested that heat transfer behavior on the micro-scale is similar to that seen in macro-scale setups and the same set of correlations as used for conventional channels, can be used for microchannel. It is believed that errors in measurements led to the previously held discrepancies in heat transfer at the micron-scale and in actuality, the heat transfer behavior at the small scale was not very different from conventional channels [48].

To approximate the heat transfer coefficients in the present microreactor, conventional relationships developed for the macro-scale flow are used. The Nusselt number, a dimensionless quantity, is often used to compare the convective and conductive heat transfer processes. The Nusselt number can be defined as:

$$\text{Nusselt Number} = Nu = \frac{\text{Convective Heat Transfer}}{\text{Conductive Heat Transfer}} = \frac{h \cdot L}{K_f}$$

where,  $h$  is the convective heat transfer coefficient of the fluid,  $L$  is the characteristic length of the channel and  $K_f$  is the thermal conductivity of the fluid. If a fully developed flow is assumed to occur in the microchannel with constant wall temperature, then for a rectangular cross-section with aspect ratio of 1:4 (height : width), the Nusselt number has a value of 4.44 [50]. The hydraulic diameter of a channel can be considered as the characteristic length for a channel with a rectangular cross-section. For the microreactor used in the reactive flow studies the hydraulic diameter can be approximated to be 100  $\mu\text{m}$ . The thermal conductivity of the fluids can be approximated as 0.5 W/m-K and thus the convective heat transfer coefficient for the microreactor can be approximated to be 22,200 W/m<sup>2</sup>-K. This high convective heat transfer coefficient (when compared to values in macro-scale flow where the coefficient usually scales on the order of 100) is due to the small length scales of the fluid flow in the microchannel. Due to such high values of heat transfer that are possible from a microfluidic device, there is a need for the heat loss from the microreactor to be accounted for.

The original code for the reactive flow simulation of the microreactor ignores heat loss from the top and bottom areas of the stagnation zone. A method for accounting for the heat loss from the reaction zone is to introduce a heat loss term in the energy equation. The energy equation for  $K$  species interacting at the reaction zone can be expressed as:

$$2U \frac{dT}{dx} - \frac{1}{c_p} \frac{d}{dx} \left( \lambda \frac{dT}{dx} \right) + \frac{\rho}{c_p} \sum_{k=1}^K Y_k c_{pk} V_k \frac{dT}{dx} + \frac{1}{c_p} \sum_{k=1}^K h_k \dot{\omega}_k = 0$$

where,  $c_p$  is the specific heat,  $h_k$  are the molar enthalpies,  $\dot{\omega}_k$  are the chemical production rates of the species due to reaction,  $W_k$  are the molecular weights of the species,  $\mu$  is the viscosity while  $\lambda$  is the thermal conductivity. Thus each individual term in the energy equation can be defined as follows :  $2U c_p \frac{dT}{dx}$  is the term that causes the convection of heat due to fluid flow,  $\frac{d}{dx} \left( \lambda \frac{dT}{dx} \right)$  is the term that is responsible for the heat transfer through the fluid due to conduction,  $\rho \sum_{k=1}^K Y_k c_{pk} V_k \frac{dT}{dx}$  represents the heat transfer due to the mass diffusion of species and  $\sum_{k=1}^K h_k \dot{\omega}_k$  signifies the energy transfer due to the production or destruction of species due to the reaction. The heat loss term can be added to this energy equation and can be coupled with the diffusion of the temperature profile along the width of the stagnation zone, thus making akin to a heat loss mechanism from the top and bottom of the reaction zone. The addition of a constant heat loss (coupled with the temperature diffusion profile) through the top and bottom of the reaction zone thus makes the simulation more physically realistic.

The numerical simulations of the reactive flow in the microreactors were run for the various reaction rates as well as for various inlet flow velocities. For each reaction rate a heat loss rate was added to the governing energy equation. This heat loss term had a constant heat loss coefficient multiplied by the change in temperature profile along the stagnation centerline. To establish the initial effects of the heat loss process on the temperatures observed in the stagnation zone, this constant heat loss coefficient was assumed to be a set percentage of the maximum heat produced by the reaction at an inlet flow velocity of 0.1 cm/s. The percentage that was used as the heat loss coefficient was varied to see what effect the heat loss mechanism introduced in the energy equation had on the temperature trends.



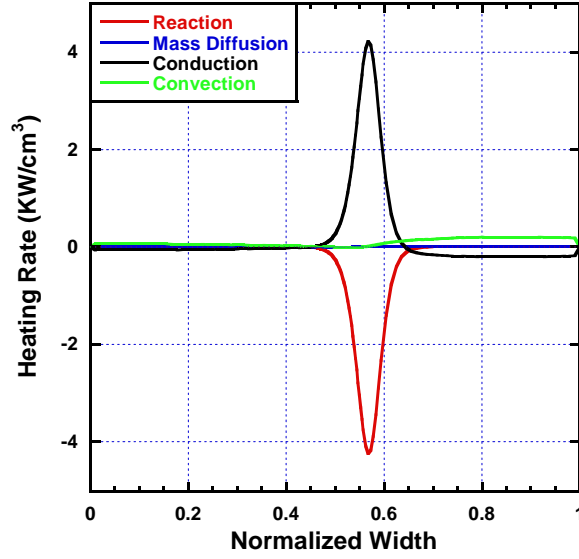


Figure 15. Heating rate along the stagnation centerline. Inlet velocity for both fuel and oxidizer is 0.1 cm/s while the reaction rate constant =  $2 \times 10^7 \text{ L}^2 \cdot \text{mol}^{-2} \cdot \text{s}^{-1}$ .

The simulations were first run with a reaction rate constant of at  $2 \times 10^7 \text{ L}^2 \cdot \text{mol}^{-2} \cdot \text{s}^{-1}$  with no heat loss term added to the energy equation. As can be seen from Figure 15, the maximum value of the heating rate due to the reaction is approximately 5 kW/cm<sup>3</sup>. The heat loss coefficient ( $\dot{q}_l$ ) was first assumed to be 20% of the maximum heating rate due to the reaction and was thus approximated to be 1 kW/cm<sup>3</sup>-K. The heat loss coefficient was then coupled to the temperature profile along the stagnation centerline so to give the heat loss term used in the energy equation. This heat loss term can be represented as:

$$\text{Heat Loss Term} = \dot{q}_l [T(x) - T_o]$$

where,  $T(x)$  provides the temperature at each point along the stagnation centerline while  $T_o$  is the temperature of the incoming fuel and oxidizer streams.

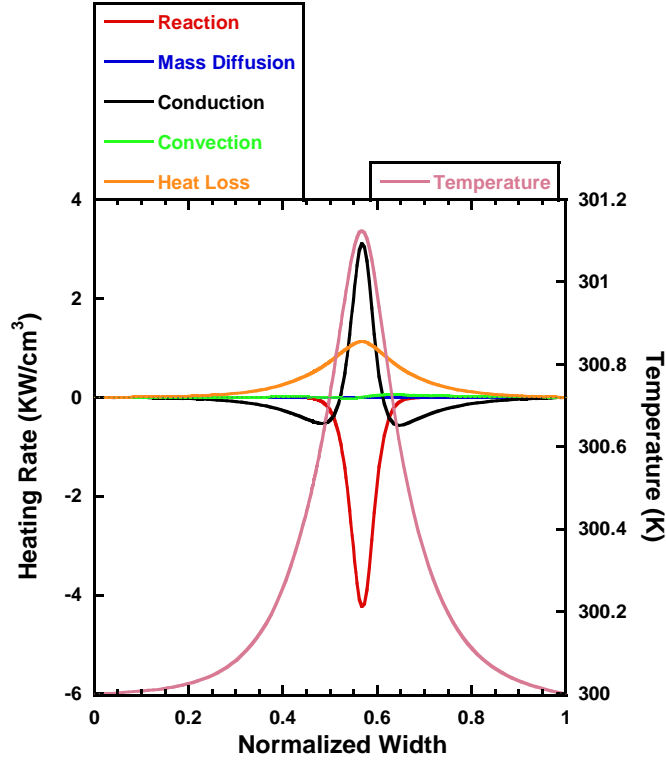


Figure 16. Heating rate and temperature profile along the stagnation centerline. Inlet velocity for both fuel and oxidizer is 0.1 cm/s while the reaction rate constant =  $2 \times 10^7 \text{ L}^2 \cdot \text{mol}^{-2} \cdot \text{s}^{-1}$ .  $\dot{q}_l = 1 \text{ kW/cm}^3 \cdot \text{K}$ .

Figure 16 shows the profiles for the various terms in the energy equation as well as the temperature profiles along the stagnation centerline in the case of an added heat loss term into the energy equation ( $\dot{q}_l = 1 \text{ kW/cm}^3 \cdot \text{K}$ ). Also from the plot, the profile of the heat loss term in the energy equation can be seen to scale similarly to the profile of the temperature along the stagnation centerline. Given that the magnitude of  $\dot{q}_l$  was chosen to represent 20% of the maximum value of the heating rate produced by the reaction, the heat loss term has a significant role to play at an inlet flow velocity of 0.1 cm/s.

Again, at the reaction zone, the energy change due to conduction through the liquid (in addition to the heat loss term) is balanced by the heat generated due to the reaction at the interface between the reagents. Very little effect of either convection of the heat due the fluid flow or energy change due to the mass diffusion of the species is observed in the simulation result. This is because at such low inlet velocities, the major changes in the energy equation are not affected by the convective forces of the fluid flow but rather by the reaction at the interface of the reagents.

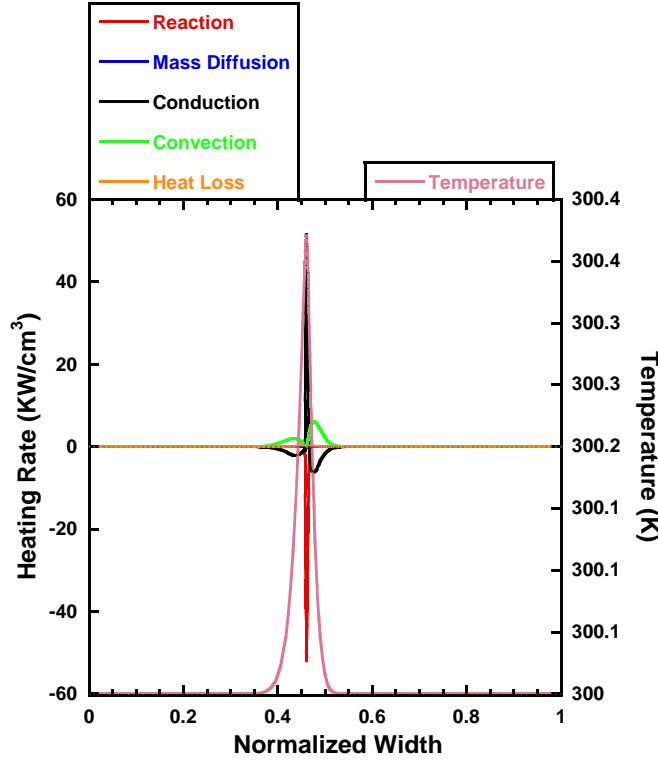


Figure 17. Heating rate and temperature profile along the stagnation centerline. Inlet velocity for both fuel and oxidizer is 50 cm/s while the reaction rate constant =  $2 \times 10^7 \text{ L}^2 \cdot \text{mol}^{-2} \cdot \text{s}^{-1}$ .  $\dot{q}_l = 1 \text{ kW/cm}^3 \cdot \text{K}$ .

With an increase in inlet velocities, it is expected that the heat loss term in the energy equation will have lesser and lesser effect on the energy equation. This is because the heat loss term has been assumed to have a constant heat loss coefficient ( $\dot{q}_l$ ) which will not change with flow rates of the reagents unlike the other terms in the energy equation which are seen to increase with an increase in flow velocities. This effect is very pronounced when the inlet velocities are raised to a large value (when compared to a flow velocity of 0.1 cm/s). Figure 17 provides the profiles for a case where the inlet velocities are 50 cm/s. Here the heat loss term is seen to be almost negligibly small when compared to the heating rates due to the reaction and the conduction through the fluid.

The fact that the heat loss will have a large effect at a low inlet velocity while the effect of the heat loss term will become negligible at higher velocities means that it can be expected that there will be a rise in temperature when the inlet flow velocities are increased. This is seen in the plot shown in 24. In the figure, the maximum temperature observed in the stagnation zone for each flow rate is plotted against the inlet flow velocities. Results in the plotted figure are for when there is no added heat loss term, for when the heat loss coefficient ( $\dot{q}_l$ ) is  $1 \text{ kW/cm}^3 \cdot \text{K}$  and also for a case in which the value of the heat loss coefficient ( $\dot{q}_l$ ) was increased to  $2.5 \text{ kW/cm}^3 \cdot \text{K}$ .

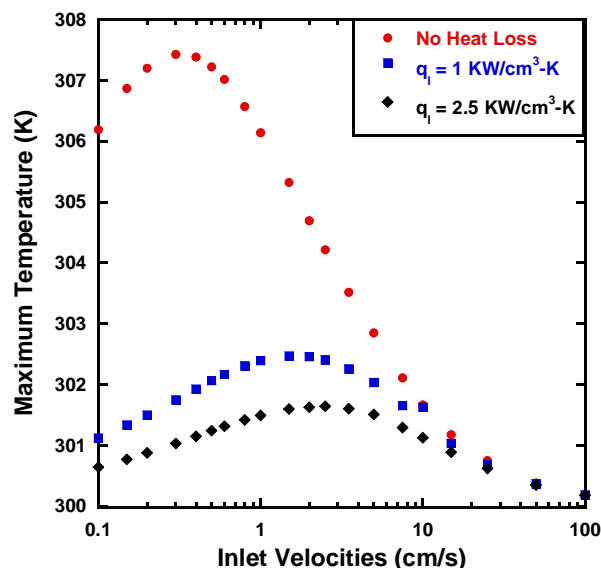


Figure 18. Maximum temperature profile at the stagnation zone from numerical simulations of flow in the microreactor with reaction rate constant  $K = 2 \times 10^7 \text{ L}^2 \cdot \text{mol}^{-2} \cdot \text{s}^{-1}$ . In addition to the temperature trends from the original simulation, temperature trends with the added heat loss term in the energy equation are also shown.

With the addition of the heat loss term in the energy equation, the peak in the temperature in the stagnation zone now occurs at a higher inlet flow velocity (1.5 cm/s) of the reagents than when there was no heat loss term in the equation (0.3 cm/s). In fact, when the heat loss coefficient is increased from  $1 \text{ kW/cm}^3\text{-K}$  to  $2.5 \text{ kW/cm}^3\text{-K}$ , the peak in temperatures occurs at an even higher inlet flow velocity (2.5 cm/s). Thus with the addition of heat loss terms in the energy equations, the rise of the temperatures with an increase in flow velocities could be easily affected. But because of the addition of the heat loss terms, there was an obvious reduction in the magnitude of the temperatures observed in the stagnation zone of the microreactor.

The reaction rate constant was then increased to a value of  $2 \times 10^9 \text{ L}^2 \cdot \text{mol}^{-2} \cdot \text{s}^{-1}$ , to observe the impact on the temperature profiles in the stagnation zone and to see if the inlet velocity at which the peak in temperatures occurred could be raised further from 2.5 cm/s. For this reaction rate, the maximum heating rate due to the reaction at an inlet velocity of 0.1 cm/s could be approximated as  $25 \text{ kW/cm}^3$ . Thus the value of the heat loss coefficients for the simulations with a reaction rate of  $2 \times 10^9 \text{ L}^2 \cdot \text{mol}^{-2} \cdot \text{s}^{-1}$  were chosen to be  $5 \text{ kW/cm}^3\text{-K}$  and  $12.5 \text{ kW/cm}^3\text{-K}$  (again, 20% and 50% of the maximum heating rate due to reaction). For these simulations as well, the heat loss term had a large effect at the low velocities but had lesser of an effect when the inlet velocities of the fuel and oxidizer stream were increased.

Figure 25 shows the maximum temperatures in the stagnation zone of the microreactor from numerical simulations run at a reaction rate constant of  $2 \times 10^9 \text{ L}^2 \cdot \text{mol}^{-2} \cdot \text{s}^{-1}$ . Along with the temperatures for the case in which there was no heat loss term added to the energy equation, temperature trends are also shown for heat loss coefficients equaling  $5 \text{ kW/cm}^3\text{-K}$  and  $12.5 \text{ kW/cm}^3\text{-K}$ . The added heat loss term reduces the overall temperature of the fluids in the microreactor (as now energy that was earlier used to heat the fluids is now lost) but also aids in shifting the peak in temperatures to a higher inlet velocity. For a heat loss coefficient of  $5 \text{ kW/cm}^3\text{-K}$  the temperatures peaked at a flow rate of 25 cm/s which was a large change from the

inlet velocity where the peak happened (0.6 cm/s) when no heat loss term was used in the energy equation. Again, just like in the case with the reaction rate constant being  $2 \times 10^7 \text{ L}^2 \cdot \text{mol}^{-2} \cdot \text{s}^{-1}$ , a higher heat loss coefficient helped in the temperature peaking at an even higher inlet flow velocity. For a heat loss coefficient of  $12.5 \text{ kW/cm}^3 \cdot \text{K}$ , the temperatures are seen to peak at a flow velocity of 50 cm/s.

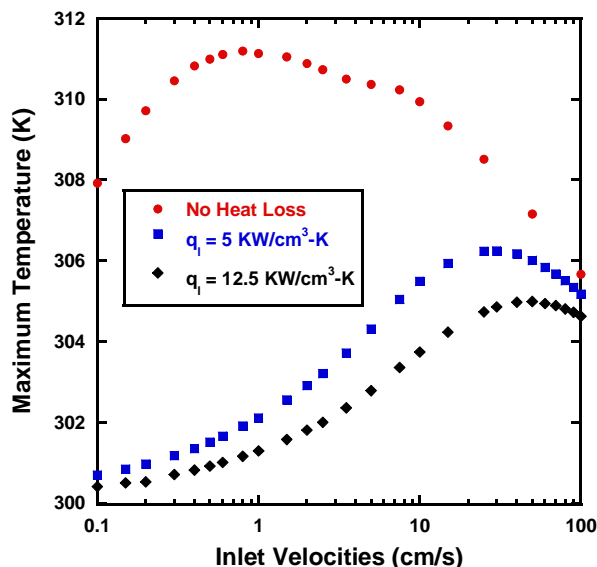


Figure 25. Maximum temperature profile at the stagnation zone from numerical simulations of flow in the microreactor with reaction rate constant  $K = 2 \times 10^9 \text{ L}^2 \cdot \text{mol}^{-2} \cdot \text{s}^{-1}$ . In addition to the temperature trends from the original simulation, temperature trends with the added heat loss term in the energy equation are also shown.

## 10. Discussion

As all the experimental runs using the micro-reactors were conducted by diluting the oxidizer, the tests were able to isolate the early condensed phase reactions from the fast gas phase reactions that occur later on. The goal of the study has been to relate these reactions to the overall transient process that leads to ignition. Amongst other factors, ignition is largely dependent on the heat released by the reaction between the two hypergols as well as how quickly this heat is released. Thus if a pair of hypergols can release a large amount of heat in a quick enough time, the ignition delay for this pair would be expected to be the least. The micro-reactors clearly show a trend in the amount of heat released by the early liquid phase reactions. And most noticeably the fuels with the higher heat release (TMEDA and triethylamine) showed by a larger temperature rise at the exit of the micro-reactor, result in the combination having the lowest ignition delay times amongst the group of fuels tested. This was also closely seen in the case of mixing DMAZ and TMEDA to form a blend which showed the highest heat release when the composition of the blend was similar to the one which had the shortest ignition delay times. The peak in the exit temperature trends occurs when the reaction shifts from a diffusion controlled or heat loss controlled regime to one that is kinetically controlled. In the diffusion controlled regime the reaction does not depend on the residence time of the reactants in the micro-reactor and instead depends on the diffusion of the reactants at the interface as the reaction occurs very quickly. In the kinetically controlled regime, on the other hand, the reaction with the reactor depends on the residence time of the reactants as the flow is now much faster and the reactants do not get enough time to react. Thus with an increase in flow rate, when in the

kinetically controlled regime, the exit temperatures of the reactants drop. It can now be correlated that if the flow rate at which the peak temperatures occur, are at a high flow rate then the reaction times between the reactants are much smaller.

Thus the hypergol pair which shows the peak at higher flow rates (like TMEDA) than a pair which has the peak at a lower flow rate (like indene), will have a faster reaction occurring at the interface. This difference in condensed phase reaction rates can also be seen from the images of the reactions between the various fuels and WFNA in the micro reactor (Figure 13). The reaction interface between TMEDA and WFNA is very thin and grows wider when moving downstream, while the reaction interface between indene and WFNA starts out quite wide at the stagnation point itself. This can be explained by the fact that the reaction between liquid TMEDA and WFNA is very quick and there is very little time available for the reactants as well as the products to diffuse at the reaction front. In the case of Indene and WFNA on the other hand the reaction between the two liquids is comparatively very slow and thus both the reactants and the products from the reaction get a lot of time to diffuse across the interface thus giving rise to an optically thick reaction zone. Thus the temperature trends from the micro-reactor experiments can also give an idea on which hypergolic pair will have a faster heat release.

Table 1. Summary of Ignition Delay times for various fuels with WFNA as well as flow rates at which peak temperatures occur in the micro-reactor.

<b>Fuel</b>	<b>Ignition Delay (ms)</b>	<b>Flow rate at which peak temperature occurs (<math>\mu\text{L}/\text{min}</math>)</b>
TMEDA	19	N/A
DMAZ	99	750
Triethylamine	45	1500
Dicyclopentadiene	No ignition but noticeable vigorous reaction at $\sim 65$ ms	500
Indene	No ignition but noticeable vigorous reaction at $\sim 300$ ms	400

From the experiments (refer summary in Table 1) it can be clearly seen that TMEDA, amongst all the fuels tested, has the highest heat release as well as has temperature trend in which no peak was noticed to occur within the range of flow rates used in the present study. On the other hand, it is also easy to see that the fuel with the lowest heat release and also with the lowest flow rate at which the peak temperature occurs is indene. These two trends showed that TMEDA would have a much shorter ignition delay time than indene and the drop tests showed similar results. In fact the heat release values and the flow rates at which the peak temperatures occurred had a trend which showed exactly what the trend for ignition delay times of the various fuels would be like.

These experimental results with the microreactor prove the relative importance of the early liquid phase reactions to the overall ignition process. A faster liquid phase reaction with a higher heat release also implies a shorter ignition delay thus implying that the gas phase reactions that occur later on between the hyperegols are intrinsically linked to the early liquid phase chemistry.

The temperature trends observed from the numerical simulations of the flow in the microreactor can be explained by reasoning used to explain trends in the counter-flow diffusion flame. In a diffusion flame, the combustion rate can be controlled by controlling the diffusion rate of reactants into the reaction zone. With an increase in diffusion rate, the combustion rate of the flame can be increased. Thus an increase of flow of the fuel and oxidizer to the reaction zone will cause an increase in the combustion rate at the flame. If the flow rates of the fuel and oxidizer are further increased, and are able to exceed a critical value, then the reaction between the fuel and oxidizer will not be able to keep up with the flow of reagents into the reaction zone, and the reaction rate will abruptly decrease.

Similarly, as the inlet flow velocities of TMEDA and nitric acid into the microreactor are increased, the residence time at the stagnation point becomes shorter. At a critical flow rate, the residence time of the reagents becomes shorter than the time required for reaction. At this critical flow rate, the temperature in the simulations starts decreasing with any further increase in inlet flow velocities of the fuel and oxidizer. As the reaction rate constant was initially chosen to reflect a relatively slow reaction between the reagents, the peak in temperature occurs at very low inlet velocities for the reagents as the time required for the reaction to occur with a rate constant of  $2 \times 10^7 \text{ L}^2 \cdot \text{mol}^{-2} \cdot \text{s}^{-1}$  is long. When the reaction rate constant is increased, then the reaction occurs at a quicker pace and thus the time required for the reaction to occur is lesser than before. For the system to switch from a mixing controlled regime, to a kinetically controlled regime, the residence times have to be much shorter than in the case when the reaction rate constant is assumed to be  $2 \times 10^7 \text{ L}^2 \cdot \text{mol}^{-2} \cdot \text{s}^{-1}$ . Thus, when the reaction rate constant is increased, the peak in the temperature trends occurs at a higher inlet flow velocity than in the case with the lower reaction rate constant. Thus for the case when the reaction rate constant is  $2 \times 10^9 \text{ L}^2 \cdot \text{mol}^{-2} \cdot \text{s}^{-1}$ , the peak in temperatures occurs at an inlet flow velocity of 0.6 cm/s. Given that the slopes of the temperature trends after the peak change with the value of reaction rate constant, thus the regime after the temperature peak can be said to be dependent on the reaction rate. Thus, this regime at the flow velocities beyond the peak in temperature is kinetically controlled. On the other hand, the slopes of the temperature trends before the peak in temperature are seen to be independent of the value of the reaction rate constant. Thus the regime for the flow velocities before the peak in temperature can be said to be influenced by the diffusional mixing between the reagents and can thus be termed as diffusion controlled.

A heat loss term was also added to the energy equation to account for heat loss from the top and bottom of the stagnation zone. The heat loss term was observed to have a large effect on the temperature trends, especially on the flow velocities at which the peak in temperatures occurred. With the addition of the heat loss term, the lower inlet velocities were affected far more than the higher inlet velocities as the heat loss term was coupled with the diffusion of temperature. Thus the heat loss term aided in suppressing the temperature of the lower inlet velocity runs far more than it suppressed the temperature for the higher flow velocity runs. This resulted in the peak in temperatures occurring at higher flow velocities like it does in the microreactor experiments. An increase in the heat loss term caused this peak in temperatures at a still higher inlet flow velocity. Even with the added heat loss terms the temperature trends in the numerical simulations are

quantitatively different from the trends observed in the experiments. The flow rates at which the peaks occur in the actual experiments are still higher than the flow rates at which the peaks occur in the numerical simulations. A possible explanation for the discrepancy between the present simulations and the experimental results could be the fact that a simple one step mechanism is used for the simulations and the fact that the salt produced by the reaction between TMEDA and nitric acid is assumed to be a fluid. Studies [51] have shown that using a simple global reaction to model condensed phase reactions can produce erroneous results and actually making use of a more detailed chemical mechanism as well as accounting for phenomena such as the cage effect to study condensed phase reactions in solutions can provide far more accurate results. Further work is thus needed to numerically model the reactive flow in the present microreactor so as to better match the experimental data.

## 11. Conclusions

Silicon-glass micro-reactors have been successfully used to isolate the initial condensed-phase chemistry of fast reactions occurring between hypergols. A series of conventional drop tests were conducted with the various fuels and WFNA to test hypergolicity as well as determine the respective ignition delay times. A correlation was found to be present between the heat released from these early reactions (observed in the micro-reactors) and the reactions that occur when the liquid and gas phase chemistry is combined as seen in the drop tests (using ignition delay times). This relationship between the heat released from the early liquid phase reactions and the ignition delay times in the drop tests was consistent over a variety of fuels as well as when mixtures of fuels were considered. Ignition delay times were also related between the rate of the liquid phase reactions occurring in the micro-reactors. It was noticed that if the reaction in the liquid phase occurred at a faster rate, they resulted in that fuel – oxidizer combination having a shorter ignition delay time. Numerical simulations of the reactive flow in the stagnation zone of the microreactor were performed using a FORTRAN code. These simulations showed temperature trends that were similar in nature to the trends seen in the microreactor. In that, the temperature first increased with an increase in reactant flow rates, it then hit a peak and any further increase in the flow rates caused a decrease in temperatures in the stagnation zone. The flow rate at which this peak in temperatures occurred could be related to the reaction rate of the reaction occurring at the interface with a higher reaction rate meaning that the peak would occur at a higher flow rate. Thus the flow rate in the experiments with the microreactor at which the peak in temperatures occurs can be used to calculate reaction rates of the condensed phase reactions between hypergols. Although these numerical simulations produced temperature trends that are qualitatively similar in nature to the trends seen in the experiments, more work is needed so as to better the simulations and thus be able to quantitatively match the experiments as well. From the correlation of the experimental drop tests and experimental microreactor tests, the liquid phase reactions can thus be said to have an effect on the later occurring gas phase reactions or reactions that occur later in the gas phase are very similar in nature to the early condensed phase reactions. Thus, although the early liquid phase reactions are slower than the eventual gas phase reactions that lead up to ignition, these condensed phase reactions cannot be ignored from computational models and analysis and should be considered important while researching safer, greener hypergolic fuels.



## 12. References

- [1] C. S. Hampton, K. K. Ramesh, and J. E. Smith, "Importance of chemical delay time in understanding hypergolic ignition behaviors," in *AIAA 41st Aerospace Sciences Meeting and Exhibit*, 2003, pp. 6–9.
- [2] W. A. Gaubatz and W. T. Webber, *Calculation of the ignition and start transient of liquid bipropellant rocket engines (Liquid bipropellant rocket engine ignition and start transient calculation for hypergolic and externally ignited starts at sea level and high altitude pressures)*. 1970.
- [3] M. J. Nusca and M. J. McQuaid, "Combustion chamber fluid dynamics and hypergolic gel propellant chemistry simulations for selectable thrust rocket engines," in *Computer Architecture, 2004. Proceedings. 31st Annual International Symposium on*, 2004, pp. 180–189.
- [4] M. J. Nusca and R. S. Michaels, "Computational Study Comparing Potential Bipropellant Compositions for the Army's Impinging Stream Vortex Engine," in *43rd JANNAF Combustion Subcommittee Meeting*, 2009.
- [5] S. V. Gunn, "The Effects of Several Variables Upon the Ignition Lag of Hypergolic Fuels Oxidized by Nitric Acid," *J. Am. Rocket Soc.*, vol. 22, no. 1, pp. 33–38, 1952.
- [6] A. J. Alfano, J. D. Mills, and G. L. Vaghjiani, "Highly accurate ignition delay apparatus for hypergolic fuel research," *Rev. Sci. Instrum.*, vol. 77, p. 45109, 2006.
- [7] J. D. Broatch, "An apparatus for the measurement of ignition delays of self-igniting fuels," *Fuel*, vol. 29, 1950.
- [8] M. A. Pino, "A Versatile Ignition Delay Tester for Self Igniting Rocket Propellants," *J. Jet Propuls.*, vol. 25, no. 9, pp. 463–467, 1955.
- [9] D. J. Ladanyi and R. O. Miller, "Two Methods for Measuring Ignition Delay of Self-Igniting Rocket Propellant Combinations," *J. Jet Propuls.*, vol. 26, no. 3, pp. 157–163, 1956.
- [10] G. Spengler and J. Bauer, "Ignition delay of hypergolic rocket propellants," *Tech. Transl. 16-US Army*, 1966.
- [11] M. A. Saad and S. R. Goldwasser, "Role of pressure in spontaneous ignition," *AIAA J.*, vol. 7, no. 8, pp. 1574–1581, 1969.
- [12] T. M. Squires and S. R. Quake, "Microfluidics: Fluid physics at the nanoliter scale," *Rev. Mod. Phys.*, vol. 77, no. 3, pp. 977–1026, 2005.
- [13] J. Atencia and D. J. Beebe, "Controlled microfluidic interfaces," *Nature*, vol. 437, no. 7059, pp. 648–655, 2004.
- [14] S. W. Mayer, D. Taylor, and L. Schieler, "Preignition products from storable propellants at simulated high-altitude conditions," 1967.
- [15] G. P. Sutton, *History of liquid propellant rocket engines*. AIAA, 2006.
- [16] O. Frota, B. Mellor, and M. Ford, "Proposed Selection Criteria for Next Generation Liquid Propellants," in *Proceedings of the 2nd International Conference on Green Propellants for Space Propulsion (ESA SP-557)*, 2004, vol. 557, p. 6.
- [17] D. M. Thompson, "Tertiary amine azides in hypergolic liquid or gel fuels propellant systems," U.S. Patent No. 6,013,143.2000.
- [18] W. H. Stevenson III, L. S. D. Felton, and Z. Slocum-Wang, "Hypergolic Liquid Or Gel Fuel Mixtures," U.S. Patent No. 8,435,364.2013.
- [19] M. J. McQuaid, W. H. Stevenson, and D. M. Thompson, "Computationally Based Design and Screening of Hypergolic Multiamines," DTIC Document, Aberdeen, MD, 2004.

- [20] G. Reddy, J. Song, M. S. Mecchi, and M. S. Johnson, "Genotoxicity assessment of two hypergolic energetic propellant compounds," *Mutat. Res. Toxicol. Environ. Mutagen.*, vol. 700, no. 1, pp. 26–31, 2010.
- [21] S. Wang, S. T. Thynell, and A. Chowdhury, "Experimental Study on Hypergolic Interaction between  $N, N, N', N'$ -Tetramethylethylenediamine and Nitric Acid," *Energy & Fuels*, vol. 24, no. 10, pp. 5320–5330, 2010.
- [22] D. M. Thompson, B. F. Wilson, and W. H. Stevenson, "Hypergolic Azide Liquid Fuels," in *Proceedings of the 1998 JANNAF Propulsion Meeting*, 1998, pp. 515–523.
- [23] C.-C. Chen, M. J. Nusca, and M. J. McQuaid, "Modeling Combustion Chamber Dynamics of Impinging Stream Vortex Engines Fueled with Hydrazine-Alternative Hypergols," Aberdeen, MD, 2008.
- [24] W. R. Anderson, M. J. McQuaid, M. J. Nusca, and A. J. Kotlar, "A Detailed, Finite-Rate, Chemical Kinetics Mechanism for Monomethylhydrazine-Red Fuming Nitric Acid Systems," US Army Research Laboratory, Aberdeen, MD, 2010.
- [25] R. Schalla and E. Pletcher, "The behavior of the system triethylamine—White fuming nitric acid under conditions of rapid mixing," *Symp. Combust.*, vol. 6, no. 1, pp. 911–917, 1957.
- [26] C. Trent and M. Zucrow, "Behavior of Liquid Hydrocarbons with White Fuming Nitric Acid," *Ind. Eng. Chem.*, vol. 44, no. 11, pp. 2668–2673, 1952.
- [27] F. Laermer and A. Schilp, "Method of anisotropically etching silicon," U.S. Patent No. 5,501,893.1996.
- [28] P. Saksena, "Study of Condensed Phase Reactions between Hypergolic Propellants using Microreactors," The Pennsylvania State University, 2014.
- [29] C. D. Meinhart, S. T. Wereley, and J. G. Santiago, "A PIV algorithm for estimating time-averaged velocity fields," *J. Fluids Eng.*, vol. 122, no. 2, pp. 285–289, 2000.
- [30] "ANSYS® FLUENT Academic Research, Release 14.0.0." ANSYS Inc.
- [31] A. Ciani, W. Kreutner, C. E. Frouzakis, and K. Lust, "An experimental and numerical study of the structure and stability of laminar opposed-jet flows," *Comput. Fluids*, vol. 39, no. 1, pp. 124–114, 2010.
- [32] M. Engler, N. Kockmann, T. Kiefer, and P. Woias, "Numerical and experimental investigations on liquid mixing in static micromixers," *Chem. Eng. J.*, vol. 101, no. 1–3, pp. 315–322, 2004.
- [33] D. Bothe, C. Stemich, and H.-J. Warnecke, "Fluid mixing in a T-shaped micro-mixer," *Chem. Eng. Sci.*, vol. 61, no. 9, pp. 2950–2958, 2006.
- [34] M. Hoffmann, M. Schlüter, and N. Rübiger, "Experimental investigation of liquid–liquid mixing in T-shaped micro-mixers using -LIF and -PIV," *Chem. Eng. Sci.*, vol. 61, no. 9, pp. 2968–2976, 2006.
- [35] A. Soleymani, E. Kolehmainen, and I. Turunen, "Numerical and experimental investigations of liquid mixing in T-type micromixers," *Chem. Eng. J.*, vol. 135, pp. S219–S228, 2008.
- [36] D. Bothe, C. Stemich, and H.-J. Warnecke, "Computation of scales and quality of mixing in a T-shaped microreactor," *Comput. Chem. Eng.*, vol. 32, no. 1–2, pp. 108–114, 2008.
- [37] M. A. Sultan, C. Fonte, and M. Dias, "Experimental study of flow regime and mixing in T-jets mixers," *Chem. Eng. Sci.*, vol. 73, pp. 388–399, 2012.
- [38] R. J. Santos and M. A. Sultan, "State of the Art of Mini/Micro Jet Reactors," *Chem. Eng. Technol.*, vol. 36, no. 6, pp. 937–949, 2013.

- [39] A. Soleymani, H. Yousefi, and I. Turunen, "Dimensionless number for identification of flow patterns inside a T-micromixer," *Chem. Eng. Sci.*, vol. 63, no. 21, pp. 5291–5297, 2008.
- [40] P. Saksena, S. Tadigadapa, and R. A. Yetter, "Control of Liquid Hypergolic Reactions in Micro-Reactors using Diffusional Mixing," in *The 12th International Workshop on Micro and Nanotechnology for Power Generation and Energy Conversion Applications*, 2012.
- [41] S. Wang and S. T. Thynell, "Experimental Investigation of Pressure Effect on Ignition Delay of Monomethylhydrazine, 1, 1-Dimethylhydrazine, Tetramethylethylenediamine and 2-Dimethylaminoethylazide with Nitric," in *8th U. S. National Combustion Meeting, Organized by the Western States Section of the Combustion Institute and hosted by the University of Utah*, 2013, pp. 1–6.
- [42] A. E. Lutz, R. J. Kee, J. F. Grcar, and F. M. Rupley, "OPPDIF: A Fortran program for computing opposed-flow diffusion flames," *Sandia Natl. Lab. Report, SAND96-8243*, 1997.
- [43] W.-G. Liu, S. Dasgupta, S. V Zybin, and W. a Goddard, "First principles study of the ignition mechanism for hypergolic bipropellants: N,N,N',N'-tetramethylethylenediamine (TMEDA) and N,N,N',N'-tetramethylmethylenediamine (TMDMA) with nitric acid.," *J. Phys. Chem. A*, vol. 115, no. 20, pp. 5221–9, 2011.
- [44] C. R. Wilke and P. Chang, "Correlation of diffusion coefficients in dilute solutions," *AIChE J.*, vol. 1, no. 2, p. 264, 1955.
- [45] B. Wang and X. Peng, "Experimental investigation on liquid forced-convection heat transfer through microchannels," *Int. J. Heat Mass Transf.*, vol. 37, pp. 73–82, 1994.
- [46] X. F. Peng and G. P. Peterson, "Convective heat transfer and flow friction for water flow in microchannel structures," *Int. J. Heat Mass Transf.*, vol. 39, no. 12, pp. 2599–2608, 1996.
- [47] S. B. Choi, R. F. Barron, and R. O. Warrington, "Fluid flow and heat transfer in microtubes," *Micromechanical Sensors, Actuators, Syst. ASME DSC*, vol. 32, pp. 123–134, 1991.
- [48] B. Xu, K. T. Ootli, N. T. Wong, and W. K. Choi, "Experimental investigation of flow friction for liquid flow in microchannels," *Int. Commun. Heat Mass Transf.*, vol. 27, no. 8, pp. 1165–1176, 2000.
- [49] D. Liu and S. V. Garimella, "Investigation of Liquid Flow in Microchannels," *J. Thermophys. Heat Transf.*, vol. 18, no. 1, pp. 65–72, 2004.
- [50] F. P. Incropera, A. S. Lavine, and D. P. DeWitt, *Fundamentals of heat and mass transfer*. John Wiley & Sons, 2011.
- [51] C. Melius and M. Piqueras, "Initial reaction steps in the condensed-phase decomposition of propellants," *Proc. Combust. Inst.*, vol. 29, pp. 2863–2871, 2002.
- [52] G. Gamrat, M. Favre-Marinet, and D. Asendrych, "Conduction and entrance effects on laminar liquid flow and heat transfer in rectangular microchannels," *Int. J. Heat Mass Transf.*, vol. 48, no. 14, pp. 2943–2954, 2005.
- [53] D. Haller, P. Woias, and N. Kockmann, "Simulation and experimental investigation of pressure loss and heat transfer in microchannel networks containing bends and T-junctions," *Int. J. Heat Mass Transf.*, vol. 52, no. 11–12, pp. 2678–2689, 2009.
- [54] W. M. Kays and M. E. Crawford, *Convective Heat and Mass Transfer*, 3rd ed. New York: McGraw-Hill, 1993.

### III.3 Reaction Mechanisms for Hypergolic Propellants (Goddard, California Institute of Technology)

#### 1. Abstract

Hypergolic bipropellants are of great importance in the application of rocket and missile technology. These propellants are fuel-oxidizer combinations that ignite spontaneously upon mixing at ambient temperatures. Fast ignition, powerful combustion and stable operation are desired properties. To achieve these goals, it is necessary to understand the combustion mechanism at the atomistic level. In collaboration with Dr. Stefan Thynell at Penn State, whose group carried out experimental spectroscopic studies, we used density functional (DFT) theory to determine the ignition reaction mechanism of hypergolic bipropellants. We focused here on two distinct types of bipropellants:

- the first type has alkylamines (N,N,N<sub>0</sub>,N<sub>0</sub>-tetramethylethylene-diamine, TMEDA, and N,N,N<sub>0</sub>,N<sub>0</sub>-tetramethylmethylenediamine, TMMDA) as the fuel and nitric acid as the oxidant.
- The second type has hydrazine derivatives (monomethyl-hydrazine, MMH, and unsymmetrical dimethyl hydrazine, UDMH) as the fuel and nitrogen tetroxide (NTO) as the oxidant.

We established the ignition reaction mechanisms at the atomistic level for these propellants, and found two key factors that affect the ignition delay:

- the heat or enthalpy of neutralization and
- the barrier heights for the most exothermic reactions.

For MMH-NTO mixture, we found that the pathway to form nitrate derivatives proceeds via the *asymmetric* N<sub>2</sub>O<sub>4</sub> dimer, but in the condensed phase not the gas phase. The predicted intermediates from the dominant reaction steps have all been identified spectroscopically, validating the predicted mechanism. With this atomistic mechanism in hand, one should be able to focus on designed changes in the fuel and/or oxidizer to achieve improved performance.

#### 2. Background and Scientific Objectives

Hypergolic bipropellants are fuel-oxidizer combinations that ignite spontaneously upon mixing at ambient temperatures. Hydrazine derivatives, such as monomethyl-hydrazine (MMH, Figure 1a) and unsymmetrical dimethylhydrazine (UDMH, Figure 1b), are commonly used as hypergolic fuel in combination with the oxidizer nitrogen tetroxide (NTO). Although ignited rapidly when two liquid surfaces touch in ambient conditions, the combustion of MMH or UDMH with NTO is rarely complete to the final products, such as H<sub>2</sub>O, N<sub>2</sub> and CO<sub>2</sub>, but in addition produce substantial amounts of condensate,<sup>1</sup> especially when the engine operates in the pulse mode with a cold engine. The residual condensate on the wall of engine is found to be organic nitrate salts, which are explosive, comparable to TNT,<sup>2</sup> resulting in pressure spikes during the engine operation. The detonation of condensate may even lead to engine destruction. Thus it is very important to understand fully the formation of this condensate, so that the fuel-oxidant combinations can be modified to reduce or minimize it. The current gas-phase combustion model for MMH reacting with red fuming nitric acid (RFNA) developed by the U.S. Army Research Laboratory (ARL)<sup>3</sup> explains the gas phase reaction mechanisms rather well, but does not account for the formation of nitrate-based condensate. This motivated us to reexamine all aspects of both the gas phase and condensate reaction mechanisms.

The other drawback of hydrazine derivatives is their carcinogenicity. To solve this problem, it is important to seek low-toxicity hypergolic fuels<sup>4</sup>. Among a wide range of organics, alkyl multi-amines have been considered as candidates to replace toxic hydrazine derivatives. Considerable experimental effort has been made to screen among saturated tertiary alkyl multi-amines with various alkyl substitutes<sup>5</sup>. A commonly used method to measure reactivity of bipropellant is the **drop-test**, which is to drop either fuel or oxidizer into the pool of the other. The time interval from the touch of two liquid surfaces to appearance of the flame is defined as the **ignition delay**, an indicator of reactivity. Among various alkylamines tested, TMEDA (Figure 1c) is considered to be most promising for its short ignition delay (14ms<sup>6</sup>) when reacting with white fuming nitric acid (WFNA). In contrast, the similar diamine linked by a methyl group, TMMDA (Figure 1d) has significant longer ignition delay (30ms<sup>7</sup>). The difference in the ignition delay depending on the length of linker has also been observed in drop-tests. Thus

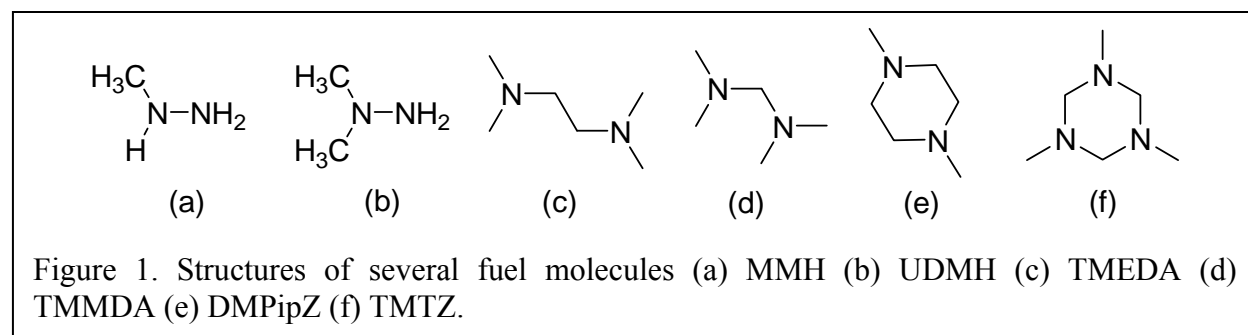
- 1,4-dimethylpiperazine (DMPipZ, Figure 1e, with 10ms ignition delay) and
- 1,3,5-trimethylhexahydro-1,3,5-triazine (TMTZ, Figure 1f, which is not hypergolic under the experimental condition) reacting with WFNA<sup>7</sup>.

The cases discussed above, show that a diamine linked by an ethyl chain has shorter ignition delay than the one linked by methyl chain. Although ignition delay is a macroscopic measurement involving many chemical and physical factors, such as diffusion, thermal conduction and chemical reaction, this dramatic dependence on the detailed molecular structure indicates that the molecular structure of fuel affects the macroscopic phenomenon. Thus to design fuel molecules with improved performance requires an atomistic level of understanding.

To establish the atomistic level understanding of the combustion reaction mechanism, we used density functional theory (DFT) to calculate the free energy reaction barriers for all plausible reactions between fuel and oxidant of hypergolic bipropellants. These studies were carried out in collaboration with Dr. Stefan Thynell's group at Penn State, who performed experimental spectroscopic studies, focusing on identifying all reaction intermediates and products generated in the pre-ignition environment for various combinations of fuel and oxidant. The atomistic reaction mechanism developed here are fully compatible with all observed combustion products, validating the mechanism. With such a complete mechanism in place, one can proceed to examine new fuels and oxidants that might minimize formation of the condensate while reducing ignition time.

### 3. Methods

The calculations of reactions of alkylamines (TMEDA and TMMDA) were carried out with Jaguar 7.5 package,<sup>8</sup> using the unrestricted hybrid density functional UB3LYP at the 6-311G\*\*



level to locate all the stationary points and calculate Hessian. This was then used to provide the vibrational frequencies for zero-point energy (ZPE) and thermocorrections to enthalpy and entropy. All transition states (TS) were validated to have only one negative eigenvalue of the Hessian, followed by the minimum energy path (MEP) calculation to connect the reactant and product. Thermal dynamic data were evaluated at normal temperature (300K) and pressure (1 atm).

Since the first step of ignition is neutralization between alkylamines and nitric acid, where the proton transfers from nitric acid to the basic nitrogen atoms on alkylamines, we obtained the reaction enthalpy by calculating the enthalpy difference between the sum of the infinitely separated reactants (alkylamines and nitric acid) and the final proton-transferred salt in the solvent of nitric acid. The solvation effects were described using the Poisson-Boltzmann (PB) continuum approximation (PBF) implemented in Jaguar.<sup>9</sup> we used the experimental dielectric constant and solvent radius for pure nitric acid ( $\epsilon=50$  and  $R_{\text{nitric acid}}=2.02\text{\AA}$ <sup>10</sup>).

The calculations of reactions between hydrazine derivatives (MMH and UDMH) and  $\text{NO}_2$  were carried out with Jaguar 7.6.<sup>8</sup> The geometry optimization and Hessian calculation were carried out at the level of M06-2X/6-311++G\*\*.<sup>11</sup> In addition, at these optimized geometries we refined the single point energy at the UCCSD(T)/6-31G\*\* level. In the reaction of HONO formation, the ONO-H distance is the key reaction coordinate, which is sensitive to the particular DFT functional being used. Comparing with geometries at the TS from CCSD/6-31+G\*\* reported by McQuaid and Ishikawa<sup>3b</sup>, the greatest difference in O-H distance is at the TS of reaction to form  $\text{CH}_3\text{NNH}_2+\text{HONO}$  (2.170 vs. 1.908 Å). For all other cases the difference in O-H is less than 0.1 Å. Fortunately, such geometric differences have little effect on the barrier heights for HONO formation, as shown below. All TS were validated by following the MEP scan to connect reactant and product. Free energies are reported at 298.15 K and 1 atm.

For reactions inside the aerosol or at the aerosol surface, we added the electrostatic interaction between reactants and surrounding ions using the PBF solvation model ( $\epsilon=80.37$  and  $R_{\text{water}}=1.4\text{\AA}$ ). We consider that the solvation effects calculated for water represent the high dielectric properties expected for these complex systems, with the results depending little on the exact values of the dielectric constant, as long as it is greater than 20 and the radius is smaller than 2.8Å.

The UCCSD(T) calculation was done with NWChem.<sup>12</sup>

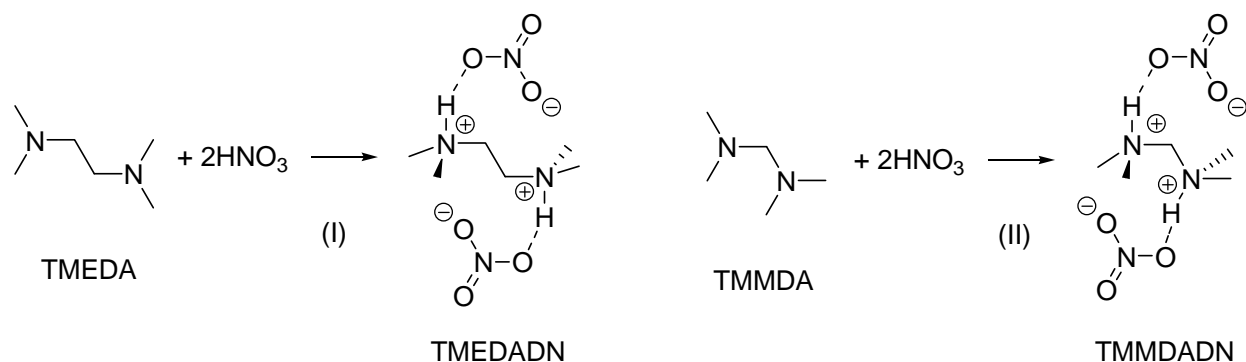
## 4. Results and Discussions

The discussion contains three parts. In the first part we discuss all reactions of TMEDA and TMMDA, including their neutralization heat with nitric acid and their oxidation by  $\text{NO}_2$ . In the second part we discuss reactions between MMH and  $\text{NO}_2$ , including aerosol formation and MMH oxidation. In the third part we discuss reactions between UDMH and  $\text{NO}_2$ .

### 4.1 DFT study of ignition mechanism of hypergolic bipropellant: TMEDA, TMMDA and nitric acid

#### 4.1.1 Exothermicity of the formation of dinitrate salt of TMEDA and TMMDA

It is observed that when TMEDA is dropped into  $\text{HNO}_3$  pool, condensed-phase TMEDA dinitrate is formed along the surface where two liquids come into contact, as the white cloud observed in the high-speed camera.<sup>6</sup> In this reaction protons on  $\text{HNO}_3$  are transferred to N atoms on TMEDA and TMMDA and make bond with lone pair electrons on N, as shown below.



For TMEDADN, the N-H distance is 1.058Å and the O-H distance is 1.647Å. For TMMDADN, the N-H distance is 1.062Å and the O-H distance is 1.639Å. The shorter N-H distance indicates that protons are fully transferred to the N atoms to form cation and anion pair.

For reaction (I), the total solution phase energy, which includes molecule's electronic energy and the interaction between molecule and dielectric solvent cavity, goes downhill by 45.0kcal/mol to form TMEDADN. For reaction (II), to form TMMDADN the energy only goes downhill by 38.7kcal/mol, 6.3kcal/mol less exothermic than the formation of TMEDADN. It can be understood that the shorter distance between two positive charged N atoms in TMMDADN results in the larger electrostatic repulsion to overcome to doubly protonate. The less heat released from forming TMMDADN can result in lower local temperature and contribute to the longer ignition delay of the reaction between TMDMA and HNO<sub>3</sub>.

#### 4.1.2 Bond energies in TMEDA, TMDMA and their alkane analogues

Although it is the barrier height to determine the reaction rate, lower bond energy in the reactant usually renders the bond easier to break and have lower barrier height for reactions. From this point of view, bond energy provides us an easy hint about chemical reactivity.

Table 1. Bond energies in TMEDA, TMMDA, and their corresponding alkane analogues

Bond Energies (kcal/mol)	TMEDA	2,5-dimethyl- hexane	TMMDA	2,5-dimethyl- pentane
C <sup>1</sup> -H	86.3	96.6	86.4	96.2
C <sup>1</sup> -N <sup>2</sup> /C <sup>2</sup>	68.3	79.6	71.7	78.4
C <sup>3</sup> -N <sup>2</sup> /C <sup>2</sup>	66.9	75.0	63.1	75.4
C <sup>3</sup> -H	84.5	91.6	85.2	92.3
C <sup>3</sup> -C <sup>4</sup>	60.5	78.9	-	-

Bond energies in TMEDA, TMMDA and their alkane analogues, 2,5-dimethyl-hexane and 2,5-dimethyl-pentane are listed in Table 1. The C<sup>1</sup>-N<sup>2</sup> bonds are about 7 to 10 kcal/mol weaker than the corresponding C-C bonds due to the atomistic difference of C and N. In the other case with no such an atomistic difference, however, the C-H bonds in TMEDA and TMMDA are significantly weaker by 10kcal/mol than C-H bonds in alkane. The C<sup>1</sup>-H bond energies in TMEDA and TMMDA are 86.3 and 86.4 kcal/mol, comparing with C-H bond energy in their alkane analogues, 96.6 and 96.2 kcal/mol. Similar reductions in bond energy are also found for C<sup>3</sup>-H bonds. The reason for the smaller C-H bond energies on TMEDA and TMMDA is because that the final product of H dissociation, the free radical on C, makes a partial bond with lone pair electrons on N, a so called three-electron-two-center bond. The extra bonding (~10 kcal/mol) between C and N stabilizes the final product and lower the C-H bond energies. Such an extra bonding can only take place if the free radical is neighboring to N atoms.

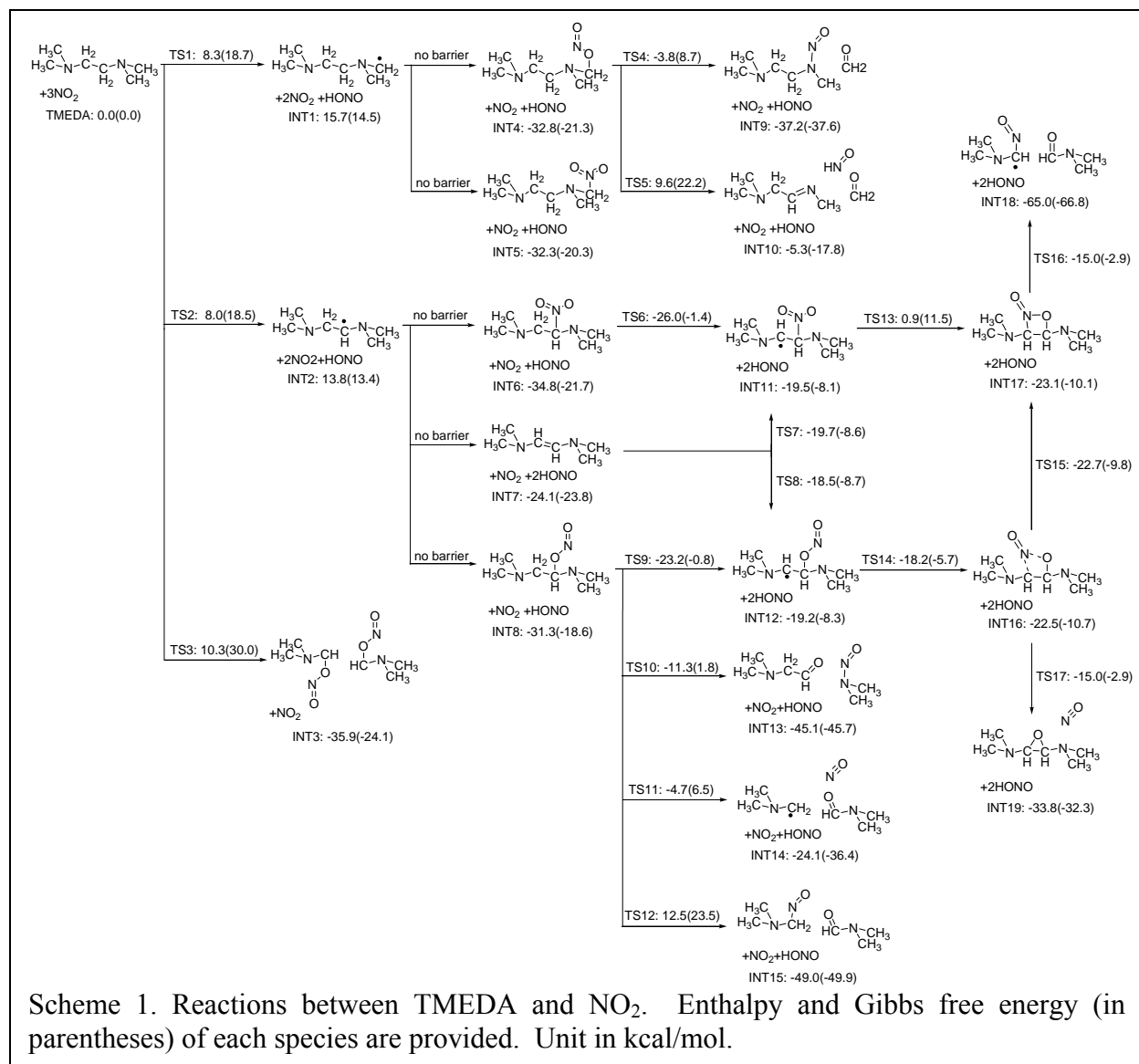
By the same stabilization effect, the C<sup>3</sup>-N<sup>2</sup> bond in TMMDA is weaker than the same C<sup>3</sup>-N<sup>2</sup> bond in TMEDA by 3 kcal/mol, and the C<sup>3</sup>-C<sup>4</sup> bond energy for TMEDA is drastically lower than the one in its alkane analogue by 18 kcal/mol due to the stabilization on both dissociation products, rendering this C-C bond the weakest bond in TMEDA, which leads to the fundamental difference in reactivity between TMEDA and TMMDA.

#### 4.1.3 Reaction mechanism of TMEDA+NO<sub>2</sub>

The reactions between TMEDA and NO<sub>2</sub> in different stages are shown in Scheme 1, which can be categorized into the following types:

1. H-abstraction by NO<sub>2</sub> (reactions to INT1, INT2, INT11 and INT12) to form HONO and leave a free radical on C.
2. Free radical recombination between the free radical after H-abstraction and NO<sub>2</sub> (reactions to INT4, INT5, INT6 and INT8).
3. C-C double bond formation and opening (reaction leading to INT7 and following reactions to INT11 and INT12).
4. C-N bond breaking and rearrangement (reactions to INT9, INT10 and INT13).
5. C-C bond breaking, which can result from the attack of two NO<sub>2</sub> simultaneously (reaction to INT3), or accompany with the O-N bond breaking in the adjacent -ONO group and





formation C-O double bond (reactions to INT14 and INT15), or through a 4-member ring intermediate (reactions from INT 16 to INT18).

#### 6. Epoxide formation (reaction to INT19).

The enthalpy and Gibbs free energy of each species are also marked in Scheme 1 with the latter in parentheses, referenced to the sum of each thermal dynamic function of individual TMEDA and NO<sub>2</sub> in gas phase.

##### 4.1.3.1 Initiating stage

Based on MMH/NTO mechanism<sup>13</sup>, where the HONO formation happens first, the reaction between TMEDA and NO<sub>2</sub> can also start with NO<sub>2</sub> abstracting hydrogen on the terminal methyl group (TS1) or the middle ethyl group (TS2). There are three possible conformations for NO<sub>2</sub> abstracting H with different NO<sub>2</sub> orientation: 1. *cis*-HONO formation, 2. *trans*-HONO formation, 3. HNO<sub>2</sub> formation. Various TS geometries are examined, and barriers for *cis*-HONO formation are always the lowest, then the HNO<sub>2</sub> and *trans*-HONO formation, so only TS for *cis*-HONO

formation is reported here. The lower barrier of *cis*-HONO formation is because of the better interaction between the C-H bond and the A<sup>1</sup> orbital on NO<sub>2</sub> containing free radical, which distributes on both oxygen ends in the same phase. At the TS of *trans*-HONO formation, the distance between H and the O on the further side of NO<sub>2</sub> is much longer, resulting in smaller interaction between free-radical orbital and C-H bond, hence the higher barrier. The trend found here that *cis*-HONO is favored is different than the trend of the HONO formation in MMH/NO<sub>2</sub> system<sup>3b</sup>, where multiple polar N-H bonds exist and *trans*-HONO interacts with not only the breaking N-H bond via the O atom but the adjacent N-H bond through N atom on NO<sub>2</sub>, lowering the barrier. The barrier to abstract H on the linker ethyl group is 8.0 kcal/mol, slightly easier than abstracting H on the terminal methyl group, 8.3 kcal/mol. The entropic effect to bring two molecules in gas phase together at TS raises the Gibbs free energy by about 10 kcal/mol for both reactions. To separate the product complex of HONO and TMEDA free radical takes the other 7~8 kcal/mol to reach intermediates INT1 and INT2.

Comparing with TMEDA, the barriers of HONO formation on 2,5-dimethyl-hexane are about 10 kcal/mol higher in average, which indicates that the N atom adjacent to the C-H bond not only reduces the C-H bond energy as shown before, but also lowers the barrier for HONO abstraction. It can be understood that at TS, the nitrogen donates its lone pair electrons to the antibonding orbital of C-H bond, stabilizes the TS and lowers the barrier.

Besides two HONO formation pathways to form INT1 and INT2, it was found that the simultaneous attack of two NO<sub>2</sub> to the both ends of the relative weak C-C bond (TS3) leads to C-C bond breaking and the formation of two ONO-CH<sub>2</sub>N(CH<sub>3</sub>)<sub>2</sub> fragments. For C-C bond breaking, this path has an unusual low enthalpy barrier, 10.3 kcal/mol, because of the lone pair electrons of two N atoms donating into the C-C antibonding orbital from both ends, just like the way it stabilizes both free radicals when C-C bond is broken as shown before. However it requires a termolecule-reaction, and the entropic effect raises the free energy at TS to 30.0 kcal/mol, which renders this pathway less possible to happen in the gas phase. However if the NO<sub>2</sub> molecule is the solute in the mixture of TMEDA and HNO<sub>3</sub>, its entropy will drop due to less degree of freedom available to move in the dense media and this pathway may be viable for the less free energy barrier.

#### 4.1.3.2 Reactions after INT1

After H-abstraction, the TMEDA free radical on terminal methyl group, INT1, recombines with other NO<sub>2</sub> radicals. The recombination to form INT4 and INT5 are about 46 kcal/mol exothermic without any barrier. In INT4, the N-O single bond in the -ONO group is weak and easily to break into an O radical and NO. The formation of C-O double bond after the N-O bond breaking is the driving force to break the C-N bond, leaving a bimolecular-like state, a formaldehyde molecule plus one N radical. The dissociating-like NO can either recombine with N radical (TS4) to form INT9 with a barrier 29.0 kcal/mol, or abstract one H from C (TS5) to form a C-N double bond plus HNO (INT10) with a higher barrier, 42.5 kcal/mol. The nitro compound INT5 is less reactive and may play little role at the initial stage when temperature is low.

#### 4.1.3.3 Reactions after INT2

Similar to INT1, the free radical on the middle ethyl of TMEDA, INT2, recombines with other NO<sub>2</sub> free radical to form nitro and nitrite compounds, INT6 and INT8, releasing more than 45 kcal/mol of heat without any barrier. The exothermic values reported here are about 10 kcal/mol less than values in the previous study to form the same intermediates.<sup>3c</sup> Besides the

recombination,  $\text{NO}_2$  can also abstract H on the carbon next to the radical site to form a C-C double bond (INT7), which is also barrierless and exothermic by 40 kcal/mol. These three reactions are very exothermic and non-reversible, therefore their relative reaction rates may not be determined by the thermodynamics of final products but determined by the orientation of incoming  $\text{NO}_2$ , resulting in the coexistence of INT6, INT7 and INT8.

With the presence of  $\text{NO}_2$ , the double bond in INT7 can be opened and converted to INT11 and INT12 via TS7 and TS8, which are products of H-abstraction from INT6 and INT8. Although the TS is located for the double bond opening (TS8) to INT12, after including the ZPE, the TS8 is lower than INT12, which means INT12 may not be a stable intermediate in gas phase, but it could have longer life time if surrounded by solvent molecules to hinder the  $\text{NO}_2$  flying away from INT12.

The formation of INT7 with the C-C double bond is important because that comparing with non-conjugated compound, the double bond is fairly easily to oxidize in acid. Some possible mechanisms for C-C bond breaking with low barrier are proposed and discussed below.

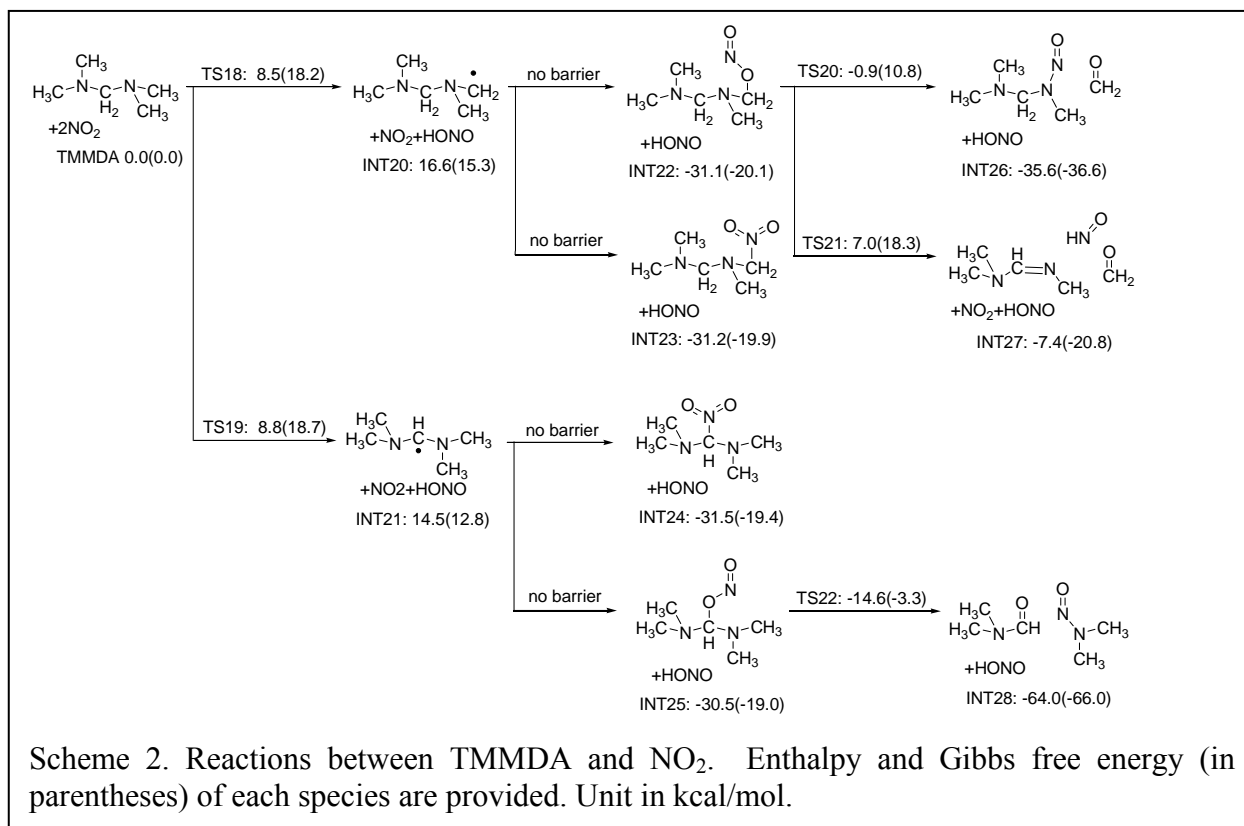
Like INT4, INT8 can undergo unimolecular reaction to break the weak N-O bond in -ONO group. The following C-O double bond formation can lead to: 1. C-N bond breaking and N-N bond formation (via TS10 to INT13, in which the  $\text{ON-N}(\text{CH}_3)_2$  was identified in the gas product of TMEDA and  $\text{HNO}_3$  by IR spectrum), 2. C-C bond breaking (via TS11 and TS12). TS11 is 17.2 kcal/mol lower than TS12 due to the less strained geometry, despite the later makes a new C-N bond and more exothermic. Although the similarity between INT14 and INT10, TS10 is 7.5 kcal/mol lower than TS5 because C-O double bond is weaker on formaldehyde than the one on the primary aldehyde of INT14.

Comparing to the unimolecular reactions above, with unfavorable entropic effect, the H-abstraction by  $\text{NO}_2$  still has the lowest enthalpy and free energy barrier, 8.1 and 17.8 kcal/mol (TS9). The product free radical can either react with the O in -ONO group to form an epoxide (INT19) plus NO, or react with the N to form a 4-member ring intermediate, INT17, with negligible barrier (<2 kcal/mol). With the help of lone pairs on N atoms, to break the C-C bond in 4-member ring intermediate has a low barrier in 8.1 kcal/mol. The ring breaking reaction starts with the N-O bond breaking, followed by C-O double bond formation and C-C bond breaking (TS16) to release heat in 41.9 kcal/mol. Not only releases considerable heat, this reaction also produces two reactive fragments, an amino aldehyde and a free radical, which can undergo further reactions. The former of products is a close-shell molecule and was observed in the gas product of the reaction between TMEDA and  $\text{HNO}_3$  via IR spectroscopy.<sup>6</sup> This is different than the free radical recombination, which reduces the number of reactive molecules and is entropically unfavorable.

#### 4.1.4 Reaction mechanism of TMMDA+ $\text{NO}_2$

The reactions between TMMDA and  $\text{NO}_2$  are very similar to the ones between TMEDA and  $\text{NO}_2$ , except there is no C-C double bond formation and C-C bond breaking. Three types of reactions are:

1. H abstraction by  $\text{NO}_2$  (reactions to INT20 and INT21) and leaves a free radical on TMMDA.
2. Free radical recombination between the product from H abstraction and  $\text{NO}_2$  (reactions to INT22, INT23, INT24 and INT25).



3. Breaking C-N bond on TMMDA to form a new N-N bond (reactions to INT26 and INT28) or a C-N double bond (reaction to INT27).

The enthalpy and Gibbs free energy of each species are marked in Scheme 2 and referenced to the sum of each thermal dynamic function of individual TMMDA and NO<sub>2</sub> in gas phase.

#### 4.1.4.1 Initiating stage: H-abstraction

The reaction starts with NO<sub>2</sub> abstracting H on the terminal methyl groups (via TS18 to INT20) or the middle -CH<sub>2</sub>- group (via TS19 to INT21). All barriers are very similar to TMEDA's. Despite the lone-pair electron on nitrogen can stabilize the TS of H-abstraction, as seen on TMEDA, to abstract H from the middle methyl group between two nitrogen atoms does not double this effect because two lone-pairs on neighboring nitrogen atoms orient perpendicularly to each other due to the steric repulsion and only one lone-pair has the right orientation to donate electron into the antibonding orbital of C-H bond to stabilize the transition state, resulting in barrier heights 8.8 kcal/mol, similar to TMEDA's.

#### 4.1.4.2 Reactions after INT20

Without the possibility to form C-C double bond, the only easy pathway to oxidize TMMDA is via free radical recombination to generate nitro or nitrite compound (INT22, INT23, INT24 and INT25). All reactions are exothermic by about 30~31 kcal/mol. The nitrite compound can undergo unimolecular reaction to break C-N bond and form C-O double bond to generate formaldehyde, followed by forming N-N bond (via TS20, see Figure 6c, to INT26) or C-N double bond (via TS21, see Figure 6d, INT27), which are similar to reactions to INT9 and INT10.

The same C-N bond breaking and C-O double bond formation can also take place on INT25 via TS22, generating an amino aldehyde and a N-nitroso fragment with a 15.9 kcal/mol barrier,

releasing a considerable amount of heat, 33.5 kcal/mol. This path also generates two reactive fragments, which can be further oxidized easily.

#### 4.1.5 Comparison between reaction mechanisms of TMEDA/NTO and TMMDA/NTO

In both systems, the initiation reaction is HONO formation, which is also observed experimentally in hydrazine derivative/NTO<sup>13-14</sup> and NH<sub>3</sub>/NTO<sup>15</sup> systems. It is a step with low barrier but endothermic, not helpful to initiate other reactions with higher barrier. The exothermic steps usually involve the oxidation of C, such as free radical recombination (a net C-N or C-O bond is formed) or C-O double bond formation. The barrier to oxidize carbon via free radical recombination pathway is similar for both TMEDA and TMMDA, since the only way to generate these free radicals is HONO formation, which has barrier around 8-9 kcal/mol for both fuels. However, C oxidation via C-O double bond formation has different barriers for TMEDA and TMMDA. In TMMDA, the easiest pathway to form C-O double bond is from INT25 to INT28, which has barrier 15.9 kcal/mol, whereas in TMEDA it is via a multistep pathway. If starting from intermediate INT7 with C-C double bond, the highest barrier on the pathway to reach the product with C-O double bond, INT18, is 8.1 kcal/mol (at TS16). A lower barrier for C oxidation leads to faster heat releasing, which may account for the shorter ignition delay observed experimentally.

Based on the comparison above, the higher reactivity of TMEDA towards NO<sub>2</sub> can attribute to the formation and oxidation of the C-C double bond on the ethyl linker. The C-H bond adjacent to N atom is easier to break due to the lone pair stabilization, and TMEDA has two such C-H bonds on the ethyl linker, making it possible to form a double bond intermediate and easier to undergo further oxidization. The double bond can also be opened and oxidized by nitric acid. On the other hand, although TMMDA has five carbon atoms adjacent to N, none of them is connected to each other, which makes the formation of C-C double bond on TMMDA impossible. The same mechanism can also be applied to explain the reactivity difference between DMPipZ and TMTZ, where the former has two adjacent carbons and short ignition delay, and the later has no carbon adjacent to each other and is non-hypergolic.

#### 4.1.6 Conclusion

We used DFT calculations to determine the atomistic mechanism for the hypergolic reaction between TMEDA, TMMDA and HNO<sub>3</sub>. Two key factors were calculated to illustrate how the molecular structure relates to the ignition delay.

- The first factor is the exothermicity of the formation of the dinitrate salt of TMEDA and TMMDA. Because of the shorter distance between basic amines in TMMDA, it is more difficult to protonate both amines for the stronger electrostatic repulsion, resulting in the heat of dinitrate salt formation being smaller by 6.3kcal/mol.
- The second factor is the rate of TMEDA and TMMDA reacting with NO<sub>2</sub>, the step that releases sufficient heat and additional reactive species to propagate the reaction.

In TMEDA, the formation of the intermediate with a C-C double bond and the low bond energy of the C-C single bond provide a route for a low barrier to oxidize C. Both factors can contribute to the shorter ignition delay of TMEDA. The same reasoning based on the molecular structure can be applied to other fuels, such as DMPipZ and TMTZ.

## 4.2 DFT Investigations of Early Reactions of Monomethylhydrazine with Mixtures of NO<sub>2</sub> and N<sub>2</sub>O<sub>4</sub>

The current ARL mechanism for MMH/NTO is a subset of the MMH/RFNA mechanism, containing reactions categorized in two domains:

1. Single-bond fission events to strip fragments from MMH and generate free radicals.
2. Radical-radical reactions to form either closed-shell or open-shell species.

Given the low temperature (<100°C) in the pre-ignition environment, direct bond fission from MMH to produce H, CH<sub>3</sub> or NH<sub>2</sub> is unlikely so that NO<sub>2</sub> is the major free radical available initially. Based on this assumption, the ARL mechanism considers the two types of initial reactions:

1. H-abstraction from MMH and sequential HONO formations.
2. Recombination between NO<sub>2</sub> and MMH free radicals generated by H-abstraction.

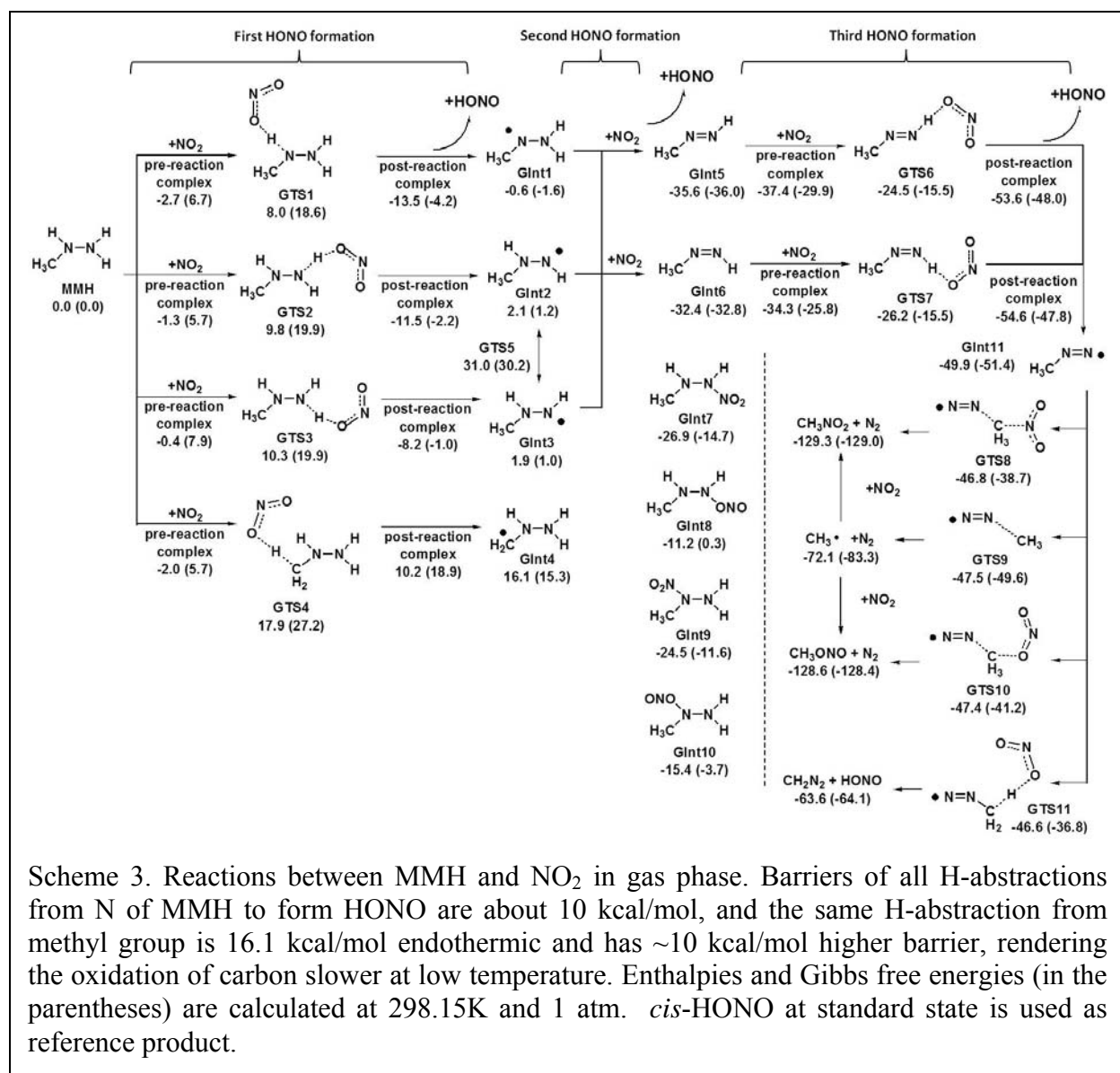
However, these reactions do not fully explain the formation of a condensate that has been observed in several previous studies involving examinations of a residue from gas-phase reactions in a stoichiometric mixture of MMH and NO<sub>2</sub>/N<sub>2</sub>O<sub>4</sub>.<sup>1c</sup> The IR properties of this residue are quite similar to the IR properties of a residue obtained from reactions between liquid-phase MMH and gaseous NO<sub>2</sub>/N<sub>2</sub>O<sub>4</sub>.<sup>2</sup> The IR properties of the residue from these two studies suggest that monomethylhydrazinium nitrate (MMH·HNO<sub>3</sub>) is formed in addition to other species.<sup>1c</sup> The formation of MMH·HNO<sub>3</sub> was also detected by Saad et al.,<sup>16</sup> who examined liquid-phase reactions between MMH and N<sub>2</sub>O<sub>4</sub> in a system diluted by CCl<sub>4</sub> at -20°C. In a recent work by Catoire et al.,<sup>14</sup> it is suggested that the MMH·HNO<sub>3</sub> detected as a major product in the residue by Semans et al. is not formed from reactions in the gas phase, since its elemental analysis matches rather poorly with that of the residue as determined by Breisacher et al.<sup>1a</sup> Catoire et al. suggest that nonionic compounds are formed and accumulate in a condensate. However, it appears that no experiments were carried out to confirm the formation of these nonionic compounds.

Based on the above discussion, there is a clear need to reexamine gas-phase reactions between MMH and NO<sub>2</sub>/N<sub>2</sub>O<sub>4</sub> at low temperatures in order to identify the relevant preignition products and reaction pathways. We applied density functional theory to help elucidate the reaction pathways, since experimentally it is rather difficult to identify and quantify radicals, as well as to identify transition-state structures.

### 4.2.1 H-atom abstraction from MMH

The oxidation of MMH via sequential HONO formation and the final N<sub>2</sub> generation were studied computationally as shown in Scheme 3. The first H-abstraction from MMH has been studied in detail by McQuaid and Ishikawa.<sup>3b</sup> Their reported barrier heights for H-abstractions from three different positions (H on N-CH<sub>3</sub> and two H on N-NCH<sub>3</sub> - *cis* and *trans* to the methyl group, respectively) to form *cis*-HONO are 10.1, 10.6 and 11.2 kcal/mol (without ZPE or thermocorrections) at CCSD(T)/6-311+G(2df,p)//CCSD/6-31+G(d,p) level relative to free NO<sub>2</sub> and MMH.

These results are close to our values of 8.0, 9.8 and 10.3 kcal/mol (including ZPE and temperature corrections, relative to free NO<sub>2</sub> and MMH). We find that the most readily abstracted H-atom is from the nitrogen with the methyl group, in agreement with the previous



study. The binding energy between the product HONO and the free radical is substantial (10-13 kcal/mol enthalpy), reducing the free energy of the post-reaction complex to even lower levels than the unbound free radicals GInt1 – GInt3. However in normal experimental conditions the partial pressure of HONO is usually much lower than 1 atm (the reference state), favoring the formation of unbound free radicals, after taking concentration correction into account. The interconversion between GInt2 and GInt3 via N-N bond rotation has a high barrier (~29 kcal/mol) because the N-N bond has some double-bond character due to the delocalization of the N lone pair. Abstraction of an H atom from a methyl group (GTS4) is ~10 kcal/mol higher in energy than from N atoms. Furthermore, this reaction is 16.1 kcal/mol endothermic, in contrast to H-abstractions from N atoms, which are almost thermoneutral. Therefore H-atom abstraction from the methyl group will not play an important role during the pre-ignition event, and experimentally we observed abundant methyl-containing compounds, indicating the inertness of methyl group at room temperature. Consequently reactions beyond GInt4 are not considered in Scheme 3.

#### 4.2.2 H-atom abstraction from CH<sub>3</sub>NNH<sub>2</sub> or CH<sub>3</sub>NHNH

The H-abstraction reactions from either CH<sub>3</sub>NNH<sub>2</sub> or CH<sub>3</sub>NHNH very likely have no barrier because of stabilization of the N *p* orbital bonded to the H with delocalization of the adjacent N lone pair. Indeed we could not find a transition state in the electronic energy surface despite an exhaustive search. The free energy surface after including ZPE might well lead to a barrier. Ishikawa and McQuaid,<sup>3d</sup> using the MPWB1K functional, found that 1-2 kcal/mol of kinetic energy is enough to activate H-atom abstraction, indicating very low barriers for H-abstraction. GInt7 - GInt10 are products from recombination between two radicals (GInt1 - GInt3 and NO<sub>2</sub>). All of them are enthalpically and entropically less stable than the product of HONO formation, GInt5 and GInt6. These recombination products are not detected in our experiment, where MMH and NO<sub>2</sub> are in gas phase diluted with N<sub>2</sub>. With higher concentration of MMH and NO<sub>2</sub> or reacting in liquid phase will change free energy profile, making the recombination products more favorable.

#### 4.2.3 H-atom abstraction from CH<sub>3</sub>N=NH

The enthalpic barrier for the H-atom abstraction is 11.1 kcal/mol for *anti*-CH<sub>3</sub>N=NH (GInt5→GTS6→GInt11) and 6.2 kcal/mol for *syn*-CH<sub>3</sub>N=NH (GInt6→GTS7→GInt11). The CH<sub>3</sub>N=N radical (GInt11) can either

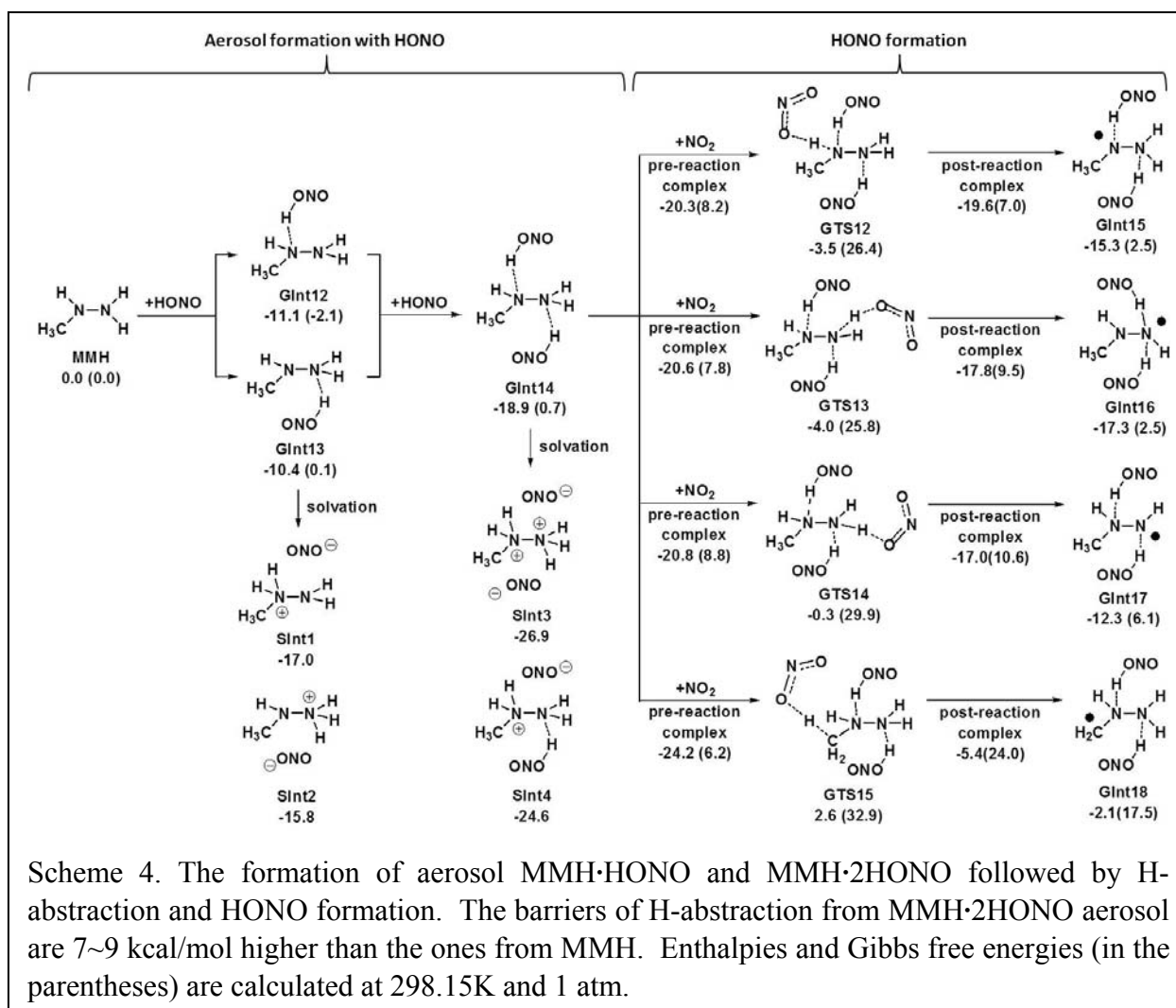
- break the C-N bond to release N<sub>2</sub> and CH<sub>3</sub> radical (ARL mechanism reaction No. 456) with only 2.4 kcal/mol barrier, or
- undergo NO<sub>2</sub> attack at different orientations to form CH<sub>3</sub>ONO and CH<sub>3</sub>NO<sub>2</sub> with barrier heights 2.5 and 3.1 kcal/mol, respectively.

Since the measured concentration of CH<sub>3</sub>ONO<sub>2</sub> is much larger than both CH<sub>3</sub>NO<sub>2</sub> and CH<sub>3</sub>ONO, and the NO<sub>2</sub> concentration is much larger than the concentration of ONONO<sub>2</sub>, the major fraction of the formation of CH<sub>3</sub>ONO<sub>2</sub> is not from reactions involving either CH<sub>3</sub> or CH<sub>3</sub>NN. For example, reactions between CH<sub>3</sub> and NO<sub>2</sub> forming the methoxy group and NO are not likely since the concentration of NO is quite small. In addition, the formation of CH<sub>2</sub>N<sub>2</sub> via H-abstraction from methyl group is also found to have a low barrier (3.3 kcal/mol). However this product was not detected experimentally, indicating that the direct dissociation of methyl free radical from GInt11 may be much faster than other bimolecular pathways.

#### 4.2.4 Formation of MMH·HONO aerosol and its lower reactivity

In each step of Scheme 3, HONO is produced, which is able to form aerosol with unreacted MMH because the basic N atoms on MMH are able to accept a proton from HONO. As shown in Scheme 4, protons in MMH·HONO complexes in gas phase prefer to stay on HONO. The enthalpies to form MMH·*n*HONO complexes (*n*=1, 2) are roughly additive (-21.5 kcal/mol from the sum of enthalpy of GInt12 and 13 vs. -18.9 kcal/mol of GInt14) and the free energies to form these complexes are about thermoneutral (-2.1, 0.1 and 0.7 kcal/mol for GInt12, GInt13 and GInt14). In the strong solvation environment (in the aerosol), the proton transfer from HONO to MMH is more favored and exothermic, which accounts for the observation of ONO<sup>-</sup> anion in the IR spectra. However, the reaction heat to transfer one and two protons from the MMH·2HONO complex in a solvated system differ little (5.7 vs. 8.0 kcal/mol exothermic), unlike complexes in the gas phase. It is because in solvated system the electrostatic repulsion between two positively charged N centers partially cancels the energy gain from the neutralization. Hence, the pathways for continued growth and composition of the aerosol can be either MMH<sup>2+</sup>·2ONO<sup>-</sup> or MMH<sup>+</sup>·ONO<sup>-</sup>. In the oxidizer-rich case, however, the former composition is more likely. The





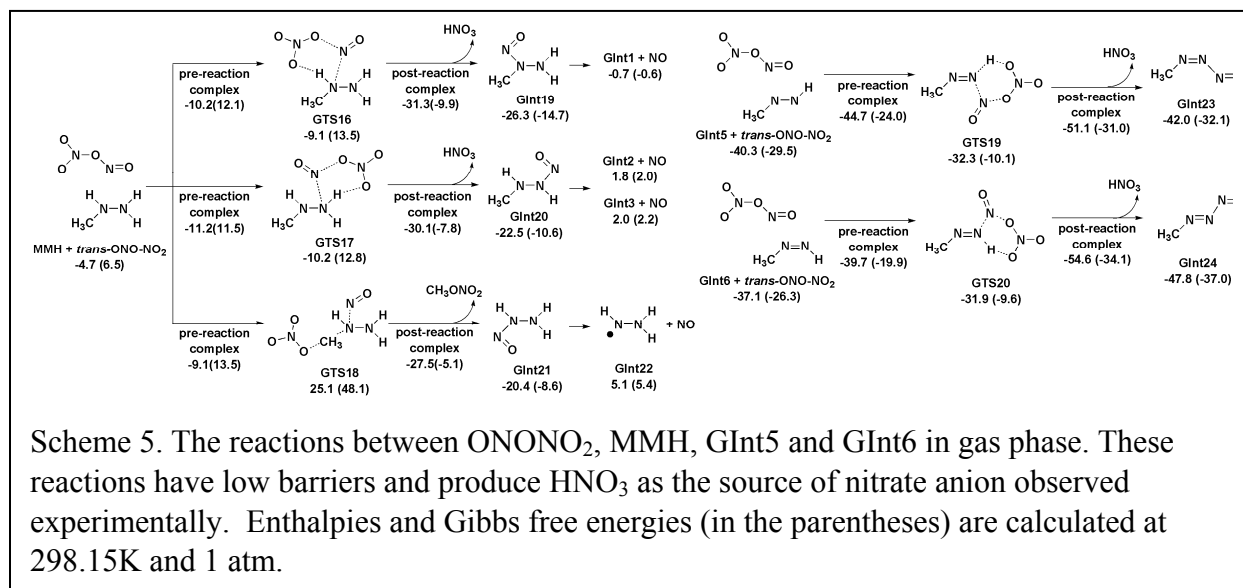
Scheme 4. The formation of aerosol MMH·HONO and MMH·2HONO followed by H-abstraction and HONO formation. The barriers of H-abstraction from MMH·2HONO aerosol are 7~9 kcal/mol higher than the ones from MMH. Enthalpies and Gibbs free energies (in the parentheses) are calculated at 298.15K and 1 atm.

spontaneous nucleation in gas phase followed by the exothermic growth make the aerosol formation a rapid process as observed in the experiment.

We also found that the MMH·HONO aerosol is less reactive than free MMH. Reactions to abstract H from MMH·HONO complex have barriers 7~9 kcal/mol higher than the same H-abstraction from MMH. The reason is that in free MMH, the lone pairs on the N can stabilize the transition state via resonance, whereas such stabilization is less available when lone pairs donate electron density to the proton, resulting in a higher barrier. The increase of the barrier for HONO formation resulting from the salt formation was also observed in the case of alkylamine and nitric acid.<sup>17</sup> As a result, growth of the particles is favored over H-abstraction reactions at the low temperatures of our experiments. As the temperature increases, particles will either undergo H-abstraction reactions or evaporate into MMH and HONO so that particles will shrink and eventually disappear. Such a phenomenon of particle disappearance is observed just prior to ignition in the MMH·HNO<sub>3</sub> reaction system.<sup>18</sup>

#### 4.2.5 Reactions of asymmetric dimer of NO<sub>2</sub>, ONONO<sub>2</sub> in gas phase

The formation of ONO<sub>2</sub><sup>-</sup> and CH<sub>3</sub>ONO<sub>2</sub> cannot be explained by simple H-atom abstractions or recombination of the radical intermediates with NO<sub>2</sub>. One potential source of nitrate is from the

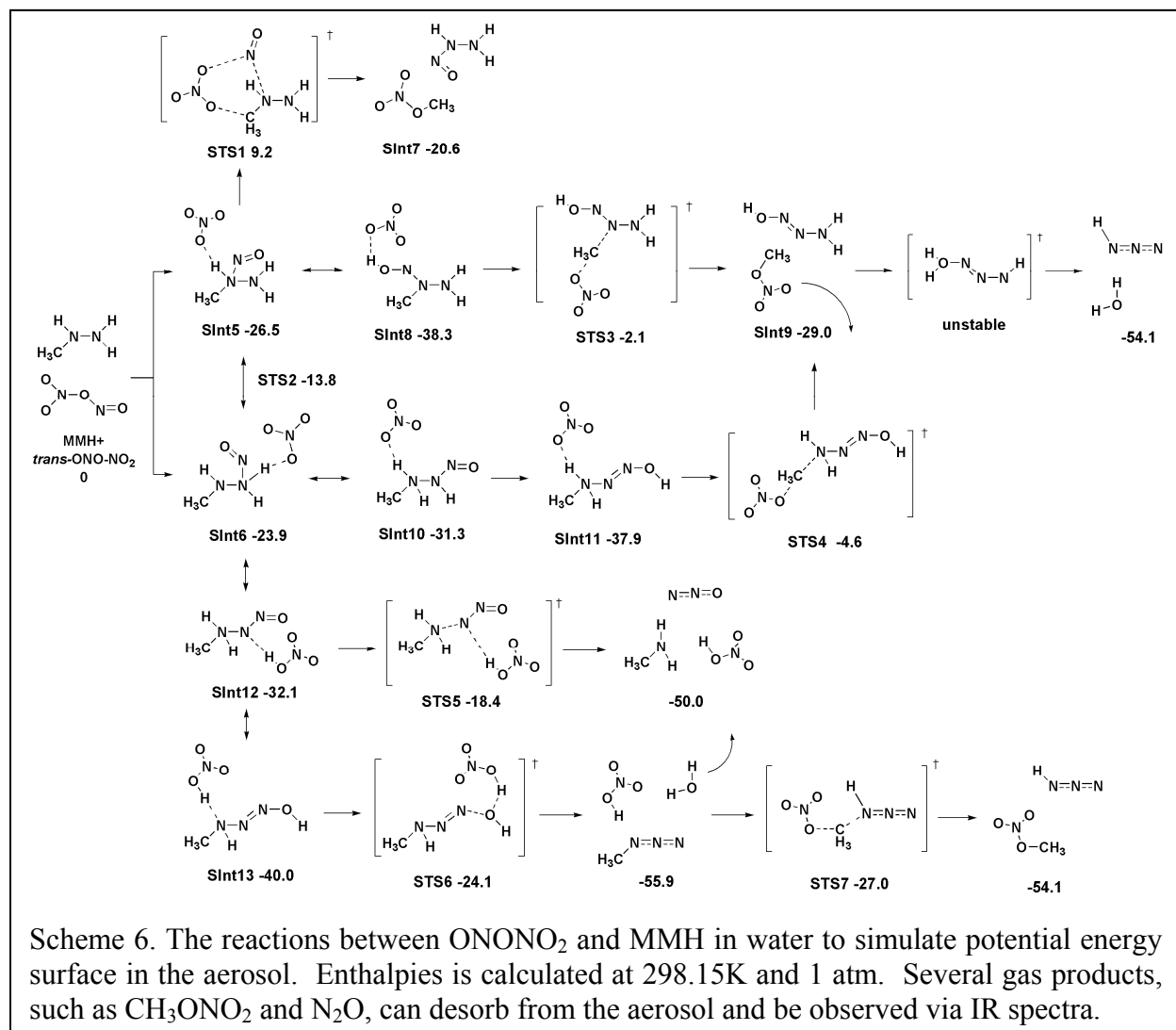


isomerization of N<sub>2</sub>O<sub>4</sub>. It is known that liquid NO<sub>2</sub> dimerizes to form N<sub>2</sub>O<sub>4</sub> and disproportionates into NO<sup>+</sup> and NO<sub>3</sub><sup>-</sup>.<sup>10</sup> NO<sub>2</sub> can also react with water vapor to give HONO and HNO<sub>3</sub>. Finlayson-Pitts and coworkers<sup>19</sup> proposed that the asymmetric isomer ONONO<sub>2</sub> is the key intermediate as the source of nitrate. Our previous study shows that the reaction to form ONONO<sub>2</sub> has low enthalpic barrier (<5 kcal/mol),<sup>20</sup> which means equilibrium between NO<sub>2</sub> and ONONO<sub>2</sub> is very fast. Recently Lai et al.<sup>21</sup> also found that ONONO<sub>2</sub> can play an important role in the hypergolic reaction between hydrazine and liquid NTO. We would also like to check if ONONO<sub>2</sub> plays the similar role in the gas phase reaction between MMH and NO<sub>2</sub>.

The easiest reactions between MMH and *trans*-ONONO<sub>2</sub> is the new N-N bond formation between NO<sup>+</sup> and electron-rich N atoms on MMH followed by the proton transferring from N-H bond to NO<sub>3</sub><sup>-</sup> to form nitric acid, as shown in Scheme 5. Although it is very easy to form nitric acid (enthalpic barrier is about 1 kcal/mol), to form methyl nitrate is difficult in gas phase (34 kcal/mol enthalpic barrier) due to the unfavorable charge separation (nitrate anion has to attack from the back of methyl group, which is far from the positive N center). Therefore, the gas phase reactions between MMH and ONONO<sub>2</sub> can easily generate HNO<sub>3</sub> and explain the experimental observation of NO<sub>3</sub><sup>-</sup>, however, they cannot explain the abundant CH<sub>3</sub>ONO<sub>2</sub> observed in the IR spectrum, which we surmised to be produced on the surface of aerosol, as studied in the section 2.6 and 2.7. ONONO<sub>2</sub> can also react with intermediates from HONO formation, such as GInt5 and GInt6, as shown in Scheme 5. N atoms on GInt5 and GInt6 are *sp*<sup>2</sup> hybridized, not as electron-rich as the *sp*<sup>3</sup> hybridized ones, therefore barriers to abstract H from GInt5 and GInt6 to form HNO<sub>3</sub> are about 10 kcal/mol higher than H-abstractions from MMH.

#### 4.2.6 Reactions facilitated by aerosol to form CH<sub>3</sub>ONO<sub>2</sub>

Several experiments indicate that NO<sub>2</sub> can react with water or alcohol heterogeneously (surface-catalyzed)<sup>19, 22</sup>, probably via the same ONONO<sub>2</sub> intermediate<sup>19</sup>. The aerosol of ONO<sup>-</sup> and MMH cation (such as Sint1-Sint4) provides polar ionic surface that can stabilize the asymmetric ONONO<sub>2</sub> and promote nitrate formation. This pathway can be favored at higher NO<sub>2</sub> concentrations because ONONO<sub>2</sub> concentration is proportional to [NO<sub>2</sub>]<sup>2</sup>, which also explain the experimental observation that the formation of methyl nitrate was only observed in the NO<sub>2</sub>-rich atmosphere. Because asymmetric ONONO<sub>2</sub> has high dipole moments (3.45D for *cis* and 2.96D



for *trans* at B3LYP/6311+G\* level),<sup>20</sup> we expect the concentration of ONONO<sub>2</sub> to be greatly increased if it is absorbed on a polar surface or formed a molecular complex with a polar molecule.

To study reactions between ONONO<sub>2</sub> and MMH on the polar surface or the sub-surface of the aerosol, we used an implicit solvation model to include the interaction between reactants and surrounding ions. Our proposed reaction mechanism between MMH and ONONO<sub>2</sub> and the corresponding enthalpies are shown in Scheme 6.

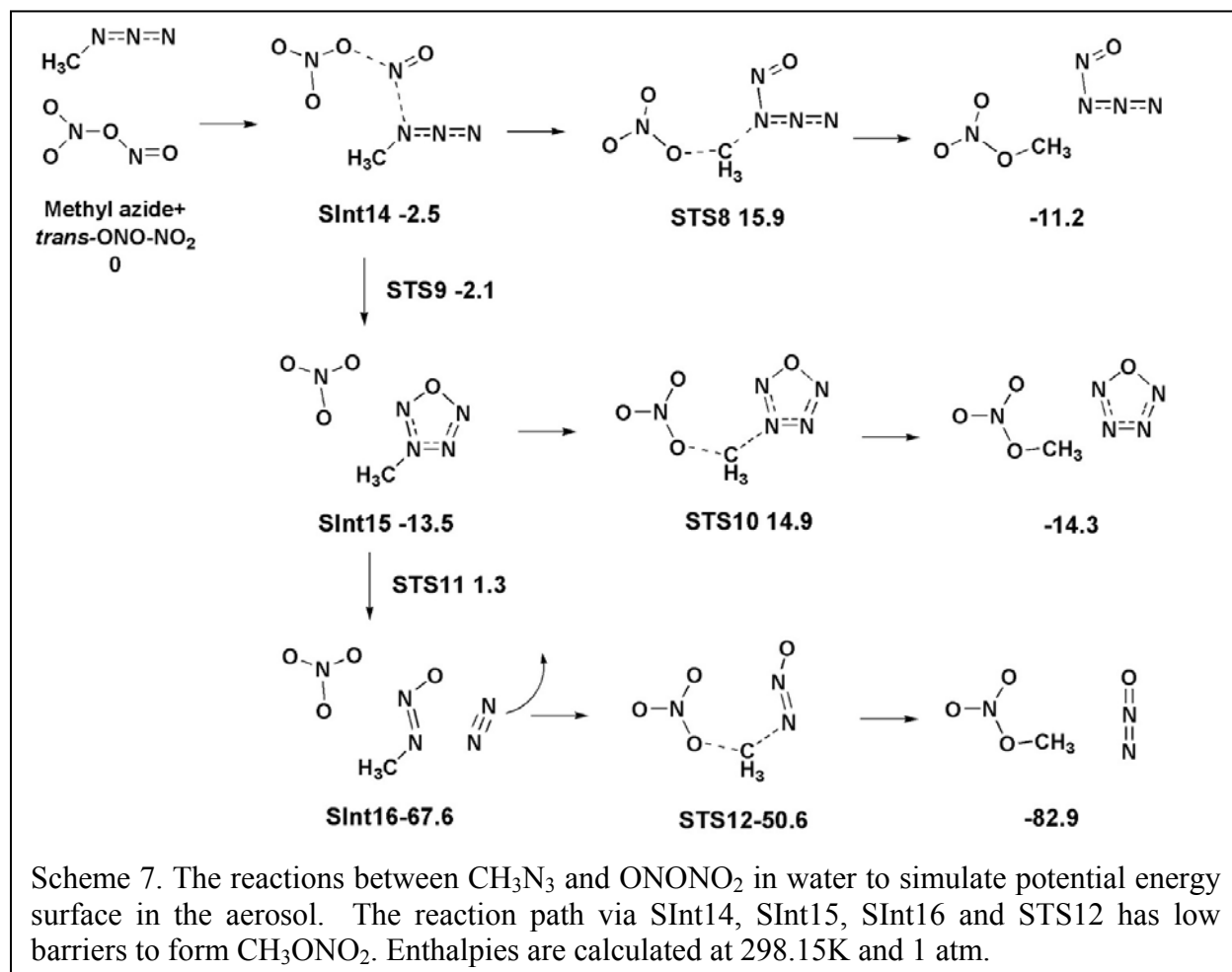
In solution phase, ONONO<sub>2</sub> has strong tendency to dissociate into NO<sub>3</sub><sup>-</sup> and NO<sup>+</sup> with the presence of electron-rich MMH. The electron-deficient NO<sup>+</sup> makes N-N bond with the electron-rich N, preferably the methyl substituted N, on MMH to form SInt5 and SInt6. From SInt5, nitrate anion can attack from the back methyl group to form methyl nitrate with 35.7 kcal/mol barrier.

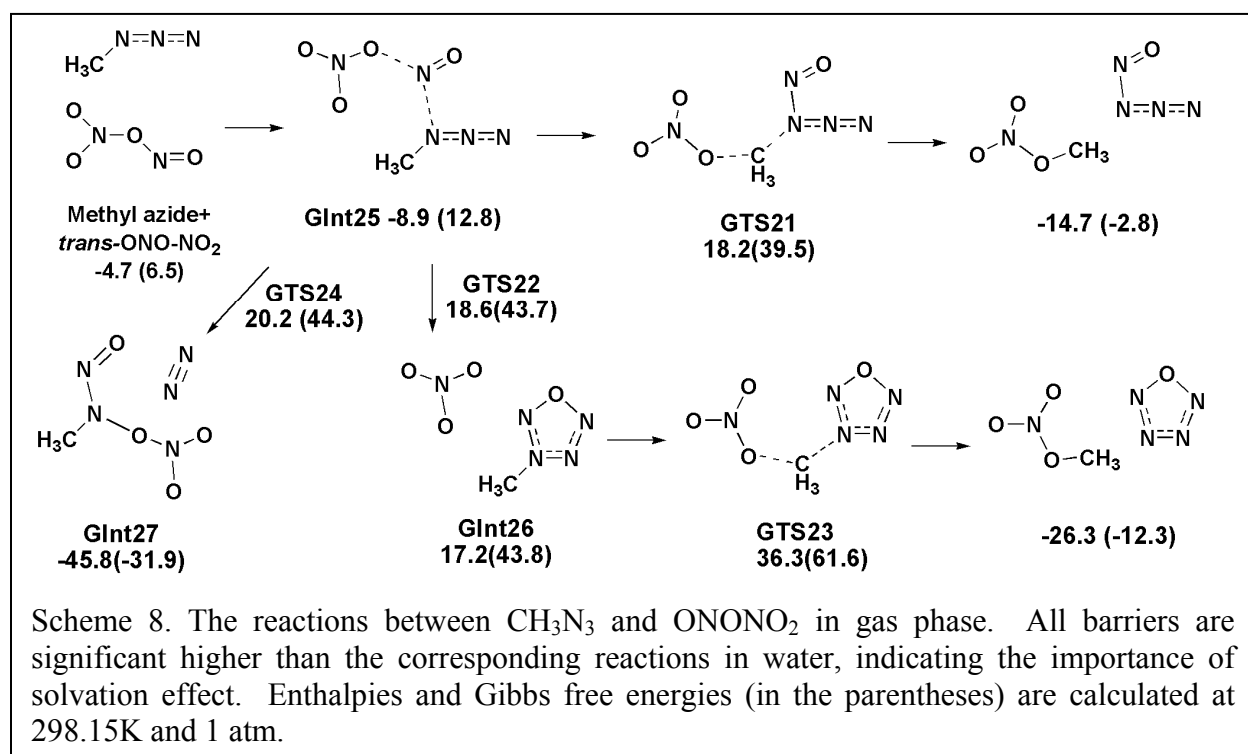
Once the N-N bond is formed, the acidity of the adjacent N-H bond increases and the overall complex is similar to the salt generated from the neutralization between HNO<sub>3</sub> and corresponding amine. We assumed that the proton transfer in such a polar environment has a

low barrier. Therefore to study tautomers as intermediates is enough to depict the potential energy surface. In our calculations, these tautomers are tightly constrained to conserve the number of protons, while in aerosol protons can exchange with the environment, implying our barriers should be the upper bounds of true barriers.

Even with free nitrate anion in aerosol, the barriers for the nucleophilic substitution of the methyl group on MMH are considerable. Among several possible tautomers, SInt8 and SInt11 are the easiest two to form  $\text{CH}_3\text{ONO}_2$  via STS3 and STS4 to SInt9, with barriers 36.2 and 33.3 kcal/mol, respectively, giving the final products, hydrazoic acid and water. It is also possible to form  $\text{N}_2\text{O}$  and methyl amine by breaking the N-N bond in SInt12 via STS5 with 13.7 kcal/mol barrier, corresponding to the experimental observation of  $\text{N}_2\text{O}$ .

An easier path to form  $\text{CH}_3\text{ONO}_2$  involves the intermediate  $\text{CH}_3\text{N}_3$  formed via STS6 with 15.9 kcal/mol enthalpic barrier. As shown in Scheme 7, in solution phase,  $\text{CH}_3\text{N}_3$  prefers to react with  $\text{ONONO}_2$  to form a 5-member ring intermediate (SInt15) with negligible barrier, which then decomposes to release  $\text{N}_2$  with 14.8 kcal/mol barrier, and the product (SInt16) undergoes nucleophilic attack of nitrate to form  $\text{CH}_3\text{ONO}_2$  and  $\text{N}_2\text{O}$  with 17.0 kcal/mol enthalpic barrier and 32.3 kcal/mol exothermicity. This mechanism fits to the fact that azide reacts completely with  $\text{NOCl}$  or  $\text{N}_2\text{O}_4$  in condense phase to give nitrate,  $\text{N}_2\text{O}$  and  $\text{N}_2$ .<sup>23</sup> The 5-member ring intermediate and its decomposition pathway have also been reported.<sup>24</sup>





The solvation effect plays an important role in facilitating the decomposition of  $\text{CH}_3\text{N}_3$ , because in gas phase, similar reactions to produce  $\text{CH}_3\text{ONO}_2$  have enthalpic barriers higher than 25 kcal/mol, as shown in Scheme 8. In gas phase, to form the same 5-member ring intermediate via GTS22 has a 27.5 kcal/mol enthalpic barrier. The STS11-like transition state, GTS24, does not connect to a 5-member ring intermediate in the MEP scan, instead it leads to the path to dissociate  $\text{N}_2$  from  $\text{CH}_3\text{N}_3$  directly, with barrier height 29.1 kcal/mol. These reaction paths do not lead to rapid production of  $\text{CH}_3\text{ONO}_2$ , leading to the conclusion that the formation of  $\text{CH}_3\text{N}_3$  and  $\text{CH}_3\text{ONO}_2$  take place on the surface of aerosol but not in gas phase.

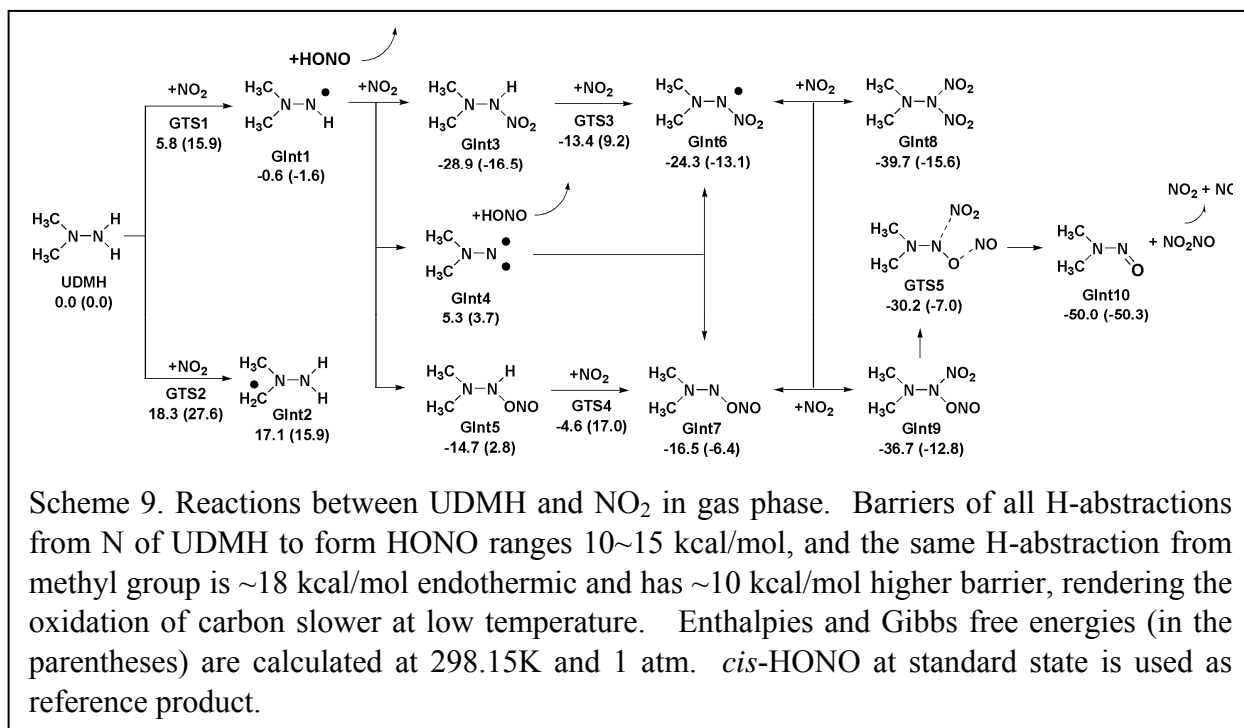
Once  $\text{N}_2\text{O}$ ,  $\text{CH}_3\text{ONO}_2$ , and  $\text{CH}_3\text{N}_3$  are formed on the surface of aerosol, they can desorb and drive reactions further towards completion. The energetics is favorable due to the partial oxidation of MMH. Also the exchange between gas phase and aerosol species is plausible -  $\text{NO}_2$  can be absorbed onto the aerosol surface and oxidize intermediates shown in Scheme 4, leading to a complicated multiphase picture of pre-ignition reactions.

#### 4.2.7 Conclusions

We determined the atomistic mechanism for the reaction between MMH and  $\text{NO}_2$  vapor to compare with spectroscopic experiments carried out in a gold-coated chamber reactor with Fourier transform infrared spectrometry at both MMH-rich and  $\text{NO}_2$ -rich conditions.

At low concentration of  $\text{NO}_2$  the major products are  $\text{MMH}\cdot\text{HONO}$  and  $\text{CH}_3\text{N}=\text{NH}$  and the minor products are  $\text{N}_2\text{O}$ ,  $\text{CH}_3\text{N}_3$ ,  $\text{CH}_3\text{NO}_2$  and  $\text{CH}_3\text{ONO}$ . Our QM calculations elucidate the various mechanisms of H-abstraction by  $\text{NO}_2$  from MMH to form HONO, which then forms condensate by reacting with MMH in fuel-rich condition. We find that  $\text{CH}_3\text{N}=\text{NH}$  is formed after a second H-abstraction from MMH. Further H-abstraction produces  $\text{CH}_3\text{ONO}$ ,  $\text{CH}_3\text{NO}_2$  and  $\text{N}_2$ .

At higher concentrations of  $\text{NO}_2$  the major products are monomethylhydrazinium nitrite and methyl nitrate. We find that formation of methyl nitrate arises from the *asymmetric* isomer  $\text{ONONO}_2$  of  $\text{N}_2\text{O}_4$ , which is favored at high  $\text{NO}_2$  concentration.



Our *ab-initio* calculations indicate that further reactions between MMH and ONONO<sub>2</sub> facilitated by the surface of the aerosol or inside can generate CH<sub>3</sub>ONO<sub>2</sub>, CH<sub>3</sub>N<sub>3</sub> and N<sub>2</sub>O, products observed in NO<sub>2</sub>-rich experimental conditions. This study illustrates the heterogeneous nature of the pre-ignition reactions between MMH and NO<sub>2</sub>.

#### 4.3 DFT Investigations of Early Reactions of Unsymmetric Dimethylhydrazine (UDMH) with Mixtures of NO<sub>2</sub> and N<sub>2</sub>O<sub>4</sub>

Based on our computational work in Section 2, we proposed the following mechanism for MMH reacting with NO<sub>2</sub>: (1) sequential H-abstraction to form HONO, which further reacts with MMH to give MMH·nHONO, and (2) reaction of MMH with asymmetric ONONO<sub>2</sub> to give nitrate salts and CH<sub>3</sub>N<sub>3</sub>. The later further reacts with ONONO<sub>2</sub> to give the production of CH<sub>3</sub>ONO<sub>2</sub>. All other reaction paths we examined to give CH<sub>3</sub>ONO<sub>2</sub> have too high barriers to account for its formation. In other words, CH<sub>3</sub>N<sub>3</sub> is the necessary intermediate for the generation of CH<sub>3</sub>ONO<sub>2</sub>. To form CH<sub>3</sub>N<sub>3</sub>, the last step is the proton transfer from the N with methyl group to the proton acceptor (nitrate in this case), as illustrated in Scheme 6. In general methyl transfer has much higher barrier than proton transfer, therefore if MMH is replaced by UDMH in this mechanism, the last step of CH<sub>3</sub>N<sub>3</sub> formation should be hindered for the higher barrier to transfer CH<sub>3</sub> group, consequently decelerating the formation of CH<sub>3</sub>ONO<sub>2</sub>. To verify this hypothesis, we carried out theoretical studies on the gas phase reaction between UDMH and NO<sub>2</sub>, aiming to further elucidate the preignition reactions between hydrazine derivatives and NO<sub>2</sub>.

### 4.3.1 H-atom abstraction from UDMH

The oxidation of UDMH via sequential HONO formation was studied computationally as shown in Scheme 9. The first H-abstraction from N-H bond has 5.8 kcal/mol enthalpic barrier, much lower than stripping H from the CH<sub>3</sub> group, 18.3 kcal/mol, and also lower than the similar H-abstraction from N-H bond in MMH, 9.8 kcal/mol, which can be attributed to the one more electron-donating CH<sub>3</sub> group.

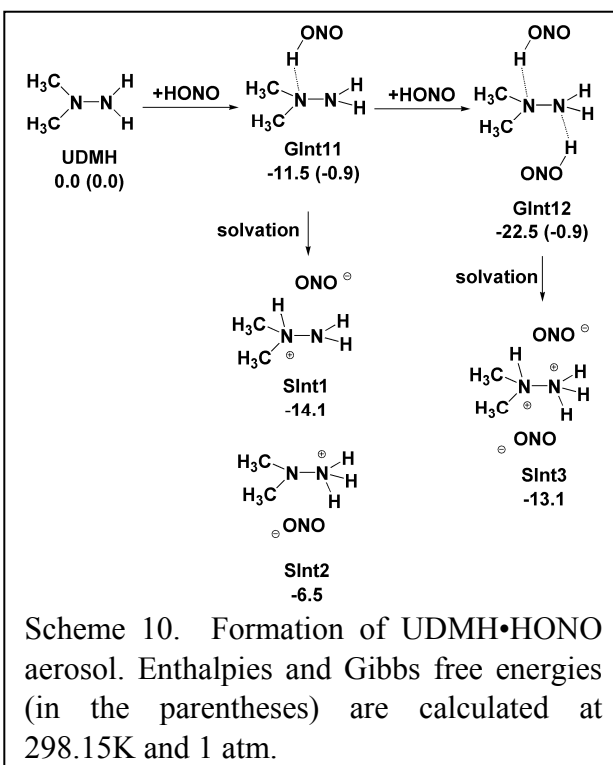
Given the more than 10 kcal/mol difference in GTS1 and GTS2, we consider only reactions beyond GInt1. This free radical can barrierlessly either recombine with the other NO<sub>2</sub> to give GInt3 and GInt5, or undergo H-abstraction to form GInt4. The second H-abstraction from GInt3 via GTS3 has barrier 15.5 kcal/mol, and from GInt5 via GTS4, 10.1 kcal/mol, both of which are thermally accessible at room temperature. The recombination between GInt6 and GInt7 with NO<sub>2</sub> gives GInt8 and GInt9. All intermediates mentioned above but GInt2 are interconvertible at room temperature because their free energy differences are within 20 kcal/mol window. The only irreversible channel is from GInt9 via GTS5 to GInt10, where a stable N-O double bond is formed. This GInt10 was experimentally detected in the gas phase reaction between UDMH and NO<sub>2</sub> as the major product.

### 4.3.2 Formation of UDMH•HONO aerosol

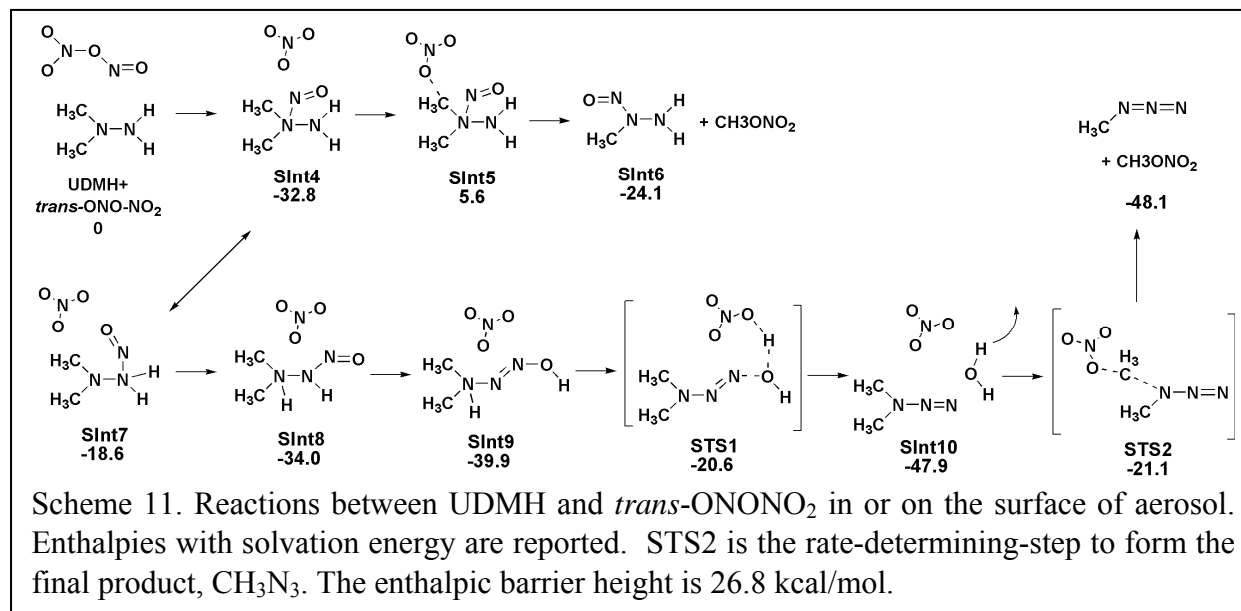
In Scheme 9, HONO is produced and able to form aerosol with unreacted UDMH because the basic N atoms on UDMH are able to accept a proton from HONO. As shown in Scheme 10, protons in UDMH•*n*HONO complexes in gas phase prefer to stay on HONO. The complexes formations are very enthalpically exothermic (-11.5 for GInt11 and -22.5 kcal/mol for GInt12) and slightly favored in free energy. In the strong solvation environment (in the aerosol), the proton transfer from HONO to UDMH is more favored and exothermic, which accounts for the observation of ONO<sup>-</sup> anion in the IR spectra. SInt1 and SInt2 are close in enthalpy, hence the pathways for continued growth and composition of the aerosol can be either UDMH<sup>2+</sup>•2ONO<sup>-</sup> or UDMH<sup>+</sup>•ONO<sup>-</sup>. In the oxidizer-rich case, however, the former composition is more likely. The spontaneous nucleation in gas phase followed by the exothermic growth make the aerosol formation a rapid process as observed in the experiment.

### 4.3.3 Reactions facilitated by aerosol to form CH<sub>3</sub>N<sub>3</sub> and then CH<sub>3</sub>ONO<sub>2</sub>

In Section 2, we concluded that NO<sub>2</sub> tends to dimerize into ONONO<sub>2</sub> on polar ionic surface of aerosol for the high dipole moments of the asymmetric ONONO<sub>2</sub> dimer.<sup>20</sup> To study reactions between ONONO<sub>2</sub> and UDMH on the polar surface or the sub-surface of the aerosol, the implicit dielectric solvation model is used to include the interaction between reactants and surrounding ions. Our proposed reaction mechanism between UDMH and ONONO<sub>2</sub> and the corresponding enthalpies are shown in Scheme 11.



Scheme 10. Formation of UDMH•HONO aerosol. Enthalpies and Gibbs free energies (in the parentheses) are calculated at 298.15K and 1 atm.



In solution phase, ONONO<sub>2</sub> has strong tendency to dissociate into NO<sub>3</sub><sup>-</sup> and NO<sup>+</sup>. The latter is electron-deficient and makes N-N bond with the dimethyl substituted nitrogen, which is electron-rich for the electron-pushing effect of CH<sub>3</sub> group. The migration of NO<sup>+</sup> from the dimethyl N to dihydro N (SInt4 to SInt7) raises the enthalpy by 14.2 kcal/mol. A series of proton migration give SInt8 and SInt9 that are more stable than SInt4 by 1.2 and 7.1 kcal/mol. From SInt9 a proton-transfer-coupled N-O bond-breaking dissociates water from UDMH and leaves cationic dimethyl-azide as the stable product. In the case of MMH, the next step is to give the proton away spontaneously to form CH<sub>3</sub>N<sub>3</sub>. However in the case of UDMH, the enthalpic barrier to transfer methyl cation to nitrate is 26.8 kcal/mol, making this TS the rate-determining step to form CH<sub>3</sub>N<sub>3</sub>. The produced CH<sub>3</sub>N<sub>3</sub> then further reacts with ONONO<sub>2</sub> to give one more CH<sub>3</sub>ONO<sub>2</sub> as previously reported.<sup>25</sup> Based on this barrier height 26.8 kcal/mol the reaction rate at 323K is estimated to be ~20 times faster than the one at 298K. This mechanism agrees well with the experimental observation that at 298K, the CH<sub>3</sub>ONO<sub>2</sub> production is very slow, and at 323K higher substantial CH<sub>3</sub>ONO<sub>2</sub> is observed.

#### 4.3.4 Conclusions

We used with DFT calculations to determine the atomistic mechanism for reactions between UDMH and NO<sub>2</sub>. The reactions between UDMH and NO<sub>2</sub> start with H-abstraction, just as for MMH. However unlike MMH, which ultimately is oxidized to N<sub>2</sub>, UDMH has one nitrogen saturated with two methyl groups, therefore at low temperature its oxidation stops at N-methyl-N-nitroso-methanamine (GInt10), which is detected in the experimental IR spectrum. Our new mechanism also predicts slower CH<sub>3</sub>ONO<sub>2</sub> production because CH<sub>3</sub>ONO<sub>2</sub> mostly comes from CH<sub>3</sub>N<sub>3</sub>. We find that it is more difficult to form CH<sub>3</sub>N<sub>3</sub> from UDMH than MMH due to the higher barrier of methyl transfer. This result is fully consistent with the experimental IR studies carried out by Penn State group.

## 5. References

1. (a) Breisach, P.; Takimoto, H. H.; Denault, G. C.; Hicks, W. A., Simultaneous mass spectrometric differential thermal analyses of nitrate salts of monomethylhydrazine and methylamine. *Combust. Flame* **1970**, *14* (1-3), 397-403; (b) Frank, I.; Hammerl, A.;



- Klapotke, T. M.; Nonnenberg, C.; Zewen, H., Processes during the hypergolic ignition between monomethylhydrazine (MMH) and dinitrogen tetroxide ( $\text{N}_2\text{O}_4$ ) in rocket engines. *Propellants Explosives Pyrotechnics* **2005**, *30* (1), 44-52; (c) Seamans, T. F.; Vanpee, M.; Agosta, V. D., Development of a fundamental model of hypergolic ignition in space-ambient engines. *AIAA Journal* **1967**, *5* (9), 1616-1624.
2. Mayer, S. W.; Taylor, D.; Schieler, L., Preignition Products from Propellants at Simulated High-Altitude Conditions. *Combust. Sci. Technol.* **1969**, *1* (2), 119-129.
  3. (a) William R. Anderson, M. J. M., Michael J. Nusca, and Anthony J. Kotlar, A Detailed, Finite-Rate, Chemical Kinetics Mechanism for Monomethylhydrazine-Red Fuming Nitric Acid Systems. **2010**; (b) McQuaid, M. J.; Ishikawa, Y., H-atom abstraction from  $\text{CH}_3\text{NHNH}_2$  by  $\text{NO}_2$ : CCSD(T)/6-311++G(3df,2p)//MPWB1K/6-31+G(d,p) and CCSD(T)/6-311+G(2df,p)//CCSD/6-31+G(d,p) calculations. *J. Phys. Chem. A* **2006**, *110* (18), 6129-6138; (c) Chen, C.-C.; Nusca, M. J.; McQuaid, M. J. *Modeling Combustion Chamber Dynamics of Impinging Stream Vortex Engines Fueled with Hydrazine-Alternative Hypergols*; 2008; (d) Ishikawa, Y.; McQuaid, M. J., Reactions of  $\text{NO}_2$  with  $\text{CH}_3\text{NHNH}$  and  $\text{CH}_3\text{NHNH}_2$ : A direct molecular dynamics study. *Journal of Molecular Structure-Theochem* **2007**, *818* (1-3), 119-124.
  4. Frota, O. M., B.; Ford, M., Proposed Selection Criteria for Next Generation Liquid Propellants. *Proceedings of the 2nd International Conference on Green Propellants for Space Propulsion (ESA SP-557)*. **2004**.
  5. Co., P. P., Petroleum Derivable Nitrogen Compounds as Liquid Rocket Fuels. In *Report 1478-56R, Phillips Petroleum Co*, 1956.
  6. Wang, S. Q.; Thynell, S. T.; Chowdhury, A., Experimental Study on Hypergolic Interaction between N,N,N',N'-Tetramethylethylenediamine and Nitric Acid. *Energy Fuels* **2010**, *24*, 5320-5330.
  7. Wang, S. Q.; Thynell, S. T., unpublished result. The experimental setting to measure the ignition delay is the same as described in Ref 6. **2010**.
  8. Jaguar, *Schrodinger, LLC, New York, NY* **2007**.
  9. Tannor, D. J.; Marten, B.; Murphy, R.; Friesner, R. A.; Sitkoff, D.; Nicholls, A.; Ringnalda, M.; Goddard, W. A.; Honig, B., Accurate first principles calculation of molecular charge-distributions and solvation energies from ab-initio quantum-mechanics and continuum dielectric theory. *J. Am. Chem. Soc.* **1994**, *116* (26), 11875-11882.
  10. Addison, C. C., Dinitrogen tetroxide, nitric-acid, and their mixtures as media for inorganic reactions. *Chem. Rev. (Washington, DC, U. S.)* **1980**, *80* (1), 21-39.
  11. Zhao, Y.; Truhlar, D. G., The M06 suite of density functionals for main group thermochemistry, thermochemical kinetics, noncovalent interactions, excited states, and transition elements: two new functionals and systematic testing of four M06-class functionals and 12 other functionals. *Theor. Chem. Acc.* **2008**, *120* (1-3), 215-241.
  12. (a) Valiev, M.; Bylaska, E. J.; Govind, N.; Kowalski, K.; Straatsma, T. P.; Van Dam, H. J. J.; Wang, D.; Nieplocha, J.; Apra, E.; Windus, T. L.; de Jong, W., NWChem: A comprehensive and scalable open-source solution for large scale molecular simulations. *Comput. Phys. Commun.* **2010**, *181* (9), 1477-1489; (b) Hirata, S., Tensor contraction engine: Abstraction

- and automated parallel implementation of configuration-interaction, coupled-cluster, and many-body perturbation theories. *J. Phys. Chem. A* **2003**, *107* (46), 9887-9897.
13. Stone, D. A., Atmospheric chemistry of propellant vapors. *Toxicol. Lett.* **1989**, *49* (2-3), 349-360.
  14. Catoire, L.; Chaumeix, N.; Paillard, C., Chemical kinetic model for monomethylhydrazine/nitrogen tetroxide gas-phase combustion and hypergolic ignition. *J. Propul. Power* **2004**, *20* (1), 87-92.
  15. Bedford, G.; Thomas, J. H., Reaction between ammonia and nitrogen-dioxide. *Journal of the Chemical Society-Faraday Transactions I* **1972**, *68* (11), 2163-2170.
  16. Saad, M. A.; Detweiler, M. B.; Sweeney, M. A., Analysis of reaction products of nitrogen tetroxide with hydrazines under nonignition conditions. *Aiaa Journal* **1972**, *10* (8), 1073-1078.
  17. Liu, W. G.; Dasgupta, S.; Zybin, S. V.; Goddard, W. A., First Principles Study of the Ignition Mechanism for Hypergolic Bipropellants: N,N,N',N'-Tetramethylethylenediamine (TMEDA) and N,N,N',N'-Tetramethylmethylenediamine (TMMDA) with Nitric Acid. *J. Phys. Chem. A* **2011**, *115* (20), 5221-5229.
  18. Wang, S. Q.; Thynell, S. T., An experimental study on the hypergolic interaction between monomethylhydrazine and nitric acid. *Combust. Flame* **2012**, *159* (1), 438-447.
  19. Finlayson-Pitts, B. J.; Wingen, L. M.; Sumner, A. L.; Syomin, D.; Ramazan, K. A., The heterogeneous hydrolysis of NO<sub>2</sub> in laboratory systems and in outdoor and indoor atmospheres: An integrated mechanism. *Phys. Chem. Chem. Phys.* **2003**, *5* (2), 223-242.
  20. Liu, W.-G.; Goddard, W. A., First-Principles Study of the Role of Interconversion Between NO<sub>2</sub>, N<sub>2</sub>O<sub>4</sub>, cis-ONO-NO<sub>2</sub>, and trans-ONO-NO<sub>2</sub> in Chemical Processes. *J. Am. Chem. Soc.* **2012**, *134* (31), 12970-12978.
  21. Lai, K. Y.; Zhu, R. S.; Lin, M. C., Why mixtures of hydrazine and dinitrogen tetroxide are hypergolic? *Chem. Phys. Lett.* **2012**, *537*, 33-37.
  22. (a) Svensson, R.; Ljungstrom, E.; Lindqvist, O., Kinetics of the reaction between nitrogen-dioxide and water-vapor. *Atmos. Environ.* **1987**, *21* (7), 1529-1539; (b) England, C.; Corcoran, W. H., Kinetics and mechanisms of gas-phase reaction of water-vapor and nitrogen-dioxide. *Industrial & Engineering Chemistry Fundamentals* **1974**, *13* (4), 373-384; (c) Fairlie, A. M.; Carberry, J. J.; Treacy, J. C., A study of the kinetics of the reaction between nitrogen dioxide and alcohols. *J. Am. Chem. Soc.* **1953**, *75* (15), 3786-3789.
  23. (a) *Nitrogen tetroxide*. Hercules Inc.: Wilmington, Del., 1968; (b) Lucien, H. W., The preparation and properties of nitrosyl azide. *J. Am. Chem. Soc.* **1958**, *80* (17), 4458-4460.
  24. Cheng, L. P.; Cao, W. Q., Theoretical study of N<sub>4</sub>X (X = O, S, Se) systems. *Journal of Molecular Modeling* **2007**, *13* (10), 1073-1080.
  25. Liu, W. G.; Wang, S. Q.; Dasgupta, S.; Thynell, S. T.; Goddard, W. A.; Zybin, S.; Yetter, R. A., Experimental and quantum mechanics investigations of early reactions of monomethylhydrazine with mixtures of NO<sub>2</sub> and N<sub>2</sub>O<sub>4</sub>. *Combust. Flame* **2013**, *160* (5), 970-981.

### III.4 Experimental Studies of Condensed-phase Interactions of Hypergolic Propellants (Thynell, Penn State)

#### 1. Abstract

The overall objective of this research is to obtain an understanding of the physical and chemical processes during the condensed-phase interactions of hypergolic propellant pairs. A drop-test setup, coupled with a high-speed camera, was developed to conduct time-resolved studies on the pre-ignition, ignition and post-ignition events during the drop-on-pool interactions of hypergolic pairs. Thin-wire thermocouples were used to trace the temperatures of the liquid reactants and the gaseous products formed during the pre-ignition process. In addition, a confined interaction setup, coupled with rapid scan Fourier transform infrared (FTIR) spectroscopy, was developed to study the gaseous species evolved from the early reactions that occur upon the mixing of small quantity of liquid hypergols. The hypergolic interactions between nitric acid ( $\text{HNO}_3$ ) and two fuels, monomethylhydrazine (MMH) and *N,N,N',N'*-tetramethylethylenediamine (TMEDA), were studied. A three-stage pre-ignition process was identified by high-speed video analysis as well as temperature profile analysis. Major species formed during the gas- and condensed-phase pre-ignition reactions between fuel/oxidizer pairs were studied. Major early reactions were proposed to enrich the ARL's MMH-RFNA and TMEDA-RFNA mechanisms. In addition, the combustion and thermal decomposition of two energetic nitrate compounds,  $\text{MMH} \cdot 2\text{HNO}_3$  and  $\text{TMEDA} \cdot 8\text{HNO}_3$ , which were synthesized from the corresponding hypergolic pairs, were studied.

#### 2. Introduction

##### 2.1 Background

A hypergolic bipropellant is a form of liquid propellant in which ignition occurs spontaneously upon contact between the oxidizer and fuel, thereby eliminating the need for a complex ignition system [1]. The reliable restart capability of these types of engines makes them ideal for spacecraft maneuvering systems. Compared to monopropellants, hypergolic propellants are also less likely to accumulate unburnt fuel and oxidizer in the combustion chamber to dangerous quantities, then detonate when starting. Such a potential catastrophic condition is known as a hard start [2].

The most commonly used hypergolic bipropellants are composed of hydrazine-based fuels and certain oxides of nitrogen such as nitrogen tetroxide (NTO,  $\text{N}_2\text{O}_4$ ) and red fuming nitric acid (RFNA), which is a mixture of nitric acid and nitrogen tetroxide [3]. The most well-known hydrazine-based fuels include hydrazine ( $\text{N}_2\text{H}_4$ ), monomethylhydrazine (MMH,  $\text{CH}_3\text{NHNH}_2$ ), unsymmetrical dimethylhydrazine (UDMH,  $(\text{CH}_3)_2\text{NNH}_2$ ), and their mixtures such as Aerozine 50 (50% hydrazine and 50% UDMH). They have been successfully deployed for decades in rocket engines such as the Russian Proton rocket, US Titan rocket, and Apollo spacecraft [4]. Hydrazine-based hypergols have many advantages such as a short ignition delay, a high density impulse, and a low freezing point, etc. However, the disadvantage of these hypergols is that they are highly toxic. Hydrazine and its derivatives have been shown to be carcinogenic in animal testing, and it is expected that the use of these fuels could pose a potential health hazard to those personnel dealing with their handling. Therefore, researchers have always been looking for potential alternative fuels which are less toxic than hydrazines. Among a series of tertiary amines and azides which have been developed and tested as alternative fuels, *N,N,N',N'*-tetramethylethylenediamine (TMEDA), 2-dimethylaminoethylazide (DMAZ) and their mixtures are of special interest because they are not only less toxic than hydrazines, but also are quite

comparable with hydrazines in terms of performance such as ignition delay and specific impulse [5-7].

In hypergolic propulsion systems, the liquid engines are known as impinging stream engines (ISEs) in which the liquid fuel and oxidizer are injected towards each other in the chamber to achieve hypergolic ignition and subsequent sustainable combustion. In conventional impinging stream engines, the fuel and oxidizer injectors point towards the chamber's axial centerline. In recent years, the U.S. Army Aviation and Missile Research, Development, and Engineering Center (AMRDEC) has also developed a novel hypergolic engine concept which is referred to as the impinging stream vortex engine (ISVE)[8-11]. The fuel and oxidizer injectors are oriented tangential to the chamber wall in an ISVE engine. It is possible that such a modified design can reduce the size of the engine and improve the combustion efficiency. Researchers in AMRDEC are currently trying to develop a computational model to simulate the fluid and combustion dynamics in the ISVE. To achieve such an attempt, they have developed reaction mechanisms for target fuel-oxidizer pairs, including MMH/RFNA, TMEDA/RFNA, DMAZ/RFNA and TMEDA-DMAZ mixture/RFNA [11,12]. The MMH/RFNA mechanism, for example, is composed of 81 species and 513 reactions which are mainly based on the research conducted by Catorie et al. [13,14] on MMH/N<sub>2</sub>O<sub>4</sub> and MMH/O<sub>2</sub> systems, Vanderhoff et al. [15] and Ilincic et al. [16] on nitramines and nitrate esters, as well as by Smith et al. [17] on natural gas combustion. In addition, these mechanisms have only covered gas-phase reactions. In order to use these mechanisms in the ISVE computational model, they have to assume that the liquid fuel and oxidizer were already vaporized at the moment of injection [10], which is of course not the case. In a hypergolic system, condensed-phase reactions will occur between the two liquid streams at the impinging point and among the liquid droplets at their interfaces. The vaporization of the liquids is in fact mainly due to the heat released from the condensed-phase reactions.

Another concern is that this mechanism contains only a few reactions between the fuel molecules and HNO<sub>3</sub> (which is in fact the dominant ingredient of RFNA). For example, only a single MMH-HNO<sub>3</sub> complexation reaction is included in the MMH/RFNA mechanism to represent the reactions between MMH and HNO<sub>3</sub> [12]. Due to these concerns, further effort to improve these mechanisms is desired and is still ongoing.

## 2.2 Objectives

The overall objective of this work is to develop an understanding of the physical and chemical processes during the hypergolic interactions between various fuel-oxidizer pairs. In the first part, the focus is on examining the liquid-phase reactions between various fuels and nitric acid from room temperature to their boiling points. In the second part, this work is focused on the early steps (or pre-ignition reactions) between the fuel and HNO<sub>3</sub> vapors at various elevated temperatures up to 300°C. These relevant species and reactions are of critical importance to accurately predicting the ignition delay.

Another objective of this work is to understand the complex physical processes that occur during the hypergolic interaction between a fuel drop and an oxidizer pool beginning with the liquid-to-liquid contact to gas-phase ignition, which is usually achieved on a very short time scale. Measurement of important parameters, such as ignition delay and transient liquid- and gas-phase temperatures, can provide useful data for further development and validation of the chemical reaction mechanisms.

The target fuels in this work include both MMH, one of the most widely used today, and TMEDA, one of the most promising alternative fuels in the future. The target oxidizer is chosen as nitric acid ( $\text{HNO}_3$ ) in this work.

### 3. Experimental Setups

In this work, several experimental setups are developed to study the physical phenomena as well as chemical reactions between various pairs of hypergolic fuel and oxidizer. Specifically, a drop-on-pool impingement setup is developed to investigate the physical phenomena that occur when a drop of fuel impinges on a liquid oxidizer pool; a confined interaction setup is developed to study the condensed-phase reactions between small amounts of liquid fuels and liquid oxidizers; a rapid thermolysis setup is used to study the thermal decomposition of the nitrates which are synthesized from hypergolic pairs; a strand burner is used to study the burn rate of the energetic nitrates compounds.

#### 3.1 Drop-test Setup

A schematic diagram of the drop test setup is presented in Figure 3.1. About 80  $\mu\text{L}$  nitric acid is placed at the bottom of a  $10 \times 10 \text{ mm}^2$ , 50 mm tall glass cuvette. A section of the cuvette is removed to facilitate the placement of thermocouples for the measurement of temperatures. Three  $\text{Al}_2\text{O}_3$ -coated thermocouples with a diameter of 0.002 inch are mounted on individual Teflon plates stacked vertically. The first thermocouple is  $\frac{1}{2}$  inch above the cuvette bottom, and the spacing between two nearby thermocouples is  $\frac{1}{2}$  inch. Liquid fuel is loaded in a syringe which is inserted into a fixed perpendicular steel holder. A drop of fuel with a volume of approximately 7  $\mu\text{L}$  is produced by releasing the plunger on the syringe, and the drop falls toward the center of oxidizer pool which is 50 mm below. The thermocouples are slightly off-centered to avoid interference with motion of the fuel drop. A He-Ne laser, and a corresponding photodiode, placed underneath the syringe and above the thermocouple assembly, triggers the data acquisition system through a reduction in the photodiode signal as the drop of fuel descends across the laser beam. The flash of luminosity from ignition is detected by a series of photodiodes placed along the wall of the cuvette. Additionally, the temperature of the liquid pool is measured by three thermocouples placed beneath the liquid pool surface. The hypergolic ignition event, as well as the pre- and post-ignition processes, is recorded by a Phantom V710 high-speed camera.

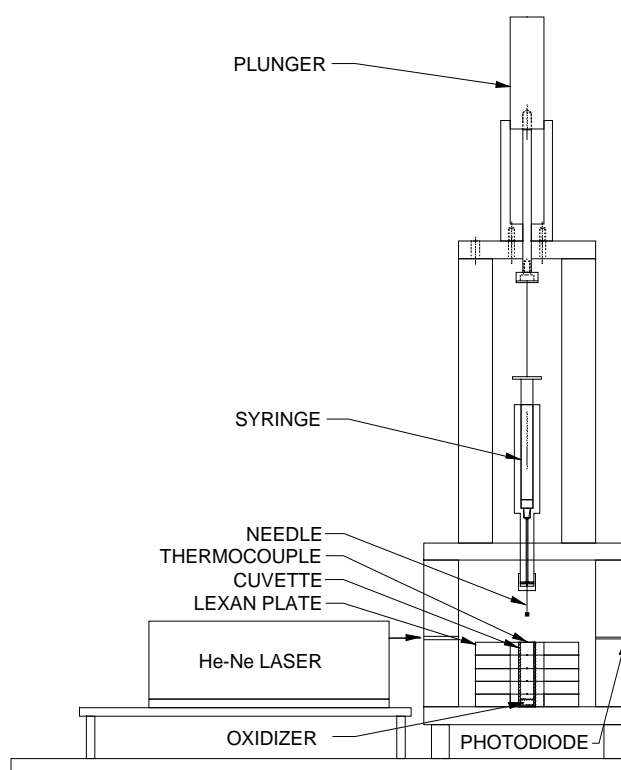


Figure 3.1 Drop-test setup.

#### 3.2 Confined-interaction Setup

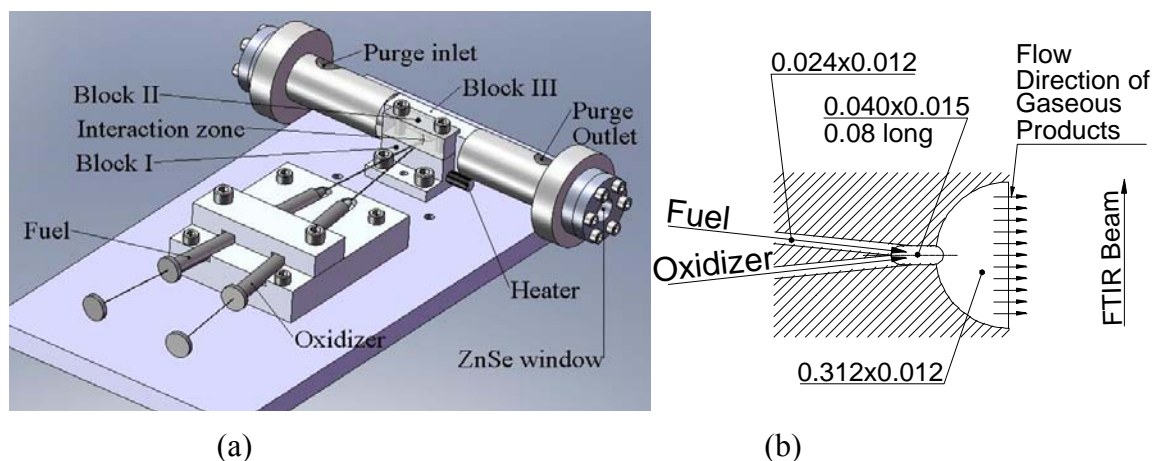


Figure 3.2. a) Overall view of the confined interaction setup, and b) top view and dimensions in inches of the interaction zone machined in block I.

Figure 3.2a shows the assembly of the confined interaction setup. Liquid fuel and oxidizer are loaded in two Hamilton 7100-series syringes, respectively, and therefore the volatile reactants can be kept for a relative long time without any significant loss due to evaporation. The syringes are placed in two rectangular slots on a polycarbonate plate. The two needles of the syringes are inserted into two small channels (0.024 in. diameter) machined on two  $\text{Al}_2\text{O}_3$ -coated stainless steel blocks (block I and II). The channels and contact interface between block I and II are sealed by a perfluoroalkoxy (PFA) polymer or aluminum film to minimize capillary effects. Shown as a partial top view of block I in Fig. 3.2b, the two reactants meet and react in an approximately flat channel (0.08 in. long, 0.04 in. wide and 0.015 in. deep), which is partially occupied by the needle tip. Gases flow into a flat channel that is 0.012 in. deep, which insures high convective heat transfer. The evolved gases from the flat channel are confined in  $\text{N}_2$  purged channel (0.3 in. diameter and 7 in. long) and detected by the modulated beam of the FTIR spectrometer. A ZnSe window is mounted at each end of the channel to provide optical access by the modulated beam of the FTIR spectrometer. A cartridge heater is mounted in block I so that the reaction zone can be heated to any desired temperature up to 300 °C. All the tests were conducted under ambient pressure. The channel is purged by  $\text{N}_2$  before each test and the purging valve is shut off during the test. The spectra of gaseous products are obtained in near real-time with a spectral resolution of  $2\text{ cm}^{-1}$  and a temporal resolution of 50 ms. In each test, 150 spectra are collected, requiring a sample time of 7.5 s. The syringes and reaction zone are cleaned after each test, and the sealing films are replaced.

### 3.3 Strand Burner

Figure 3.3 shows the schematic diagram of the strand burner used for studying the combustion of energetic nitrates which are synthesized from hypergolic pairs. The strand burner is composed of

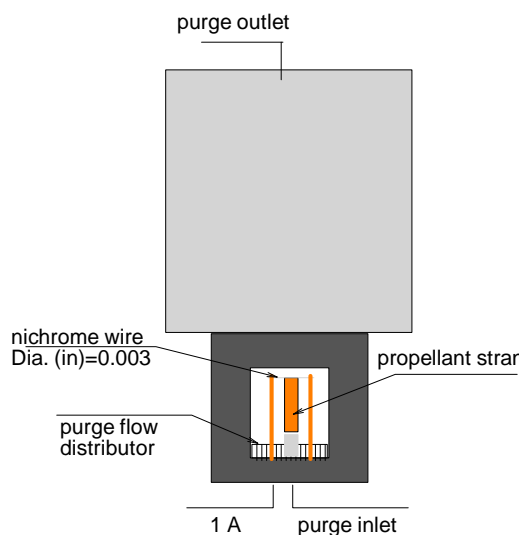


Figure 3.3. Strand burner.

a combustion chamber (bottom portion) and an exhaust chamber (top portion). The strands of monopropellants are placed in the bottom chamber which is purged and pressurized by  $N_2$ . A nichrome wire ( $D = 0.1$  mm), which is mounted on two copper poles and buried straight along the top surface of strand, is used to ignite the monopropellants. A constant electric current of 1 A, which is slightly lower than the maximum allowable current (1.27A) above which the nichrome wire will melt and break apart, is provided by a DC power supply through a high pressure feedthrough. The purging flow is kept running through the chamber from the bottom inlet to the top outlet during the test so that the exhaust gases can be carried out of the chamber rapidly to avoid a sudden chamber pressure increase. Meanwhile, the soot of carbon particles (smoke) from incomplete combustion can also be rapidly blown out of the chamber to maintain a clear optical access to the liquid strand and the flame. The purge gas flow is evenly distributed across the chamber by running through many tiny holes punched on a round plastic piece. The ignition and combustion processes were recorded a Phantom V710 high-speed camera, though an optical access glass window with a thickness of 1 inch. A piece of paper with a printed ruler is placed just behind the strand to record the instantaneous position of the burning surface, which allows the calculation of the regression rates.

### 3.4 Confined rapid Thermolysis (CRT)/FTIR Setup

The experimental technique utilized to study the rapid thermal decomposition of the MMH nitrates is known as confined rapid thermolysis (CRT). Detailed discussion of this technique and the associated data reduction techniques are available in earlier works [18,19]. A short summary of the process is as follows. A small quantity of the nitrates (1.5 mg) is confined and heated rapidly between two heated, parallel, and isothermal surfaces in a constant pressure chamber purged by  $N_2$ . The heated surfaces are achieved by a stationary top heater and a mobile bottom heater, both of which are fitted with a cartridge heater, while temperature control is maintained by PID controllers. The use of a small sample volume enclosed in a confined space, roughly 300  $\mu\text{m}$  in height, enables heating rates in the range of 2000 K/s. The IR-active gaseous species emerging from the condensed phase are quenched by the relatively cooler atmosphere, and detected in real-time by the modulated beam of a Bruker IFS66/S FTIR spectrometer in the rapid scanning mode, scanning at  $2\text{ cm}^{-1}$  with a temporal resolution of 50 ms. In each test, a total of 150 spectra are collected, requiring a sample time of 7.5s.

## 4. Results and Discussion

In this work, results were obtained from drop-on-pool impingement tests and confined-interaction/FTIR tests for hypergolic pairs MMH/ $HNO_3$  and TMEDA/ $HNO_3$ . Detailed discussions on the physical interactions as well as early chemical reactions are available in publications [20-23]. The gas-phase reactions between MMH and  $HNO_3$  were also studied by cooperating with Caltech MURI group and the results were discussed in publication [24]. The combustion characteristics and decomposition chemistry of energetic nitrates, which were prepared from corresponding hypergolic pairs, were studied and detailed discussions are available in publications [25, 26]. In addition, the pressure effect on ignition delay of several hypergolic pairs was investigated and the results were discussed in conference paper [27]. The following is a brief discussion on the results obtained from this work.

#### 4.1 Drop-on-pool Impingement Tests

Drop-on-pool impingement interactions between MMH and three nitric acid solutions are studied. The three nitric solutions are: (1) 90% $\text{HNO}_3$  that contains 10% of  $\text{H}_2\text{O}$ ; (2) white fuming nitric acid (WFNA) that contains less than 0.5% of impurities; and (3) red fuming nitric acid (RFNA) that contains about 12-24%  $\text{N}_2\text{O}_4$  by weight.

##### 4.1.1 MMH/90% $\text{HNO}_3$

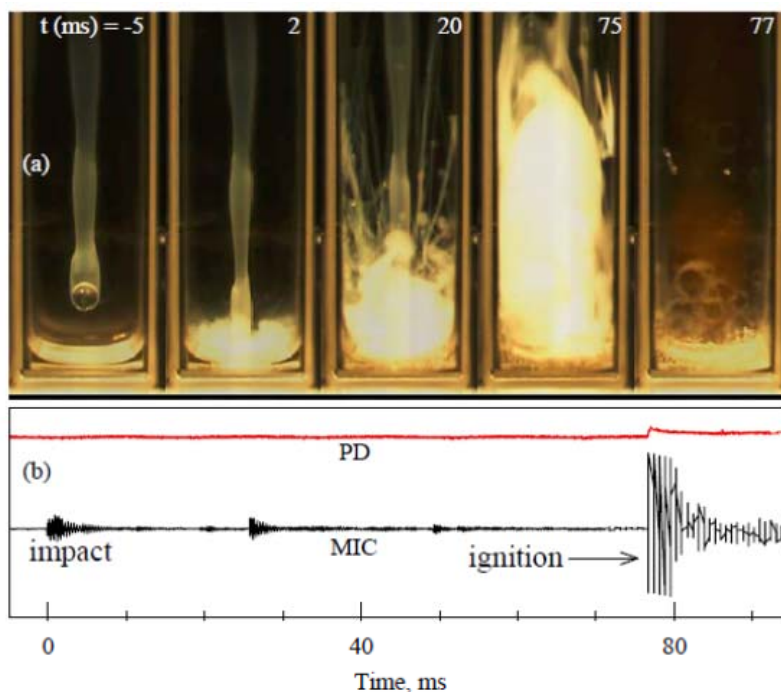


Figure 4.1. a) Selected images from a drop test of MMH (drop) / 90% $\text{HNO}_3$  (pool); and b) signals acquired by photodiode (PD) and microphone (MIC).

Figure 4.1a shows a few selected images from a typical drop test in which a MMH drop ( $7 \mu\text{L}$ ) falls into a 90% $\text{HNO}_3$  pool ( $80 \mu\text{L}$ ). When the MMH droplet traveled vertically down in the cuvette, an aerosol trace was formed from reactions with  $\text{HNO}_3$  vapor which was initially filled in the cuvette. Liquid-phase reactions occurred rapidly upon contact between the two liquids, and a large amount of products accumulated above the liquid surface to form a particulate aerosol cloud. As shown in the images at  $t = 2, 20$ , and  $75$  ms, the aerosol cloud kept growing in the gas phase until at  $t = 77$  ms, it vanished rapidly and a faint luminous flame was observed. Therefore, the ignition delay of this test is about  $77$  ms. The same ignition delay was determined by the photodiode and microphone signals shown in Fig. 4.1b.

Figure 4.2a shows the liquid-phase temperature trace obtained in a typical drop test of MMH/90% $\text{HNO}_3$ . The liquid temperatures increased from room temperature to about  $100^\circ\text{C}$  within a few milliseconds. Temperatures then fluctuated between  $80$  and  $100^\circ\text{C}$  (the boiling point is  $87^\circ\text{C}$  for MMH and  $102^\circ\text{C}$  for 90% $\text{HNO}_3$ ). Since the thermocouple was buried in the liquid, it did not sense the rapid temperature rise at about  $t = 100$  ms due to gas-phase ignition as detected by the photodiode. Figure 4.2b shows the gas-phase temperature traces at two locations as indicated in the figure. The gas-phase temperatures show three distinct stages. In the first stage, temperatures increased from ambient values to around  $100^\circ\text{C}$ , which is close to the boiling point



of 90%  $\text{HNO}_3$ ; in the second stage, gas-phase temperatures gradually increased from 100 to about  $280^\circ\text{C}$  due to the exothermic gas-phase reactions; in the third stage, temperatures increased rapidly from  $280^\circ\text{C}$  to a flame temperature of about  $1350^\circ\text{C}$  at  $t = 95$  ms.

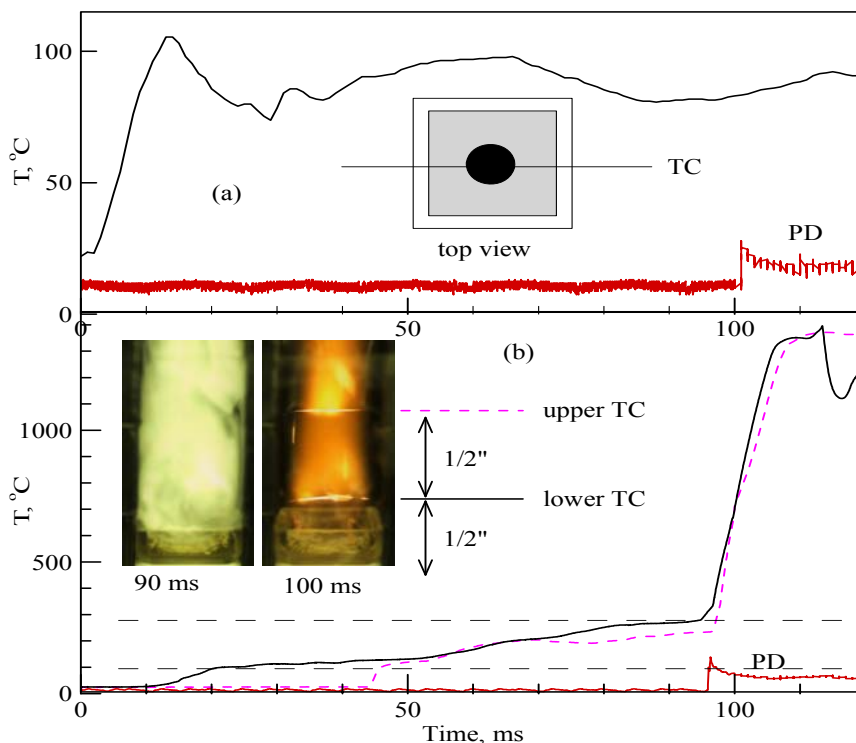


Figure 4.2. Liquid-phase temperature trace (a) and gas-phase temperature traces (b) in a drop test of MMH (drop) / 90% $\text{HNO}_3$  (pool).

#### 4.1.2 MMH/WFNA

Twenty tests were conducted by releasing an MMH droplet into 80  $\mu\text{L}$  of WFNA, with ignition delays varying from 19 to 22 ms. Although all tests were conducted by carefully following the same procedure, two different types of interaction phenomena, shown in Figs. 4.3 and 4.4, respectively, were observed.

In case I (Fig. 4.3), the MMH droplet exploded at  $t = 10$  ms, and the cuvette was quickly filled with a well-mixed mist. At  $t = 22$  ms, the mist suddenly turned into a luminous flame. As shown in Fig. 4.3b, the luminosity from a likely pre-mixed flame lasted only a very short time, and simultaneously, a very loud sound was recorded by the microphone.

In case II (Fig. 4.4), the MMH droplet was ejected from the WFNA pool at  $t = 22$  ms. The aerosol cloud around the droplet vanished rapidly and a luminous flame was formed between the droplet and the pool. From  $t = 22$  to 216 ms, the MMH droplet was smoothly floating on and rolling along the surface of the WFNA pool. A force balance was established between the droplet due to gravity and the repelling force at the interface due to gas flow. At  $t = 218$  ms, the gas flow increased and the drop was pushed further away from the pool. Subsequently, the gas flow decreased causing the droplet to impact the pool again at  $t = 330$  ms. This impacting-repelling type of interaction continued until finally the drop disintegrated. Figure 4.4b shows the photodiode and microphone signals from the same test.

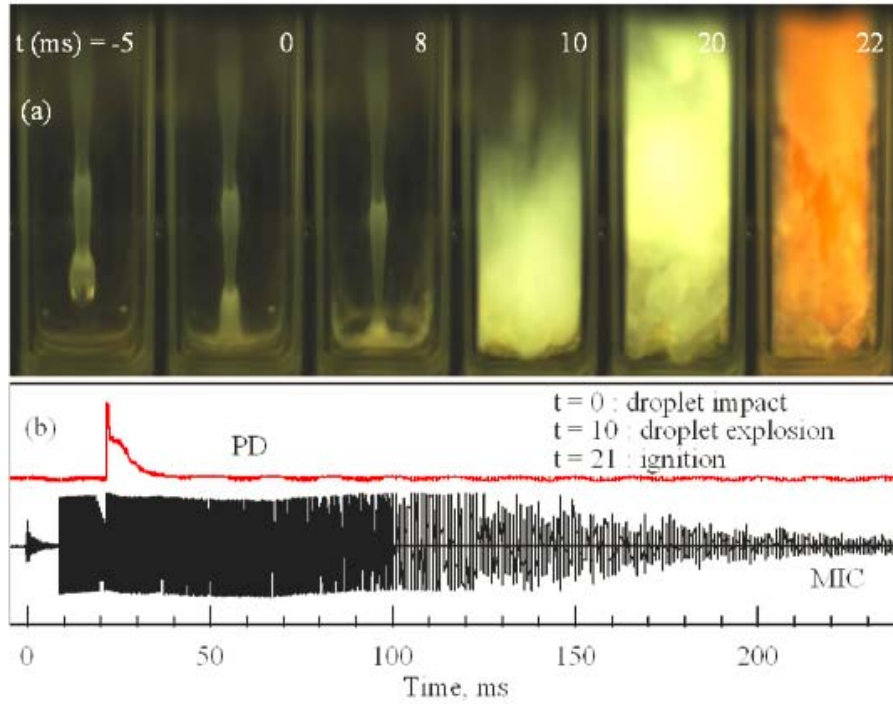


Figure 4.3. a) Selected images from a drop test of MMH (drop) / WFNA (Case I); and b) signals acquired by photodiode (PD) and microphone (MIC).

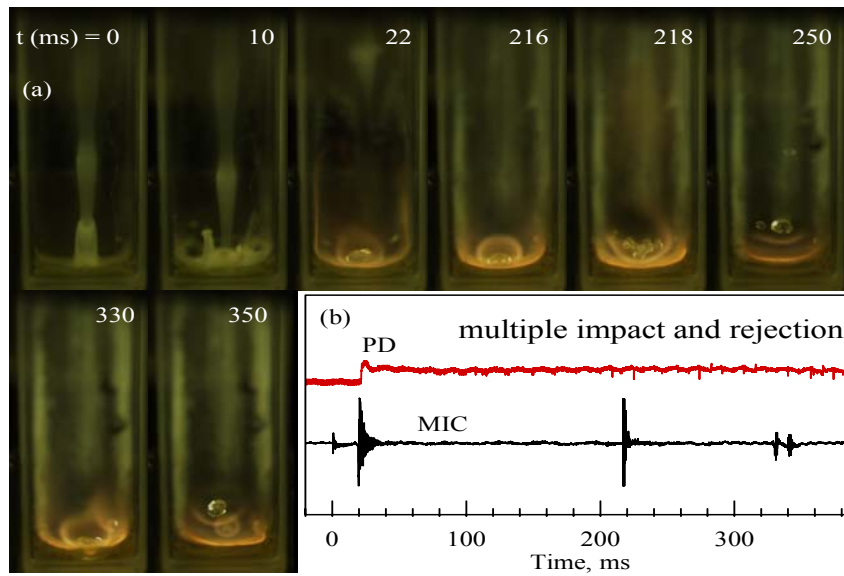


Figure 4.4. a) Selected images from a drop test of MMH (drop) / WFNA (Case II); and b) signals acquired by photodiode (PD) and microphone (MIC).

### 4.1.3 MMH/RFNA

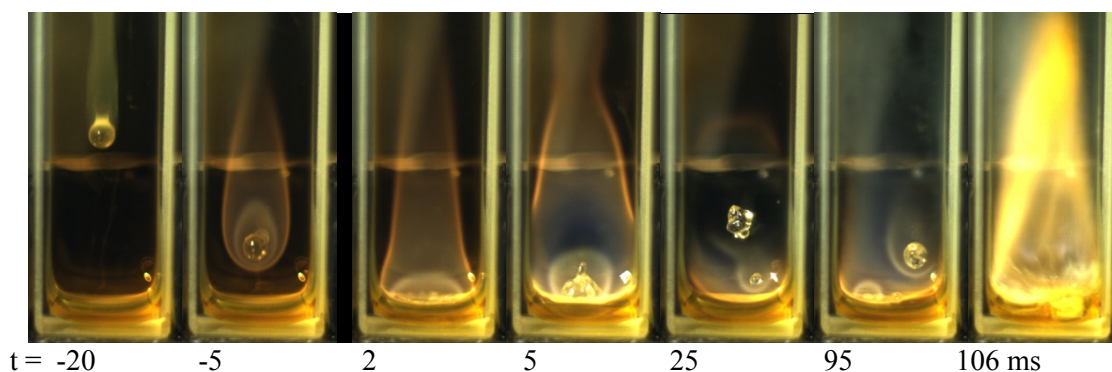


Figure 4.5. Selected images from a drop test of MMH (drop) / RFNA (80  $\mu$ L).

A total of 20 videos were acquired for the interaction between a drop of MMH and RFNA pool. Quite similar to that discussed in the MMH-WFNA section, the MMH droplet may be ejected from the pool or simply exploded after the impact. Figure 4.5 shows a test in which droplet-ejection occurred. A columnar particulate trace was formed due to the reactions with pre-occupied  $\text{HNO}_3$  vapor (as shown at  $t = -20$  ms). However, this particulate trace vanished as the droplet approached closer to the RFNA pool, and an oval-shape luminous flame was observed, as shown at  $t = -5$  ms. This pre-contact ignition was observed only when RFNA was used, which means it is most likely caused by reactions with gaseous  $\text{NO}_2$ . The droplet then plunged into and was ejected from the pool, surrounded with a diffusion flame. At  $t = 106$  ms, the droplet exploded on its second contact with the pool.

### 4.1.4 TMEDA/90% $\text{HNO}_3$

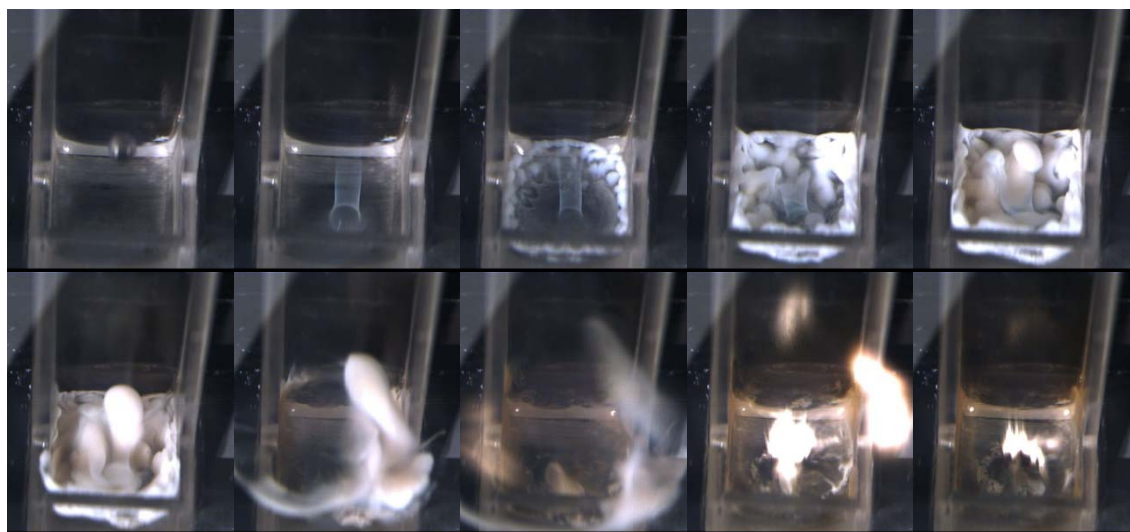


Figure 4.6. Selected frames from a high-speed video for TMEDA (drop) and 90%  $\text{HNO}_3$  (pool),  $t = -5, 0, 10, 30, 45, 60, 75, 90, 110, 130$  ms, respectively.

Figure 4.6 shows a series of selected frames from the drop test of TMEDA and 90%  $\text{HNO}_3$  as the event progresses from the free fall of the droplet to ignition and self-sustained combustion. Figure 4.7 shows the temperatures traces of the liquid pool as well as the gases above the pool.

Time  $t = 0$  corresponds to the instant when the drop hits the pool. When the droplet of TMEDA impacts on the pool of  $\text{HNO}_3$ , exothermic reactions occur rapidly between the two liquids and the liquid temperature increases to about  $100^\circ\text{C}$  within a few milliseconds (the boiling points of  $90\%\text{HNO}_3$  and TMEDA are  $95^\circ\text{C}$  and  $120^\circ\text{C}$ , respectively). The vaporization of the two liquids lead to the formation of a white particulate cloud above the liquid. The particulate cloud is due to the accumulation of TMEDA nitrate that is formed by reactions between the vapors of two reactants. The cloud is growing gradually until a luminous flame is observed at  $t=90\text{ms}$ , which is recorded by the photodiode signal as shown in Fig. 4.7. The particulate cloud disappears due to the rapid temperature increase in the gas region above the liquid.

The transient temperature traces of in the gases above the liquid pool (Fig. 4.7b) show three distinct stages: Stage A (0–63 ms): In this stage, all three thermocouples do not show any appreciable increase of temperature. Stage B (63–94 ms): The bottom and middle thermocouples show a rapid temperature rise from room temperature to around  $120^\circ\text{C}$ , which is probably due to the rapid gasification of nitric acid or a rapid release of gaseous species from condensed-phase reactions. The middle thermocouple senses the temperature rise about 10 ms later than the bottom thermocouple because the gases reach the bottom thermocouple first. The top-most thermocouple did not sense the temperature increase in this stage, because it is too far from the pool's surface. Stage C (94 –125 ms): In this stage, all there thermocouples sense a rapid temperature increase due to the combustion of gaseous species in the cuvette. The maximum temperatures at position 1, 2 and 3 are  $960$ ,  $650$  and  $260^\circ\text{C}$ , respectively.

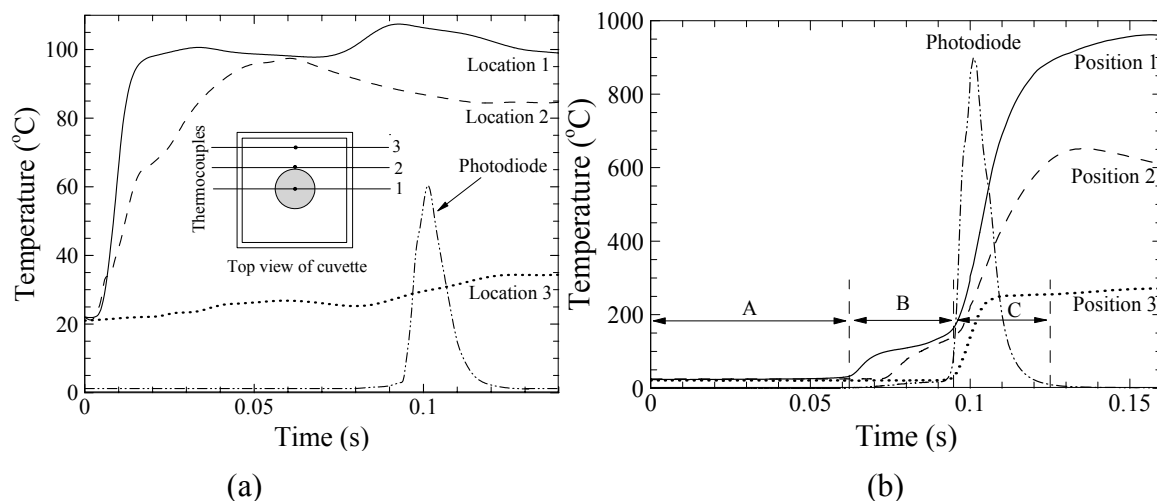


Figure 4.7. Temperature traces of the liquid pool (a) and the gases above the pool (b) in a drop test involving  $80\ \mu\text{L}$  of  $90\%\text{HNO}_3$  and a  $7\ \mu\text{L}$  drop of TMEDA.

## 4.2 Results from confined-interaction/FTIR studies

### 4.2.1 IR analysis of MMH/ $\text{HNO}_3$ interaction

Confined-interaction/FTIR experiments were conducted at a series of preset temperatures ( $20$ ,  $50$ ,  $100$ ,  $150$ ,  $200$  and  $250^\circ\text{C}$ ) in order to identify the pre-ignition products between the interaction of MMH and  $\text{HNO}_3$ .

Figure 4.8 shows the IR spectra of species evolved from the confined interaction between  $0.5\ \mu\text{L}$  of MMH and  $0.5\ \mu\text{L}$  of  $\text{HNO}_3$  at  $20^\circ\text{C}$ . The spectra in Figs. 4.8(a) and (b) were obtained by averaging the first 30 and last 30 spectra out of a total of 150 spectra obtained in the same test.

The major products include monomethylhydrazinium nitrate, methyl nitrate ( $\text{CH}_3\text{ONO}_2$ ), methyl azide ( $\text{CH}_3\text{N}_3$ ),  $\text{N}_2\text{O}$  and  $\text{H}_2\text{O}$ . Figure 4.8(c) shows the time-resolved profiles of major species from the same test discussed above. The IR absorption intensity of each species was normalized to 1. Liquid-phase reactions occurred very fast and all the species evolved almost simultaneously. MMH nitrate then gradually disappeared from IR the spectra. It is most likely that this nitrate salt has extremely low volatility at these temperatures and condensed out on the chamber walls. It is also possible that this salt was further converted to the other species, whose concentrations increased slowly. The IR spectra obtained from confined interaction tests at  $50^\circ\text{C}$  are quite similar with those obtained at  $20^\circ\text{C}$ , thus are not presented and discussed here.

When the interaction zone was preheated to temperatures above the boiling points of reactants, a major portion of the reactants was gasified prior to their liquid-liquid contact. Thus, the reactions mainly occurred in the gas phase. Confined-interaction tests were conducted at 100, 150, 200 and  $250^\circ\text{C}$ .

At 100, 150 and  $200^\circ\text{C}$ , the vapors of MMH and  $\text{HNO}_3$  reacted to form an aerosol cloud which was mainly composed of monomethylhydrazinium nitrate. This type of gas-phase acid-base reactions are usually called ‘gas-to-particle’ or ‘gas-to-aerosol’ reactions. Figure 4.9 shows the averaged IR spectrum of products evolved from a confined interaction experiment at  $200^\circ\text{C}$ , using  $0.1\ \mu\text{L}$  of MMH and  $0.1\ \mu\text{L}$  of  $\text{HNO}_3$ . The dominant product was monomethylhydrazinium nitrate, and minor products were oxidation products  $\text{CH}_3\text{ONO}_2$ ,  $\text{CH}_3\text{N}_3$ ,  $\text{N}_2\text{O}$ ,  $\text{NO}$  and  $\text{H}_2\text{O}$ .

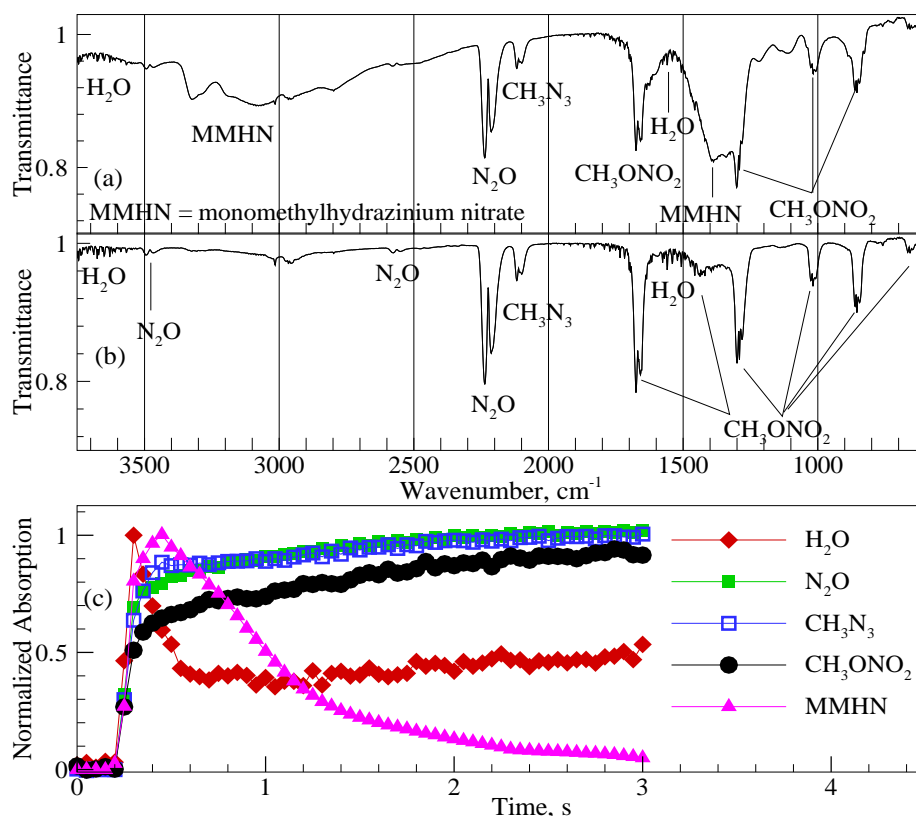


Figure 4.8. a) Average IR spectrum of the first 30 spectra obtained from confined interaction between MMH and  $\text{HNO}_3$  at  $20^\circ\text{C}$  and 1 atm  $\text{N}_2$ ; b) average IR spectrum of the last 30 spectra obtained from the same test; and c) Time-resolved IR absorption of species evolved from the same test (maximum absorption of all species were normalized to 1).

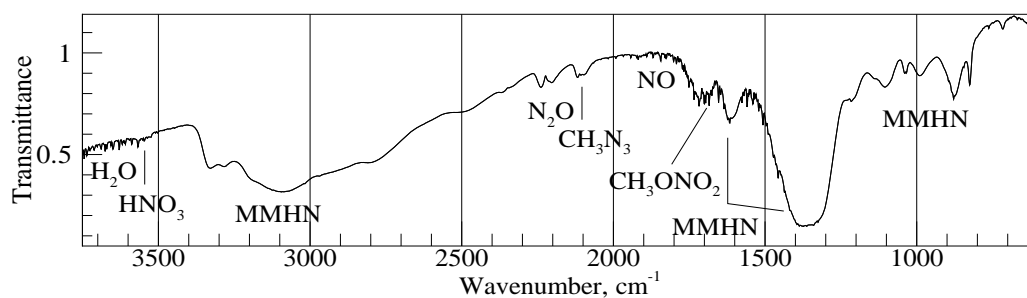


Figure 4.9. IR spectrum from a confined interaction of MMH/ $\text{HNO}_3$  at  $200^\circ\text{C}$ .

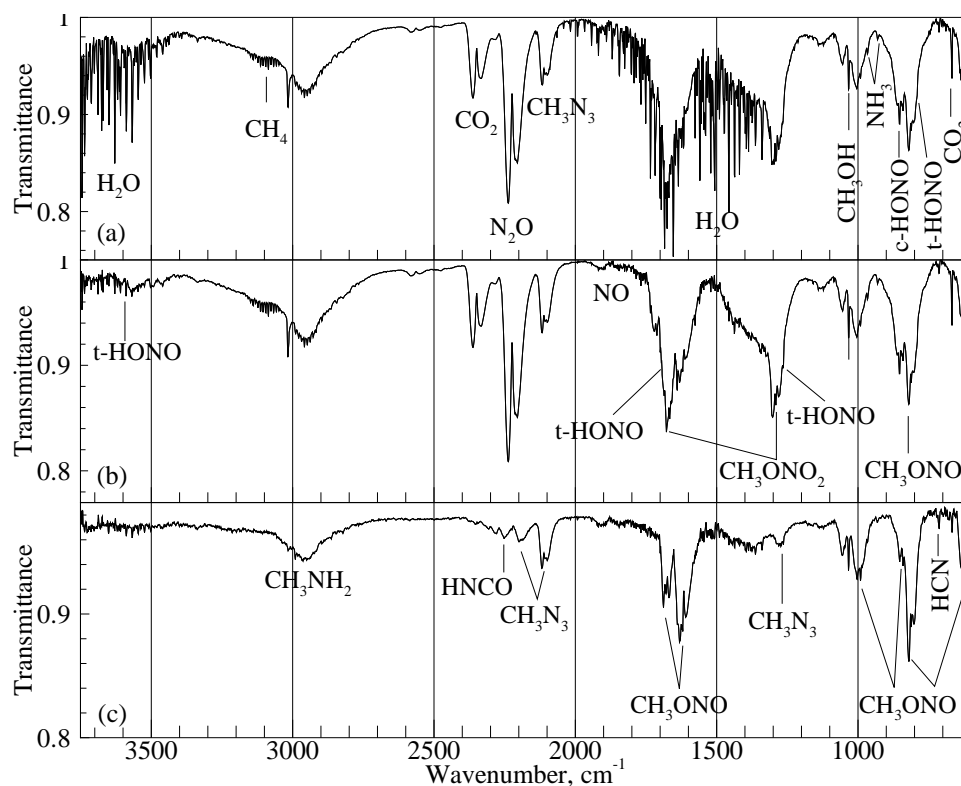


Figure 4.10. a) Average IR spectra from confined interaction between MMH and WFNA at  $250^\circ\text{C}$  and 1 atm  $\text{N}_2$ ; b) IR spectrum obtained by subtracting  $\text{H}_2\text{O}$  from (a); and c) IR spectrum obtained by subtracting  $\text{HONO}$ ,  $\text{CH}_3\text{ONO}_3$ ,  $\text{N}_2\text{O}$ ,  $\text{CO}_2$ , and  $\text{CH}_4$  from b).

Table 4.1. IR frequencies of species in Fig. 4.10 (vs=very strong, s=strong, m=medium)

Species	Major IR bands observed in this work (cm <sup>-1</sup> )	Refs.
HNO <sub>3</sub> , H <sub>2</sub> O, NO <sub>2</sub> , NO, N <sub>2</sub> O, CO <sub>2</sub> , CH <sub>4</sub> , HCN, CH <sub>3</sub> OH and NH <sub>3</sub>	See HITRAN data base	[28]
MMH	3261(s), 2960(vs), 2852(vs), 2785(vs), 1595(m), 1480(s), 1451(s), 1293(m), 1119(s), 968(s), 888(vs), 771(vs)	[29]
MMH Nitrate	3322(s), 3080(s), 2796(m, br), 2495(m), 1617(s), 1460(s), 1383(vs), 1215(m), 1106(m), 1000(m), 882(m), 827(m)	[30]
trans-HONO	3590(m), 1699(s), 1264(s), 791(s)	[31]
cis-HONO	1640(s), 853(s)	[31]
	2269	[31]
HNCO	2190(m), 2107(s), 1276(m)	[32]
CH <sub>3</sub> N <sub>3</sub>	2965(m), 1666(vs), 1435(m), 1290(vs), 1017(s), 855(s), 759(m)	[33]
CH <sub>3</sub> ONO <sub>2</sub>	1678(s), 1620(vs), 991(s), 811(vs)	[34]
CH <sub>3</sub> ONO	2955(s), 1621(m), 1046(m), 782(s)	[35]
CH <sub>3</sub> NH <sub>2</sub>		[36]

Figure 4.10a shows the averaged IR spectrum of products evolved from a confined interaction experiment at 250°C, using 0.1 µL of MMH and 0.1 µL of HNO<sub>3</sub>. The spectra in Fig. 4.10b and 4.10c were obtained by spectral subtraction on the original spectrum in Fig. 4.10a. At 250°C, the formation of monomethylhydrazinium nitrate was not favored. Instead, large amounts of H<sub>2</sub>O and HONO were produced. Other IR-active products include CH<sub>3</sub>ONO<sub>2</sub>, CH<sub>3</sub>ONO, CH<sub>3</sub>N<sub>3</sub>, CH<sub>3</sub>OH, CH<sub>3</sub>NH<sub>2</sub>, CH<sub>4</sub>, N<sub>2</sub>O, NO, and small amounts of HNCO, NH<sub>3</sub>, HCN and CO<sub>2</sub>. IR-inactive species N<sub>2</sub> was also identified in the mass spectrum. The IR bands of each species and corresponding references are listed in Table 4.1.

#### 4.2.2 Early reactions between MMH and HNO<sub>3</sub>

The possible liquid-phase reactions (R1-R14) of MMH/HNO<sub>3</sub> are suggested in Fig. 4.11 and a short description of these reactions is given as follows: MMH contains two electrophilic nitrogen atoms, and as such, it can be mono-protonated (R1) and diprotonated (R2) by nitric acid. The monomethylhydrazinium salt can be further oxidized by excess nitric acid through pathways R3-R14. The initial step of the oxidation of hydrazinium ion in nitric acid solution is believed to be the formation of nitrous acid, H<sub>2</sub>O and a diazene intermediate [37], based on which, reactions R3 and R4 are proposed. In this process, an N-nitrohydrazinium compound [CH<sub>3</sub>NH<sup>+</sup>(NO<sub>2</sub>)NH<sub>2</sub>], which is unstable in acidic solution [38], is suggested as an intermediate species. Similarly, the methyl diazenium cation (CH<sub>3</sub>NH<sup>+</sup>=NH) from reaction R4 can react with nitric acid to form an N-nitrodiazenium intermediate [CH<sub>3</sub>N<sup>+</sup>(NO<sub>2</sub>)=NH] (R5), which can convert into a methyldiazonium ion (CH<sub>3</sub>N<sub>2</sub><sup>+</sup>) through an HONO elimination step (R6). A well-known reaction of diazonium ion is called ‘replacement of nitrogen’ [39], in which the nitrogen is lost as N<sub>2</sub>. For example, methyldiazonium ion can react with H<sub>2</sub>O to form CH<sub>3</sub>OH, N<sub>2</sub> and H<sup>+</sup> [40]. In nitric acid solution, methyldiazonium cation may react with NO<sub>3</sub><sup>-</sup> to form methyl nitrate and N<sub>2</sub> (R7). In addition, monomethylhydrazinium ion can also react with nitrous acid from reactions R4 and R6 to form methyl azide (CH<sub>3</sub>N<sub>3</sub>) and H<sub>2</sub>O (R8-R9). MMH was reported to be oxidized by nitrous acid to form methyl azide [41]. Studies on the reactions





An N-nitrosohydrazinium compound can decompose through two parallel routes, to an azide and  $\text{H}_2\text{O}$  at high acidities and to an amine and  $\text{N}_2\text{O}$  at low acidities [42]. In nitric acid solution, the N-nitrosohydrazinium compound from reaction R8 will decompose through rearrangement and dehydration to form methyl azide and  $\text{H}_2\text{O}$  (R9) [46]. It should be noted that reaction R9 is a global reaction with the possible elementary steps discussed by Smith [47]. Methyl azide from reaction R9 may further react with nitric acid (R10) or nitrous acid (R11) through the displacement of azido group by hydroxyl group, which is a well-known reaction of alkyl azides in acidic medium [48]. Based on the studies conducted by Stedman [49] and Doyle et al. [50], two intrinsically unstable oxides of nitrogen, nitryl azide ( $\text{N}_3\text{NO}_2$ ) and nitrosyl azide ( $\text{N}_3\text{NO}$ ), were proposed as the intermediate species. Nitryl azide and nitrosyl azide can only be prepared at very low temperatures [50,51], and can easily decompose to  $2\text{N}_2\text{O}$  (R12) and  $\text{N}_2 + \text{N}_2\text{O}$  (R13), respectively [52]. Reaction R12 is a global reaction with the possible elementary steps discussed by Zeng et al. [53]. The methanol from reactions R10 and R11 can further react with nitric acid to form methyl nitrate and  $\text{H}_2\text{O}$  (R14).

Figure 4.12 shows some gas-phase reactions (R17-R37) suggested for MMH/ $\text{HNO}_3$ . At temperatures below  $250^\circ\text{C}$ , the ‘gas-to-aerosol’ type of reactions is favored between the vapors of MMH and  $\text{HNO}_3$ , and it is generally believed that the first step of this type of reactions is the formation of a hydrogen-bonded complex (R17). Proton transfer from the acid to the base forms an ion pair as the complex grows (R18) [54-57]. At temperatures above  $250^\circ\text{C}$ , the gas-phase salt formation reactions are not favored and replaced by a more favorable gas-phase oxidation mechanism. Since  $\text{HNO}_3$  vapor is thermally unstable and can decompose rapidly at temperatures above  $250^\circ\text{C}$  [58-60], it may react with MMH through an oxidation mechanism suggested in Fig. 4.12 (R19-R37) other than the salt formation reactions. A short description of these reactions is given next.

In the gas phase, the first step of  $\text{HNO}_3$  decomposition is the  $\text{HO}-\text{NO}_2$  bond breaking, which forms OH and  $\text{NO}_2$  radicals (R19) [58]. The activation energy of this reaction is about 40 kcal/mol, much lower than the other potential pathways,  $\text{H} + \text{ONO}_2$  (100 kcal/mol) and  $\text{HONO} + \text{O}$  (80 kcal/mol) [58]. The OH and  $\text{NO}_2$  radicals can react with MMH through H-atom abstraction steps (R20-R22) to form  $\text{H}_2\text{O}$  and HONO, respectively. These reactions were studied by McQuaid and Ishikawa using ab initio techniques [61, 62]. In this process, an N-nitro compound is proposed as an intermediate, which can decompose into methyl diazene ( $\text{CH}_3\text{N}=\text{NH}$ ) through a HONO elimination step (R22). HONO is a very reactive species, and it can generate NO (R23). The NO then reacts with the MMH radical to form an N-nitroso intermediate (R24, R28). N-nitroso compound (I) may decompose through an HNO elimination reaction (R25) to form methyl diazene, or through rearrangement and dehydration steps (R26) to form methyl azide. Reaction (R26) is well-known [41,46], and the possible elementary steps are described by Smith [47]. N-nitroso compound (II) can decompose through rearrangement (R29) and  $\text{N}_2\text{O}$  elimination (R30) steps to form methylamine ( $\text{CH}_3\text{NH}_2$ ) [43,63]. N-nitroso compound (I) can also transform to (II) when heated (R27) [56]. Methyl diazene ( $\text{CH}_3\text{N}=\text{NH}$ ) intermediate can further react with the OH or  $\text{NO}_2$  radicals to form methyl diazene radical ( $\text{CH}_3\text{N}=\text{N}\cdot$ ) through  $\text{H}_2\text{O}$  elimination (R31) or HONO elimination (R32). The methyl diazene radical may with other radicals to form methanol or methyl nitrite ( $\text{CH}_3\text{ONO}$ ) through an  $\text{N}_2$  elimination reaction (R33-R36). Methanol can further react with  $\text{HNO}_3$  to form  $\text{CH}_3\text{ONO}_2$  through an  $\text{H}_2\text{O}$  elimination reaction (R37).

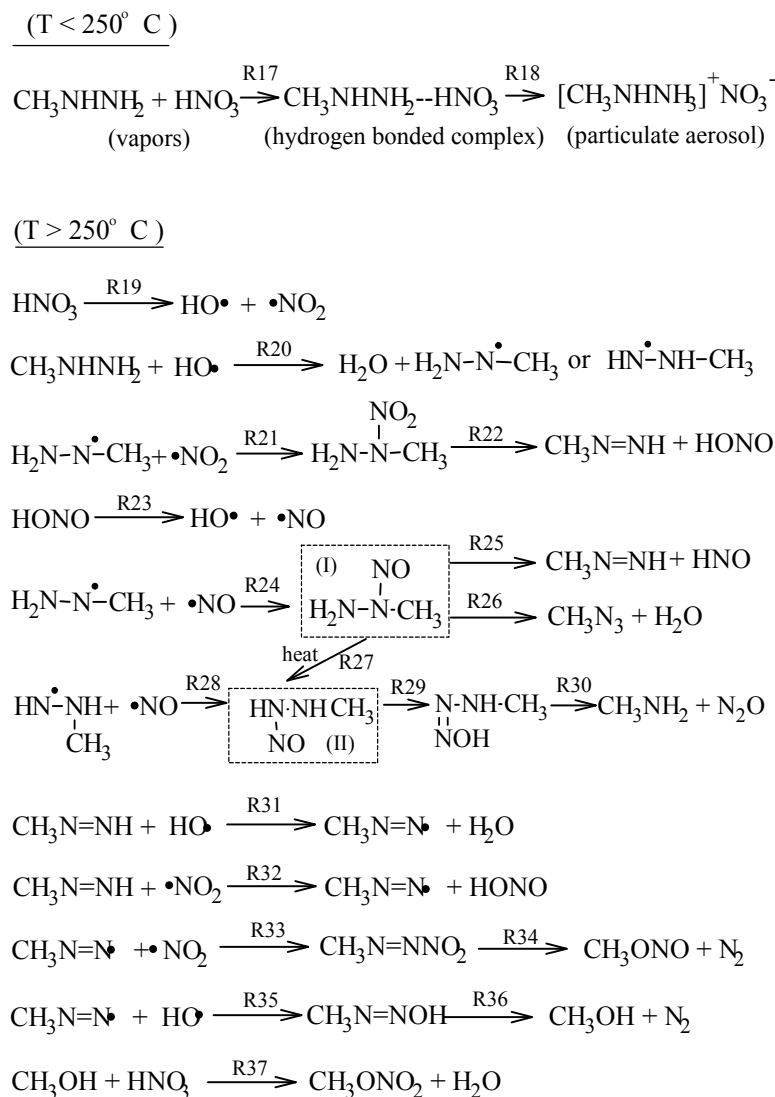


Figure 4.12. Gas-phase pre-ignition reactions of MMH/HNO<sub>3</sub>.

#### 4.2.3 IR analysis of TMEDA/HNO<sub>3</sub> interaction

Confined-interaction tests were conducted at 20, 50, 100, 150, 200 and 250°C to identify species formed during the condensed-phase and gas-phase interaction between TMEDA and HNO<sub>3</sub>.

Figure 4.13 shows a selected spectrum of species evolved from the interaction between 0.5  $\mu\text{L}$  TMEDA and 1  $\mu\text{L}$   $\text{HNO}_3$  at 20°C. The only product formed between TMEDA and  $\text{HNO}_3$  at room temperature is TMEDA dinitrate (TMEDADN). Small amounts of  $\text{HNO}_3$ ,  $\text{H}_2\text{O}$  and TMEDA are also detected in the spectrum. The reactants are mainly consumed by condensed-phase reaction which forms a white residue accumulating in the reaction zone. In addition, TMEDA and  $\text{HNO}_3$  are partially evaporated and reactions occur in the vapors to form TMEDADN in the gas phase, which is detected in the IR spectrum. The formation of this cloud is most probably due to the condensation of TMEDADN in the gas phase, producing a slope in the baseline of the spectral transmittance. The work by Kravets et al. contains an excellent discussion on the effects of small particles on the spectral transmittance [64].

When the initial temperature of the confinement is increased to 50°C, the species observed in the spectrum are the same as those observed when the initial temperature is 20°C; thus, only a nitrate salt is formed. However, many more IR-active species evolve when the initial temperature of the confinement is increased to 100, 150 and 200°C. Figure 4.14 shows selected IR spectra of species evolved from the interaction between 0.2  $\mu\text{L}$  TMEDA and 0.2  $\mu\text{L}$   $\text{HNO}_3$  at an initial temperature of 100 and 200°C, respectively. As shown in Fig. 4.14, TMEDADN is still the dominant product detected at these temperatures. Other IR-active species include  $\text{H}_2\text{O}$ ,  $\text{NO}_2$ ,  $\text{NO}$ ,  $\text{CO}_2$ ,  $\text{N}_2\text{O}$ ,  $\text{CH}_2\text{O}$ ,  $\text{HONO}$ .

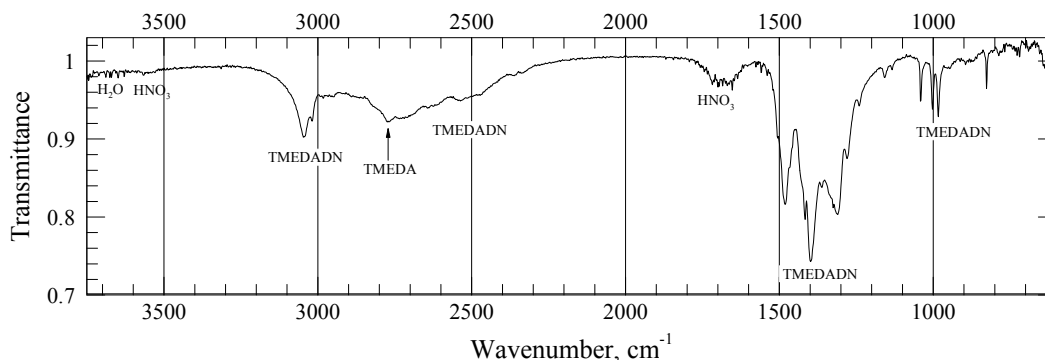


Figure 4.13. Selected IR spectrum of species evolved from confined interaction between TMEDA and  $\text{HNO}_3$  at 20°C and 1 atm  $\text{N}_2$ .

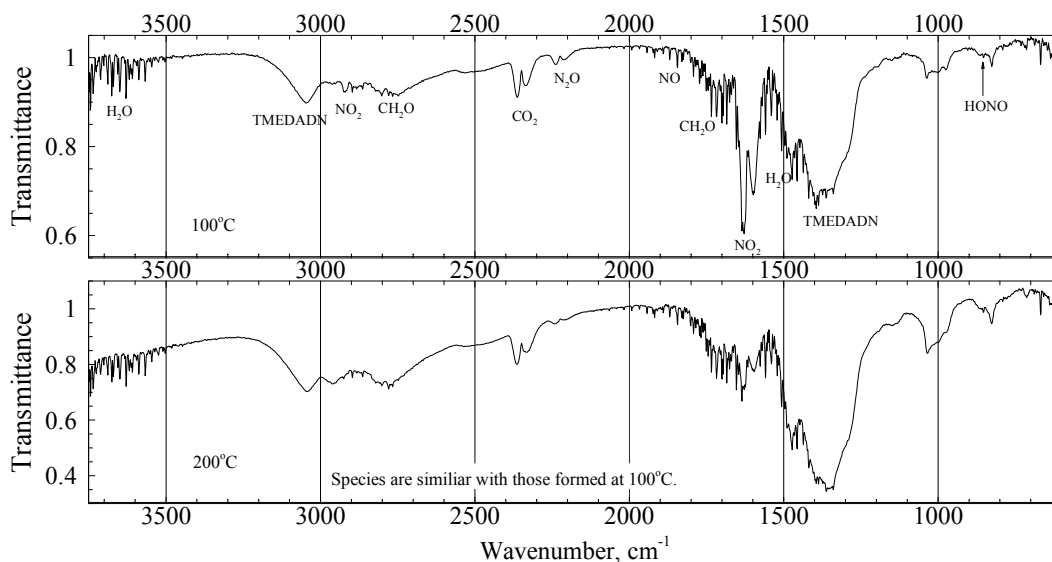


Figure 4.14. Selected IR spectrum of species evolved from confined interaction between TMEDA and  $\text{HNO}_3$  at 100 and 200°C, 1 atm  $\text{N}_2$ .

Figure 4.15 shows a selected IR spectrum of species evolved from the interaction between 0.2  $\mu\text{L}$  TMEDA and 0.2  $\mu\text{L}$   $\text{HNO}_3$  at an initial temperature of 250°C. In Fig. 4.15, part A is the original spectrum; part B is the spectrum after subtracting  $\text{H}_2\text{O}$ ,  $\text{NO}_2$  and  $\text{CO}_2$ ; part C is the spectrum after further subtracting  $\text{N}_2\text{O}$ ,  $\text{NO}$ ,  $\text{CH}_2\text{O}$  and  $(\text{CH}_3)_2\text{NNO}$ . Spectral subtraction is an important method to simplify the product spectrum [65]. The IR spectra of  $(\text{CH}_3)_2\text{NNO}$  and

$(\text{CH}_3)_2\text{NCHO}$  were obtained separately on the same setup and at the same temperature for comparison with the product IR spectrum.

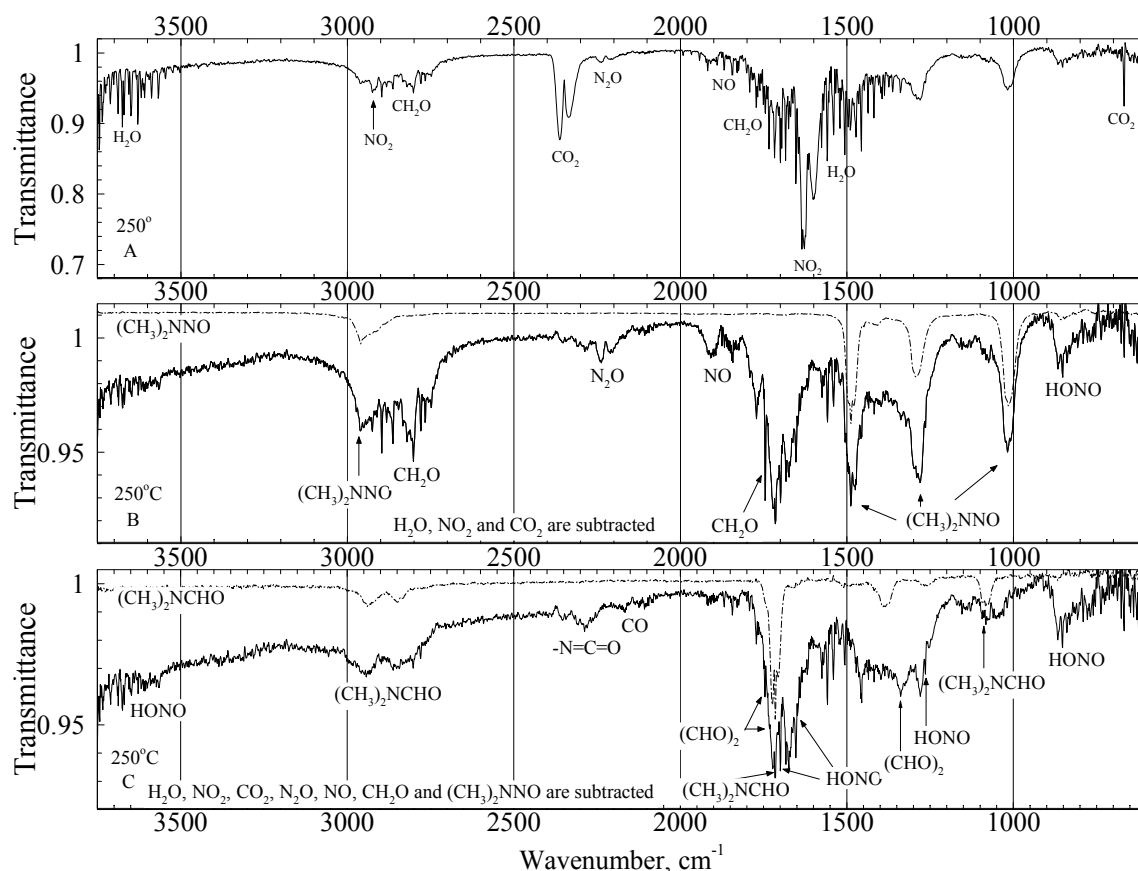


Figure 4.15. IR spectrum of species evolved from confined interaction between TMEDA and  $\text{HNO}_3$  at  $250^\circ\text{C}$  and 1 atm  $\text{N}_2$ ; (A – original spectrum; B – spectrum after subtraction of  $\text{H}_2\text{O}$ ,  $\text{NO}_2$  and  $\text{CO}_2$  from the original spectrum; C – spectrum after subtraction of  $\text{H}_2\text{O}$ ,  $\text{NO}_2$ ,  $\text{CO}_2$ ,  $\text{N}_2\text{O}$ ,  $\text{NO}$ ,  $\text{CH}_2\text{O}$  and  $(\text{CH}_3)_2\text{NNO}$  from the original spectrum.).

#### 4.2.4 Early reactions between TMEDA and $\text{HNO}_3$

Based on the product analysis from the interaction of TMEDA/ $\text{HNO}_3$  as well as rapid thermolysis of TMEDADN, some major pre-ignition reactions in the condensed and gas phases are proposed in Fig. 4.16. The initiation reaction between TMEDA and  $\text{HNO}_3$  is an exothermic salt formation reaction with the formation of TMEDADN, as shown in reaction R1. This Lewis-type acid-base reaction is well-known in many amine- $\text{HNO}_3$  systems [66–68]. In the condensed phase (solution or solid), TMEDADN is most likely a nitrate salt or zwitter ion,  $[(\text{CH}_3)_2\text{NHCH}_2\text{CH}_2\text{NH}(\text{CH}_3)_2]^{2+}[\text{NO}_3^-]_2$ ; in the gas phase, TMEDADN is most likely a complex  $\text{TMEDA} \cdot 2\text{HNO}_3$ . The heat of reaction predicted by Gaussian03 (B3LYP/6-31G(d,p)), using a method suggested by Osmont et al. [69] is approximately -30 kcal/mol. This acid-base type of reaction normally has a low activation energy and thus is very rapid. Therefore, the salt formation is the dominant reaction between TMEDA and nitric acid until TMEDADN starts to rapidly decompose at temperatures above approximately  $250^\circ\text{C}$ . At elevated temperatures, liquid  $\text{HNO}_3$  starts to decompose through a self-acceleration process, which produces  $\text{NO}_2$ ,  $\text{O}_2$  and  $\text{H}_2\text{O}$

as the final products, as shown in reaction R2. At elevated temperatures, TMEDA may react with  $\text{NO}_2$  through hydrogen abstraction reaction to form a TMEDA radical and HONO (R3). The TMEDA radical then reacts with  $\text{NO}_2$  to give a nitro compound or nitrite (R4). This mechanism is well-known in alkane nitration [70]. An unstable alkyl nitrite derivative may rearrange to give a nitrosamine and elimination of a carbonyl compound, as shown in reaction (R5).  $(\text{CH}_3)_2\text{NCH}_2\text{CHO}$  can react with  $\text{NO}_2$  in a similar way as shown in reactions R6-R9. The C-nitroso compound in reaction (R9) may be unstable and can readily isomerize to the corresponding oxime compound [26, 71], as shown in reaction R10. This type of reaction is the principal synthetic method used to generate  $\text{C}=\text{N}$  structures [72].

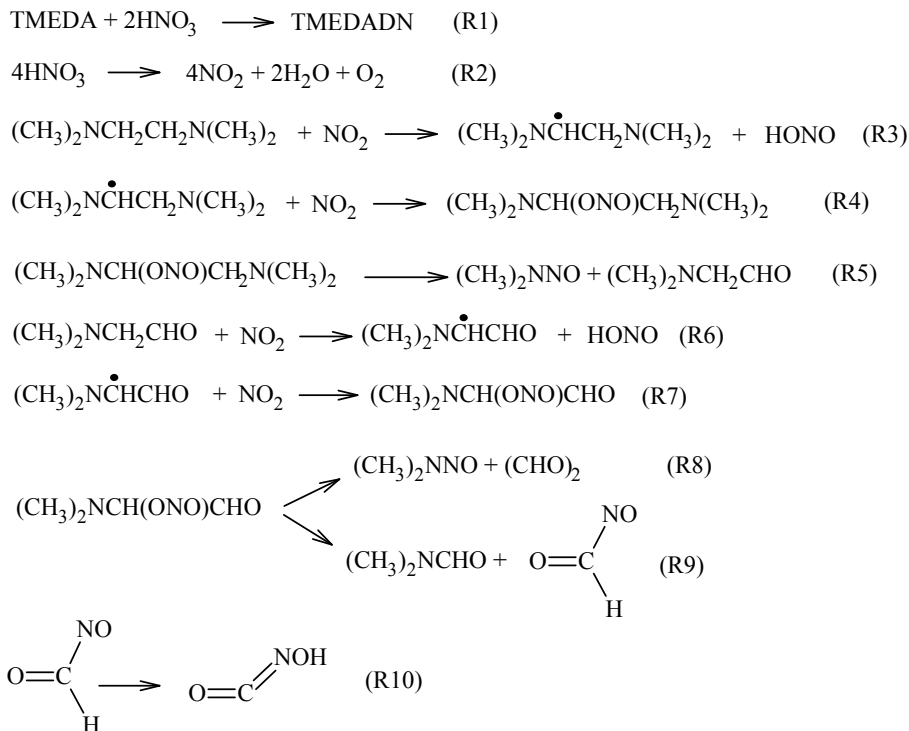


Figure 4.16. Pre-ignition reactions of TMEDA/ $\text{HNO}_3$ .

### 4.3 Study on nitrates $\text{MMH} \cdot 2\text{HNO}_3$ and $\text{TMEDA} \cdot 8\text{HNO}_3$

#### 4.3.1 Preparation

Hypergolic fuels MMH and TMEDA will ignite spontaneously upon contact with nitric acid. The hypergolic ignition is initiated by exothermic nitrate salt formation reactions which generate enough heat to activate the secondary reactions. If the heat from the salt formation reactions is removed quickly enough in order to prevent the secondary reactions from occurring, the reactions between the hypergolic pair will end with the nitrate salt formation.

Two nitrate salts,  $\text{MMH} \cdot 2\text{HNO}_3$  and  $\text{TMEDA} \cdot 2\text{HNO}_3$ , are synthesized by following two steps: 1) slowly mix the aqueous solutions of MMH (or TMEDA) and  $\text{HNO}_3$  in an ice bath with a mole ratio of 1:2 to obtain an aqueous solution of  $\text{MMH} \cdot 2\text{HNO}_3$  or  $\text{TMEDA} \cdot 2\text{HNO}_3$ ; 2) remove the water by keep the solutions in a vacuum dryer ( $< 1$  torr) for 24 hours. As shown in Fig. 4.17a and b, the collected  $\text{MMH} \cdot 2\text{HNO}_3$  and  $\text{TMEDA} \cdot 2\text{HNO}_3$  are white powder with a density of 1.55 and 1.67  $\text{g}/\text{cm}^3$ , respectively.  $\text{MMH} \cdot 2\text{HNO}_3$  is slightly hygroscopic and has a melting point of  $74^\circ\text{C}$ .

It has a stoichiometric F/O (fuel-to-oxidizer) ratio, and the overall combustion reaction can be written as follows:

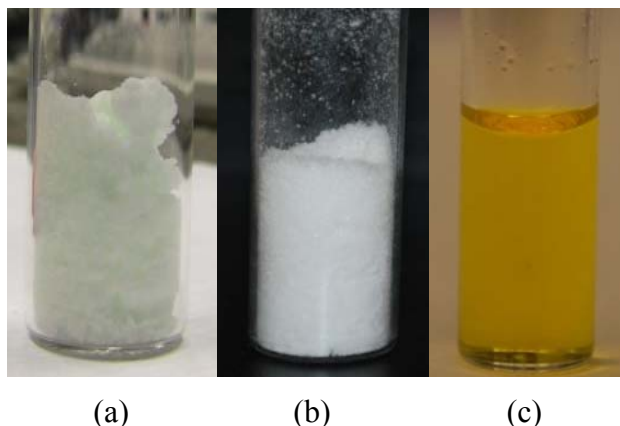
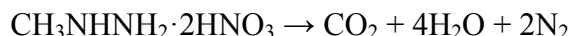


Figure 4.17. a) MMH·2HNO<sub>3</sub>; b) TMEDA·2HNO<sub>3</sub>; and c) TMEDA·8HNO<sub>3</sub>.

However, TMEDA·2HNO<sub>3</sub>, which can also be written as C<sub>6</sub>H<sub>18</sub>O<sub>6</sub>N<sub>4</sub>, is extremely oxidizer lean, and therefore this nitrate itself can not be considered as a monopropellant. A liquid compound with a stoichiometric F/O ratio, which can be written as TMEDA·8HNO<sub>3</sub> or C<sub>6</sub>H<sub>24</sub>O<sub>24</sub>N<sub>10</sub>, was synthesized by adding 6 moles of HNO<sub>3</sub> to 1 mole of TMEDA·2HNO<sub>3</sub>. As shown in Fig. 4.17c, TMEDA·8HNO<sub>3</sub> is a viscous yellow liquid with a density of 1.49 g/ml which is almost the same as that of WFNA. Complete combustion of TMEDA·8HNO<sub>3</sub> can be written as follows:



It is important to note that TMEDA·8HNO<sub>3</sub> is a thermally unstable liquid and will decompose rapidly after about 6-7 hours even when it is stored at room temperature. Therefore, one should not store TMEDA·8HNO<sub>3</sub> in capped vessels in order to avoid potential explosive hazards due to the pressure buildup.

#### 4.3.2 Combustion of TMEDA·8HNO<sub>3</sub>

Liquid strands of TMEDA·8HNO<sub>3</sub>, with a diameter of 8 mm and a height of 1 cm, were ignited and burned in the strand burner at various pressures ranging from atmospheric pressure to 1000 psig (gauge pressure). Figure 4.18 contains images from combustion tests at several gauge pressures, showing the typical gas- and liquid-phase processes and flame structures during the combustion and regression of the liquid strands.

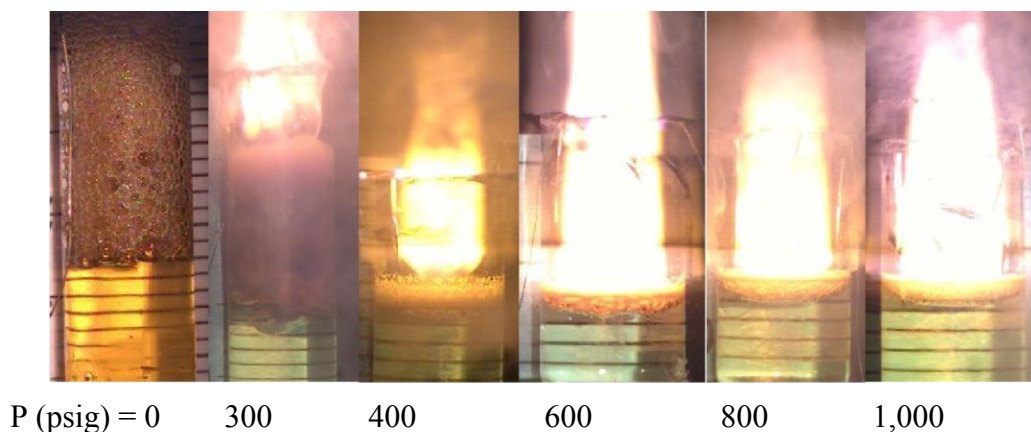


Figure 4.18. Combustion of  $\text{TMEDA} \cdot 8\text{HNO}_3$  at various gauge pressures (unit: psig).

At one atmosphere (0 psig), the liquid strand begins to decompose when its surface is heated by the hot nichrome wire, but it failed ignite. A bubbling zone is formed above the liquid surface due to the release of gases. The thermal decomposition and secondary reactions of  $\text{TMEDA} \cdot 8\text{HNO}_3$  are exothermic and a self-sustained regression of the liquid strand, with a rate of approximately 0.3 mm/s, is observed. At 100 and 200 psig, a similar non-luminous self-sustained liquid strand regression was observed. At 300 psig and higher pressures, the liquid strands were ignited by the hot nichrome wire and a bright luminous flame was observed above the liquid surface. At 300 psig, the flame positions itself quite far away from the liquid surface, with a foam layer (approximately 6 mm) and a dark zone (approximately 1 mm) sitting between the flame and the liquid. The foam layer is a two-phase region that is composed of liquid and gas bubbles which are formed by decomposition and evaporation. The dark zone is a gas-phase region where relatively slow reactions occur, usually involving  $\text{NO}$ ,  $\text{N}_2\text{O}$  and  $\text{HCN}$  [73,74]. The temperature increases from the liquid's boiling point (or decomposition temperature) to its adiabatic flame temperature in this transition zone (foam layer and dark zone). At this pressure, the flame is not quite stable. It moves up and down frequently with respect to the bubbling surface of the foam layer. When the pressure is increased to 400 psig, the foam layer and dark zone are substantially reduced. A stable flame stays close to and regresses with the liquid surface at an almost constant rate. It should be noted that the regression rate increases slightly with time because the liquid strand becomes preheated by the glass wall, which is heated by the foam layer and hot combustion gases. At higher pressures, such as 600-1,000 psig, the foam layer is further reduced in size and the flame is almost in contact with the liquid surface. At these pressures, dark zone is almost undetectable. The glass strand holder cracked after each test due to the heat transfer from the very hot combustion products.

The burn rates of  $\text{TMEDA} \cdot 8\text{HNO}_3$  strands from 400 to 1,000 psig are plotted in Fig. 4.19. The data represent average values of three tests at each pressure and the error bars indicate that the burn-rate measurements are quite repeatable. At these pressures, the burn rate increases with pressure almost linearly. The burn rate of  $\text{TMEDA} \cdot 8\text{HNO}_3$  is slower than that of hydroxylammonium nitrate based liquid propellants [75].

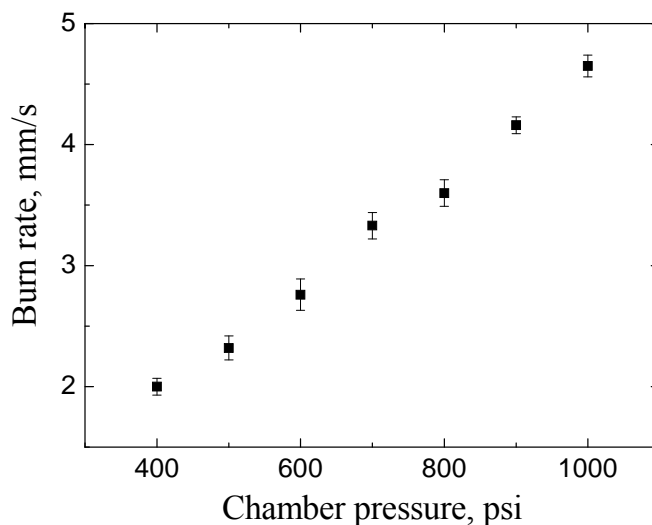


Figure 4.19. Burn rate of  $\text{TMEDA} \cdot 8\text{HNO}_3$ .

#### 4.3.3 Combustion of $\text{MMH} \cdot 2\text{HNO}_3$

Strands of  $\text{MMH} \cdot 2\text{HNO}_3$  were prepared by pressing the nitrates powder into a glass vial ( $D=8$  mm) with a length of 2 cm. To be cautious, a small amount of these nitrates was initially tested (grinding and pressing) to check their sensitivity to shock and friction. No detonation or any sensible changes were observed. It was also reported in literature that MMH nitrates showed poor sensitivity to drop hammer test [76]. The average density of the strand is about  $1.3 \text{ g/cm}^3$ , which is estimated by (mass of filled nitrates / volume of glass via). The density of the strand is smaller than that of the nitrate ( $1.55 \text{ g/cm}^3$ ).

Figure 4.20a and b show selected images from typical combustion tests of  $\text{MMH} \cdot 2\text{HNO}_3$  at a gauge pressure of 400 and 1,000 psig, respectively. In each test, an average burn rate was estimated by: height of strand (mm) / total time consumed (s). For example, at 400 psig, it takes about 2 s to burn a strand with a height of 12 mm. Therefore, the estimated burn rate in this test is about 6 mm/s. At 1,000 psig, it takes about 0.033 s to burn a strand with a height of 14 mm, and the estimated burn rate in this test is about 424 mm/s. The images in Fig. 4.20a were acquired with a frame rate of 1000 fps and an exposure time of 400  $\mu\text{s}$ . In Fig. 4.20b, higher frame rate (5000 fps) and lower exposure time (40  $\mu\text{s}$ ) were used due to the much shorter event.

Burn rates of  $\text{MMH} \cdot 2\text{HNO}_3$  at various gauge pressures were measured. Averaged data of three tests at each pressure is plotted in Fig. 4.21. From atmospheric pressure to 800 psig, the burn rate increases with pressure almost linearly from 0.54 to 14 mm/s. At 1000 psig, the burn rate suddenly rises to about 400 mm/s.



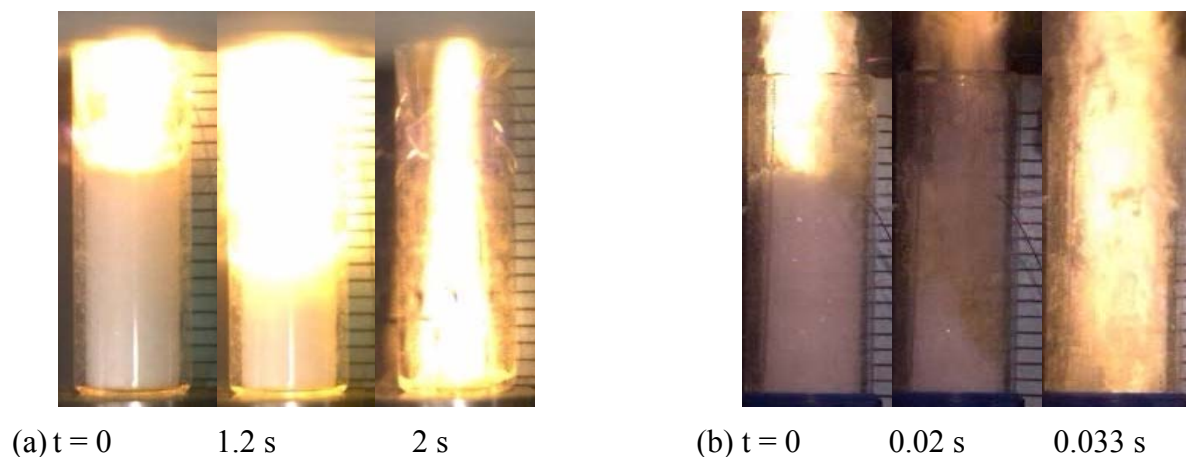


Figure 4.20. Combustion of MMH·2HNO<sub>3</sub> at gauge pressure 400 (a) and 1000 psig (b).

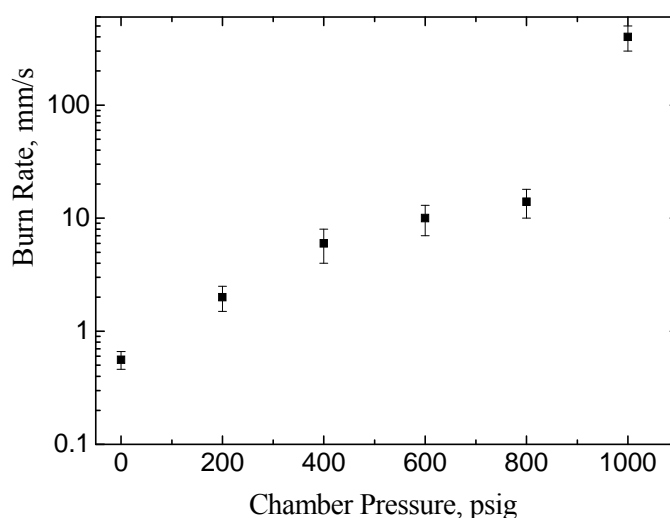


Figure 4.21. Burn Rates of MMH·2HNO<sub>3</sub>.

#### 4.3.4 Decomposition of TMEDA·8HNO<sub>3</sub>

The decomposition of TMEDA·8HNO<sub>3</sub> was investigated by conducting confined rapid thermolysis experiments at various temperatures from room temperature to 120°C with a step of 10°C. In each test, only a very small amount of TMEDA·8HNO<sub>3</sub> (5  $\mu$ L) was used so that it can be heated to the preset temperature rapidly. Figure 4.22 shows the infrared spectra of gaseous IR-active species evolved from the decomposition of TMEDA·8HNO<sub>3</sub> at three selected temperatures (40, 80 and 120°C). The spectrum in each plot is an average of 150 spectra from one test.

At 40°C and lower temperatures, the dominant species is nitric acid vapor (HNO<sub>3</sub>) which is due to the evaporation of nitric acid, which is a major constituent of this liquid propellant. Small amounts of NO<sub>2</sub> and H<sub>2</sub>O, which are typical products from the decomposition of nitric acid [60], were also detected, as shown in Fig. 4.22a. At 50-80°C, the major IR-active species evolved from the condensed-phase decomposition include NO<sub>2</sub>, H<sub>2</sub>O, HNO<sub>3</sub>, HCOOH, CO<sub>2</sub> and glyoxylic acid

(HOCCOOH) which has infrared absorption bands at 1798 and 1748  $\text{cm}^{-1}$  due to the carbonyl and carboxylic groups [7], as shown in Fig. 4.22b. The formation of carbon containing species indicates that TMEDA cation,  $(\text{CH}_3)_2\text{NH}^+\text{CH}_2\text{CH}_2\text{NH}^+(\text{CH}_3)_2$ , is involved in the reactions and decomposes at these temperatures. At 90-120°C, additional species such as  $\text{CH}_2\text{O}$ ,  $\text{N}_2\text{O}$ , NO and a small amount of dimethylnitrosamine  $(\text{CH}_3)_2\text{NNO}$  (1015, 1292 and 1488  $\text{cm}^{-1}$ ) are also detected, as shown in Fig. 4.22. TMEDA·8HNO<sub>3</sub> decomposes at much lower temperatures than TMEDA dinitrate (TMEDA·2HNO<sub>3</sub>) which requires quite high temperatures (around 290°C) to overcome the lattice energy to form TMEDA and HNO<sub>3</sub>,  $\text{TMEDA} \cdot 2\text{HNO}_3 \rightarrow \text{TMEDA} + 2\text{HNO}_3$ . Decomposition and reaction of TMEDA·8HNO<sub>3</sub>, however, is much easier because the TMEDA cation can be directly oxidized by the existing HNO<sub>3</sub> in this liquid.

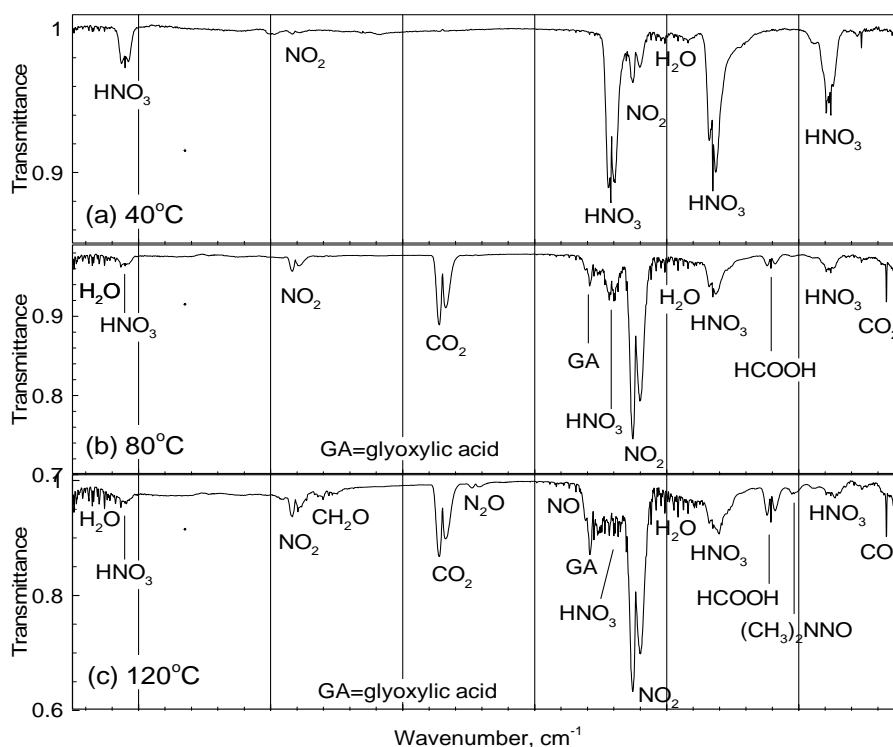


Figure 4.22. IR spectra of gaseous species evolved from rapid thermolysis of TMEDA·8HNO<sub>3</sub> at various temperatures: a) 40°C; b) 80°C; ad c) 120°C.

The temporal evolution of IR-active gaseous species at 80°C is shown in Fig. 4.23. The species concentrations of various species, such as H<sub>2</sub>O, HNO<sub>3</sub>, NO<sub>2</sub>, CO<sub>2</sub> and HCOOH are extracted by a non-linear, least-squares method by comparison with theoretical transmittance. The radiative properties, such as partition function, half-width of spectral lines, and its temperature exponent, are determined from HITRAN database [28]. A more detailed introduction of this data reduction technique is available in an earlier work.<sup>19</sup> It should be note that glyoxylic acid (HOCCOOH) has not been quantified due to the lack of its theoretical transmittance in the HITRAN database. As indicated by the temporal species profiles in Fig. 4.23, HNO<sub>3</sub> and NO<sub>2</sub> evolve rapidly as soon as TMEDA·8HNO<sub>3</sub> is heated ( $t = 0$ ). Meanwhile, H<sub>2</sub>O and glyoxylic acid evolve slowly due to slow decomposition in the condensed phase. The rapid decrease of concentrations of species in this plot is caused by the purge-gas flow of N<sub>2</sub>. At  $t = 1.7$  s, rapid condensed-phase decomposition release large amounts of NO<sub>2</sub> and H<sub>2</sub>O. Glyoxylic acid, formic acid and CO<sub>2</sub> also

evolve rapidly. Compared to other species,  $\text{HNO}_3$  only increases slightly at  $t = 1.7$  s because it rapidly reacts to form other species. The evolution of large amounts of  $\text{NO}_2$  and  $\text{H}_2\text{O}$  indicates the condensed-phase decomposition of nitric acid is of great importance in the decomposition mechanism. Nitric acid and its aqueous solutions decompose to form  $\text{NO}_2$ ,  $\text{O}_2$  and  $\text{H}_2\text{O}$  as the final products. The global reaction can be written as follows:



The formation of  $\text{HCOOH}$  and glyoxylic acid has been reported in the oxidation of many aliphatic alkylamines [78].

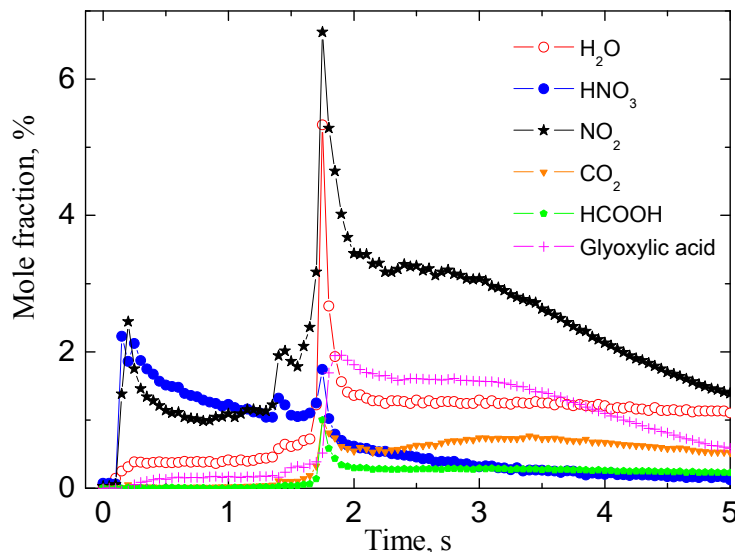


Figure 4.23. Temporal evolution of species from rapid thermolysis of  $\text{TMEDA} \cdot 8\text{HNO}_3$  at  $80^\circ\text{C}$  and 1 atm  $\text{N}_2$ .

The oxidation paths of TMEDA cation  $(\text{CH}_3)_2\text{NH}^+\text{CH}_2\text{CH}_2\text{NH}^+(\text{CH}_3)_2$  by nitric acid are proposed in Fig. 4.24. Oxidation of alkyl groups generally follows two steps: 1) oxidation of alkyl groups to carbonyl groups such as aldehydes ( $-\text{CHO}$ ); and 2) further oxidation of carbonyl groups to carboxylic groups ( $-\text{COOH}$ ). Reactions R1-R4 show the paths through which the TMEDA cation is oxidized by  $\text{HNO}_3$  to form aldehyde intermediates such as  $(\text{CH}_3)_2\text{NHCH}_2\text{CHO}$  and  $\text{HOC-CHO}$ , involving the elimination of  $\text{H}_2\text{O}$  and the formation of an unstable nitrite ( $-\text{ONO}$ ) intermediate. The remaining part is converted to dimethylnitrosamine  $(\text{CH}_3)_2\text{NNO}$  which has a relative high boiling point ( $153^\circ\text{C}$ ) and tends to stay in the condensed phase, and therefore only a very small amount of  $(\text{CH}_3)_2\text{NNO}$  was detected at these temperatures. Reactions R5 and R6 involve the further oxidation of glyoxal ( $\text{HOC-CHO}$ ) to glyoxylic acid ( $\text{HOC-COOH}$ ) which was observed in the experiments. Reactions R7 and R8 represent the further oxidation of glyoxylic acid ( $\text{HOC-COOH}$ ) to oxalic acid ( $\text{HOOC-COOH}$ ), through the same paths as R5-R6, involving the formation of a nitrite intermediate and  $\text{ONONO}_2$  which is the isomer of dinitrogen tetroxide ( $\text{N}_2\text{O}_4$ ).  $\text{ONONO}_2$  will decompose to  $\text{NO}_2$  through the equilibrium reactions R9 and R10 [79]. Reaction R11 is the decomposition of oxalic acid, which was reported [80,81] to form formic acid  $\text{HCOOH}$  and  $\text{CO}_2$  which were observed in the experiments. Reaction R12 is the decomposition of glyoxylic acid to form formaldehyde  $\text{CH}_2\text{O}$  and  $\text{CO}_2$  [82]. These reactions

(R1-R12) are exothermic from a global reaction point of view, and can cause a self-sustained regression of the liquid strand at atmosphere conditions as discussed in Fig. 4.18.

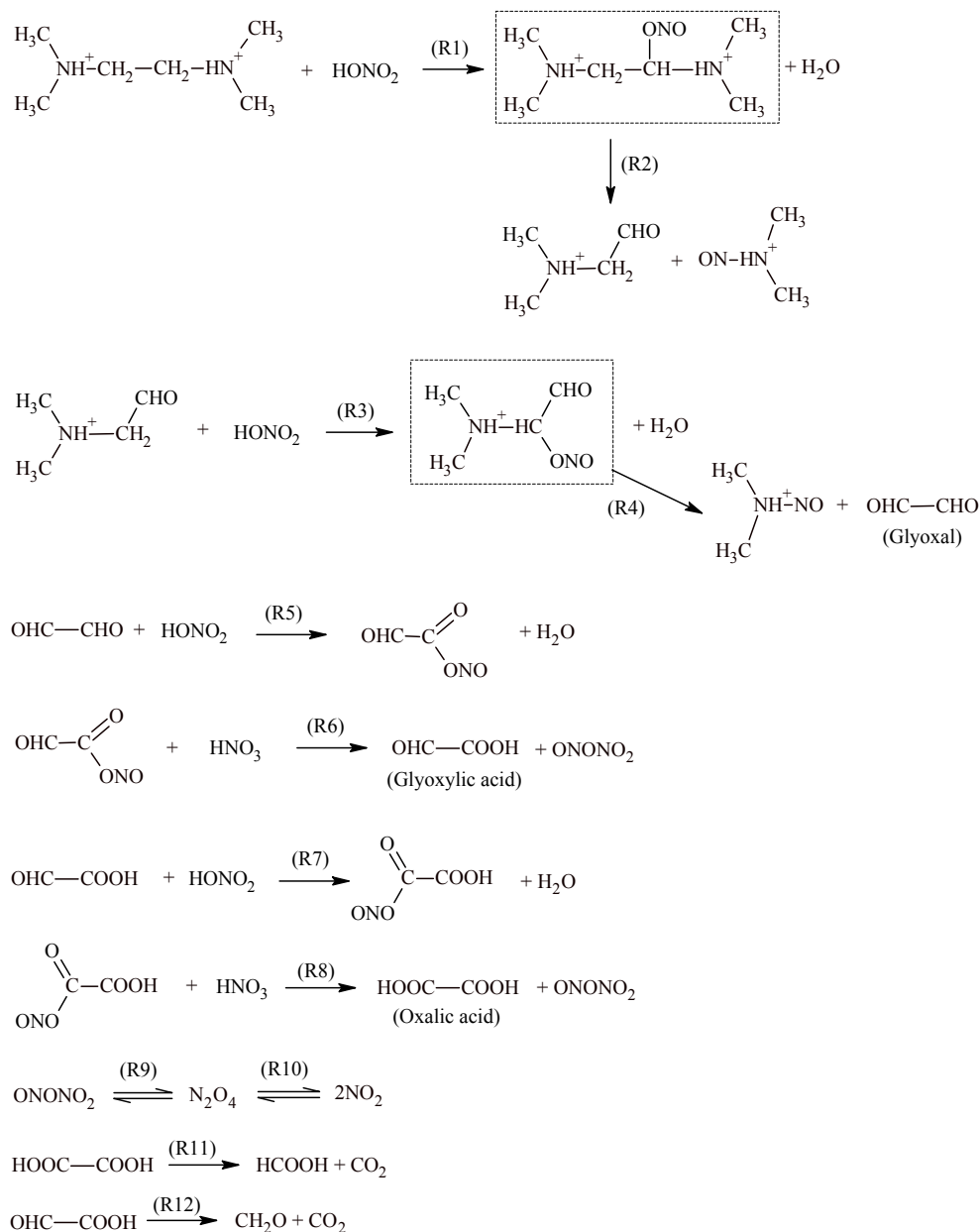


Figure 4.24. Oxidation of TMEDA cation by  $\text{HNO}_3$ .

#### 4.3.5 Decomposition of $\text{MMH} \cdot 2\text{HNO}_3$

The thermal decomposition of  $\text{MMH} \cdot 2\text{HNO}_3$  was examined by the CRT/FTIR setup at various temperatures up to  $300^\circ\text{C}$ . In this rapid thermolysis setup,  $\text{MMH} \cdot 2\text{HNO}_3$  starts to decompose at about  $120^\circ\text{C}$ , and the identified IR-active species include  $\text{HNO}_3$ ,  $\text{CH}_3\text{ONO}_2$ ,  $\text{CH}_3\text{N}_3$ ,  $\text{HN}_3$ ,  $\text{H}_2\text{O}$ ,  $\text{N}_2\text{O}$ ,  $\text{NO}$ ,  $\text{NO}_2$ ,  $\text{CH}_4$  and  $\text{CO}_2$ . It should be noted that IR-inactive species (i.e.,  $\text{N}_2$ ) may also exist. Figure 4.25a shows an IR spectrum obtained by averaging a total 150 spectra obtained in a test at  $160^\circ\text{C}$ . Figure 4.25b is the remaining spectrum after subtracting the IR bands of  $\text{H}_2\text{O}$  and

$\text{HNO}_3$  from Fig. 4.25a. Spectral subtraction can help to separate and identify the species whose major IR bands overlap with those of  $\text{HNO}_3$ , such as  $\text{CH}_3\text{ONO}_2$  in this case.

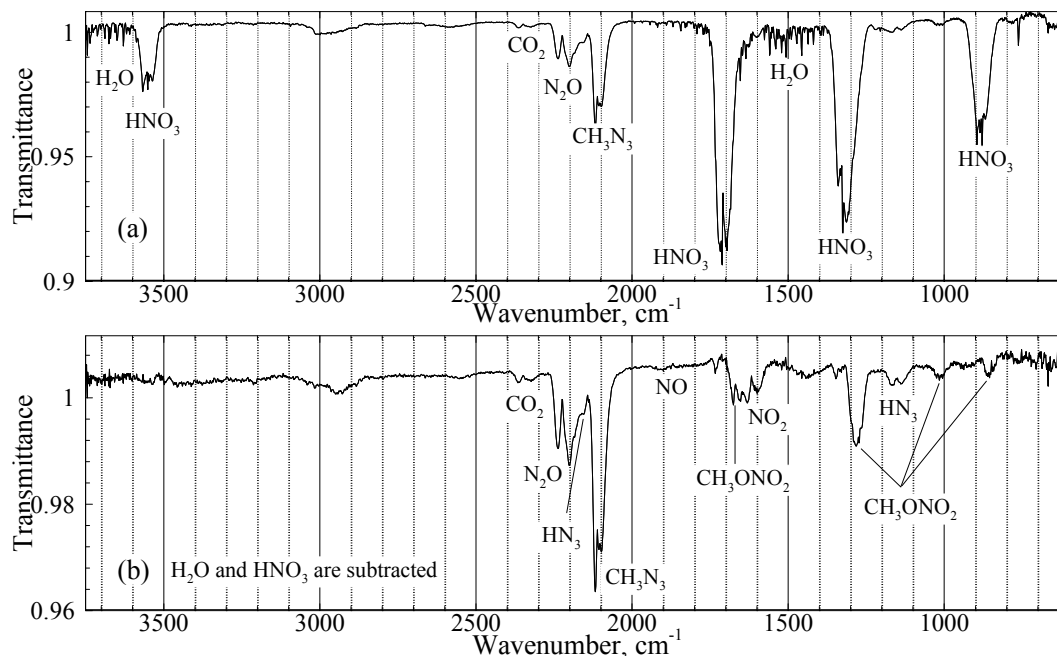
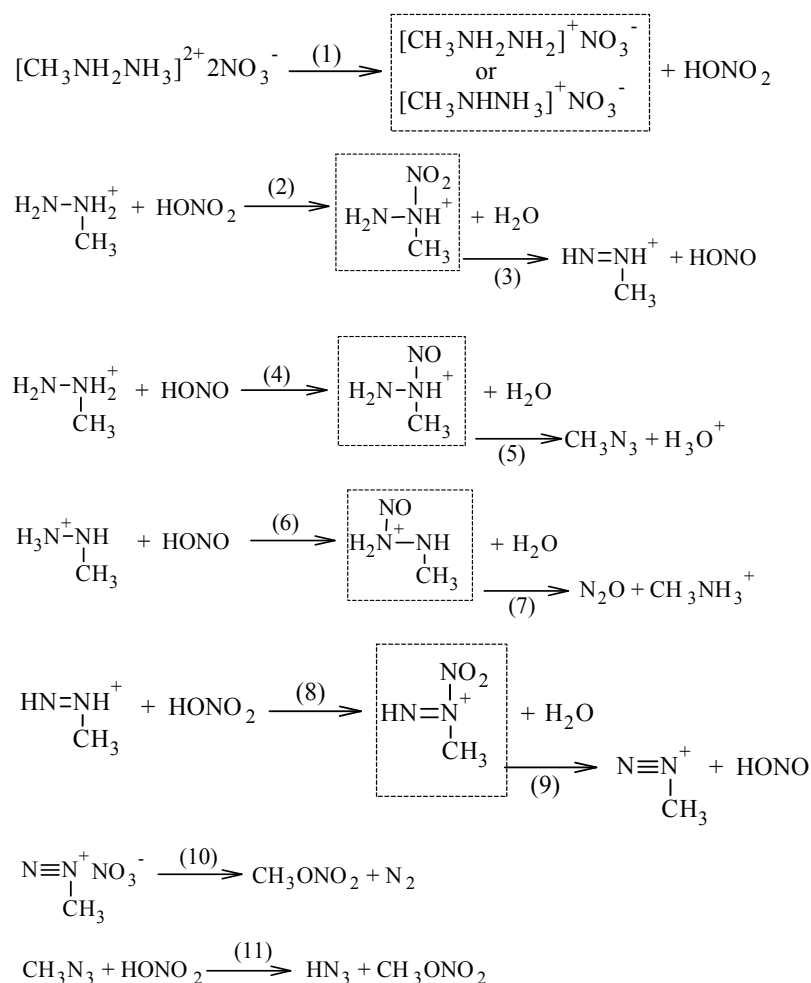


Figure 4.25. a) Average IR spectrum of a total 150 spectra obtained from  $\text{MMH} \cdot 2\text{HNO}_3$  decomposition at  $160^\circ\text{C}$  and 1 atm  $\text{N}_2$ ; b) IR spectrum obtained by subtracting  $\text{H}_2\text{O}$  and  $\text{HNO}_3$  bands from (a).

A large amount of  $\text{HNO}_3$  was released from the decomposition of  $\text{MMH} \cdot 2\text{HNO}_3$  nitrates and only a very small amount of  $\text{NO}_2$  is detected. This observation does not agree with the work of Breisacher et al. [46], in which  $\text{NO}_2$  rather than  $\text{HNO}_3$  was believed to be a major product based on data from mass spectrometry. This observation is likely caused by their use of electron-impact ionization which will dissociate  $\text{HNO}_3$  to produce lower molecular-weight species, such as  $\text{NO}_2^+$  and  $\text{NO}^+$  [83]. Therefore, the mass spectrometric analysis of Breisacher et al. was unable to differentiate  $\text{HNO}_3$  from  $\text{NO}_2$ . For the same reason, they were unable to identify methyl nitrate  $\text{CH}_3\text{ONO}_2$  which will also dissociate upon electron impact [84].

The suggested pathways for  $\text{MMH} \cdot 2\text{HNO}_3$  decomposition are provided in Fig. 4.26. In reaction (1), the nitrate decomposes to release  $\text{HNO}_3$ , which is identified as a major early product in the IR spectra. In reaction (2), the monomethylhydrazium cation reacts

Figure 4.26. Proposed MMH·2HNO<sub>3</sub> decomposition reactions.

with nitric acid to form an unstable nitro intermediate which decomposes to methyldiazenium cation through a HONO elimination step (reaction 3). In reaction (4) and (6), monomethylhydrazinium cation reacts with HONO to form N-nitrosohydrazinium intermediates which can decompose to form methyl azide through H<sub>2</sub>O elimination step (reaction 5) or to form methyl ammonium cation through the N<sub>2</sub>O elimination step (reaction 7) [43]. In reaction (8), methyldiazenium cation reacts with nitric acid to form a nitro intermediate which decomposes to a methyldiazonium cation through a HONO elimination step (reaction 9). In reaction (10), the methyldiazonium nitrate decomposes to methyl nitrate through a step which is well-known as ‘replacement of nitrogen’ [39], in which the nitrogen is lost as N<sub>2</sub>. Methyl azide may also react with nitric acid to form hydrazoic acid and methyl nitrate [24] both of which are detected in the IR spectra. The minor species, such as CH<sub>4</sub>, NO and CO<sub>2</sub>, can be formed by many reactions included in the MMH/RFNA mechanism by Anderson et al. [12], thus are not discussed in this study.

#### 4.4 Pressure effect on ignition delay

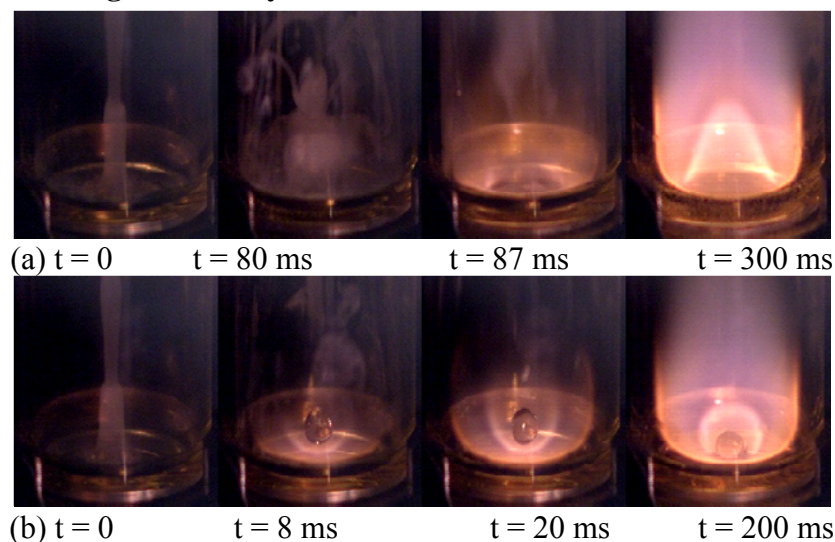


Figure 4.27. Drop tests: a) MMH/WFNA at -20 kPa; b) MMH/WFNA at 50 kPa

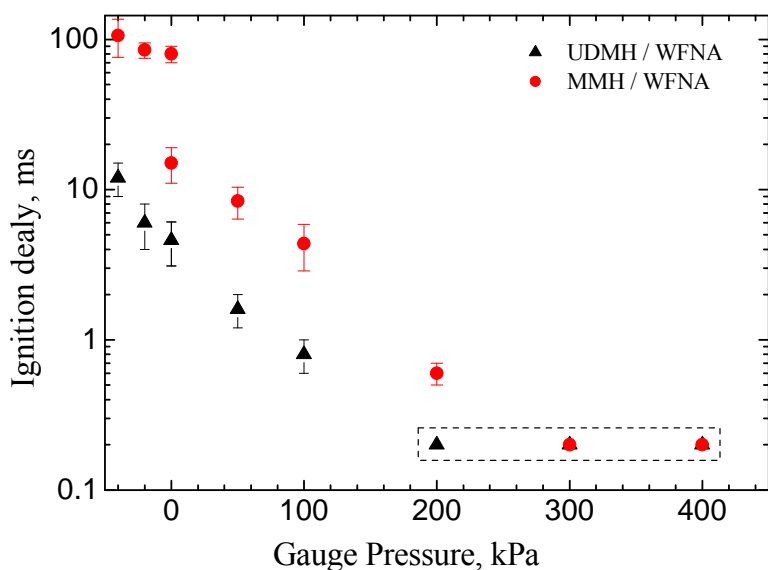


Figure 4.28. Ignition delay of MMH/WFNA and UDMH/WFNA

The drop-on-pool impingement interactions and ignition delays of MMH and UDMH with WFNA were studied at various pressures from -40 kPa to 400 kPa (gauge pressure). The pressurization gas is  $N_2$ . For MMH/WFNA, two different types of drop-pool interactions were observed. At pressures below 0 kPa (gauge), the droplet stays in the nitric acid pool after the impact, as shown in Fig. 4.27a, while at elevated pressures the droplet is ejected from the oxidizer pool and then suspended above the pool surface, as shown in Fig. 4.27b. Upon impact, liquid-phase reactions will occur at the contact surface which forms nitrates, generate abundant heat, and produce plenty of gases. It is generally believed that a gas layer (or vapor layer) will be formed between the droplet and pool surface [85]. If the repelling force generated by the gas flow is larger than the gravity of the droplet, the droplet will be ejected from the pool; otherwise,

the droplet will stay in the pool. Figure 4.28 shows the ignition delays of MMH/WFNA and UDMH/WFNA at various pressures. For MMH/WFNA, the ignition delays decrease with increasing pressure. At 0 kPa (gauge), the ignition delay is about 14 ms if the droplet is ejected from the surface; or the ignition delay can be as long as 80 ms if the droplet stays in the pool. At pressures below 0 kPa, the droplet always stays in the pool and the ignition delays are longer than 80 ms. At pressures above 0 kPa, the droplet is always ejected from the pool and the ignition delays are less than 14 ms. At 200 kPa, the ignition delay is less than 1 ms. It should be noted the ignition delays measured in this work have a resolution of 0.2 ms since a frame rate of 5000 fps is used for the camera. The data in the dashed frame in Fig. 4.28 indicate that the ignition delay is shorter than 0.2 ms. UDMH reacts with WFNA more violently and has a shorter ignition delay compared to MMH/WFNA. For UDMH/WFNA, the droplet is always ejected from the pool even at pressures down to -40 kPa.

The ignition delays of a tertiary amine TMEDA, an azide DMAZ and a mixture of 66.7% TMEDA with 33.3% DMAZ were studied at various pressures, and the results were plotted in Fig. 4.29. In general, the ignition delay increases with increasing pressure. The ignition delay of TMEDA is shorter than that of DMAZ. The mixture of TMEDA and DMAZ has a shorter ignition delay than pure TMEDA and DMAZ. In addition, the ignition delay of this mixture shows little dependence on pressure. The ignition delay is around 10 ms which is close to the value (9 ms) obtained in Stevenson's work [6].

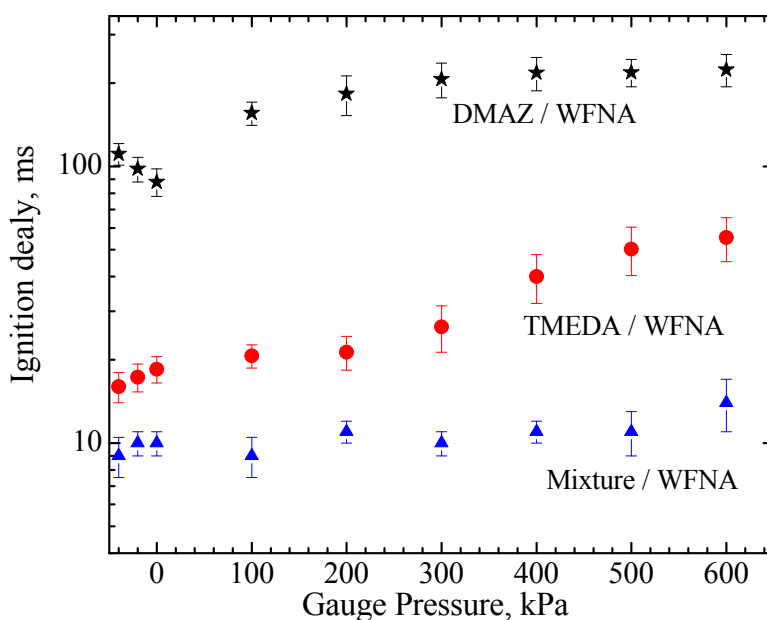


Figure 4.29. Ignition delay of TMEDA, DMAZ and their mixture with WFNA.

## 5. References

- [1]. J. D. Clark, "Ignition! An Informal History of Liquid Rocket Propellants", Rutgers University Press: New Brunswick, NJ, 1972.
- [2]. R. T. Holtzmann, "Chemical Rockets", Marcel Dekker: New York, NY, 1969.
- [3]. E. W. Schmidt, "Hydrazine and Its Derivatives: Preparation, Properties, Applications (2nd Ed.)", Wiley-Interscience: New York, NY, 2001.



- [4]. G. P. Sutton, "History of Liquid Propellant Rocket Engines", American Institute of Aeronautics and Astronautics: Alexandria, VA, 2006.
- [5]. D. M. Thompson, "*Tertiary amine azides in hypergolic liquid or gel fuels propellant systems*", Patent No.: US 6013143 A, 2000.
- [6]. W. H. Stevenson, "*Hypergolic Liquid Or Gel Fuel Mixtures*", Patent No.: US 20080127551 A1, 2008.
- [7]. M. J. McQuaid, W. H. Stevenson, D. M. Thompson, "Computationally Based Design and Screening of Hypergolic Multiamines", ARL Technical Report, NTIS ADA433347, 2004.
- [8]. M. J. Nusca, "Computational model of impinging-stream/swirl injectors in a hypergolic fuel engine", AIAA 2003-5062, 39th AIAA/ASME/SAE/ASEE Joint Propulsion Conference & Exhibit, Huntsville, AL, 2003 and references therein.
- [9]. M. J. Nusca, R. S. Michaels, "Utility of Computational Modeling for the Study of Combustion Instability in Small MMH-NTO Liquid Rocket Engines", AIAA 2007-5562, 43rd AIAA/ASME/SAE/ASEE Joint Propulsion Conference & Exhibit, Cincinnati, OH, 2007 and references therein.
- [10]. M. J. Nusca, R. S. Michaels, Proceedings of the 50th JANNAF Propulsion Meeting, 2002, Vol.1, 179-191.
- [11]. C.-C. Chen, M. J. Nusca, M. J. McQuaid, "Modeling Combustion Chamber Dynamics of Impinging Stream Vortex Engines Fueled With Hydrazine-Alternative Hypergols", ARL Technical Report, NTIS ADA503941, 2008.
- [12]. W. A. Anderson, M. J. McQuaid, M. J. Nusca, A. J. Kotlar, "A detailed, finite-rate, chemical kinetics mechanism for monomethylhydrazine-red fuming nitric acid systems", ARL Technical Report, ARL-TR-5088, 2010.
- [13]. L. Catoire, N. Chaumeix, C. Paillard, ""Chemical Kinetic Model for Monomethylhydrazine/Nitrogen Tetroxide Gas-Phase Combustion and Hypergolic Ignition"", J. Propul. Power, 2004, 20, 87-92.
- [14]. L. Catoire, T. Ludwig, X. Bassin, G. Dupr, C. Paillard, ""Kinetic Modeling of the Ignition Delays in Monomethylhydrazine/Oxygen/Argon Mixture", Proc. Combust. Inst., 1998, 27, 2359-2365.
- [15]. J. A. Vanderhoff, W. R. Anderson, A. J. Kotlar, "Dark zone modeling of solid propellant flames", Proceedings of 29th JANNAF Combustion Subcommittee Meeting, 1992, Vol.2, 225-237.
- [16]. N. Ilincic, W. R. Anderson, K. Seshadri, N. E. Meagher, "Chemical mechanisms for the dark zones of double base and nitramine gun propellants", Proc. Combust. Inst., 1996, 26, 1997-2006.
- [17]. G. P. Smith, D. M. Golden, M. Frenklach, N. W. Moriarty, B. Eiteneer, M. Goldenberg, C. T. Bowman, R. K. Hanson, S. Song, W. C. Gardiner, V. V. Lissianski, Z. Qin, GER-MECH 3.0, [http://www.me.berkeley.edu/gri\\_mech/](http://www.me.berkeley.edu/gri_mech/)
- [18]. Chowdhury, S. T. Thynell, "Confined rapid thermolysis/FTIR/ToF studies of methyl-amino-triazolium-based energetic ionic liquids", Thermochem. Acta, 2010, 505, 33-40.
- [19]. A. Chowdhury, "Confined rapid thermolysis/FTIR/ToF Studies of energetic ionic liquids", Ph.D. Thesis, The Pennsylvania State University, 2010.
- [20]. S.Q. Wang and S.T. Thynell, "An experimental study on the hypergolic interaction between methylhydrazine and nitric acid", Combustion and Flame, 2012, 159(1), pp 438-447.

- [21]. S.Q. Wang, S.T. Thynell and A. Chowdhury, "Experimental study on the hypergolic interaction between N,N,N',N'-Tetramethylethylenediamine and nitric acid", *Energy and Fuels*, 2010, 24, 5320-5330.
- [22]. S.Q. Wang and S.T. Thynell, "Experimental study on hypergolic interaction between MMH and nitric acid", 44th Joint-Army-Navy-NASA-Air Force Combustion Subcommittee Meeting, Apr 2011, Arlington.
- [23]. S.Q. Wang, S.T. Thynell, Condensed- and gas-phase reactions between monomethylhydrazine and nitric acid from 20 to 250°C, 7th U.S. National Combustion Meeting, Mar 2011, Atlanta, GA.
- [24]. W.-G. Liu, S. Wang, S. Dasgupta, S. T. Thynell, W. A. Goddard III, S. Zybin, and R. A. Yetter, "Experimental and Quantum Mechanics Investigations of Early Reactions of Monomethylhydrazine with Mixtures of NO<sub>2</sub> and N<sub>2</sub>O<sub>4</sub>," *Combustion and Flame*, Vol. 160, Issue 5, May 2013, pp. 970-981.
- [25]. S.Q. Wang and S.T. Thynell, "Decomposition and Combustion of Energetic Ionic Compound Synthesized from N,N,N',N'-Tetramethylethylenediamine and nitric acid", *ACS Symposium Series*, 2012, 1117, pp 51-66.
- [26]. S.Q. Wang and S.T. Thynell, "Decomposition and Combustion of Monomethylhydrazinium Nitrates", 8th U.S. National Combustion Meeting, Park City, Utah, May 2013.
- [27]. S.Q. Wang and S.T. Thynell, "Experimental Investigation of Pressure Effect on Ignition Delay of Hypergolic Pairs", 8th U.S. National Combustion Meeting, Park City, Utah, May 2013.
- [28]. L. S. Rothman, D. Jacquemart, A. Barbe, D. Chris Benner, M. Birk, L. R. Brown, M. R. Carleer, J. C. Chackerian, K. Chance, L. H. Coudert, V. Dana, V. M. Devi, J. M. Flaud, R. R. Gamache, A. Goldman, J. M. Hartmann, K. W. Jucks, A. G. Maki, J. Y. Mandin, S. T. Massie, J. Orphal, A. Perrin, C. P. Rinsland, M. A. H. Smith, J. Tennyson, R. N. Tolchenov, R. A. Toth, J. Vander Auwera, P. Varanasi, G. Wagner, *J. Quant. Spectrosc. Radiat. Transfer*, 2005, 96, 139-204.
- [29]. J. R. Durig, T. K. Gounev, C. Zheng, A. Choulakian, V. N. Verma, "Conformational stability from temperature-dependent FT-IR spectra of liquid xenon solutions, ab initio calculations, and  $r_0$  parameters for methylhydrazine", *J. Phys. Chem. A*, 2002, 106, 3395-3402.
- [30]. E. A. Lawton, C. M. Moran, "Methylhydrazinium Nitrate", *J. Chem. Eng. Data*, 1984, 29, 357-358.
- [31]. L. H. Jones, R. M. Badger, G. E. Moore, "The Infrared Spectrum and the Structure of Gaseous Nitrous Acid", *J. Chem. Phys.*, 1951, 19, 1599-1604.
- [32]. S. S. Brown, H. L. Berghout, F. F. Crim, "Raman spectroscopy of the N-C-O symmetric ( $\nu_3$ ) and antisymmetric ( $\nu_2$ ) stretch fundamentals in HNCO", *J. Chem. Phys.*, 1997, 107, 9764-9771.
- [33]. M. Khlifi, P. Paillous, P. Bruston, F. Raulin, J. C. Guillemin, "Absolute IR band intensities of CH<sub>2</sub>N<sub>2</sub>, CH<sub>3</sub>N<sub>3</sub>, and CH<sub>3</sub>NC in the 250-4300 cm<sup>-1</sup> region and upper limits of abundance in Titan's stratosphere", *Icarus*, 1996, 124, 318-328.
- [34]. J. C. D. Brand, T. M. Cawthon, "The vibrational spectrum of methyl nitrate", *J. Am. Chem. Soc.*, 1955, 77, 319-323.
- [35]. F. L. Rook, "Preparation, vapor pressure, and infrared spectrum of methyl nitrite", *J. Chem. Eng. Data*, 1982, 27, 72-73.

- [36]. P. J. Linstrom, W. G. Mallard, NIST Chemistry WebBook, NIST Standard Reference Database Number 69, <http://webbook.nist.gov>.
- [37]. D. G. Karraker, "Oxidation of hydrazine by nitric acid", *Inorg. Chem.*, 1985, 24, 4470-4477.
- [38]. V. Kalinin, É. T. Apasov, S. L. Ioffe, V. A. Tartakovskii, "N-nitrohydrazines and their salts", *Russ. Chem. Bull.*, 1991, 40, 988-995.
- [39]. R. T. Morrison, R. N. Boyd, "Organic Chemistry (4th Ed.)", Allyn and Bacon Inc.: Newton, MA, 1983, 933-938.
- [40]. R. H. Smith, S. R. Koepke, Y. Tondeur, C. L. Denlinger, C. J. Michejda, "The methyldiazonium ion in water: Competition between hydrolysis and proton exchange", *J. Chem. Soc., Chem. Commun.*, 1985, 936-937.
- [41]. W. N. Latimer, J. H. Hildebrand, "Reference Book of Inorganic Chemistry (3<sup>rd</sup> Ed.)", The Macmillan Company: New York, 1964, p.19.
- [42]. E. W. Schmidt, "Hydrazine and Its Derivatives: Preparation, Properties, Applications (2nd Ed., Vol. 1)", Wiley-Interscience: New York, NY, 2001, 465-466.
- [43]. J. R. Perrott, G. Stedman, N. Uysal, "Kinetic and product study of the reaction between nitrous acid and hydrazine", *J. Chem. Soc., Dalton Trans.*, 1976, 2058-2064.
- [44]. J. R. Perrott, G. Stedman, "The kinetics of nitrite scavenging by hydrazine and hydrazoic acids at high acidities", *J. Inorg. Nucl. Chem.*, 1977, 39, 325-327.
- [45]. M. M. Doherty, K. R. Howes, G. Stedman, M. Q. Naji, "Is hydrazoic acid ( $\text{HN}_3$ ) an intermediate in the destruction of hydrazine by excess nitrous acid?", *J. Chem. Soc., Dalton Trans.*, 1995, 3103-3107.
- [46]. P. Breisacher, H. H. Takimoto, G. C. Denault, W. A. Hicks, "Simultaneous mass spectrometric differential thermal analyses of nitrate salts of monomethylhydrazine and methylamine", *Combust. Flame*, 1970, 14, 397-403.
- [47]. P. A. S. Smith, "Chemistry of Open-Chain Organic Nitrogen Compounds (Vol. 2)", W.A. Benjamin, Inc.: New York, NY, 1966, p. 129.
- [48]. J. H. Boyer, F. C. Canter, "Alkyl and aryl azides", *Chem. Rev.*, 1954, 54, 1-57.
- [49]. G. Stedman, "Mechanism of the azide-nitrite reaction. Part II", *J. Chem. Soc.*, 1959, 2949-2954.
- [50]. M. P. Doyle, J. J. Maciejko, S. C. Busman, "Reaction between azide and nitronium ions. Formation and decomposition of nitryl azide", *J. Am. Chem. Soc.*, 1973, 95, 952-953.
- [51]. H. W. Lucien, "The preparation and properties of nitrosyl azide", *J. Am. Chem. Soc.*, 1958, 80, 4458-4460.
- [52]. R. D. Harcourt, "Examples of valence bond representations for the decompositions of  $\text{N}_3\text{NO}$  and  $\text{N}_3\text{NO}_2$ ", *J. Mol. Struct. Theochem*, 1995, 342, 51-57.
- [53]. X. Zeng, M. Ge, Z. Sun, J. Bian, D. Wang, "Gaseous nitryl azide  $\text{N}_4\text{O}_2$ : A joint theoretical and experimental study", *J. Mol. Struct.*, 2007, 840, 59-65.
- [54]. M. Luria, B. Cohen, "Kinetics of gas to particle conversion in the  $\text{NH}_3$ -HCl system", *Atmos. Environ.*, 1980, 14, 665-670.
- [55]. J. A. Lloyd, K. J. Heaton, M. V. Johnston, "Reactive uptake of trimethylamine into ammonium nitrate particles", *J. Phys. Chem. A*, 2009, 113, 4840-4843.

- [56]. S. N. Eustis, A. Whiteside, D. Wang, M. Gutowski, K. H. Bowen, "Ammonia-Hydrogen Bromide and Ammonia-Hydrogen Iodide Complexes: Anion Photoelectron and ab Initio Studies", *J. Phys. Chem. A*, 2009, 114, 1357-1363.
- [57]. F.-M. Tao, "Gas phase proton transfer reaction of nitric acid-ammonia and the role of water", *J. Chem. Phys.*, 1998, 108, 193-202.
- [58]. H. S. Johnston, L. Foering, Y.-S. Tao, G. H. Messerly, "The kinetics of the thermal decomposition of nitric acid vapor", *J. Am. Chem. Soc.*, 1951, 73, 2319-2321.
- [59]. H. S. Johnston, L. Foering, R. J. Thompson, "Kinetics of the thermal decomposition of nitric acid vapor. II. Mechanism", *J. Phys. Chem.*, 1953, 57, 390-395.
- [60]. S. A. Stern, J. T. Mullhaupt, W. B. Kay, "The physicochemical properties of pure nitric acid", *Chem. Rev.*, 1960, 60, 185-207.
- [61]. M. J. McQuaid, Y. Ishikawa, "H-atom abstraction from  $\text{CH}_3\text{NHNH}_2$  by  $\text{NO}_2$ : CCSD(T)/6-311++G(3df,2p)//MPWB1K/ 6-31+G(d,p) and CCSD(T)/6-311+G(2df,p)//CCSD/ 6-31+G(d,p) calculations", *J. Phys. Chem. A*, 2006, 110, 6129-6138.
- [62]. Y. Ishikawa, M. J. McQuaid, "Reactions of  $\text{NO}_2$  with  $\text{CH}_3\text{NHNH}$  and  $\text{CH}_3\text{NNH}_2$ : A direct molecular dynamics study", *J. Mol. Struct. Theochem*, 2007, 818, 119-124.
- [63]. M. A. Saad, M. B. Detweiler, M. A. Sweeney, "Analysis of reaction products of nitrogen tetroxide with hydrazines under nonignition conditions", *AIAA Journal*, 1972, 10, 1073-1078.
- [64]. V. G. Kravets, C. Meier, D. Konjhodzic, A. Lorke, "Infrared properties of silicon nanoparticles", *J. Appl. Phys.*, 2005, 97, 084306
- [65]. Smith, "Infrared Spectral Interpretation: A Systematic Approach", CRC Press LLC: Boca Raton, FL, 1999, p. 25.
- [66]. R. L. Schalla, E. A. Fletcher, "Ignition behavior of various amines with white fuming nitric acid", *ARS Journal*, 1959, 29, 33-39.
- [67]. R. P. Rastogi, N. L. Munjal, "Mechanism kinetics of preignition reactions. I. Aniline red-fuming nitric acid propellants", *Indian J. Chem.*, 1966, 4, 463-468.
- [68]. M. L. Bernard, A. Cointot, M. Auzanneau, B. Sztal, B. "Role of surface reactions in hypergolic ignition of liquid-solid systems", *Combust. Flame*, 1974, 22, 1-7.
- [69]. Osmont, L. Catoire, I. Gökalp, V. Yang, "Ab initio quantum chemical predictions of enthalpies of formation, heat capacities, and entropies of gas-phase energetic compounds", *Combust. Flame*, 2007, 151, 262-273.
- [70]. G. A. Olah, R. Malhotra, S. C. Narang, "Nitration: Method and Mechanisms", VHC Publishers: New York, NY, 1989, 220-228.
- [71]. L. H. Williams, "Nitrosation", Cambridge University Press: New York, NY, 1988, p. 37.
- [72]. Dayagi, Y. Degani, "The Chemistry of the Carbon-Nitrogen Double Bond", Ed. S. Patai, Interscience Publishers: New York, NY, 1970, p. 85.
- [73]. N. Kumbhakarna, S. T. Thynell, A. Chowdhury, P. Lin, "Analysis of RDX-TAGzT pseudo-propellant combustion with detailed chemical kinetics", *Combust. Theor. Model*, 15, 933-956.
- [74]. W. R. Anderson, N. E. Meagher, J. A. Vanderhoff, "Dark zones of solid propellant flames: Critically assessed datasets, quantitative model comparison, and detailed chemical analysis", *Combust. Flame*, 158, 1228-1244.
- [75]. B. Kondrikov, V. Annikov, V. Egorshv, L. De Luca, "Burning of hydroxylammonium nitrate", *Combust. Explos. Shock Waves*, 2000, 36, 135-145.

- [76]. de Bonn, A. Hammerl, T. M. Klapotke, P. Mayer, H. Piotrowski, H. Zewen, "Plume Deposits from Bipropellant Rocket Engines: Methylhydrazinium Nitrate and N,N-Dimethylhydrazinium Nitrate", *Z. Anorg. Allg. Chem.*, 2001, 627, 2011-2015.
- [77]. R. L. Redington, C.-K. J. Liang, "Vibrational spectra of glyoxylic acid monomers", *J. Mol. Spectrosc.*, 1984, 104, 25-39.
- [78]. M. Takasaki, K. Harada, "Oxidation reaction of aliphatic amines and aminoalcohols in aqueous solution induced by argon arc plasma", *Tetrahedron*, 1985, 41, 4463-4473.
- [79]. S. Pimentel, F. C. A. Lima, A. B. F. da Silva, "The isomerization of dinitrogen tetroxide: O<sub>2</sub>N-NO<sub>2</sub> ↔ ONO-NO<sub>2</sub>", *J. Phys. Chem. A*, 2007, 111, 2913-2920.
- [80]. T. Kakumoto, K. Saito, A. Imamura, "Unimolecular decomposition of oxalic acid", *J. Phys. Chem.* 1987, 91, 2366-2371.
- [81]. J. Higgins, X. Zhou, R. Liu, T. T. S. Huang, "Theoretical Study of Thermal Decomposition Mechanism of Oxalic Acid", *J. Phys. Chem. A*, 1997, 101, 2702-2708.
- [82]. R. A. Back, S. Yamamoto, "The gas-phase photochemistry and thermal decomposition of glyoxylic acid", *Can. J. Chem.*, 1985, 63, 542-548.
- [83]. R. A. Friedel, J. L. Shultz, A. G. Sharkey, "Mass spectrum of nitric acid", *Anal. Chem.*, 1959, 31, 1128-1128.
- [84]. J. Lindstrom, W. G. Mallard, Eds., NIST Chemistry WebBook, NIST Standard Reference Database Number 69, National Institute of Standards and Technology, Gaithersburg MD, 20899, <http://webbook.nist.gov>.
- [85]. W. Daimon, Y. Gotoh, I. Kimura, "Mechanism of Explosion Induced by Contact of Hypergolic Liquids", *J. Propul. Power*, 1991, 7, 946-952.

## IV. IGNITION AND REACTION MECHANISMS IN GAS PHASE

### IV.1 Aerosol Shock Tube Experiments (Hanson, Stanford University)

#### 1. Abstract

A unified experimental and theoretical approach is used to establish detailed and reduced reaction mechanisms for hypergolic propellants. Initial studies focused on the chemistry of nitrogen-containing species including MMH (monomethylhydrazine), TMEDA (tetramethylethylenediamine), Morpholine, EA (ethylamine), and DMA (dimethylamine). Shock tubes are used to provide a well-understood, near-ideal constant volume test platform. Laser diagnostics are used to measure species time-histories during pyrolysis and oxidation of GHPs and related species and their subsequent reaction products. Shock tube/laser absorption experiments include measurements of ignition delay time, time-histories of gas-phase species concentrations, and elementary reaction rate constants. To this end, we have developed an extensive database of multi-species time-history measurements during MMH oxidation and pyrolysis (including MMH, OH, NH<sub>2</sub>, NH<sub>3</sub> and CH<sub>4</sub>), high-pressure ignition delay time measurements of TMEDA and morpholine, NH<sub>2</sub> time-history measurements during the reaction of MMH+NO<sub>2</sub>, and rate constant measurements for key reactions in the MMH and N/H/O pyrolysis and oxidation systems. Mechanisms and refinements to mechanisms for GHP archetypal fuels have also been developed.

#### 2. Experimental Facilities and Methods

Three different shock tubes were used for this research. Laser absorption diagnostic methods were used to monitor different species during the combustion processes of the fuels. This section covers the fundamental theory and detailed descriptions of these facilities and of the laser absorption measurements.

##### 2.1 Shock Tube Facility

A shock tube is a test facility close to be an ideal zero-dimension reactor with uniform temperature and pressure that can be readily generated by shock heating. A diaphragm is used to separate the tube into the driver and driven section. When the diaphragm breaks a shock wave will form, travel down the tube, reach the end wall of the shock tube then reflect back. Optical diagnostics can be implemented in the heated test gas behind the incident or the reflected shock waves. With accurate measurement of the incident shock speed, the test conditions behind shock waves can be determined accurately using the ideal shock jump relations. A schematic for shock tube operation is shown in Figure 1.

##### 2.2 Stanford High Pressure Shock Tube (HPST)

This shock tube has a stainless steel driven section of 5 m length with a 5 cm inner diameter and a driver section that is 3 m long with an inner diameter of 7.5 cm. Shock tube driver inserts were used to achieve uniform test conditions at lower temperatures where facility effects at long test times ( $dP/dt$  and  $dT/dt$ ) are most significant. In the current study, a test time about 2.5 ms was achieved with uniform test conditions using helium driver gas. The incident shock speed, which is critical to the accurate determination of reflected shock pressure and temperature, was determined using five piezoelectric pressure transducers that were spaced at approximately 30 cm intervals over the last 2 m of the shock tube. The driven section was heated to 86 °C to mitigate condensation of fuel on the wall. Temperatures and pressures in the post-shock region were determined from the incident shock speed at the end wall using standard normal shock

relations. Ignition pressure was monitored using a piezoelectric pressure transducer (Kistler Model 603B1) located 1 cm from the end wall.

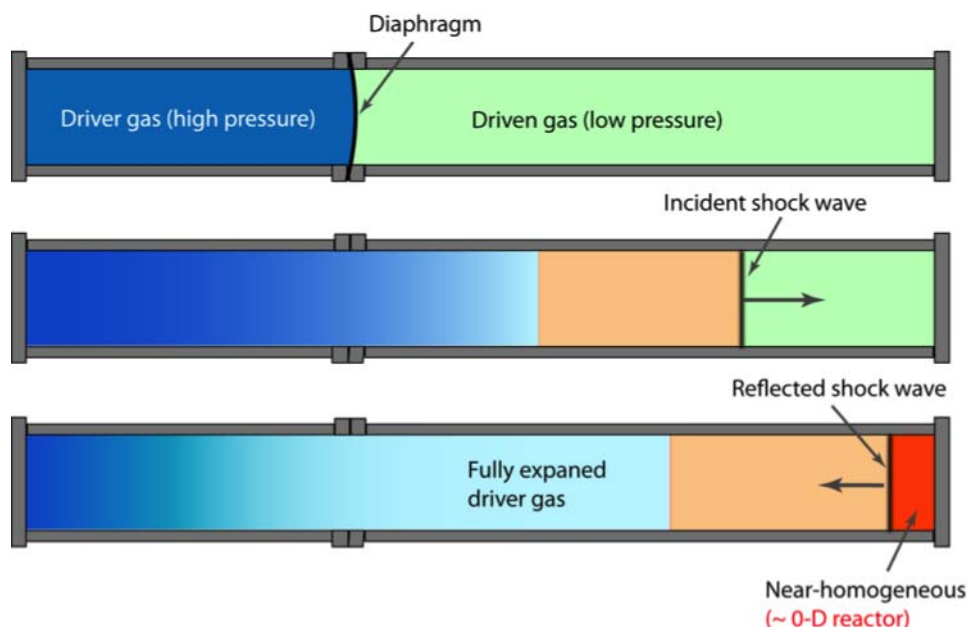


Figure 1. Schematic of shock tube operation.

### 2.3 Stanford Kinetic Shock Tube (KST)

This shock tube has a 3.35 m driver section and an 8.54 m driven section, both with an inner diameter of 14.13 cm. Shock tube driver inserts were used to achieve uniform test conditions. In the current study, a test time about 2 ms was achieved with uniform test conditions using helium driver gas. The incident shock speeds were measured using five piezoelectric pressure transducers near the driven section endwall. Between experiments, the shock tube was routinely evacuated to  $\sim 5$   $\mu$ torr to ensure purity of the test mixtures.

### 2.4 Stanford NASA Shock Tube (NASA)

This shock tube has a 3.7 m driver section and a 10 m driven section, both with an inner diameter of 15.24 cm. The incident shock speeds were measured using five piezoelectric pressure transducers over the last 1.5 meters of the shock tube and linearly extrapolated to the endwall. The ignition pressures were monitored using a piezoelectric pressure transducer (Kistler Model 603B1) located 2 cm from the end wall; laser absorption measurements were conducted at the same axial location.

### 2.5 Laser Absorption Strategy

The primary laser diagnostic method utilized is the fixed-wavelength direct absorption technique, which is a power tool for chemical kinetics study. One advantage of this laser absorption diagnostic method is that it enables rapid real-time measurement at kHz-MHz rates, which can be used to determine the time evolution of important species in combustion processes. As well, laser absorption is non-intrusive, and does not perturb the kinetic process. In this work, species time-history measurements for important combustion compounds were used to provide kinetic information for mechanism validation and modification.

Species concentration can be inferred from laser absorption measurement via the Beer-Lambert law  $\alpha = -\ln(T) = -\ln(I/I_0) = P \times k \times L$ , where  $\alpha$  is the absorbance,  $T$  is the transmission,  $I$  is the transmitted laser intensity with absorption through the test region,  $I_0$  is the laser intensity without absorption,  $P$  is the pressure,  $x$  is the mole fraction of the absorbing species, and  $k$  is the absorption coefficient of the target species,  $L$  is the laser pathlength in the test region. With the measured absorbance and pressure inside the shock tube, and the known absorption coefficient and the laser pathlength, the mole fraction of the absorbing species can be derived directly.

## 2.6 Ring Dye Laser Diagnostics

Species time-history measurements of selected species such as OH, CH<sub>3</sub> and NH<sub>2</sub> were measured using the outputs of narrow-linewidth ring dye lasers. NH<sub>2</sub> is probed in the following manner. Visible light near 597.4 nm was generated by pumping Rhodamine 6G dye in a Spectra Physics 380 laser cavity with the 5 W, continuous wave, output of a Coherent Verdi laser at 532 nm. Using a common-mode rejection detection setup, a minimum NH<sub>2</sub> detection sensitivity of 5 ppm could be achieved for most conditions studied in this work. A schematic of the NH<sub>2</sub> diagnostic is shown in Figure 2. OH was measured near 306.7 nm using the frequency-doubled output of the same ring dye laser system as for the NH<sub>2</sub> diagnostic. The chosen wavelength was the peak of the well-characterized R<sub>1</sub>(5) absorption line in the OH A-X(0,0) band. Visible light near 613.4 nm generated in the Spectra Physics 380 laser cavity was intracavity frequency-doubled using a temperature-tuned AD\*A nonlinear crystal to generate ~1 mW of UV light near 306.7 nm. Using a common-mode rejection detection setup, a minimum OH detection sensitivity of 0.5 ppm could be easily achieved.

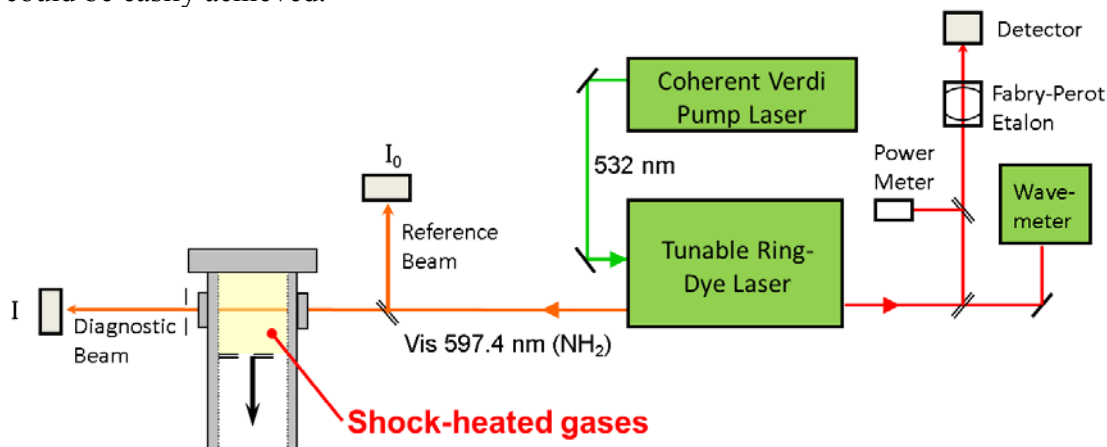


Figure 2. Ring dye laser diagnostic of NH<sub>2</sub>, using the fundamental output of a Spectra Physics 380 ring dye laser.

## 3. Summary of Results

### 3.1 MMH Pyrolysis and Oxidation

This section is adapted from the following studies:

D. F. Davidson, R. D. Cook, S. H. Pyun, R. K. Hanson, "MMH Pyrolysis and Oxidation: Species Time-History Measurements behind Reflected Shock Waves," Paper #9, 23rd ICDERS Meeting July 24-29, 2011 Irvine, CA.



R. D. Cook, S. H. Pyun, J. Cho, D. F. Davidson, R. K. Hanson, "Shock tube measurements of species time-histories in monomethylhydrazine pyrolysis," *Combustion and Flame* 158 (2011) 790-795.

Monomethyl hydrazine ( $\text{CH}_3\text{NHNH}_2$ , MMH) is a widely used rocket propellant. It is particularly important because the combination of MMH and nitrogen tetroxide is hypergolic, meaning that the components ignite spontaneously when they are combined. As researchers have tried to develop comprehensive oxidation mechanisms for a variety of different oxidizers, MMH pyrolysis kinetics has become very important. Unfortunately, there is currently little data from which to establish the important decomposition channels and corresponding reaction rate coefficients in MMH pyrolysis. In addition, the experimental database of species time-histories in MMH oxidation is very limited, resulting in very few targets for the evaluation of MMH oxidation mechanisms.

The earliest pyrolysis study was performed in a flow reactor by Kerr et al. using the toluene carrier method at pressures of 0.01 – 0.04 atm [1]. Eberstein and Glassman performed atmospheric flow reactor studies of MMH pyrolysis between 750 – 1000 K in a nitrogen carrier gas [2]. That study showed the overall reaction order to be close to 1. Subsequently, Golden et al. studied MMH decomposition at very low pressures and temperatures between 923 – 1273 K, suggesting that the  $\text{H}_2$  and  $\text{NH}_3$  molecular elimination channels were dominant [3]. The first shock tube study of MMH pyrolysis was performed by Catoire et al., using mixtures of 1 – 3 % MMH in Ar at pressures of 1.4 – 4.5 atm and temperatures of 1040 – 1370 K [4]. MMH concentration time-histories were measured using absorption at 220 nm. Catoire et al. also measured ignition delay times with  $\text{O}_2$  as the oxidizer in mixtures of 1 – 8% MMH,  $\phi = 1 - 4.3$ , in Ar bath gas and developed a comprehensive MMH pyrolysis and oxidation mechanism [5,6] (referred to here as the Catoire mechanism). Recently Sun and Law developed an MMH pyrolysis mechanism based on quantum Rice-Ramsperger-Kassel (QRRK) theory and a master equation analysis for pressure falloff [7]. In contrast to previous studies, the dominant MMH decomposition channels were determined to be N-N and C-N bond scission. Sun et al. also used the pyrolysis data of Catoire et al. [4] to validate their comprehensive pyrolysis mechanism [8]. The most recent calculation of MMH decomposition was performed by Zhang et al. [9] using *ab initio* transition state theory and master equation analysis. That calculation agreed with the dominant decomposition channels proposed by Sun et al. [7], and provided refined pressure-dependent rates for both decomposition channels. An oxidation mechanism for MMH and red fuming nitric acid has also been developed by Anderson et al. [10] (referred to here as the Anderson mechanism). That work contains much of the same MMH pyrolysis chemistry as the Catoire mechanism, but has updated  $\text{NH}_3$  and  $\text{NO}_x$  chemistry. Recent pyrolysis studies by Sun et al. [7] and Zhang et al. [9] have not previously been incorporated into the Catoire or Anderson oxidation mechanisms.

This work augments the MMH pyrolysis experimental database by adding two additional species time-histories,  $\text{NH}_2$  and  $\text{NH}_3$ , as well as measuring MMH at an IR wavelength where interference could be measured and subtracted from the signal. We used a mixture composition of 1% MMH in an Ar bath gas, and covered temperatures from 941 – 1252 K and pressures from 1.7 – 2.6 atm. Quantitative  $\text{NH}_2$  time-histories were made using laser absorption of the doublet feature at  $16739.90\text{ cm}^{-1}$  (597.4 nm).  $\text{NH}_3$  was measured using the 9R(30) line of a  $\text{CO}_2$  laser at  $9.22\text{ }\mu\text{m}$ . MMH was measured using the 10R(24) line of a  $\text{CO}_2$  laser at  $10.22\text{ }\mu\text{m}$ . These three diagnostics give substantial new insight into the MMH pyrolysis mechanism. The MMH

oxidation experimental database is expanded by providing OH and NH<sub>2</sub> species time-histories. In addition, this work addresses the considerable challenge of modeling shock tube gasdynamics in the MMH oxidation system, due to the presence of significant pre-ignition energy release. Finally, new oxidation mechanisms were developed by replacing the outdated pyrolysis submechanism in the Anderson and Catoire mechanisms with pyrolysis chemistry based on the most recent MMH pyrolysis studies [8, 9, 11]. The mixture used was 1% MMH, 2.5% O<sub>2</sub>, in an Ar bath gas, at pressures near 1.6 atm and temperatures from 1136 – 1287 K. The time-histories of two species, improved treatment of MMH pyrolysis, and improved gasdynamic modeling give substantial new insight into the MMH oxidation system.

### 3.1.1 Experimental Setup

All experiments were performed behind reflected shock waves in a high-purity, 15 cm diameter, helium-driven, stainless-steel shock tube. Optical measurements were made at a location 2 cm from the endwall of the shock tube. Incident shock velocities were calculated based on 5 piezoelectric pressure transducer measurements spread over the last two meters of the shock tube and linearly extrapolated to the endwall. Temperatures and pressures in the reflected shock region were calculated using a frozen-chemistry, ideal-shock code, resulting in an uncertainty of <1% in the initial reflected-shock temperature and pressure.

Mixtures were prepared manometrically in a high-purity mixing assembly and stored in a 14L stainless-steel mixing vessel. A magnetically driven stirrer was used to ensure homogeneous mixtures. Details of the methods used to prepare accurate mixtures have been reported elsewhere [12]. Research grade Ar (99.99%), He (99.99%), and a premixed cylinder of 1% NH<sub>3</sub> in Ar were supplied by Praxair. MMH (98%) was supplied by Sigma-Aldrich. Catalytic decomposition and wall adsorption of MMH can be a problem with some materials, so great care was taken to determine the initial concentration of MMH in the shock tube. MMH concentration in the shock tube at room temperature was measured using 244 nm laser absorption and the room temperature absorption cross section of Vaghjiani [13]. In order to determine if any decomposition or wall adsorption occurred in the mixing tank, MMH concentration was measured using 3 different mixing times: 15 minutes, 1 hour, and 1 day. In addition, an MMH mixture was measured after sitting in the shock tube for 5 minutes (typical) and 1 hour. For all cases, the measured initial MMH concentration in the shock tube remained in the narrow range 0.95 – 1%. The nominal mixtures in the mixing tank based on partial pressures were 0.99 – 1.01% MMH. The good agreement between these two independent measurements gives us confidence in our initial mixture composition. Between experiments, the shock tube and mixing manifold were routinely pumped down to  $\sim 5 \times 10^{-6}$  torr and  $\sim 10^{-3}$  torr, respectively, to ensure the purity of the test mixture. The leak-plus-outgassing rate was  $\sim 10 \times 10^{-6}$  torr/min.

NH<sub>2</sub> concentration was measured using narrow-linewidth laser absorption at 16739.90 cm<sup>-1</sup>. The chosen NH<sub>2</sub> wavelength (597.4 nm) was the peak of the overlapping  $\tilde{A}A_1 \leftarrow X^2B_1(090 \leftarrow 000)\Sigma^P Q_{1,N}7$  doublet lines. Absorption coefficients were calculated using the spectroscopic parameters of Kohse-Hoinghaus et al. [14] and Votsmeier et al. [15]. Votsmeier et al. [15] carefully validated the absorption coefficient from 1600 – 2000 K, and pressures below 5 atm, resulting in an estimated uncertainty in that range of +/-10%. Since our work was done at much lower temperatures, we estimate the uncertainty near 1000 K to be larger, about +/- 30% based on uncertainty in the average oscillator strength of the doublet and uncertainty associated with collision broadening. Laser light at 16739.90 cm<sup>-1</sup> (597.4 nm) was generated by a Spectra Physics 380 dye laser pumped by a 5W Coherent Verdi at 532 nm. Over 10 mW of light near

597.4 nm was easily achievable, however about 90% of the light was blocked with a neutral density filter to avoid saturating the detector (Thorlabs PDA36A). The wavelength was measured using a Bristol 621A visible wavemeter with an accuracy of 0.2 ppm. Common mode rejection was used to reduce laser intensity noise to  $< 0.3\%$  in the reflected shock region, resulting in a minimum detection sensitivity of  $\sim 5$  ppm for most conditions studied. Quantitative  $\text{NH}_2$  concentration was calculated using Beer's law. Measurements were also performed with the laser tuned off the  $\text{NH}_2$  absorption line and with the laser turned off to verify that there was no significant interfering absorption or emission.

$\text{NH}_3$  concentration was measured at  $9.22\text{ }\mu\text{m}$  using the 9R(30) line of a  $\text{CO}_2$  laser. The line was chosen because strong room temperature absorption of  $\text{NH}_3$  has been previously observed at this wavelength. However, the high-temperature behavior of this absorption feature has not previously been studied. The absorption coefficient was directly measured by shock heating mixtures of 1%  $\text{NH}_3$  in Ar at pressures near 1.8 atm and temperatures from 942 – 1426 K, resulting in an uncertainty of less than 15%. The  $\text{CO}_2$  laser (Access Laser Co. LASY-4G) produced  $\sim 20$  mW at this wavelength. The laser light was focused through the shock tube and then focused onto a custom, photovoltaic, thermoelectrically-cooled MCT detector built by Boston Electronics. A portion of the beam was also split off before passing through the shock tube for common mode rejection, resulting in laser intensity noise of  $< 0.2\%$  in the reflected shock region. The wavelength was measured using a Bristol 721B infrared wavemeter/spectrum analyzer with an accuracy of 0.75 ppm. The spectrum analyzer was also used to verify single-mode operation of the laser. Measurements were performed with the laser turned off and also using an adjacent  $\text{CO}_2$  laser line to verify that there was no significant interfering absorption or emission.

MMH concentration was measured at  $10.22\text{ }\mu\text{m}$  using the 10R(24) line of the  $\text{CO}_2$  laser. Previous measurements of MMH at 220 nm demonstrate significant non-exponential behavior at low temperatures that cannot be reproduced by the most recent MMH pyrolysis mechanism [5]. One potential explanation for this phenomenon is the presence of significant interference absorption. Both  $\text{CH}_3$  and  $\text{NH}_3$  are known to absorb at 220 nm over the temperature range of their work. Initially in this study, absorption measurements were performed at 244 and 306 nm, since both  $\text{CH}_3$  and  $\text{NH}_3$  absorbance are expected to decrease at longer UV wavelengths. Unfortunately, absorption traces at both wavelengths still exhibited signs of significant interference absorption, especially at low temperatures (Figure 3) where we expect MMH to undergo decomposition beginning at early times. Neither the 244 nm nor the 306 nm signals exhibit this expected behavior. At higher temperatures it was also observed that the UV absorption traces did not decay to zero, indicating that there was interference absorption from some of the product species as well. We conclude that interference effects may preclude the use of UV absorption for quantitative detection of MMH.

Approximately 100 mW of light was available at the 10R(24)  $\text{CO}_2$  laser line. The wavelength was chosen based on room temperature measurements of the FTIR absorption spectra of MMH and  $\text{NH}_3$ , which are shown in Figure 4. The 10R(24) line shows significant sensitivity to MMH and is away from any strong  $\text{NH}_3$  absorption features. However, there is no available high-temperature data for either species. High-temperature absorption coefficients of MMH and  $\text{NH}_3$  were measured by shock heating mixtures of 1% MMH in Ar and 1%  $\text{NH}_3$  in Ar, respectively. At pressures near 1.8 atm, MMH could be successfully isolated from 950 – 1130 K.  $\text{NH}_3$  absorption interference varied from being negligible at the lowest temperatures to as much as

40% of the absorbance at the highest temperatures. The upper bound of the temperature range was set by the appearance of interference absorption at long times that could not be corrected by accounting for  $\text{NH}_3$  alone. The optical setup and detection scheme were identical to the  $\text{NH}_3$  absorption diagnostic.

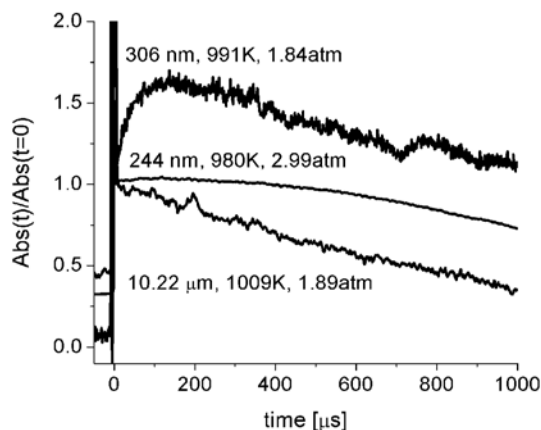


Figure 3. Comparison of measured absorbance in the pyrolysis of 1% MMH/Ar mixtures at 244 nm, 306 nm and 10.22  $\mu\text{m}$ .

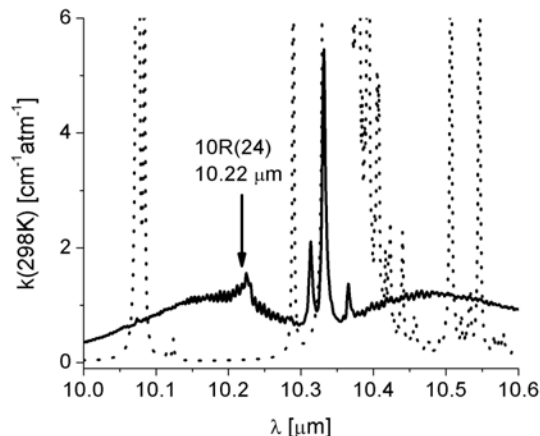


Figure 4. Room temperature FTIR spectra of  $\text{NH}_3$  (dotted line) and MMH (solid line), and  $\text{CO}_2$  laser line chosen for the MMH diagnostic. ( $\text{NH}_3$  absorption extends beyond the scale of the plot near 10.35  $\mu\text{m}$ )

OH concentration was measured using narrow-linewidth laser absorption near 306.7 nm. The chosen OH wavelength was the peak of the well-characterized  $\text{R}_1(5)$  absorption line in the OH A-X (0,0) band. Laser light at 613.4 nm was generated by a Spectra Physics 380 dye laser pumped by a 5W Coherent Verdi at 532 nm. Light at 306.7 nm was generated by intracavity frequency-doubling, using a temperature-tuned AD\*A crystal. Common mode rejection was used to reduce laser intensity noise to  $< 0.1\%$ , resulting in a minimum detection sensitivity of  $< 1$  ppm for most conditions in this work. OH concentration was calculated using Beer's law and the estimated uncertainty in measured  $X_{\text{OH}}$  is  $\sim 3\%$ . Measurements were also performed with the laser tuned off the OH absorption line and with the laser turned off to verify that there was no significant interfering absorption or emission. Further details of the OH laser absorption diagnostic are available elsewhere [16].

### 3.2 MMH Pyrolysis

#### 3.2.1 Kinetic and Gasdynamic Modeling

The MMH pyrolysis reaction mechanism used in analyzing the data presented here was the most recent mechanism by Sun et al. [7], modified with the pressure-dependent MMH decomposition rates from Zhang et al. [9]. For convenience, this mechanism will be referred to as the "Princeton mechanism". The Princeton mechanism was chosen because of its comprehensive treatment of MMH decomposition pathways and its subsequent fragments. The CHEMKIN PRO package was used to interpret the mechanism and generate all of the modeling results. Choosing the appropriate gasdynamic model for this work is somewhat difficult. Since the MMH decomposition process is exothermic, even our relatively dilute 1% mixtures can result in significant increases in temperature and pressure when the standard assumption of constant volume is applied to modeling chemical reactions in the reflected shock region. For example, using the constant volume assumption, the modeled pressure increases by about 7% during the

test time at the conditions shown in Figure 5. However, the measured pressure remains constant throughout the experiment. In fact, it is already known that the temperature and pressure increases predicted by the constant volume assumption are often exaggerated in cases where significant energy release is present. Since all of the experiments in this study demonstrated no measurable pressure increase during the test time, the gasdynamic model chosen was adiabatic and constant pressure. This reduces the modeled temperature rise during the test time by a factor of two compared to the constant volume model (Figure 6).

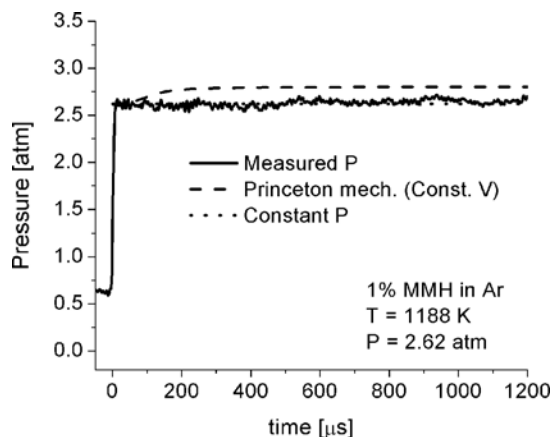


Figure 5. Comparison of measured pressure to constant volume and constant pressure models. Initial conditions are  $T_5 = 1188$  K and  $P_5 = 2.62$  atm.

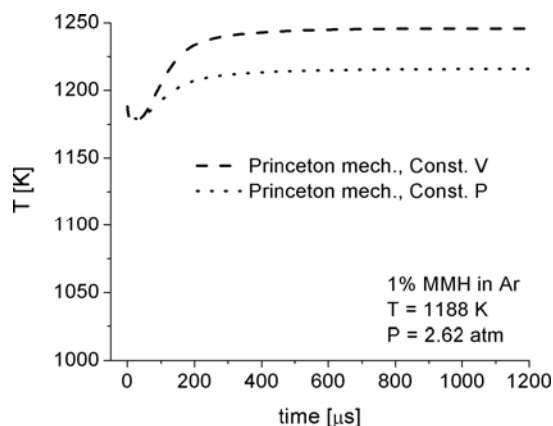


Figure 6. Comparison of modeled temperature using constant volume and constant pressure models. Initial conditions are  $T_5 = 1188$  K and  $P_5 = 2.62$  atm.

### 3.2.2 Results and Discussion

$\text{NH}_3$  was measured from 942 – 1426 K and at pressures near 1.8 atm. As expected, significant  $\text{NH}_3$  was detected, but the initial rate of formation is much faster than predicted by the Princeton mechanism. An example trace and the corresponding sensitivity analysis are shown in Figure 7.

The initial formation rate of  $\text{NH}_3$  is primarily dependent on the following two rates:

- (1)  $\text{CH}_3\text{NHNH}_2 \rightarrow \text{CH}_3\text{NH} + \text{NH}_2$
- (2)  $\text{CH}_3\text{NHNH}_2 + \text{NH}_2 \rightarrow \text{CH}_3\text{NNH}_2 + \text{NH}_3$

While it is obvious that one or both of those rates must be increased in the Princeton mechanism, there is no unique solution based on the  $\text{NH}_3$  data alone. However, the addition of  $\text{NH}_2$  measurements helps the situation greatly.

$\text{NH}_2$  was measured from 1111 – 1252 K and at pressures near 2.6 atm. At temperatures significantly below 1111 K, the amount of  $\text{NH}_2$  produced was too small to be measured accurately with the available diagnostic. An example  $\text{NH}_2$  measurement and sensitivity plot are shown in Figure 8.

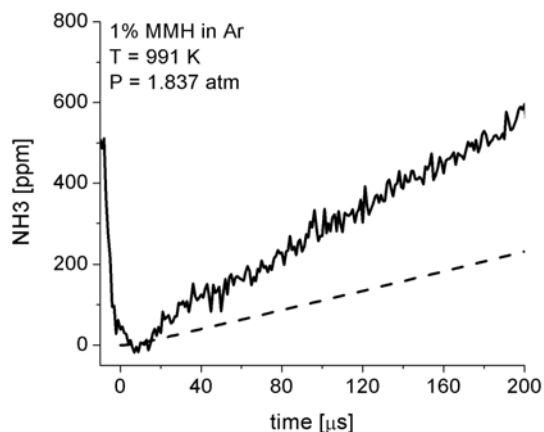


Figure 7(a). Comparison of measured  $\text{NH}_3$  (solid line) with the original Princeton mechanism (dashed line)

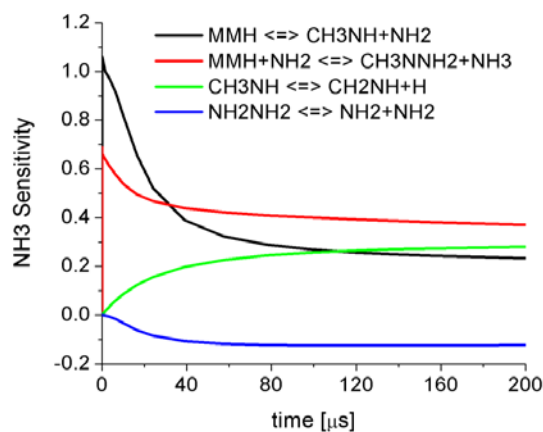


Figure 7(b).  $\text{NH}_3$  sensitivity at 991 K and 1.837 atm.

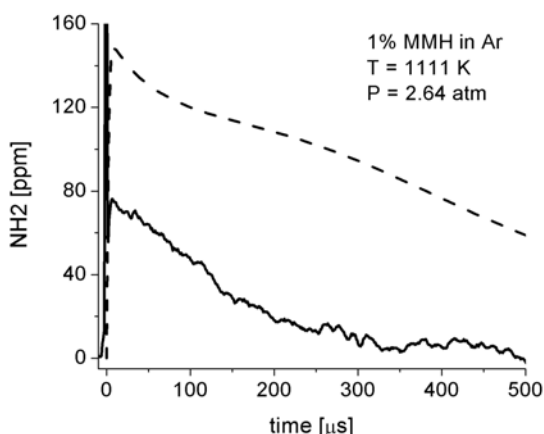


Figure 8(a). Comparison of measured  $\text{NH}_2$  (solid line) with the original Princeton mechanism (dashed line)

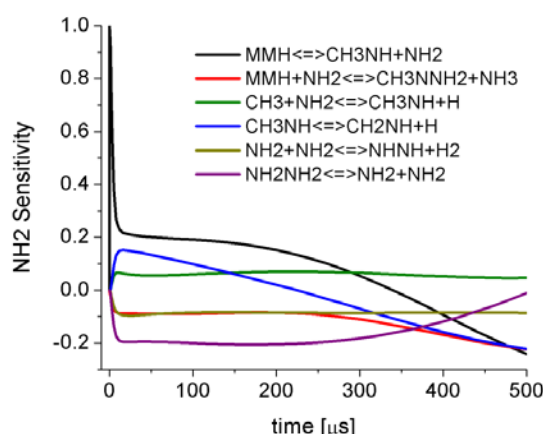


Figure 8(b).  $\text{NH}_2$  sensitivity at 1111 K and 2.64 atm.

The initial peak of  $\text{NH}_2$  is greatly overpredicted by the Princeton mechanism. The corresponding sensitivity plot (Figure 8b) shows that, like  $\text{NH}_3$ ,  $\text{NH}_2$  is sensitive to both Reactions (1) and (2) at early times, but the sensitivities are in opposite directions: Reaction (1) produces  $\text{NH}_2$  while Reaction (2) removes it. There is also significant sensitivity to the hydrazine decomposition rate, but it was not adjusted here since it has been extensively studied previously. Based on the relationship between Reactions (1) and (2), it was possible to find a unique set of values for the rates  $k_1$  and  $k_2$ . The procedure for doing this is to choose a value for  $k_1$ , adjust  $k_2$  until  $\text{NH}_3$  is modeled well, and then compare the measured and modeled values of the  $\text{NH}_2$  peak. This was repeated until the best agreement for both the early formation of  $\text{NH}_3$  and the peak of  $\text{NH}_2$  were obtained. The best agreement was found by decreasing  $k_1$  by 30% and increasing  $k_2$  by a factor of 10 in the Princeton mechanism (Figures 9 and 10).

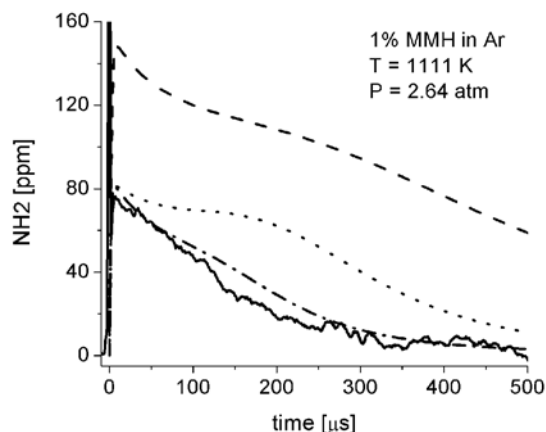


Figure 9(a). Comparison of measured  $\text{NH}_2$  (solid line) with the Princeton mechanism (dashed line), the Princeton mechanism with modified  $k_1$  and  $k_2$  (dotted line), and the Princeton mechanism with modified  $k_1$ ,  $k_2$ , and  $k_4$  (dashed-dotted line) at 1111 K.

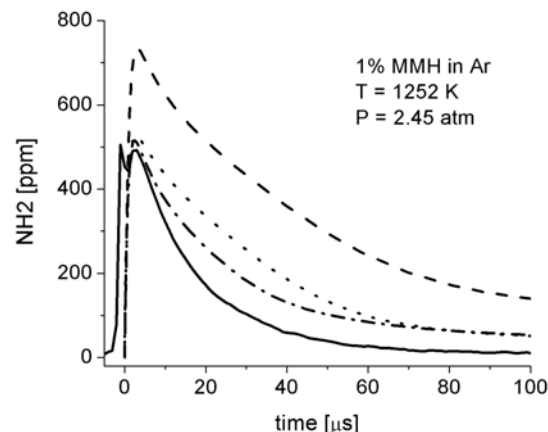


Figure 9(b). Comparison of measured  $\text{NH}_2$  (solid line) with the Princeton mechanism (dashed line), the Princeton mechanism with modified  $k_1$  and  $k_2$  (dotted line), and the Princeton mechanism with modified  $k_1$ ,  $k_2$ , and  $k_4$  (dashed-dotted line) at 1252 K.

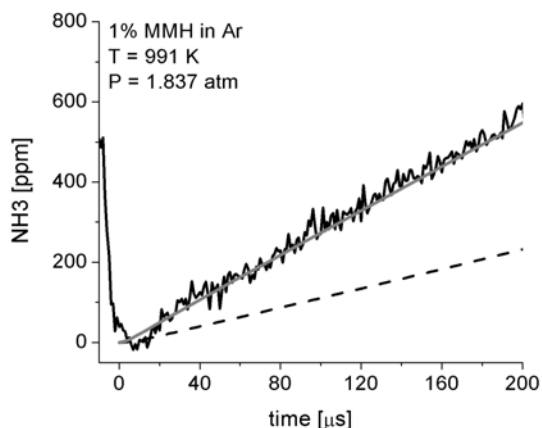


Figure 10(a). Comparison of measured  $\text{NH}_3$  (solid line) with the Princeton mechanism (dashed line) and the Princeton mechanism with modified  $k_1$  and  $k_2$  (gray line) at 991 K.

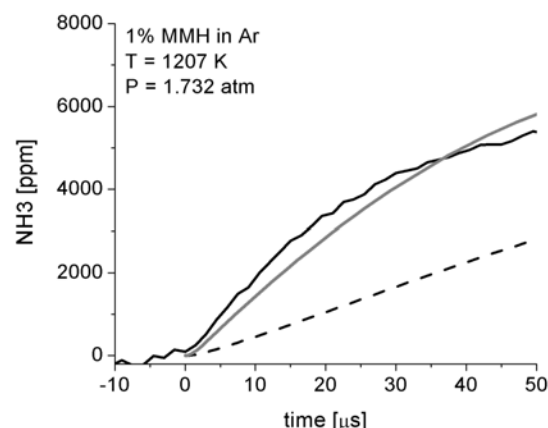
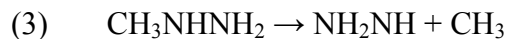
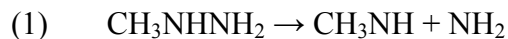


Figure 10(b). Comparison of measured  $\text{NH}_3$  (solid line) with the Princeton mechanism (dashed line) and the Princeton mechanism with modified  $k_1$  and  $k_2$  (gray line) at 1207 K.

MMH was measured at temperatures from 961 – 1112 K. These measurements were carried out to improve upon the 220 nm absorption measurements by Catoire et al. [4]. At 220 nm, significant absorption interference is expected from both  $\text{CH}_3$  and  $\text{NH}_3$ . By contrast, at 10.22  $\mu\text{m}$  only a relatively small amount of  $\text{NH}_3$  interference is expected. Furthermore, the absorption coefficient of  $\text{NH}_3$  was measured at 10.22  $\mu\text{m}$  and the concentration of  $\text{NH}_3$  was measured at 9.22  $\mu\text{m}$ , which allowed  $\text{NH}_3$  absorbance to be subtracted, leaving only MMH absorbance at temperatures below about 1130 K. Results of our measurements at two temperatures are shown in Figure 11.

According to previous theoretical investigations, MMH initially decomposes via the following channels [4-6]:



MMH can also be eliminated by attack from radicals like  $\text{NH}_2$  and  $\text{CH}_3$ . The dashed lines in Figure 11 show that the rate of MMH decay is underpredicted by the Princeton mechanism. However, when the adjustments to  $k_1$  and  $k_2$  from the previous section are applied to the Princeton mechanism, the measured and modeled MMH decay rates agree very well. The most recent theoretical investigation of MMH decomposition by Zhang et al. [9] suggests a value for  $k_3$  that is about 7% of the value of  $k_1$  in the temperature and pressure range of this study. While the value of  $k_1$  is fixed by the  $\text{NH}_3$  and  $\text{NH}_2$  measurements, it should be noted that values of  $k_3$  from 0 – 20% of  $k_1$  are consistent with the measured MMH data. Hence, with regard to  $k_3$ , we can only conclude that the value in the Princeton mechanism is valid to  $\pm 100\%$ . When this estimate of  $k_3$  is combined with the measured value of  $k_1$ , the overall MMH unimolecular decomposition rate can also be determined (See Table 1).

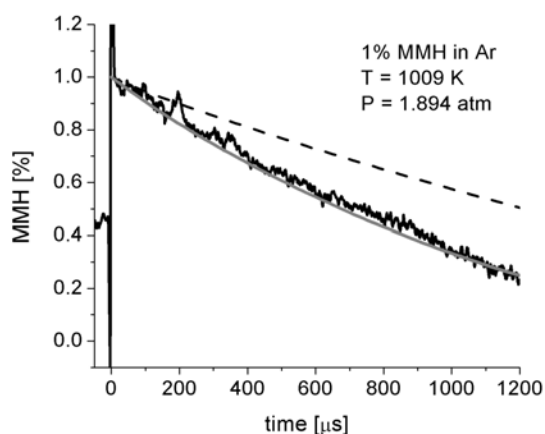


Figure 11(a). Comparison of measured MMH with the Princeton mechanism (dashed line) and the Princeton mechanism with modified  $k_1$  and  $k_2$  (gray line) at 1111 K.

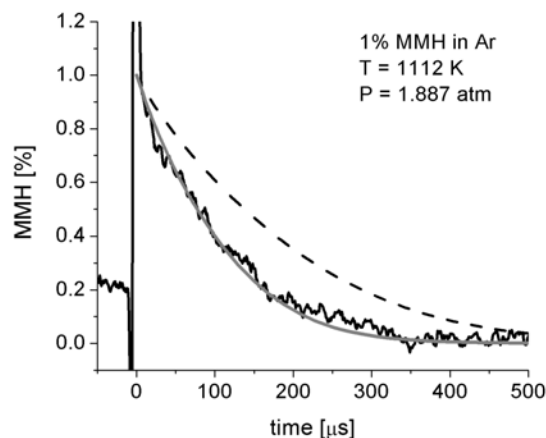


Figure 11(b). Comparison of measured MMH with the Princeton mechanism (dashed line) and the Princeton mechanism with modified  $k_1$  and  $k_2$  (gray line) at 1252 K.

Adjustments to  $k_1$  and  $k_2$  alone are sufficient to match the initial peak of  $\text{NH}_2$ , the early formation rate of  $\text{NH}_3$ , and the overall decomposition rate of MMH. However, there is still a significant discrepancy between measured and modeled  $\text{NH}_2$  after the initial peak, especially at lower temperatures. To address this problem,  $\text{NH}_2$  sensitivity was calculated using the Princeton mechanism with our updated rates for  $k_1$  and  $k_2$ .

In addition to Reactions (1) and (2), the following reaction was found to be relatively important at later times:



When this reaction was increased by a factor of 5, agreement between modeled and measured  $\text{NH}_2$  at later times improved significantly, and is shown by the dash-dot lines in Figure 9. This change in the Princeton mechanism does not have any significant impact on modeled  $\text{NH}_3$  or MMH, however this solution is not entirely unique. Altering the rate of any reaction in which  $\text{NH}_2$  abstracts a hydrogen atom can achieve the desired effect. The recommendation here was



chosen because it requires changing the fewest reactions by the least amount. A summary of recommended rate changes to the Princeton mechanism is shown in Table 1.

Table 1. Summary of rate recommendations based on new  $\text{NH}_2$ ,  $\text{NH}_3$ , and MMH measurements in MMH pyrolysis

Reaction	Recommended Rates, 2 atm, 900 – 1300 K
(1) $\text{MMH} \rightarrow \text{CH}_3\text{NH} + \text{NH}_2$	$1.50 \times 10^{58} \times T^{-12.84} \exp(-39580/T) [\text{s}^{-1}]$
(2) $\text{MMH} + \text{NH}_2 \rightarrow \text{CH}_3\text{NNH}_2 + \text{NH}_3$	$1.65 \times 10^3 \times T^{3.009} \exp(-435/T) [\text{cm}^3\text{mol}^{-1}\text{s}^{-1}]$
(4) $\text{CH}_3\text{NNH} + \text{NH}_2 \rightarrow \text{CH}_3\text{NN} + \text{NH}_3$	$3.70 \times 10^{14} \exp(-2620/T) [\text{cm}^3\text{mol}^{-1}\text{s}^{-1}]$
MMH $\rightarrow$ products	$1.64 \times 10^{58} \times T^{-12.84} \exp(-39580/T) [\text{s}^{-1}]$

### 3.3 MMH Oxidation

#### 3.3.1 Kinetics and Gasdynamics Modeling

The MMH oxidation reaction mechanisms used in analyzing the data presented here are all based on the Catoire and Anderson oxidation mechanisms. The original Catoire and Anderson oxidation mechanisms were used, as well as updated mechanisms including MMH pyrolysis chemistry from the Modified Princeton pyrolysis mechanism. The modified oxidation mechanisms were constructed by replacing all pyrolysis reactions with the Modified Princeton mechanism. Then, reactions of OH and O with MMH and the earliest fragments were added to provide early removal pathways for those key radicals. Finally, reactions of MMH and the earliest fragments with  $\text{O}_2$  were removed because they caused far too much early OH and suppressed early  $\text{NH}_2$  formation. Table 2 summarizes the mechanisms described here.

Table 2. Summary of MMH mechanisms used in this work.

Mechanism Name	Mechanism Description and References
Modified Princeton pyrolysis	Based on Sun et al. [7,8] $\text{MMH} \rightarrow \text{CH}_3\text{NH} + \text{NH}_2$ [this work] $\text{MMH} \rightarrow \text{NHNH}_2 + \text{CH}_3$ [this work] $\text{MMH} + \text{NH}_2 \rightarrow \text{products}$ [this work]
Catoire oxidation	Catoire et al. [5,6]
Anderson oxidation	Anderson et al. [10]
Modified Catoire oxidation	Catoire oxidation + Modified Princeton pyrolysis
Modified Anderson oxidation	Anderson oxidation + Modified Princeton pyrolysis

Choosing the appropriate gasdynamic model for this work is extremely difficult due to significant pre-ignition energy release, even in relatively dilute mixtures of only 1% MMH. This effect is most clearly illustrated by comparing the measured pressure and the predicted pressure based on the standard constant U,V assumption and the Catoire oxidation mechanism (Figure 12(a)). Based on that assumption, the modeled pre-ignition pressure increase is ~15%, while the pressure measurement shows no increase prior to ignition. This phenomenon appears to be similar to the previous observations that temperature and pressure increases predicted during ignition by the constant volume assumption are often exaggerated in cases where significant

energy release is present [17]. This result is somewhat intuitive since the reflected shock region is not literally a fixed volume, 0-D reactor. Energy release occurs earlier near the endwall than farther downstream, resulting in an inhomogeneous mixture. In addition, when energy release is present, the increasing pressure of the reacting mixture can cause the reflected shock to accelerate. The result is that the reacting volume is not as constrained as the constant volume assumption implies. These changes in pressure and temperature prior to ignition significantly impact ignition delay time [18]. If the chosen gasdynamic model does not reproduce the basic features of the measured pressure, it cannot adequately model the experiment. The 15% pre-ignition pressure increase predicted by the constant UV model would increase the pre-ignition temperature by 5%, or over 60 K, based on an isentropic relationship. This issue must be addressed to make meaningful comparisons between the kinetic mechanism and experimental data.

One strategy is to use the measured pressure as an input when performing the kinetic computations. The CHEMKIN PRO computational package can calculate the kinetics at the observation location, using the measured pressure as an input and then solving the energy equation. For a given pressure trace, the result is nearly identical to that obtained with the CHEMSHOCK model developed by previous workers in our laboratory [17]. The drawback of prescribing pressure is that the measured ignition event is embedded in the pressure, making the model less predictive. It would be more predictive, and therefore preferable, to use a model that accepts only the initial conditions, and then calculates P, T, and species time-histories.

Another strategy is to use a 1-D, reacting, inviscid, CFD model to model P, T, and species time-histories throughout the reflected shock region. This method has been previously used to model pressure and temperature increases during ignition experiments [17]. The 1-D model has the advantage of being fully predictive (i.e. does not require pressure input), but it is very computationally expensive. While CHEMKIN PRO can perform calculations with a pressure input in less than one minute, the 1-D model requires nearly 24 hours on a similar computer. However, the 1-D model captures several key features, such as variations in T and P along the axis of the shock tube, and the acceleration of the reflected shock as the test mixture releases energy and ignites. The modeled pressure for one case is shown in Figure 12(b). Using the 1-D model, the pre-ignition pressure increase is only ~4%, and the pressure increase after ignition is much closer to the measured increase. The 1-D model still slightly overpredicts the pre-ignition pressure increase relative to the observed pressure, but shows that when a better gasdynamic model is used, the Catoire mechanism predicts ignition delay times that are significantly longer than measured.

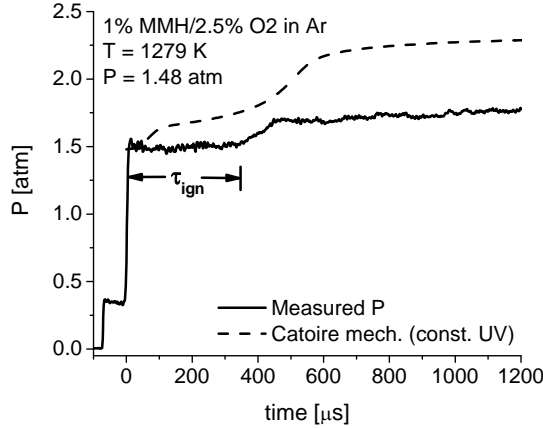


Figure 12(a). Comparison of measured pressure to constant volume model. Initial conditions are  $T_5 = 1279$  K and  $P_5 = 1.48$  atm.

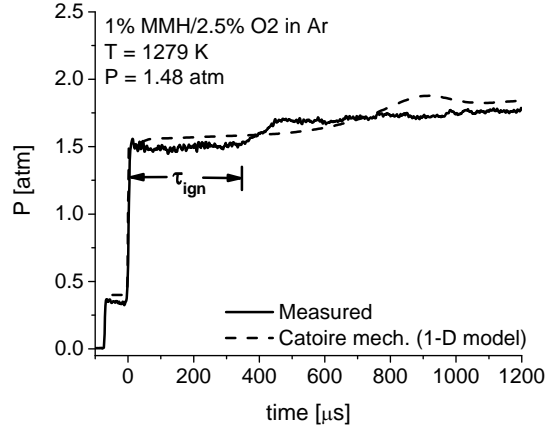
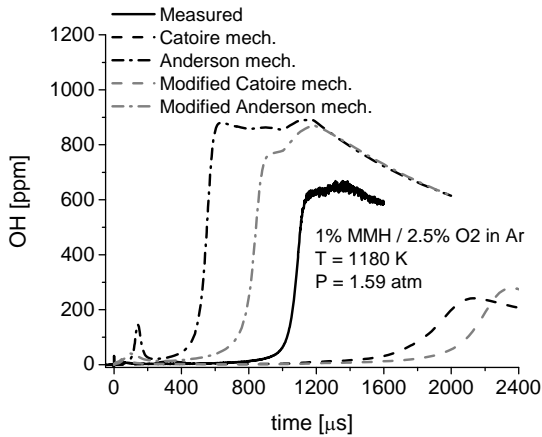


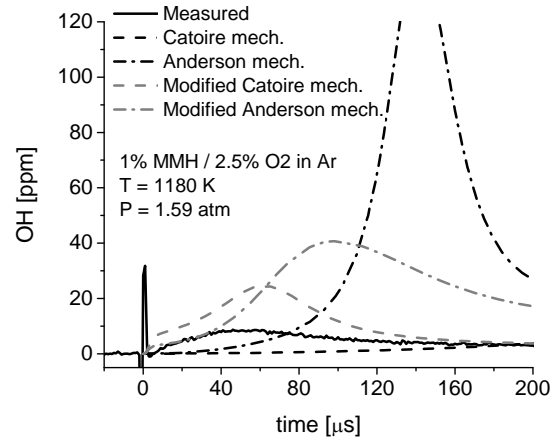
Figure 12(b). Comparison of measured pressure to 1-D model. Initial conditions are  $T_5 = 1279$  K and  $P_5 = 1.48$  atm.

### 3.3.2 Results and Discussion

Initially, all four oxidation mechanisms were considered in this work. Figures 13 and 14 show a comparison of simulations based on these mechanisms at the intermediate temperature, using the measured (i.e., specified) pressure in the simulations. The Modified Anderson mechanism predicts ignition delay time better than the other mechanisms, and its performance with regard to early OH and  $\text{NH}_2$  is also reasonably good. Therefore, further detailed analysis presented here is limited to the Modified Anderson mechanism.



(a)



(b)

Figure 13. Comparison of measured OH to Catoire (black, dash), Anderson (black, dash-dot), Modified Catoire (gray, dash), and Modified Anderson (gray, dash-dot) mechanisms using measured pressure (a) over the entire test time and (b) at early times. Initial conditions are  $T_5 = 1180$  K and  $P_5 = 1.59$  atm.

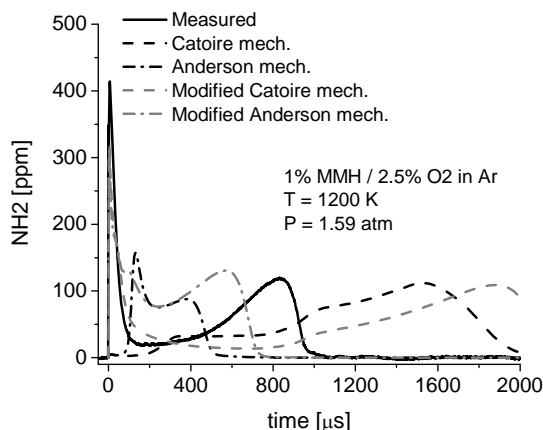


Figure 14. Comparison of measured  $\text{NH}_2$  to Catoire (black, dash), Anderson (black, dash-dot), Modified Catoire (gray, dash), and Modified Anderson (gray, dash-dot) mechanisms using measured pressure. Initial conditions are  $T_5 = 1200$  K and  $P_5 = 1.59$  atm.

$\text{NH}_2$  time-histories were measured at temperatures of 1136, 1200, and 1287 K and pressures near 1.6 atm. Figures 15-17 show the comparison between measured  $\text{NH}_2$  and modeled  $\text{NH}_2$  based on the Modified Anderson mechanism using both measured pressure and the 1-D gasdynamic models. Modeled  $\text{NH}_2$  based on the constant U,V model is also shown for comparison at the intermediate temperature (Figure 16). The first notable feature of the measured  $\text{NH}_2$  time-histories is the initial peak. At 1136 K, the first peak is 136 ppm, which is very similar to the peak of 134 ppm when using the measured pressure. The measured  $\text{NH}_2$  peak increases rapidly at higher temperatures to 410 ppm at 1200 K and 1220 ppm at 1287 K (Figures 16 and 17). The Modified Anderson mechanism increases more moderately, to 310 ppm at 1200 K and 770 ppm at 1287 K. At the two lowest temperatures, after the initial peak, there is also a fluctuation in modeled  $\text{NH}_2$  that is not present in the measurement.

The second notable feature is the second  $\text{NH}_2$  peak, immediately prior to ignition. The measured value of the second peak is much less temperature dependent, 80 ppm at 1136 K, 120 ppm at 1200 K, and 170 ppm at 1287 K (Figures 15-17). The Modified Anderson mechanism predicts this peak reasonably well, ranging from 30% higher at 1136 K to matching within a few ppm at 1287 K. The time to the second peak, indicating the beginning of ignition, is uniformly underpredicted by about 30% using Modified Anderson mechanism with the measured pressure. The 1-D model performs slightly worse, underpredicting ignition delay by about 50%. Figure 16 also shows a comparison based on the same mechanism, but using the less accurate constant U,V gasdynamic model. It is encouraging that the Modified Anderson mechanism captures ignition delay time reasonably well since it was originally developed for a different oxidizer and initially contained an outdated MMH pyrolysis submechanism. Reactions of oxygen-containing species appear to be handled well, and updated MMH pyrolysis chemistry was all that was required to get ignition delay time nearly right. The differences between the different gasdynamic models also demonstrate the great importance of choosing the appropriate gasdynamic model when developing and validating comprehensive reaction mechanisms. Generally, the measured pressure traces demonstrated no pre-ignition pressure increase, while the 1-D model predicted a small pre-ignition pressure increase, and the constant U,V model predicted a comparatively larger pre-ignition pressure increase. These differences are apparent in Figure 16. While the 1-D

model is definitely an improvement over constant U,V modeling, it could still use some refinement as it does not quite capture the measured pressure in the shock tube.

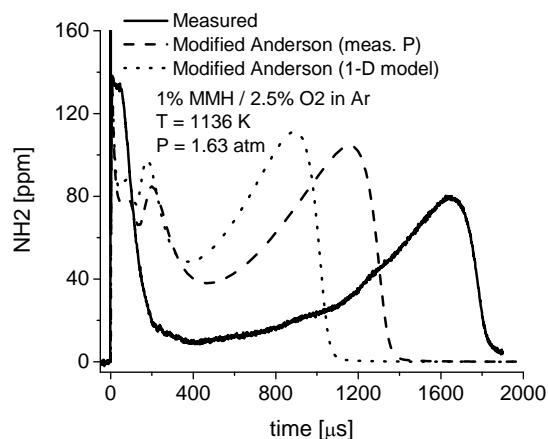


Figure 15. Comparison of measured  $\text{NH}_2$  to Modified Anderson mechanism using measured P (dashed) and 1-D model (dotted). Initial conditions are  $T_5 = 1136$  K and  $P_5 = 1.63$  atm.

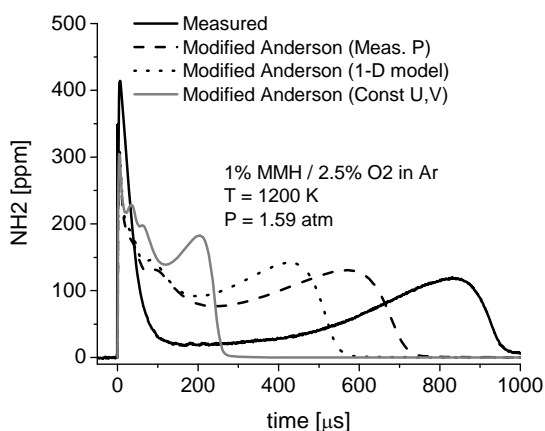


Figure 16. Comparison of measured  $\text{NH}_2$  to Modified Anderson mechanism using measured P (dashed), 1-D model (dotted), and constant U,V model (gray). Initial conditions are  $T_5 = 1200$  K and  $P_5 = 1.59$  atm.

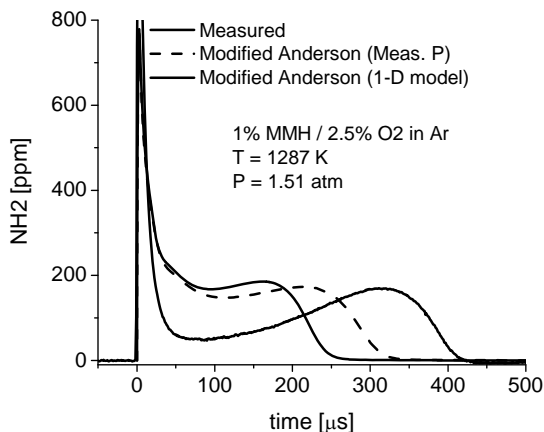
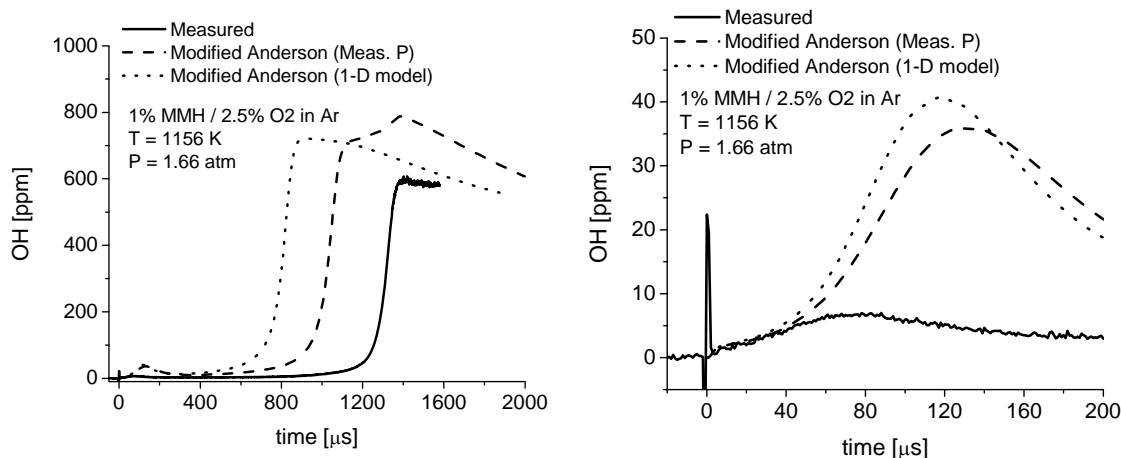


Figure 17. Comparison of measured  $\text{NH}_2$  to Modified Anderson mechanism using measured P (dashed) and 1-D model (dotted). Initial conditions are  $T_5 = 1287$  K and  $P_5 = 1.51$  atm.

OH was measured at temperatures of 1156, 1180, and 1279 K, and pressures near 1.6 atm. Figures 18-20 show the comparisons between measured OH and modeled OH based on the Modified Anderson mechanism using both measured pressure and the 1-D gasdynamic models. Modeled OH based on the constant U,V model is also shown for comparison at the intermediate temperature (Figure 19). The first notable feature is the initial OH peak at the beginning of the time-history. The measured peak at 1156 K is 7 ppm, compared to the modeled peak of 36 ppm. The measured peak increases to 8 ppm at 1180 K and 19 ppm at 1279 K, compared to modeled values of 41 and 62 ppm, respectively. Ignition delay times based on OH are consistent with those based on  $\text{NH}_2$ , and the Modified Anderson mechanism uniformly predicts values that are

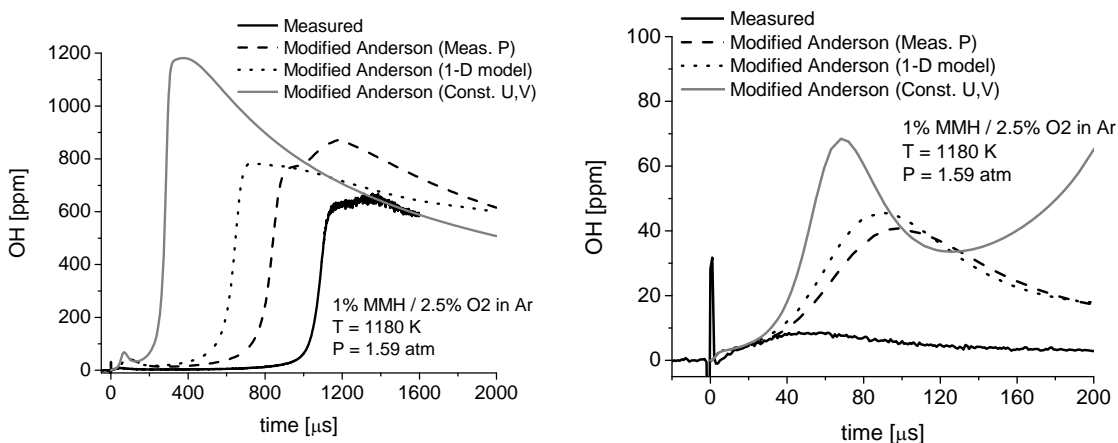
too short by about 30%. Peak OH after ignition is overpredicted by about 30 – 35%. Figure 19 also includes a comparison to the constant U,V gasdynamic model, showing that the magnitudes of both OH peaks are significantly increased when the constant U,V model is used, and ignition delay time is considerably shortened. The deficiencies (and inherent error) of the constant U,V model in simulating reflected shock experiments with energy release are clearly shown here. Also apparent is the comparatively good agreement between the 1-D simulation and that based on use of the specified (measured) pressure.



(a)

(b)

Figure 18. Comparison of measured OH to Modified Anderson mechanism using measured P (dashed) and 1-D model (dotted) (a) over the entire test time and (b) at early times. Initial conditions are  $T_5 = 1156$  K and  $P_5 = 1.66$  atm.



(a)

(b)

Figure 19. Comparison of measured OH to Modified Anderson mechanism using measured P (dashed), 1-D model (dotted), and constant U,V model (gray) (a) over the entire test time and (b) at early times. Initial conditions are  $T_5 = 1180$  K and  $P_5 = 1.59$  atm.

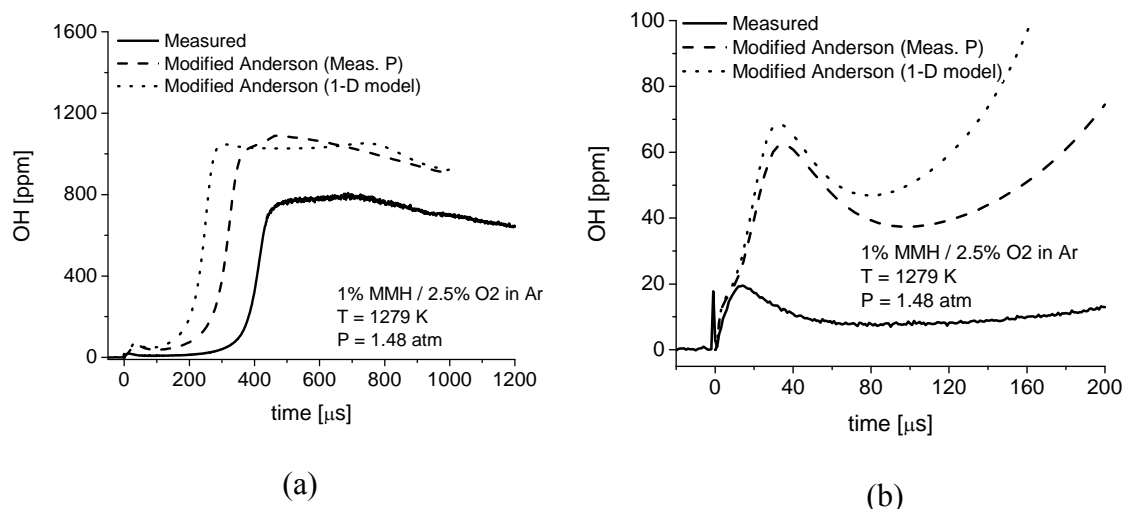


Figure 20. Comparison of measured OH to Modified Anderson mechanism using measured P (dashed) and 1-D model (dotted) (a) over the entire test time and (b) at early times. Initial conditions are  $T_5 = 1279$  K and  $P_5 = 1.48$  atm.

Generally, the Modified Anderson mechanism, using measured pressure models OH fairly well, as shown in Figures 18-20. The most problematic discrepancy is that the mechanism makes too much OH at early times, e.g. see the peaks at 40 to 120  $\mu$ s, depending on temperature. Eliminating reactions of O<sub>2</sub> with MMH and the larger fuel fragments successfully prevented significant OH formation at very early times in the Modified Anderson mechanism. However, some OH is inevitably formed by small radical reactions during the initial pyrolysis of MMH in the mixtures used here. Reactions of OH with MMH and the larger fuel fragments are included in the Modified Anderson mechanism as one possible removal pathway for OH. However, there are many more species in the Modified Princeton pyrolysis mechanism than were in the original Anderson pyrolysis submechanism. We were unable to find any individual major OH removal pathways that clearly needed to be added, so it may be possible that a larger set of OH removal pathways is necessary. The strange fluctuation in NH<sub>2</sub> at early times also implies that there is some problem in the interface between pyrolysis and oxidation chemistry in the Modified Anderson mechanism. Nonetheless, the mechanism developed here is a significant improvement over previous MMH/O<sub>2</sub> modeling efforts, and we hope that publication of our NH<sub>2</sub> and OH time-history data will facilitate further refinements in MMH mechanisms by other researchers.

### 3.4 Conclusions

MMH pyrolysis was studied behind reflected shock waves in a shock tube at temperatures from 942 – 1426 K and pressures near 2 atm. Three laser absorption diagnostics were used to measure NH<sub>2</sub>, NH<sub>3</sub>, and MMH time-histories. These were the first time-histories of NH<sub>2</sub> and NH<sub>3</sub>, and the first MMH measurements free of CH<sub>3</sub> interference, performed during MMH pyrolysis. The results were modeled using the Princeton MMH pyrolysis mechanism [7.8]. The rate for the NH<sub>2</sub> channel of MMH decomposition needed to be decreased by about 30% and the rate of MMH + NH<sub>2</sub> needed to be increased by a factor of 10. Adjusting those two rates successfully captured the rate of MMH decomposition, the rate of NH<sub>3</sub> formation, and the initial peak of NH<sub>2</sub> very well over the entire range of the study. Further analysis of measured MMH allowed us to determine that the CH<sub>3</sub> channel of MMH decomposition used in the Princeton mechanism is accurate to

$\pm 100\%$ . An additional adjustment to  $k_4$  in the mechanism led to improved agreement between measured and modeled  $\text{NH}_2$  at later times.

MMH oxidation was studied behind reflected shock waves in a shock tube at temperatures from 1136 – 1287 K and pressures near 1.6 atm. Laser absorption diagnostics were used to measure OH and  $\text{NH}_2$  time-histories. These were the first measurements of important radical time-histories in MMH oxidation. In addition, the measured pressure traces were used to examine gasdynamic modeling in the presence of significant pre-ignition energy release. It was determined that the constant U,V model typically used in shock tube studies is inappropriate for modeling the MMH system because it predicts a pre-ignition pressure increase that is far too large. Two alternative models were used to provide a more meaningful comparison between the kinetic mechanism and the measured species time-histories. The first option was to simply use the measured pressure as an input when modeling the reaction system. The second was to use a more accurate (and more computationally expensive), 1-D, reacting, inviscid, CFD calculation to calculate temperature, pressure, and species time-histories. We conclude that the use of specified pressure can provide an economical simulation that reasonably approximates the correct 1-D modeling. Both of these methods were then used to compare measured time-histories to predictions based comprehensive MMH oxidation mechanisms.

The MMH oxidation mechanisms of Catoire et al. [6] and Anderson et al. [10] were modified to include the results of our new MMH pyrolysis measurements and other recent studies [8, 9, 11]. The Modified Anderson mechanism was a significant improvement over previous oxidation mechanisms, and modeled all the major OH and  $\text{NH}_2$  features reasonably well. The biggest improvement in the Modified Anderson mechanism was the appearance of an initial  $\text{NH}_2$  peak, similar in magnitude to the peak observed in the measurements. The ignition delay times of the Modified Anderson mechanism were about 30% shorter than the measured values, while the modeled peak OH after ignition was about 30 – 35% higher. The biggest discrepancy between the Modified Anderson mechanism and the measurements occurred with the OH peak at very early times. The modeled values are about 3 – 5 times higher than measured. In addition, the model demonstrates a small  $\text{NH}_2$  fluctuation after the initial peak that is not present in the measurements. These two discrepancies may represent some small issues with the interface between the pyrolysis chemistry added to the Modified Anderson mechanism and the original Anderson mechanism. However, the overall agreement between the Modified Anderson mechanism and the species measured here is very encouraging. The updated mechanism, combined with gasdynamic modeling using measured pressure is a significant step forward in modeling the MMH/ $\text{O}_2$  system.

### 3.5 Morpholine and Related Chemistry

This section is adapted from the following studies:

S. Li, D. F. Davidson, R. K. Hanson, “Shock tube study of the pressure dependence of monomethylhydrazine,” *Combustion and Flame* 161 (2014) 16-22.

S. Li, D. F. Davidson, R. K. Hanson, N. J. Labbe, P. R. Westmoreland, P. Oßwald, K. Kohse-Höinghaus, “Shock Tube Measurements and Model Development for Morpholine Pyrolysis and Oxidation at High Pressures,” *Combustion and Flame* 160 (2013) 1559-1571.

S. Li, D. F. Davidson, R. K. Hanson, “Shock Tube Study of Dimethylamine Oxidation,” Submitted for publication, *Fuel*, April 2014.



S. Li, D. F. Davidson, R. K. Hanson, "Shock tube study of ethylamine pyrolysis and oxidation," *Combustion and Flame* April 2014, available on-line DOI: 10.1016/j.combustflame.2014.04.002.

S. Li, D. F. Davidson, R. K. Hanson, K. Moshhammer, K. Kohse-Höinghaus, "Shock tube study of ethylamine pyrolysis and oxidation," Paper 070RK-0075, 8<sup>th</sup> U.S. National Combustion Meeting, University of Utah, May 19-22, 2013.

S. Li, D. F. Davidson, R. K. Hanson, "High-temperature measurements of the reaction of OH with ethylamine and dimethylamine," Submitted to *Journal of Physical Chemistry A*, November 2013.

The combustion chemistry for nitrogen-containing fuels is important and has not been well-studied before. The primary objective of the research presented in this dissertation is to augment the experimental database and to improve understandings of the chemical kinetics for four nitrogen-containing fuels: morpholine, dimethylamine, ethylamine and monomethylhydrazine.

Morpholine ( $C_4H_9NO$ , 1-oxa-4-aza-cyclohexane) is a good representative candidate of a nitrogen-containing fuel because of its unique cyclic structure and wide industrial applications. Morpholine ignition delay times and species time histories were measured behind reflected shock waves. A morpholine mechanism was updated based on this shock tube data. The simulations from the updated mechanism were in good agreement with the current experiments as well as previous flame data. Further refinement of the morpholine mechanism required improvements in the sub-mechanisms of two major intermediate species dimethylamine and ethylamine.

The overall rate constants of hydroxyl radicals (OH) with dimethylamine (DMA:  $CH_3NHCH_3$ ) and ethylamine (EA:  $CH_3CH_2NH_2$ ) were measured behind reflected shock waves using UV laser absorption of OH radicals near 306.7 nm. The overall rate constants were determined by fitting the measured OH time-histories with the computed profiles using the detailed amine sub-mechanism contained in the morpholine mechanism. Variational transition state theory was used to compute the H-abstraction rates by OH for dimethylamine and ethylamine. The calculated reaction rate constants are in good agreement with the experiment. The calculated reaction rate constants were used to update the morpholine mechanism.

Dimethylamine (DMA) ignition delay times and OH time-histories were investigated behind reflected shock waves. The dimethylamine ignition delay time measurements were carried out in 4% oxygen/argon. OH time-histories were measured in stoichiometric mixtures of 500 ppm DMA/ $O_2$ /argon. The morpholine mechanism was then updated by adding the DMA unimolecular decomposition channel:  $DMA = CH_3NH + CH_3$ . The simulation results using the modified morpholine mechanism are in excellent agreement with both the dimethylamine ignition delay times and OH time-history data.

Ethylamine ( $CH_3CH_2NH_2$ ) pyrolysis and oxidation were studied behind reflected shock waves. For ethylamine pyrolysis,  $NH_2$  time-histories were measured in 2000 ppm ethylamine/argon mixtures. For ethylamine oxidation, ignition delay times,  $NH_2$  and OH time-histories were measured in ethylamine/ $O_2$ /argon mixtures. By fitting the simulations to the early time-histories of  $NH_2$  and OH, the rate constants for the two major ethylamine decomposition pathways were updated for better agreement with the experiment. In addition, recommendations from recent theoretical studies of ethylamine radical reactions were implemented. With these modifications, the modified morpholine mechanism provides significantly improved agreement with the species time-history measurements and the ignition delay times of ethylamine.

The morpholine mechanism, after implementing the aforementioned updates based on the dimethylamine and ethylamine data, was compared with the morpholine ignition delay time data again. It was shown that the modifications, based on the dimethylamine and ethylamine works, to the morpholine mechanism slightly improve the agreements of the mechanism with the data.

Amine groups are common structural features for rocket propellants as well, and using the same approach as above, the pyrolysis of an important propellant monomethylhydrazine (MMH) was studied using  $\text{NH}_2$  time-histories in MMH/argon mixtures. The MMH pyrolysis mechanism developed by Sun et al. (2009) [8], with the updates by Cook et al. (2011) [11], was used to compare with the experiment. The rate constant of the reaction:  $\text{MMH} = \text{CH}_3\text{N.H} + \text{NH}_2$  was determined based on early time of the  $\text{NH}_2$  time-histories. Pressure dependence of this reaction was observed at 0.3-5 atm. The measured reaction rate constants follow a pressure dependence trend close to the theoretical results by Zhang et al. (2011) [9] based on transition state theory master equation analysis. Using the high and low-pressure limit expressions by Zhang et al., a new Troe expression in the fall-off region was proposed base on the current experimental data. Utilizing the later times of the  $\text{NH}_2$  time-histories, a new reaction rate expression was recommended for the reaction:  $\text{NHNH}_2 + \text{H} = \text{NH}_2 + \text{NH}_2$ .

### 3.5.1 Morpholine

Morpholine ignition delay times were measured in the Stanford high pressure shock tube, covering temperatures from 866 to 1197 K, equivalence ratios of 0.5, 1 and 2, two pressure groups near 15 and 25 atm, and two oxygen concentration values of 4%  $\text{O}_2$  in Ar and synthetic air with 21%  $\text{O}_2$ . (See Figure 21) The current shock tube work extends the morpholine combustion experimental database and a morpholine mechanism was updated using the current data.

The morpholine mechanism originally developed for low-pressure flames in [19] significantly over-predicts the ignition delay times under all conditions. Current model predictions are much closer matches with the morpholine ignition delay times than those from the previous mechanism developed in [19], and can successfully capture the equivalence ratio dependence near 15 atm. Future shock tube measurements of different species time-histories will help to improve the current mechanism further.

On the other hand, combustion of morpholine as a 6-membered cyclic amine starts with ring opening and pyrolysis process to form smaller aliphatic amine compounds, in particular, dimethylamine and ethylamine radicals. Further refinement of the morpholine mechanism requires improvements in the sub-mechanisms of dimethylamine and ethylamine. In the following sections, shock tube studies of dimethylamine and ethylamine combustion are presented, to improve understanding of the reaction kinetics of those two important aliphatic amines, and also to improve the morpholine mechanism.

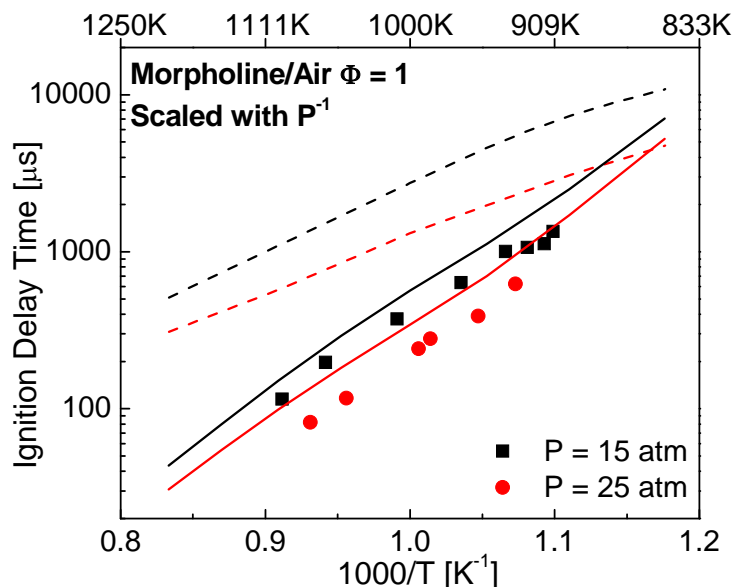


Figure 21. Comparison of model predictions to morpholine/air ignition delay time measurements for stoichiometric mixtures around 15 and 25 atm, respectively. Dashed lines: Simulation results using the previous mechanism [19]. Solid lines: Simulation results using the current mechanism.

### 3.5.2 OH + DMA, OH + EA

The overall rate constants of hydroxyl radicals (OH) with dimethylamine and ethylamine were investigated using UV laser absorption of OH near 306.7 nm, behind reflected shock waves over the temperature range of 901 to 1368 K and at pressures near 1.2 atm. Over the temperature range studied, the measured values can be expressed as  $k_{DMA+OH} = 2.26 \times 10^4 \cdot T^{2.69} \exp(1797/T)$   $\text{cm}^3 \text{mol}^{-1} \text{s}^{-1}$  and  $k_{EA+OH} = 1.10 \times 10^7 \cdot T^{1.93} \exp(1450/T)$   $\text{cm}^3 \text{mol}^{-1} \text{s}^{-1}$ . Detailed error analyses were performed to estimate the overall uncertainties of these reactions, and the estimated ( $2\sigma$ ) uncertainties were found to be  $\pm 29\%$  at 925 K and  $\pm 21\%$  at 1307 K for  $k_{DMA+OH}$ , and  $\pm 31\%$  at 901 K and  $\pm 22\%$  at 1368 K for  $k_{EA+OH}$  (See Figure 22). Variational transition state theory was used to compute the H-abstraction rates by OH for dimethylamine and ethylamine, with potential energy surface geometries, frequencies and electronic energies calculated by Galano and Alvarez-Idaboy [20] at CCSD(T)/6-311++G(2d,2p) level of theory. The calculated reaction rate constants are in good agreement with the experimental data. To the authors' best knowledge, the current work presents the first direct high-temperature measurements and theoretical study of the overall rate constants for dimethylamine and ethylamine with OH. The resulted reaction rate constants in this chapter were implemented into the morpholine mechanism and will be used for further analysis in the following sections.

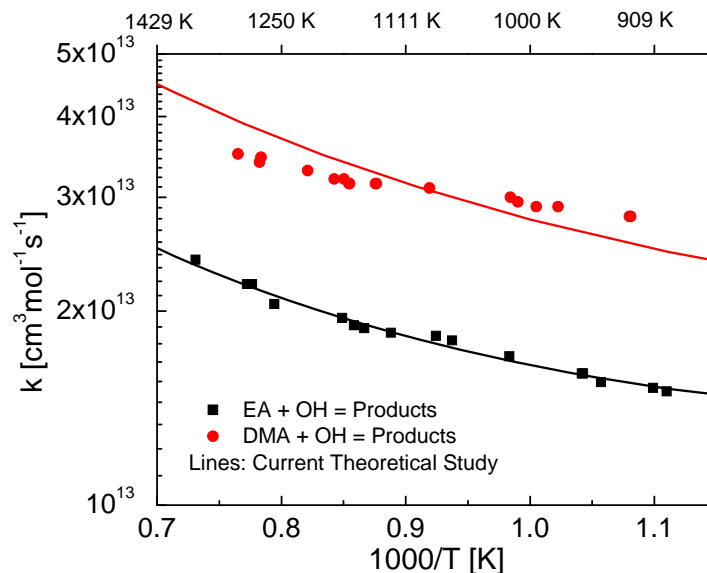


Figure 22. Comparison of the measured reaction rates and theoretical study results for DMA + OH and EA + OH.

### 3.5.3 Dimethylamine Oxidation

The combustion database of nitrogen-containing fuels were augmented with dimethylamine ignition delay times and OH time-histories, studied behind reflected shock waves. The measured dimethylamine ignition delay times covered the temperature range of 1181-1498 K, with pressures near 0.9, 1.5 and 2.8 atm, and equivalence ratios of 0.5, 1 and 2, in 4% oxygen/argon (See Figure 23). The current dimethylamine ignition delay time data feature low scatter and can be correlated into a single expression ( $R^2 \sim 0.99$ ):  $\tau_{\text{ign}} = 7.30 \times 10^{-4} P^{-0.68} \Phi^{0.45} \exp(18265/T)$ , with  $\tau_{\text{ign}}$  in  $\mu\text{s}$ ,  $P$  in atm, and  $T$  in K. OH time-histories were measured in stoichiometric mixtures of 500 ppm DMA/O<sub>2</sub>/argon, using laser absorption of OH near 306.7 nm. The mechanism of Lucassen et al. [19] was used to simulate the measured dimethylamine ignition delay times and OH time-histories. The mechanism, which was originally developed for morpholine combustion, overpredicts the measured dimethylamine ignition delay times, and cannot capture the measured OH time-histories. Modification to the mechanism was recommended by adding the DMA unimolecular decomposition channel:  $\text{DMA} = \text{CH}_3\text{NH} + \text{CH}_3$ , with the reaction rates estimated by analogy to dimethyl ether decomposition previously investigated by Cook et al. [21] The reactions of DMA + OH were also updated. The morpholine mechanism with the aforementioned modifications is in good agreement with both the dimethylamine ignition delay times and OH time-histories (See Figure 24).

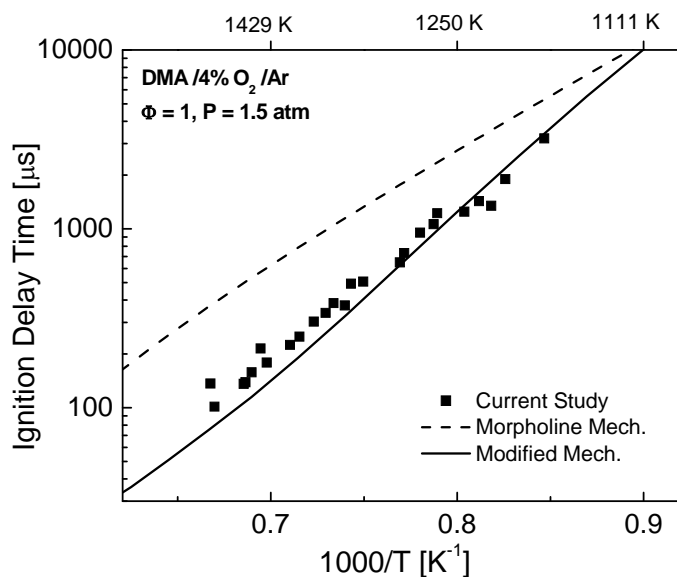


Figure 23. Measured dimethylamine ignition delay times in 4% O<sub>2</sub>/argon, scaled to  $\Phi = 1$  and  $P = 1.5$  atm, in comparison with the simulations with and without modifications.

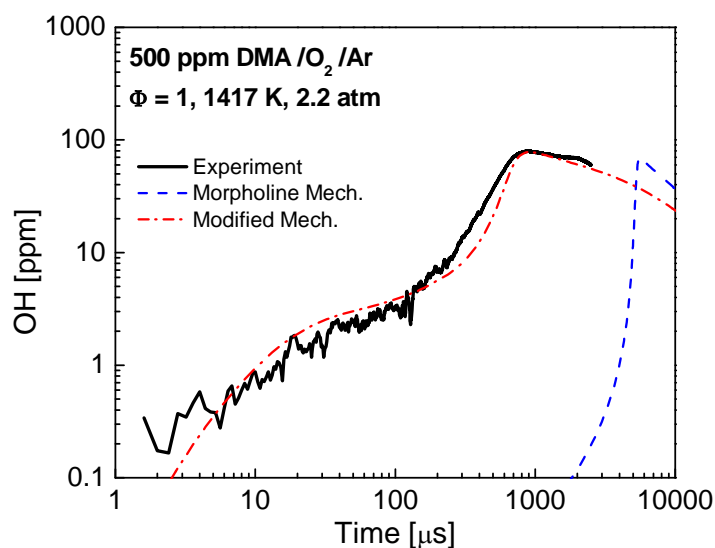


Figure 24. Comparison of the simulated OH time-histories, using the morpholine mechanism with and without modifications, to the experiment in stoichiometric mixture of 500 ppm DMA/O<sub>2</sub>/argon at 1417 K and 2.2 atm.

### 3.5.4 Ethylamine Pyrolysis and Oxidation

Ethylamine (CH<sub>3</sub>CH<sub>2</sub>NH<sub>2</sub>) pyrolysis and oxidation were studied behind reflected shock waves using shock tube/laser absorption methods. In addition to extending the shock tube database for ethylamine combustion, the morpholine mechanism was improved with this experimental data.

For ethylamine pyrolysis,  $\text{NH}_2$  time-histories in 2000 ppm ethylamine/argon mixtures were measured and compared with the morpholine mechanism. The mechanism overpredicts the  $\text{NH}_2$  formation during ethylamine pyrolysis process and cannot capture the measured  $\text{NH}_2$  time-histories.

For ethylamine oxidation, ignition delay times,  $\text{NH}_2$  and  $\text{OH}$  time-histories were measured in ethylamine/oxygen/argon mixtures and were also analyzed using the mechanism. (See Figure 25). The mechanism significantly underpredicts the measured ethylamine ignition delay times. The mechanism also overpredicts the initial formation rate and the peak concentration of  $\text{NH}_2$  for ethylamine oxidation in 2000 ppm ethylamine/0.8%  $\text{O}_2$ /argon mixtures. Finally, the mechanism cannot capture the measured  $\text{OH}$  time-histories in 500 ppm ethylamine/0.2%  $\text{O}_2$ /argon mixtures.

The unimolecular decomposition reaction rates, for  $\text{EA} = \text{CH}_2\text{NH}_2 + \text{CH}_3$  and  $\text{EA} = \text{C}_2\text{H}_5 + \text{NH}_2$ , were determined based on the current experimental data. Modifications to the ethylamine decomposition reactions and the ethylamine + radical reactions in the reaction mechanism were also recommended based on recent theoretical studies. With these modifications, simulations are in much better agreement with all the ethylamine species time-histories and the ignition delay time data (See Figures 26 and 27).

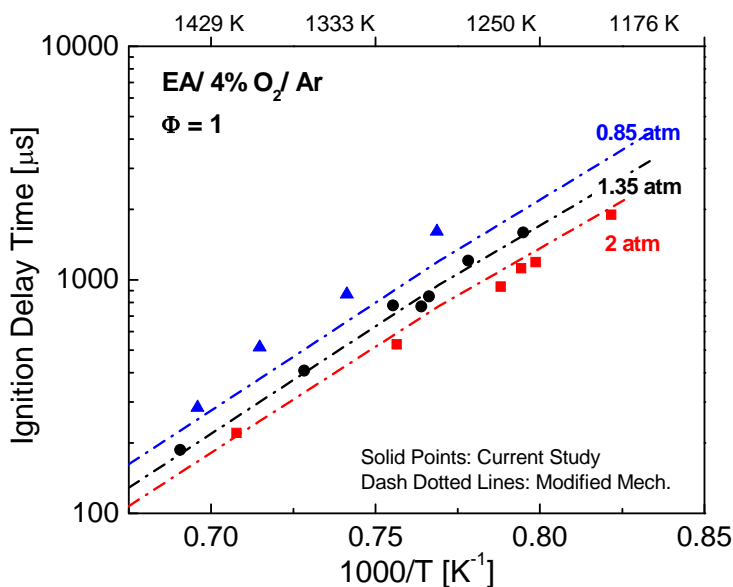


Figure 25. Measurements of ethylamine ignition delay times near 0.85, 1.35 and 2 atm in stoichiometric mixture of ethylamine/4%  $\text{O}_2$ /Ar; simulation results utilize the modified morpholine mechanism.

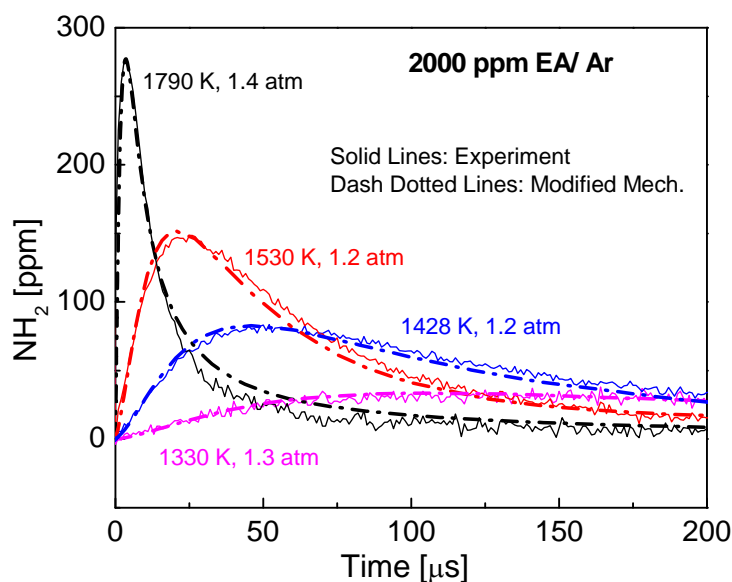


Figure 26. Measured  $\text{NH}_2$  time-histories in 2000 ppm ethylamine/Ar mixtures; simulation results are based on the modified morpholine mechanism.

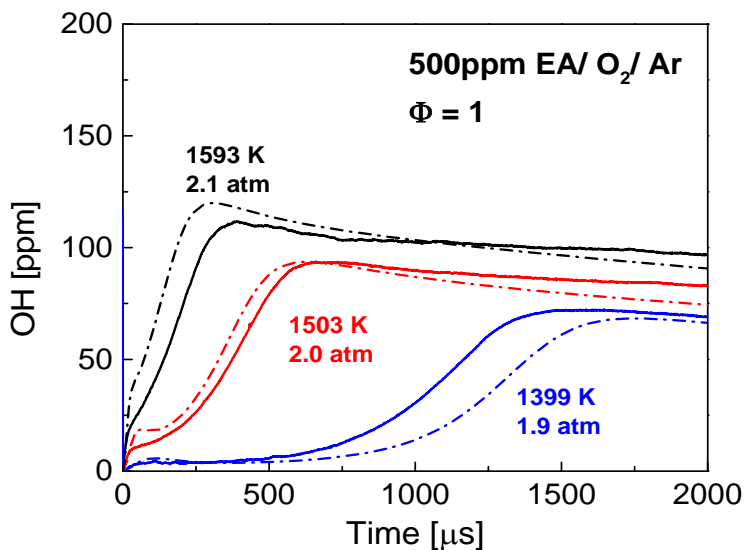


Figure 27. OH time-histories in 500 ppm ethylamine/0.2%  $\text{O}_2$ /Ar mixtures: measurements (solid lines) and simulation results using the modified morpholine mechanism (dash-dotted lines).

### 3.5.5 MMH Pyrolysis

Monomethylhydrazine (MMH,  $\text{CH}_3\text{NHNH}_2$ ) pyrolysis was studied behind reflected shock waves using laser absorption method.  $\text{NH}_2$  concentration time-histories in MMH/argon mixtures were measured over the temperature range of 1100-1400 K and pressures 0.3-5 atm (See Figure 28 and 29). The MMH pyrolysis mechanism developed by Sun et al.[7,8], with the updates by

Cook et al.[11], was used to simulate the  $\text{NH}_2$  time-histories. Sensitivity analyses of  $\text{NH}_2$  show that, under the current test conditions, the  $\text{NH}_2$  formation at the early time is primarily controlled by the MMH decomposition reaction:  $\text{MMH} = \text{CH}_3\text{N.H} + \text{NH}_2$ . The reaction rate constant of this N-N bond scission reaction was determined based on the  $\text{NH}_2$  time-history measurements. Clear pressure dependence of the rate constant was observed at 0.3-5 atm. The measured reaction rate constants follow a pressure dependence trend which is similar to the theoretical results by Zhang et al., and a new Troe's expression for the rate constant was recommended based on the current experimental data in the fall-off region. The pressure dependence of this MMH decomposition reaction determined experimentally in the current study provides important information for MMH pyrolysis.

Using the experimentally determined rate constant for the MMH decomposition  $\text{NH}_2$  producing channel, the simulation results match closely with the measured  $\text{NH}_2$  time-histories at early times. The current study also shows that increasing the rate constant for the reaction:  $\text{NHNH}_2 + \text{H} = \text{NH}_2 + \text{NH}_2$  to 3 times of the values used in the Cook et al. mechanism greatly improves the match of the simulated  $\text{NH}_2$  time-histories with the data at later times. Based on the current study, the rate constant for this rate constant is recommended to be:  $k = 1.5 \times 10^{14} \exp(-755/T) \text{ cm}^3/\text{mol/s}$ . The modified Cook et al. mechanism [11] with these two updated rate constants match well with the measured  $\text{NH}_2$  time-histories throughout the test conditions of the current study.

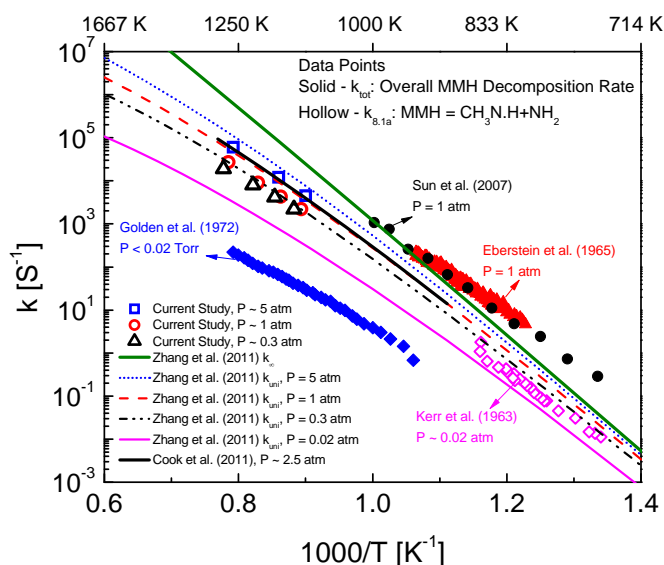


Figure 28. Representative MMH N-N bond scission reaction rate constants in comparison with the previous studies.



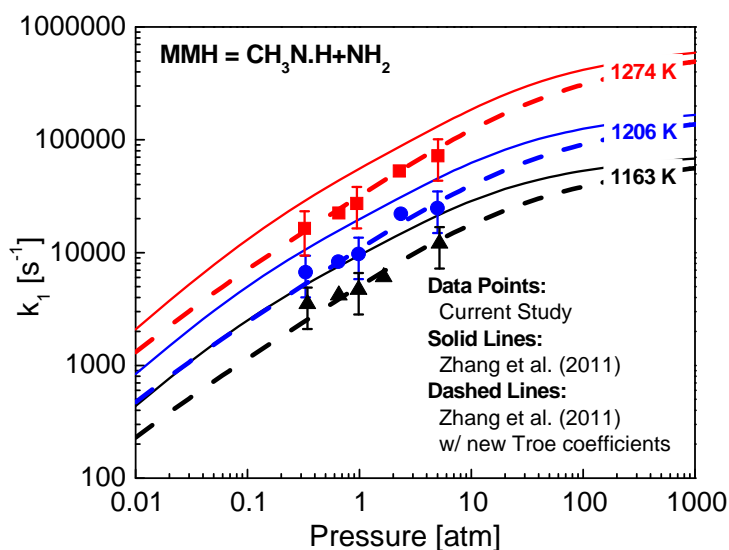


Figure 29. Pressure dependence of the measured  $k$  at representative temperatures, in comparison with the theoretical study by Zhang et al. [9].

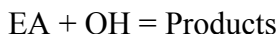
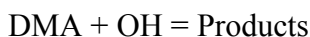
### 3.5.6 Conclusions

#### 3.5.6.1 Morpholine Oxidation

Ignition delay times for morpholine were measured at 866-1197 K, with pressures near 15 and 25 atm, oxygen mole fractions of 4 and 21%, and equivalence ratios of 0.5, 1, and 2. The experimental data, together with recently published rate constants for relevant reactions and newly calculated thermochemistry, were used to update the morpholine mechanism in the literature. The model predictions with those updates match with the experimental data much better than those from using the previous mechanism developed in [19] and can successfully capture the equivalence ratio dependence of morpholine ignition delay times near 15 atm. This mechanism was further validated and updated using dimethylamine and ethylamine shock tube data.

#### 3.5.6.2 Dimethylamine and Ethylamine Combustion

A shock tube and the OH laser diagnostic were used to measure the reaction rate constants for the overall reactions of dimethylamine and ethylamine with OH



The OH radical was generated by near-instantaneous pyrolysis of tert-butyl hydroperoxide. The pseudo-first order decay of OH behind reflected shock waves was monitored using laser absorption at 306.7 nm, and the reaction rate constants of amine with OH were inferred from the measured OH time-histories. The rate constants were measured at temperatures from 901 to 1368 K and at pressures near 1.2 atm. Variational transition state theory was used to compute the H-abstraction rates by OH for dimethylamine and ethylamine, with potential energy surface geometries, frequencies and electronic energies calculated by Galano and Alvarez-Idaboy at CCSD(T)/6-311++G(2d,2p) level of theory [20]. The calculated reaction rate constants are in good agreement with the experimental data.

Ignition delay times and OH time-histories during the oxidation of dimethylamine were studied behind reflected shock waves. The ignition delay time measurements of dimethylamine covered the temperature range of 1181-1498 K, with pressures near 0.9, 1.5 and 2.8 atm, and equivalence ratios of 0.5, 1 and 2, in 4% oxygen/argon. OH time-histories were measured in stoichiometric mixtures of 500 ppm DMA/O<sub>2</sub>/argon. The mechanism developed for morpholine, with amine sub-mechanisms, was used to simulate the measured dimethylamine ignition delay times and OH time-histories. That mechanism, which was originally developed for morpholine combustion, overpredicts the measured dimethylamine ignition delay times, and cannot capture the measured OH time-histories. Modification to the morpholine mechanism was implemented by adding the DMA unimolecular decomposition channel:  $\text{DMA} = \text{CH}_3\text{NH} + \text{CH}_3$  with the reaction rates estimated by analogy to dimethyl ether decomposition previously investigated by Cook et al. [21]. The reactions of DMA + OH were also updated based on the study mentioned earlier. This modified morpholine mechanism is in good agreement with both the dimethylamine ignition delay times and OH time-histories data.

Ethylamine (CH<sub>3</sub>CH<sub>2</sub>NH<sub>2</sub>) pyrolysis and oxidation were studied behind reflected shock waves using shock tube/laser absorption methods. For ethylamine pyrolysis, NH<sub>2</sub> time-histories in 2000 ppm ethylamine/argon mixtures were measured behind reflected shock waves and compared with the morpholine mechanism. The morpholine mechanism overpredicts the NH<sub>2</sub> formation during ethylamine pyrolysis process and cannot capture the measured NH<sub>2</sub> time-histories. For ethylamine oxidation, ignition delay times, NH<sub>2</sub> and OH time-histories were measured in ethylamine/oxygen/argon mixtures and also analyzed using the morpholine mechanism. The morpholine mechanism significantly underpredicts the measured ethylamine ignition delay times. That mechanism also overpredicts the initial formation rate and the peak concentration of NH<sub>2</sub> for ethylamine oxidation in 2000 ppm ethylamine/0.8% O<sub>2</sub>/argon mixtures. For OH measurement in 500 ppm ethylamine/0.2% O<sub>2</sub>/argon mixtures, the mechanism cannot capture the measured OH time-histories. The unimolecular decomposition reaction rates, for  $\text{EA} = \text{CH}_2\text{NH}_2 + \text{CH}_3$  and  $\text{EA} = \text{C}_2\text{H}_5 + \text{NH}_2$ , were determined based on the current experimental data. Modifications to the ethylamine decomposition mechanism and the ethylamine + radical reactions in the mechanism were also recommended based on recent theoretical studies. With the modifications in the current work, the Modified morpholine mechanism is in much better agreement with the species time-history measurements and the ignition delay time data of ethylamine.

Using this approach, the current experimental works of dimethylamine and ethylamine not only augmented the combustion database of aliphatic amines, but also led to an improved morpholine mechanism.

### 3.5.6.3 MMH Pyrolysis

Monomethylhydrazine (MMH, CH<sub>3</sub>NHNH<sub>2</sub>) pyrolysis was studied behind reflected shock waves using the NH<sub>2</sub> diagnostic. NH<sub>2</sub> concentration time-histories in MMH/argon mixtures were measured over the temperature range of 1100-1400 K and pressures of 0.3-5 atm. The MMH pyrolysis mechanism developed by Sun et al., with the updates by Cook et al., was used to simulate the NH<sub>2</sub> time-histories. Sensitivity analyses of NH<sub>2</sub> show that, under the current test conditions, the NH<sub>2</sub> formation at the early time is primarily controlled by the MMH decomposition reaction:  $\text{MMH} = \text{CH}_3\text{N.H} + \text{NH}_2$ . The reaction rate constant of this N-N bond scission reaction was determined based on the NH<sub>2</sub> time-histories at early times. Clear pressure dependence was observed at 0.3-5 atm. The measured reaction rate constants follow a pressure

dependence trend which is similar to the theoretical results by Zhang et al. Using the high- and low-pressure limit expressions by Zhang et al., a new set of Troe coefficients were proposed based on the current data in the fall-off region. The pressure dependence of the MMH decomposition reaction determined experimentally in the current study provides important information for MMH pyrolysis.

With the experimentally determined rate constant above, the simulation results match closely with the measured  $\text{NH}_2$  time-histories at early times. The current study also shows that increasing the rate constant for the reaction  $\text{NHNH}_2 + \text{H} = \text{NH}_2 + \text{NH}_2$  to 3 times the values used in the Cook et al. mechanism greatly improves the match of the simulated  $\text{NH}_2$  time-histories with the data at later times. Based on the current study, the rate constant for Reaction 8.2 is recommended to be  $k = 1.5 \times 10^{14} \exp(-755/T) \text{ cm}^3/\text{mol/s}$ . The modified Cook et al. mechanism match well with the measured  $\text{NH}_2$  time-histories throughout the test conditions of the current study.

#### 4. References

- [1] Kerr, J.A., Sekhar, R.C., Trotman-Dickenson, A.F., *J. Chem. Soc. B* (1963) 3217 – 3225.
- [2] Eberstein, I.J. and Glassman, I., *Proc. Combust. Inst.* 10 (1965) 365 – 374.
- [3] Golden, D.M., Solly, R.K., Gac, N.A., Benson, S.W., *Int. J. Chem. Kinet.* 4 (1972) 433 – 448.
- [4] Catoire, L., Bassin, X., Dupre, G., Paillard, C., *Shock Waves* 6 (1996) 139 – 146.
- [5] Catoire, L., Bassin, X., Dupre, G., Paillard, C., *Comb. Flame* 99 (1994) 573 – 580.
- [6] Catoire, L., Ludwig, T., Bassin, X., Dupre, G., Paillard, C., *Proc. Combust. Inst.* 27 (1998) 2359 – 2365.
- [7] Sun, H. and Law, C.K., *J. Phys. Chem. A* 111 (2007) 3748 – 3760.
- [8] Sun, H., Catoire, L., Law, C.K., *Int. J. Chem. Kinet.* 41 (2009) 176 – 186.
- [9] Zhang, P., Klippenstein, S.J., Sun, H., Law, C.K., *Proc. Combust. Inst.* 33 (2011) 425 – 432.
- [10] W. Anderson, M. McQuaid, M. Nusca, A. Kotlar, A Detailed, Finite-Rate, Chemical Kinetics Mechanism for Monomethylhydrazine-Red Fuming Nitric Acid Systems, 2010.
- [11] Cook, R.D., Pyun, S., Cho, J., Davidson, D.F., Hanson, R.K., *Comb. Flame* 158 (2011) 790 – 795.
- [12] Horning, D.C., Davidson, D.F., Hanson, R.K., *J. Propul. Power* 18 (2002) 363 – 371.
- [13] Vaghjiani, G.L., *J. Phys. Chem. A* 101 (1997) 4167 – 4171.
- [14] Kohse-Hoinghaus, K., Davidson, D.F., Chang, A.Y., Hanson, R.K., *J. Quant. Spec. Rad. Trans.* 42 (1989) 1 – 17.
- [15] Votsmeier, M., Song, S., Davidson, D.F., Hanson, R.K., *Int. J. Chem. Kinet.* 31 (1999) 323 – 330.
- [16] Herbon, J. T., Hanson, R. K., Golden, D. M., Bowman, C. T. *Proc. Combust. Inst.* 29 (2002) 1201.
- [17] Li, H., Owens, Z.C., Davidson, D.F., Hanson, R.K., *Int. J. Chem. Kinet.* 40 (2008) 189 – 198.
- [18] Pang, G.A., Davidson, D.F., Hanson, R.K., *Proc. Combust. Inst.* 32 (2009) 181 – 188.
- [19] Lucassen, N. Labbe, P. Westmoreland, K. Kohse-Hoinghaus, *Combust. Flame* 158 (2011) 1647.
- [20] Galano, A., J. Alvarez-Idaboy, *J. Chem. Theory Comput.* 4 (2008) 322.
- [21] Cook, R. D., D.F. Davidson, R.K. Hanson, *J. Phys. Chem. A* 113 (2009) 9974.

## IV.2 Studies on MMH Reaction Mechanism (Law, Princeton University)

### 1. Objective

The objective of this program is to develop elementary reaction paths and their kinetics in the pyrolysis and oxidation of MMH with IRFNA and the related intermediates. The detailed reaction mechanisms developed will be validated by comparison with experimental results and further reduced for computational expediency. Reaction mechanisms and rate coefficients governing the oxidation of monomethylhydrazine (MMH) and its subsequent reactions with various oxidizing agents are of central importance to the design and operation of liquid-propellant rockets employing MMH or its derivatives as propellant.

### 2. Background

Ignition is one of the most crucial events governing the satisfactory performance of many practical combustion devices including the diesel engine which powers most of the Army's tactical vehicles and civilian fleet. In the diesel engine the liquid fuel is sprayed into the combustion chamber during the compression stroke. The atomized liquid subsequently penetrates into the interior of the combustor in the form of a spray jet, undergoing simultaneous vaporization and mixing with air. Ignition occurs, either locally or globally, when a combustible mixture is formed and is heated to its ignition temperature. Performance of the diesel engine therefore depends sensitively on the chemical process leading to ignition. In addition to diesel combustion, the Army is also interested in combustion within rocket engines. Here ignition and spray processes are of primary interest, especially to rocket motors fueled by hypergolic bipropellants, notably monomethylhydrazine (MMH). Because of the low volatility of the gelled fuel, ignition can take place either between the gelled fuel droplet and vaporized oxidizer (IRFNA) at the droplet surface, or between the liquid fuel and oxidizer when they collide and merge as jets or droplets. The associated ignition chemistry and hydrodynamics are necessarily quite complicated and not well studied.

*Interactions with others within MURI team:*

- Prof. Ron Hanson's group at Stanford University

*Collaborations with the Personnel of National Labs*

- Dr. Stephen J. Klippenstein at Argonne National Laboratory
- Dr. Karol Kowalski at Pacific Northwest National Laboratory

### 3. Theoretical Approach

In the investigation of elementary reaction mechanism of MMH pyrolysis and oxidation and also the associated thermochemical and kinetic parameters, several advanced ab initio multireference quantum chemistry approaches and sophisticated kinetic theories were applied.

#### 3.1 Multireference second-order perturbation theory (CASPT2)

Multireference second-order perturbation theory (CASPT2) [1] with Dunning's augmented correlation-consistent double- $\xi$  basis set, aug-cc-pVDZ, and then triplet- $\xi$  basis set, aug-cc-pVTZ [2], were applied to optimize the geometries of reactants and transition states and then to calculate the rovibrational frequencies. The active space for the reactant, complexes, and transition states was carefully chosen to ensure that it represents the characteristics of frontier molecular orbitals.

### 3.2 High-accuracy Multireference coupled-cluster theory with Brillouin-Wigner (BW-MRCCSD(T)) and Mukherjee (Mk-MRCCSD(T)) approaches

Higher level stationary point energies were obtained from quadratic configuration interaction, coupled-cluster, and locally renormalized coupled-cluster methods. Specifically, the QCISD(T), CCSD(T), and LR-CCSD(T) [3] calculations employed the correlation-consistent, polarized - valence, triplet- $\xi$  (cc-pVTZ) and quadruple- $\xi$  (cc-pVQZ) basis sets [2b]. The energies were then extrapolated to the complete basis set (cc-pV $\infty$ Z) limit by the asymptotic form [4]. To further improve accuracy of the potential energy surface, the stationary point energies were from high-level state selective multireference coupled-cluster theory with single and double excitations and correction for triple excitations including Brillouin-Wigner and Mukherjee's BW-MRCCSD(T) and Mk-MRCCSD(T) approaches [5].

### 3.3 Variable reaction coordinate transition state (VRC-TST) theory

In VRC-TST calculations, the intermolecular degrees of freedom describing the separation of the fragments and the relative orientation are treated as fully coupled anharmonic modes via classical phase space integrals [6]. This analysis requires an interaction potential for these degrees of freedom, which was determined here with on-the-fly CASPT2 calculations employing the cc-pVDZ and aug-cc-pVDZ basis sets. Orientation independent corrections for limitations in the basis set and for the effects of conserved mode geometry relaxation are included. Specifically, two correction terms are included in the final potential energy: an  $R$ -dependent one-dimensional correction term from CASPT2/aug-cc-pVTZ electronic structure calculations, and a multi-dimensional correction for the effect of relaxing the internal structure of the reacting fragments along the minimum energy path [7].

### 3.4 Rice–Ramsperger–Kassel–Marcus (RRKM) theory

The pressure dependence of dissociation rate coefficients was determined by solving the two-dimensional master equation [8]. The energy transfer probability was approximated with a single-exponential-down model employing the temperature-dependent form for the average downwards energy transfer. The energy levels for the underlying density and number of states calculations were evaluated on the basis of rigid-rotor harmonic oscillator assumptions for all but the torsional degrees of freedom. For the latter, hindered rotor corrections were obtained from one-dimensional fits to the torsional potentials employing Pitzer-Gwinn like approximations and the moments of inertia [9].

## 4. Major Findings

### 4.1 *Ab Initio* Kinetics for the Primary Decomposition of Monomethylhydrazine

The simple N–N and C–N bond fissions of MMH to produce the radicals  $\text{CH}_3\text{NH} + \text{NH}_2$  (R1) or  $\text{CH}_3 + \text{NHNH}_2$  (R2) was found to dominate the thermal decomposition of MMH. The transition states for these two bond fissions are studied with variable reaction coordinate transition state theory employing directly determined CASPT2/aug-cc-pVDZ interaction energies. Orientation independent corrections for limitations in the basis set and for the effects of conserved mode geometry relaxation are included. Specifically, two correction terms are included in the final potential energy: an  $R$ -dependent one-dimensional correction term from CASPT2/aug-cc-pVTZ electronic structure calculations, and a multi-dimensional correction for the effect of relaxing the internal structure of the reacting fragments along the minimum energy path. The CASPT2/aug-cc-pVDZ relaxed potentials along the MEPs are illustrated in Fig. 1.

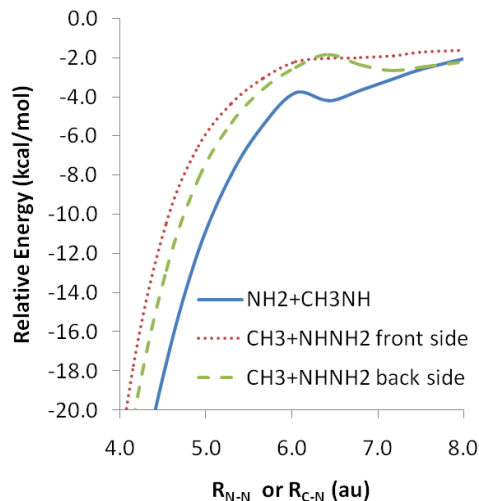


Figure 1. Potential curves for  $\text{NH}_2 + \text{CH}_3\text{NH}$  (solid line), and the front (dotted line) and back (dashed line) sides of  $\text{CH}_3 + \text{NHNH}_2$ .

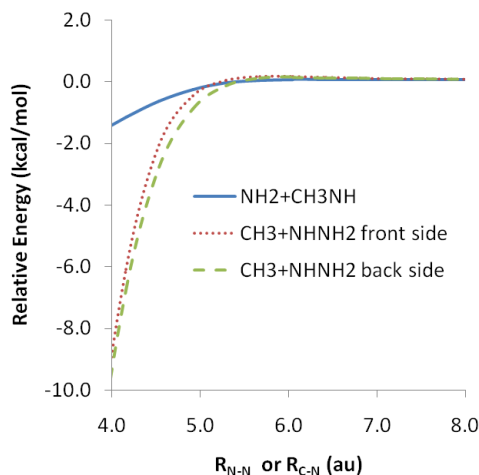


Figure 2. Total potential correction curves for  $\text{NH}_2 + \text{CH}_3\text{NH}$  (solid line), and the front (dotted line) and back (dashed line) sides of  $\text{CH}_3 + \text{NHNH}_2$ .

The total basis set and relaxation correction is illustrated in Fig. 2 for the aug-cc-pVDZ cases. For the  $\text{NH}_2 + \text{CH}_3\text{NH}$  case, the correction is only a small fraction of the total interaction potential at any given separation. In contrast, for the  $\text{CH}_3 + \text{NHNH}_2$  cases, the corrections, which are primarily a relaxation effect, are a significant fraction of the total interaction at shorter separations. The relatively large magnitude of the latter corrections is likely due to the transformation from  $\text{sp}^2$  to  $\text{sp}^3$  hybridization in the  $\text{CH}_3$  fragment as the CN bond is formed.

The bond dissociation energies are evaluated at the QCISD(T)/CBS//B3LYP/6-311++G(d,p) level. The bond energies of N–N and C–N bond are 62.7 and 64.6 kcal/mol, respectively.

The high pressure capture kinetics for the barrierless R-1 and R-2 reactions was studied with the VRC-TST method. The recombination rate coefficient for reaction R-1 is significantly greater than that for R-2 due to the differences in attractivity. The rate coefficient for R-1, denoted by  $k_{-1}^\infty$ , is well fit by the expression  $8.34 \times 10^{-10} T^{-0.429} \exp(20.1/T) \text{ cm}^3 \text{ molecule}^{-1} \text{ s}^{-1}$  over the temperature

range of 200-2500 K. Similarly, the rate coefficient  $k_{-2}^{\infty}$  for R-2 may be reproduced by the expression  $3.99 \times 10^{-12} T^{0.085} \exp(404.2/T) \text{ cm}^3 \text{ molecule}^{-1} \text{ s}^{-1}$  over the same temperature range.

The pressure dependence of the MMH dissociation rate coefficients was determined by solving the two-dimensional master equation. The energy transfer probability was approximated with a single-exponential-down model employing the temperature-dependent form  $\Delta E_{down} = 200(T/300)^{0.85} \text{ cm}^{-1}$  for the average downwards energy transfer. The energy levels for the underlying density and number of states calculations were evaluated on the basis of rigid-rotor harmonic oscillator assumptions for all but the torsional degrees of freedom.

The total MMH decomposition rate constant is compared with previous experimental and simulation data in Figure 3. It shows that our theoretical rate coefficients agree very well with the experimental data of Kerr et al., especially at 0.04 atm. The very low pressure pyrolysis study of Golden et al. measures the rate constant for unimolecular decomposition induced by wall collisions and then extracts high pressure rate constants via comparison with RRK and RRKM predictions, therefore their directly measured unimolecular rate constants are not readily compared with the present pressure dependent predictions due to their convolution with gas-surface instead of gas-gas energy transfer effects.

This work is reported in Publication “*Ab Initio* Kinetics for the Decomposition of Monomethylhydrazine ( $\text{CH}_3\text{NHNH}_2$ )”, P. Zhang, S. J. Klippenstein, H. Sun, and C. K. Law, *Proc. Combust. Inst.*, **2011**, 33, 425-432.

#### 4.2 *Ab Initio* Kinetics for the Secondary Decomposition of Monomethylhydrazine

Potential energy surface of MMH decomposition is central to a kinetic mechanism for modeling the overall MMH decomposition and its product formation. Several new reaction channels were found to be important for direct MMH decomposition, therefore potential energy surface of MMH decomposition is updated from the previous work.<sup>[10]</sup> First, it was found that MMH can undergo isomerization via a three-member-ring transition state TS1 ( $E_a = 60.2 \text{ kcal/mol}$ ) to an MMH isomer  $\text{CH}_3\text{NH}_2\text{NH}$ , which decomposes to three product sets:  $\text{CH}_3\text{NH}_2 + \text{NH}$ ,  $\text{CH}_3\text{NNH} + \text{H}_2$ , and  $\text{N}_2\text{H}_4 + \text{CH}_4$ . Secondly, MMH can undergo isomerization via a three-member-ring TS2 ( $E_a = 62.9 \text{ kcal/mol}$ ) to another MMH isomer  $\text{CH}_3\text{NNH}_3$ , which decomposes to two product sets:  $\text{NH}_3 + \text{CH}_3\text{N}$ , and  $\text{CH}_3\text{NNH} + \text{H}_2$ . Furthermore, a direct  $\text{H}_2$  elimination channel of MMH via a five-member-ring transition state TS3 was found with energy barrier of  $61.6 \text{ kcal/mol}$ . These three reaction channels have relatively lower energy barriers, 60 – 63 kcal/mol, which are comparable to those of two N–N and C–N bond fissions, and are important to model  $\text{NH}_2$ ,  $\text{NH}_3$ , and  $\text{H}_2$  product formation. The other reaction channels via three (or four)-member-ring TS3, TS4, and TS5 are responsible for  $\text{NH}_2$ ,  $\text{NH}_3$  and  $\text{CH}_4$  product formations, though they have relatively higher energy barriers, 66 – 78 kcal/mol.

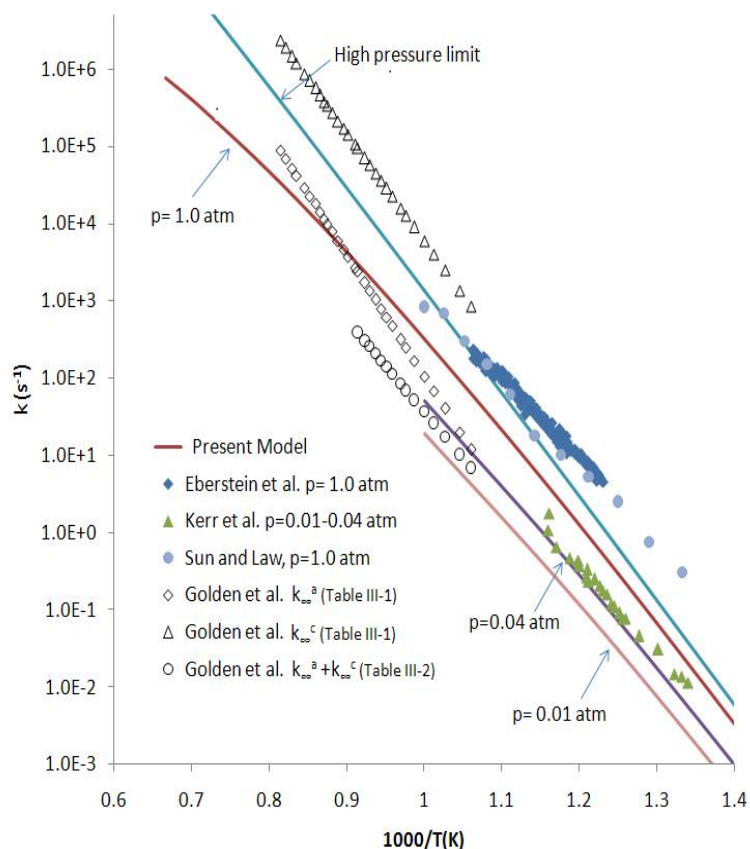


Figure 3. Comparison of the predicted total decomposition rate constant through  $\text{MMH} \rightarrow \text{NH}_2 + \text{CH}_3\text{NH}$  and  $\text{MMH} \rightarrow \text{CH}_3 + \text{NHNH}_2$  with previous experimental and simulation data for the overall thermal decomposition of MMH.

The energies for the stationary points of above potential energy surface were calculated by two ab initio methods. One is composite CBS-QB3 method, one is quadratic configuration interaction with singles doubles and perturbative inclusion of triples (QCISD(T)) method. In the latter, the geometries and zero-point energies are obtained with B3LYP/6-311++G(d,p) density functional theory, and the QCISD(T) single point energies were performed using the cc-pVTZ and cc-pVQZ basis sets and then were extrapolated to the complete basis set limit (CBS).

This work is reported in Publication “Secondary Channels in the Thermal Decomposition of Monomethyl-hydrazine ( $\text{CH}_3\text{NHNH}_2$ )”, P. Zhang, H. Sun, and C. K. Law, 7th US National Technical Meeting of the Combustion Institute, the Georgia Institute of Technology, Atlanta, GA, March 20-23, 2011.

#### 4.3 Gas-phase Kinetics Study of Reaction of OH Radical with $\text{CH}_3\text{NHNH}_2$ by Second-Order Multireference Perturbation Theory and Two-Transition State Theory

Reactions of  $\text{MMH} + \text{NO}_2$  and  $\text{MMH} + \text{OH}$  are important in rocket engine combustion, since  $\text{NO}_2$  and OH are the decomposition products of NTO and nitric acid. Furthermore, the H-abstraction of MMH by  $\text{NO}_2$  produces nitrous acid (HONO) which undergoes further decomposition and chain reactions to regenerate the OH radical. Recently, the reactions of  $\text{MMH} + \text{OH}$  at temperatures of 1000 – 1250 K have been found to play a critical role in the modeling of earlier OH time histories



in the ignition of MMH with  $O_2$  as an oxidizer. Consequently the theoretical rate data for each individual channel need to be quantified accurately.

Theoretically, we have found that the reaction of MMH + OH proceeds via direct and indirect abstraction mechanisms. Specifically, the abstraction of methyl H atoms by the OH radical is a direct abstraction reaction, while the indirect abstraction of amine H atoms proceeds via addition of the OH radical to the diamine N atoms to form an intermediate and subsequently rapid dissociation into products.

The T1 diagnostic of Lee *et al.* for the transition states of the abstraction of amine hydrogen atoms from the QCISD(T) calculations was found to be 0.04, implying significant multi-reference character of the wave function. Therefore multireference second-order perturbation theory (CASPT2) with Dunning's augmented correlation-consistent double- $\xi$  basis set, aug-cc-pVDZ, and then triplet- $\xi$  basis set, aug-cc-pVTZ, were applied to optimize the geometries of reactants and transition states and then to calculate the rovibrational frequencies. Higher level single-point energies were obtained from the quadratic configuration interaction with single, double and perturbative triple excitation QCISD(T) calculations.

In the CASPT2 calculations, the active space for the reactant, complexes, and transition states was carefully chosen to ensure that it represents the characteristics of frontier molecular orbitals. Specifically, the active space (4e,3o) consisting of the  $s$ ,  $s^*$  orbital pair of N—N bond and the  $s$  orbital of amine N atom was selected for the reactant MMH, the state-averaged (3e,2o) active space consisting of the two degenerated  $p$  orbitals of the OH radical was used for the pre-reactivated reactant complexes, the active space (3e,3o) consisting of the OH radical orbital and the  $s$ ,  $s^*$  orbital pair of the H being abstracted was used for the transition states of the abstraction of amine H atoms (Fig. 4), and the active space (9e,6o) consisting of the  $s$ ,  $s^*$  orbital pair of the methyl H being abstracted, two  $p$  orbitals of the hydroxyl O atom, and two hybrid  $s$  orbitals of hydroxyl O and hydroxyl H was used for the transition states of the abstraction of methyl hydrogen.

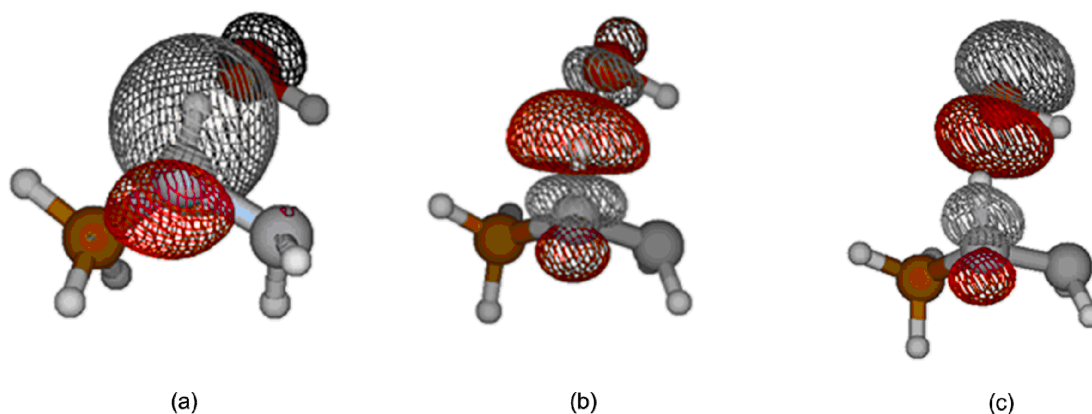


Figure 4. Transition state geometry of abstracting central amine H of MMH optimized at the CASPT2(3e,3o)/aug-cc-pVTZ level, with mesh contour showing the active space (3e,3o) of the  $\sigma$ ,  $\sigma^*$  orbital pair of the central amine hydrogen being abstracted and the OH radical orbital. (a)  $\sigma$  orbital of central amine H, (b)  $\sigma^*$  orbital of central amine H, and (c)  $p$  orbital of the OH.

For the reactions of OH + MMH, there are multiple transition states associated with the abstraction of different H atoms (Fig. 5). Since the abstraction of the methyl H atom has an energy barrier higher than that of the reactants, it is appropriate to apply the E/J resolved micro-canonical transition state theory for the rate calculation. The abstraction reaction of the amine H atoms proceeds through the formation of two hydrogen bonded pre-activated complexes and it has submerged energy barriers lower than that of the reactants. The two-transition-state model proposed by Georgievskii and Klippenstein was used to determine the rate coefficients for such type of reactions, especially at low to intermediate temperatures.

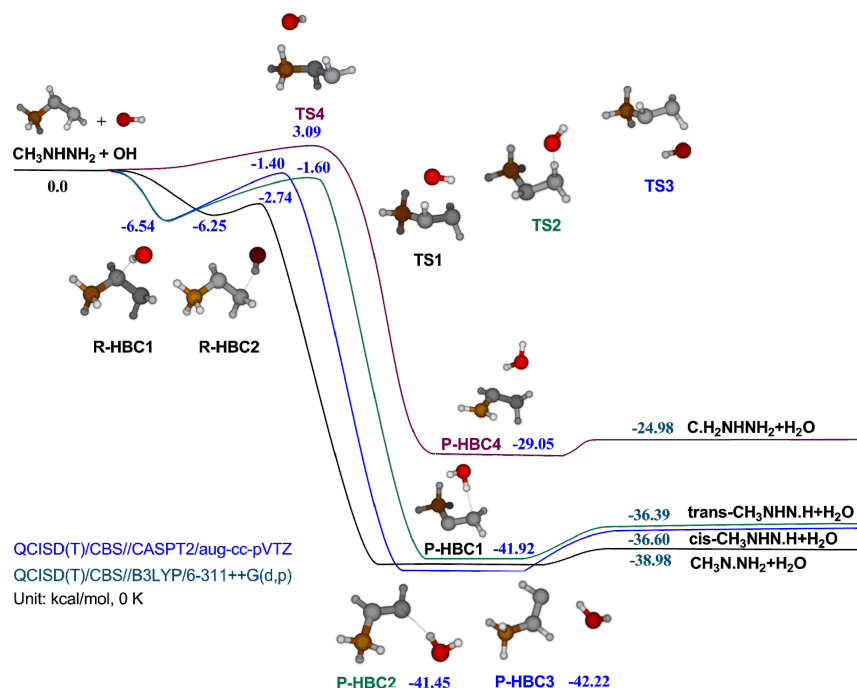


Figure 5. Potential energy surface of the reactions of MMH + OH calculated at the QCISD(T)/CBS//CASPT2/aug-cc-pVTZ level, except the geometry of OH radical was optimized at the UCCSD(T)/cc-pVTZ level and the geometries of radical products were optimized at the B3LYP/6-311++G(d,p) level.

The calculated rate coefficients for the abstraction of different H atoms in MMH by OH are shown in Fig. 6, with the abstraction of the central amine H atom illustrated by black curve, and the abstraction of the terminal amine H atom to form trans-CH<sub>3</sub>NHN•H–H<sub>2</sub>O and cis-CH<sub>3</sub>NHN•H–H<sub>2</sub>O by red and green curves, respectively. It is seen that the rate coefficients for the abstraction of the amine H atoms have negative temperature dependence, i.e., the rate constant decreases with increasing temperature below 600 K.

In units of cm<sup>3</sup> molecule<sup>-1</sup> s<sup>-1</sup>, the rate coefficient was fitted as  $k_1 = 3.37 \times 10^{-16} T^{1.295} \exp(1126.17/T)$  for the abstraction of the central amine H to form the CH<sub>3</sub>N•NH<sub>2</sub> radical;  $k_2 = 2.34 \times 10^{-17} T^{1.907} \exp(1052.26/T)$  for the abstraction of the terminal amine H to form the trans-CH<sub>3</sub>NHN•H radical;  $k_3 = 7.41 \times 10^{-20} T^{2.428} \exp(1343.20/T)$  for the abstraction of the terminal amine H to form the cis-CH<sub>3</sub>NHN•H radical; and  $k_4 = 9.13 \times 10^{-21} T^{2.964} \exp(-114.09/T)$  for the abstraction of the methyl H atom to form the C•H<sub>2</sub>NHNH<sub>2</sub> radical. Assuming the rate coefficients are

additive, the total rate coefficient  $k_{total} = 1.94 \times 10^{-18} T^{2.306} \exp(1272.81/T) \text{ cm}^3 \text{ molecule}^{-1} \text{ s}^{-1}$  is obtained by summing the rate coefficients of above individual channels, which again exhibits negative temperature dependence. Excellent agreement is observed by comparing this total rate coefficient  $k_{total}$  (blue curve) with the two available experimental data over 232 – 637 K (Vaghjiani, *Int. J. Chem. Kinet.*, 2001), as shown in Fig.6.

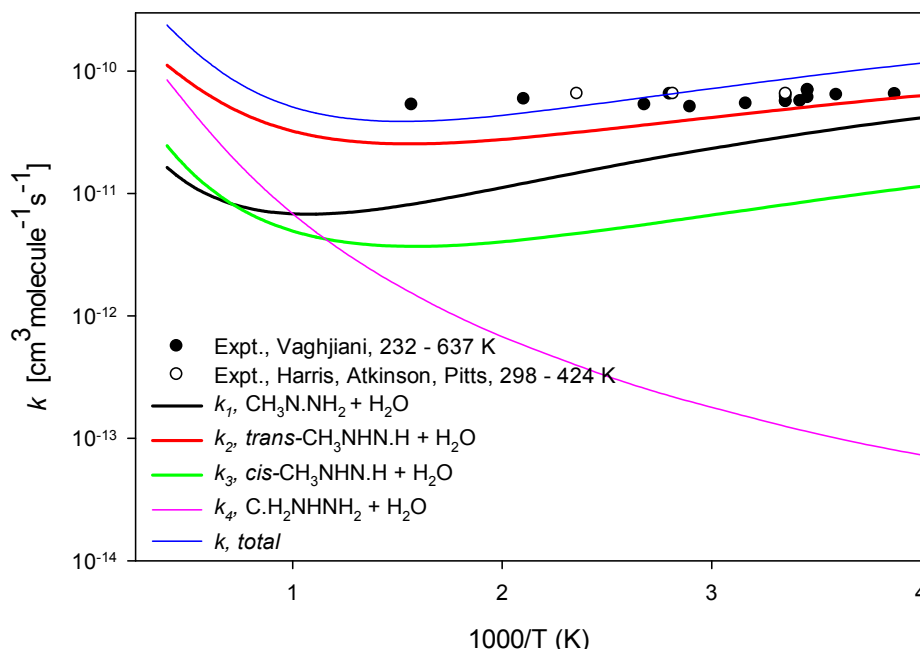


Figure 6. Theoretical rate coefficients for the abstraction of different H atoms in MMH by OH radical, with a total rate compared with the experimental data.

This work is reported in Publication “Gas-Phase Kinetics Study of Reaction of OH Radical with  $\text{CH}_3\text{NHNH}_2$  By Second-Order Multireference Perturbation Theory”, H. Sun, P. Zhang, C. K. Law, *Journal of Physical Chemistry A*, **2012**, 116 (21), 5045-5056.

#### 4.4 *Ab Initio* Kinetics for Thermal Decomposition of $\text{CH}_3\text{N}\cdot\text{NH}_2$ , $\text{cis-CH}_3\text{NHN}\cdot\text{H}$ , $\text{trans-CH}_3\text{NHN}\cdot\text{H}$ , and $\text{C}\cdot\text{H}_2\text{NNH}_2$ Radicals

The H-abstraction of MMH leads to the formation of four MMH radicals:  $\text{CH}_3\text{N}\cdot\text{NH}_2$ ,  $\text{cis-CH}_3\text{NHN}\cdot\text{H}$ ,  $\text{trans-CH}_3\text{NHN}\cdot\text{H}$ , and  $\text{C}\cdot\text{H}_2\text{NNH}_2$ , where the cis and trans notations indicate the orientation of the terminal amine H atom to the methyl group. These MMH radicals undergo further decomposition reactions to produce H,  $\text{NH}_2$ , and  $\text{CH}_3$  radicals, which further lead to many chain reactions. Consequently the decomposition of the MMH radicals is crucial to the understanding of the ignition chemistry of MMH and its derivatives.

The potential energy surface (PES) for the decomposition of the MMH radicals consists of multiple, interconnected potential wells and multiple product channels (Fig. 7). The results reveal that the  $\beta$ -scission of  $\text{NH}_2$  to form methyleneimine is the predominant channel for the decomposition of the  $\text{C}\cdot\text{H}_2\text{NNH}_2$  radical because of its small energy barrier of  $13.8 \text{ kcal mol}^{-1}$ , and as such the rate coefficient exhibits relatively weak temperature dependence at 1000 - 2500 K. The

cis-CH<sub>3</sub>NHN•H radical and trans-CH<sub>3</sub>NHN•H radical are the two distinct spatial isomers with an energy barrier of 26 kcal mol<sup>-1</sup> for their isomerization. The  $\beta$ -scissions of CH<sub>3</sub> from the cis- and the trans-CH<sub>3</sub>NHN•H radicals have energy barriers of 35.2 kcal mol<sup>-1</sup> and 39.8 kcal mol<sup>-1</sup>, respectively. The CH<sub>3</sub>N•NH<sub>2</sub> radical undergoes the  $\beta$ -scission of methyl hydrogen and amine hydrogen to form CH<sub>2</sub>=NNH<sub>2</sub>, trans-CH<sub>3</sub>N=NH (Fig. 7) and cis-CH<sub>3</sub>N=NH products, with energy barriers of 42.8, 46.0, and 50.2 kcal mol<sup>-1</sup>, respectively.

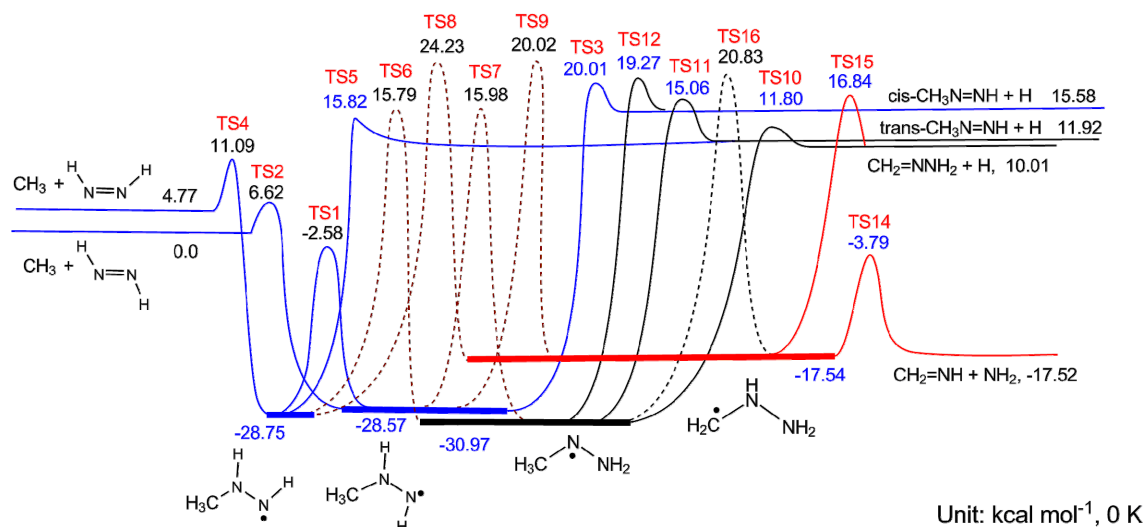


Figure 7. Potential energy surface of decomposition of the CH<sub>3</sub>N•NH<sub>2</sub>, cis-CH<sub>3</sub>NHN•H, trans-CH<sub>3</sub>NHN•H, and C•H<sub>2</sub>NNH<sub>2</sub> radicals calculated at the QCISD(T)/cc-pV $\infty$ Z//CASPT2/aug-cc-pVTZ level (data marked by blue) and at the QCISD(T)/cc-pV $\infty$ Z//B3LYP/6-311++G(d,p) level (data marked by black).

Microcanonical rate coefficients as functions of total rotational-vibrational energy ( $E$ ) and total angular momentum ( $J$ ) were calculated using Rice–Ramsperger–Kassel–Marcus (RRKM) theory and the multi-well master equation analysis. The transition states were treated with the conventional transition-state theory employing rigid-rotor harmonic oscillator assumptions using optimized geometries and vibrational frequencies from the CASPT2/aug-cc-pVTZ or the B3LYP/6-311++G(d,p) calculations for most modes. Hindered rotor corrections for the CH<sub>3</sub> and NH<sub>2</sub> torsional modes were obtained from one-dimensional fits of the torsional potentials, employing Pitzer-Gwinn like approximations and the  $I^{(2,3)}$  moments of inertia.

The pressure-dependent kinetics analysis for the decomposition of the MMH radicals was performed by solving the time-dependent, multiple-well master equation at the  $E, J$  resolved level (Figs. 8-11). The collisional energy transfer probability in the master equation analysis was approximated by a single-exponential-down model, employing the temperature dependent form  $\Delta E_{down} = 200(T/300)^{0.85}$  cm<sup>-1</sup> for the average downward energy transfer. This energy transfer model is used for the collider of argon, which has been considered in the MMH pyrolysis and oxidation mechanism. Nitrogen was also considered as a collider in the study for comparison.

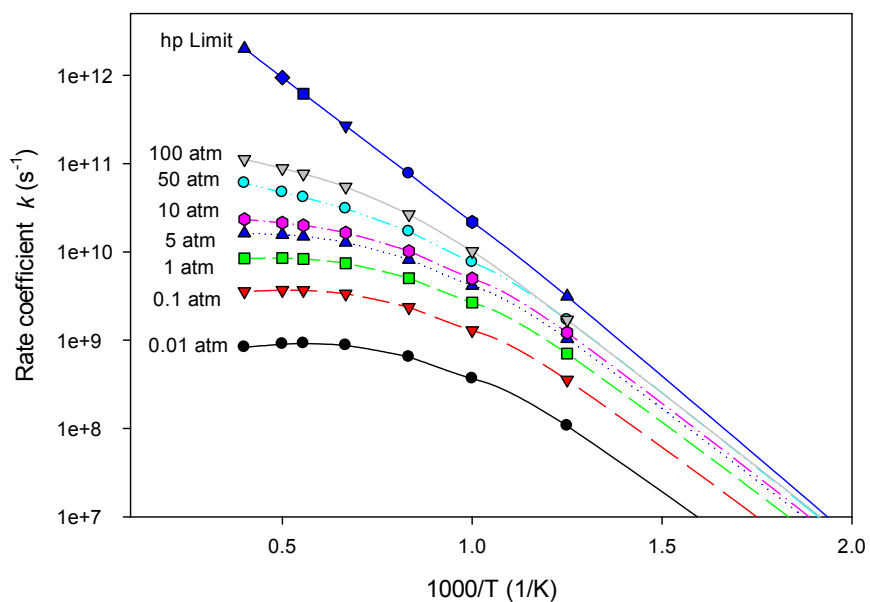


Figure 8. The temperature dependence of rate coefficients in the dissociation channel of  $\text{C}\cdot\text{H}_2\text{NHNH}_2 \rightarrow \text{CH}_2=\text{NH} + \text{NH}_2$  at pressures of  $p = 0.01, 0.1, 1, 5, 10, 50, 100$  atm, and high pressure limit.

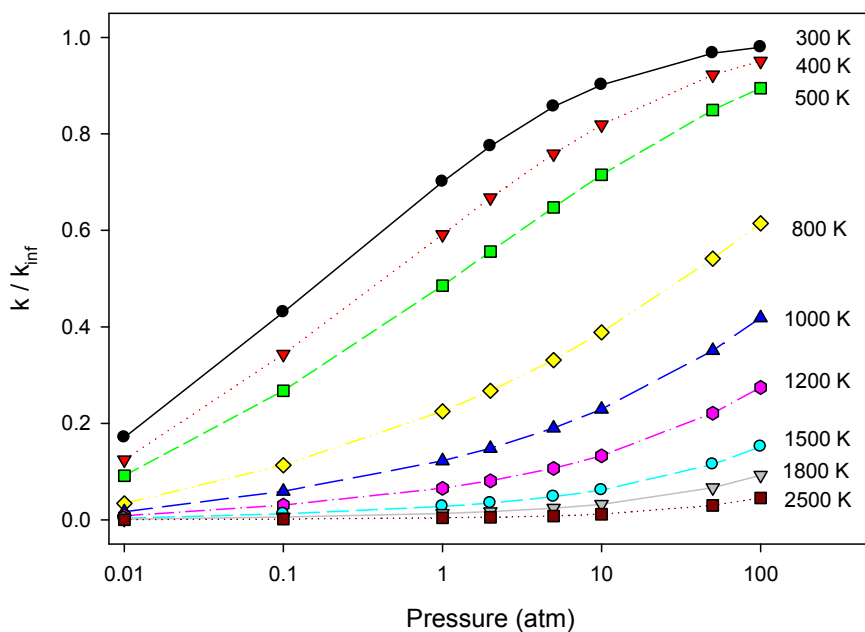


Figure 9. A plot of  $k/k_\infty$  as a function of pressure at  $T = 300, 400, 500, 800, 1000, 1200, 1500, 1800,$  and  $2500$  K, for the dissociation channel of  $\text{C}\cdot\text{H}_2\text{NHNH}_2 \rightarrow \text{CH}_2=\text{NN} + \text{NH}_2$ .

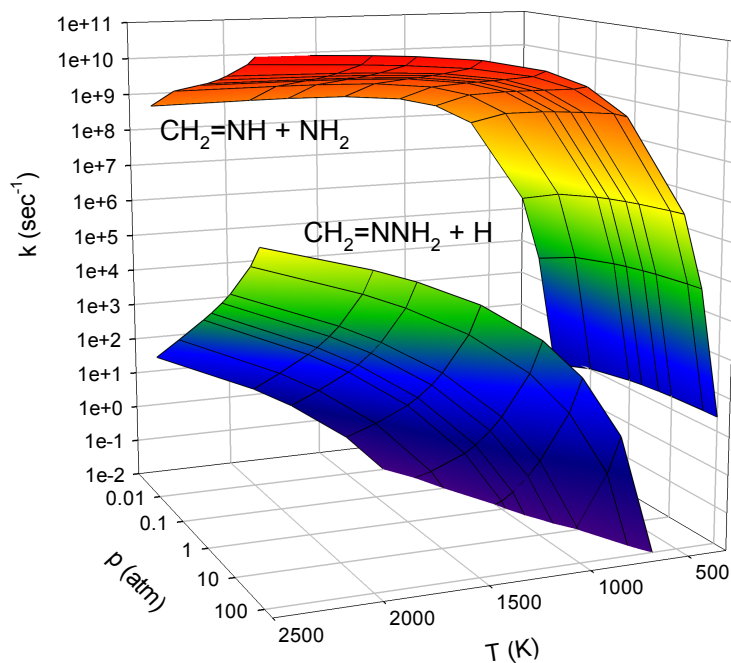


Figure 10. Theoretical rate coefficients of the dissociation channels of  $\text{C}\cdot\text{H}_2\text{NHNH}_2 \rightarrow \text{CH}_2=\text{NH} + \text{NH}_2$  and  $\text{C}\cdot\text{H}_2\text{NHNH}_2 \rightarrow \text{CH}_2=\text{NNH}_2 + \text{H}$  as functions of temperature and pressure.

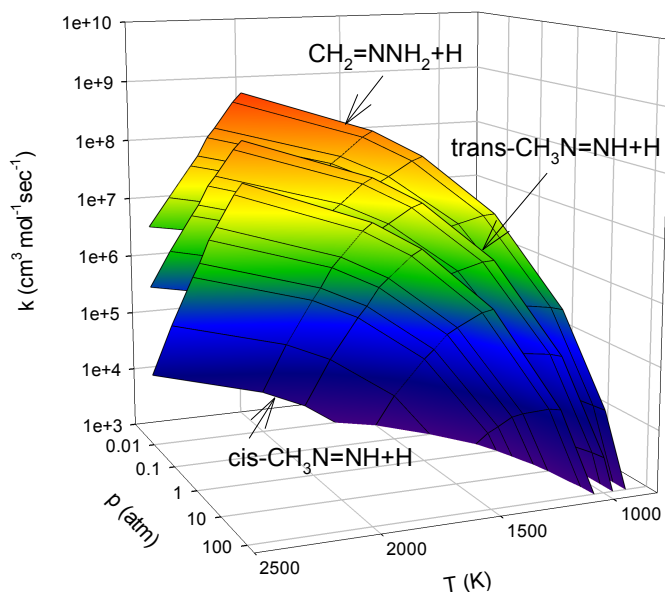


Figure 11. Theoretical rate coefficients for the dissociation of  $\text{CH}_3\text{N}\cdot\text{NH}_2$  radical to three product channels of  $\text{CH}_2=\text{NNH}_2 + \text{H}$ ,  $\text{trans-CH}_3\text{N}=\text{NH} + \text{H}$ , and  $\text{cis-CH}_3\text{N}=\text{NH} + \text{H}$  as functions of temperature and pressure.

This work is reported in Publication “*Ab Initio* Kinetics for Thermal Decomposition of  $\text{CH}_3\text{N}\cdot\text{NH}_2$ , *cis*- $\text{CH}_3\text{NHN}\cdot\text{H}$ , *trans*- $\text{CH}_3\text{NHN}\cdot\text{H}$ , and  $\text{C}\cdot\text{H}_2\text{NNH}_2$  Radicals”, H. Sun, P. Zhang, C. K. Law, *Journal of Physical Chemistry A*, **2012**, 116 (33), 8419–8430.

#### 4.5 Kinetics of $\text{CH}_3\text{N}\cdot\text{NH}_2 + \text{OH}$ by Multireference Second-Order Perturbation Theory and Multireference Coupled-Cluster Theory

As found above, the  $\beta$ -scission of H atom from the  $\text{CH}_3\text{N}\cdot\text{NH}_2$  radical is not as feasible as the  $\beta$ -scission of  $\text{NH}_2$  and  $\text{CH}_3$  radicals from the other three MMH radicals (*cis*- $\text{CH}_3\text{NHN}\cdot\text{H}$ , *trans*- $\text{CH}_3\text{NHN}\cdot\text{H}$ , and  $\text{C}\cdot\text{H}_2\text{NNH}_2$ ) due to the higher energy barriers. Consequently, the  $\text{CH}_3\text{N}\cdot\text{NH}_2$  radical undergoes further oxidation to decompose to final products.

The oxidation of  $\text{CH}_3\text{N}\cdot\text{NH}_2$  radical by OH radical was found to occur with submerged energy barriers with large exothermicity. Furthermore, multireference characters of the wave function in transition states of the reaction are very significant. Consequently, the accuracy of theoretical rate coefficient for this reaction greatly depends on the accurate description of electron correlation effects for both the outer and multiple inner transition states.

Due to the strong quasi-degeneracy effect, the multireference second-order perturbation theory (CASPT2) with Dunning’s augmented correlation consistent basis set, aug-cc-pVDZ was applied to optimize the geometries of the stationary point of the potential energy surface and then to calculate the ro-vibrational frequencies. For the OH addition to the central and terminal nitrogen of the  $\text{CH}_3\text{N}\cdot\text{NH}_2$  radical, the state-averaged active space (4e,3o) consists of two degenerated  $p$  orbitals of the OH and the  $p$  orbitals of N atoms in the transition states and the H-bonded complexes. For the dissociation of the addition adducts, larger active space was applied.

Higher level stationary point energies were obtained from quadratic configuration interaction, coupled-cluster, and locally renormalized coupled-cluster methods. Specifically, the QCISD(T), CCSD(T), and LR-CCSD(T) calculations employed the correlation-consistent, polarized -valence, triplet- $\xi$  (cc-pVTZ) and quadruple- $\xi$  (cc-pVQZ) basis sets of Dunning. The energies were then extrapolated to the complete basis set (cc-pV $\infty$ Z) limit by the asymptotic form. To improve quality of the potential energy surface, the stationary point energies were further explored from high-level state selective multireference coupled-cluster theory with single and double excitations and correction for triple excitations including Brillouin-Wigner and Mukherjee’s BW-MRCCSD(T) and Mk-MRCCSD(T) approaches.

With the CASPT2/aug-cc-pVDZ geometries, scrutinizing the energies obtained at CASPT2/aug-cc-pVDZ, QCISD(T)/cc-pV $\infty$ Z, CCSD(T)/cc-pV $\infty$ Z, LR-CCSD(T)/cc-pV $\infty$ Z, and Mk-MRCCSD(T)/cc-pVTZ calculation levels, it was found that all these energies show agreement in few kcal/mol, as shown in Figure 12. The energies from multireference CASPT2/aug-cc-pVDZ and Mk-MRCCSD(T)/cc-pVTZ calculations were found to better account for the quasi-degeneracy effect.

For the OH addition to the  $\text{CH}_3\text{N}\cdot\text{NH}_2$  radical, it was found that the reaction proceeds via two hydrogen-bonded complexes (HBC1 and HBC2) for the OH addition to the central and terminal nitrogen of the  $\text{CH}_3\text{N}\cdot\text{NH}_2$  radical, respectively. The HBC1 and HBC2 are formed by an H-bonding between the central N atom of  $\text{CH}_3\text{N}\cdot\text{NH}_2$  and the hydroxyl H of OH radical, and they are optical isomers with an energy of -5.73 kcal/mol.



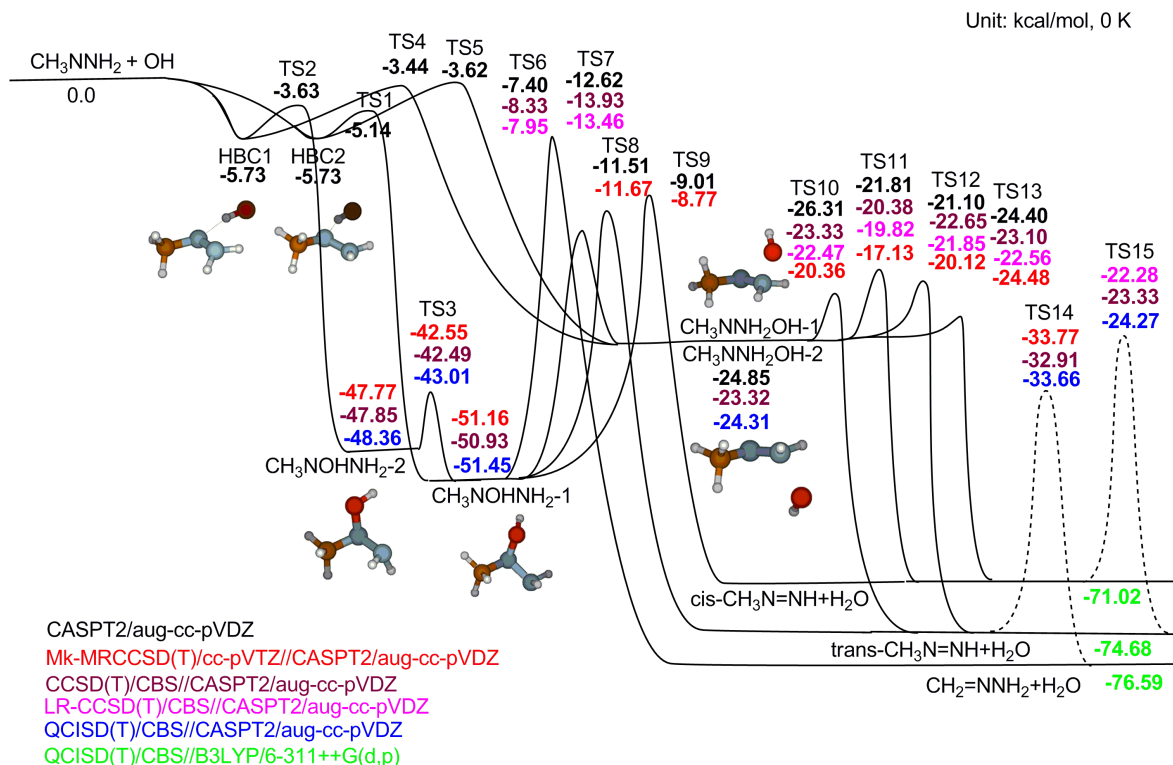


Figure 12. Potential energy surface of  $\text{CH}_3\text{N}\cdot\text{NH}_2 + \text{OH}$  calculated by several *ab initio* methods.

For the OH addition to the central N atom of  $\text{CH}_3\text{N}\cdot\text{NH}_2$  radical, it was found that the reaction proceeds through TS1 (-5.14 kcal/mol) via HBC2 to form  $\text{CH}_3\text{N}(\text{OH})\text{NH}_2\text{-1}$  adduct, and it also proceeds through TS2 (-3.63 kcal/mol) via HBC1 to form  $\text{CH}_3\text{N}(\text{OH})\text{NH}_2\text{-2}$  adduct. The energy of  $\text{CH}_3\text{N}(\text{OH})\text{NH}_2\text{-1}$  is 3.08 kcal/mol lower than that of  $\text{CH}_3\text{N}(\text{OH})\text{NH}_2\text{-2}$ , and it has energy barrier of 8.44 kcal/mol via TS3 to isomerize to  $\text{CH}_3\text{N}(\text{OH})\text{NH}_2\text{-2}$  by the rotation of the N—N bond. The  $\text{CH}_3\text{N}(\text{OH})\text{NH}_2\text{-1}$  is more stable than  $\text{CH}_3\text{N}(\text{OH})\text{NH}_2\text{-2}$  is ascribed to the fact that there are four H-bonding existing between the hydroxyl O, methyl H and amine H atoms in  $\text{CH}_3\text{N}(\text{OH})\text{NH}_2\text{-1}$ , while there are only two H-bonding existing between the hydroxyl O and methyl H atoms in  $\text{CH}_3\text{N}(\text{OH})\text{NH}_2\text{-2}$ . For the OH addition to the terminal N atom of  $\text{CH}_3\text{N}\cdot\text{NH}_2$  radical, it proceeds through TS4 (-3.44 kcal/mol) via HBC1, and it also proceeds through TS5 (-3.62 kcal/mol) via HBC2 to form two  $\text{CH}_3\text{NNH}_2\text{OH}$  adducts which are optical isomers with energies of -24.85 kcal/mol.

The lower energy adduct  $\text{CH}_3\text{N}(\text{OH})\text{NH}_2\text{-1}$  undergoes an intramolecular methyl H abstraction by OH via TS6 with energy of ca. -8 kcal/mol to form the  $\text{CH}_2=\text{NNH}+\text{H}_2\text{O}$  products. It also undergoes isomerization via TS7 with energy of -13 kcal/mol to form its higher  $\text{CH}_3\text{NNH}_2\text{OH}$  isomer. Furthermore, it undergoes intermolecular amine H abstractions via TS8 (-11.67 kcal/mol) and TS9 (-8.77 kcal/mol) to form  $\text{trans-CH}_3\text{N}=\text{NH}+\text{H}_2\text{O}$  and  $\text{cis-CH}_3\text{N}=\text{NH}+\text{H}_2\text{O}$  product sets. For each  $\text{CH}_3\text{NNH}_2\text{OH}$  optical isomeric adduct, there is a distinct transition state corresponding to intramolecular abstraction of each amine H atom. Specifically, the two optical isomeric adducts undergo intramolecular amine H abstraction via TS10 (-20.36 kcal/mol), TS11 (-17.13 kcal/mol), TS12 (-20.12 kcal/mol), TS13 (-24.48 kcal/mol), forming  $\text{trans-}$  and  $\text{cis-}$  methyldiazene and water, respectively. The isomerization of  $\text{trans-}$  methyldiazene to  $\text{CH}_2\text{N}=\text{NH}_2$  was found to have energy barrier of 41.02 kcal/mol, and the isomerization of  $\text{cis-}$  methyldiazene to  $\text{trans-}$  methyldiazene has



an energy barrier of 46.75 kcal/mol. In addition, direct intermolecular OH abstraction of hydrogen at different positions of  $\text{CH}_3\text{N}\cdot\text{NH}_2$  radical were found to have energies of -2.63 to 0.55 kcal/mol with exothermicities of 71.02 kcal/mol to 76.59 kcal/mol, forming trans- and cis-methyldiazene and water, respectively.

This work is reported in Publication “Kinetics Study of Reaction  $\text{CH}_3\text{N}\cdot\text{NH}_2 + \text{OH}$  by Multireference Second-Order Perturbation Theory and Multireference Coupled-Cluster Theory, H. Sun, K. Kowalski, K. Bhaskaran-Nair, and C. K. Law, 8th US National Combustion Meeting, University of Utah, Canyons resort in Park City, Utah, May 19-22, 2013.

#### 4.6 Kinetic Modeling of Monomethylhydrazine Decomposition and Product Formation

A kinetic mechanism was developed by incorporating pressure-dependent rate coefficients on the N—N and C—N bond fissions of MMH, and also the pressure-dependent rate coefficients for new reaction channels of MMH decomposition, MMH radical decomposition, new rate coefficients of H-abstraction reaction of MMH by  $\text{NH}_2$ ,  $\text{CH}_3$ , H radicals, and recently published rate coefficients of subsequent reactions for MMH decomposition to model the thermal decomposition of gaseous MMH.

The kinetic model was used to predict the MMH decomposition profiles at temperatures of 900 - 1370 K and pressures of 140 - 450 kPa for seven groups of MMH/Ar mixtures containing 97.5 - 99 mol % argon, and also the half-life decomposition times from shock tube experiments. Good agreement was observed below 940 K and above 1150 K for diluted MMH/Ar mixtures.

The model predictions further show that the overall MMH decomposition rate follows first-order kinetics, and that the N—N bond scission is the most sensitive reaction path for the modeling of the homogeneous decomposition of MMH at elevated pressures.

The kinetic model was used to predict the overall MMH decomposition, and  $\text{NH}_2$  and other product formation profiles at temperatures of 900 - 1300 K and pressures up to 2.7 atm from shock tube experiments (Figs. 13-15). Good agreement was observed between modeling and experimental data for the MMH/Ar mixtures.

The model predictions further show that the overall MMH decomposition rate follows first-order kinetics, and that the N—N bond and C—N bond scission are the most important reaction channels for the modeling of decomposition of MMH and also its product formation, while the  $\text{NH}_2+\text{CH}_3\text{NH}$  and  $\text{CH}_3+\text{NHNH}_2$  radical roaming channels has contribution for modeling overall MMH decomposition at temperatures below 900 K.

This work is reported in Publication “Detailed Chemical Kinetic Mechanism For Modeling MMH Pyrolysis and Oxidation, H. Sun, P. Zhang, and C. K. Law, The 7th International Conference on Chemical Kinetics, MIT, Cambridge, MA, July 10-14, 2011.

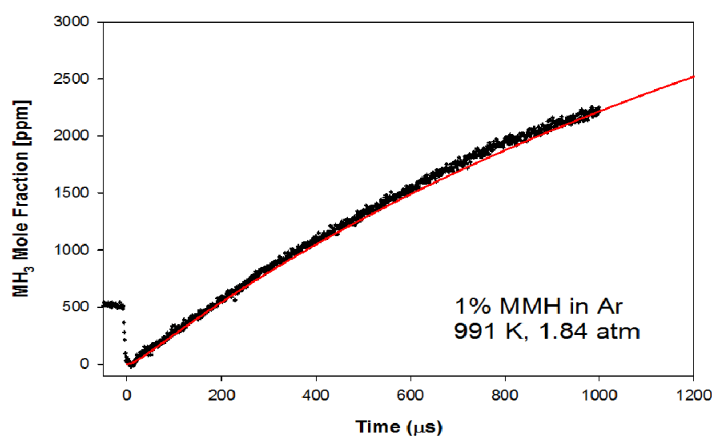


Figure 13. Modeling of experimental data of  $\text{NH}_3$  product formation. Experimental condition: 991K, 1.84atm, 1%MMH in Ar.

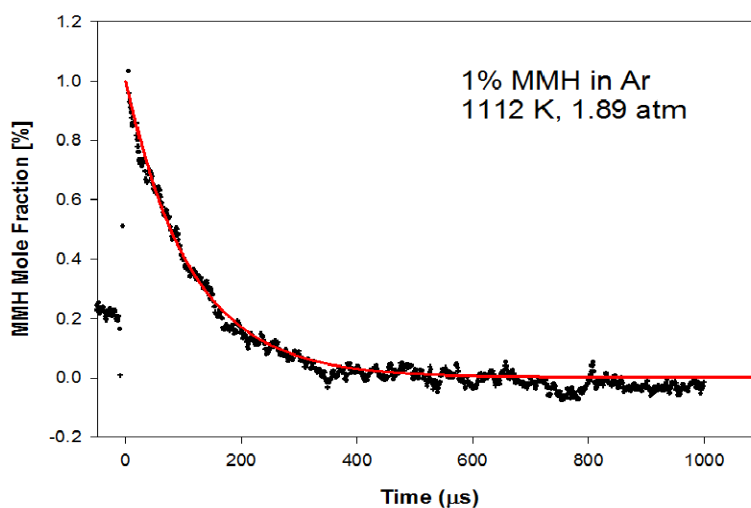


Figure 14. Modeling of experimental data of MMH decomposition. Experimental condition: 1112K, 1.89 atm, 1%MMH in Ar.

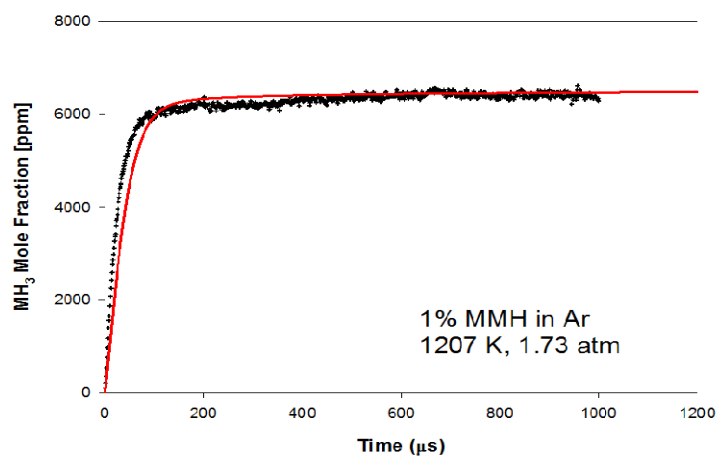


Figure 15. Modeling of experimental data of  $\text{NH}_3$  product formation. Experimental condition: 1207K, 1.73atm, 1%MMH in Ar.

## 5. References

- [1] P. Celani, H.-J. Werner, *The Journal of Chemical Physics* **2000**, *112*, 5546-5557.
- [2] (a) T. H. Dunning, *The Journal of Chemical Physics* **1989**, *90*, 1007-1023; (b) R. A. Kendall, J. Thom H. Dunning, R. J. Harrison, *The Journal of Chemical Physics* **1992**, *96*, 6796-6806.
- [3] K. Kowalski, *The Journal of Chemical Physics* **2005**, *123*, 014102.
- [4] (a) J. M. L. Martin, *Chemical Physics Letters* **1996**, *259*, 669-678; (b) D. Feller, D. A. Dixon, *Journal of Chemical Physics* **2001**, *115*, 3484.
- [5] K. Bhaskaran-Nair, O. Demel, J. Pittner, *The Journal of Chemical Physics* **2008**, *129*, 184105.
- [6] L. B. Harding, S. J. Klippenstein, A. W. Jasper, *Physical Chemistry Chemical Physics* **2007**, *9*, 4055-4070.
- [7] L. B. Harding, Y. Georgievskii, S. J. Klippenstein, *The Journal of Physical Chemistry A* **2005**, *109*, 4646-4656.
- [8] (a) J. A. Miller, S. J. Klippenstein, *The Journal of Physical Chemistry A* **2006**, *110*, 10528-10544; (b) A. Fernández-Ramos, J. A. Miller, S. J. Klippenstein, D. G. Truhlar, *Chemical Reviews* **2006**, *106*, 4518-4584.
- [9] A. L. L. East, L. Radom, *The Journal of Chemical Physics* **1997**, *106*, 6655-6674.
- [10] H. Sun, C. K. Law, *The Journal of Physical Chemistry A* **2007**, *111*, 3748-3760.

### **IV.3 Theoretical and Experimental Counterflow Ignition and Combustion Studies (Williams, University of California at San Diego)**

#### **1. Abstract**

Theoretical and experimental studies were completed on counterflow ignition and combustion of fuels related to gelled hypergolic propellants. Both generic models and specific propellant combinations were considered. A model employing activation-energy asymptotics was derived for an exothermic ignition reaction occurring at the interface between the two reactants. A model employing rate-ratio asymptotics was derived for the counterflow combustion and extinction of a hydrocarbon flowing against a mixture of oxygen and nitrous oxide. The latter provided good agreement with experiments that were performed in the counterflow apparatus during this project. Measurements were made of the structures and extinction conditions for counterflow flames with methane and ethane as fuels and with oxygen and nitrous oxide as oxidizers. Two distinct reaction zones were identified at low strain rates. The structures of these zones were calculated computationally with detailed chemistry. They also were modeled with reduced chemistry, improving knowledge and understanding of their structures. The two zones were observed to merge into one at high strain rates. Good agreement was obtained between experiment and computation for the merged reaction-zone structure and for extinction conditions. The major findings in this work thus were improvements in descriptions of the combustion processes of such fuels.

#### **2. Background and Scientific Objectives**

The objectives of this component of the MURI effort in general were to clarify the characteristics of the combustion processes of the relevant fuels and oxidizers with special reference to their chemical kinetics. More specifically, this research was intended to improve insight into the chemical kinetics and heat and mass transfer of hypergolic ignition of gelled propellants by experimental, computational, and theoretical analyses of counterflow combustion configurations and by theoretical analyses of more general configurations based on asymptotic methods. Critical conditions for ignition were to be determined, and from the results appropriate reduced chemical-kinetic descriptions were to be developed which can be used in computer simulations of combustion-chamber processes. The consequent improvements in understanding of hypergolic gelled propellant ignition were intended to be helpful to designs of propulsion systems with storable fuels.

The work fell under Task 4 of the MURI proposal, namely research concerning ignition and reaction mechanisms for hypergolic propellants. As such, it complemented research at Stanford, Princeton, and Cal Tech. In addition, it provided input to the computational research of Task 5. There thus were interactions in a number of different directions in this MURI program, and this particular work extended into more than one of the original tasks.

The background for this study arose from the realization that research in two different directions at UCSD would contribute to the objective of furthering knowledge of combustion of gelled hypergolic propellants. One direction was asymptotic analysis, not only activation-energy asymptotics, which had been advanced continuously over the years, extending back to 1966, but also the more recent method of rate-ratio asymptotics, which had begun to be developed only in the 1990's. The other direction was the development of counterflow combustion methods, both experimentally and computationally, with the former, in particular, being improved towards perfection by the nearly unique scree-type of experimental design. A great deal of progress in clarifying combustion chemistry had been obtained through these counterflow studies, and a

high-pressure combustion facility had just been completed at UCSD under ARO support. There thus was an opportunity to employ these unique methods to advance knowledge concerning these propulsion applications.

### 3. Facilities

**Laboratory:** A well equipped combustion laboratory is available for conducting the experiments. Several counterflow burners are available. These burners can be used in studies on nonpremixed, premixed, and partially premixed combustion. At UCSD we have constructed a “High Pressure Combustion Experimental Facility” (HPCEF) that can be used to carry out experiments at elevated pressures up to 2.5MPa. In the HPCEF different types of counterflow burners can be placed inside a high-pressure chamber. This project made extensive use of our counterflow burners.

**Computer:** Several computers are available for carrying the proposed numerical computations. Extensive computations were made in this project.

**Major Equipment:** Major equipment include gas chromatograph for measurements of concentrations of stable chemical species, an LDV for velocity measurements in reacting flow, a three-component PDPA, and a high-speed camera. Especially the last of these was used in this research.

### 4. Major Findings

The major findings are described in the following sections.

#### 4.1 A Generic Model for Hypergolic Ignition of Gelled Propellants

An analytical model was developed for calculating ignition histories of gelled propellants when the heat release occurs at the interface between the fuel and oxidizer. The model is based on one-step activation-energy asymptotics. General parametric analytical results were derived. The model was used by other members of the MURI team in computational investigations of hypergolic ignition.

#### 4.2 The Structure and Extinction of Methane/Nitrogen Dioxide Flames

The structure and burning velocities, of premixed flames were calculated for various values of the equivalence ratio,  $\phi$ . The calculations were performed using the complete San Diego Mechanism and simplified mechanisms. The flame structure was found to be qualitatively different from the structure of hydrocarbon air flames. Unlike hydrocarbon/air flames, both reactants,  $\text{CH}_4$  and  $\text{NO}_2$  were found to be consumed at the same location in the flame, called the reactant-consumption layer. At this location many intermediate species were formed. This includes nitric oxide (NO), oxygen ( $\text{O}_2$ ), and carbon monoxide (CO). These compounds were consumed downstream from the reactant-consumption layer. The elementary step  $\text{NO} + \text{T-CH}_2 \leftrightarrow \text{HNCO} + \text{H}$  was found to have a significant influence on the value of the burning velocity. The structure and critical conditions for extinction were calculated for nonpremixed combustion of  $\text{CH}_4$  and  $\text{NO}_2$ . Steady, axisymmetric, laminar flow of two reactant streams toward a stagnation plane was considered. One reactant stream, the fuel stream, was made up of methane, and the other stream, the oxidizer stream, was made up of a mixture of nitrogen dioxide, oxygen and nitrogen. Two sets of calculations were performed. In one set of calculations the ratio of mass fractions of oxygen and nitrogen in the oxidizer stream was the same as in air. The strain rate at extinction was calculated for various values of mass fraction of  $\text{NO}_2$ . In another set of calculations, the effective mass fraction of oxygen from air and  $\text{NO}_2$  was

fixed. The critical conditions for extinction were calculated for various values of the mass fraction of  $\text{NO}_2$ . Both set of calculations showed that  $\text{NO}_2$  inhibits the flame. An illustration of this is that, in the second set of calculations, the strain rate at extinction was found to decrease with increasing amounts of  $\text{NO}_2$ .

### 4.3 The Structure and Extinction of Nonpremixed Methane/Nitrous Oxide and Ethane/Nitrous Oxide Flames

An experimental and kinetic-modeling study was carried out to elucidate aspects of nonpremixed combustion of methane ( $\text{CH}_4$ ) and nitrous oxide ( $\text{N}_2\text{O}$ ), and ethane ( $\text{C}_2\text{H}_6$ ) and  $\text{N}_2\text{O}$ . Experiments were conducted, at a pressure of 1 atm, on flames stabilized between two opposing streams. One stream is a mixture of oxygen ( $\text{O}_2$ ), nitrogen ( $\text{N}_2$ ), and  $\text{N}_2\text{O}$ , and the other a mixture of  $\text{CH}_4$  and  $\text{N}_2$  or  $\text{C}_2\text{H}_6$  and  $\text{N}_2$ . Figure 1 shows a schematic illustration of the counterflow configuration.

The counterflow burner used in the experimental study has two ducts. From one duct, a fuel stream made up of methane and nitrogen or ethane and nitrogen is injected toward the mixing layer. At the exit of the fuel duct, the mass fraction of fuel is represented by  $Y_{F,1}$ , the temperature by  $T_1$ , and the injection velocity by  $V_1$ . From the other duct an oxidizer stream made up of a mixture of oxygen, nitrous oxide, and nitrogen is injected. At the exit of the oxidizer duct, the mass fraction of oxygen, and nitrous oxide is represented by,  $Y_{\text{O}_2,2}$ , and  $Y_{\text{N}_2\text{O},2}$  respectively, the temperature by  $T_2$ , and the injection velocity by  $V_2$ . The diagram is a cut through the centerline of the axisymmetric system. The flame is shown to be on the oxidizer side of the stagnation plane because it usually is located there. Experimental conditions can be established with the flame on the fuel side, as well, or it could be adjusted to be right at the stagnation plane. Since in most practical cases the flame is on the oxidizer side, it is shown to be there in the figure.

There are a variety of ways to analyze such counterflow experiments. One approach is to measure the flow field by methods such as PIV. Such approaches, however, are very expensive and time-consuming. It is more direct to use a formula for a representative residence time. This is especially appropriate for screen counterflows because the parameters in the formula are readily measured experimentally and also are readily input into computational programs so that direct correspondences can be made between the measurements and the computations.

A convenient parameter to characterize the residence time is the reciprocal of the strain rate,  $a_2$ , given by

$$a_2 = \frac{2|V_2|}{L} \left( 1 + \frac{|V_1|\sqrt{\rho_1}}{|V_2|\sqrt{\rho_2}} \right). \quad (1)$$

Here  $\rho_1$  and  $\rho_2$  are the densities at the reactant streams at the injection plane of the fuel duct and at the injection plane of the oxidizer duct respectively. The separation distance between the ducts is  $L$ .

Critical conditions for extinction were measured. It has been established from asymptotic analysis that the critical extinction conditions depend on the strain rate, the stoichiometric mixture fraction,  $Z_{\text{st}}$  and the adiabatic flame temperature  $T_{\text{st}}$ . The adiabatic temperature is a function of temperature and mass fraction and of the reactants at the boundaries. To elucidate the influence of  $\text{N}_2\text{O}$  on the structure and mechanisms of extinction of  $\text{CH}_4$  and  $\text{C}_2\text{H}_4$  flames, several sets of experimental data were obtained. In each set the values of  $Z_{\text{st}}$ ,  $T_{\text{st}}$  are the same.

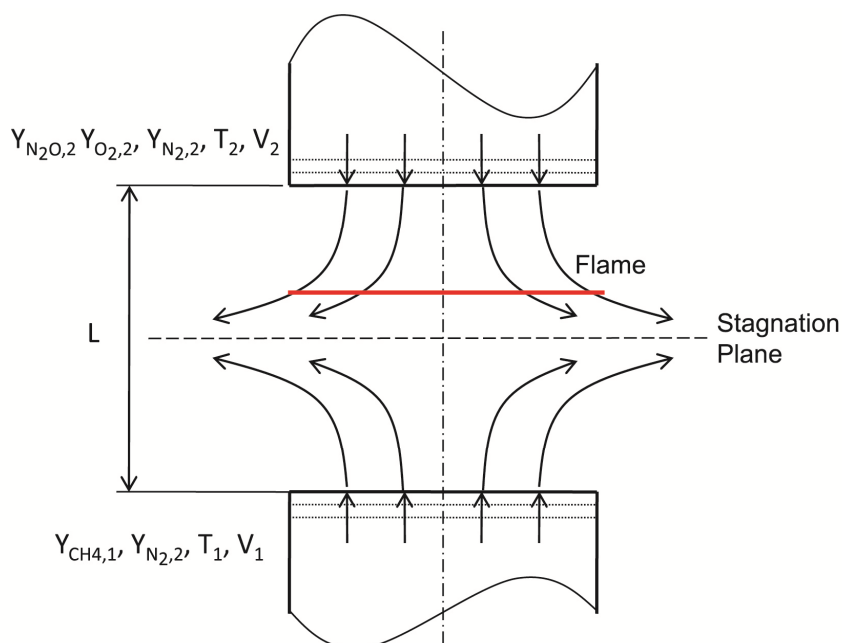


Figure 1. Schematic illustration of the counterflow configuration.

Figure 2 is a photograph of a flame stabilized in the counterflow burner. The photograph shows two reaction zones. After the flame is established, the values of the flow velocities of the reactants were increased until extinction was observed. The strain rate at extinction,  $a_{2,e}$ , was recorded as a function of the mass fraction of  $N_2O$  in the reactant streams,  $Y_{N_2O,2}$ . This photograph demonstrates clearly the two-zone character of the flame, mentioned in the abstract. One reaction zone is on the fuel side, and the other is on the oxidizer side. The major fuel consumption occurs in the reaction zone on the fuel side, and the major consumption of nitrous oxide occurs in the reaction zone on the oxidizer side. This is noteworthy because it is not observed with other oxidizers. For example, when only oxygen is employed as the oxidizer, only one reaction zone is visible. The reason for the difference lies in the different chemical kinetics of the two oxidizers. As will be described in greater detail below, nitrogen-containing oxidizers differ in important ways from oxidizers that do not contain nitrogen because of the appreciably different chemical kinetics involved.

The primary chemical-kinetic scheme employed in this study is the San Diego mechanism. This mechanism is made up of 288 elementary reactions among 53 species. The set of elementary reactions that include species that have the element nitrogen in their molecule is referred to here as nitrogen chemistry. The code employs mixture-averaged diffusion coefficients for various species and thermal (Soret) diffusion. Discretization of differential equations is carried out using conventional finite differencing techniques for non-uniform mesh spacing. To account for steep gradients within the computational domain, dynamical adaptive meshing techniques are used. Standard calculations employ more than 300 grid points. To ensure grid insensitivity, at selected conditions simulations were performed with up to 2000 grid-points and results were compared with those calculated using less number of grid points. Figures 3 shows critical conditions for extinction for  $CH_4/N_2-N_2O/O_2/N_2$  flames at two different values of  $Z_{st}$  and two different values of  $T_{st}$ . The symbols are experimental data and the lines are results of computations performed

using the San Diego Mechanism. The predictions agree well with experimental measurements, supporting the accuracy of the San Diego Mechanism in prediction extinction.

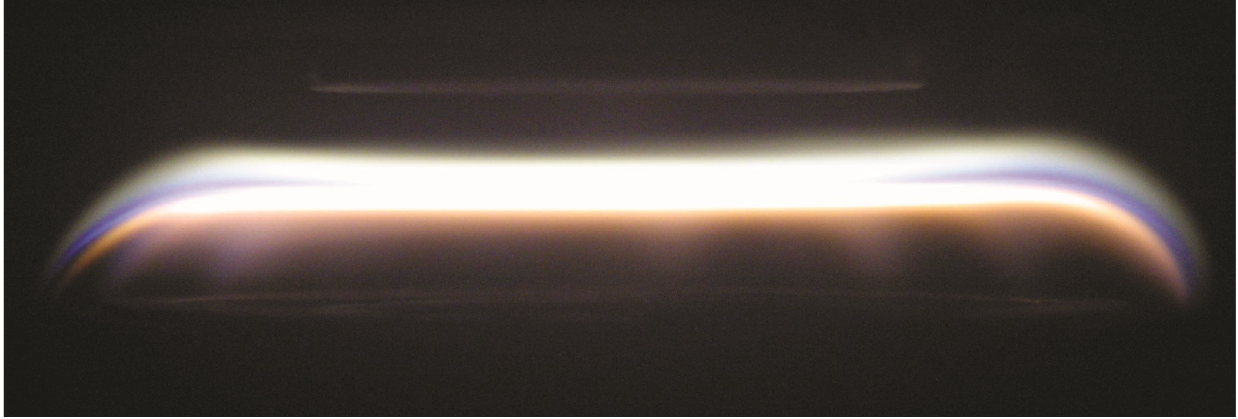


Figure 2. Photograph of a nonpremixed  $\text{CH}_4/\text{N}_2\text{-N}_2\text{O}/\text{O}_2/\text{N}_2$  flame. Strain rate,  $a_2 = 175 \text{ s}^{-1}$ .

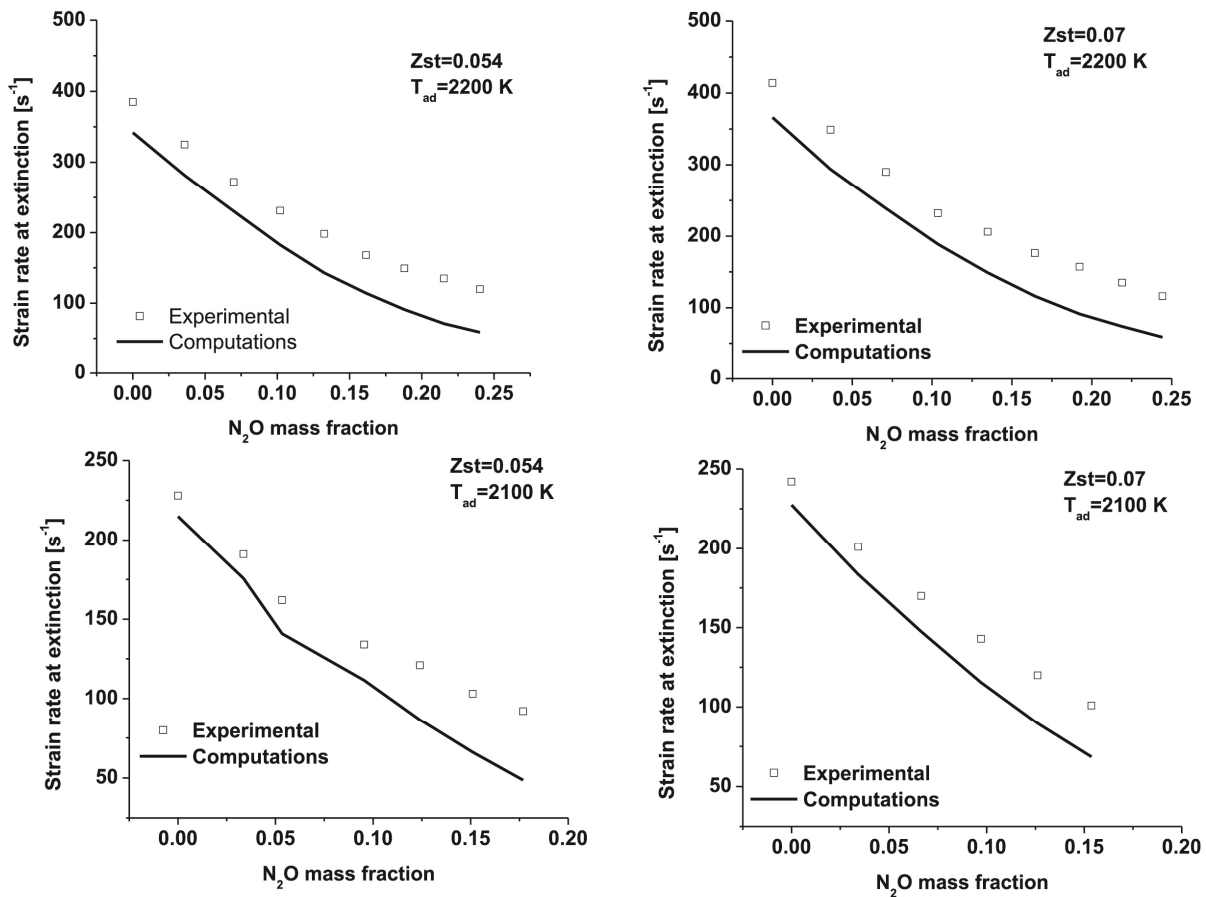


Figure 3. The mass fraction of nitrous oxide,  $Y_{\text{N}_2\text{O},2}$ , as a function of the strain rate at extinction,  $a_{2,e}$  at fixed values of  $Z_{\text{st}}$  and  $T_{\text{st}}$ . The fuel is methane. The symbols represent experimental data and the lines are predictions of the San Diego Mechanism.

Figure 4 shows the corresponding critical conditions for extinction for ethane flames. These critical conditions measure experimentally exhibit excellent agreement with the extinction



conditions calculated using the San Diego mechanism. The agreement is better than those for methane flames. With increasing  $Y_{N_2O,2}$ , the value of  $a_{2,e}$  decreases. Thus  $N_2O$  inhibits the flame. The better agreement than in Fig. 3 suggests that, although the nitrogen chemistry in the San Diego Mechanism was developed for air-pollution rather than propellant problems, it seems to work well for propellants. It also suggests that deficiencies remain in the mechanism for methane. The chemistry for this fuel definitely deserves further study. Since methane is not a candidate for a hypergolic propellant, that further investigation was not pursued in this program.

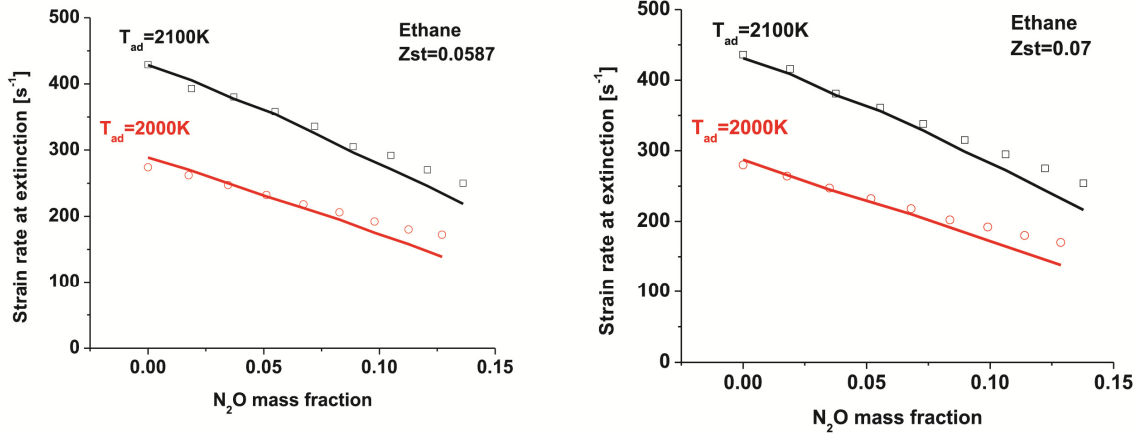


Figure 4. The mass fraction of nitrous oxide,  $Y_{N_2O,2}$ , as a function of the strain rate at extinction,  $a_{2,e}$  at fixed values of  $Z_{st}$  and  $T_{st}$ . The fuel is ethane. The symbols represent experimental data and the lines are predictions of the San Diego Mechanism.

The flame structure is calculated to elucidate the inhibiting effect of  $N_2O$ . Figure 5 shows the computed structure of a  $CH_4/N_2-N_2O/O_2/N_2$  flame at different strain rates. The structure at  $a_2 = 100 \text{ s}^{-1}$  is far from extinction and the structure at  $a_2 = 180 \text{ s}^{-1}$  is close to extinction. The normalized carbon mass fraction in Fig. 5 is the ratio of the mass fraction of carbon at a given location to the mass fraction of carbon in the fuel stream. It represents the mixture fraction.

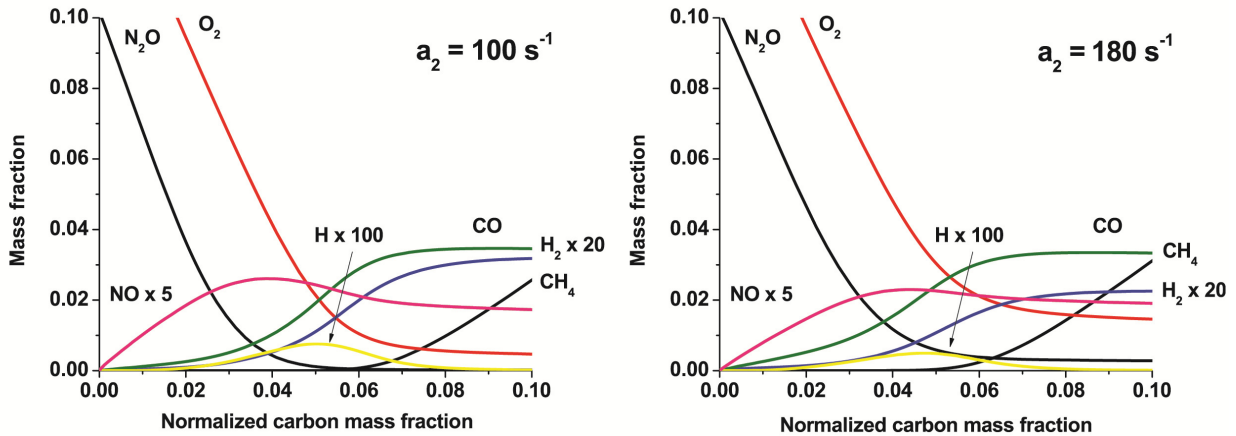


Figure 5. Computed structure of  $CH_4/N_2-N_2O/O_2/N_2$  flames at fixed values of  $T_{st} = 2200K$ ,  $Z_{st} = 0.054$ , and  $Y_{N_2O,2} = 0.102$ . The left side shows flame structure at strain rate of  $100 \text{ s}^{-1}$ , and the right side the flame structure at strain rate of  $180 \text{ s}^{-1}$ . The computations were done using the San Diego Mechanism.

Figure 5 clearly shows that consumption of  $\text{CH}_4$  and  $\text{N}_2\text{O}$  takes place in two separate regions. This is also evident in the photograph of the flame shown in Fig. 2, as mentioned earlier. In the region where  $\text{CH}_4$  is consumed, the intermediate species  $\text{CO}$  and  $\text{H}_2$  are formed. In the region where  $\text{N}_2\text{O}$  is consumed,  $\text{NO}$  is formed. As extinction is approached the concentration of  $\text{H}$  decreases. Also the concentration of  $\text{N}_2\text{O}$  and  $\text{O}_2$  in the reaction zone increases with increasing strain rate. This indicates that the leakage of  $\text{N}_2\text{O}$  and  $\text{O}_2$  increases as the strain approaches its extinction value.

Figure 6 shows the contribution of various elementary reactions to rates of production of  $\text{CH}_4$ ,  $\text{N}_2\text{O}$ ,  $\text{O}_2$ , and  $\text{H}$  in a  $\text{CH}_4/\text{N}_2\text{--N}_2\text{O}/\text{O}_2/\text{N}_2$  flame at  $T_{\text{st}} = 2200$ ,  $Z_{\text{st}} = 0.054$ ,  $Y_{\text{N}_2\text{O},2} = 0.102$ , and  $a_2 = 100 \text{ s}^{-1}$ . The elementary steps  $\text{CH}_4 + \text{H} \leftrightarrow \text{CH}_3 + \text{H}_2$  and  $\text{CH}_4 + \text{OH} \leftrightarrow \text{CH}_3 + \text{H}_2\text{O}$  are the main contributors to the rate of consumption of  $\text{CH}_4$ , the elementary propagation step  $\text{N}_2\text{O} + \text{H} \leftrightarrow \text{N}_2 + \text{OH}$  is the main contributor to the rate of consumption of  $\text{N}_2\text{O}$ , and the main contributor to the rate of consumption of  $\text{O}_2$  and rate of production of  $\text{H}$  is the branching reaction  $\text{H} + \text{O}_2 \leftrightarrow \text{OH} + \text{O}$ . This reaction is followed by fast reactions  $\text{H}_2 + \text{O} \leftrightarrow \text{OH} + \text{H}$ , and  $\text{H}_2 + \text{OH} \leftrightarrow \text{H}_2\text{O} + \text{H}$  giving the overall branching reaction  $3\text{H}_2 + \text{O}_2 \leftrightarrow 2\text{H}_2\text{O} + 2\text{H}$ . This is evident from Fig. 6 because it shows that the net rate of production of  $\text{H}$  is positive in the region where the branching step  $\text{H} + \text{O}_2 \leftrightarrow \text{OH} + \text{O}$  is active. The reactions that consume  $\text{H}$  are the elementary steps  $\text{CH}_4 + \text{H} \leftrightarrow \text{CH}_3 + \text{H}_2$ , and  $\text{N}_2\text{O} + \text{H} \leftrightarrow \text{N}_2 + \text{OH}$ . In the regions where these reactions are active the net rate of production of  $\text{H}$  is negative. The reaction  $\text{N}_2\text{O} + \text{H} \leftrightarrow \text{N}_2 + \text{OH}$ , followed by the fast reaction  $\text{H}_2 + \text{OH} \leftrightarrow \text{H}_2\text{O} + \text{H}$  gives the overall step  $\text{N}_2\text{O} + \text{H}_2 \leftrightarrow \text{N}_2 + \text{H}_2\text{O}$ . Thus addition of  $\text{N}_2\text{O}$  leads to a net consumption of  $\text{H}_2$  and the formation of the products  $\text{H}_2\text{O}$  and  $\text{N}_2$ . Inhibition of  $\text{N}_2\text{O}$  arises from the competition of this overall step with the overall branching reaction  $3\text{H}_2 + \text{O}_2 \leftrightarrow 2\text{H}_2\text{O} + 2\text{H}$ . To further test the contribution of the elementary step  $\text{N}_2\text{O} + \text{H} \leftrightarrow \text{N}_2 + \text{OH}$  to critical conditions of extinction, computations were performed with and without this reaction included in the kinetic mechanism. The results show that critical conditions of extinction can be calculated accurately by excluding all reactions in the nitrogen chemistry except  $\text{N}_2\text{O} + \text{H} \leftrightarrow \text{N}_2 + \text{OH}$ .

Figure 7 shows the net rates of production of  $\text{CH}_4$ ,  $\text{N}_2\text{O}$ ,  $\text{O}_2$ , and  $\text{H}$  computed for  $T_{\text{st}} = 2200$ ,  $Z_{\text{st}} = 0.054$ ,  $Y_{\text{N}_2\text{O},2} = 0.102$ , and  $a_2 = 100 \text{ s}^{-1}$ . These net rates are the same as those shown in Fig. 6. They are reproduced here to elucidate the flame structure. Figure 7 shows that consumption of  $\text{CH}_4$ ,  $\text{N}_2\text{O}$  and  $\text{O}_2$  take place in different layers of the reaction zone. They are called the  $\text{CH}_4$  consumption layer,  $\text{N}_2\text{O}$  consumption layer and  $\text{O}_2$  consumption layer. In the  $\text{CH}_4$  consumption layer fuel reacts with the radicals to form the intermediate species  $\text{CO}$  and  $\text{H}_2$ . In the  $\text{N}_2\text{O}$  consumption layer nitrous oxide reacts with radicals. Consumption of  $\text{O}_2$  takes place between the  $\text{CH}_4$  consumption layer and  $\text{N}_2\text{O}$  consumption layer. Here the radicals are produced.

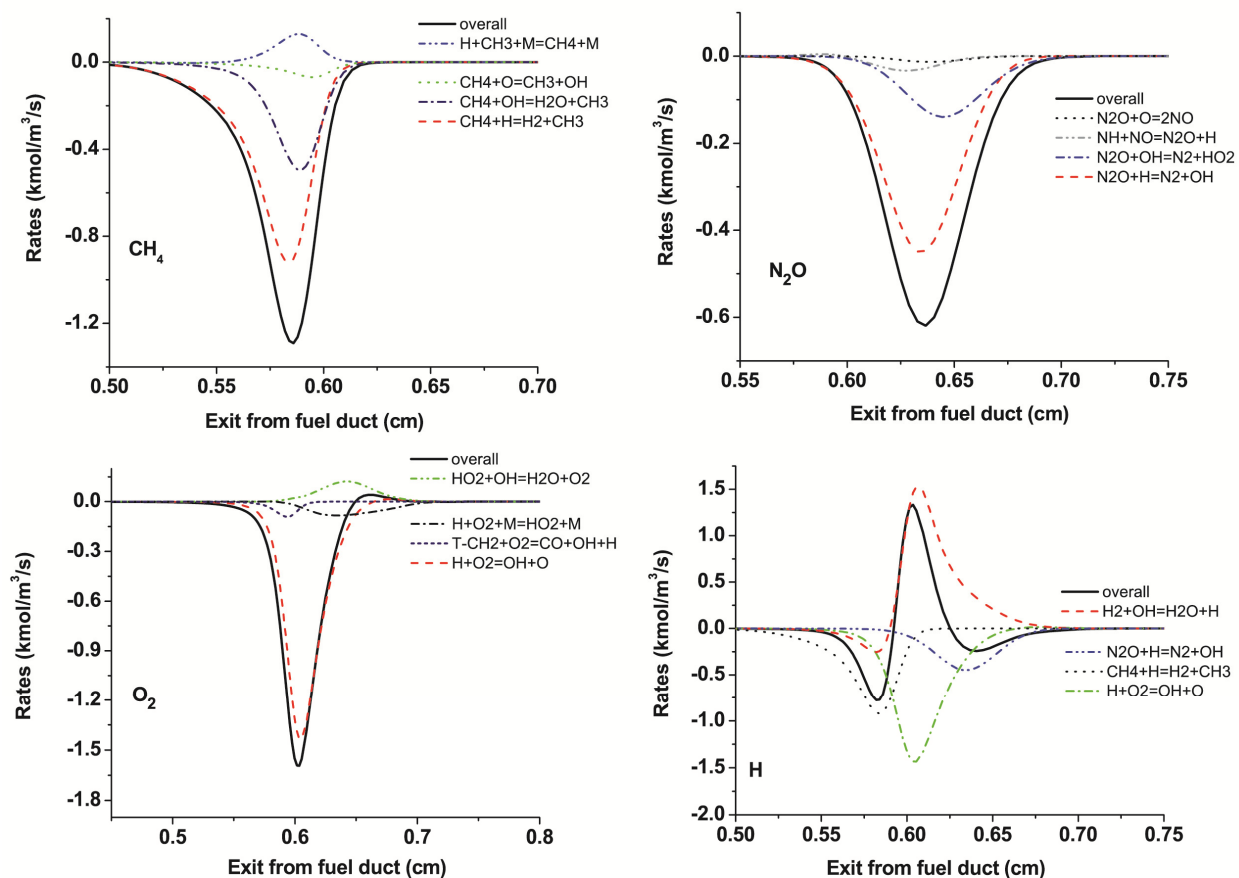


Figure 6. Contribution of elementary reactions to rates of production of  $\text{CH}_4$ ,  $\text{N}_2\text{O}$ ,  $\text{O}_2$ , and  $\text{H}$ . Positive values indicate production and negative values consumption. The computations were done using the San Diego Mechanism at  $T_{\text{st}} = 2200$ ,  $Z_{\text{st}} = 0.054$ ,  $Y_{\text{N}_2\text{O},2} = 0.102$ , and  $a_2 = 100 \text{ s}^{-1}$ .

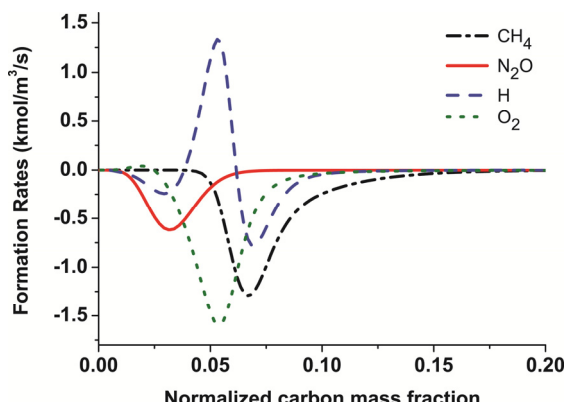


Figure 7. Net rates of production of  $\text{CH}_4$ ,  $\text{N}_2\text{O}$ ,  $\text{O}_2$ , and  $\text{H}$ . The computations were done using the San Diego Mechanism at  $T_{\text{st}} = 2200$ ,  $Z_{\text{st}} = 0.054$ ,  $Y_{\text{N}_2\text{O},2} = 0.102$ , and  $a_2 = 100 \text{ s}^{-1}$ .

#### 4.4 Experimental and Computational Studies of Ignition of Nonpremixed C<sub>2</sub>H<sub>6</sub>/N<sub>2</sub> with oxidizer mixtures of N<sub>2</sub>O/O<sub>2</sub>/N<sub>2</sub>

An experimental and computational study was carried out to elucidate the influence of nitrous oxide (N<sub>2</sub>O) on the ignition of ethane (C<sub>2</sub>H<sub>6</sub>). Experiments were conducted, at a pressure of 1 atm, employing the counterflow configuration. In this configuration two streams flow toward a stagnation plane. One stream is a mixture of oxygen (O<sub>2</sub>), nitrogen (N<sub>2</sub>), and N<sub>2</sub>O, and the other a mixture of C<sub>2</sub>H<sub>6</sub> and N<sub>2</sub>. Figure 1 is a schematic illustration of the experimental configuration. Here the mass fraction of ethane in the fuel stream is  $Y_{C_2H_6,1}$ . The strain rate is given by Eq. 1.

The structure of the reactive flowfield depends on the five boundary parameters represented by the mass fraction of the reactants,  $Y_{F,1}$ ,  $Y_{O_2,2}$ , and  $Y_{N_2O,2}$  and the temperatures  $T_1$  and  $T_2$ . The experiments were conducted with  $Y_{F,1} = 0.15$ ,  $T_1 = 298$  K. This reduces the number of independent parameters to three. To evaluate the influence of N<sub>2</sub>O on critical conditions of ignition, experiments are conducted at fixed  $Y_{O_2,x} = 0.233$ , where

$$Y_{O_2,x} = Y_{O_2,2} + Y_{N_2O,2}(16/44) \quad (2)$$

This constraint reduces the independent parameter to 2. Several sets of data are obtained. In each set the strain rate is fixed. For a given set of experiments, a value of  $Y_{N_2O,2}$  is selected and the flow field is established. The temperature of air is increased until autoignition takes place. The onset of autoignition is observed using a high-speed camera to make sure that ignition takes place close to the axis of symmetry. The temperature of the oxidizer stream,  $T_2$  is recorded as a function of  $Y_{N_2O,2}$ . The accuracy of the measurement of the temperature of air is expected to be  $\pm 30$  K, the strain rate  $\pm 10\%$ , and fuel mass fraction  $\pm 3\%$  of recorded value. The experimental repeatability in the measurement of the temperature of air at autoignition is expected to be  $\pm 6$  K, that of strain rate  $\pm 5\%$  of recorded value and that of the fuel mass fraction  $\pm 1\%$  of recorded value.

Figure 8 shows photographs of the transient autoignition process recorded by a high-speed camera at 500 frames per second. Such photographs were taken to assure accuracy in establishing ignition conditions. Extinction conditions are obtained with accuracy more easily. Ignition sometimes is difficult to detect because the flame is not clearly seen in the hot flow when it first appears. The high-speed photographs, however, clearly reveal at just what conditions the flame is established. It is for this reason that the photography is so helpful in these experiments.

Computations were performed employing the San Diego Mechanism. Figure 9 shows critical conditions for autoignition of ethane with no nitrous oxide added to the oxidizer stream. At all values of strain rate, the predicted temperature of the oxidizer stream at ignition is higher than the measured value. This is another disagreement that in the future needs to be addressed in the mechanism. It is helpful to see this, however, because it provides the background needed for proper interpretation of results with nitrous oxide.

Figure 10 show critical autoignition conditions with nitrogen-containing oxidizers added. The symbols represent experimental data and the lines are predictions obtained using the San Diego Mechanism. At all values of  $a_2$  the predicted temperature at ignition is higher than the measured value. Experimental data show that small amounts of N<sub>2</sub>O promotes ignition and large amounts

$\text{N}_2\text{O}$  inhibits ignition. In this respect the effects on ignition are not the same as the effects on extinction.

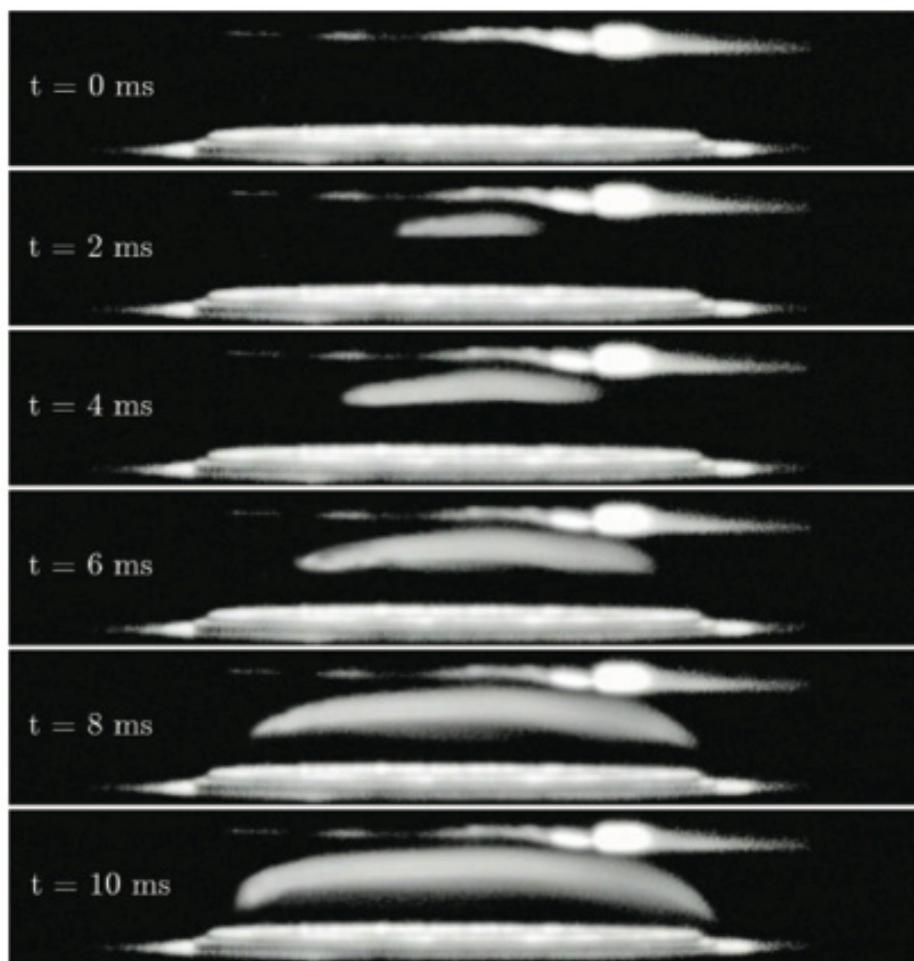


Figure 8: Photograph of an Ignition Event of  $\text{C}_2\text{H}_6/\text{N}_2\text{—N}_2\text{O}/\text{O}_2/\text{N}_2$ ,  $Y_{\text{F},\text{L}} = 0.15$ ,  $T_1 = 298 \text{ K}$ ;  $Y_{\text{N}_2\text{O},2} = 0.4$ ,  $Y_{\text{O}_2,2} = 0.088$ ,  $T_2 = 1189 \text{ K}$ ; Strain rate  $a_2 = 350 \text{ s}^{-1}$

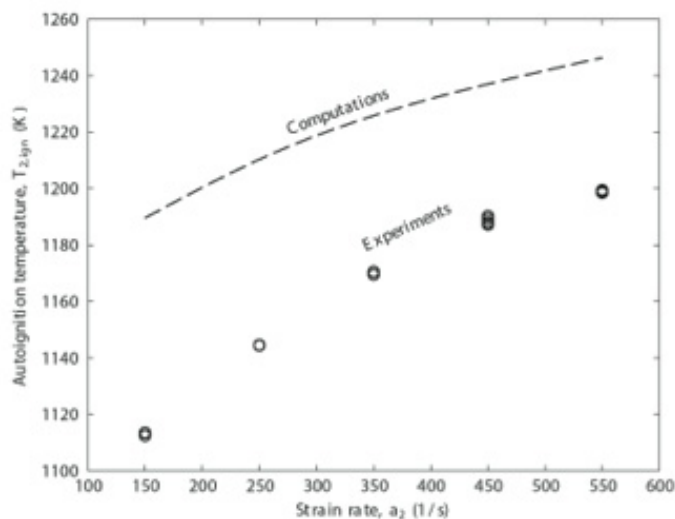


Figure 9: Critical conditions of ignition  $\text{C}_2\text{H}_6/\text{N}_2\text{-Air}$ . Symbols represent experimental data and the line is prediction obtained using San Diego Mechanism

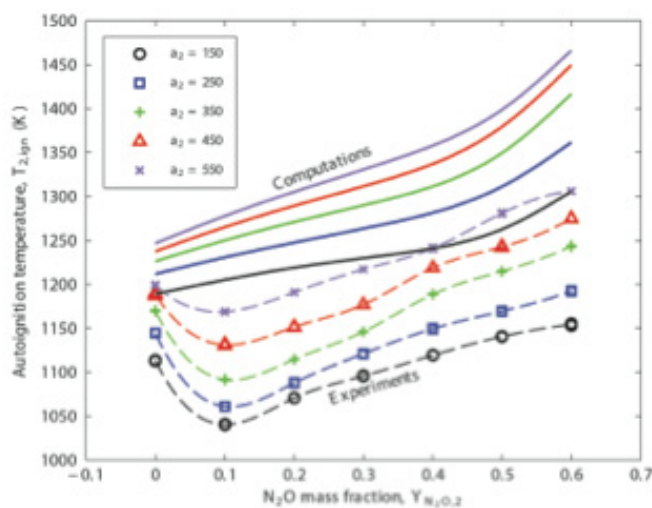
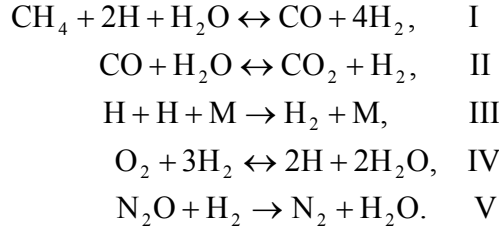


Figure 10: Critical conditions of ignition  $\text{C}_2\text{H}_6/\text{N}_2\text{-N}_2\text{O}/\text{O}_2/\text{N}_2$ . Symbols represent experimental data and the line is prediction obtained using San Diego Mechanism

#### 4.5 Rate-Ratio Asymptotic Analysis of the Structure and Mechanisms of Extinction of Nonpremixed $\text{CH}_4/\text{N}_2\text{-O}_2/\text{N}_2\text{O}/\text{N}_2$ Flames

Rate-ratio asymptotic analysis was also carried out to elucidate the influence of nitrous oxide on the structure and critical conditions for extinction of nonpremixed methane flames, as indicated in the abstract. Steady, axisymmetric, laminar flow of two counterflowing streams toward a stagnation plane is considered. One stream is made up of a mixture of methane and nitrogen. The other stream is a mixture of oxygen, nitrous oxide, and nitrogen. A reduced mechanism of five global steps is employed in the analysis. The reduced mechanism is



Chemical reactions are presumed to take place in a thin reaction zone that is established in the vicinity of the stagnation plane. On either side of this thin reaction zone, the flow field is inert. These inert regions are called outer zones. Methane and nitrous oxide are completely consumed in the reaction zone, while oxygen is presumed to leak through the reaction zone. In the reaction zone, chemical reactions are presumed to take place in two layers—the inner layer and the oxidation layer. In the inner layer fuel (methane) is consumed and the intermediate species hydrogen and carbon monoxide are formed. These intermediate species are oxidized in the oxidation layer to water vapor and carbon dioxide. Radicals are produced in the oxidation layer from chain-branching reactions that consume hydrogen.

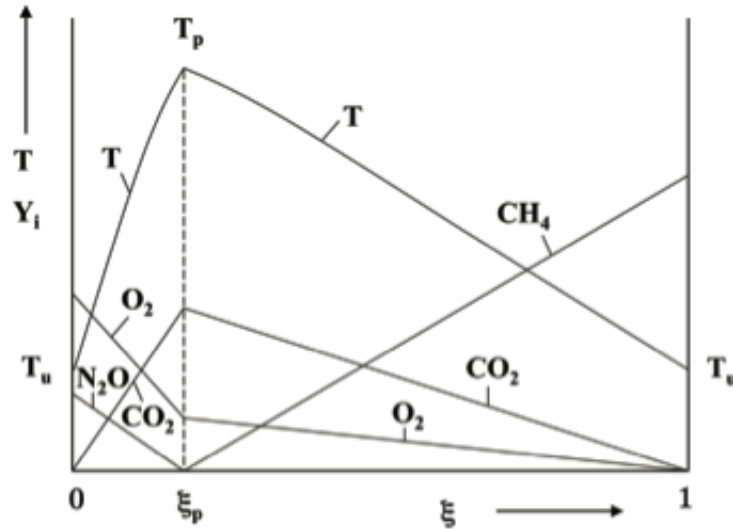


Figure 11. Schematic illustration of the outer structure of the flame.

Figure 11 shows the outer structure with the reaction zone located at  $\xi_p$ , where  $\xi$  represents a conserved scalar quantity. To the leading order, oxygen is presumed to leak through the reaction zone.

Asymptotic analysis gives the scalar dissipation rate,  $\chi_p$  at extinction. Figure 12 shows the flame temperature,  $T_p$  as a function of the scalar dissipation rate,  $\chi_p$ . The minimum value of  $\chi_p^{-1}$  for each curve in the figure represents the critical condition at extinction.

Asymptotic analysis predicts the scalar dissipation rate at extinction, while measurements give the strain rate at extinction,  $a_q$ . At fixed values of the stoichiometric mixture fraction and adiabatic temperature it has been shown that the scalar dissipation rate at extinction,  $\chi_{q,st}$  is proportional to the strain rate. Figure 13 compares predictions of critical conditions for extinction predicted by the asymptotic model with experimental data. Here  $a_{q,0}$  represents the strain rate at



extinction with no  $N_2O$  added to the oxidizer stream. Critical conditions for extinction predicted by the analysis agree well with previous experimental data. Nitrous oxide is found to have an inhibiting effect on the flame, promoting extinction. The inhibiting effect is attributed to the competition between the net reaction of nitrous oxide with hydrogen to form water vapor and nitrogen and the chain-branching reaction between oxygen and hydrogen that produces radicals.

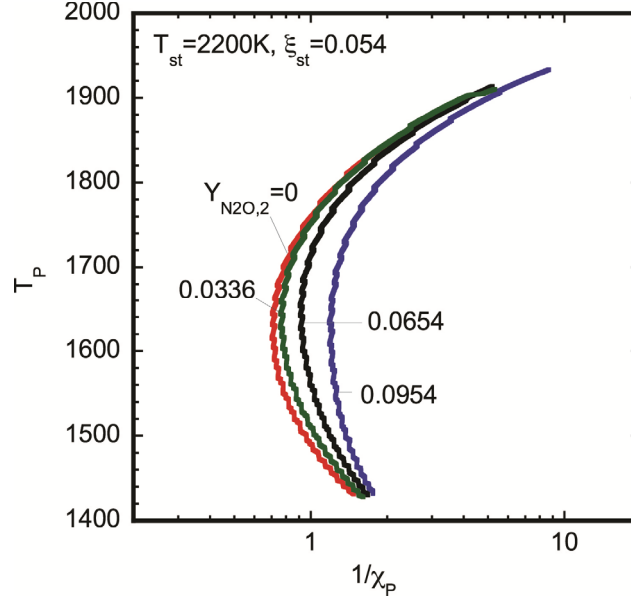


Figure 12. The flame temperature  $T_p$  as a function of  $\chi_p^{-1}$  for various values of  $Y_{N_2O}$ .

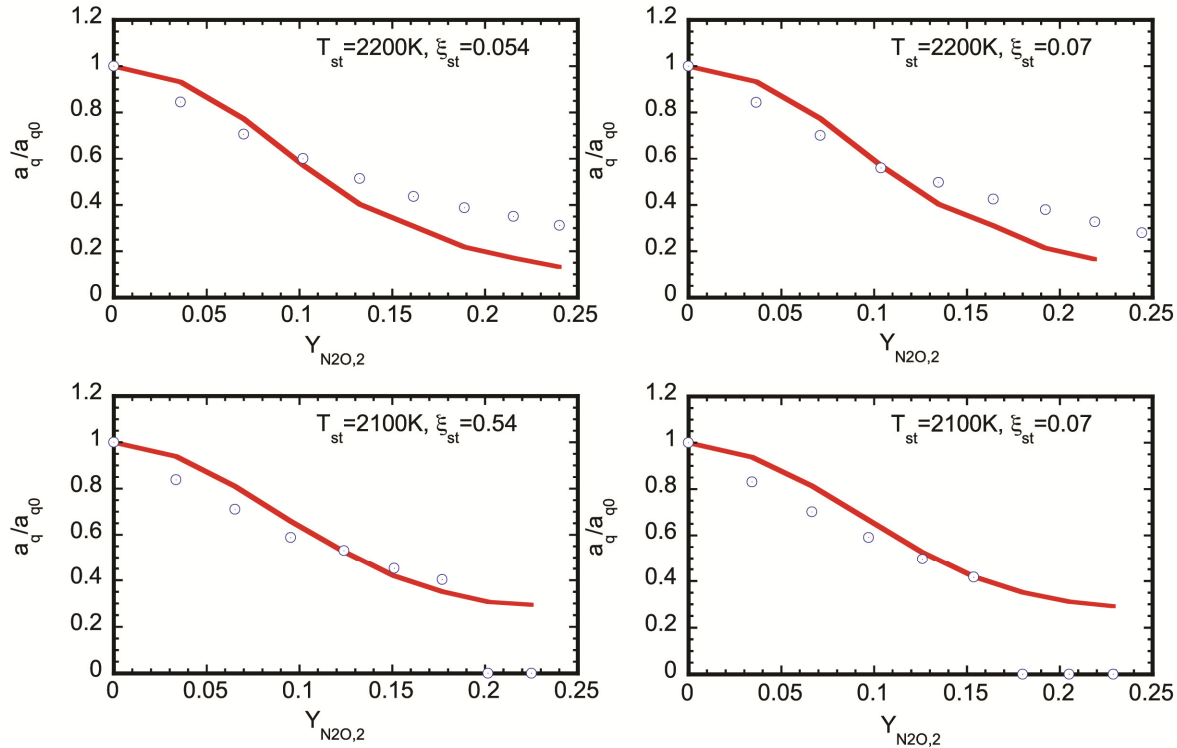


Figure 13. The ratio  $a_q/a_{q,0}$  at extinction for various values of  $Y_{N_2O}$ . The symbols represent experimental data and the lines are predictions of the asymptotic analysis.



#### 4.6 Experimental and Computational Studies of the Influence of Hydrogen and Carbon Monoxide on the Structure and Extinction of Methane Flames

An experimental and computational study was carried out to elucidate the influence of hydrogen and carbon monoxide on the structure and extinction of nonpremixed methane flames. Experiments were conducted on flames stabilized between two counterflowing streams. The fuel stream was made up of  $\text{CH}_4$  and  $\text{N}_2$  and the oxidizer stream, was made up of  $\text{O}_2$ , and  $\text{N}_2$ . Carbon monoxide was added either to the fuel stream or to the oxidizer stream. The mass fraction of  $\text{CH}_4$  in the fuel stream is  $Y_{\text{F},1}$ , and that of  $\text{O}_2$  in the is  $Y_{\text{O}_2,2}$ . The temperature of the fuel stream is  $T_1$  and the temperature of the oxidizer stream is  $T_2$ . When  $\text{H}_2$  or  $\text{CO}$  is added to the fuel stream their mass fractions, respectively, are  $Y_{\text{H}_2,1}$  and  $Y_{\text{CO},1}$ , and when added they are added to the oxidizer stream their mass fractions, respectively, are  $Y_{\text{H}_2,2}$  and  $Y_{\text{CO},2}$ . In comparing influences of  $\text{CO}$  addition to different streams, choices must be made about what parameters to keep fixed. It has been established from activation energy asymptotic analysis and rate-ratio asymptotic analysis that the Damkohler number,  $D_a = \tau_f/\tau_c$ , plays a key role in establishing the critical conditions of extinction, where  $\tau_f$  is the characteristic flow time and  $\tau_c$  the characteristic chemical time. The characteristic flow time depends on the scalar dissipation rate, which in turn depends on the strain rate, and the stoichiometric mixture fraction,  $Z_{\text{st}}$ . The chemical time depends on the mass fraction of reactants and the temperatures,  $T_1$ , and  $T_2$ . Because of the strong temperature dependencies of reaction rates, it is most important to make comparisons at fixed values of the adiabatic temperature,  $T_{\text{st}}$ . Otherwise differences associated with different reaction-zone temperatures are likely to dominate the results. After removal of effects of temperature variations, structures of reaction zones still vary with the stoichiometric mixture fraction. It is therefore also desirable to make comparisons at fixed values of  $Z_{\text{st}}$ .

Figure 14 shows critical extinction conditions for methane flames with hydrogen added to the oxidizer side, and Figure 15 show critical extinction conditions with hydrogen added to the fuel side. In these figures the symbols represent experimental data, and the curves represent computational predictions obtained using the San Diego mechanism. In both of these figures the experimental data and predictions show that the value of extinction strain rate increases with increasing amounts of hydrogen in the reactant streams. Thus, addition of hydrogen delays extinction, as expected because of its high reactivity.

The data in Figs. 14 and 15 are best plotted as a function of a quantity  $r$ , where  $r$  is the ratio of the oxygen flux that reacts with hydrogen to the oxygen flux that reacts with methane. Figure 16, shows the extinction strain rate, normalized by the extinction strain rate without hydrogen addition, as a function of  $r$ , for both oxidizer-side and fuel-side addition of hydrogen. The extremely close agreement seen in this figure, for both computation and experiment and for both fuel side and oxidizer side hydrogen addition, is truly remarkable. It shows that, even though the detailed structures of the reaction zones differ in the different cases, the extinction behavior is the same as it would be if they were the same.

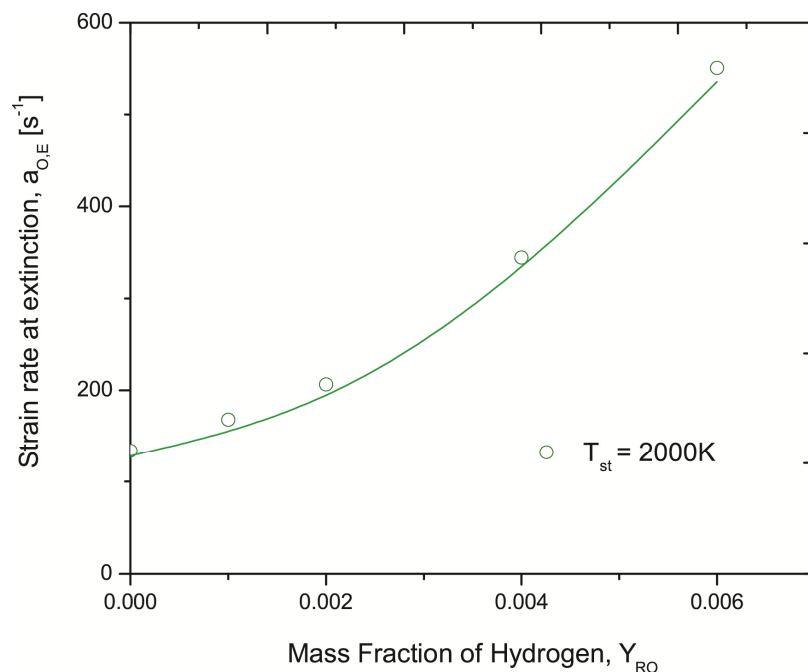


Figure 14. The strain rate at extinction, as a function of mass fraction of hydrogen in the oxidizer stream,  $Y_{H_2,2}$ , at fixed  $Z_{st} = 0.055$ , and  $T_{st} = 2000$  K. The symbols represent experimental data and the curve represents predictions obtained using the San Diego Mechanism.

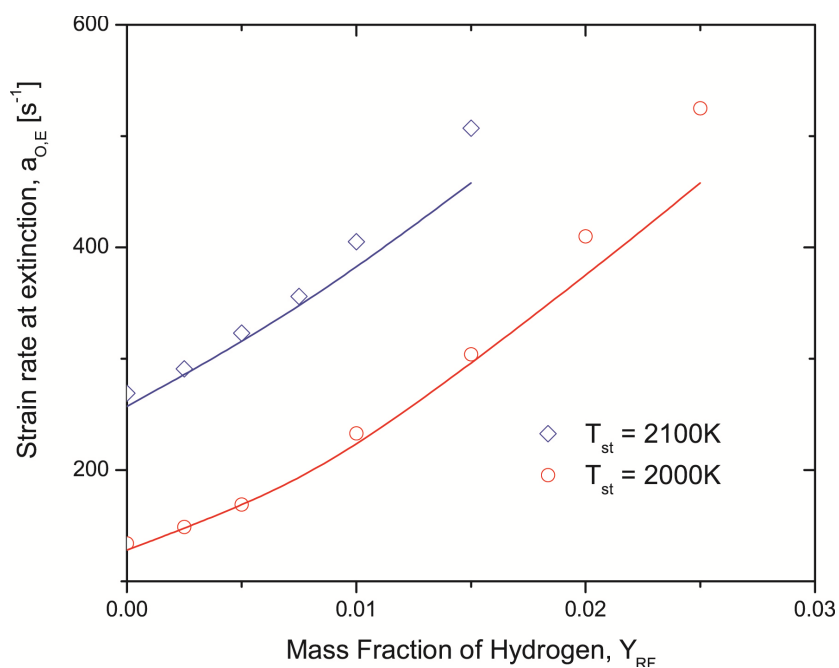


Figure 15. The strain rate at extinction, as a function of mass fraction of hydrogen in the fuel stream,  $Y_{H_2,1}$ , at fixed  $Z_{st}$  and  $T_{st}$ . The symbols represent experimental data and the curve represents predictions obtained using the San Diego Mechanism.

Figures 17 and 18 show the strain rate at extinction, as a function of the mass fraction of CO in the oxidizer stream,  $Y_{\text{CO},2}$  and the mass fraction of CO in the fuel stream,  $Y_{\text{CO},1}$ . In these figures the symbols represent experimental data and the solid lines and broken lines represent predictions obtained using the San Diego Mechanism. Figure 17 shows results obtained at fixed  $Z_{\text{st}} = 0.055$ , and  $T_{\text{st}} = 2000$  K, while Fig. 18 shows results obtained at fixed  $Z_{\text{st}} = 0.055$ , and  $T_{\text{st}} = 2100$  K. The experimental data and predictions in both figures show that with increasing amounts of CO in the oxidizer stream the strain rate at extinction first increases and then decreases. Thus addition of CO to the oxidizer stream first increases the overall reactivity and then decreases the reactivity. The experimental data and predictions in Fig. 17 and in Fig. 18 show that addition of CO to the fuel stream does not have a significant influence on the overall reactivity of methane flames.

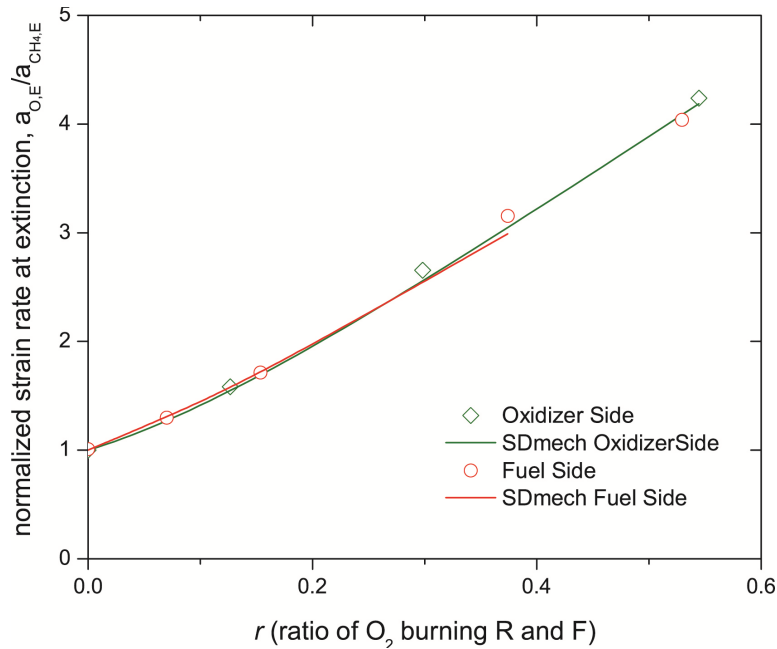


Figure 16. The normalized strain rate at extinction, as a function of  $r$  at fixed  $Z_{\text{st}} = 0.055$ , and  $T_{\text{st}} = 2000$  K. The symbols represent experimental data and the curves represent predictions obtained using the San Diego Mechanism.

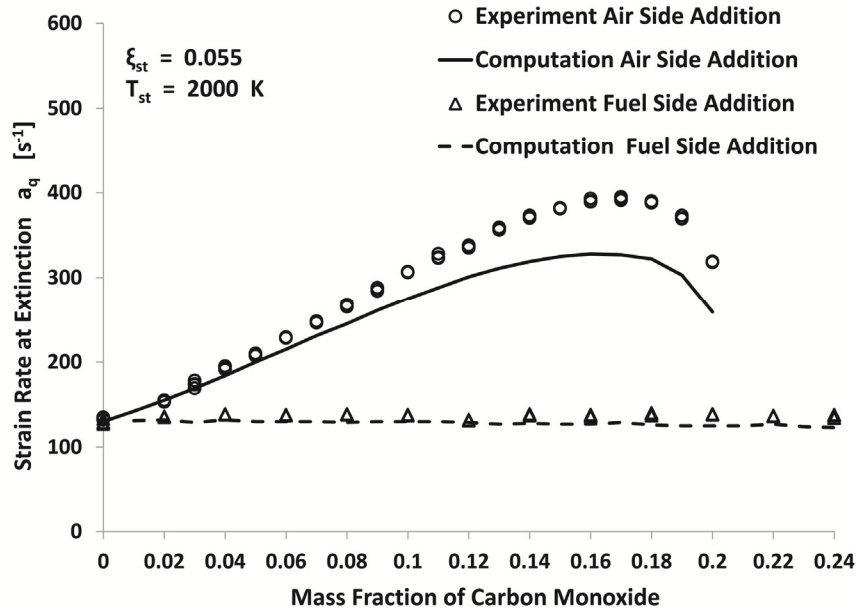


Figure 17. The strain rate at extinction, as a function of mass fraction of CO in the oxidizer stream,  $Y_{CO,2}$ , and mass fraction of CO in the fuel stream,  $Y_{CO,1}$  at fixed  $Z_{st} = 0.055$ , and  $T_{st} = 2000$  K. The symbols represent experimental data and the solid line and broken line are predictions obtained using the San Diego Mechanism.

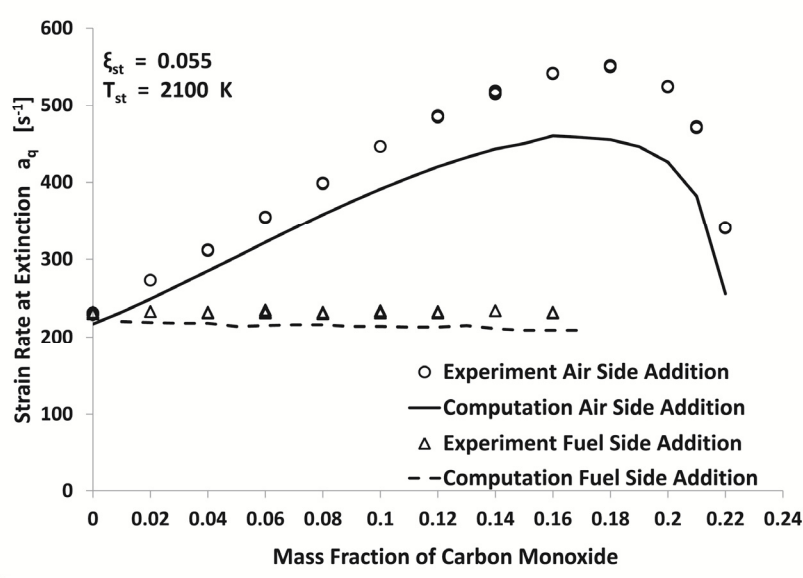


Figure 18. The strain rate at extinction, as a function of mass fraction of CO in the oxidizer stream,  $Y_{CO,2}$ , and mass fraction of CO in the fuel stream,  $Y_{CO,1}$  at fixed  $Y_{st} = 0.055$ , and  $T_{st} = 2100$  K. The symbols represent experimental data and the solid line and broken line are predictions obtained using the San Diego Mechanism.

Figure 19 shows the predicted ratio of the extinction strain rate with CO addition to that without as a function of  $r$ , for both oxidizer-side and fuel-side addition of CO. At a given value of  $r$ , the predicted strain rate at extinction for CO addition to the oxidizer stream is greater than that for CO addition to the fuel stream. With increasing values of  $r$  the strain rate at extinction first increases and then decreases. The increase is small for CO addition to the fuel side. Thus the influence of CO addition on critical conditions of extinction of methane flames is qualitatively different from the influence of  $H_2$  addition on critical conditions of extinction of methane flames.

These last results help further to improve our understanding of these types of flame structures. The results supplement those discussed previously, which are more directly connected to the studies of hypergolic propellant combinations. They are included here for their general interest and because they were partially supported by the same program. The major findings of more direct relevance to the main program are those discussed at the beginning of this section.

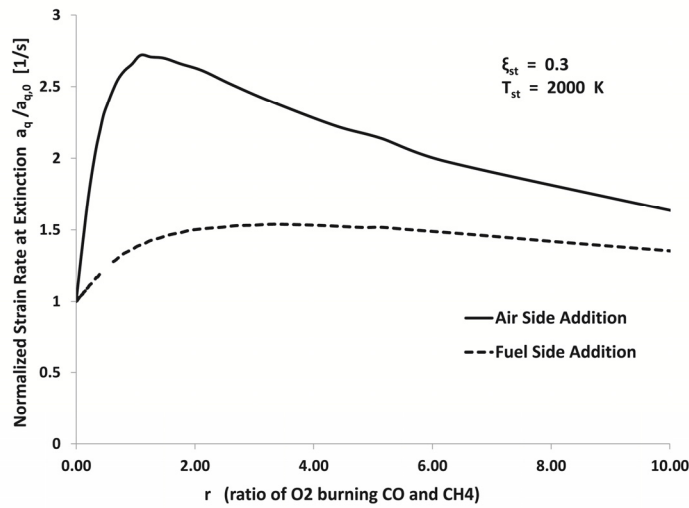


Figure 19. The predicted normalized strain rate at extinction, as a function of  $r$  at fixed  $Z_{st} = 0.3$ , and  $T_{st} = 2000$  K, for CO addition to the fuel side and to the oxidizer side. Predictions were made using the San Diego Mechanism.

## V. MODELING, SIMULATION, AND DIAGNOSTICS OF OVERALL PROCESSES

### V.1 High-Fidelity Modeling and Simulation of Spray and Combustion of Gelled Hypergolic Propellants (Yang, Georgia Institute of Technology)

#### 1. Abstract

A unified theoretical, high-fidelity numerical framework is established to model and simulate the injection, spray formation, ignition, and combustion of gelled hypergolic propellants over a broad range of operating conditions. An Eulerian-Eulerian, volume-of-fluid (VOF) based numerical algorithm, augmented with adaptive mesh refinement (AMR) methodology, is used to investigate the underlying physics for both Newtonian and non-Newtonian fluids. The results are systematically compared with existing experimental data. Impinging jet atomization is investigated first. Several different patterns of sheet and rim configurations are obtained, including liquid chain, closed rim, fish-bone, disintegrating sheet, disintegrating rim and impact wave. Binary collision of equal and unequal sized droplets are studied next. All possible collision outcomes (including bouncing, coalescence, reflexive and stretching separation) are obtained over a wide range of the Weber numbers and impact parameters. Generalized correlations of the collision regime boundaries are obtained for a wide variety of liquid droplets and ambient fluids. Finally, the approach developed here is used to analyze in detail the physics of four different breakup regimes -- oscillatory, bag, multimode, and shear breakup. A generalized regime diagram valid for  $Oh < 0.1$  is developed to predict the mode of droplet dynamics at a wide range of operating pressures ( $1-p_{critical}$ ) using data from previous experimental investigations and the current study. Child droplet size diameters follow a universal log-normal distribution for  $We > 300$ , and the Sauter mean diameter (SMD) of the droplet size distribution varies as a power law function:  $d_{32}/D = 8We^{-0.72}/C_d$ . A correlation for the time-mean drag coefficient for deforming and fragmenting droplet is also developed. It decreases with increasing Weber number as a power law given by  $C_d/C_{d,0} = 2We^{-0.175}$ . Deformation and fragmentation of non-Newtonian liquid droplets is also studied. It is found that the breakup behavior of pseudoplastic, non-Newtonian liquids is drastically different from that of Newtonian droplets. Several flow features commonly exhibited by non-Newtonian fluids are observed during the breakup process. The breakup begins with the formation of beads-in-a-string. This is followed by rapid rotation of the droplet with the appearance of helical instability and liquid bulges, which form the sites for primary and satellite droplet shedding.

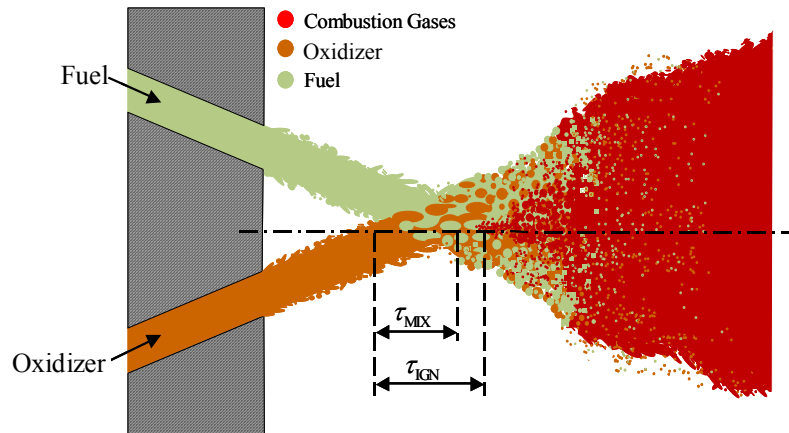
#### 2. Research objectives

Figure 1 shows the process of concern from propellant injection to flame development. Primary atomization takes place as the fuel and oxidizer jets leave the injectors and impinge on each other under the action of aerodynamic, viscous, inertial, and tensile forces. The dynamic head of the injected propellant destabilizes the liquid streams, creating a liquid sheet, which disintegrates into ligaments and droplets of various shapes and sizes via different mechanisms depending on the flow conditions. These fluid structures further disintegrate to form the final droplet distribution.

The overall objectives of the present study were high-fidelity modeling and simulation of fluid injection, spray formation, ignition, and combustion of gelled hypergolic propellants over a broad range of operating conditions. The specific objectives (both for Newtonian and non-Newtonian fluids) includes:

- development of a general theoretical framework and numerical methods for multi-scale, multi-phase, and multi-component reacting flows,
- study of droplet dynamics and breakup, including a detailed analysis of the drag coefficient of deforming and fragmenting droplets,
- study of impinging jet breakup and dynamics, and
- study of collision and dynamics of droplets of equal and unequal sizes.

The major scientific challenges involved in the phenomena under consideration include modeling of fluid primary atomization, dense spray formation, and heterogeneous reactions of multi-phase, multi-component systems. In addition, the presence of widely disparate length and time scales, along with complex physics, makes this a formidable problem, both theoretically and experimentally.



#### ***Gelled Propellant Formation, Processing, and Characterization***

- propellant synthesis
- intrinsic and constitutive properties
- physics-based formulation rules

#### ***Multiphase Processes***

- primary atomization and secondary breakup
- dilute spray dynamics, vaporization
- mixing and interfacial dynamics
- droplet-wall, film-wall interactions

#### ***Initiation and Reaction Mechanisms***

- initiation mechanisms at contact surface
- heterogeneous reactions near interface
- homogeneous reactions in gas phase
- condense-phase reactions

#### ***Local Flow and Chemical Processes***

- turbulence/chemistry interactions
- multiple-scalar mixing processes
- extinction, re-ignition processes

#### ***Injector and Combustor Dynamics***

- overall flow and flame evolution

Figure 1. Combustion of impinging jets of gelled hypergolic propellants.

### **3. Theoretical formulation**

The theoretical formulation accommodates dense multi-component fluids in the Eulerian frame. The present research poses stringent numerical challenges. To render calculations manageable with reasonable turn-round time, efforts were made to improve the effectiveness of both software and hardware technologies. An efficient numerical algorithm is used to solve the theoretical model, and an efficient data communication algorithm is used to make full use of a distributed computing facility. The code is equipped with a multi-block domain decomposition feature to facilitate parallel processing in a distributed computing environment using the Message Passing

Interface (MPI) library. In addition, a highly flexible and efficient data structure is established to facilitate code development for two-phase flow simulations.

A critical issue in the present study is the treatment of multi-scale liquid-liquid and gas-liquid interfaces with mass, momentum, and energy transport arising from chemical reactions and phase transition. A state-of-the-art, high resolution, volume-of-fluid (VOF) interface capturing method is adopted for large-scale interfacial evolution. Surface tension is accommodated as a Dirac distribution function on the interface. The theoretical and mathematical formulation of this multi-phase, multi-fluid problem is based on a complete set of incompressible Navier-Stokes equations with surface tension. The numerical methods presented in this section are based on Popinet (2003) (2009), Khare (2014) and Zakerzadeh (2008).

### 3.1 Governing equations

The governing equations are based on three basic assumptions: the continuum hypothesis, the hypothesis of sharp interfaces, and fluid incompressibility. To shed light on the validity of the continuum assumption for the current problem, consider the measurement of density inside a box. When the box is small, the density fluctuates. It becomes smoother as the box dimension increases and can be approximated by a continuous function  $\rho$  (Batchelor 2000). For liquids at NTP, this happens for length scales of the order of  $10^{-9}$  m (Tryggvason 2011), much smaller than the length scales of liquids considered in this research effort. For gases, the important length scale dictating the validity of the continuum hypothesis is the mean free path. If the length scales under investigation,  $l \gg \lambda$ , the gas obeys Navier-Stokes equations to a very good approximation. The continuum hypothesis is thus an excellent assumption for studying droplet breakup phenomena. The second assumption made during this study is the hypothesis of sharp interfaces, according to which it can be assumed that the interface has a vanishing thickness and the transition from one phase to another takes place at very small scales. The most important intermolecular force influencing the droplet breakup physics, capillarity, is modeled by surface tension concentrated on the sharp interface. Owing to the operating conditions ( $M \ll 1$ ) considered in the current research, the last major assumption is that of fluid incompressibility. A detailed and rigorous description of fluid incompressibility can be found in Batchelor (2000).

Conservation of mass is written as follows

$$\frac{\partial \rho}{\partial t} + \nabla \cdot (\rho \vec{u}) = 0 \quad (1)$$

$\vec{u} = (u, v, w)$  is the fluid velocity and  $\rho = \rho(\vec{x}, t)$  is the density. By definition,  $\nabla \cdot (\rho \vec{u}) = \vec{u} \cdot \nabla \rho + \rho \nabla \cdot \vec{u}$ . For incompressible flows the velocity field is divergence-free and equation 1 translates to the evolution equation of density as

$$\frac{\partial \rho}{\partial t} + \vec{u} \cdot \nabla \rho = 0 \quad (2)$$

and the mass conservation equation transforms to:

$$\nabla \cdot \vec{u} = 0 \quad (3)$$

At this point, it is useful to note that there is no requirement for the density to be constant everywhere for incompressible flows. To explain this more clearly, we consider the Lagrangian description of fluid flow. For incompressible flows, the density of a fluid packet can vary from



one packet to another, but it should remain constant for a particular parcel. Since the fluid packets are distributed spatially and their distribution can change with time because of advection, the density distribution also varies in time and space. It is evaluated using equation 2.

Conservation of momentum is given by:

$$\frac{\partial \rho \vec{u}}{\partial t} + \nabla \cdot (\rho \vec{u} \vec{u}) = -\nabla p + \nabla \cdot \tilde{\tau} + \vec{F}_{st} \quad (4)$$

$\vec{F}_{st}$  is the surface tension force per unit volume and  $\tilde{\tau}$  is the shear stress tensor given by:

$$\tilde{\tau} = \mu (\nabla \vec{u} + (\nabla \vec{u})^T) \quad (5)$$

Here  $\mu = \mu(\vec{x}, t)$  is the dynamic viscosity.  $\mu$  is only a function of temperature for Newtonian fluids but can vary with shear strain for non-Newtonian fluids. The governing equations are written in an Eulerian reference frame to capture the gas-liquid interface. A volume of fluid scalar variable,  $f$  is introduced to trace the multi-fluid interface. It is defined as the volume fraction of a given fluid in each computational cell.  $f$  is mathematically given by

$$f = \begin{cases} 0 & \text{fluid 1} \\ 1 & \text{fluid 2} \end{cases} \quad (6)$$

The density and viscosity in each computational cell is defined as a linear function  $f$  given by:

$$\rho(f) = f \rho_1 + (1 - f) \rho_2 \quad (7)$$

$$\mu(f) = f \mu_1 + (1 - f) \mu_2 \quad (8)$$

The advection equation for density can then be written as an equivalent equation for the volume fraction

$$\frac{\partial f}{\partial t} + (\vec{u} \cdot \nabla) f = 0 \quad (9)$$

The mathematical formulation described above is often referred to as "one-fluid" or "whole-domain" approach in the literature. The conservation equations are written for the different phases without using the jump condition at the interface, which translates to singularities in the governing equations. It can easily be shown that this formulation is equivalent to that written for each phase separately with the pressure jump condition at the interface. As pointed out by Tryggvason *et al.* (2011), the one-fluid approach can be interpreted in two ways, in a weak sense, in which the governing equations are satisfied only in the integral form, or by admitting solutions using step and delta functions. In the current research, we have resorted to the latter approach by modeling the surface tension effects using the continuum surface force (CSF) model developed by Brackbill *et al.* (1992)

$$\vec{F}_{st}(\vec{x}_1) = \sigma \int_S \kappa(\vec{x}_2) \hat{n}(\vec{x}_2) \delta(\vec{x}_1 - \vec{x}_2) dS \quad (10)$$

$\sigma$  is the surface tension force,  $\kappa$  the local curvature and  $\delta$  the Dirac delta function. The curvature is evaluated by:

$$\kappa = \frac{1}{R_1} + \frac{1}{R_2} \quad (11)$$

$R_1$  and  $R_2$  are the principal radii of curvature of the interface. The surface tension force in each computational cell at the interface is approximated by:

$$\vec{F}_{st} \approx \sigma \kappa \delta \hat{n} \quad (12)$$

Pressure in incompressible flows is not a thermodynamic property and is solely a function of the velocity field. If the velocity field is solenoidal, divergence of equation 4 yields the following:

$$\nabla^2 p = -\rho \frac{\partial^2 (u_i u_j)}{\partial x_i \partial x_j} \quad (13)$$

This Poisson equation must be satisfied to enforce incompressibility and the solenoidal nature of the velocity field. Since the density,  $\rho$ , viscosity,  $\mu$ , and surface tension,  $\sigma$ , are not functions of temperature in the current study (all the numerical experiments being conducted at constant temperature conditions), continuity and momentum equations are decoupled from the energy equation.

### 3.2 Numerical model and spatial discretization

The governing equations described in the previous section are solved using a projection method based on variable density fractional step numerical methodology. Interim velocity is computed in the first step, and then the pressure field is computed by solving the Poisson equation and the projection of the interim velocity onto a divergence-free velocity field. Quad/octree spatial discretization is used in combination with a multi-level Poisson solver to obtain the pressure distribution. The primitive variables -- momentum components, pressure and volume fraction -- are volume averaged and collocated at the cell centers of the discretized volume. This collocated definition of primitive variables is useful for mesh adaptation, and facilitates the implementation of the Gudunov scheme for the non-linear convective terms. To treat the viscous terms accurately, an approximate projection method developed by Almgren *et al.* (2000) is used. The scalar VOF variable,  $f$ , is obtained by solving the advection equation for the volume fraction. A piecewise-linear geometrical VOF scheme (Scardovelli & Zaleski 1999) generalized for quad/octree spatial discretization is used to solve equation 9. The value of the volume fraction in each cell then corresponds to the fraction of each cell filled with the reference phase. Computational cells completely filled with fluid 1 are characterized by  $f = 0$  and fluid 2 by  $f = 1$ , and cells containing the interface are characterized by  $0 < f < 1$ . Since face-centered velocities are divergence-free, the function  $f$  is then advected using the computed velocity field.

Multiphase flow problems often involve length and time scales varying over several orders of magnitude. Impinging jets, liquid jets in cross flows, droplet breakup, and droplet collision and impact are a few examples. Even though fixed mesh algorithms have been used successfully for dynamically evolving interfacial flows, this approach is extremely computationally expensive and often cost prohibitive. The adaptive mesh refinement technique is one of the most efficient ways to mitigate this problem; the numerical grid dynamically adapts according to a pre-specified criterion in regions where higher resolution is needed, while the rest of the computational domain uses a coarser mesh. The AMR implementation used in this research effort is based on structured grids. Structured mesh offers simplification in implementing the various numerical algorithms and reduces the computational overhead, in addition to providing



#### 4.1 Flow patterns of impinging jets

The jet diameter is  $400\ \mu\text{m}$ , and the impingement angle is fixed at  $60^\circ$ . Figure 3 shows the various flow patterns observed at jet velocities varying from 2.2 to 11.2 m/s. The different flow patterns are dependent on the Reynolds and Weber numbers. Figure 3(a) shows a well-defined liquid chain structure at  $u_j = 2.2\ \text{m/s}$ . Both a liquid sheet and a closed rim form in the first ring. No sheet, however, exists after the second chain link due to viscous dissipation and the resultant reduction in the inertial energy of the combined liquid streams. The colliding streams from the two sides of the rim coalesce into a single column oscillating under the inertial-capillary interaction. Finally, breakup takes place at the end of the column because of the Plateau-Rayleigh instability. As the jet velocity increases, a larger liquid sheet is established, as shown in Fig. 3b. Since the sheet and rim formed afterwards are much smaller, this pattern is usually referred to as a closed rim.

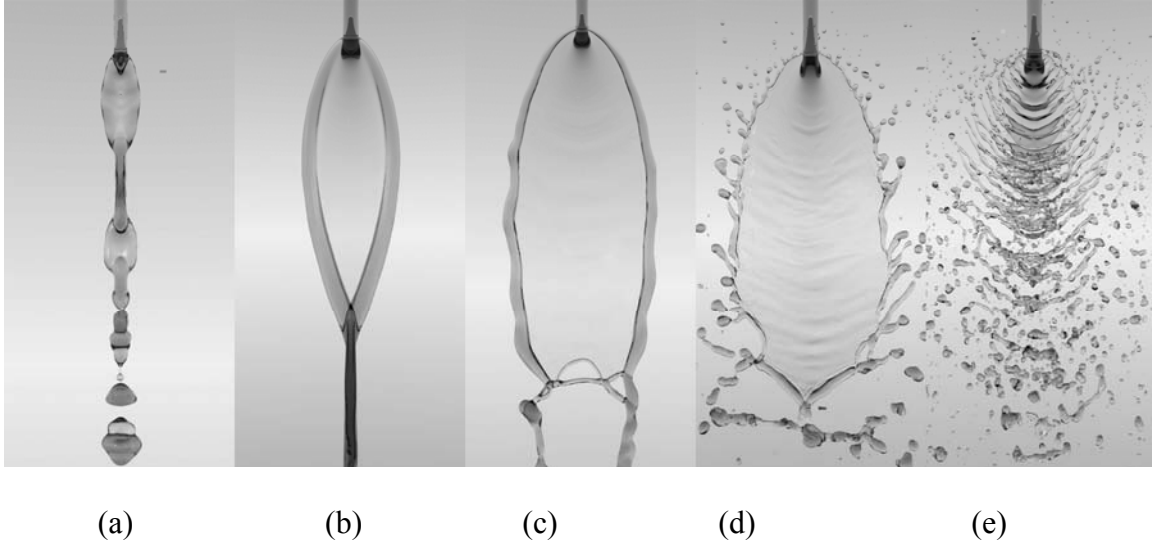


Figure 3. Impinging-jet flow patterns of glycerin-water solution obtained from simulations.  $D = 400\ \mu\text{m}$ ,  $2\alpha = 60^\circ$ , (a) liquid chain ( $u_j = 2.2\ \text{m/s}$ ,  $We=27.5$ ,  $Re=1000$ ); (b) closed rim ( $u_j = 3.3\ \text{m/s}$ ,  $We=58.8$ ,  $Re=40.4$ ); (c) open rim ( $u_j = 5.3\ \text{m/s}$ ,  $We=152$ ,  $Re=294$ ); (d) unstable rim ( $u_j = 7.9\ \text{m/s}$ ,  $We=343.5$ ,  $Re=3536$ ); (e) impact wave ( $u_j = 11.2\ \text{m/s}$ ,  $We=687$ ,  $Re=5000$ ).

At a higher jet velocity, the liquid sheet becomes unstable, with an oscillating boundary. Figure 3(c) shows a pattern known as a disintegrating sheet. The thin liquid sheet in the downstream region is prone to small disturbances. Holes are formed and grow progressively, eventually reaching the sheet boundary to open the rim. The ligaments downstream of the opening break up because of capillary action. The disintegrating sheet is also referred to as an open-rim structure. As the jet velocity further increases to  $7.9\ \text{m/s}$ , the liquid rim becomes unstable, as shown in Fig. 3(d). Disturbances originate at the impingement point and grow, while propagating downstream along the liquid rim. Ligaments are then formed and break up into droplets via the end-pinching mechanism. In the extreme case of  $u_j = 11.2\ \text{m/s}$ , shown in Fig. 3(e), the liquid sheet becomes unstable and undergoes violent flapping, followed by rapid atomization into droplets.

#### 4.2 Impact wave dynamics and atomization

Figure 4 shows the spatial distribution of the flow-field obtained from the simulation with the finest grid. Direct insight can be achieved into the atomization process. The liquid jet velocity is  $18.5\ \text{m/s}$ . The corresponding Weber and Reynolds numbers are 2860 and 11748, respectively.

As shown in Fig. 4(a), the entire flow evolution can be divided into four regions: jet impingement, flapping sheet, ligaments, and droplets. The impact waves arising from hydrodynamic instabilities generate high-amplitude disturbances and cause the sheet to fragment. The collision of the two liquid jets in Region A forms a liquid sheet expanding from the impingement point. The sheet thickness is uneven because of the non-uniform velocity profiles of the incoming streams. In Region B, impact waves are generated and propagate radially outwards from the impingement point. The liquid sheet is then ruptured by the impact wave and breaks along the waves to form arc-shaped structures in Region C. Capillary instabilities further cause the ligaments to break up, as shown in Region D. In general, the droplet and ligament sizes decrease radially outwards from the core.

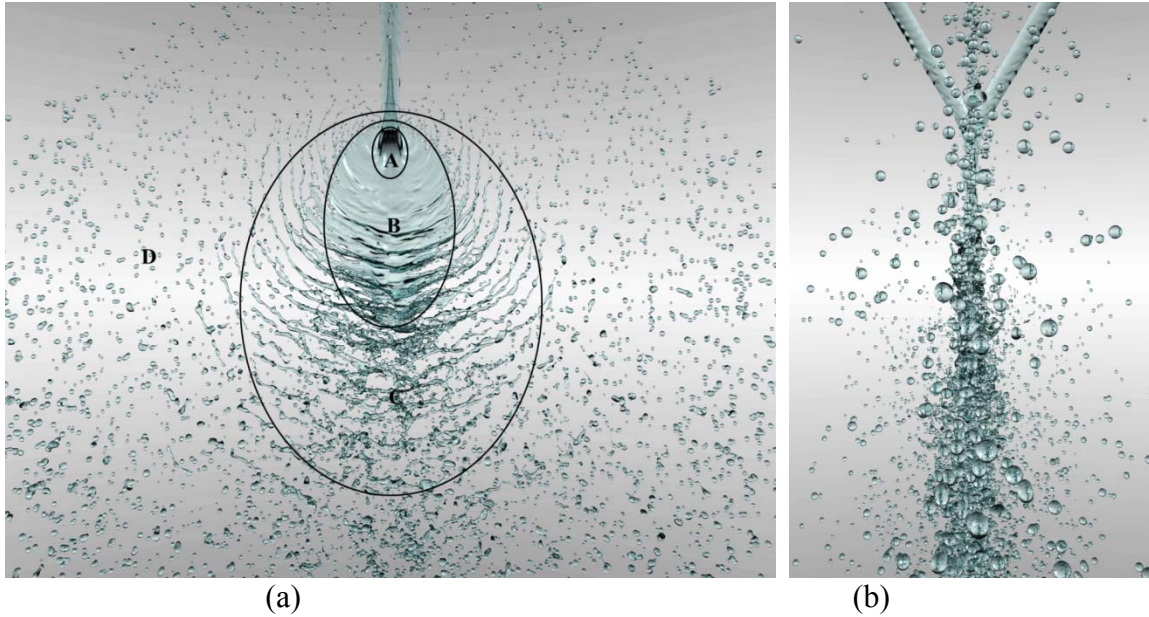


Figure 4. Spatial distribution of flow-field predicted by level-9 simulation: (a) front view; (b) side view. Various regions in impinging-jet atomization dominated by impact wave. A: jet impingement region; B: flapping sheet region; C: ligaments region; D: droplet region. (water jets,  $D = 635 \mu\text{m}$ ,  $u_j = 18.5 \text{ m/s}$ ,  $2\alpha = 60^\circ$ ,  $We = 2987$ ,  $Re = 11724$ ).

A more detailed view, Fig. 5 shows a snapshot of the impact wave under lower flow conditions corresponding to those shown in Fig. 3(e). The liquid surface is colored by the  $z$  coordinate to show the location with respect to the center plane. The impact waves and ligaments are distributed in an interlaced manner on their respective sides of the injected liquid streams. Rupture of the liquid sheet takes place near the rear point where the thickness is smallest. As indicated by the black arrow, the location of the rupture is between the wave crests and troughs. The discontinuity in the liquid phase created at the rupture point enlarges as the liquid sheet moves down stream. Under the effect of local acceleration introduced by the wave motion, the resultant ligaments are located along the wave crests and troughs, and are attached to the flapping liquid sheet. When the openings on the two lateral sides connect, long ligaments are detached from the liquid sheet in the downstream region. The process becomes even more complex as the impact waves superimpose, resulting in different interference patterns.

### 4.3 Non-Newtonian impinging jets

Gelled propellants feature many advantages over non-gelled liquid and solid rocket propellants. They are safe to store and handle, and meet insensitive munitions requirements. The inherent thrust modulation capability provides good application flexibility for utilization in tactical rocket engines. Gelled propellants are non-Newtonian fluids, since their viscosity depends on the shear rate. They are difficult to atomize and require relatively high injection pressures. As a result, it would be advantageous for the gelled propellants to be shear thinning liquids whose viscosity decreases with increasing shear rate. The formation and breakup mechanisms of non-Newtonian liquid sheets formed by impinging jets are poorly understood.

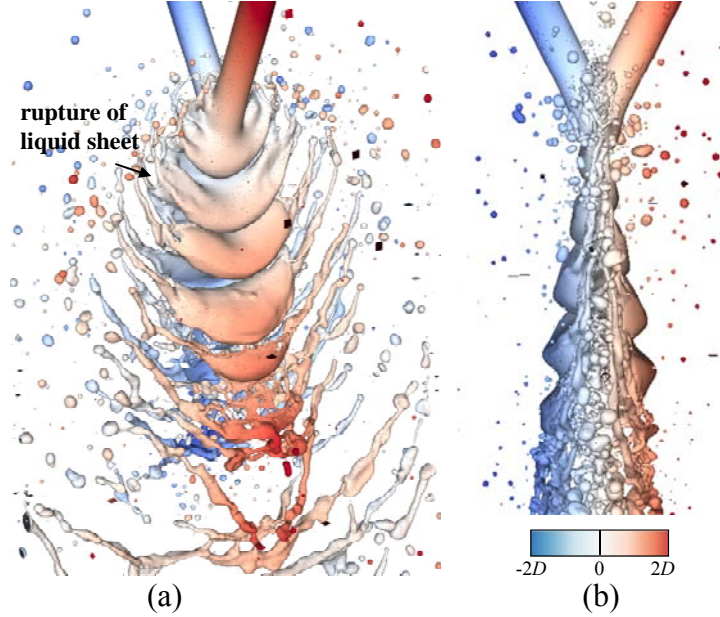


Figure 5. Detailed image showing the process of ligament formation with interface colored by  $z$  coordinate. (a) oblique view; (b) side view. (glycerine-water jets,  $D = 400 \mu\text{m}$ ,  $u_j = 11.2 \text{ m/s}$ ,  $2\alpha = 60^\circ$ ,  $We = 687$ ,  $Re = 5000$ ).

The rheology and flow characteristics of non-Newtonian fluids are different from those of Newtonian fluids. Newtonian fluids have constant viscosities, while the viscosities of non-Newtonian fluids vary with applied shear rate. The composition of the working fluid used here was adopted from Fakhri (2009). It consists of TS-720 silica (5 wt. %) and 981A Carbopol (0.1 wt. %) in a 75/25 by volume ethanol/water mixture. This simulant gel is used to match the rheological and physical properties of typical Gelled Hypergolic Propellants (GHPs). The results of numerical simulations are compared with the experimental data. The relationship between shear rate and viscosity can be represented accurately using the extended Herschel-Bulkley model:

$$\mu = \frac{\tau_0}{\gamma} + K\gamma^{n-1} + \mu_\infty \quad (14)$$

Figure 6 shows rheological property of the gel employed in this work. The Weber number of the simulant gel takes the same form as that of a Newtonian liquid. A modified formula for Reynolds number is used, since the viscosity of the gel changes with shear rate.



Figure 7 compares the near field transients of liquid sheet formation with experimental images at three different inlet velocities (corresponding Weber numbers for the three cases from top to bottom are 1549, 6195 and 12390 respectively). Good qualitative agreements are obtained in terms of the flow patterns and sheet topology at steady state. The flow patterns obtained in numerical simulation appear to be more stable than the experimental ones. For example, with  $We=1549$ , a flat liquid sheet is obtained in the simulation, in contrast to the irregular ripples noticed in the experimental images. This difference is caused by the inlet turbulence in the experiments. The shapes of the liquid jets are disturbed, as shown in the experimental images. It must be noted that the turbulence of the inlet liquid jets is not taken into account in the present model. Adaptive mesh refinement provides highly resolved images of the flow structures and atomization process.

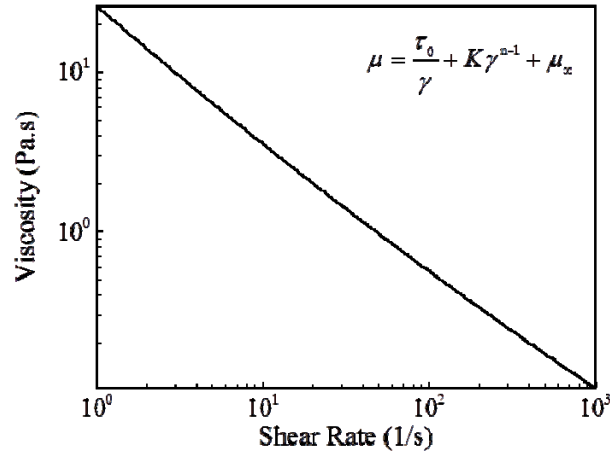
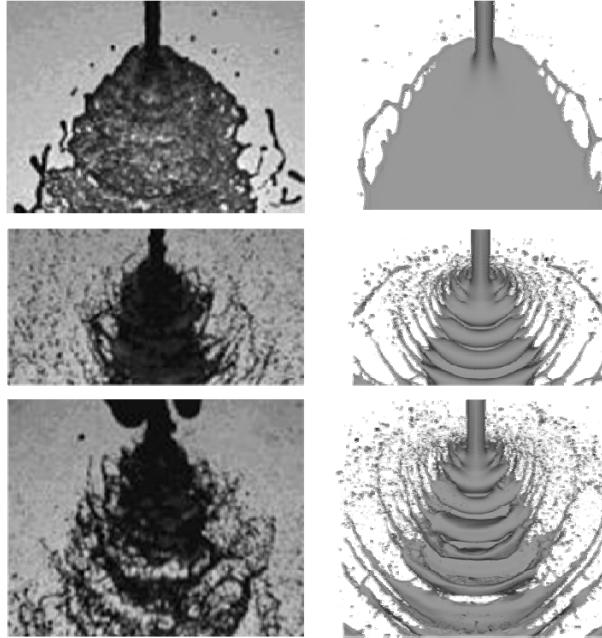


Figure 6. Variation of average drag coefficient with Weber number.



**Figure 7.** Comparison of flow patterns under different Weber numbers. (Images in left column obtained from experiments by Fakhri (2009), right column depicts present simulation results.

The Weber numbers for the three cases from top to bottom are 1549, 6195 and 12390, respectively).

#### 4.3.1 Rim instability

Figure 8 consists of a series of images showing the development of the flow pattern at  $We=1549$ . A flat liquid sheet bounded by the rim is formed at the center when the two liquid sheets come in contact. As the size of the liquid sheet increases, an asymmetrical wave appears, as shown in Fig. 8(c). As the liquid sheet continuously expands, it ruptures near the rear point as shown in Fig. 8(d). After that, the liquid rim at the rear point is disturbed. The disturbances propagate and develop along the two sides of the liquid sheet. The boundary of the liquid sheet ruptures, resulting in the shedding of the rim to form ligaments, as shown in Fig. 8(f) to (l). The ligaments break into droplets under the effect of surface tension. Due to fluid viscosity, the shedding of the liquid rim results in web-like structures and the droplets are less visible, as shown in Fig. 8(k). The steady state of this process is shown in Fig. 8(l). It is interesting to notice the small amplitude surface waves on the liquid sheet. The damped amplitude is caused by the high viscosity of the simulant gel.

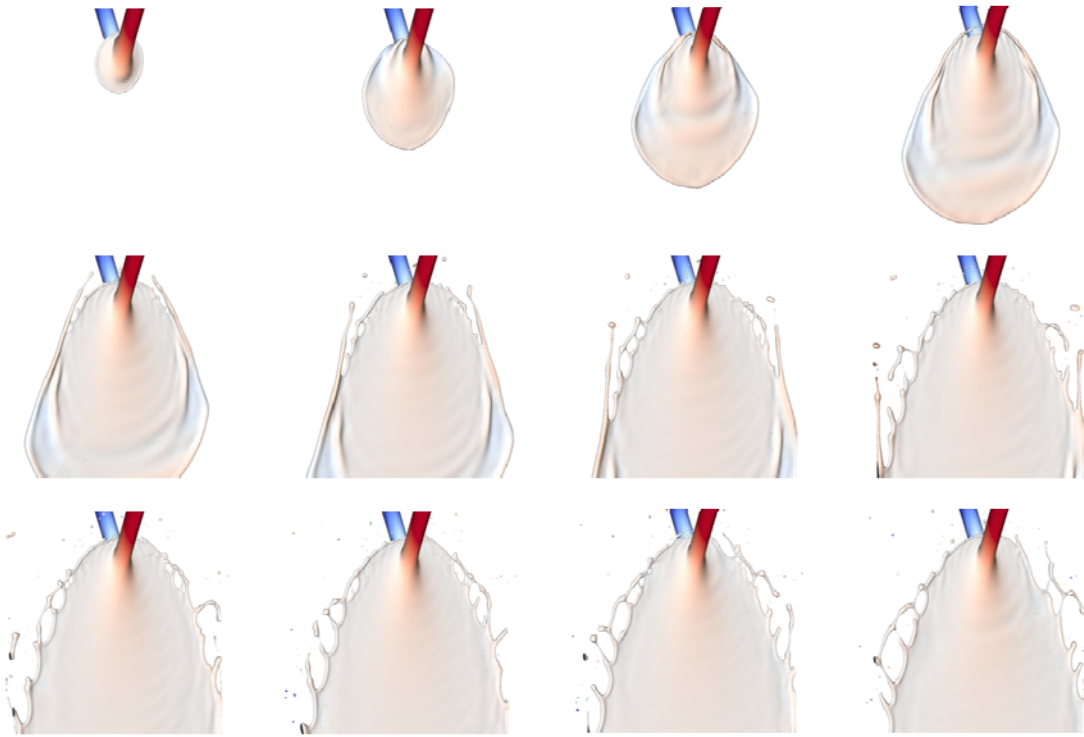


Figure 8. Development of flow pattern under  $We=1549$  (interface colored by  $y$  coordinate).

#### 4.3.2 Impact wave

Figure 9 shows a series of images describing the development of the flow pattern at  $We = 6195$ . In this case, the velocity of the liquid rim is high enough to cause capillary instabilities, which lead to the formation of ligaments and droplets near the boundary of the liquid sheet. When the two liquid jets fully impact each other, as shown in Fig. 9(d), wave structures appear from the rear point. The wave propagates downstream with the liquid sheet, as shown in Fig. 9(e) to (i). The overall wave pattern is similar to that seen in previous simulation results on a Newtonian fluid. This wave is usually called “impact wave.” The thin regions of the liquid sheet are torn off by the impact wave, and the gaps contract into liquid ligaments distributed by the two sides of the liquid sheet.



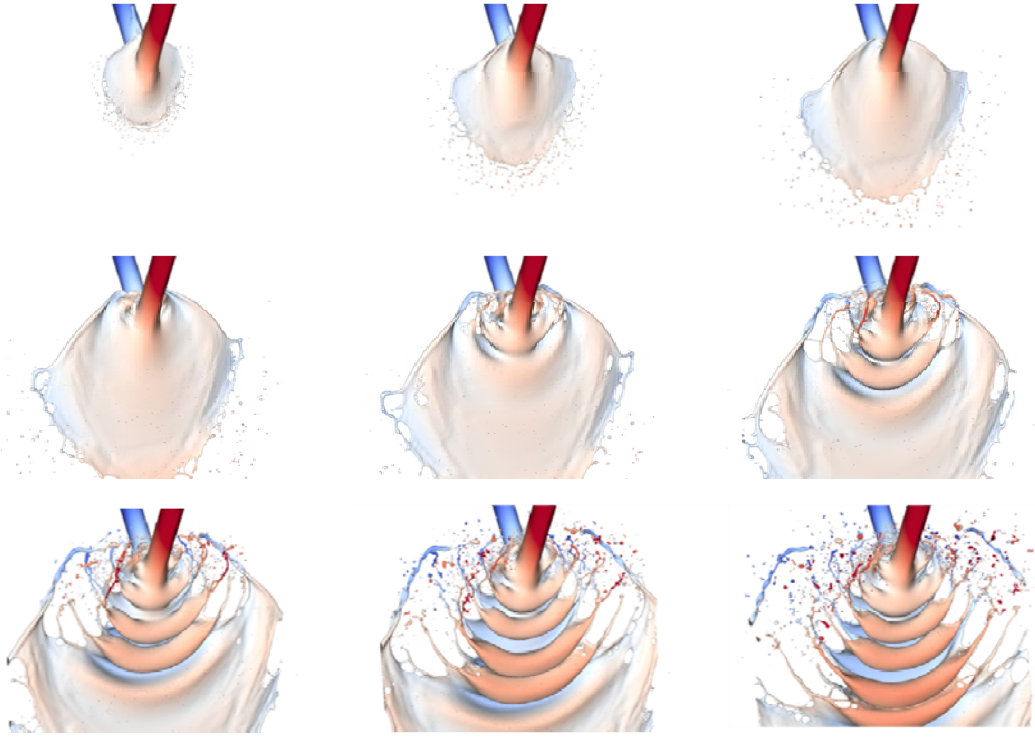


Figure 9. Development of flow pattern under  $We=6195$  (interface colored by  $y$  coordinate).

A similar case depicting the propagation of impact waves at  $We = 12390$  is shown in Fig. 10. Since the inlet velocity is higher, the droplet shedding at the beginning of the impingement process results in formation of a droplet cloud (see Figure 10(a) to (d)). The amplitudes of the impact waves are higher compared to the previous case with  $We = 6195$ . As the waves propagate downstream, the thickness of the liquid sheet decreases dramatically. The liquid sheet fully ruptures at about four to five wavelengths from the impact point. This observation agrees well with the experimental images. The ligaments under this higher inlet velocity are longer and thinner.

Strouhal number is defined as  $St=fD/U_s=D/\lambda$ , where  $f$  is wave propagation frequency,  $D$  the jet diameter,  $U_s$  the velocity of liquid sheet, and  $\lambda$  is the wavelength. The values of  $St$  under different  $We$  are plotted in Fig. 11. It is clear that the Strouhal numbers are almost the same for the three cases. The simulations carried out in this paper are in the range of locking-on. The Strouhal number is locked below  $We = 1000$  for Newtonian liquids. Present results indicate that the critical Weber number may be the same for all the liquid considered here. Also, the locking-on value of the Strouhal number for this non-Newtonian liquid is similar to that seen before. This indicates that the wavelength is independent of viscosity and depends only on geometrical parameters, that is, jet diameter and impingement angle.

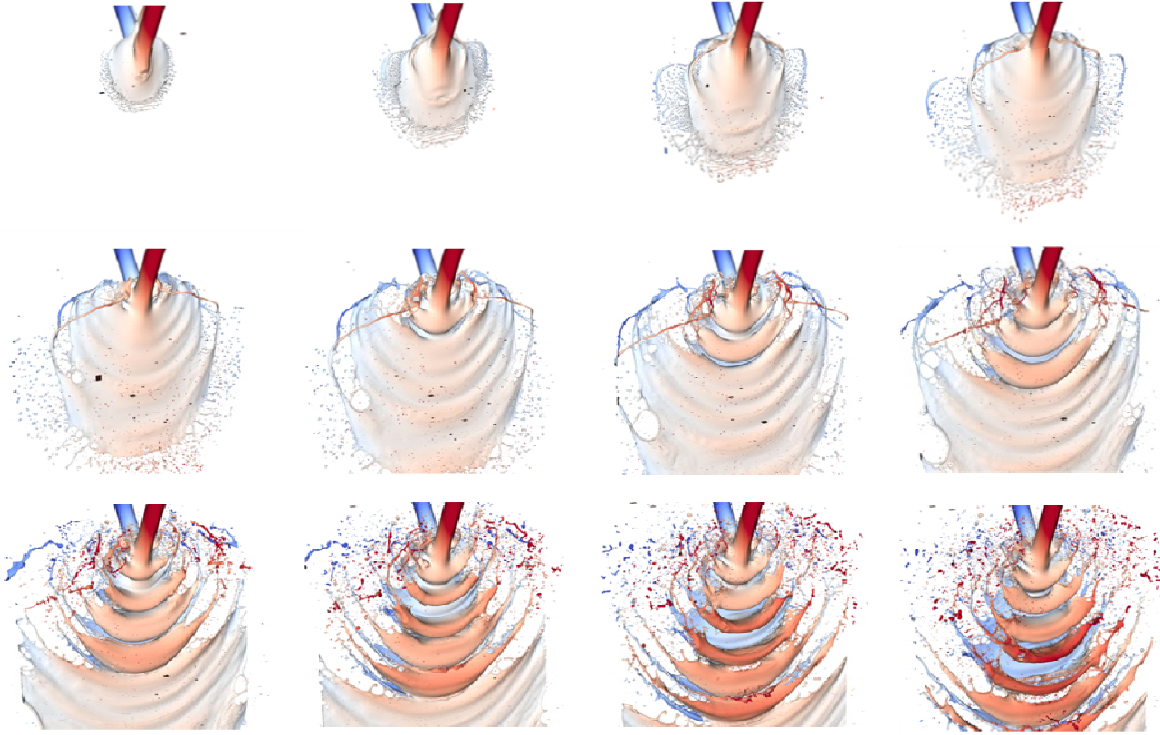


Figure 10. Development of flow pattern under  $We = 12390$  (interface colored by  $y$  coordinate).

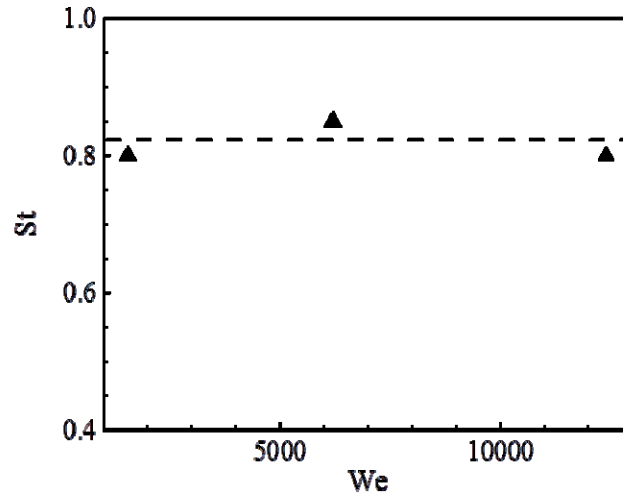


Figure 11. Locking-on of Strouhal number.

#### 4.3.3 Shear thinning effect

Figure 12 shows the distribution of shear rate at the interfaces for the three cases. For  $We=1549$ , high shear rate is found on the liquid sheet near the rear point and also on the liquid rim. When  $We$  increases to 6195, the high shear rate region near the rear point widens. The shear rates on the wave crest and trough are higher than at other locations on the waves. Since the ligaments are formed by the ruptured liquid sheet, the shear rate on the ligaments is higher than that in inlet jets. This contributes to better atomization. The shear rates in the thin part of the liquid ligaments are highest, as shown in Fig. 12(b), because of the stretching of liquid ligaments, which results in higher shear rate and lower viscosity. This is a well-known phenomenon for a shear-thinning

non-Newtonian liquid, and is called “beads on a string” (spherical droplets connected by thin ligaments). Figure 12(c) shows the more complicated breakup process of liquid ligaments with higher inlet velocity. There are more twisted ligaments, long ligaments with dramatically changed diameters, and finer droplets.

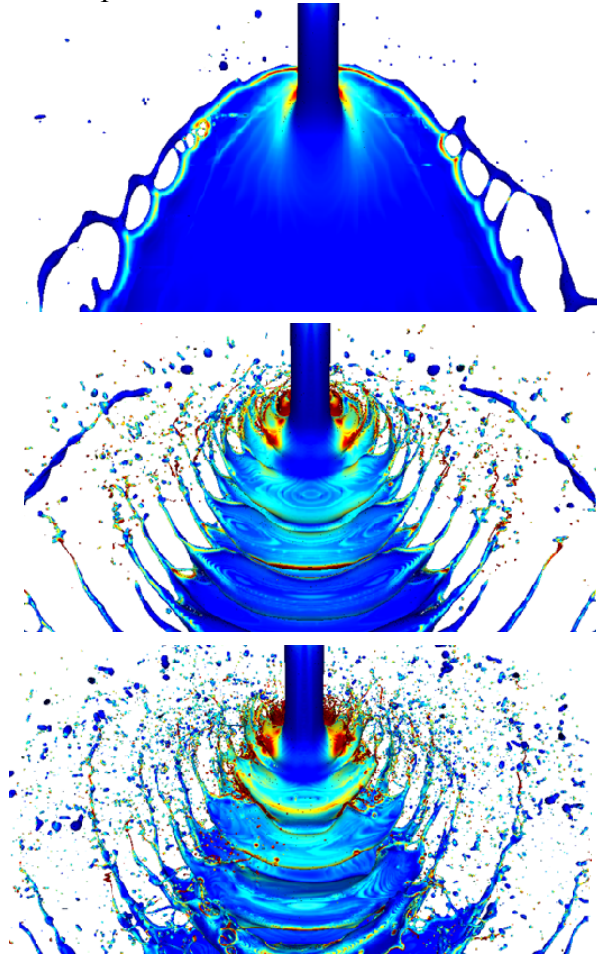


Figure 12. Distribution of shear rate on the interface under different Weber numbers. (a)  $We=1549$ ; (b)  $We=6195$ ; (c)  $We=12390$ .

### 5. Deforming and fragmenting Newtonian liquid droplets

Deforming and fragmenting liquid droplets are of interest in a wide range of applications, including, but not limited to, dense spray combustion (Faeth 1996; Faeth 2002), industrial and agricultural sprays, gas-liquid separators, and two-phase flows in chemical reactors. In the particular case of liquid-fueled propulsion systems, such as diesel, gas-turbine and rocket engines, system performance is conditioned by the fuel and oxidizer droplet size distribution and droplet dynamics is usually the rate-controlling process in dense sprays (Berthoumieu *et al.* 1999; Faeth 2002). In addition, fuel spray/droplet penetration is an important parameter in determining combustor size, which depends on the drag experienced by the liquid spray.

Figure 13 shows the schematic of the computational setup. Physically, a single water droplet is impulsively started in a quiescent air environment. The spherical droplet deforms due to the action of aerodynamic forces and eventually breaks up. The deformation and fragmentation are

resisted by surface tension and viscous forces. The Weber number dictates the breakup mechanism. Even though numerous experiments have been conducted over the last two decades to explore the physics of breakup, no experimental investigation has been successful in measuring the local drop and ambient flowfield that leads to the deformation and breakup of the droplets (López-Rivera 2010). This is primarily because the droplet deformation and breakup process involves a myriad of time and length scales, in addition to the accelerating and unsteady nature of the problem. We resolve these length and time scales associated with droplet deformation and breakup phenomena in the present work.

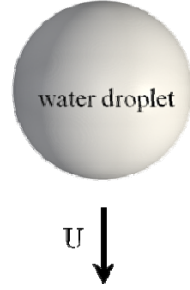


Figure 13. Computational Setup.

As a first step, we compare our simulation results with those of Han & Tryggvason (2001), who studied similar configurations and comparable Weber number and density ratio. As shown in Fig. 14, the current approach is capable of capturing the various shapes involved in the breakup process, including the bowl and backward facing droplet structure, and shows excellent agreement with results presented in (Han & Tryggvason 2001). It should be noted that the published numerical data were obtained from an axisymmetric calculation in which breakup of the droplet was not considered. We present results using a 3-D numerical simulation coupled with the capability to model breakup.

As the droplet moves in the ambient environment, momentum is exchanged between the liquid droplet and the surrounding air. The drag coefficient is defined by:

$$C_d(t) = \frac{\frac{d}{dt}(mu_{rel}(t))}{\frac{1}{2}\rho_g u_{rel}^2(t)A_{frontal}(t)} \quad (15)$$

where  $A_{frontal}(t) = \pi r_{effective}^2(t)$

The numerator is the time-dependent drag force acting on the droplet. The projected frontal area,  $A_{frontal}$ , is defined as the frontal area of a sphere of equivalent surface area. The droplet shape evolves in time, and as a result the frontal area is also a time-varying quantity. Data extraction for the current research is conducted by tracking the temporal location and associated properties of the liquid phase. Droplet momentum, relative velocity, location and surface area are calculated at each time step. Using these properties, the drag coefficient is calculated using equation 15, as the droplet moves in the ambient environment. A broad range of Weber numbers from 0.1 to 1400 was considered during the current work, encompassing bag, multimode and shear breakup mechanisms. Most of the practical operating conditions lie in Newton's regime,

where the drag coefficient over a solid sphere has a constant value independent of  $Re$ . Therefore, all the results pertaining to the drag coefficient presented in the paper are normalized by a constant value,  $C_{d,0} = 0.45$  (Efsthios & Clayton 2005). Consequently, the drag coefficient of deforming and breaking liquid droplets is solely treated as a function of Weber number. Three different breakup mechanisms, namely, bag, multimode, and shear breakup modes, are addressed during the current research effort. Weber number governs the transition from one breakup mechanism to another. In the next three sections, the different breakup modes will be discussed in detail, along with the evaluation of drag coefficient.

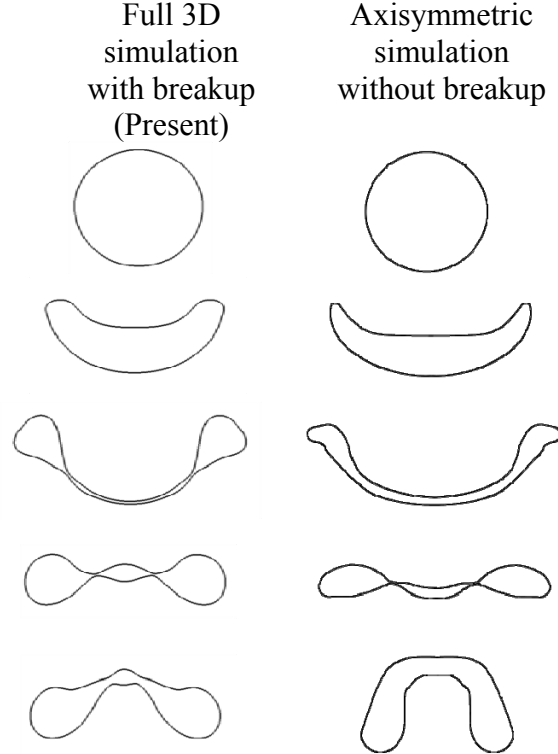


Figure 14. Comparison of present results for  $We = 24$ ,  $\rho_l / \rho_g = 8.29$  with results for  $We = 18.7$ ,  $\rho_l / \rho_g = 10$ .

### 5.1 Bag breakup

Typical temporal evolution of droplet structure for the bag breakup mechanism is shown in Fig. 15. The figure corresponds to a water droplet of  $100 \mu\text{m}$  with a velocity of  $22 \text{ m/s}$ . As the droplet starts to move in the ambient environment, it first deforms laterally into a disk with a lid, and then into a bowl. Because of inertia and the movement of the liquid from the bottom to the rim, the bowl is further transformed into a thin bag. The bag becomes progressively thinner and finally breaks up starting with the formation of a web-like structure, followed by the disintegration of the rim. The detailed physics pertaining to these phenomena is discussed in (Khare *et al.* 2012).

The physics we are interested in exploring in the current paper pertain to the time history of the drag coefficient as the droplet moves. As reflected by equation 15,  $C_d$  for deformable objects is primarily dependent on the time history of momentum and the frontal area. Therefore, it is

informative to look at the bottom view of the droplet structure to appreciate the extent of area change during the droplet lifetime. This is shown in Fig. 16. It is quite clear from the figure that there is a tremendous increase in the frontal, as well as the overall, surface area of the droplet as it deforms and breaks up. Once breakup is initiated, there are two competing forces affecting the surface area -- externally imposed inertial forces and the formation of child droplets -- which are trying to increase the surface area. The surface tension force, on the other hand, causes surface retraction preventing the surface area growth.

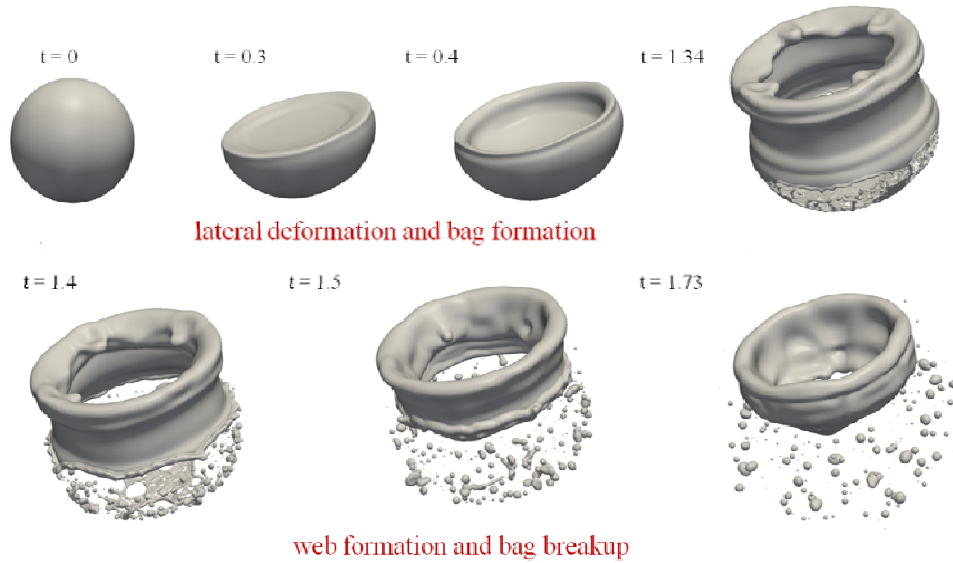


Figure 15. Perspective view of the temporal evolution of droplet structure for bag breakup mechanism.  $We = 80$ ,  $Re = 13951$ ,  $\rho_l / \rho_g = 8.29$ ,  $t = T^*U/D$ .

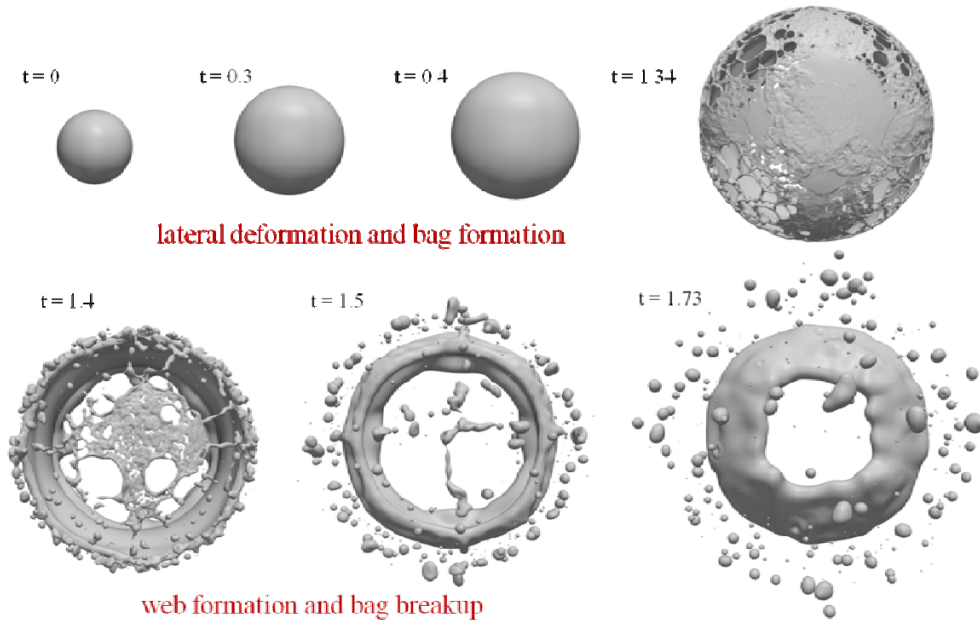


Figure 16. Bottom view of the temporal evolution of droplet structure for bag breakup mechanism.  $We = 80$ ,  $Re = 13951$ ,  $\rho_l / \rho_g = 8.29$ ,  $t = T^*U/D$ .



Figure 17 shows the time history of momentum and surface energy during the bag breakup process and elucidates this complex physics in a more quantitative manner. Momentum is normalized by its initial value, so that it takes a maximum value of 1. On the horizontal axis, non-dimensional time is defined as  $t = T*U/D$ , where  $D$  and  $U$  are the initial diameter and velocity of the droplet respectively. The droplet starts with some initial value of momentum, corresponding to the initial velocity imparted to the droplet. As it moves further, it is resisted by surface tension and viscous forces and the momentum is transferred to the surroundings. The surface energy, defined as the product of surface tension and surface area, has its minimum value at the beginning of the simulation, when the droplet is spherical. It is normalized by this minimum value and hence has a value of 1 at  $t = 0$ . As the droplet deforms, the surface energy increases to the point of breakup, at which point it falls suddenly, due to surface retraction. Qualitatively, we can expect the drag coefficient to increase initially due to the rapid decrease of momentum owing primarily to pressure drag. Once the droplet starts to break up, the drag coefficient should decrease. Figure 18 shows the variation of  $C_d$  for bag breakup process. This was calculated from the gradient of momentum (shown in Fig. 17) using the definition of the drag coefficient from equation 15.

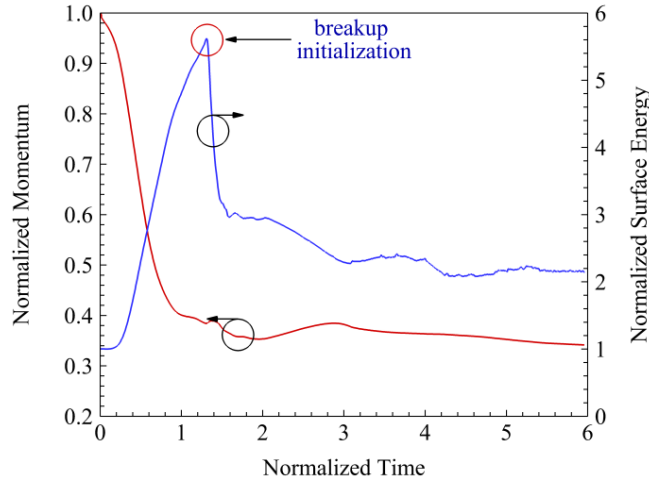


Figure 17. Time evolution of momentum and surface energy for  $We = 80$ .

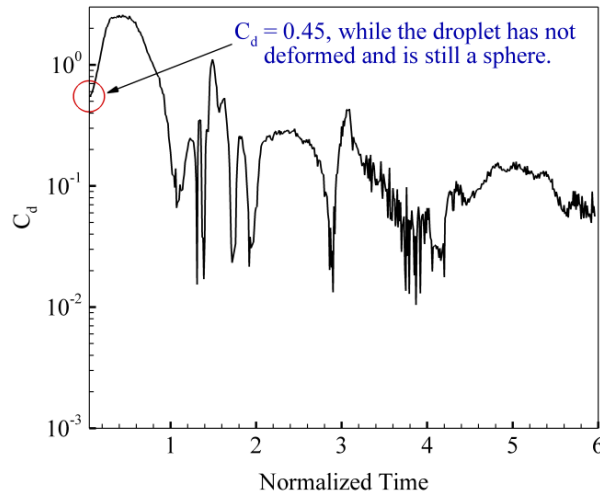


Figure 18. Time history of drag coefficient for bag breakup.

Initially, while the droplet is still spherical, the drag coefficient has a value corresponding to that of flow over a solid sphere. As expected, the drag coefficient first increases to a maximum value and then dips. Once the droplet starts to break up via the formation of webs and holes, as seen in Fig. 16, the surface area, and thus the surface energy, fall rapidly. By this time the droplet has already lost most of its momentum and hence the drag coefficient decreases. The instantaneous Weber number of the droplet decreases as time progresses and the surface tension force becomes comparable to the inertial forces acting on the droplet. This causes the droplet to oscillate. Oscillations of the droplet have a much more prominent effect on the surface area as compared to the momentum, and as a result the drag coefficient oscillates between moderately small values (owing to a very small change in the droplet momentum).

## 5.2 Multimode breakup

At progressively higher Weber numbers, the multimode mechanism becomes the dominant mode of breakup. Due to an even higher inertial force, the bag development is accompanied by the formation of a lip and a stamen. The breakup process can either start from the lip or from the bag, depending on the flow conditions. This is followed by the disintegration of the rim and the stem to form ligaments and child droplets, as shown in Fig. 19. The droplet diameter and velocity in this case were  $100\text{ }\mu\text{m}$  and  $47\text{ m/s}$  respectively. The detailed physics associated with this breakup mode are presented elsewhere (Khare *et al.* 2012). Figure 20 shows the time evolution of momentum and surface energy associated with a droplet undergoing multimode breakup. The initial events of this breakup process are similar to bag breakup, as shown in the 3D figures, as are the evolution of momentum and surface energy associated with the droplet. As noted previously, there are two competing effects affecting the overall surface area: the liquid surface tension, which tries to minimize the liquid surface area, and the formation of child droplets, which increases the effective surface area. Depending on the breakup mechanism, the beginning of breakup is accompanied with a sharp or a gradual reduction in surface energy. In this case, the decrease in surface energy is rather gradual, indicating that increase in surface area due to child droplet formation plays a significant role, and compensates for the surface retraction effect caused due to surface tension to a much larger extent than in bag breakup.

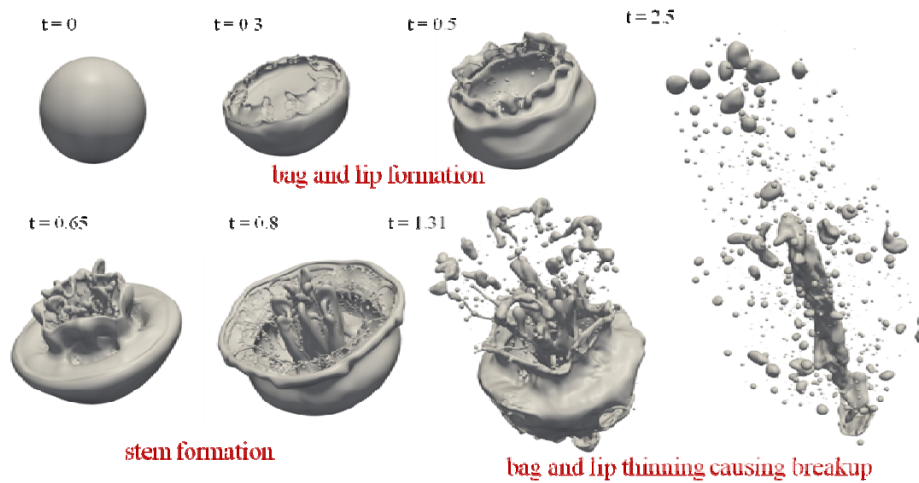


Figure 19. Multimode breakup mechanism.  $We = 365$ ,  $Re = 29805$ ,  $\rho_l / \rho_g = 8.29$ ,  $t = T^*U/D$ .



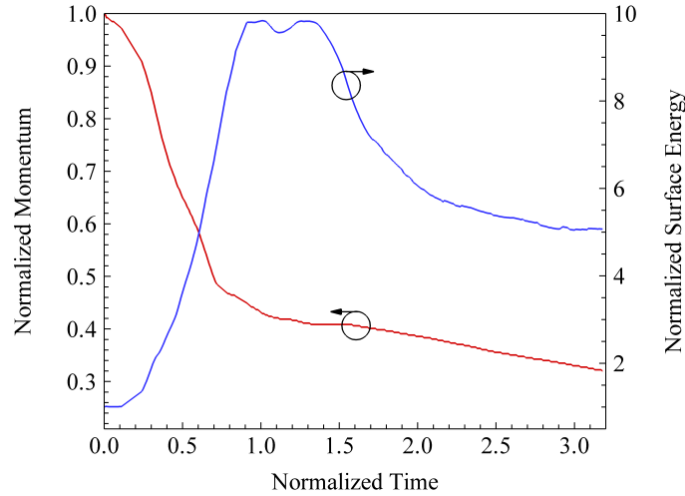


Figure 20. Time evolution of momentum and surface energy for  $We = 365$ .

Figure 21 shows the evolution of drag coefficient for the multimode breakup mechanism. As the droplet starts to move, the drag coefficient is about 0.45, corresponding to that of flow over a sphere. As in bag breakup, once the droplet starts deforming laterally the drag coefficient starts to increase and reaches a maximum value. As shown in Fig. 22, the frontal area of the water droplet increases multiple folds in the lateral direction before it breaks up. As the droplet starts to break up and holes and webs are developed in the parent droplet, the drag coefficient starts to drop, since ambient fluid can pass through the droplet without any resistance. The end of the breakup process corresponds to a stationary value of surface and kinetic energies and the result is a steady distribution of child droplets. As a consequence, once the droplet breaks up completely, the drag coefficient also reaches a steady value.

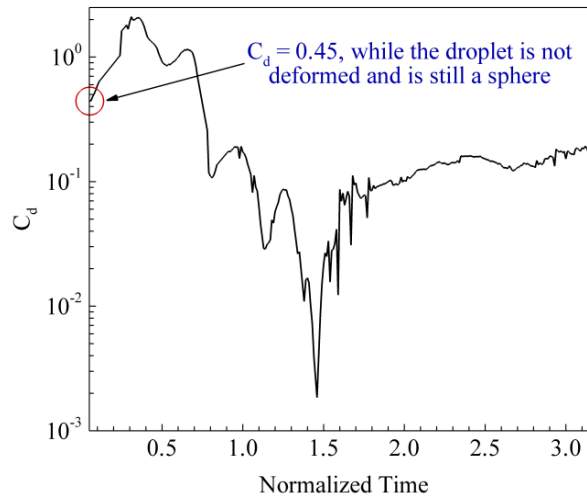


Figure 21. Time history of drag coefficient for multimode breakup.

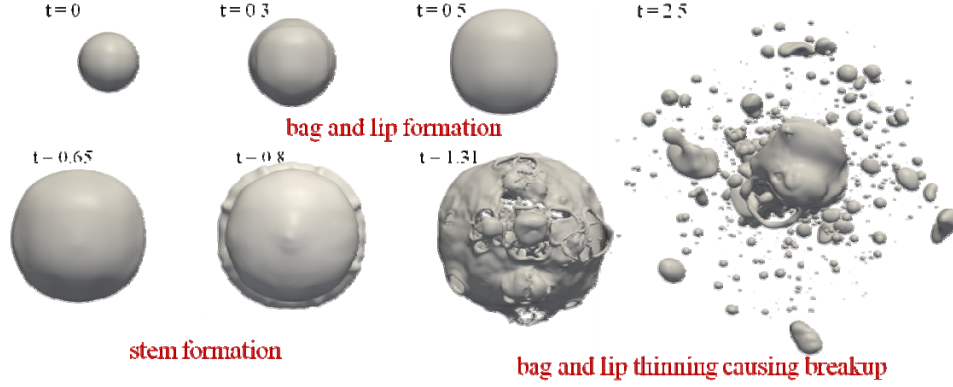


Figure 22. Multimode breakup mechanism (bottom view).  $We = 365$ ,  $Re = 29805$ ,  $\rho_l / \rho_g = 8.29$ ,  $t = T^*U/D$ .

### 5.3 Shear breakup

Shear breakup is the most explosive breakup mode observed in the present research. The droplet breaks up due to the formation of Rayleigh-Taylor (R-T) waves, which causes shear thinning of the droplet at the periphery, leading to child droplet formation. Temporal evolution of the front and bottom view of the droplet structure corresponding to  $We = 1112$  is shown in Figs. 23 and 24. Multimode and shear breakup phenomena differ in two ways: 1) formation of strong R-T waves on the droplet surface in case of shear breakup, and 2) formation of a hollow bag before the protrusion of the stem, which is unique to multimode breakup. A detailed discussion of the characteristics of the shear breakup mechanism can be found in (Khare *et al.* 2012).

Typical temporal variation of momentum and surface energy for shear breakup phenomena is shown in Fig. 25. As is clear from the figure, the decrease in surface area is much more gradual in this case because child droplets are constantly being generated by extremely high external forcing. The slopes of momentum and surface energy stay almost constant after  $t = 1$  and  $t = 1.5$  respectively. Because of this, the drag coefficient tends to a stationary value in the later stages of the breakup process. The variation of drag coefficient for this case is shown in Fig. 26.

### 5.4 Time averaged drag coefficient of deforming and fragmenting droplets

As pointed out previously, practical multiphase engineering problems are often investigated using a Eulerian-Lagrangian framework. To account for the steady-state drag force experienced by a liquid droplet in such a framework, accurate knowledge of time-averaged drag coefficient is of immense importance. Average value of drag coefficient is obtained by calculating the area under the curve of the temporal evolution of drag coefficient, and dividing it by the droplet lifetime. Time averaged drag coefficient is calculated for a range of Weber numbers, and a correlation is developed to predict the value of drag coefficient for a given Weber number. The correlation is given by:

$$\frac{C_d}{C_{d,0}} = 2We^{-0.175} \quad We > 0.1, \quad Oh < 0.1 \quad (16)$$

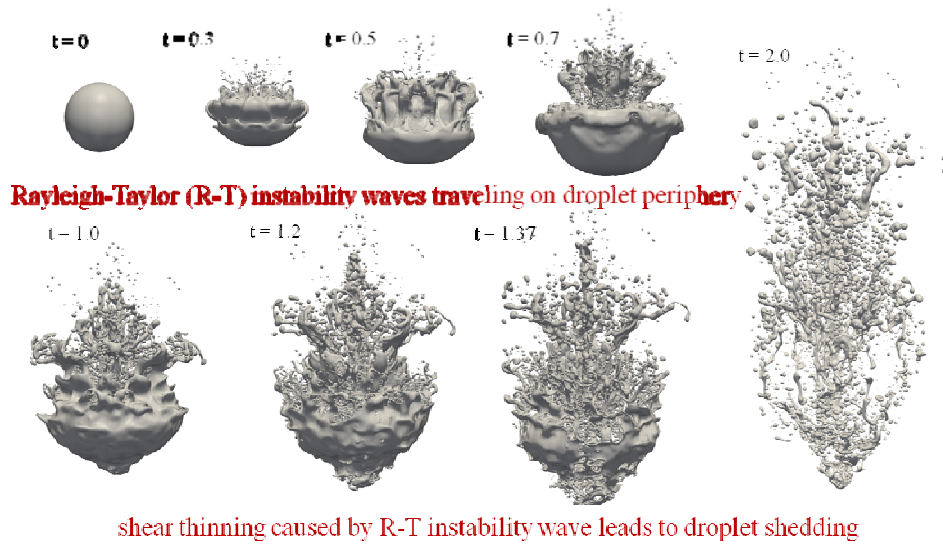


Figure 23. Shear breakup mechanism.  $We = 1112$ ,  $Re = 52000$ ,  $\rho_l / \rho_g = 8.29$ ,  $t = T*U/D$ .

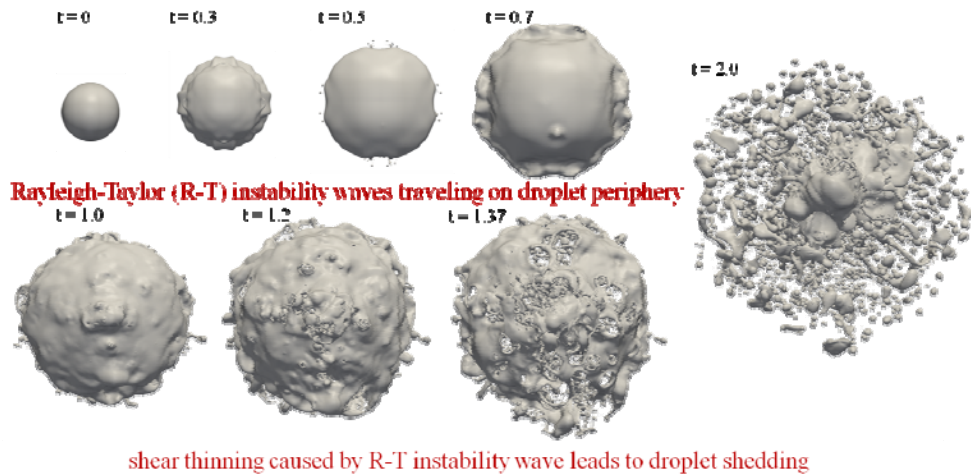


Figure 24. Bottom view of the shear breakup mechanism.  $We = 1112$ ,  $Re = 52000$ ,  $\rho_l / \rho_g = 8.29$ ,  $t = T*U/D$ .

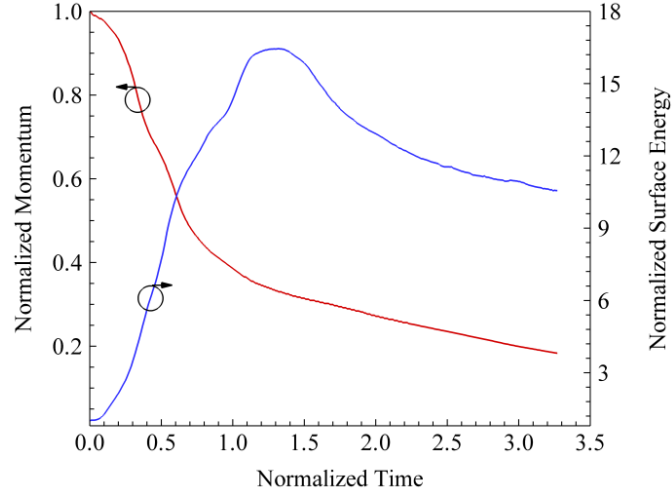


Figure 25. Time evolution of momentum and surface energy for  $We = 1112$ .

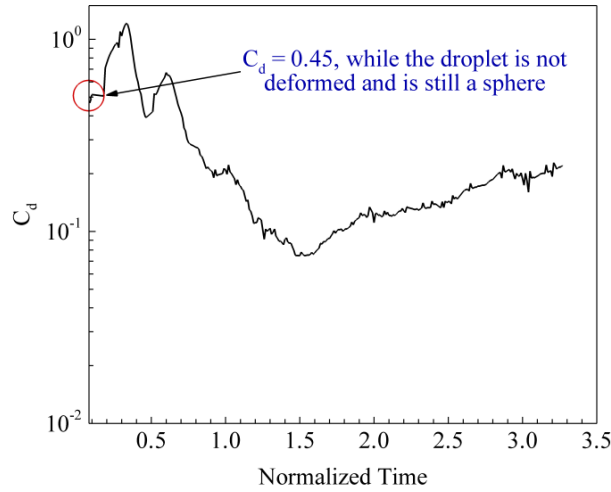


Figure 26. Evolution of coefficient of drag with time for  $We = 1112$ .

The variation of time-mean drag as a function of Weber number is shown in Fig. 27. The time averaged drag coefficient decreases as the Weber number is increased. To explain this phenomenon, it is useful to look at the breakup mechanisms dominant at various Weber numbers. When the Weber number is small, the breakup process usually proceeds via the bag breakup mechanism and the droplet deformation before the initiation of breakup is large. In addition, the time associated with this large deformation is usually very large. This in effect corresponds to a larger drag coefficient, in comparison to the processes taking place at higher Weber numbers, where fragmentation proceeds quickly. Maximum value of drag coefficient was also investigated for the range of Weber numbers investigated in this research and is shown in Table 1. If the value of maximum drag coefficient is linearly extrapolated for  $We = 10$ , we obtain a value of 2.58, which agrees closely with the value obtained by Wadhwa *et al.* (2007). The decreasing trend of the maximum and average drag coefficient was also observed in experiments conducted by Warnica *et al.* (1995), although the Weber numbers studied during their experiments were very low.

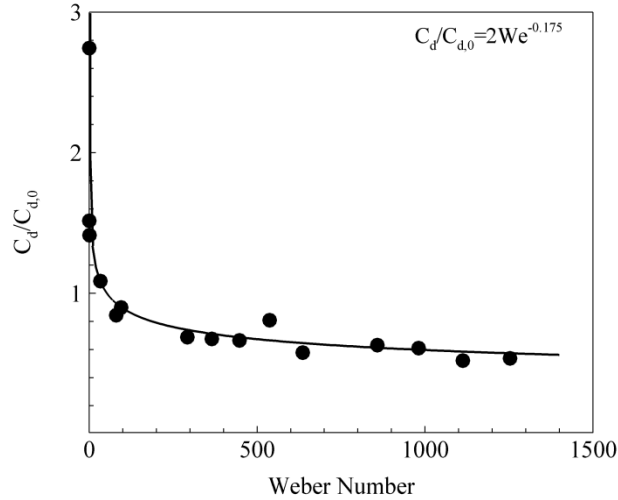


Figure 27. Variation of average drag coefficient with Weber number.

Table 1. Maximum value of drag coefficient as a function of Weber number.

Weber number	Maximum $C_d$
23	2.44
33	2.56
66	2.60
80	2.58
95	2.62
292	2.15
365	2.11
447	2.10
537	2.04
636	1.75
858	1.37
981	1.33
1112	1.21
1253	1.08
1400	1.03

The time-mean drag coefficient for fragmenting liquid droplets at different operating pressures can be predicted using the generalized regime diagram developed by Khare *et al.* (2012), along with the correlation given by equation 16.

### 5.5 Generalized regime diagram and child droplet size distributions

A thorough parametric study was conducted to identify the critical Weber numbers for the various breakup modes. They are dependent on the density ratio, which can be regarded as a manifestation of pressure, along with the more important Weber number. In particular, for 100 atm pressure conditions, the critical Weber numbers were found to be approximately 33, 110 and 1000, for the bag, multimode and shear breakup regimes, respectively. These numbers are much

different from those found in the literature for higher density ratios, or equivalent lower pressure conditions, even though the experimental data consisted of quite a wide range of density ratios. It should be pointed out that the density ratio in the experiments was varied by changing the liquid, as opposed to changing the ambient fluid density, as in the present numerical study. The differences observed in critical Weber numbers at elevated pressure conditions can be explained using the fact that at higher pressures, the drag experienced by the droplet is much higher. This means that the effective relative velocity between the droplet and the ambient fluid decreases at a much higher rate as compared to lower-pressure cases, that is, the rate of change of momentum is much higher at lower density ratios created by high pressures. This reduction in relative velocity reduces the instantaneous relative velocity and hence a higher Weber number is required for the droplet to undergo deformation and breakup at higher pressure conditions. A model was developed to take into account the pressure effect on the critical Weber number. Figure 28 shows the generalized regime diagram based on the developed model. The black, green, red and blue symbols represent the critical Weber numbers for bag, multimode and shear breakup regimes at 1, 25, 60 and 100 atm pressures, respectively.

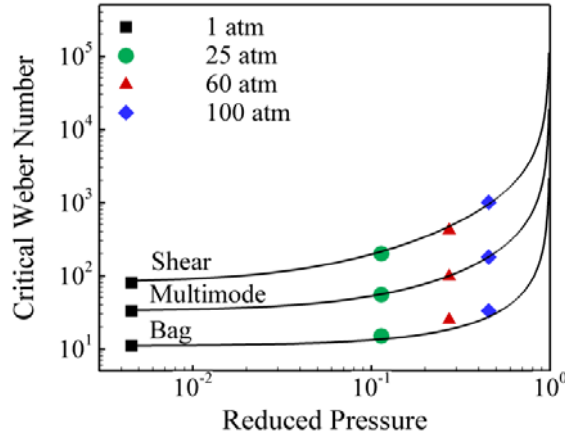


Figure 28. Generalized regime diagram.

Child droplet diameters were studied for a wide range of Weber numbers. Interestingly, it was found that the probability density distribution of the droplet diameter, shifted by a probability of 0.05, could be correlated using a log-normal distribution for  $We > 300$ , given by the equation below and as shown in Table 2 and Fig. 29:

$$pdf = \frac{1}{d\sigma\sqrt{2\pi}} \exp\left\{-\frac{(\ln(d) - \mu)^2}{2\sigma^2}\right\} \quad \text{for } We > 300 \quad (17)$$

where  $d$  is the representative child droplet diameter, and  $\mu$  and  $\sigma$  are the correlation constants, respectively.

In order to quantify the liquid volume, we develop a correlation to predict the Sauter mean diameter of the droplet distribution. The end of breakup is marked by the equilibrium of surface tension and inertial aerodynamic forces. If an effective representative sphere of diameter,  $d$ , is assumed for a given volume of liquid, the surface tension and aerodynamic forces can be written as:

Table 2. Correlation coefficients  $\mu$  and  $\sigma$  for a range of Weber numbers.

Weber number	$\mu$	$\sigma$
365	0.2395	0.4010
447	0.2417	0.3646
537	0.2357	0.3753
636	0.2384	0.4005
858	0.2586	0.3884
981	0.248	0.4041
1112	0.2879	0.412
1253	0.3182	0.4218
1400	0.2926	0.3947

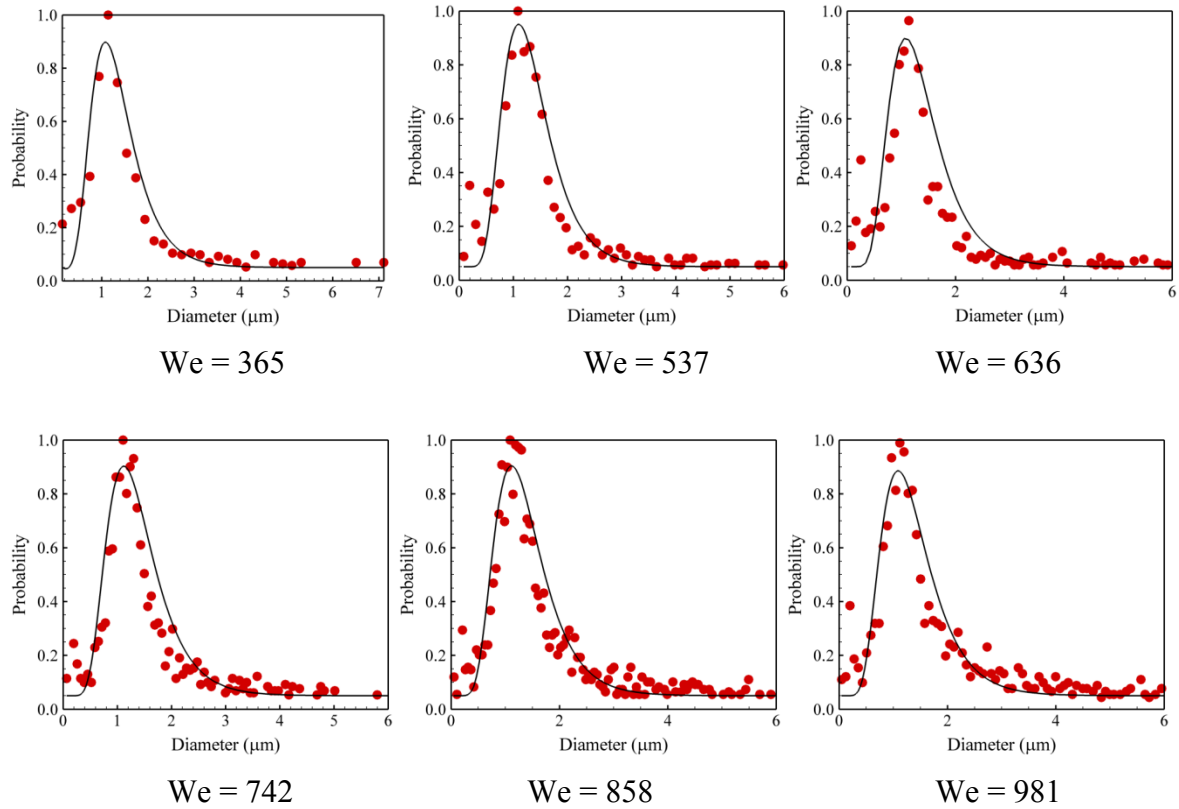


Figure 29. PDF of child droplet diameter for Weber numbers of 365, 537, 636, 742, 858 and 981.

$$F_{aerodynamic} = \frac{1}{2} C_d \rho_g u_{rel}^2 A_{frontal}$$

$$\text{where } A_{frontal} = \frac{\pi d^2}{4} \quad (18)$$

$$F_{surf.tension} = \sigma \pi d \quad (19)$$

At equilibrium,  $F_{aerodynamic} = k F_{surf.tension}$

$$k = \text{proportionality constant } d = \frac{8k\sigma}{C_d \rho_g u_{rel}^2} \Rightarrow \frac{d}{D} = \frac{8k}{C_d We} \quad (20)$$

The Sauter mean diameter (SMD),  $d_{32}$ , was calculated. It can be correlated using the above analysis by assuming that  $d_{32}$  is proportional to  $d$ , given by:

$$\frac{d_{32}}{D} = f(We) \frac{d}{D} = kf(We) \frac{8}{C_d We} \quad (21)$$

where  $f(We)$  is chosen not only because it is the most important non-dimensional quantity in the present physical situation but also since it represents a quantity similar to  $d_{32}$ . Figure 30 shows the predicted SMD, along with the SMD obtained from the simulation.  $f(We)$  is given by:

$$f(We) = We^{0.28} \quad (22)$$

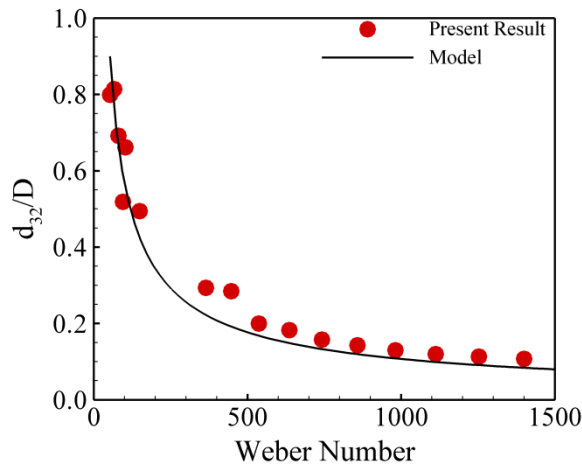


Figure 30. Sauter mean diameter,  $d_{32}$ , correlated using an analytical model.



Excellent agreement is observed between the model and the numerical data. The correlation predicts that the SMD distribution does not change significantly beyond  $We$  of 300, which also supports the previous finding that the PDF of droplet diameter follows a universal log-normal distribution for  $We > 300$ . The results for SMD for the shear breakup regime, defined for Weber numbers greater than approximately 1000 for  $p=100$  atm, seems to asymptote to a value near 0.1. This agrees well with the quasi steady correlation developed by Chou *et al.* (1997), in which they propose  $SMD/D = 0.09$  (with a 22% standard deviation) for the shear breakup regime. If we use our generalized correlation to obtain the corresponding Weber number at 100 atm, which involves the same breakup physics as exhibited by Weber number of 125 for the water/air system at 1 atm, and use the SMD correlation, we find that our SMD correlation yields a value of 0.11, which is quite close to the experimental predictions and lies with the range of experimental error. This further validates the approach and the generalized regime diagram developed during the course of this study.

## 6. Dynamics and mass transfer of unequal-sized droplet collision

In order to fully understand the physics for the entire parameter regime for unequal-sized droplet collision, topology-oriented adaptive mesh refinement methods (TOAMR) were developed and applied to simulate the gas film drainage and ligament breakup during the approach and separation of colliding droplets. Figure 31 shows selected simulation results with various collision outcomes.

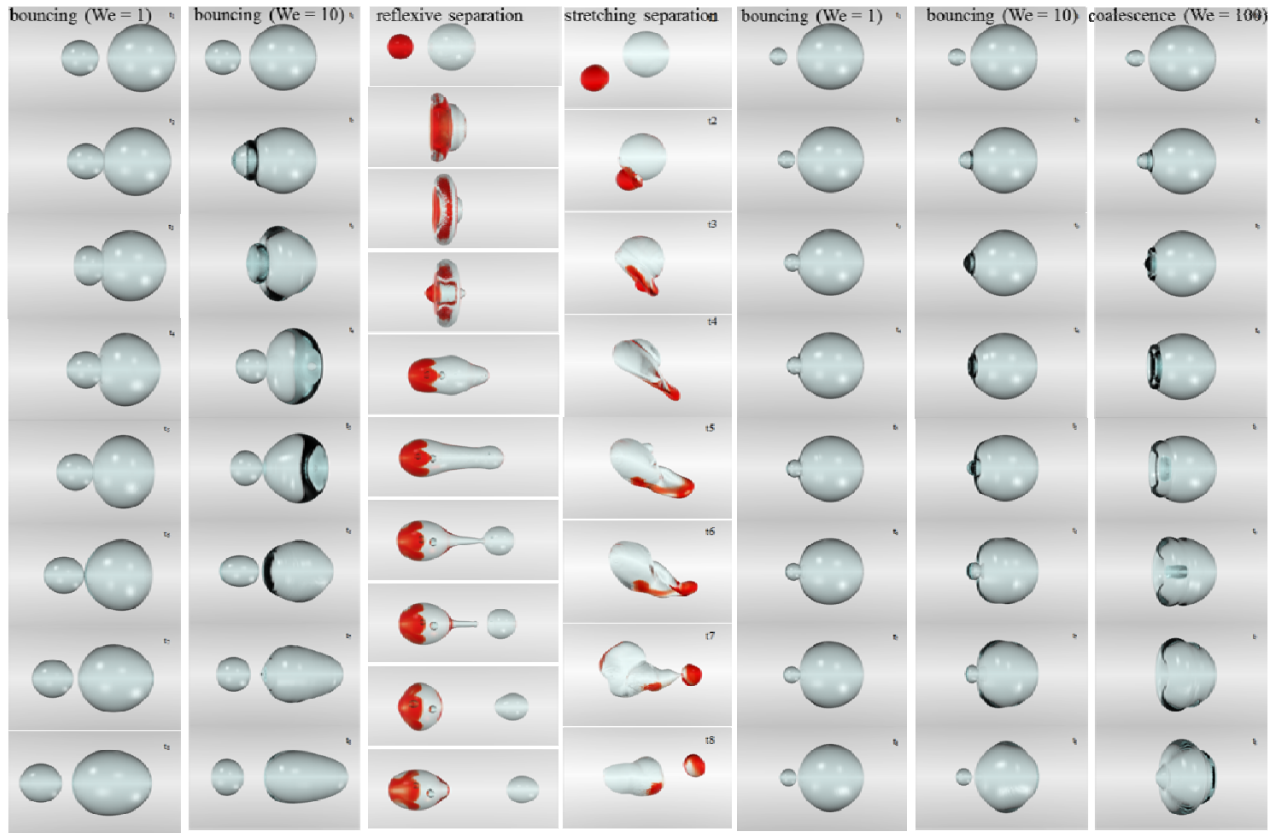


Figure 31. Rendered results of collision of unequal-sized droplets.

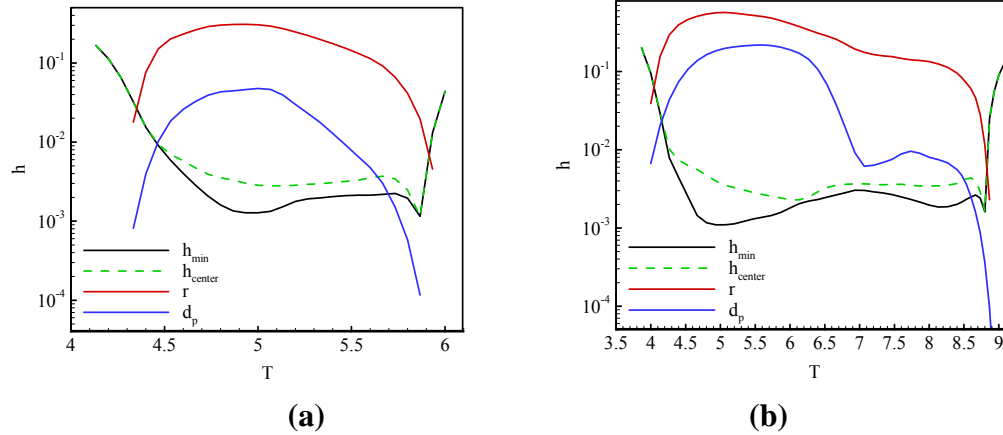


Figure 32. Evolution of shape parameters during bouncing process. Water droplets in air at 1 atm: (a)  $We=1$ ,  $Re=85.2$ ,  $B=0$ ,  $D_s=100 \mu m$ ,  $U=0.85$  m/s; (b)  $We=10$ ,  $Re=269.4$ ,  $B=0$ ,  $D_s=100 \mu m$ ,  $U=2.69$  m/s.

When two droplets approach each other, a gas film is trapped between them. The pressure generated within the film prevents further motion of the approaching droplets. This is analogous to the fluid film lubrication that occurs when two opposing bearing surfaces are completely separated by a fluid film. The term “gas film lubrication” is used here to indicate that the lubricant is gas. Figure 32 shows the time evolutions of  $h_{rim}$ ,  $h_{center}$ ,  $r$ , and  $d_p$ , where  $h_{rim}$  is the minimum film thickness,  $h_{center}$  is the maximum film thickness (at the center of the film),  $r$  the radial extent of the film and also the radius of the dimple, and  $d_p$  the penetration distance of the film. For  $We = 1$ , as shown in Fig. 32(a), when the two droplets approach each other,  $h_{rim}$  and  $h_{center}$  decrease at a rate equal to the relative velocity. When the drop surfaces are about  $1.08 \times 10^{-2} D_s$  apart from each other at  $t = 4.46$ , the surface becomes flat and a dimple pattern with a radius of  $r$  begins to form a gas film. A positive pressure field is established in the gas film. As the droplets continue to approach each other, the drainage slows, with a gradual change in the film thickness and dimple radius. Since the pressure is different between the two droplets, the small droplet can penetrate into the large one, as shown by the increasing trend of  $d_p$  with the development of the gas film. After  $r$  reaches a maximum value at around  $t = 4.95$ , the kinetic energy of the droplet is not sufficient to continue the drainage of the gas film, and the droplet starts to recover its original shape, due to surface tension. After that,  $r$  begins to decrease, while  $h_{rim}$  begins to increase slowly. It is interesting to notice that when  $h_{rim}$  and  $r$  reach their extreme values,  $h_{center}$  and  $d_p$  continue to decrease and increase, respectively. They reach their extreme values at around  $t = 5.06$ . This means that while the shapes of droplets are restored, there is still a compression motion near the center between the two droplets. The shape recovery due to surface tension for the small droplet introduces not only an inverse motion that causes the bounce-off of the two droplets, but also a motion in the original collision direction. It is this recovery-induced opposite motion that causes continued compression near the center. At  $t = 5.26$ , the bouncing process becomes nearly stationary when the variations of  $h_{rim}$  and  $h_{center}$  are small, while  $r$  and  $d_p$  decrease nearly linearly. Negative pressure exists near the boundary of the dimple pattern during the bounce-off process. It is induced by the shrinkage motion of the dimple. When  $r$  approaches zero at  $t = 5.69$ , the negative pressure affects the pressure distribution in the gas film near the center and causes a sudden decrease in  $h_{rim}$  and  $h_{center}$ . When the dimple pattern quickly changes to a tip pattern, the curves of  $h_{rim}$  and  $h_{center}$  coincide. The value of  $h_{rim}$  at this point is even smaller than the minimum value of  $h_{rim}$  during the approaching process. This means the sudden

decrease in the film thickness can also induce coalescence. The distance between the two droplets then increases, thus finishing the bouncing process. For  $We = 10$ , as shown in Fig. 32(b), the evolutions of  $h_{rim}$ ,  $h_{center}$ ,  $r$  and  $d_p$  show similar trends. The mismatching of the minimum values of  $h_{rim}$  and  $h_{center}$  is clearly caused by stronger deformation of the small droplet. While the variation of  $h_{center}$  levels off at  $t = 6.61$ ,  $h_{rim}$ ,  $r$ , and  $d_p$  show sinuous variations due to the oscillation of the small droplet.

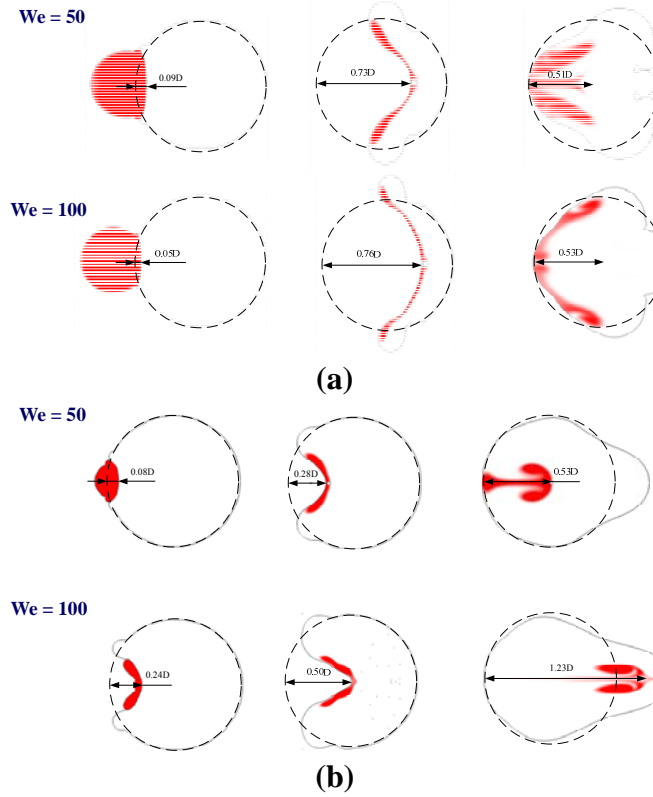


Figure 33. Liquid phase mixing during head-on collision for  $We = 50$  and  $100$  with diameter ratio of (a)  $0.5$  and (b)  $0.25$ .

The simulation results of four head-on unequal-sized collisions, with  $We = 50$  and  $100$ , are used to study the liquid phase mixing of the two droplets. Figure 33(a) shows snapshots of a droplet collision with  $\lambda = 0.5$ . The embedded distances from the gas film to the original shape of the large droplet for the two cases are  $0.09$  and  $0.05 D_l$ , respectively. At a higher  $We$  number, the high kinetic energy of the droplet more rapidly decreases the film thickness at the rim boundary. The gas-film rupture happens around the liquid rims formed by the impact motion. After rupture, the gas film shrinks quickly under the effect of surface tension. The connected droplets further interact with each other. The mass is distributed around the impact plane, whose shape changes during the collision process. The maximum deformation for each case is shown in the second image for the respective case. Gas bubbles formed by the ruptured gas film can be found in the center of the collision. The deformation distances for the two cases are  $0.73$  and  $0.76 D_l$ , respectively. Even with higher kinetic energy, the maximum deformation is only slightly larger. However, the liquid rim is thinner and the mass radial distribution of the small droplet is wider. After the maximum deformation is reached, the droplets restore their shapes due to surface tension, while the rims formed by the impact motion move to the other side to form a body wave. It is clear that the mass of the small droplets moves in a direction opposite to its original

direction with the restoring motion of the merged droplet. The penetration distances of the small droplets are 0.51 and 0.53  $D_1$ , respectively. After that, the merged droplet continues to elongate, but the mass of the small droplet remains in the left side. Similar processes can be observed in Fig. 33(b) for  $\lambda = 0.25$ . The kinetic energy within the small droplet is large enough to cause continuous penetration after the maximum deformation.

### 7. Equal-sized droplet collision and mixing

In order to fully understand all the regimes existing in droplet collision, distance-based and thickness-based refinement methods were developed and applied to simulate bouncing outcomes. Phenomena similar to film drainage was successfully captured, and the change in shape and pressure between two colliding droplets was analyzed. Figure 34 shows two simulation results with head-on and off-center droplet bouncing, rendered by an advanced visualization technique, which uses Ray-tracing to gain direct insight into the detailed physics of droplet interaction. The head-on collision was simulated by an axis-symmetric model to reduce the numerical cost. Distance-based refinement was used with a minimum grid size of about 0.015  $\mu\text{m}$ . Off-centered collisions cannot be simulated using an axisymmetric approach, so a 3-D simulation was conducted for this case. The particular conditions chosen for the off-centered bouncing case were selected such that the minimum grid size requirement was about 0.7  $\mu\text{m}$  (Fig. 34(b)).

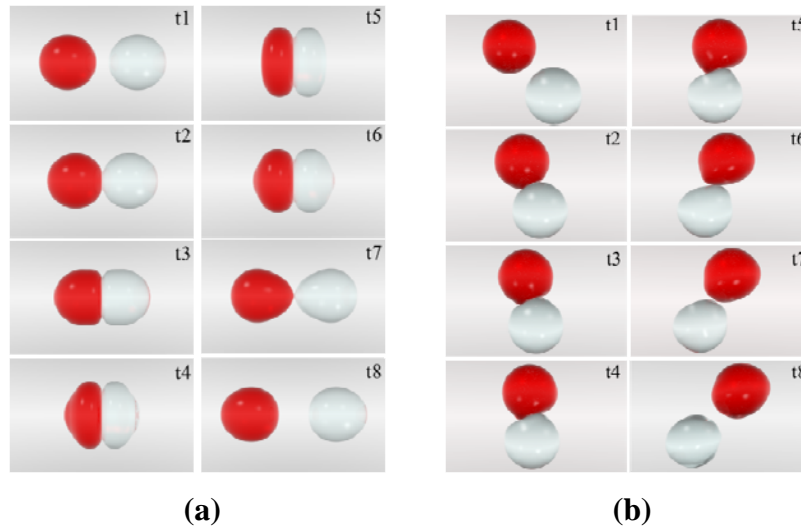


Figure 34. Rendered results for simulation of head-on and off-center bouncing outcome. Conditions: (a) Tetradecane droplets in 1 atm. Nitrogen,  $We=8.6$ ,  $Re=105.9$ ,  $B=0$ ,  $D=306 \mu\text{m}$ ,  $U_{\text{relative}}=0.97 \text{ m/s}$ ; (b) Tetradecane droplets in 1 atm. Nitrogen,  $We=48.8$ ,  $Re=260.3$ ,  $B=0.9$ ,  $D=306 \mu\text{m}$ ,  $U_{\text{relative}}=2.31 \text{ m/s}$ .

The simulation results in the low Weber number range, in general, differed from the experimental data because van der Waals forces were not considered in the analysis. In spite of this assumption, the effect of gas film lubrication was isolated, and it was observed that the minimum film thickness varies non-monotonically with an increasing Weber number. This non-monotonic behavior takes place because, for a fixed impact parameter, the collision outcome transitions from coalescence, to bouncing, and then back to coalescence with an increasing Weber number.

Following previous studies on equal-sized droplet collisions, unequal-sized collision of water droplets was studied under two diameter ratios, 0.5 and 0.25. Figure 35 shows the comparison

between experimental images and rendered simulation results. Good agreement was achieved for both the shape changing and mass transfer processes. Forty-five and forty cases were simulated for diameter ratios of 0.5 and 0.25, respectively. Mass transfer contours for diameter ratios of 0.5 and 0.25 are shown in Fig. 36(a) and (b), respectively. It can be seen that the mass transfer ratio is almost independent of the Weber number and is affected strongly by the impact parameter,  $B$ . A model for the mass transfer ratio of unequal-sized droplet collision was developed and it showed good agreement with simulation results, as shown in Fig. 36(c) and (d).

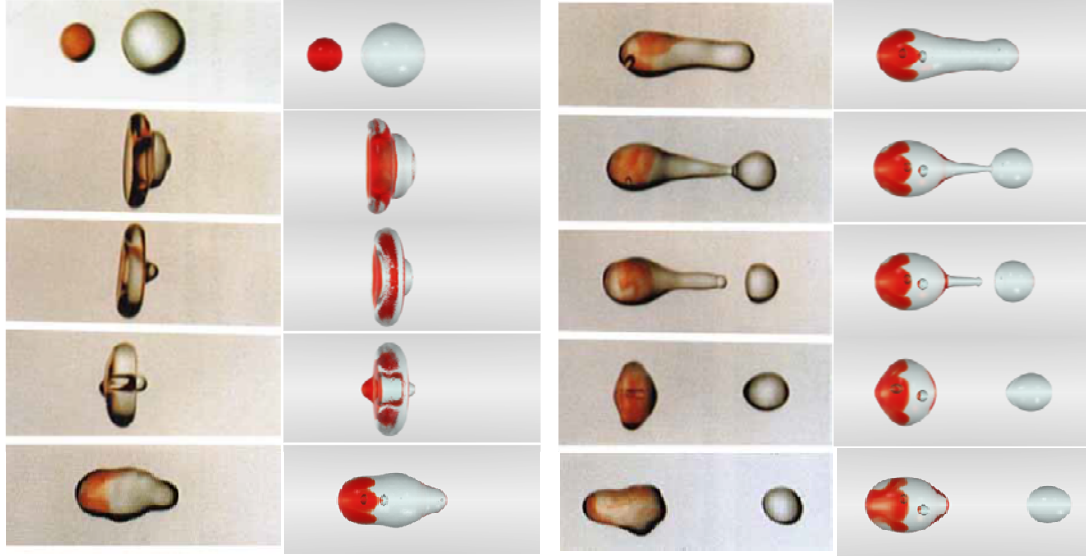


Figure 35. Comparison of unequal reflexive separation with experimental images. Conditions: water droplets with diameter ratio of 0.50 in 1 atm. air,  $We_{small} = 102$ ,  $B=0$ ,  $D_{larger}=400 \mu m$ ,  $U_{relative}=6.10 \text{ m/s}$  (Ashgriz & Poo 1990).

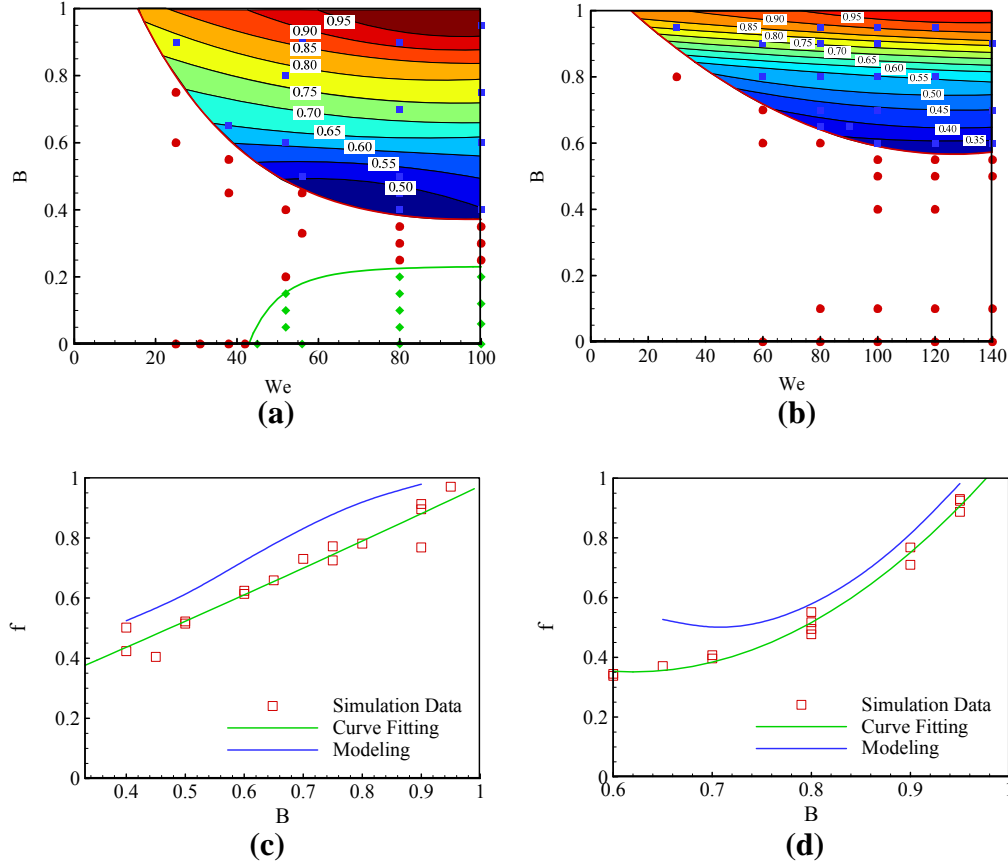


Figure 36. Results and modeling of mass transfer ratio under different diameter ratios: (a) results under diameter ratio of 0.5; (b) results under diameter ratio of 0.25; (c) modeling under diameter ratio of 0.5; (d) modeling under diameter ratio of 0.25.

## 8. Non-Newtonian droplet breakup and dynamics

The motivation to study non-Newtonian liquid droplet breakup stems from the various advantages offered by gelled propellants, as compared to traditional liquid or solid propellants in combustion systems, particularly in rocket engines. According to Natan & Rahimi (2002), “From the atomization point of view, very little is known about the atomization mechanism of non-Newtonian fluids and even less regarding gel propellants.” They further note that, “From the combustion point of view, gels burn at a lower burning rate than non-gelled fuels and exhibit lower combustion efficiency. Secondary atomization seems to be a key parameter in order to obtain complete burning within a reasonable combustion chamber length.

Figure 37 shows the temporal evolution of droplet structure for a drop of diameter  $512\ \mu\text{m}$  subjected to an initial velocity of  $55\ \text{m/s}$ . As is clear from the figures, the breakup mechanism is drastically different from that of Newtonian liquids. The droplet, as it is decelerating downwards, stretches in the flow direction. The stretching quickly becomes asymmetric because the fluid is non-Newtonian and experiences different values of stresses at different regions of the droplet. This is attributed to differential shear rates, which lead to different values of viscosity at different points on the droplet. Eventually two things happen: 1) droplet stretching creates a dimple and eventually a bowl, and 2) it creates a torque due to unbalanced forces and the droplet starts rotating. This process continues for some time before the bag becomes thin enough to



break up. The initial breakup, shown in Fig. 38, resembles a very common non-Newtonian phenomenon, the beads-on-a-string (BOAS) structure (Bhat *et al.* 2010). This breakup creates additional non-uniformity in the shear strain experienced by the droplet leading to additional unbalanced forces. As a result, the droplet starts to rotate rapidly. This is analogous to a uniformly rotating liquid column where planar disturbances rotate with the stretched droplet. Twisting and growth of these disturbances evolve into helical instabilities with a central core. Over time, secondary capillary instabilities appear, forming droplet ejection sites in the form of liquid knots. Primary and secondary satellite drops result from these sites due to pinching. These instabilities are shown more clearly in Fig. 39.

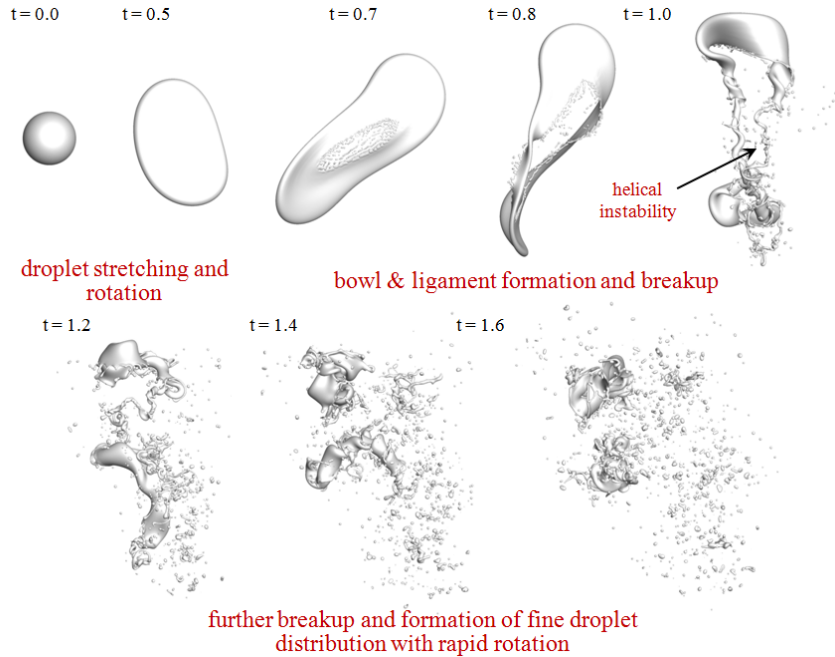


Figure 37. Non-Newtonian droplet breakup -  $We = 2411$ . Perspective view of temporal evolutions of 3D droplet structure in non-dimensional time. Non-dimensional time,  $t = T^*U/D$ .

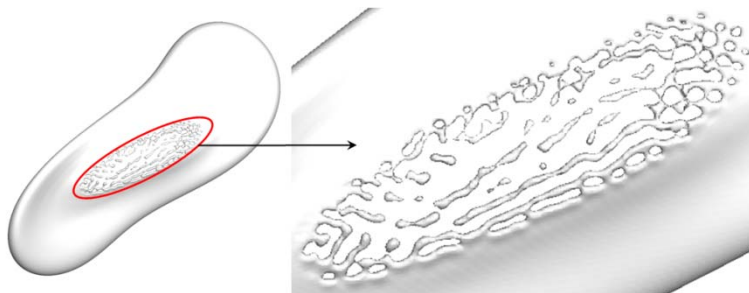


Figure 38. Beads-on-a-string structure during the breakup of non-Newtonian liquid drops.

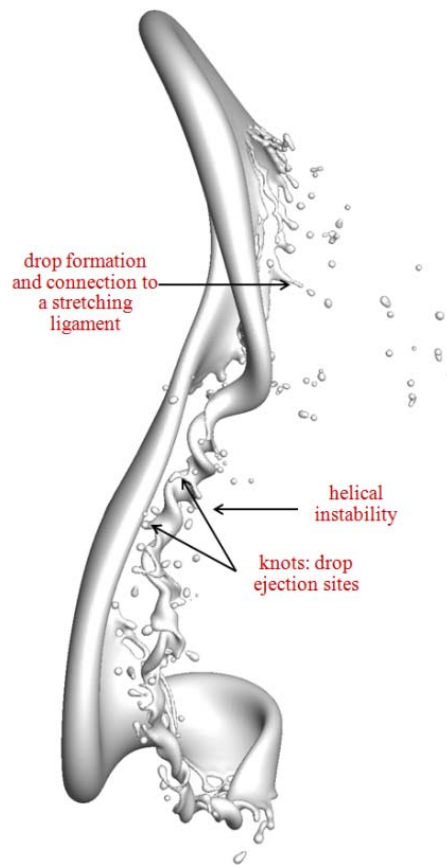


Figure 39. Helical instability, liquid drop ejection sites and formation of primary and satellite droplets during the breakup of non-Newtonian liquid drops.

## 9. References

- ALMGREN, A., BELL, J. & CRUTCHFIELD, W. 2000 Approximate Projection Methods: Part I. Inviscid Analysis. *SIAM Journal on Scientific Computing* **22**, 1139-1159.
- ASHGRIZ, N. & POO, J. Y. 1990 Coalescence and Separation in Binary Collisions of Liquid Drops. *Journal of Fluid Mechanics* **221**, 183-204.
- BATCHELOR, G. K. 2000 *An Introduction to Fluid Dynamics*. Cambridge University Press.
- BELL, J. (2005). Amr for Low Mach Number Reacting Flow. Adaptive Mesh Refinement - Theory and Applications. PLEWA, T., LINDE, T. and GREGORY WEIRS, V., Springer Berlin Heidelberg. **41**: 203-221.
- BERGMANS, J., KEPPENS, R., ODYCK, D. E. A. & ACHTERBERG, A. (2005). Simulations of Relativistic Astrophysical Flows. Adaptive Mesh Refinement - Theory and Applications. PLEWA, T., LINDE, T. and GREGORY WEIRS, V., Springer Berlin Heidelberg. **41**: 223-233.
- BERTHOUMIEU, P., CARENTZ, H., VILLEDIEU, P. & LAVERGNE, G. 1999 Contribution to Droplet Breakup Analysis. *International Journal of Heat and Fluid Flow* **20**, 492-498.
- BHAT, P. P., APPATHURAI, S., HARRIS, M. T., PASQUALI, M., MCKINLEY, G. H. & BASARAN, O. A. 2010 Formation of Beads-on-a-String Structures During Break-up of Viscoelastic Filaments. *Nature Physics* **6**, 625-631.



- BRACKBILL, J. U., KOTHE, D. B. & ZEMACH, C. 1992 A Continuum Method for Modeling Surface Tension. *Journal of Computational Physics* **100**, 335-354.
- BRYAN, G. & NORMAN, M. (2000). A Hybrid Amr Application for Cosmology and Astrophysics. Structured Adaptive Mesh Refinement (Samr) Grid Methods. BADEN, S., CHRISOCHOIDES, N., GANNON, D. and NORMAN, M., Springer New York. **117**: 165-170.
- CHOPTUIK, M. (2000). Making Arbitrarily Small Black Holes: Experiences with Amr in Numerical Relativity. Structured Adaptive Mesh Refinement (Samr) Grid Methods. BADEN, S., CHRISOCHOIDES, N., GANNON, D. and NORMAN, M., Springer New York. **117**: 153-163.
- CHOU, W. H., HSIANG, L. P. & FAETH, G. M. 1997 Temporal Properties of Drop Breakup in the Shear Breakup Regime. *International Journal of Multiphase Flow* **23**, 651-669.
- EFSTATHIOS, M. & CLAYTON, C. (2005). Basic Concepts and Definitions. *Multiphase Flow Handbook*, CRC Press: 1-1-1-79.
- FAETH, G. M. 1996 Spray Combustion Phenomena. *Twenty-Sixth Symposium (International) on Combustion. The Combustion Institute* **26**, 1593-1612.
- FAETH, G. M. 2002 Dynamics of Secondary Drop Breakup—a Rate Controlling Process in Dense Sprays. *ILASS-Europe*.
- FAKHRI, S. A. K. 2009 A Study on the Atomization and Spray Characteristics of Gelled Simulants Formed by Two Impinging Jetsthesi, The Pennsylvania State University.
- HAN, J. & TRYGGVASON, G. 2001 Secondary Breakup of Axisymmetric Liquid Drops. II. Impulsive Acceleration. *Physics of Fluids* **13**, 1554-1565.
- JOURDREN, H. (2005). Hera: A Hydrodynamic Amr Platform for Multi-Physics Simulations. Adaptive Mesh Refinement - Theory and Applications. PLEWA, T., LINDE, T. and GREGORY WEIRS, V., Springer Berlin Heidelberg. **41**: 283-294.
- KHARE, P. 2014 Breakup of Liquid Droplets. Ph.D. thesis, Georgia Institute of Technology.
- KHARE, P., MA, D., CHEN, X. & YANG, V. (2012). Breakup and Dynamics of Liquid Droplets. ILASS Americas, 24th Annual Conference on Liquid Atomization and Spray Systems. San Antonio, TX.
- LÓPEZ-RIVERA, C. 2010 Secondary Breakup of Inelastic Non-Newtonian Liquid Drops. PhD thesis, Purdue University.
- MYERS, C. (2000). The Dynamics of Localized Coherent Structures and the Role of Adaptive Software in Multiscale Modeling. Structured Adaptive Mesh Refinement (Samr) Grid Methods. BADEN, S., CHRISOCHOIDES, N., GANNON, D. and NORMAN, M., Springer New York. **117**: 111-125.
- NATAN, B. & RAHIMI, S. 2002 The Status of Gel Propellants in Year 2000. **5**, 172-194.
- PERNICE, M., BOCKELIE, M. J., SWENSEN, D. & SMITH, P. J. (2000). Progress, Results, and Experiences in Developing an Adaptive Solver for Steady State Turbulent Reacting Flows in Industrial Boilers and Furnaces. Structured Adaptive Mesh Refinement (Samr) Grid Methods. BADEN, S., CHRISOCHOIDES, N., GANNON, D. and NORMAN, M., Springer New York. **117**: 127-151.
- POPINET, S. 2003 Gerris: A Tree-Based Adaptive Solver for the Incompressible Euler Equations in Complex Geometries. *Journal of Computational Physics* **190**, 572-600.
- PÓPINET, S. 2009 An Accurate Adaptive Solver for Surface-Tension-Driven Interfacial Flows. *Journal of Computational Physics* **228**, 5838-5866.
- SCARDOVELLI, R. & ZALESKI, S. 1999 Direct Numerical Simulation of Free-Surface and Interfacial Flow. *Annual Review of Fluid Mechanics* **31**, 567-603.

- TRYGGVASON, G., SCARDOVELLI, R. & ZALESKI, S. 2011 *Direct Numerical Simulations of Gas-Liquid Multiphase Flows*. Cambridge University Press.
- WADHWA, A. R., MAGI, V. & ABRAHAM, J. 2007 Transient Deformation and Drag of Decelerating Drops in Axisymmetric Flows. *Physics of Fluids* **19**, 113301.
- WARNICA, W. D., RENKSIZBULUT, M. & STRONG, A. B. 1995 Drag Coefficients of Spherical Liquid Droplets Part 1: Quiescent Gaseous Fields. *Experiments in Fluids* **18**, 258-264.
- ZAKERZADEH, S. A. 2008 Applying Dynamic Contact Angles to a Three-Dimensional Vof Model. PhD thesis, University of Toronto (Canada).

## V.2 Impinging Jet Experimentation (Risha, Penn State – Altoona)

### 1. Summary

The major objective of this part of the program effort is to characterize ignition and combustion of non-gelled and gelled hypergolic propellants using an impinging jet experiment. Impinging jet experimentation is required to (1) provide insights into the entire flow and combustion process of GHPs; and (2) evaluate the overall effect of propellant formation, flow condition, and injector geometry on the combustion characteristics and ensuing engine performance. Further, new combinations of fuels with classical oxidizers such as N,N,N',N'-tetramethylethylenediamine (TMEDA), dimethyle-2-azidoethylamine (DMAZ), white fuming nitric acid (WFNA), red fuming nitric acid (RFNA) were examined to provide potential viable replacements for highly toxic fuels such as hydrazine. Experiments were conducted to determine the ignition delay as a function of: volumetric flow rate, momentum ratio, L/D ratio, fuel/oxidizer combination, gel, fuel/oxidizer lead times, and equivalence ratio. As the reactant volumetric flow rate increased by a factor of six, the ignition time delay decreased from ~17 ms down to ~5 ms. The effect of  $\phi$  on ignition delay shows that at very fuel rich conditions ( $\phi = 5.8$ ) the ignition delay was approximately 3 times longer. However, for cases at  $\phi = 3.2$  and below, the ignition delay is not significantly affected by stoichiometry (indicating that stoichiometry is more important for combustion rather than ignition) nor the introduction of inert gelling agents.

### 2. Nomenclature

L/D	= length-to-diameter ratio of injector
O/F	= oxidizer-to-fuel ratio
WFNA	= white fuming nitric acid
RFNA	= red fuming nitric acid
DMAZ	= dimethyle-2-azidoethylamine
TMEDA	= N,N,N',N'-tetramethylethylenediamine
JATO	= Jet Assisted Take-Off
$\phi$	= equivalence ratio
$t_0$	= time oxidizer and fuel streams initiate impingement
$t_{\text{ign}}$	= time of first light subsequent impingement

### 3. Introduction

A Soviet researcher by the name of the Valentin Glushko originally experimented with hypergolic fuels early in 1931.<sup>1</sup> The chemical ignition from dissolving phosphorus in carbon disulfide was used to start kerosene and nitric acid engines. Later, in 1935, Professor O. Lutz of the German Aeronautical Institute began experimenting with over 1000 self-igniting combinations. He helped develop C-Stoff, which is a chemical that ignites when mixed with concentrated hydrogen peroxide.<sup>1</sup> The United States, then through GALCIT and Navy Annapolis researchers, developed an engine powered by aniline and nitric acid. This was used throughout the 1940's for small missiles and Jet Assisted Take-Off (JATO).<sup>1</sup>

Rocket propellants are often classified with broad terminology; such as, lithergols (mixture of solid and liquid propellants), hypergols (bipropellant mixture requiring no external ignition), non-hypergols (bipropellant mixture requiring external ignition), and monergols (monopropellant chemical or chemical mixture, which reacts when exposed to different environments).<sup>1</sup> Previously cryogenics such as liquefied oxygen were used as the preferred method in space launchers. However, since most missiles and rockets require a high-level of readiness prior for

any launch, they can be stored for months at a time before being used in the fleet. This state of so-called hibernation proves to be unrealistic for cryogenics and therefore paved the way for hypergolic propellants to supersede. The ignition process of hypergolic materials usually is initiated by the impinging of a liquefied fuel and oxidizer combination. Hypergolic ignition, although not confirmed, is a two step process, at first substantial heat is generated by an acid based neutralization, then a slower, rate controlling gas phase oxidation process occurs.<sup>2</sup> A recent study reveals that once the oxidizer and fuel impinge, droplets form at the bottom of the sheet that is created. These droplets contain a mixture of fuel and oxidizer. Within the drops, an initial liquid phase reaction forms and releases vapor. Hot vapor rapidly fills the surrounding area and shortly after, ignition between the fuel and the oxidizer occurs.<sup>3</sup>

Even though hypergolic propellants provide many advantages such as a more sensible propulsive fuel, these materials have several unwanted characteristics. In particular, the materials are often very toxic and can be hazardous if a leak would occur. The potential of leakages led to their substitution of solid-propellant boosters. In addition, to providing more possible propulsive power, hypergolic propellants offer some other unique advantages such as: ignition does not occur until fuel and oxidizer impinge, and the ignition can be aborted at anytime by stopping the oxidizer or fuel stream. Furthermore, thrust can be throttled by changing the flow conditions of the fuel and/or oxidizer. In contrast, once a solid propellant rocket booster is ignited, it is often difficult or even impossible to stop the ignition process until the solid propellant has been completely consumed.

The focus of this research work was to characterize ignition and combustion of blends of TMEDA / DMAZ fuels and white fuming nitric acid (WFNA) oxidizer using a single-element injection system to provide characteristics on hypergolic propellant reactants in terms of ignition delays under atmospheric pressure and ambient temperature conditions. This study assists in determining whether TMEDA and DMAZ are viable replacements for highly toxic fuels such as hydrazine. Specific operating conditions such as volumetric flow rate of the fuels and oxidizer, momentum ratio, L/D ratio of the injectors, and equivalence ratio were varied throughout the experimental matrix. High-speed images of the ignition transient were ascertained to determine the ignition delay times.

#### 4. Background

Usually hypergols are composed of highly corrosive oxidizers (Red-Fuming Nitric Acid-RFNA, nitrogen tetroxide-NTO) and toxic fuels (hydrazines).<sup>4</sup> Dealing with these chemicals in a large scale environment can be quite dangerous and they must be handled with extreme care. Hydrazine based rockets have been used in years past in rocket engines such as the U.S. Titan Rocket and the Apollo spacecraft.<sup>5</sup> Studies however, have shown that hydrazine based fuels are carcinogenic in animal testing and highly toxic, exposure creates potential danger.<sup>6</sup> As a result, there is a need for alternative fuels, that would be less toxic, but suitable as a replacement for hydrazine based fuels.<sup>4</sup> The alternative fuels must possess suitable ignition delay times, less hazardous handling, and ease of reproduction. Recently, new forms of ionic liquids<sup>7,9</sup> and tertiary amines (or amine azides)<sup>10-12</sup> fuels have been examined which include dimethyl-2-azidoethylamine (DMAZ) and N,N,N',N'-tetramethylethylenediamine (TMEDA), which is of special interest due to its close proximity to monomethylhydrazine (MMH). MMH is believed to be a much more toxic fuel because of its hydrazine base.<sup>13</sup> As a result of the current interest in TMEDA and DMAZ, many publications have set forth to prove that these fuels and fuel blends may meet the requirements of MMH.

Previously, many studies have been conducted using RFNA as the oxidizer for igniting TMEDA.<sup>4</sup> Most of the current studies employ WFNA since it is less toxic than RFNA, while offering most of the same characteristics. Researchers have blended TMEDA and 2-N,N-dimethylaminoethylazide (DMAZ) and found decreases in overall ignition delay.<sup>11,14</sup> One study in particular, examined various amounts of DMAZ mixed into the TMEDA fuel. According to Stevenson, fuel mixtures showed lower ignition delay times, compared to unmixed fuels such as TMEDA alone.<sup>14</sup> The results of their patent is given in Fig. 1. TMEDA/DMAZ blends containing between 20-40% DMAZ (by wt%) in both rocket engine and drop-test experiments resulted in the lowest ignition delay times, nearly a 50% reduction. For this study, mixtures containing 20-80% DMAZ were tested for graphical analysis of the effect DMAZ has on ignition delay time.

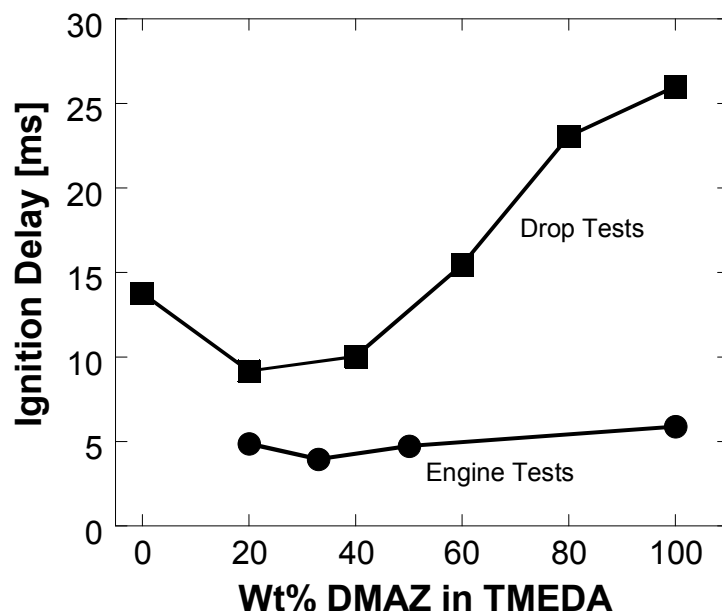


Figure 1. Ignition delays from drop tests and rocket engine firings of TMEDA/DMAZ blends.<sup>14</sup>

According to McQuaid, DMAZ is an aliphatic amine azide and its ignition process is quite surprising, because aliphatic azides are not hypergolic. Although aliphatic amines appear to be hypergolic, they still produce much longer ignition delay times than hydrazine. In the study, it is thought that the proton transfer from nitric acid to the amine starts the azide breakdown.<sup>15</sup> Due to this decomposition, it is considered the most important exothermic ignition initiation step within the ignition process.<sup>16</sup> When the azide decomposition starts, it then speeds up the sluggish oxidation process of the amine.<sup>15</sup> This amine oxidation causes the hot vapors to form around the liquids and eventually ignition occurs. Therefore, the most important group within DMAZ to suppress the reactivity to become a hypergolic fuel, are the azides.<sup>16</sup> Results from this study indicate that the interaction between TMEDA/WFNA and TMEDA-DMAZ/WFNA may offer a viable bi-propellant replacement of a more hazardous and toxic combination (MMH/NTO).

Previously, studies of hypergolic material jet atomization characteristics have been based off of empirical models using adaptive mesh refinement (AMR).<sup>17</sup> Impingement of two cylindrical jets offers a great deal of advantages for spray atomization and sheet formation in liquid propellant engines.<sup>18-21</sup> As a result of the study, conclusions based on sheet formation and

material break-up were documented. Revealing that a sheet is formed perpendicular to the plane of the two jets and that the break-up of the sheet is dominant by the viscosity and surface tension effects. Depending on surface tension, Reynolds number, and Weber number; the sheet will form waves that propagate into small droplets farther downstream.<sup>17</sup> Although simulation and empirical models are great for sheet and mixture characteristics, it is often difficult to develop simulations of the ignition process, since several other factors can deter or enhance ignition. Several researchers have experimentally studied optimum mixing conditions for impinging jet configurations. According to Rupe, optimum mixing time occurs when the streams of the propellants are 45° degrees apart. Because lower impingement angles are desirable for optimum mixing time and higher impingement angles are desirable for turbulence induced mixing (90°), an angle of impingement was chosen to be 60° to allow for a balance of the two. With an impingement angle of 60° and properly spaced apart, the flow stream should form a perfect equilateral triangle from each nozzle exit as shown in Fig. 2. Furthermore, instead of momentum ratio, Rupe et al<sup>22</sup> found that when the product of the ratio of the mean velocity head of the two streams and the ratio of the diameters of the two streams is equal to unity, the mixture is at a maximum uniformity regardless of impingement angle.<sup>22</sup>

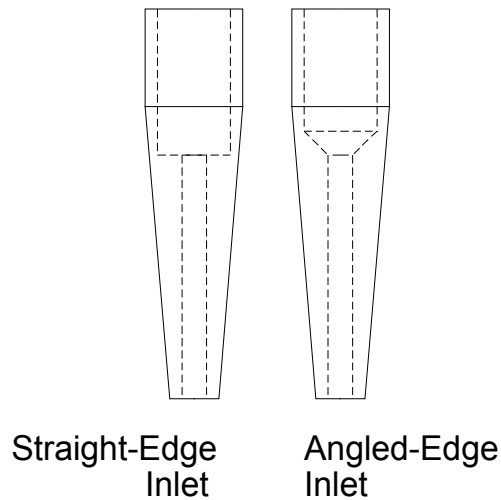


Figure 2. Schematic diagram of the injector configuration.

Although Rupe<sup>22</sup> suggests that the momentum ratios of each stream being equal do not provide optimum mixing, for the existing system, early experiments indicate to the contrary. Thus, for the preliminary optimization calculations to determine the injector diameters, a momentum ratio of 1.0 was chosen for optimum mixing to occur. At momentum ratios above or below 1.0 the mass distribution significantly changes. The mass flow moves in the direction of the higher momentum stream along the impinging plane. Also, in a study on optimum mixing for impinging jets, Riebling found that at higher mixture ratios and with a varying orifice area ratio from 1-8.3, the mixing factor forms a bell curve. At the top of the curve is a point where the highest mixing factor occurs. This point is where optimum mixing occurs for the two streams. Indicating that efficient mixing is dependent on the combination of the mixture ratio and orifice area ratio.<sup>23</sup> Jet velocities of the fuel and oxidizer streams were optimized based upon dynamic similarity and stoichiometry, i.e. momentum ratio and chemical reactivity (equivalence ratio). Equation 1 illustrates the definition of the momentum ratio for the current research and Eq. (2) exhibits the Rupe number.

$$\frac{M_{\text{TMEDA}}}{M_{\text{WFNA}}} = \frac{(\rho V^2 D^2)_{\text{TMEDA}}}{(\rho V^2 D^2)_{\text{WFNA}}} = 1 \quad (1)$$

$$\text{Rupe\#} = \frac{(\rho V^2 D)_{\text{TMEDA}}}{(\rho V^2 D)_{\text{WFNA}}} = 1 \quad (2)$$

## 5. Experimental Method of Approach

### 5.1 Injector Configuration

Based on concurrent orifice design studies within the MURI team by Fakhri et. al.,<sup>24,25</sup> a series of injectors has been designed to deliver the reactants to the impingement zone. Two injector contours were designed and tested: (1) straight edge inlet; (2) 120° angled inlet as shown in Fig. 2. From Fakhri's results, there is no significant difference between the type of inlet. Thus, angled inlets were chosen for all of the injectors due to simplicity in the manufacturing process. In order to realize the range of injector diameters that were required to achieve a broad range of stoichiometric and momentum ratios to optimized both chemistry and mixing, several calculations were performed. Figure 3 shows the dependence of momentum ratio (Eq. 1) and equivalence ratio on the oxidizer orifice diameters. The fuel orifice size was held constant at 0.020 in. Assuming ideal chemical reaction ( $\phi \sim 1$ ) and the jet momentum of each stream to be identical, the oxidizer orifice diameter was determined to be 0.065 in. These parameters were considered to be the baseline flow conditions.

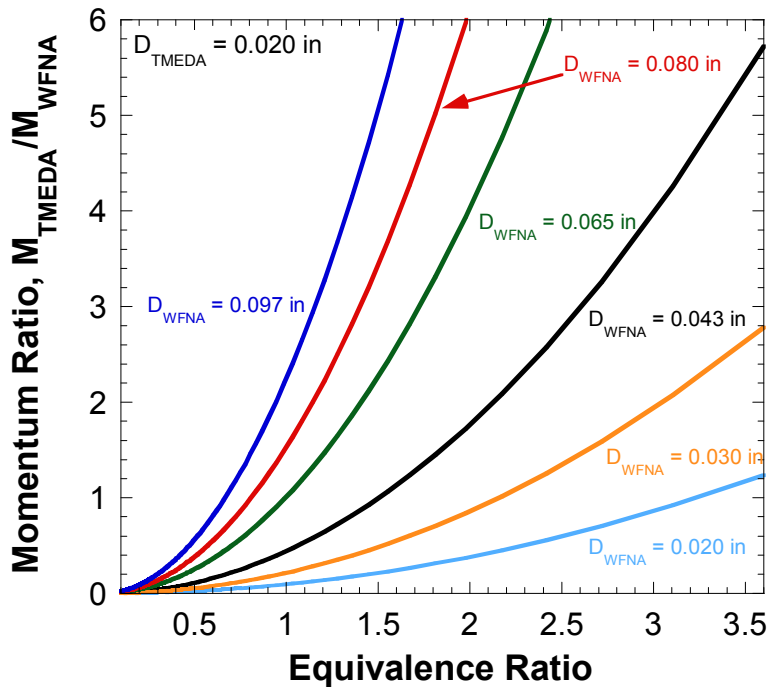


Figure 3. Effect of oxidizer jet diameter on momentum ratio and equivalence ratio.

As mentioned, all of the experiments conducted in this study employed injectors with angled inlets. The injectors were designed to have different length-to-diameter (L/D) ratios and orifice sizes while mounted in a universal housing assembly. Figure 4 shows several images of the injectors, orientation, and housing. This injector design allows a modular enclosure to enable

high pressure operation since the large dump chamber cannot sustain high pressure. A close-up view of the injector configuration is also given in the figure. The injectors are oriented at an impingement angle of  $60^\circ$  and the jet impingement point is located 5-mm from the jet exit, while the jet exits are positioned 5-mm apart, forming an equilateral triangular configuration. The L/D ratio of 20 was used for most of the experiments. The injector assembly (Fig. 5) allows a modular enclosure to enable high pressure operation since the large dump chamber cannot sustain high pressure.

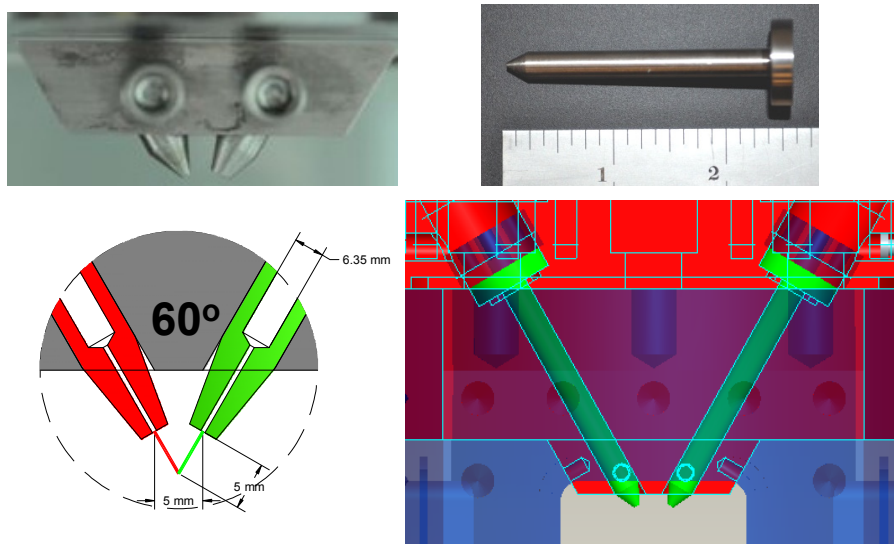


Figure 4. Schematic and photographs of the injector assembly.

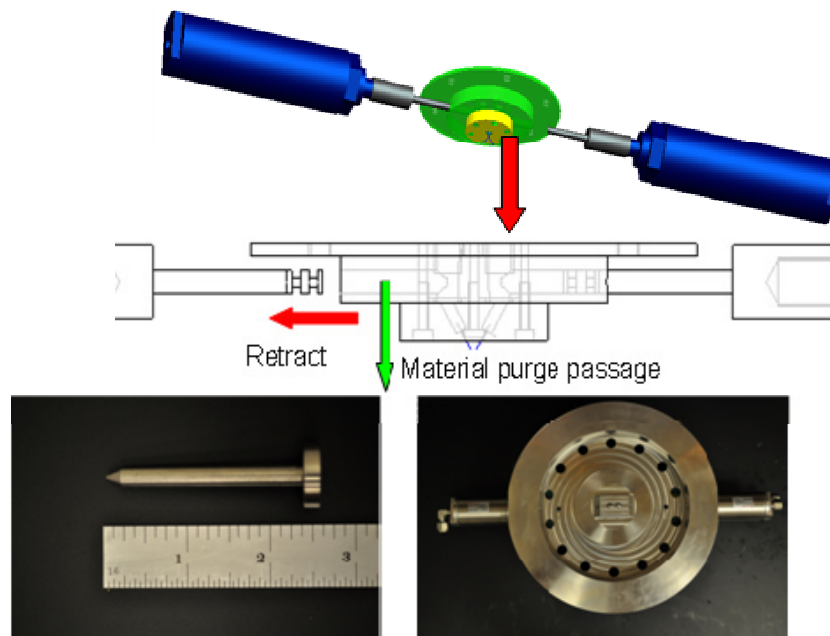


Figure 5. Schematic of the injector assembly purge passage.



### 5.1.1 Inert Impingement Results

A series of experiments was conducted with inert materials to examine the evolution of the impingement location as well as the fan. In order to identify each individual stream and to evaluate mixing degree, each water stream was doped with a food dye. The resulting fan shows an atomized mixture of the two streams. In Figs. 6a and 6b, two water streams with food dye coloring impinge against one another. Fig. 6a is a captured image of the impingement location. The stream which represents the oxidizer was colored green (right side injector) and the fuel stream was colored red (left side injector). Fig. 6b is a captured image that shows the resulting fan of the atomized mixture of the two streams. Neither color is visible in the image. This viewpoint is  $90^\circ$  from the image in Fig. 6a.

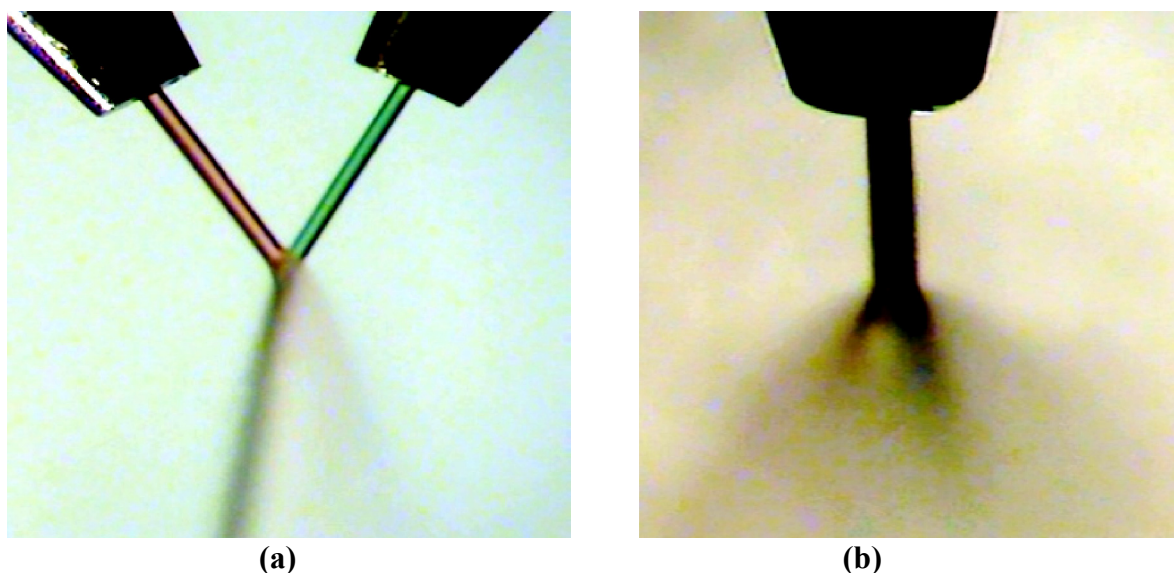
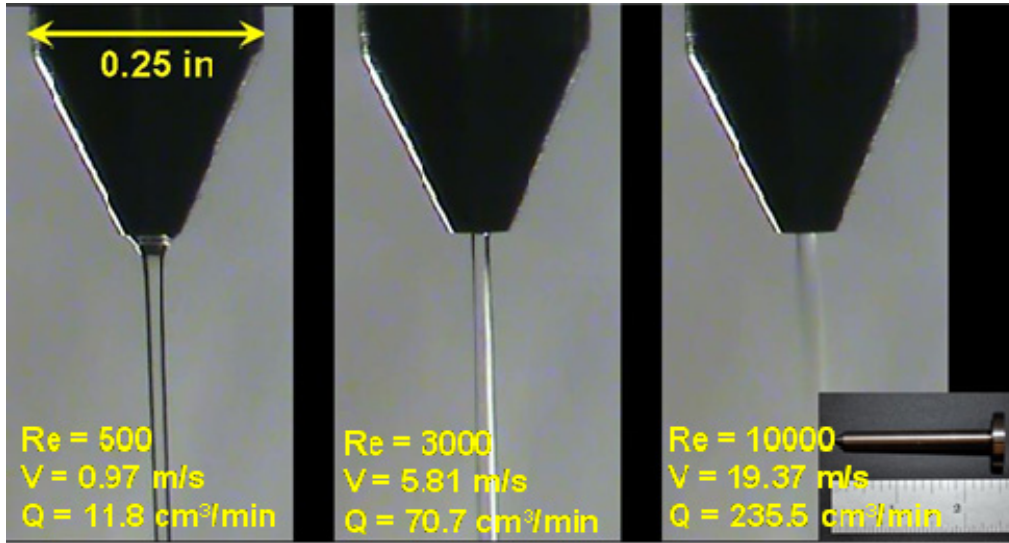


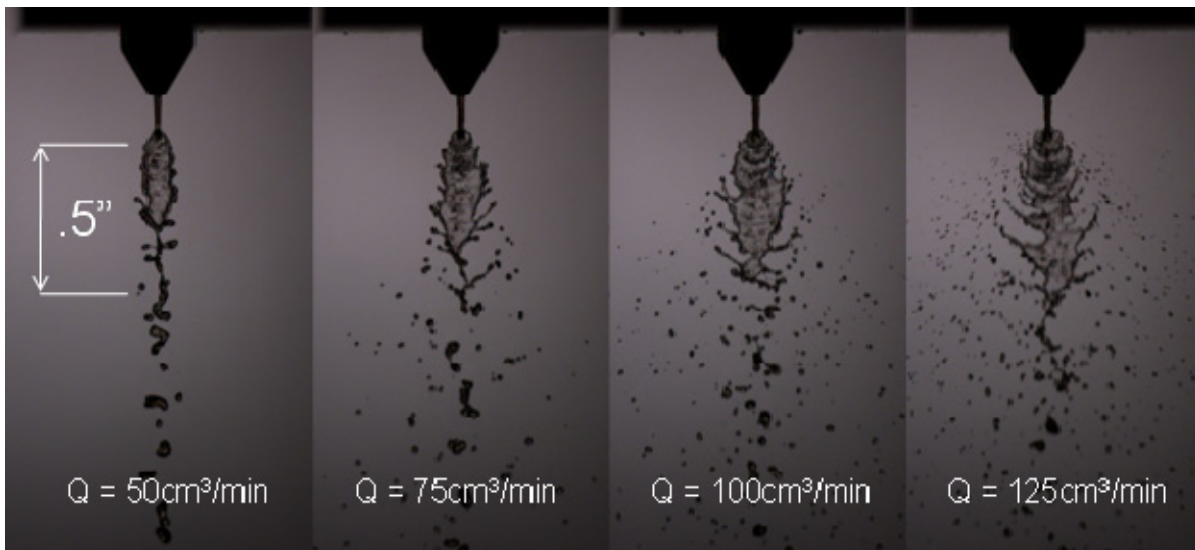
Figure 6. Impinging water jets: (a) impingement angle of  $60^\circ$ , (b) fan created by jet impingement.

### 5.1.2 Single Element Characterization with Liquid Water

Each injector element was characterized independently using water and an impingement mode to examine the flow details of the specific injector (Fig. 7). The images were captured using a Phantom V310 high-speed color camera at a framing rate of 6000 fps and a resolution of 512x512. As the flow rate is increased, the Reynolds number ( $Re$ ) and the Velocity ( $V$ ) increase proportional to the change in flow as expected. At lower flow rates the fluid produces laminar flow (as seen in image Fig. 7a on the far upper left). Higher flow rates produced turbulent flow (Fig. 7a, third image, the flow lines become less evident due to higher velocities). The Reynolds number, velocity, and volumetric flow rate were calculated for both configurations. Figure 7b represents the breakup lengths of impinging jets using water at different flow rates ranging from 50 to 125 cc/min. As the flow increased, the core jet elongated and smaller, finer particles became more evident.



(a)



(b)

Figure 7. Captured images of single and impinging injectors using water as the liquid.

### 5.1.3 Gel Preparation for Inert Materials

Gelled water streams, surrogate fuels, and oxidizers were used to characterize injector flow velocity, volumetric flow rate, Weber number and Reynolds numbers, gel break-up length, and system response times. Carbopol 981A and silica were used to create the gels, which are inert, and will allow for safe handling and testing. Initially, the gels were prepared with tap water. The gel characteristics were very good having no bubbles after gelling. The lack of bubbles present was attributed to the salt in tap water, which was important since the gelling process was affected. Therefore, gels comprised of distilled and de-ionized water were used for comparison. Images of the impingement characteristics of the sprays are shown in Fig. 8.

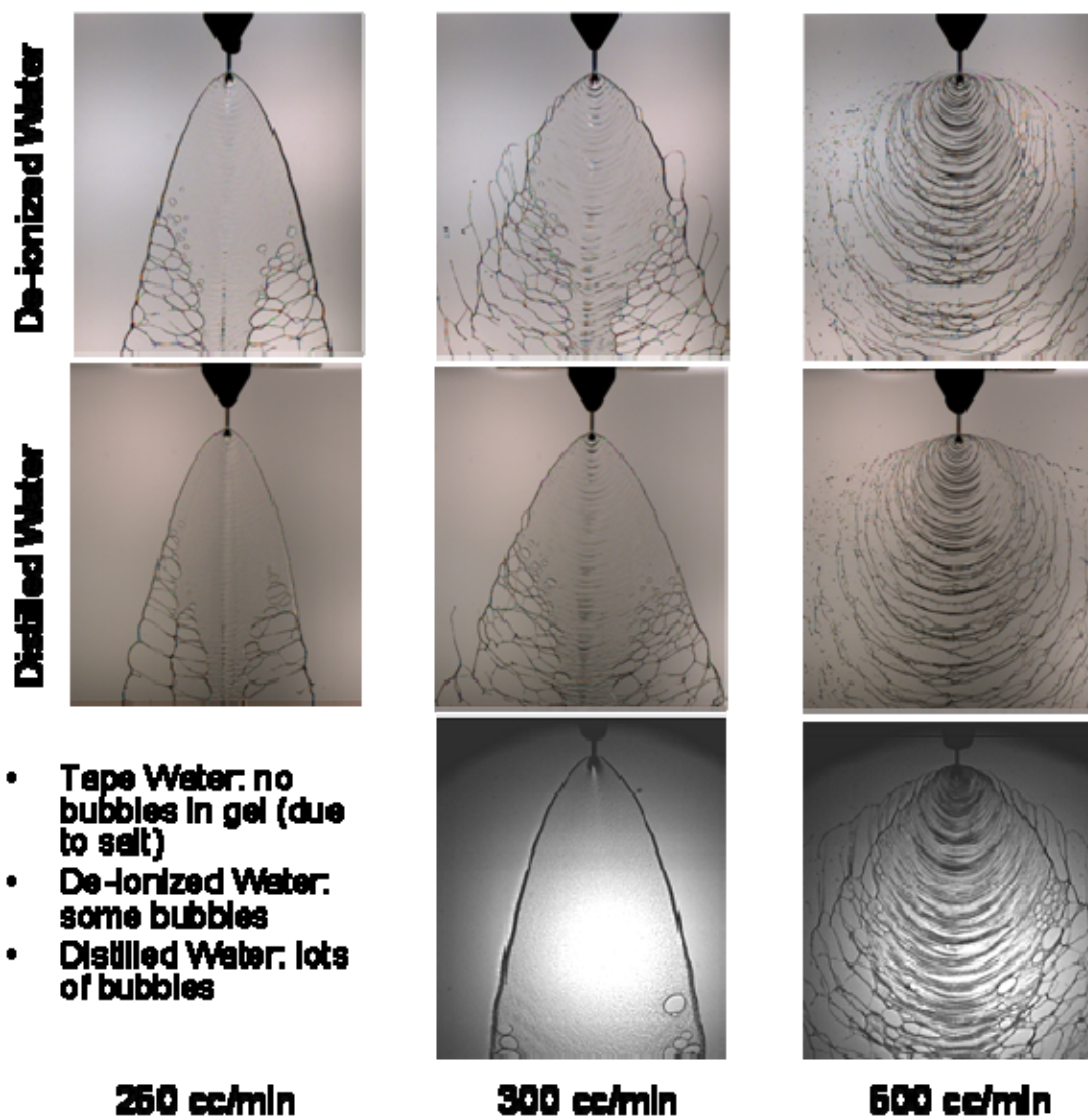


Figure 8. Images of the effect of water type of fan characteristics using Carbopol gels.

Although the tap water based gel created a bubble free gel, the spray characteristics were significantly different from both DI and distilled water showing less break-up at the same flow rate. However, there was no significant difference in performance between DI and distilled water. Thus, distilled water was chosen to continue the testing series. All gels were prepared using distilled water and 5% (by mass) of Carbopol 981. The water was mixed using a paddle mixer at approximately 300 rpm while the gelling agent was added slowly, which avoided agglomeration and bubble introduction. After all of the gelling agent was added, the mixer speed was increased to approximately 700-1000 rpm for 5-10 minutes, adjusting speed to reduce bubble introduction. The water-Carbopol mixture was then placed in vacuum chamber for approximately 10 minutes and lightly agitating the container to promote bubble rise and breakage. The pH of the gel was measured before addition of NaOH and progressively until mixture reached  $7.0 \pm 0.3$  while mixing at approximately 1000-3000 rpm (also careful to avoid bubble introduction.) as prescribed by the gelling agent manufacturer. The final mixture of water and 5wt% Carbopol yielded a gel consistency similar hair gel.

Figure 9 to 15 are captured images of the evolution the jets impinging on one another. This is a very important characteristic to understand for controllability and accuracy of the flow times. Figures 9 to 11 represent images of the impinging jets at 90° views. In each figure, images *a* and *b* show the fan size, with *b* being a close-up view. Image *c* in the figures shows the actual impingement of both streams. Overall, the gel delivery system responds rather well being such a large system. As the flow is increased, the fan becomes larger and larger in diameter due to the increased velocity and mass of each jet until the core flow begins to atomize. Furthermore, the core flow elongates as shown in the high-speed images. Atomization is not observed until the jet flow rates reach approximately 250 cc/min, which in this case, the break-up occurs at the tail end of the fan.

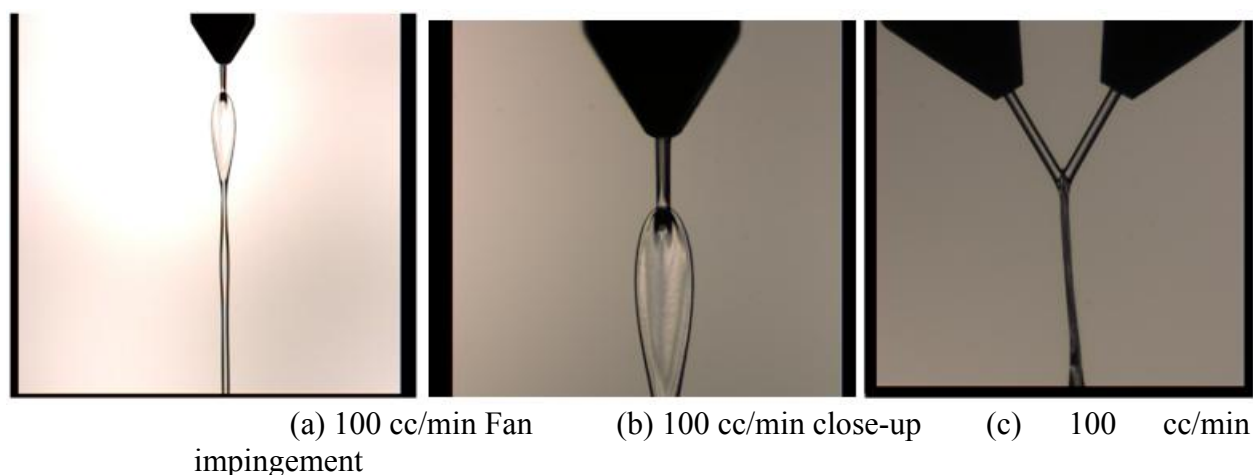


Figure 9. High-speed images of the fan and impingement gel streams at 100 cc/min for each stream.

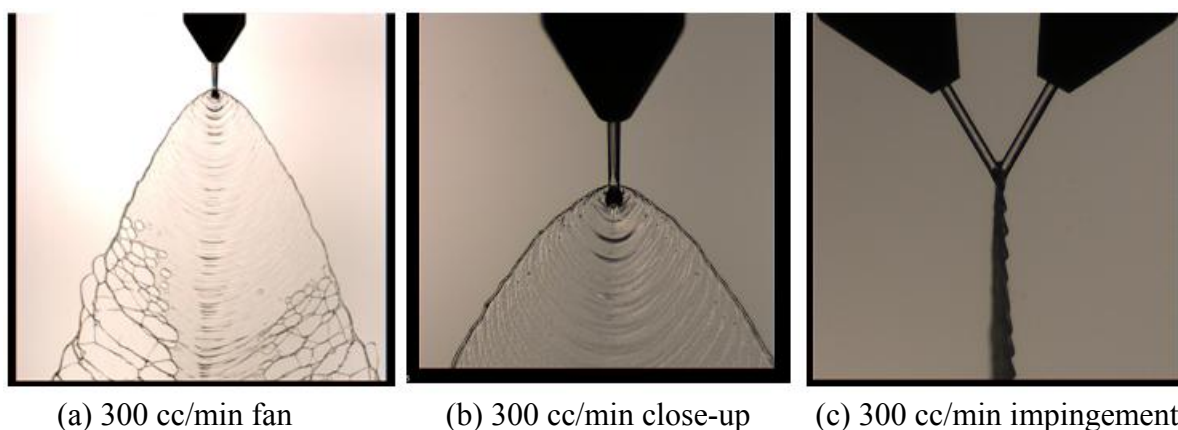
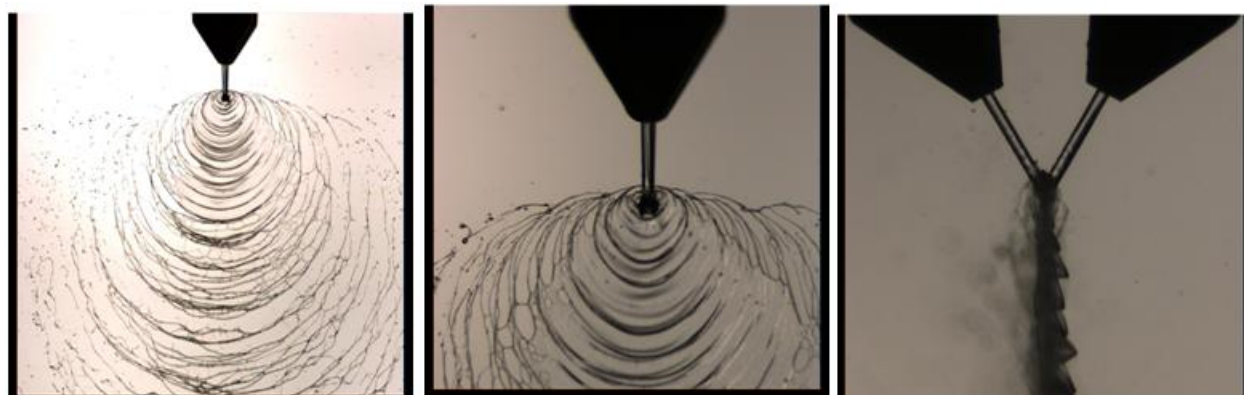


Figure 10. High-speed images of the fan and impingement gel streams at 300 cc/min for each stream.





(a) 500 cc/min Fan

(b) 500 cc/min close-up

(c) 500 cc/min impingement

Figure 11. High-speed images of the fan and impingement gel streams at 500 cc/min for each stream.

Figures 12 to 15 exhibit the evolution of the high speed gelled jet exiting the injector. Examining the entire flow rate range, the jets fully impinge on one another in 40 ms at the slowest flow rate and as short as 9 ms at the highest flow rate. Close to the jet exit, the gel surface tension prevents the stream to exit strongly until the stress is exceeded. The slow flows reduce droplet generation. In order to obtain smaller droplets, high flow velocities are required.

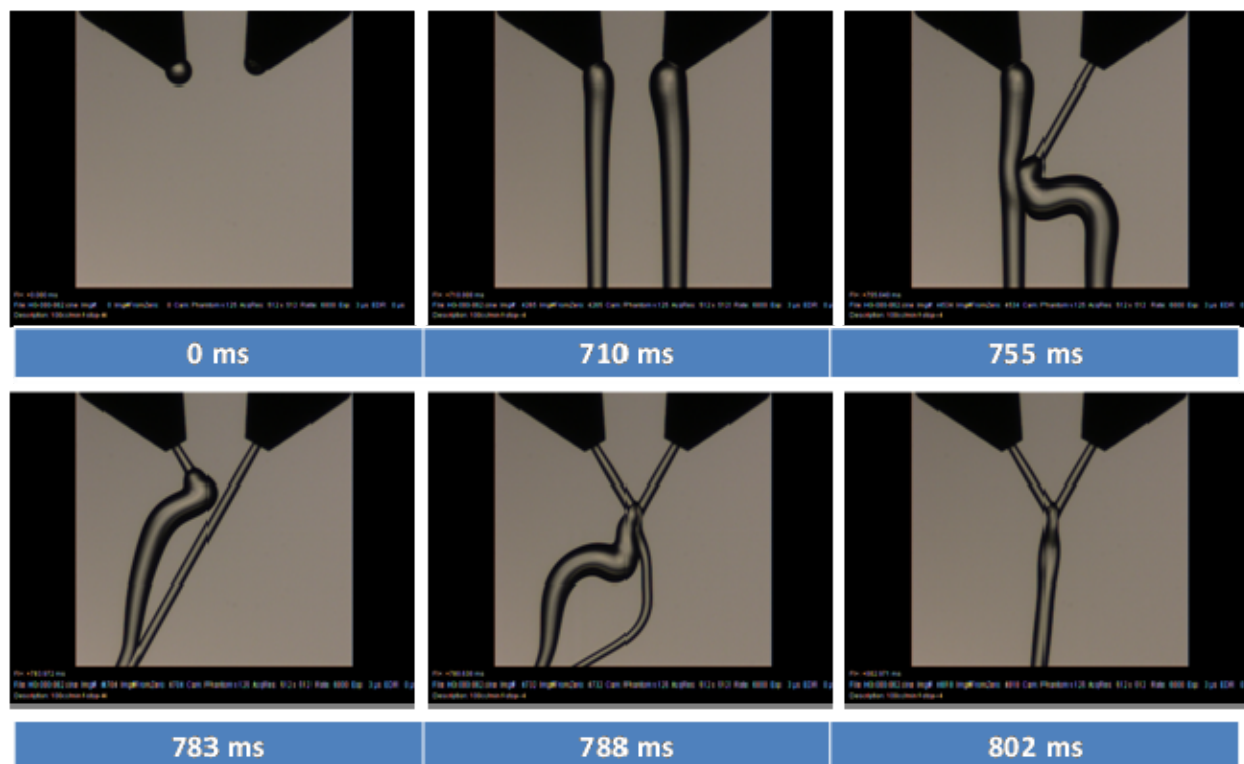


Figure 12. Sequence of images of the gel stream evolution at a flow rate of 100 cc/min.

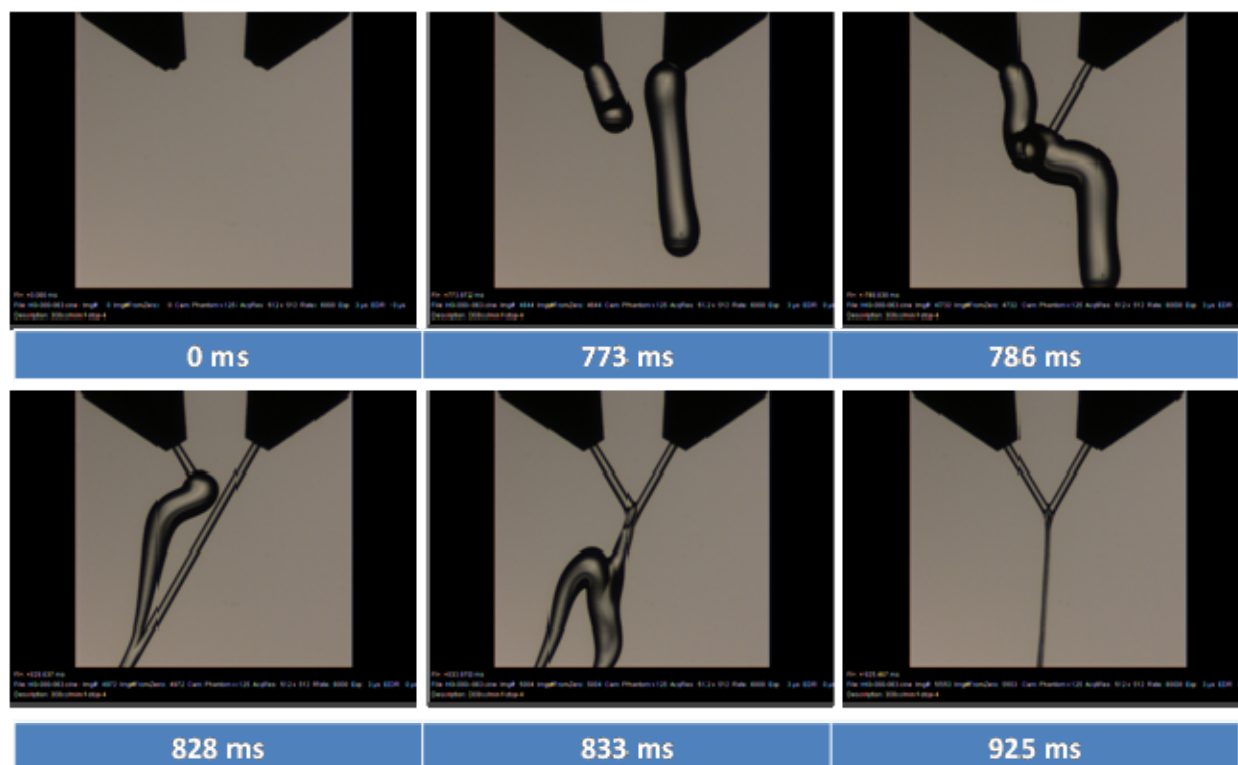


Figure 13. Sequence of images of the gel stream evolution at a flow rate of 300 cc/min.

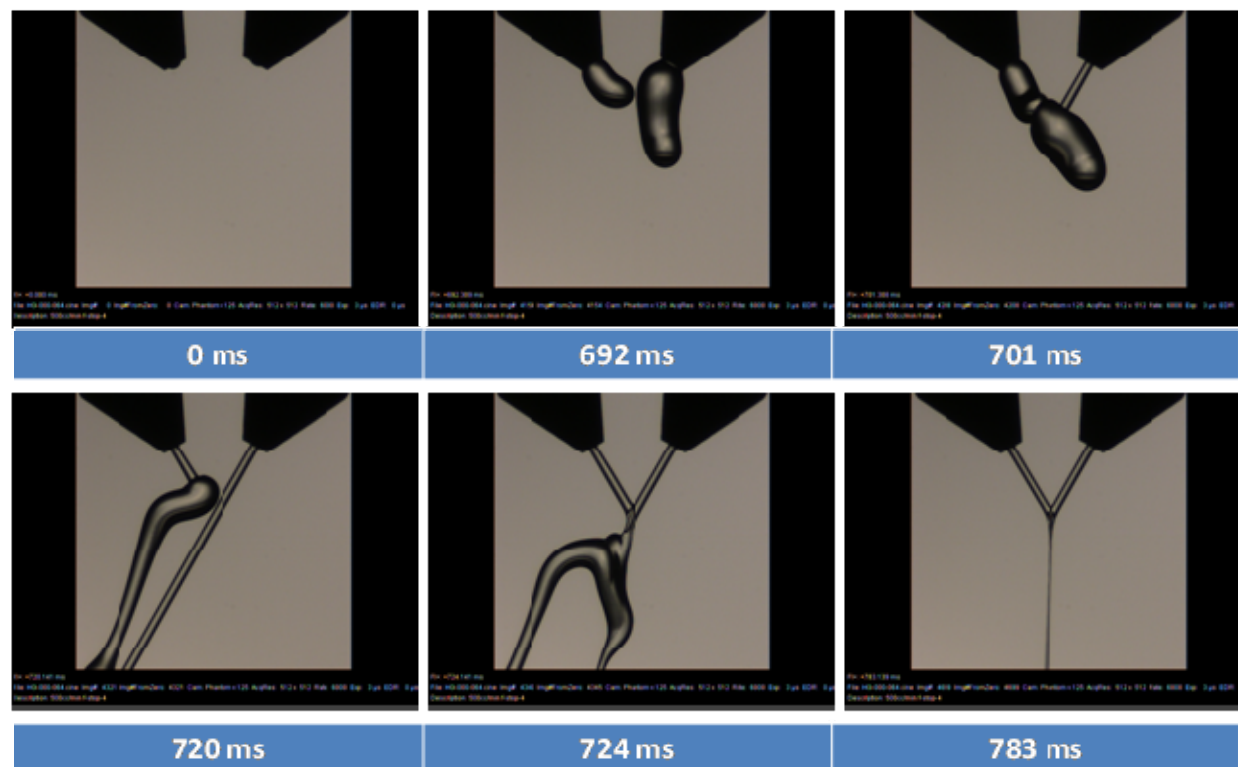


Figure 14. Sequence of images of the gel stream evolution at a flow rate of 500 cc/min.

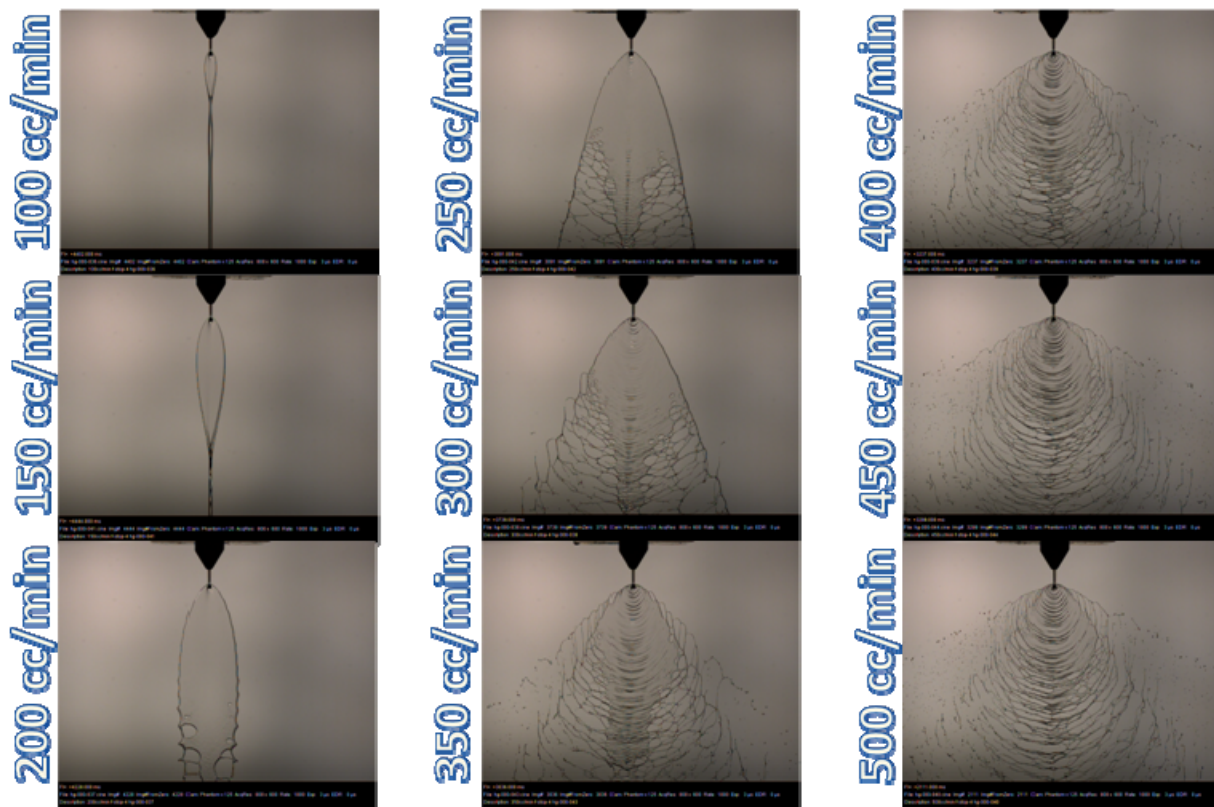


Figure 15. Series of images of jet atomization for flow rates ranging from 100 to 500 cc/min.

#### 5.1.4 Gel Preparation for Reactive Materials

The gelling procedure for reactive materials, i.e. TMEDA and WFNA, are substantially different than the cases using water. In the water gels, a chemical reaction occurs to create the gel; thus no particulates are in the final mixture. In reactive materials, it is mandatory for no chemical reactions to occur during mixing, gelling, or storage since the stability of the reactive material is important. With this in mind, inert particulates have to be introduced into the reactant materials. Cab-O-Sil (silica dioxide,  $\text{SiO}_2$ ) was chosen as the gelling agent. Silica dioxide is extremely inert with many reactive materials. Moreover, there are various grades of Cab-O-Sil that characteristics of the material are different such as surface area, surfactants, etc. Figure 16 includes photographs of the volumetric proportions of the gelling agent (Cab-O-Sil) and the liquid. Figure 17 shows the ignition delay results as a function of gellant added percentage examined by Wang and Thynell. Their goal was to determine a gellant percentage that gel consistency was adequate, while the amount of inert material introduced into the reactant mixture was not excessive to influence the ignition delay. All gels were prepared under a fume hood using 4.5wt% (EH-5) for fuels and 3wt% (M5) for oxidizers. The reactant material was mixed using a paddle mixer at approximately 750 rpm while the gelling agent was added in one-minute increments ( $\sim 20\text{wt}\%$  of gellant amount), which avoided agglomeration and bubble introduction. The final gelled mixtures (shown in Figure 18) is the result after all of the gelling agent was added and subsequently placed in a sonication bath for 20 minutes.



CAB-O-SIL (EH-5)

Liquid

Cab-O-Sil	Surface Area
EH-5 (fuel)	385 m <sup>2</sup> /g
M-5 (oxidizer)	200 m <sup>2</sup> /g

Figure 16. Photograph of the volumetric proportions of the gelling agent (Cab-O-sil) and the liquid.

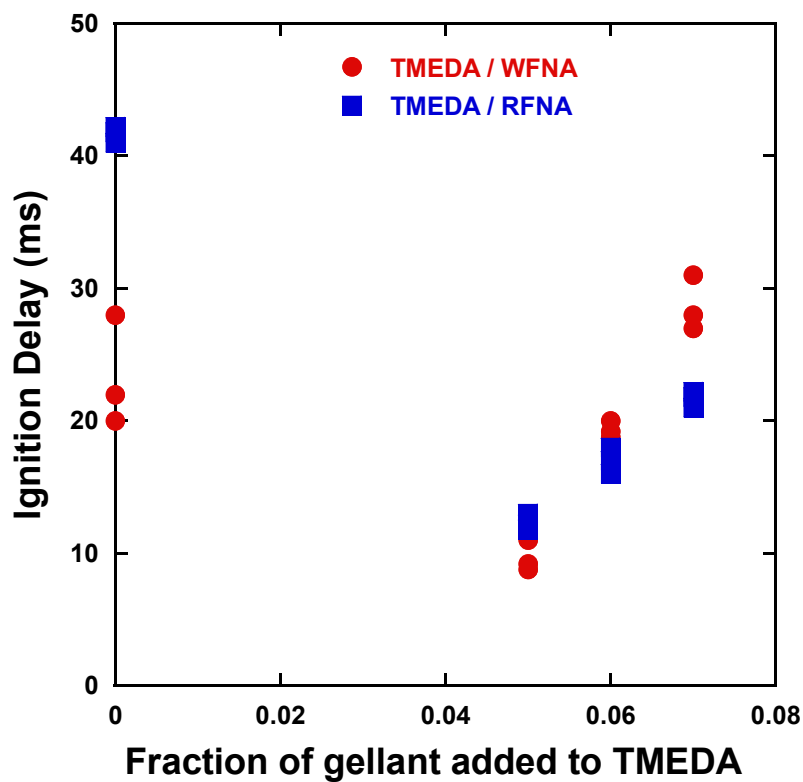


Figure 17. Drop test results of gelled TMEDA with WFNA and RFNA.



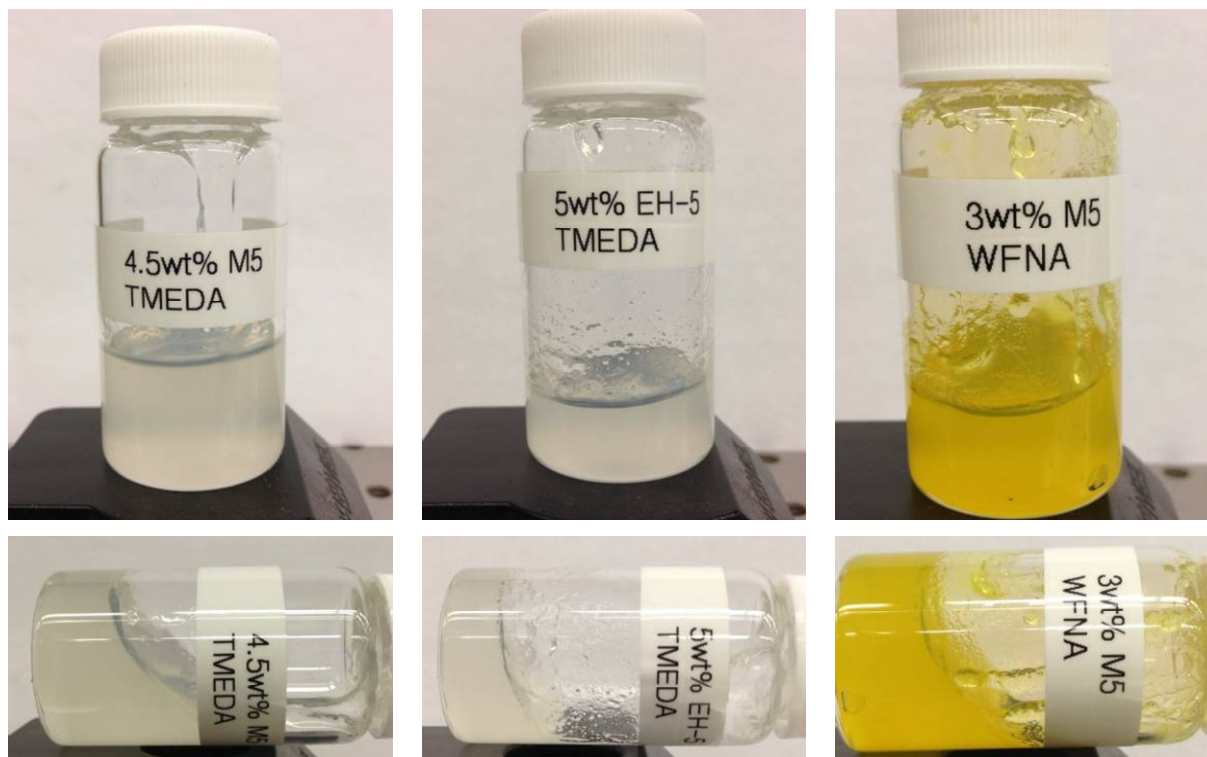


Figure 18. Images of various gelled reactants including TMEDA (at two different Cab-O-sil wt%) and WFNA.

## 5.2 Reactant Delivery System

An injector apparatus has been designed and manufactured to study the characteristics of the hypergolic propellants. The apparatus, based on modeling and simulation results, has been designed and tested for specific propellant formulations and flow conditions. The system employs a modular injector housing to allow for different injector configurations. The reactants are delivered individually through the injector to the impingement location via a high-thrust (6000 lb<sub>f</sub>) linear actuator pushing the piston of a stainless steel syringe at a constant velocity by regulating the force applied to the syringe (reservoir). Since the linear velocity of the actuator is regulated, the volumetric flow rate of the liquids is controlled. Although the LabVIEW program is used to drive the actuators, the actual movement of the linear drives is controlled by two Agilent function generators. These function generators supply a square wave to the actuators which can start and stop the actuator function for a specific duty cycle for very accurate time durations. The system is also equipped with high-precision timers to allow for delays in each stream to examine reactant lead times. A typical test run time was 1.5 seconds. The reactants flow through their respective injector and impinge on one another in a large volume dump chamber as shown in Fig. 19. The dump chamber is continually evacuated with a high flow exhaust fan and a continuous stream of water to remove any combustion products.

The active monitoring system with pressure and temperature sensors in each stream allows instantaneous purging of the fuel and oxidizer if the pressure or temperature exceeds desired limits due to clogging. Specific fuel and oxidizer flow rates are inputted in the program and the linear actuator velocity is adjusted to a velocity which provides the desired volumetric flow rate of the reactant. Each reactant stream is controlled and monitored separately.

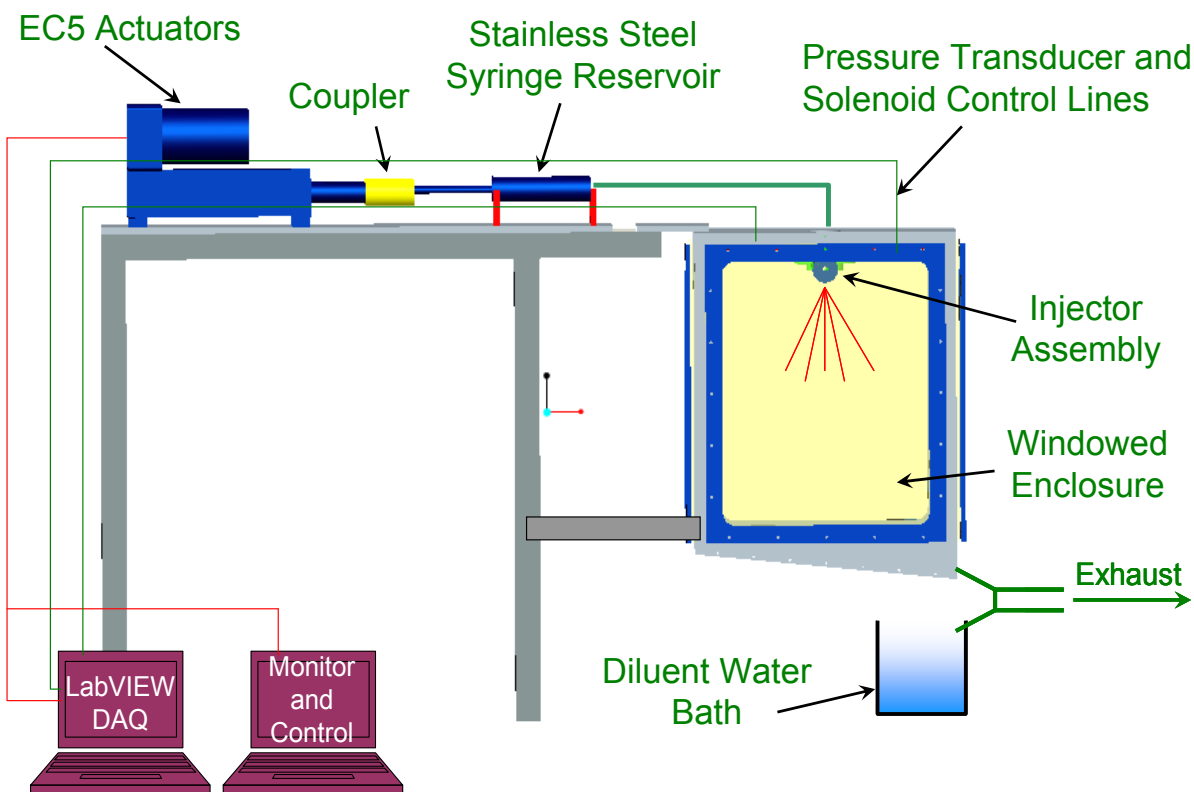


Figure 19. Schematic diagram of hypergolic experiment.

To prevent flames from extending beyond the desired ignition zone and to dilute any unburned reactants, a water diluent system has been incorporated. This water diluent system serves both as a safety extinguishing system and cooling system. The dump chamber is a 26" × 26" × 22" stainless steel welded rectangular chamber with four o-ring sealed glass windows on each side. The ignition and combustion event was captured using a color Phantom V310 high speed camera at 2,000 fps. The camera is equipped with Nikon Nikkor 50mm lens and is placed about 12 inches away from the impingement point, perpendicular to the fan.

### 5.3 Curved Surface Impingement

In a study by Coil<sup>3</sup>, a flat ceramic plate at a 45° angle was placed at the impingement point to promote reaction and ignition. Due to the presence of the ceramic plate, the ignition delay was accelerated. As an addition to the tests that were performed for this study and to initiate further mixing of the fuel and oxidizer, a curved quartz-glass surface was constructed and placed at the exit of the two injectors. This curved glass surface should simulate a chamber wall impingement between the chemicals (see Fig. 20). The chamber wall simulation should promote mixing between the chemicals and therefore could result in lower ignition delay times. The curved surface assembly consists of a circular quartz piece (1/4 of a circle in cross-section) that begins at the impingement point and ends at a point farther down along the circular plane.

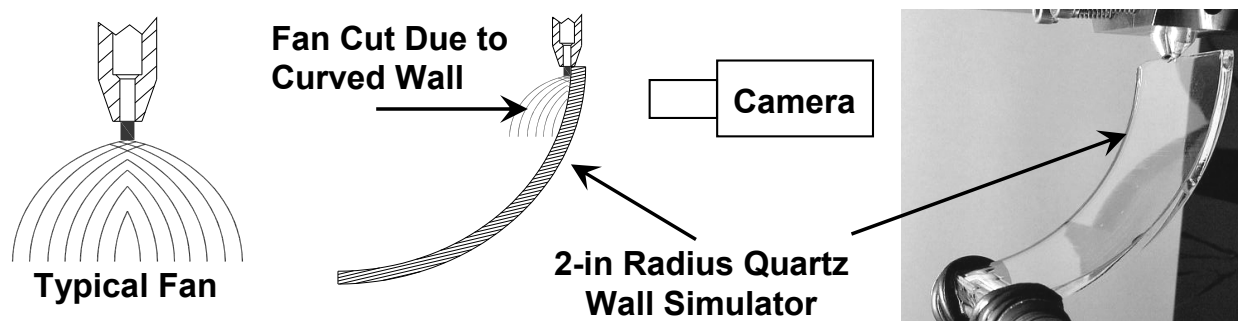


Figure 20. Diagram of the curved impingement wall configuration.

For the tests, the camera is positioned at the back side of the glass, to protect it from any chemicals that may splash during the test. It also is positioned at this location so that vapor and fragments from the test do not obstruct the view for the camera during the test. To the left in Fig. 20 is a diagram showing the fan that is created by a pair of impinging jets without the use of the curved surface. The center image indicates how the fan is affected by the curved surface. As one can see, the right side of the fan is affected by the chamber wall impingement. The curved surface was then incrementally moved 1-mm at a time away from the injector exit until the curved surface was 6-mm away from the impingement point. This will offer a different fan effect at every increment.

#### 5.4 Propellant Formulation and Reservoir Filling Process

To characterize the ignition process, several chemical combinations were considered: several fuels and two oxidizers. The two fuels were N,N,N',N'-tetramethylethylenediamine (TMEDA) and dimethyle-2-azidoethylamine, while the oxidizer was white fuming nitric acid (WFNA). Most of the tests conducted, consisted of pure TMEDA and WFNA. WFNA was chosen over red fuming nitric acid (RFNA) for most of the testing because it is less toxic and has very similar performance. Table 1 includes several key properties of the fuels and oxidizer used in this study.

**Table 1. Properties of selected fuels and oxidizers.**

Name	Chemical Formula	Molecular Weight	Density [g/cc]	Viscosity [N-s/m <sup>2</sup> ]	Boiling Point [°C]
TMEDA <sup>1</sup>	C <sub>6</sub> H <sub>16</sub> N <sub>2</sub>	116.21	0.775	1 × 10 <sup>-3</sup>	120-122
DMAZ <sup>2</sup>	C <sub>4</sub> H <sub>10</sub> N <sub>4</sub>	114	0.930	2 × 10 <sup>-3</sup>	135
WFNA <sup>3</sup>	HNO <sub>3</sub>	63.01	1.400	0.9 × 10 <sup>-3</sup>	100
RFNA <sup>3</sup>	HNO <sub>3</sub>	63.01	1.480	0.9 × 10 <sup>-3</sup>	100
MMH <sup>1</sup>	CH <sub>6</sub> N <sub>2</sub>	46.072	0.874	<sup>4</sup> 0.86 × 10 <sup>-3</sup>	87.5

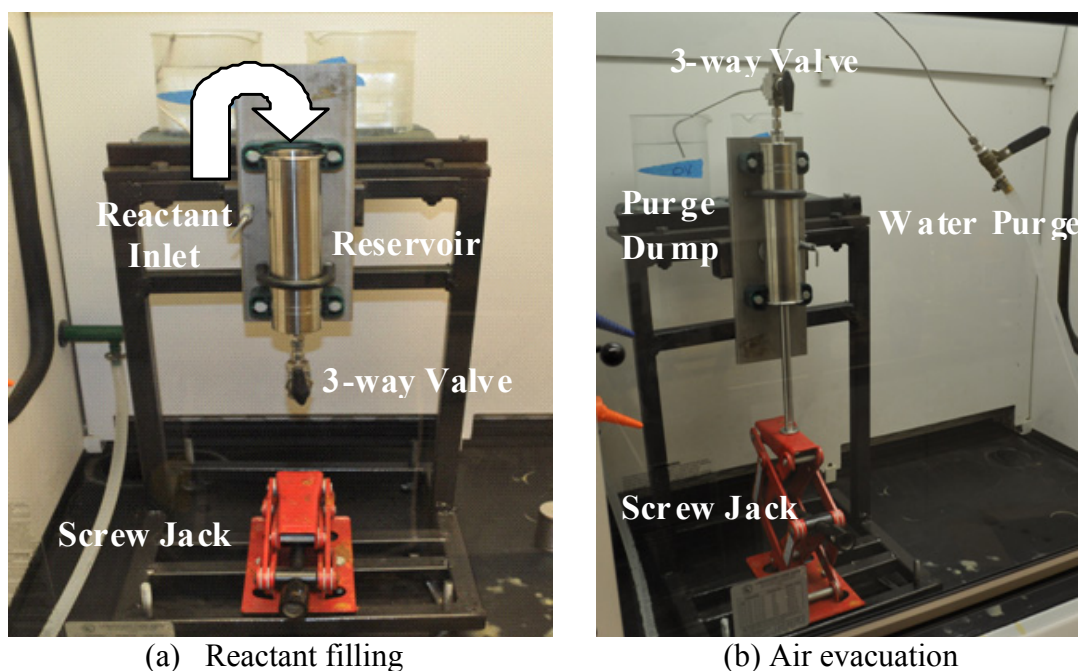
<sup>1</sup>ICT database, 2000.

<sup>2</sup>MSDS from MACH I

<sup>3</sup>MSDS from Sigma Aldrich

<sup>4</sup>ARCH Lonza Website (major supplier of MMH)

Each reactant stream has its separate reservoir. The reservoirs consisted of Harvard Apparatus stainless steel syringes that were capable of holding 250 mL of liquid material and could handle the high thrust/pressure (1,500 psig) that were applied during testing. The stainless steel syringes were removed from the cradle on the experimental system to the filling station located in a fume hood. After each test, the syringes were thoroughly cleaned with water and dried before being re-filled with their respective chemicals. The O-rings were checked and/or replaced to ensure a tight fit around the piston. The syringe is then placed into the filling harness and held by a C-style clamp as indicated in Fig. 21a. The chemicals, 200ml of fuel or oxidizer, are then poured slowly into the syringe with a beaker, leaving a small amount of volume. The O-ring sealed piston is greased and then placed in the open end of the syringe and loosely compressed.



(a) Reactant filling

(b) Air evacuation

Figure 21. Photographs of the filling/evacuation station configuration during reactant filling and air evacuating processes.

The syringe is then rotated 180° to remove any air inside of the reservoir and then the piston is moved using a manual screw style jack shown in Fig. 21b. A three-way valve located at the exit of the syringe is opened to allow any excess air to escape up through the fume hood. Once the air is evacuated, the valve is purged with water to ensure all escaped chemicals are released from the syringe while closing off the main pathway to the bulk material. The syringe is re-installed on the experimental system. Each test duration is usually 1.5 seconds, thus approximately 15 experiments per fill can be conducted depending on the flow rates of the streams. Once the fuel and oxidizer are placed on the system, they are connected to the injectors with a 1/8" stainless steel line. The syringes are secured and the actuators are pushed against the syringe piston. The actuators will push any remaining air out of the lines connected to the injectors to ensure a quick response once the test is initiated. Once the lines have been cleared of all existing air, the hypergolic system is locked inside a well ventilated testing chamber which keeps any fumes or unexpected reactions away from operating personnel.



## 6. Results and Discussion

Over 300 experiments were conducted to investigate the ignition delay time of blends of TMEDA and DMAZ fuels (both gelled and non-gelled) combusting with WFNA or RFNA (gelled and non-gelled) oxidizers. Results include ignition delays of the hypergolic combinations as a function of momentum ratio, injector diameter, equivalence ratios, fuel composition, L/D ratio, non-gelled or gelled, and fuel / oxidizer volumetric flow rates. The jet velocity of the fuel stream,  $V_{\text{TMEDA}}$ , ranged from 8 to 66 m/s yielding a Reynolds number ranging from 1,600 to 30,000, while the jet velocity in the oxidizer stream,  $V_{\text{WFNA}}$ , ranged from 2 to 60 m/s yielding a Reynolds number from 2,400 to 40,000. In order to determine the ignition delay for each test, post-processing was required on the high-speed video. The lights in the cell were left on to provide enough ambient light to capture the exact time that the oxidizer and fuels streams impinge on one another prior to ignition. The time at which this impingement occurs is considered time zero ( $t_0$ ) as shown in Fig. 22. Thus, the ignition delay time is defined as the time duration between first impingement ( $t_0$ ) to the time that first light occurs ( $t_{\text{ign}}$ ). Figure 22 is a series of images showing the critical times during the ignition event. For this particular test, once the two streams impinge, 11.5 ms elapsed and the mixture is not ignited. At time = 16 ms, first light has occurred, which the ignition delay can then be determined. The figure has both monochrome and color images, with one image being shown in both. This illustrates how the image had to be adjusted to see impingement prior to ignition. The dump chamber windows and injectors were thoroughly cleaned after each tests to ensure adequate viewing.

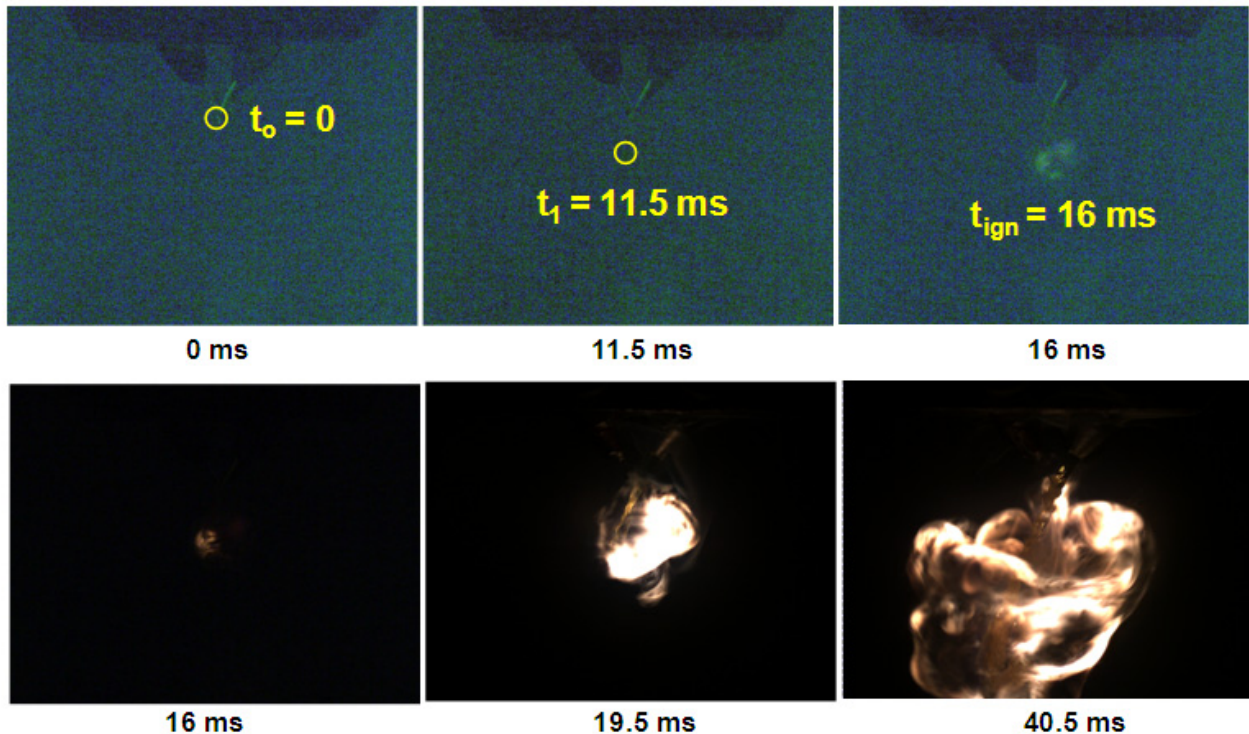


Figure 22. Series of captured images of the impingement and ignition processes of TMEDA and WFNA.

### 6.1 Effect of Volumetric Flow Rate and Oxidizer Type

The effect of volumetric flow rate is essentially the amount of chemical input introduced in the impingement region. The fuel (TMEDA) stream volumetric flow rate ranged from 100 to 800 cc/min and the oxidizer (WFNA/RFNA) stream ranged from 213 to 1929 cc/min. Various combinations of these rates were tested to examine the effect of momentum ratio and equivalence ratio as well. Figure 23 shows the ignition delay times as a function of fuel volumetric flow rates for WFNA as the oxidizer and Figure 24 displays the delays for RFNA as the oxidizer. In each of these tests, there were no fuel or oxidizer leads, the momentum ratio was fixed at 1, and the equivalence ratio was 1. For an equivalence ratio of 1, the corresponding oxidizer-to-fuel ratio was 4.35. The points on the graph represent at least 3 repeat tests at each condition. The ignition delays for repeat tests were averaged and represented as a single point including error bars. The general trend indicates that as the chemical input is increased, the ignition delay decreases. This can be attributed to more vigorous mixing due to the increase in Reynolds number for each stream. For the baseline case (213 cc/min of TMEDA and 513 cc/min of WFNA), the average ignition delay time was approximately 17 ms. The 213/513 fuel-to-oxidizer combination was chosen as the baseline case due to the calculations shown previously that this specific combination produces a momentum ratio and an equivalence ratio of one for a reasonable fuel injector size of 0.020 in and oxidizer injector size of 0.065 in. Injectors much smaller than 0.020 in are very difficult to manufacture. A significant 3.5 ms drop was observed in ignition delay time from the 300/723 combination to 513/1237 combination. It is believed that the ignition delay time will continue to decrease until a critical flow combination where the ignition point will be too strained to promote ignition and the residence time of the two flows is too short.

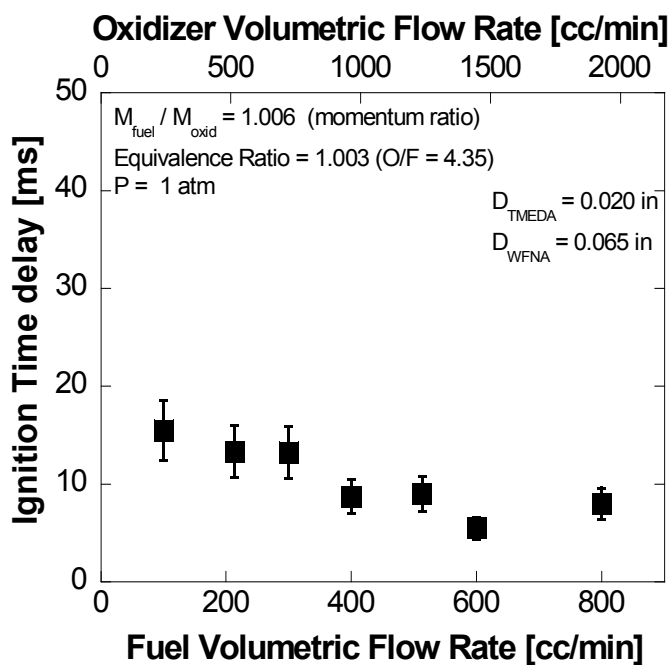


Figure 23. Ignition delay as a function of total flow rate.

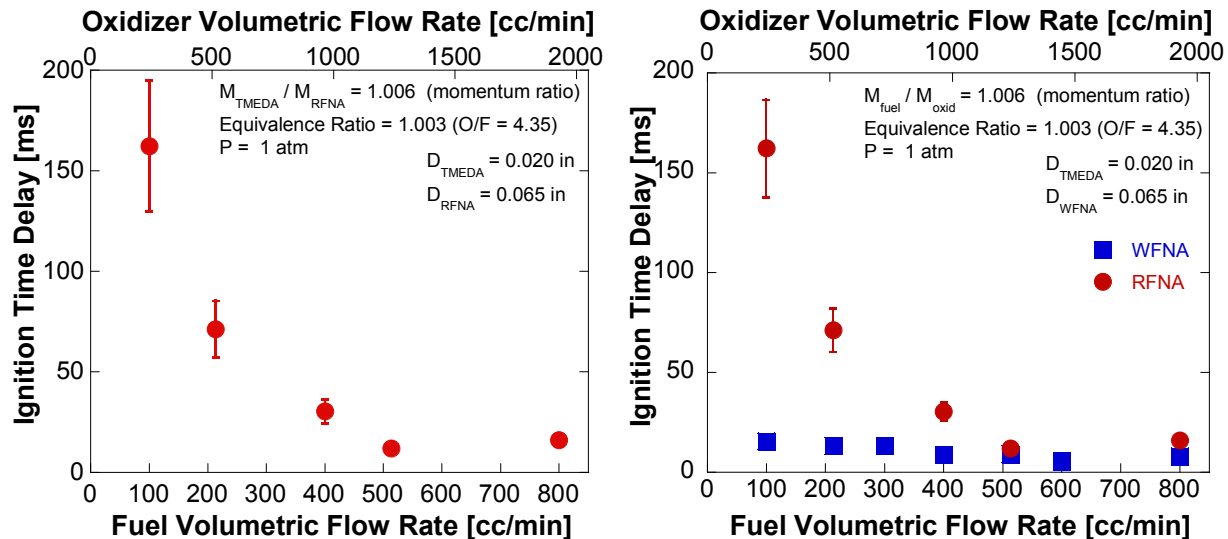


Figure 24. Influence of oxidizer type on ignition delay for various flow conditions.

## 6.2 Effect of Momentum Ratio and Equivalence Ratio

The WFNA injectors that were analyzed were; 0.020, 0.030, 0.043, 0.065, 0.080, and 0.097 in. Each of these injectors having a specific momentum ratio of 0.095, 0.215, 0.44, 1.006, 1.527, and 2.26, respectively. Ignition delays as a function of momentum ratio ranges from 16.5 to 23.5 ms at the conditions described above. For the range examined, the shortest ignition delay occurs at a momentum ratio of 1. This result is in contrast to the earlier experiments conducted by Rupe *et al.*<sup>22</sup> The discrepancy may be due to the limited momentum ratio range conducted in this study.

Injector sizes were varied in both the TMEDA and WFNA stream to achieve the desired momentum ratio as a function of equivalence ratio. Injector orifices ranged from 0.010 to 0.097 in. Figure 25 shows that as momentum ratio is increased, ignition delay time is decreased for a variety of equivalence ratios, which suggests that the deficiency in chemical stoichiometry can be somewhat remedied if the momentum ratio of the reactants is sufficiently high to overcome the lack of oxidizer required for ignition. This further reinforces that the mixing is more important than the chemical composition for the spray during the ignition process. At fuel rich conditions ( $\phi = 5.8$ ) and a momentum ratio of 2.4, the ignition delay is over 50 ms. As the momentum ratio of the same stoichiometry is increased to nearly 34, the ignition delay is reduced to 22 ms, which is a factor of 2.5. reduction. At equivalence ratios of 3.2 and below, the equivalence ratio has little effect on the ignition delay time. At equivalence ratios equal to 1 and 3.2, the ignition delay times show a small variation between 15-18 ms. Although equivalence ratio may have greater effects on ignition delay times at higher ratios, it appears that momentum ratio had the greatest effect on time delays within the conditions that were examined.

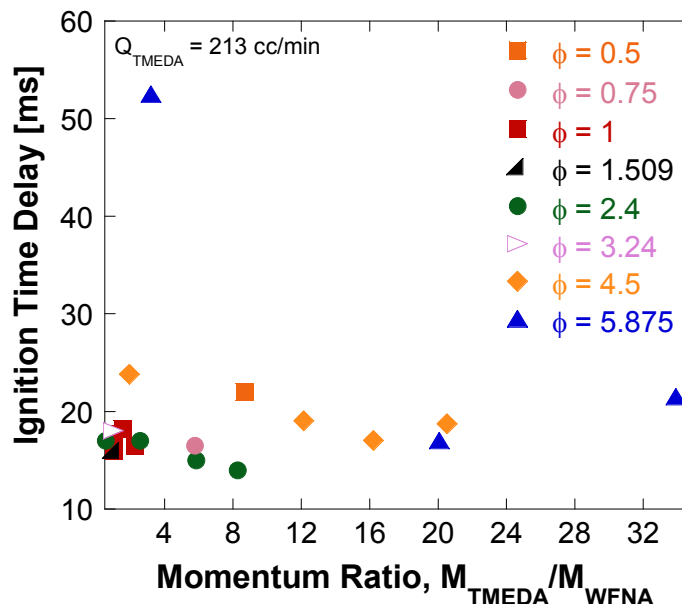


Figure 25. Effect of equivalence ratio and momentum ratio on ignition delay.

The momentum ratio,  $M_{TMEDA} / M_{WFNA}$ , ranged from 0.096 to 2.4 for an equivalence ratio of 1 as shown in Fig. 26. Examining the momentum ratio addresses the effect of mixing of the two impinging streams. For this set of tests, the TMEDA volumetric flow rate was fixed at 213 cc/min, 513 cc/min for WFNA, and the TMEDA orifice diameter was 0.020 in. The WFNA injector orifice diameter was changed to provide six different nozzle combinations, which in turn provides six momentum ratios at the same stoichiometry. Reynolds number is the independent parameter. For the ranges tested, the ignition delay tends to slightly decrease as the momentum ratio approaches unity. Time delays are same order as drop tests performed by Wang and Thynell.<sup>4</sup> As shown in the figure, optimum Rupe number (at momentum ratio of 0.5) also yields comparable ignition delays.

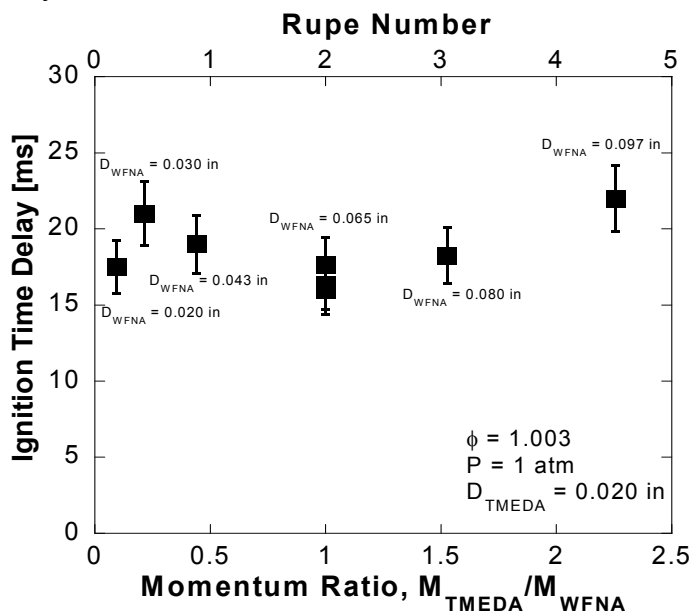


Figure 26. Momentum Ratio versus ignition delay for TMEDA/WFNA reactants.



Figure 26 is a more concise arrangement of the data. The figure displays two ranges of momentum ratios as a function of equivalence ratio. The ranges are 0.06 to 3.3 and greater than 5.5. It is apparent higher momentum ratios perform better at a wider range of equivalence ratios, indicating that for the ignition process, mixing may be able to promote ignition in spite of undesirable stoichiometric conditions.

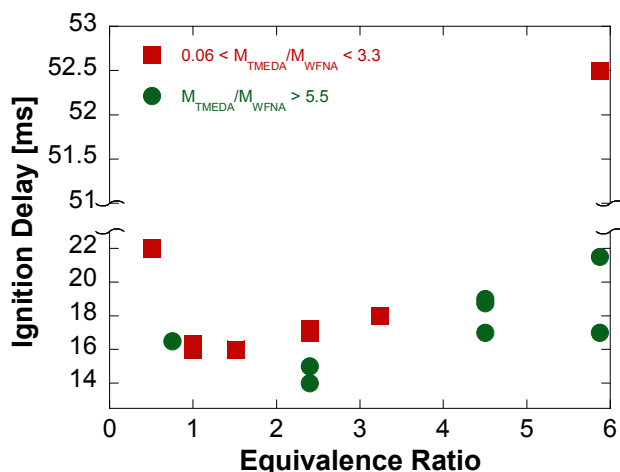


Figure 27. Influence of momentum and equivalence ratios on ignition delay.

### 6.3 Effect of Gellant of Ignition Delay

A series of tests were performed to examine the effect of gellant on the ignition process of hypergolic materials. The fuel was TMEDA and the oxidizer was WFNA. Based upon results from Sakensa, Yetter, and Thynell in the research group, the gelling agents were different for each reactant due to their varying chemical properties. Both the fuel and oxidizer were gelled using Cab-O-Sil, but employed different grades. TMEDA was gelled with EH-5, which has a much higher surface area ( $\sim 385 \text{ m}^2/\text{g}$ ), and the WFNA was gelled with M5 ( $\sim 200 \text{ m}^2/\text{g}$ ), a more typical grade of Cab-O-Sil. Figure 28 shows there is no significant effect when gellant is added, which is consistent with Wang and Thynell's results.

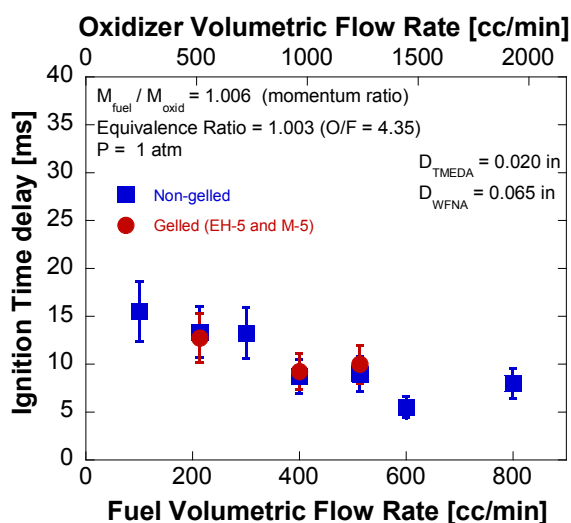


Figure 28. Ignition delay for both non-gelled and gelled reactants as a function of reactant flow rate.

#### 6.4 Effect of Fuel and Oxidizer Leads

Figures 29 to 31 show the effect of fuel and oxidizer leads on the ignition process of non-gelled and gelled TMEDA and WFNA. The term “lead” means that the particular reactant is delivered into the mixing/combustion zone prior to the second reactant. This allows more time for the specific reactant stream to become more established, steady, atomized, etc before the other is introduced. In the figures, it is clear that the oxidizer flow lead has a strong effect on reducing ignition delay due to the prevaporized oxidizer readily available for reaction since WFNA has a high vapor pressure. This effect may not be as significant when other oxidizers are used that have less volatile characteristics, e.g. lower vapor pressure.

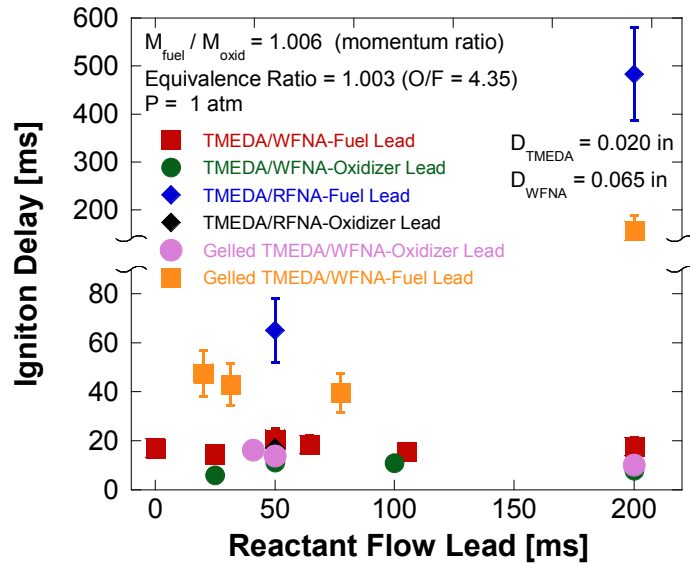


Figure 29. Ignition delay for both non-gelled and gelled reactants as a function of reactant flow lead time.

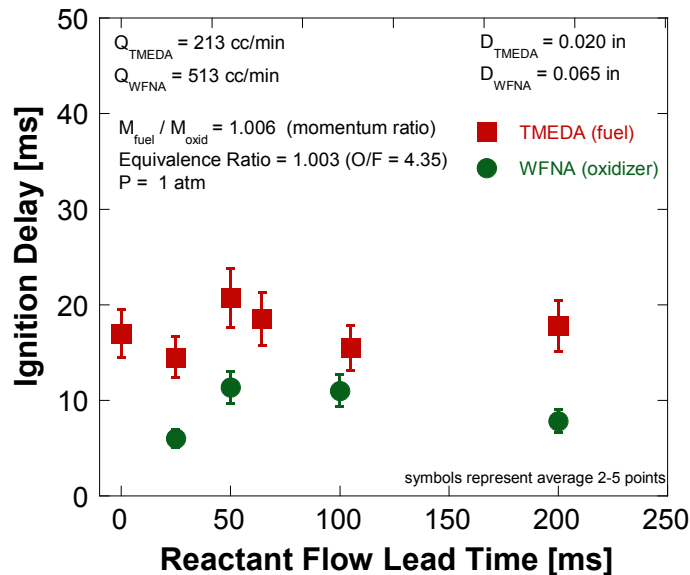


Figure 30. Effect of oxidizer and fuel lead time on ignition delay.

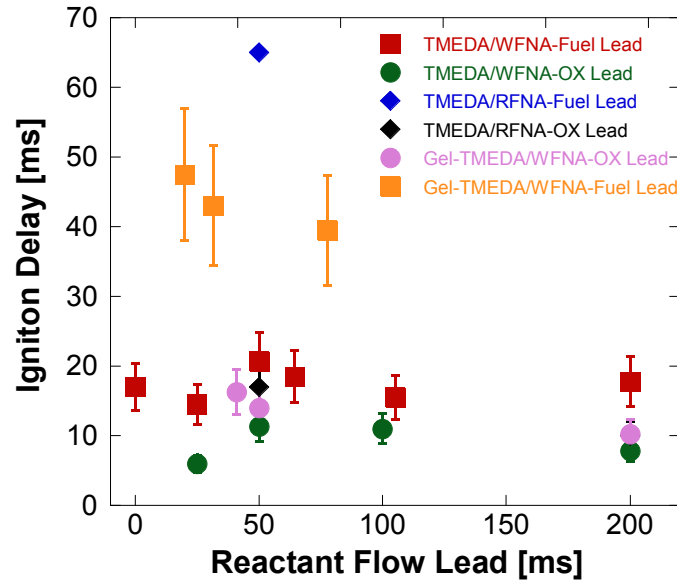


Figure 31. Effect of oxidizer and fuel lead time on ignition delay.

### 6.5 Effect of Length-to-Diameter Ratio of Injector

A limited amount of experiments were performed to determine the effect of injector L/D ratio on the ignition delay. The volumetric flow rates of the TMEDA and WFNA were held constant at 231 and 513 cc/min, respectively. Fully developed flow occurs typically when the  $L/D > 10$  for turbulent flow. Thus, for most of the testing series,  $L/D$  was 20. According to Heywood<sup>26</sup>, the optimum  $L/D$  for diesel fuel droplet sizing is 4.  $L/D$  ratios were varied from 2 to 20. Figure 32 shows that the ignition delay is relatively independent of  $L/D$  ratio. However,  $L/D = 5$ , has the shortest ignition delay which is consistent with Heywood. Further studies are warranted to determine if the gelled reacts truly have a slightly lower ignition delay for different  $L/D$  ratios. The data still fall within experimental error.

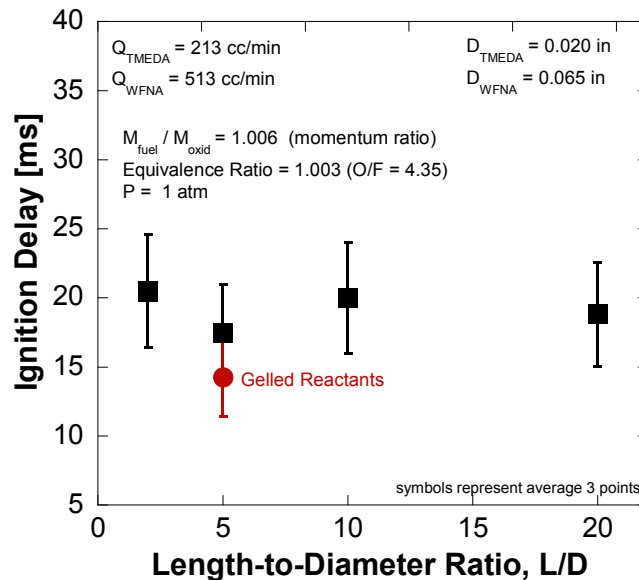


Figure 32. Ignition delay as a function of  $L/D$  ratio for one flow rate.

### 6.6 Effect of DMAZ Fuel Additive

Experiments performed by Stevenson et al.<sup>11,14</sup> showed promise for DMAZ/TMEDA fuel blends in terms of decreasing ignition delays. According to Stevenson et al., small percentages of DMAZ (20-40%) mixed with TMEDA, resulted in the lowest ignition delay times<sup>14</sup> (see Fig. 1). Further reducing ignition delays provide evidence for potential substitutes for hydrazine without significantly sacrificing performance. Several experiments were conducted to show the effect of adding DMAZ to the TMEDA fuel. First, each fuel was characterized as a function for fuel flow rate as shown in Fig. 33. Even at the highest flow conditions tested, the TMEDA has an ignition delay that is 60% of DMAZ. The amount of DMAZ added to TMEDA ranged from 0 to 100% (by wt). A series of 3-4 repeat experiments were performed at each DMAZ/TMEDA mixture combination. In Fig. 33, as the amount of DMAZ present in the mixture increases from 0 to 30% DMAZ, the ignition delay times decreased respectively. The region of interest is magnified in Fig. 33 for clarity. At a critical DMAZ amount of 30%, the ignition delay time is at its lowest value of approximately 11 ms. At percentages of DMAZ beyond 30%, the ignition delay times continue to increase. At high percentages (80% DMAZ), the delay times increased dramatically in the tests performed where in some cases the ignition even takes place off screen where the high speed camera cannot capture it (>100 ms). This dramatic increase could be caused by a significant fraction of the fuel is now less energetic or a slightly higher momentum ratio. Since the composition for these tests is continuously changing, the momentum ratio slightly varied from 1.006 to 1.161. As a comparison, Fig. 35 illustrates the data of the current study superimposed on a plot including the data for hot-fire engine tests by Stevenson et al.<sup>14</sup>

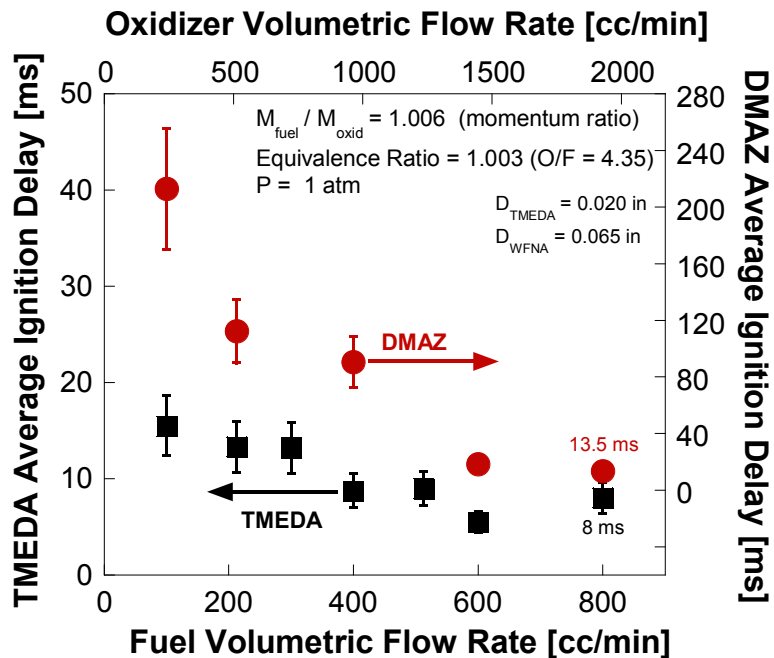


Figure 33. Ignition delays for TMEDA and DMAZ as a function of fuel flow rate.

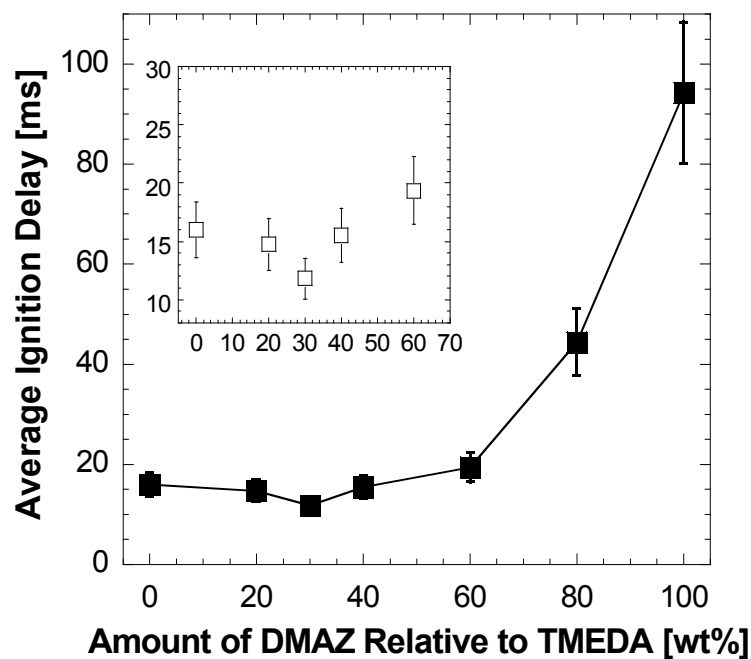


Figure 34. Effect of DMAZ additive in the TMEDA fuel on ignition delay.

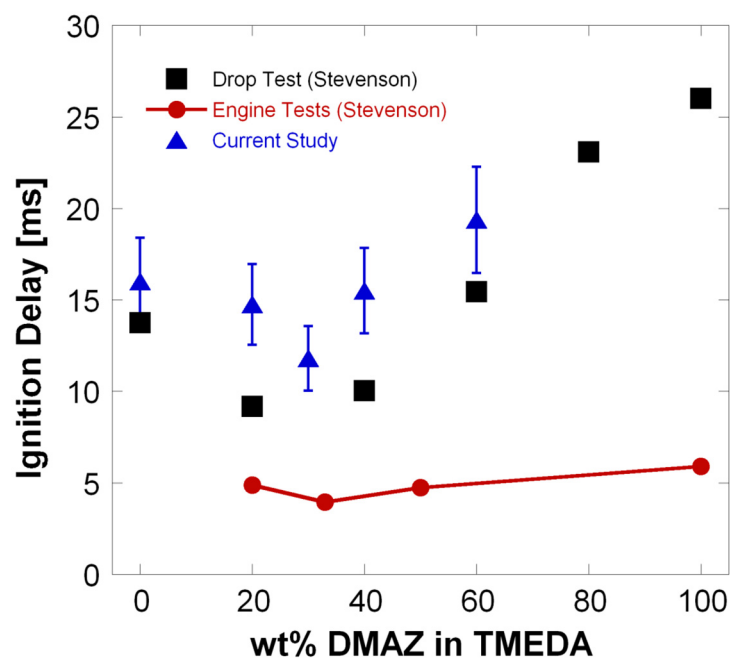


Figure 35. Ignition delay of DMAZ additive superimposed on the data for engine tests by Stevenson et al.<sup>14</sup>

### 6.7 Effect of Curved Wall Impingement

A cold wall curved surface was placed near the injector exit to simulate the initial start-up of an actual combustor. The wall was placed at 1-mm increments from the exit of the injector exit. It was configured in a tangential orientation with respect to the jet as shown previously in Fig. 17. As given in Fig. 36, results indicate that the presence of the curved surface at the exit of the injectors increases the ignition delay. This can be caused by the heat loss to the surface. Tests conducted immediately, consecutively show a slight decrease in ignition delay due to the gals plate heating up. The average ignition delay now falls in the 22 ms range, where the maximum is nearly 27 ms. In comparison, tests conducted with no curved surface, ignition delay times are around 17 ms. This condition is represented by the diamond points at a 0-mm distance. The horizontal trend in Fig. 36 indicates that from a distance of 0 (tangent to injector exit) to 6-mm away from the injector exit, there is no significant effect on ignition delay caused by moving the curved glass surface farther away from the jet. Figures 37a and 37b show images of typical ignition with and without a curved surface present. Figure 37b reveals how the reactants impinge on the curved surface to spread and mix against the quartz and therefore ignite.

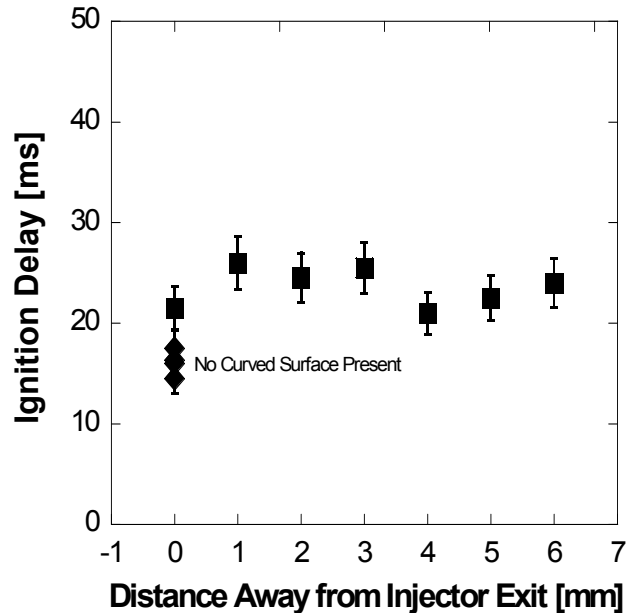


Figure 36. Effect of curved surface on ignition delay.

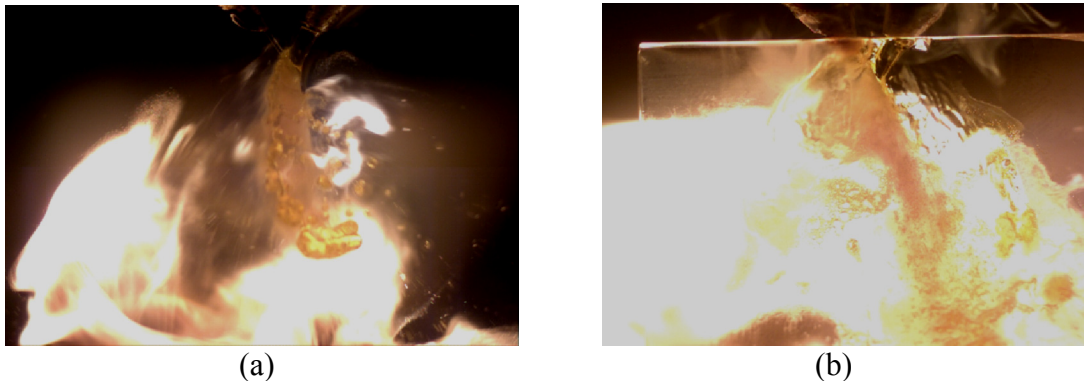


Figure 37. Captured high speed images of a typical TMEDA and WFNA ignition event: (a) without curved quartz wall; (b) with curved quartz wall tangent to the nozzle exit.

## 7. Conclusions

A series of tests were conducted to ascertain the ignition delay time of hypergolic propellants as a function of flow rate, momentum ratio, gellant, L/D ratio, equivalence ratio, and blends of DMAZ and TMEDA. It was found that maintaining constant stoichiometry, the ignition delay time decreased by a factor of 3 (nearly 17 ms to 5 ms) when the total propellant flow rate was increased by a factor of six. This may be attributed to the enhanced mixing at the impingement point as a result of larger Reynolds numbers. The effect of equivalence ratio on ignition delay shows that at very fuel rich conditions conditions ( $\phi = 5.8$ ), ignition delay was approximately 3 times longer. However, for cases at  $\phi = 3.2$  and below, it is evident that the ignition delay is not affected by stoichiometry. From these results, it suggests that stoichiometry is much more important for combustion rather than ignition. Blends of DMAZ/TMEDA fuels were reacted with WFNA. The DMAZ fuel was varied from 0 to 100% (by wt) yielding ignition delays from 11 to 96 ms. It was found that adding small percentages of DMAZ fuel in TMEDA can significantly decrease the ignition delay times of the oxidizer and fuel mixtures. The most predominate case was a mixture of 30%DMAZ to 70% TMEDA decreasing the ignition delay from 17 ms (100% TMEDA) to around 11 ms (30% DMAZ + 70%TMEDA). For DMAZ concentrations of >50%, the ignition delay continued to rapidly increase to values beyond 100 ms. These data relatively agree well with data published by Stevenson et al. for hot-fire engine tests and Saksena and Yetter. A cold wall curved surface was added to simulate the initial start-up of an actual combustor. The wall was placed at various distances from 0 to 6 mm (in 1-mm increments) away from the nozzle exits. For the range tested, the presence of the surface increased the ignition delay time from 17 to a maximum of 27 ms, independent of the location of the surface. Gellant had no significant effect on ignition delay for any of the fuel/oxidizer combinations tested in this study since hypergolic ignition is promoted due to surface contact. However, it is believed that the combustion performance may be affected by adding an inert gellant. Oxidizer flow lead has a strong effect on reducing ignition delay due to the prevaporized oxidizer readily available for reaction since WFNA has a high vapor pressure. This effect may not be as significant when other oxidizers are used that have less volatile characteristics, e.g. lower vapor pressure.

## 8. References

- <sup>1</sup>Clark, John D., *"Ignition! An Informal History of Liquid Rocket Propellants"*; Rutgers University Press, New Brunswick, New Jersey, 1972, pp. 7-73.
- <sup>2</sup>Schalla, R.L., Fletcher, E.A., "The Ignition Behavior of Various Amines With White Fuming Nitric Acid," Lewis Research Center, NASA, Cleveland, OH; 1959.
- <sup>3</sup>Coil, M.A., "Hypergolic Ignition of a Gelled Ionic Liquid Fuel;" Orbital Technologies Corporation; American Institute of Aeronautics and Astronautics; 2010-6901-396; 2010.
- <sup>4</sup>Shiqing Wang, Stefan T. Thynell, and Arindrajit Chowdhury, "Experimental Study on Hypergolic Interaction between *N,N,N',N'*-Tetramethylethylenediamine and Nitric Acid," *Energy Fuels*, 2010, 24 (10), pp. 5320–5330, DOI: 10.1021/ef100593s.
- <sup>5</sup>Sutton, G. P., "History of Liquid Propellant Rocket Engines," American Institute of Aeronautics and Astronautics: Alexandria, VA, 2006; pp. 5-21.
- <sup>6</sup>Mellor, B. In Proceedings of the 2nd International Conference on Green Propellants for Space Propulsion (ESA SP-557) 2004, Sardinia, Italy.
- <sup>7</sup>Chambreau, S. D.; Schneider, S.; Rosander, M.; Hawkins, T.; Gallegos, C. J.; Pastewait, M.F.; Vaghjiani, G. L., *J. Phys. Chem. A* 2008, 112, 7816–7824.

- <sup>8</sup>Schneider, S.; Hawkins, T.; Rosander, M.; Vaghjiani, G.; Chambreau, S.; Drake, G., *Energy & Fuels* 2008, 22, 2871–2872.
- <sup>9</sup>He, L.; Tao, G. H.; Parrish, D. A.; Shreeve, J. M., *Chem. Eur. J.* 2010, 16, 5736–5743.
- <sup>10</sup>Thompson, D. M. Tertiary Amine Azides in Hypergolic Liquid or Gel Fuels Propellant Systems. U.S. Patent No. 6013143, 2000.
- <sup>11</sup>Stevenson, W. H., Hypergolic Liquid or Gel Fuel Mixtures. U.S. Patent No. 0127551, 2008.
- <sup>12</sup>McQuaid, M. J.; Stevenson, W. H.; Thompson, D. M., “Computationally Based Design and Screening of Hypergolic Multiamines,” Technical Report, NTIS No. ADA433347; US Army Research Laboratory: Aberdeen Proving Ground, MD, 2004.
- <sup>13</sup>Reddy, G.; Song, J.; Mecchi, M. S.; Johnson, M. S. *Mutat. Res.* 2010, 700, 26–31.
- <sup>14</sup>Stevenson, W.H., Felton L.D.; Wang Z.S., Hypergolic Liquid or Gel Fuel Mixtures. U.S. Patent No. 0272071 A1, 2011
- <sup>15</sup>McQuaid, M.J., “Computational Characterization of 2-Azidocycloalkanamines: Notional Variations on Hypergol 2-Azido-N,N-Dimethylethanamine (DMAZ),” Army Research Laboratory; ARL-TR-2806, 2002.
- <sup>16</sup>Zhang, P., Law, C.K., “Density Functional Theory Study of the Ignition Mechanism of 2-Azido-N, N-Dimethylethanamine (DMAZ),” Princeton University, Department of Mechanical and Aerospace Engineering; Combustion Institute; 2011.
- <sup>17</sup>Dong-Jun Ma; Xiao-Dong Chen; Prashant Khare; Vigor Yang, Atomization patterns and breakup characteristics of liquid sheets formed by two impinging jets, Chapter DOI: 10.2514/6.2011-97, Publication Date: 04 January 2011 - 07 January 2011.
- <sup>18</sup>Bayvel, L. P. and Orzechowski, Z., *Liquid Atomization*, Taylor and Francis, Washington, DC, 1993.
- <sup>19</sup>Lefebvre, A. H., *Atomization and Sprays*, CRC Press, 1989.
- <sup>20</sup>Sutton, G. P., *Rocket Propulsion Elements: An Introduction to The Engineering of Rockets*, Wiley, New York, 6th ed., 1992, p. 298.
- <sup>21</sup>Bush, J. W. M. and Hasha, A. E.: “On the collision of laminar jets: fluid chains and fishbones,” Massachusetts Institute of Technology; *J. Fluid Mech.*, Vol. 511, 2004, pp. 285{310. DOI: 10.1017/S002211200400967X.
- <sup>22</sup>Rupe, J.H.; A Correlation Between The Dynamic Properties Of A Pair Of Impinging Streams And The Uniformity Of Mixture-Ratio Distribution In the Resulting Spray; progress report No.20-209; Department of the Army; ORDCIT Project.
- <sup>23</sup>Riebling, R.W.; Criteria for Optimum Propellant Mixing in Impinging-Jet Injection Elements; Jet Propulsion Laboratory, Pasadena, Calif; American Institute of Aeronautics and Astronautics; DOI:10.2514/3.28966, 1967.
- <sup>24</sup>Fakhri, S.A., “A study on the atomization and spray characteristics of gelled simulants formed by two impinging jets,” The Pennsylvania State University, M.S. Thesis, 2009.
- <sup>25</sup>Lee, J.G., Fakhri, S., Yetter, R.A., “Atomization and Spray Characteristics of Gelled-Propellant Simulants Formed by Two Impinging Jets,” 45<sup>th</sup> AIAA/ASME/SAE/ASEE Joint Propulsion Conference & Exhibit, 2009, AIAA Paper, 2009-5241.
- <sup>26</sup>Heywood, J.B., *Internal Combustion Engine Fundamentals*, McGraw-Hill, New York, 1988.



## ARCHIVAL PUBLICATIONS AND PRESENTATIONS IN CHRONOLOGICAL ORDER

### Archival Publications

1. F. Shuang, M. Zhou, A. Pechen, R. Wu, O. Shir, and H. Rabitz, "Control of quantum dynamics by optimized measurements," *Phys. Rev. A*, 78, 063422 (2008).
2. F. A. Williams, "Simplified Theory for Ignition Times of Hypergolic Gelled Propellants", *Journal of Propulsion and Power*, Vol. 25 (2009) 1354-7.
3. H. Sun, L. Catoire, and C. K. Law, "Thermal Decomposition of Monomethyl-hydrazine: Shock Tube Experiments and Kinetic Modeling", *International Journal of Chemical Kinetics*, 2009, 41(3), 176-186.
4. V. Beltrani, P. Ghosh, and H. Rabitz, "Exploring the capabilities of quantum optimal dynamic discrimination," *Journal of Chemical Physics*, 130, 164112 (2009).
5. A. Oza, A. Pechen, J. Dominy, V. Beltrani, K. Moore and H. Rabitz, „Optimization search effort over the control landscapes for open quantum systems with Kraus-map evolution," *J. Phys. A*, 42, 205305 (2009).
6. M. Roth, L. Guyon, J. Roslund, V. Boutou, F. Courvoisier, J.-P. Wolf and H. Rabitz, "Quantum control of tightly competitive product channels," *Physics Review Letters*, 102, 253001 (2009).
7. J. Roslund and H. Rabitz, "Experimental quantum control landscapes: inherent monotonicity and artificial structure," *Physics Review A*, 80, 013408 (2009).
8. A. Chowdhury, C. Bapat, and S. T. Thynell, "Apparatus for probing preignition behavior of hypergolic materials," *Review of Scientific Instruments*, (2009), 80(4), 044101/1-044101/4.
9. K. Chenoweth, A. C. T. van Duin, S. Dasgupta, and W. A. Goddard III, "Initiation Mechanisms and Kinetics of Pyrolysis and Combustion of JP-10 Hydrocarbon Jet Fuel", *J. Phys.Chem. A*, 113 (9), pp. 1740-1746, 2009.
10. L. Zhang, A.C.T. van Duin, S.V. Zybin, W.A. Goddard III, "Thermal Decomposition of Hydrazines from Reactive Dynamics Using the ReaxFF Reactive Force Field", *Journal of Physical Chemistry B*, 113 (31), 10770-10778, 2009.
11. Fakhri, S., Lee, J.G., and Yetter, R.A., "Effect of nozzle geometry on the atomization and spray characteristics of gelled-propellant simulants formed by two impinging jets," *Atomization and Sprays*, Vol. 20, No. 12, 2010, pp. 1033-1046. doi: 10.1615/AtomizSpr.v20.i12.20
12. S. Wang, S.T. Thynell, and A. Chowdhury, "Experimental Study on Hypergolic Interaction between N,N,N',N'-Tetramethylethylenediamine and Nitric Acid," S. Wang, S.T. Thynell, and A. Chowdhury, *Energy & Fuels*, 24(10), pp. 5320-5330, 2010.
10. Liu, WG; Dasgupta, S; Zybin, SV; Goddard, WA, "First Principles Study of the Ignition Mechanism for Hypergolic Bipropellants: N,N,N',N'-Tetramethylethylenediamine (TMEDA) and N,N,N',N'-Tetramethylmethylenediamine (TMMDA) with Nitric Acid," *J. Phys. Chem. A*, 115(20): 5221-5229 (2011).

11. R. D. Cook, S. H. Pyun, J. Cho, D. F. Davidson, R. K. Hanson, "Shock Tube Measurements of Several Species Time-Histories in Monomethyl Hydrazine Pyrolysis," *Combustion & Flame* 158 (2011) 790–795.
12. S. H. Pyun, J. Cho, D. F. Davidson, R. K. Hanson, "Interference-Free Mid-IR Laser Absorption Detection of Methane," *Measurement Science and Technology* 22 (2011) 025303 (9pp).
13. C. K. Law, "Fuel Options for Next-Generation Chemical Propulsion," *AIAA J.*, Vol. 50, No. 1, pp. 19-36, 2012.
14. C. Tang, P. Zhang, and C. K. Law, "Bouncing, coalescence, and separation in head-on collision of unequal size droplets," *Phys. Fluids* 24, 022101 (2012); doi: 10.1063/1.3679165
15. P. Zhang and C. K. Law, "An analysis of head-on droplet collision with large deformation in gaseous medium," *Physics of Fluids*, 23, 042102 (2011).
16. X. Hong, H. Sun, and C. K. Law, "Rate coefficients of the reactions of isopentane with H and CH<sub>3</sub> radicals: Quantum mechanical approach," *Computational & Theoretical Chemistry*, 963 (2011) 357–364.
17. P. Zhang, S. J. Klippenstein, H. Sun, and C. K. Law, "Ab initio kinetics for the decomposition of monomethylhydrazine (CH<sub>3</sub>NHNH<sub>2</sub>)," *Proceedings of the Combustion Institute* 33 (2011) 425–432.
18. H. Sun, P. Zhang, C. K. Law, "Gas-Phase Kinetics Study of Reaction of OH Radical with CH<sub>3</sub>NHNH<sub>2</sub> By Second-Order Multireference Perturbation Theory," *Journal of Physical Chemistry A*, 2012, 116 (21), 5045-5056
19. H. Sun, P. Zhang, C. K. Law, "Ab Initio Kinetics for Thermal Decomposition of CH<sub>3</sub>N•NH<sub>2</sub>, cis-CH<sub>3</sub>NHN•H, trans-CH<sub>3</sub>NHN•H, and C•H<sub>2</sub>NNH<sub>2</sub> Radicals," *Journal of Physical Chemistry A*, 2012, 116, 8419-8430.
20. J. Roslund, M. Roth, L. Guyon, V. Boutou, F. Courvoisier, J.-P. Wolf, and H. Rabitz, "Resolution of strongly competitive product channels with optimal dynamic discrimination: Application to flavins," *The Journal of Chemical Physics*, 134, 034511 (2011).
21. F. O. Laforge, J. Roslund, O. M. Shir, and H. Rabitz, "Multi-objective adaptive feedback control of two-photon absorption coupled with propagation through a dispersive medium," *Phys. Rev. A* 84, 013401 (2011)
22. S. D. McGrane, M. T. Greenfield, J. Scharff, D. S. Moore, J. Roslund, and H. Rabitz, "SPECTROSCOPY: Optimal Dynamic Detection enhances sensitivity of explosives detection," *Laser Focus World* (2011)
23. Liu, W.G., and Goddard, W.A., "First-Principles Study of the Role of Interconversion Between NO<sub>2</sub>, N<sub>2</sub>O<sub>4</sub>, cis-ONO-NO<sub>2</sub>, and trans-ONO-NO<sub>2</sub> in Chemical Processes," *J. Am. Chem. Soc.*, 134(31), 12970-12978, 2012. DOI: 10.1021/ja300545e
24. Liu, Y., Zybin, S.V., Guo, J., van Duin, A.C.T. and Goddard, W.A., "Reactive Dynamics Study of Hypergolic Bipropellants: Monomethylhydrazine and Dinitrogen Tetroxide," *J. Phys. Chem. B*, 116(48), 14136-14145, 2012. DOI: 10.1021/jp308351g

25. S. Q. Wang and S. T. Thynell, "Decomposition and Combustion of Ionic Liquid Compound Synthesized from *N,N,N',N'*-Tetramethylethylenediamine and Nitric Acid", in book: *Ionic Liquids: Science and Applications*, A. Visser, N.J. Bridges and R.D. Rogers (Eds.), ACS Symposium Series, Vol. 1117, pp. 51-66, 2012. <http://dx.doi.org/10.1021/bk-2012-1117.ch003>.
26. S.Q. Wang and S.T. Thynell, "An experimental study on the hypergolic interaction between monomethylhydrazine and nitric acid," *Combustion & Flame*, 159 (2012) 438–447.
27. T. Neumann-Lehman, R. Grana, K. Seshadri, and F. A. Williams, "The Structure and Extinction of Non-Premixed Methane/Nitrous Oxide and Ethane/Nitrous Oxide Flames," *Proceedings of the Combustion Institute*, Vol. 34, 2013, pp. 2147-2153. <http://dx.doi.org/10.1016/j.proci.2012.05.102>
28. D. Liu, P. Zhang, C. K. Law and Yincheng Guo, Collision dynamics and mixing of unequal-size droplets," *International Journal of Heat and Mass Transfer*, Vol. 57, pp. 421-428 (2013).
29. Zhang, P., S. J. Klippenstein and C. K. Law, "Ab initio kinetics for the decomposition of hydroxybutyl and butoxy radicals of n-butanol," *Journal of Physical Chemistry A*, Vol. 117(9), pp. 1890-1906 (2013); doi: 10.1021/jp400155z.
30. W.-G. Liu, S. Wang, S. Dasgupta, S. T. Thynell, W. A. Goddard III, S. Zybin, and R. A. Yetter, "Experimental and Quantum Mechanics Investigations of Early Reactions of Monomethylhydrazine with Mixtures of NO<sub>2</sub> and N<sub>2</sub>O<sub>4</sub>," *Combustion and Flame*, Vol. 160, Issue 5, May 2013, pp. 970-981.
31. U. Niemann, K. Seshadri, and F. A. Williams, "Effect of Addition of a Nonequidiffusional Reactant to an Equidiffusional Diffusion Flame," *Combustion Theory and Modelling*, 17, 2013, pp. 563-576.
32. Chen, X., Ma, D., Yang, V. and Popinet, S. "High-Fidelity Simulations of Impinging Jet Atomization," *Atomization and Sprays*, 23(12), 2013.
33. R. Rey-de-Castro, Z. Leghtas, and H. Rabitz, "Manipulating Quantum Pathways on the Fly", *Phys. Rev. Lett.*, 110, 223601 (2013).
34. S. Li, D. F. Davidson, R. K. Hanson, N. J. Labbe, P. R. Westmoreland, P. Oßwald, K. Kohse-Höinghaus, "Shock Tube Measurements and Model Development for Morpholine Pyrolysis and Oxidation at High Pressures," *Combustion and Flame* 160 (2013) 1559-1571.
35. S. Li, D. F. Davidson, R. K. Hanson, "Shock tube study of the pressure dependence of monomethylhydrazine," *Combustion and Flame* 161 (2014) 16-22.
36. Chen, X. and Yang, V., "Thickness-based adaptive mesh refinement methods for multi-phase flow simulations with thin regions," *J. Computational Physics*, Vol. 269, pp 22–39, 2014.
37. N. Kumbhakarna, and S.T. Thynell, "Development of a reaction mechanism for liquid-phase decomposition of guanidinium 5-amino tetrazolate," *Thermochimica Acta*, Vol. 582(20), pp. 25-34, 2014.

38. S. Li, D. F. Davidson, R. K. Hanson, "Shock Tube Study of Dimethylamine Oxidation," Submitted for publication, *Fuel*, April 2014.
39. S. Li, D. F. Davidson, R. K. Hanson, "Shock tube study of ethylamine pyrolysis and oxidation," Accepted by *Combustion and Flame* April 2014.
40. Ramasubramanian, C., Notaro, V. and Lee, J.G., "Characterization of Near-field Spray of Non-gelled and Gelled Impinging Doublets in Air under High Pressure," Accepted for publication in *Journal of Propulsion and Power*, May, 2014.
41. K. Seshadri, X. S. Bai, and F. Williams, "Rate-Ratio Asymptotic Analysis of the Structure and Mechanisms of Extinction of Nonpremixed  $\text{CH}_4/\text{N}_2\text{-O}_2/\text{N}_2\text{O}/\text{N}_2$  Flames," *Proceedings of the Combustion Institute*, 35, 2015, in press.
42. V. Amin, G. Katzlinger, P. Saxena, E. Pucher, and K. Seshadri, "The Influence of Carbon Monoxide and Hydrogen on the Structure and Extinction of Nonpremixed and Premixed Methane Flames," *Proceedings of the Combustion Institute*, 35, 2015, in press.
43. S. Li, D. F. Davidson, R. K. Hanson, "High-temperature measurements of the reaction of OH with ethylamine and dimethylamine," submitted to *Journal of Physical Chemistry A*, November 2013.
44. Zhang, P., Lidong Zhang and Chung K. Law, "Density functional theory study of the ignition mechanism of 2-azido-*N*, *N*-dimethylethanamine with nitric acid and nitrogen dioxide," *Combustion and Flame*, submitted, 2014.
45. Zhang, P., S. J. Klippenstein, H. Sun, and C. K. Law, "Secondary channels in the thermal decomposition of monomethylhydrazine ( $\text{CH}_3\text{NHNH}_2$ )," submitted, 2014.
46. K. Seshadri, and X. S. Bai, "Rate-Ratio Asymptotic Analysis of the Influence of Addition of Hydrogen on the Structure and Mechanisms of Extinction of Nonpremixed Methane Flames," *Combustion Science and Technology*, submitted, 2014.
47. Khare, P., Wang, S. and Yang, V., "Modeling of Finite-Size Droplets and Particles in Multiphase Flows," *Int. J. Multiphase Flow*, (in review), 2014.

#### **Papers Presented at Conferences**

1. S. Fakhri, J.G. Lee and R.A. Yetter, "Atomization and Spray Characteristics of Gelled-Propellant Simulants Formed by Two Impinging Jets," AIAA 2009-5241, 45th AIAA/ASME/SAE/ASEE Joint Propulsion Conference & Exhibit, 2-5 August 2009, Denver, Colorado.
2. Chowdhury, A., S. Wang, and Stefan T. Thynell, "Ignition Behavior of Novel Hypergolic Materials," AIAA-2009-5352 presented at 45th AIAA/ASME/SAE/ASEE Joint Propulsion Conference and Exhibit, Denver, Colorado, Aug. 2-5, 2009.
3. H. Sun and C. K. Law, "Kinetics of H-Abstraction Reactions of Monomethyl-hydrazine by OH Radical", Fall Technical Meeting, the Eastern States Section of the Combustion Institute at University of Maryland, College Park, October 18-21, 2009.
4. D. Liu, P. Zhang, C.K. Law, and Y. Guo, "Collision dynamics and mixing of unequal-size droplets," 2009 Fall Technical Meeting of the Eastern States Section of the Combustion Institute, October 18-21, 2009, College Park, MD.

5. C. Norscia, K. Seshadri, and F. A. Williams, "The Structure and Extinction of Methane/Nitrogen Dioxide Flames," 43rd Combustion, 31st Airbreathing Propulsion, 25th Propulsion Systems, Hazards, Joint Subcommittee Meeting, 7-11 December 2009, La Jolla, California.
6. P. Saxena, and K. Seshadri, "The Influence of Hydrogen and Carbon Monoxide on Structure and Burning Velocity of Methane Flames," Paper # 09F-86, 2009 Fall Technical Meeting, Western States Section of the Combustion Institute, University of California at Irvine, Irvine, October 26-27, 2009.
7. P. Saxena, V. Raghavan, and K. Seshadri, "The Influence of Hydrogen and Carbon Monoxide on Structure and Burning Velocity of Methane Flames," 8th Asia-Pacific Conference on Combustion, Hyderabad, India, December 2010.
8. S.Q. Wang and S.T. Thynell, "Experimental study on hypergolic interaction between MMH and nitric acid", 44th Joint-Army-Navy-NASA-Air Force Combustion Subcommittee Meeting, Apr 2011, Arlington.
9. S.Q. Wang, S.T. Thynell, Condensed- and gas-phase reactions between monomethylhydrazine and nitric acid from 20 to 250°C, 7th U.S. National Combustion Meeting, Mar 2011, Atlanta, GA.
10. R. D. Cook, D. F. Davidson, S. H. Pyun, R. K. Hanson, "MMH Pyrolysis and Oxidation: Species Time-History Measurements behind Reflected Shock Waves," 23<sup>rd</sup> ICDERS meeting, Irvine CA July 2011.
11. K. Seshadri, K., Bai, X. S., Williams, F. A., and Newman-Lehman, T., "Rate-Ratio Asymptotic Analysis of the Structure and Mechanisms of extinction of Nonpremixed  $\text{CH}_4/\text{N}_2\text{-O}_2/\text{N}_2\text{O}/\text{N}_2$  Flames," Paper # 316, 23rd International Colloquium on the Dynamics of Explosions and Reactive Systems, University of California, Irvine, Irvine, California, July 24-29, 2011.
12. K. Seshadri, T. Newmann-Lehman, R. Grana, U. Niemann, and F. A. Williams, F.A., "The Structure and Extinction of Nonpremixed Methane/Nitrous Oxide and Ethane/Nitrous Oxide Flames," JANNAF, 44th Combustion, 32nd Airbreathing Propulsion, 32nd Exhaust Plumes and Signatures, 25th Propulsion Systems Hazards, Joint Subcommittee Meeting, 18-21 April 2011, Hyatt Regency Crystal City, Arlington, Virginia.
13. Saksena, P., S. Tadigadapa, R. A. Yetter, "Study of Hypergolic Propellants using Micro-reactors," presented at the 15th International Conference on Miniaturized Systems for Chemistry and Life Sciences, October 2-6, 2011, Washington State Convention Center, Seattle, WA.
14. S. Wang and S.T. Thynell, "Experimental Study on Hypergolic Interaction between Monomethylhydrazine and Nitric Acid," Proceedings of the 44th JANNAF Subcommittee Combustion Meeting, Arlington, VA, April 2011.
15. S. Q. Wang and S. T. Thynell, "Condensed- and Gas-phase Reactions between Monomethylhydrazine and Nitric Acid from 20 to 250°C," 7th U.S. National Technical Meeting of the Combustion Institute, Georgia Institute of Technology, Atlanta, GA, March 20-23, 2011.

16. K. Seshadri, X. S. Bai, and F. A. Williams, "Rate Ratio Asymptotic Analysis of the Influence of Hydrogen on the Structure and Mechanisms of Extinction of Methane Flames in Laminar Nonpremixed Flows," Paper # M26.01, American Physical Society, 65th Annual Fall DFD Meeting, San Diego, California, November 18–20, 2012.
17. R. Gehmlich, and K. Seshadri, "The Influence of Nitrogen Oxide Addition on the Autoignition Temperature of Ethane/Air Flames," JANNAF Interagency Propulsion Committee, 45th Combustion, 33rd Airbreathing Propulsion, 33rd Exhaust Plume and Signatures, 27th Propulsion Systems Hazards, Joint Subcommittee Meeting, Hyatt Regency Monterey/Naval Postgraduate School, December 3-7, 2012.
18. Saksena, P., S. Tadigadapa, and R.A. Yetter, "Control of Liquid Hypergolic Reactions in Micro-Reactors using Diffusional Mixing," in The 12th International Workshop on Micro and Nanotechnology for Power Generation and Energy Conversion Applications, 2012, Atlanta, Georgia, USA.
19. P. Khare, D. Ma, X. Chen and V. Yang, "Phenomenology of Secondary Breakup of Newtonian Liquid Droplets," 50th AIAA Aerospace Sciences Meeting including the New Horizons Forum and Aerospace Exposition, AIAA 2012-0171, 9-12 January 2012, Nashville, Tennessee.
20. X. Chen, D. Ma, and V. Yang, "Collision Outcome and Mass Transfer of Unequal-sized Droplet Collision," AIAA 2012-1090, 50th AIAA Aerospace Sciences Meeting including the New Horizons Forum and Aerospace Exposition, AIAA 2012-1090, 9-12 January 2012, Nashville, Tennessee.
21. X. Chen, D. Ma, and V. Yang, "Mechanism Study of Impact Wave in Impinging Jets Atomization Atomization," 50th AIAA Aerospace Sciences Meeting including the New Horizons Forum and Aerospace Exposition, AIAA 2012-1089, 9-12 January 2012, Nashville, Tennessee.
22. X. Chen, D. Ma and V. Yang, "High-Fidelity Numerical Simulations of Impinging Jet Atomization," 48th AIAA/ASME/SAE/ASEE Joint Propulsion Conference & Exhibit, AIAA 2012-4328, 30 July - 01 August 2012, Atlanta, Georgia.
23. X. Chen, D. Ma and V. Yang, "Dynamics and Stability of Impinging Jets," ILASS Americas, 24th Annual Conference on Liquid Atomization and Spray Systems, San Antonio, TX, May 2012.
24. P. Khare, D. Ma, X. Chen and V. Yang, "Breakup and Dynamics of Liquid Droplets," ILASS Americas, 24th Annual Conference on Liquid Atomization and Spray Systems, San Antonio, TX, May 2012.
25. X. Chen and V. Yang, A Multi-Scale Study of Droplet Collision Dynamics: From Gas Film Lubrication to Liquid Phase Mixing, ILASS Americas, 24th Annual Conference on Liquid Atomization and Spray Systems, San Antonio, TX, May 2012.
26. P. Khare, D. Ma, X. Chen and V. Yang, "Breakup of Liquid Droplets", ICLASS 2012, 12th Triennial International Conference on Liquid Atomization and Spray Systems, Heidelberg, Germany, September 2-6, 2012.
27. K. Seshadri, X. S. Bai, and F. A. Williams, "Rate-Ratio Asymptotic Analysis of the Influence of Addition of Hydrogen on the Structure and Mechanisms of Extinction of

- Nonpremixed Methane Flame” Paper # 070LT-0325, 8th U.S National Combustion Meeting, Organized by the Western States Section of the Combustion Institute, University of Utah May 19-22, 2013.
28. G. Katzlinger, V. Amin, K. Seshadri, and E. Pucher, “The Influence of Carbon Monoxide on the Structure and Extinction of Nonpremixed Methane Flames,” Paper # 084LF-0023, 2013 Fall Meeting of the Western States Section of the Combustion Institute, Colorado State University, Fort Collins, CO. October 7-9, 2013.
  29. G. Katzlinger, V. Amin, P. Saxena, andn K. Seshadri, K, “The Influence of Carbon Monoxide on the Structure and Extinction of Nonpremixed Methane Flames,” 23<sup>rd</sup> National Conference on I. C. Engine and Combustion (NCICEC 2013) SVNIT, Surat, India, December 13-16, 2013.
  30. S. Li, D. F. Davidson, R. K. Hanson, K. Moshhammer, K. Kohse-Höinghaus, “Shock tube study of ethylamine pyrolysis and oxidation,” Paper 070RK-0075, 8<sup>th</sup> U.S. National Combustion Meeting, University of Utah, May 19-22, 2013.
  31. X. Chen and V. Yang, "Numerical Simulation of Primary Atomization of Non-Newtonian Impinging Jets", ILASS Americas, 25th Annual Conference on Liquid Atomization and Spray Systems, Pittsburgh, PA, May 2013.
  32. P. Khare and V. Yang, "Drag Coefficients of Deforming and Fragmenting Liquid Droplets", ILASS Americas, 25th Annual Conference on Liquid Atomization and Spray Systems, Pittsburgh, PA, May 2013.
  33. S. Q. Wang and S. T. Thynell, "Experimental Investigation of Pressure Effect on Ignition Delay of Monomethylhydrazine, 1,1-Dimethylhydrazine, Tetramethylethylenediamine and 2-Dimethylaminoethylazide with Nitric Acid," 8th U. S. National Combustion Meeting, Organized by the Western States Section of the Combustion Institute and hosted by the University of Utah, Salt Lake City, Utah, May 19-22, 2013.
  34. S. Q. Wang and S. T. Thynell, " Decomposition and Combustion of Monomethylhydrazinium Nitrates," 8th U. S. National Combustion Meeting, Organized by the Western States Section of the Combustion Institute and hosted by the University of Utah, Salt Lake City, Utah, May 19-22, 2013.
  35. H. Sun, K. Kowalski, K. Bhaskaran-Nair, and C. K. Law, „Kinetics Study of Reaction  $\text{CH}_3\text{N}\cdot\text{NH}_2 + \text{OH}$  by Multireference Second-Order Perturbation Theory and Multireference Coupled-Cluster Theory,” 8th US National Combustion Meeting, University of Utah, Canyons Resort in Park City, Utah, May 19-22, 2013.
  36. P. Saksena, S. Tadigadapa and R. A. Yetter, “Studies of Condensed-Phase Hypergolic Reactions in a Counter-Flow Stagnation Reactor,” in The Eastern States Section of The Combustion Institute, Fall Technical Meeting. 2013. Clemson, South Carolina, USA.
  37. Drew E. Bittner, Jordan L. Sell, and Grant A. Risha, "Effect of Jet Momentum Ratio and Equivalence Ratio on the Ignition Process of TMEDA and White Fuming Nitric Acid (WFNA)," 49th AIAA/ASME/SAE/ASEE Joint Propulsion Conference, July 14 - 17, 2013, San Jose, CA
  38. Notaro, V., Ramasubramanian, C. and Lee, J.G., “Mixing Measurement of Like Doublet Impinging Jets in High Pressure Environments for Gelled Propellant Simulant,” to be

presented at AIAA Propulsion and Energy Forum and Exposition 2014, Cleveland, OH, 2014.

39. V. Amin, R. van Duren, and K. Seshadri, "The Influence of Hydrogen and Carbon Monoxide on the Structure and Extinction of Counterflow Premixed Flames," Paper # 087LF-0063, 2014 Spring Meeting of the Western States Section of the Combustion Institute, California Institute of Technology, Pasadena, CA, March 23-25, 2014.
40. K. Seshadri, X. S. Bai, and F. A. Williams "Rate-Ratio Asymptotic Analysis of the Influence of Addition of Hydrogen on the Structure and Mechanisms of Extinction of Nonpremixed Methane Flame," Proceedings of Combustion Institute Canadian Section, Spring Technical Meeting, University of Windsor, May 12-15, 2014.
41. Khare, P. and Yang, V., "Breakup of Non-Newtonian Liquid Droplets," Accepted for 44th AIAA Fluid Dynamics Conference, 2014.
42. S. Li, "Shock tube study of nitrogen-containing fuels," Ph.D. thesis submitted to the Mechanical Engineering Department, Stanford University, May 2014.



## LIST OF TEAM MEMBERS IN ALPHABETICAL ORDER

### **Dr. James H. Adair**

Professor of Materials Science and Engineering, The Pennsylvania State University  
[jha3@psu.edu](mailto:jha3@psu.edu)

### **Dr. William A. Goddard, III**

Charles and Mary Ferkel Professor of Chemistry, Materials Science, and Applied Physics  
 California Institute of Technology  
[wag@wag.caltech.edu](mailto:wag@wag.caltech.edu)

### **Dr. Ronald K. Hanson**

Woodard Professor of Mechanical Engineering, Stanford University  
[rkhanson@stanford.edu](mailto:rkhanson@stanford.edu)

### **Dr. Chung K. Law**

Robert H. Goddard Professor of Mechanical and Aerospace Engineering, Princeton University  
[cklaw@Princeton.edu](mailto:cklaw@Princeton.edu)

### **Dr. Jongguen Lee**

Professor of Aerospace Engineering and Engineering Mechanics, University of Cincinnati  
[Lee3jn@ucmail.uc.edu](mailto:Lee3jn@ucmail.uc.edu)

### **Dr. Herschel A. Rabitz**

Charles Phelps Smythe Professor of Chemistry, Princeton University  
[hrabitz@princeton.edu](mailto:hrabitz@princeton.edu)

### **Dr. Grant A. Risha**

Professor of Mechanical Engineering, The Pennsylvania State University - Altoona  
[gar108@psu.edu](mailto:gar108@psu.edu)

### **Dr. Stefan Thynell**

Professor of Mechanical Engineering, The Pennsylvania State University  
[Thynell@psu.edu](mailto:Thynell@psu.edu)

### **Dr. Forman A. Williams**

Professor of Engineering Physics and Combustion, University of California, San Diego  
[faw@ucsd.edu](mailto:faw@ucsd.edu)

### **Dr. Vigor Yang**

William R. T. Oakes Professor and Chair of School of Aerospace Engineering  
 Georgia Institute of Technology  
[Vigor.Yang@aerospace.gatech.edu](mailto:Vigor.Yang@aerospace.gatech.edu)

### **Dr. Richard A. Yetter**

Professor of Mechanical Engineering, The Pennsylvania State University  
[Ray8@psu.edu](mailto:Ray8@psu.edu)